5-2019

Diffuse Reflectance Spectroscopy to Quantify In Vivo Tissue Optical Properties: Applications in Human Epithelium and Subcutaneous Murine Colon Cancer

Gage Joseph Greening
University of Arkansas, Fayetteville

Diffuse Reflectance Spectroscopy to Quantify *In Vivo* Tissue Optical Properties: Applications in Human Epithelium and Subcutaneous Murine Colon Cancer

A dissertation submitted in partial fulfillment
of the requirements for the degree of
Doctor of Philosophy in Engineering with a concentration in Biomedical Engineering

by

Gage Joseph Greening
University of Arkansas
Bachelor of Science in Biomedical Engineering, 2014

May 2019
University of Arkansas

This dissertation is approved for recommendation to the Graduate Council.

_____
Timothy J. Muldoon, M.D., Ph.D.
Dissertation Director

_____
Narasimhan Rajaram, Ph.D.
Committee Member

_____
Yong Wang, Ph.D.
Committee Member

_____
Kyle P. Quinn, Ph.D.
Committee Member

Abstract

Colorectal cancer is the 4th most common and 2nd deadliest cancer. Problems exist with predicting which patients will respond best to certain therapy regimens. Diffuse reflectance spectroscopy has been suggested as a candidate to optically monitor a patient's early response to therapy and has been received favorably in experimentally managing other cancers such as breast and skin. In this dissertation, two diffuse reflectance spectroscopy probes were designed: one with a combined high-resolution microendoscopy modality, and one that was optimized for acquiring data from subcutaneous murine tumors. For both probes, percent errors for estimating tissue optical properties (reduced scattering coefficient and absorption coefficient) were less than 5% and 10%, respectively. Then, studies on tissue-simulating phantoms were performed to test probe sensitivity and to serve as testing platforms for investigators in biomedical optics. Next, the diffuse reflectance spectroscopy probe was applied to subcutaneous murine colon tumors (n=61) undergoing either antibody immunotherapy or standard 5-fluorouracil chemotherapy. Mice treated with a combination of these therapies showed reduced tumor growth compared to saline control, isotype control, immunotherapy, and chemotherapy groups ($p<0.001$, <0.001, <0.001, and 0.046, respectively) 7 days post-treatment. Additionally, at 7 days post-treatment, oxyhemoglobin, a marker currently being explored as a functional prognostic cancer marker, trended to increase in immunotherapy, chemotherapy, and combination therapy groups compared to controls ($p=0.315$, 0.149, and 0.190). Also of interest, an oxyhemoglobin flare (average increase of 1.44x from baseline, $p=0.03$ compared to controls) was shown in tumors treated with chemotherapy, indicating that diffuse reflectance spectroscopy may be useful as a complimentary tool to monitor early tumor therapeutic response in colon cancer. However, subject-to-subject variability was high and studies correlating survival to early oxyhemoglobin flares are suggested.

Dedication

In loving memory of Charles Robert Abernathy

Acknowledgements

There are many people I would like to thank. I am especially indebted to Dr. Timothy Muldoon, who trusted me to make appropriate research decisions and design my own methodology, and, most importantly, gave me constant encouragement in times of uncertainty. I am also indebted to my wonderful committee members, Dr. Narasimhan Rajaram, Dr. Kyle Quinn, and Dr. Yong Wang, who taught me a great deal about scientific research, and worked to provide me time and resources to pursue my research goals. Additionally, I'd like to thank Mr. Keith Tucker and Dr. Matthew Leftwich, who hired me for internships and have been excellent career mentors.

Financially, this work would not have been possible without the support of the National Science Foundation Graduate Research Fellowship Program and the University of Arkansas Doctoral Academy Fellowship.

I would like to thank my fellow colleagues, past and present, Sandra Gordon, Amy Powless, Haley James, Josh Hutcheson, Ariel Mundo, and Shelby Bess for their willingness to review manuscripts, constructively critique my research, discuss science, and talk about life. A most sincere thank you for your friendship and all you've done for me.

I would like to thank my parents, Greg and Stacie, whose guidance has always been strong in whatever I chose to pursue. My sister, Haleigh, has been my greatest role model as to what a good person should be. My best friend, Logan, was always open to intellectual discussions and provided constant support. Most importantly, I wish to thank my wife, Codi, who provided unwavering love, inspiration, and encouragement, even in the most challenging of times, and who always knows how to make me laugh and smile. I love you all. Without you, I would not have been able to complete this endeavor.

Table of Contents

List of Published Work

Published Manuscripts

Greening GJ, Bess SN, Muldoon TJ. "Immunohistochemistry staining for tumor-associated macrophage polarization in murine subcutaneous colon tumor allografts," *Bio-101*, 3106, (2018).
[Dissertation Chapter 6]

Greening GJ, Mundo AI, Rajaram N, Muldoon TJ. "Sampling depth of a diffuse reflectance spectroscopy probe for in vivo physiologic quantification of murine subcutaneous tumor allografts," *Journal of Biomedical Optics*, 23(8), (2018).
[Dissertation Chapter 4]

Tabassum S, Pera V, **Greening GJ**, Muldoon TJ, Roblyer D. "Two-layer inverse model for improved longitudinal preclinical tumor imaging in the spatial frequency domain," *Journal of Biomedical Optics*, 23(7), (2018).
[Dissertation Chapter 3]

Greening GJ, Miller KP, Spainhour CR, Cato MD, Muldoon TJ. "Effects of isoflurane anesthesia on physiological parameters in murine subcutaneous tumor allografts measured via diffuse reflectance spectroscopy," *Biomedical Optics Express*, 9(6), (2018).
[Dissertation Chapter 5]

Greening GJ, Rajaram N, Muldoon TJ. "Multimodal imaging and spectroscopy fiber-bundle microendoscopy platform for non-invasive in vivo tissue analysis," *Journal of Visualized Experiments*, 116, (2016).
[Dissertation Chapter 2]

Greening GJ, James HM, Dierks MK, Vongkittiargorn N, Osterholm SM, Rajaram N, Muldoon TJ. "Towards monitoring dysplastic progression in the oral cavity using a hybrid fiber-bundle imaging and spectroscopy probe," *Scientific Reports*, 6(26734), (2016).
[Dissertation Chapter 2]

Greening GJ, Powless AJ, Hutcheson JA, James HM, Dierks MK, Rajaram N, Muldoon TJ, "Fiber-bundle microendoscopy with sub-diffuse reflectance spectroscopy and intensity mapping for multimodal optical biopsy of stratified epithelium," *Biomedical Optics Express*, 6(12), (2015).
[Dissertation Chapter 2]

Greening GJ, Istfan R, Higgins LM, Balachandran K, Roblyer D, Pierce MC, Muldoon TJ, "Characterization of thin poly (dimethylsiloxane)-based tissue simulating phantoms with tunable reduced scattering and absorption coefficients at visible and near infrared wavelength," *Journal of Biomedical Optics*, 19(11), (2014).
[Dissertation Chapter 3]

Published Books

Greening GJ, James HM, Muldoon TJ. "Optical Phantoms: Diffuse and sub-diffuse imaging and spectroscopy validation," *SPIE Spotlights,* (2015).
[Dissertation Chapter 3]

Conference Proceedings

Greening GJ, Rajaram N, Muldoon TJ. "In vivo measurement of non-keratinized squamous epithelium using a spectroscopic microendoscope with multiple source-detector separations," *Proceedings of SPIE,* 9715, (2016).

Greening GJ, Powless AJ, Hutcheson JA, Prieto SP, Majid AA, Muldoon TJ, "Design and validation of a diffuse reflectance and spectroscopic microendoscope with poly (dimethylsioxane)-based phantoms," *Proceedings of SPIE,* 9332, (2015).

Conference Presentations

Greening GJ, Rajaram N, Muldoon TJ, (May 2018). "Sampling depth of a diffuse reflectance spectroscopy probe in murine subcutaneous tumor allografts," **Poster presentation** at the SPIE Translational Biophotonics Conference, Houston, TX.

Greening GJ, Gordon SP, James HM, Muldoon TJ, (Jan 2018). "Monitoring therapeutic response of murine tumor allografts of colon carcinoma in response to combined immunotherapy and chemotherapy," **Oral presentation** at the SPIE Photonics West BiOS Conference, San Francisco, CA.

Greening GJ, Rajaram N, Muldoon TJ, (May 2016). "A hybrid imaging and spectroscopy probe for monitoring dysplasia," **Poster presentation** at the SPIE Translational Biophotonics Conference, Houston, TX.

Greening GJ, Rajaram N, Muldoon TJ, (Feb 2016). "In vivo measurement of non-keratinized squamous epithelium using a spectroscopic microendoscope with multiple source-detector separations," **Oral presentation** at the SPIE Photonics West BiOS Conference, San Francisco, CA.

Greening GJ, Powless AJ, Hutcheson JA, Prieto SP, Majid AA, Muldoon TJ, (Feb 2015). "Design and validation of a diffuse reflectance and spectroscopic microendoscope with poly (dimethylsioxane)-based phantoms," **Oral presentation** at the SPIE Photonics West BiOS Conference, San Francisco, CA.

Greening GJ, Balachandran K, Muldoon TJ, (Apr 2014). "Thin-film polydimethylsiloxane-based optical phantoms for epithelial tissue simulation," **Poster presentation** at the OSA Biomedical Optics Conference, Miami, FL.

Chapter 1: Introduction

1. Background

The overall health focus of this dissertation is colorectal cancer (CRC). Murine subcutaneous allografts were used as a model for CRC. No clinical human work was performed in CRC. Mice with subcutaneous CRC were treated with chemotherapy and immunotherapy, and the tumor therapeutic response was measured using a non-invasive optical technique, diffuse reflectance spectroscopy (DRS).

Figure 1 shows the general dissertation workflow. Before DRS was implemented in the scientific investigation of therapy response in murine subcutaneous CRC allografts, an engineering approach was taken to design a DRS probe, design tissue-simulating phantoms with tunable optical properties, and perform calibration and validation of DRS hardware to ensure robust results.

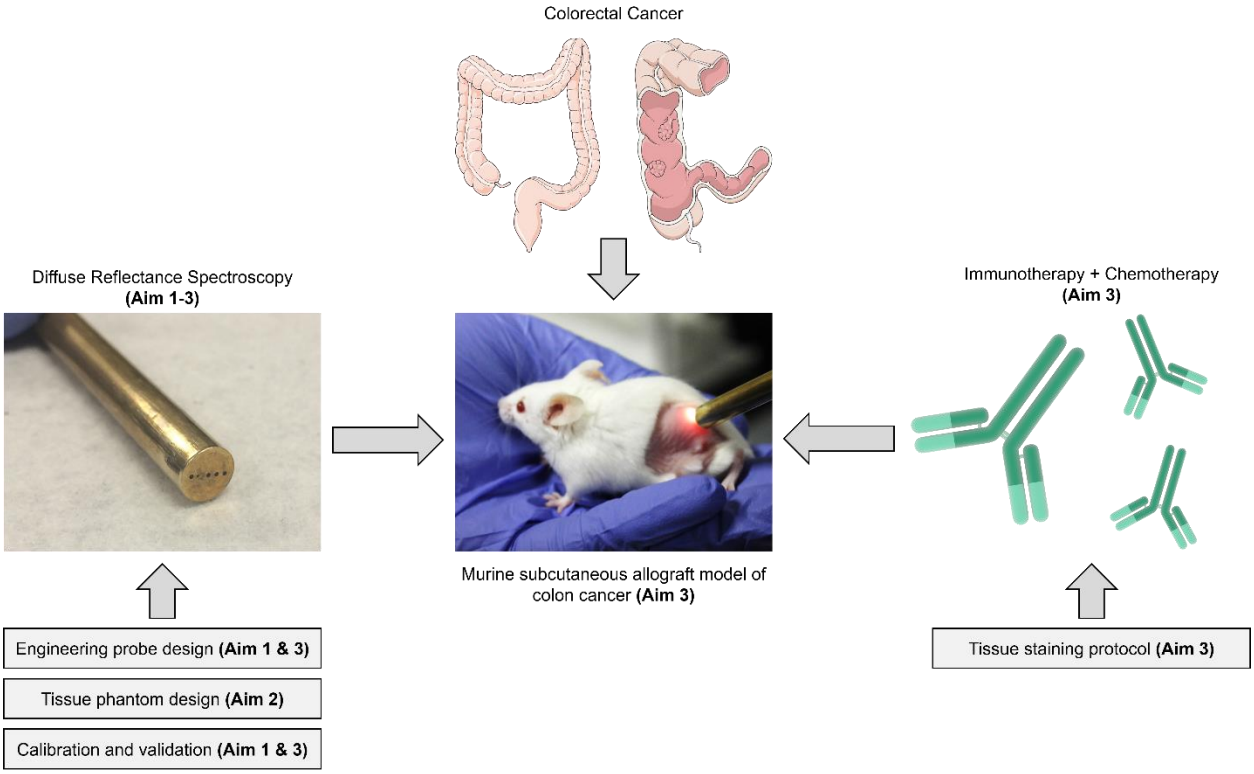

Figure 1. DRS was used as a non-invasive optical tool to monitor tumor therapeutic response to chemotherapy and immunotherapy in a subcutaneous mouse model of CRC. Aims 1 and 2 primarily focus on engineering design and testing of a DRS probe and the calibration and validation of DRS hardware using tissue-simulating phantoms. Aim 3 primarily focuses scientific results from treating murine subcutaneous CRC allografts with chemotherapy and immunotherapy. Photo of DRS probe and mouse taken by author. *Image of colon and colon cancer sourced from the Smart Servier Medical Art, which are free to share, copy, and redistribute under Create Commons License CC BY 3.0. Image of antibodies sourced from the Library of Science Medical Figures by somersault1824, which are free to share, copy, and redistribute under Create Commons License CC BY-NC-SA 4.0.*

Therefore, this introduction opens with a discussion on the overall clinical health problem: CRC. This discussion introduces basic CRC epidemiological statistics, the biology of tumorigenesis, hypoxia, and angiogenesis, the current diagnostic and treatment standards for CRC, the emerging role of immunotherapy in CRC, and the current methods to assess CRC tumor response to therapy, and how DRS can offer additional clinically relevant information to better assess CRC tumor response to therapy. The

introduction next turns to describing DRS in detail, including the exact DRS platforms used for various studies in this dissertation. We discuss the optical physics of DRS, and how information gathered from light that has scattered and absorbed in body tissues relates to both structural and functional biological characteristics. Finally, the introduction closes with a brief summary of all three specific aims. Chapters 2 and 3 represent specific aims 1 and 2, respectively. Aim 3, on the other hand, is longer, and consists of chapters 4, 5, and 6.

1.1 Clinical health focus: colorectal cancer

In the United States, CRC is the 4th most common cancer with 140,000 new cases and 50,000 deaths in the United States annually. CRC has the 7th worst 5-year survival rate (~65%) of all cancers (Siegel *et al.*, 2018). CRC makes up 8.1% of all cancers cases and 8.3% of all cancer-related death (Siegel *et al.*, 2018). It has been estimated that individuals have a 2% and 0.9% cumulative lifetime risk of developing and dying from CRC, respectively (Stigliano *et al.*, 2014), and the disease is more prevalent in males (54% of cases) compared to females (46% of cases) (Siegel *et al.*, 2018). Although the incidence of CRC in the U.S. has been decreasing over the past several decades, there are still nearly 1.25 million U.S. residents (~0.4% of the population) living with CRC (Marley *et al.*, 2016), costing the U.S. $14 billion annually (Yabroff *et al.*, 2007; Yabroff *et al.*, 2011). Furthermore, per person costs

Summary of acronyms	
5-FU	5-fluorouracil
CCL2	Monocyte chemoattractant protein-1
CSF2	Colony-stimulating factor 2
DRS	Diffuse reflectance spectroscopy
Hb	Hemoglobin
LACC	Locally advanced colorectal cancer
LCC	Left-sided colorectal cancer
pCR	Pathological complete response
RCC	Right-sided colorectal cancer
RTE	Radiative transport equation
StO_2	Tissue oxygen saturation
SDS	Source-detector separation
TAM	Tumor-associated macrophage
THC	Total hemoglobin concentration
TME	Tumor microenvironment
TNM	Tumor, node, and metastasis
μ_a	Absorption coefficient
μ_s'	Reduced scattering coefficient

associated with CRC treatment are $30 thousand within a year of diagnosis (Luo *et al.*, 2009). In developing countries, on the other hand, CRC incidence is expected to increase over the next decade as population and life expectancy increase (Stigliano *et al.*, 2014). Although there has been a steady reduction in CRC incidence and mortality since the 1970's, primarily attributed to reduction in preventable risk factors, advances in early detection, and nationwide screening initiatives (Siegel *et al.*, 2018; Levin, 2016), research into monitoring tumor therapeutic response to better personalize patient treatment is still needed and an active area of research in the field of CRC (Park *et al.*, 2014).

CRC (Figure 2) is classified in multiple ways. CRCs can either be sporadic (70-85% of cases) (Yamagishi *et al.*, 2016; Mundade *et al.*, 2014) or familial (15-30% of cases) (Stigliano *et al.*, 2014; Jasperson *et al.*, 2010). Sporadic cases arise as a result of multiple rare variants, which are genetic variants occurring in < 1% of the population. Familial cases arise when individuals have a genetic disposition or family history of CRC, although family history is often unreported which contributes to the large percent range of cases (Stigliano *et al.*, 2014). Treatment of sporadic vs. familial CRC currently does not differ significantly as chemotherapy and surgical resection remain the curative standard, although patients with certain subtypes of familial CRC may be screened and treated earlier (Esplin *et al.*, 2014). Alternatively, CRC can be classified on where the disease occurs. CRC can arise in the rectum (31% of cases), left colon (30% of cases), or right colon (39% of cases) (Mik *et al.*, 2017; Siegel *et al.*, 2018). The left and right colon have different embryological origins (hindgut vs. midgut, respectively) (Baek, 2017) and many believe that left-sided (LCC) and right-sided CRC (RCC) should be considered separate diseases because they have different characteristics and oncological outcomes (Lim *et al.*, 2017; Qin *et al.*, 2017; Hussain *et al.*, 2016). Although LCC and RCC are currently treated identically, these

diseases may be screened and treated differently in the future (Mik *et al.*, 2017). Next, CRC can be histologically classified into adenocarcinomas (>90% of cases) or other types (<10% of cases), such as neuroendocrine, squamous cell, adenosquamous, spindle cell, and undifferentiated carcinoma (Fleming *et al.*, 2012). Finally, a recent 2015 collaborative gene expression-based subtyping initiative has classified CRC into four distinct subtypes: CMS1 (14%), CMS2 (37%), CMS3 (13%), CMS4 (23%), as well as 13% of cases with mixed features. It is anticipated that the CMS subtype classification will have the biggest impact on future targeted therapies (Guinney *et al.*, 2015).

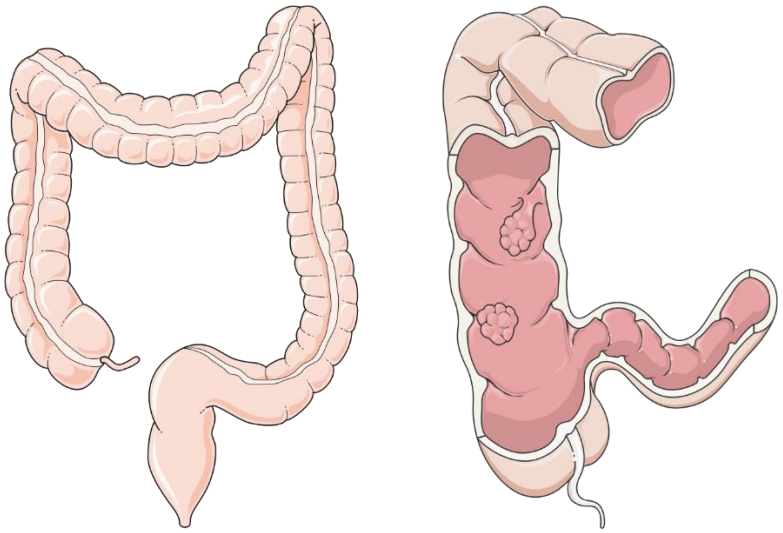

Figure 2. The primary health focus of this dissertation is CRC. *Images sourced from the Smart Servier Medical Art, which are free to share, copy, and redistribute under Create Commons License CC BY 3.0.*

1.1.1 Hypoxia in colorectal cancer

Hypoxia is a condition of insufficient tissue oxygen saturation and arises due to uncontrolled and rapid proliferation of cancer cells in the absence of efficient vasculature (Eales *et al.*, 2016). Initial tumor growth occurs without angiogenesis (Tafani *et al.*, 2016). When intercapillary distances exceed the diffusion limit of oxygen (200 μm), average oxygen partial pressure (pO_2) drops from ~35 mmHg to ~10 mmHg (Tafani *et al.*, 2016). Intratumoral hypoxia

is spatially heterogenous, with between 50-60% of a solid tumor's mass being hypoxic on average (Vadde *et al.*, 2017). While much is known about how hypoxia affects the tumor microenvironment, the exact biological mechanism by which cells first detect low oxygen levels is under active investigation (Hamanaka *et al.*, 2009). Despite this knowledge gap, hypoxia has several broad effects on tumors which will be briefly described here, including maintaining cancer cell stemness (Vadde *et al.*, 2017), inducing release of damage-associated molecular patterns (DAMPs) (Tafani *et al.*, 2016), increasing production of reactive oxygen species (ROS) (Tafani *et al.*, 2016), and triggering angiogenesis and vascularization of the tumor mass (Eales *et al.*, 2016).

In the colon and rectum, superficial glandular epithelial cells (of which > 95% of CRC cases arise)(Marley *et al.*, 2016; Hinck *et al.*, 2014; Xue *et al.*, 2012) ubiquitously express a family of transcription factors, known as hypoxia inducible factors (HIF) (Ulivi *et al.*, 2016), of which HIF-1 is the best studied (Vadde *et al.*, 2017). HIF-1 consists of two subunits: HIF-1α and HIF-1β (Ulivi *et al.*, 2016). HIF-1β is constitutively active whereas the activity of HIF-1α is oxygen-regulated (Ulivi *et al.*, 2016). HIF-1α gene expression has been shown to significantly increase with increased CRC stage (Mansour *et al.*, 2016). In normoxic conditions, HIF-1α undergoes hydroxylation of two proline residues (P402 and P564) via prolyl hydroxylase 2 (PHD-2) (Ulivi *et al.*, 2016; Vadde *et al.*, 2017; Cejudo-Martin *et al.*, 2005). Hydroxylated HIF-1α then binds to the Hippel-Lindau tumor suppression protein (pVHL) located on the E3 ubiquitin ligase complex, which mediates ubiquitination and proteasomal degradation of HIF-1α (Maxwell *et al.*, 2001; Vadde *et al.*, 2017). Alternatively, in hypoxic conditions, HIF-1α circumvents ubiquitination. From here, HIF-1α, or the structurally related HIF-2α, can act alone to regulate the tumor microenvironment or move inside the cell to the nucleus where it

dimerizes with HIF-1β to form a complex which serves as a transcription factor for a variety of genes that support CRC progression (Ulivi *et al.*, 2016). An extensive list of HIF-1 or HIF-1α target genes that support cancer progression has been previously published (Semenza, 2010).

In the stem cell theory of cancer, stemness is defined as the property of self-renewal and proliferative and differentiation potential of a subpopulation of cancer cells (Lathia *et al.*, 2017). With regards to maintaining stemness of CRC in hypoxic conditions, activated HIF-1α interacts with the intracellular domain of the transmembrane protein, Notch1. In the presence of HIF-1α, the half-life of Notch1 increases which stimulates the Notch signaling cascade (Vadde *et al.*, 2017; Cejudo-Martin *et al.*, 2005). The Notch signaling cascade, described in detail elsewhere (Wang *et al.*, 2012), maintains cancer cell stemness by increasing proliferation and differentiation potential (Vadde *et al.*, 2017). Additionally, HIF-2α (also known as EPAS 1, HLF, or HRF), which is also expressed in CRC, acts as a transcription factor for the Octamer-binding transcription factor 4 gene (*Oct-4*) and thus upregulates Oct-4 expression (Covello *et al.*, 2006; Santoyo-Ramos *et al.*, 2014). Oct-4 expression has been shown to increase going from normal tissue to benign polyps to CRC tissue with expression ratios of 4.4%, 12.7%, and 42,4%, respectively (Zhou *et al.*, 2015). Specifically, Oct-4 maintains cell stemness within the CRC tumor microenvironment and is also a useful biomarker and potential therapeutic target (Vadde *et al.*, 2017; Lathia *et al.*, 2017), Therefore, hypoxic conditions contribute to stemness, progression, and malignancy of CRC.

Next, hypoxia induces necrosis and the subsequent release of DAMPs (Hernandez *et al.*, 2016). DAMPs are a broad array of intracellularly sequestered molecules, which, upon necrosis or other cellular injury or stress, are actively secreted or passively released extracellularly (Land, 2015; Eppensteiner *et al.*, 2018). In CRC, DAMPs include adenosine, ATP, calreticulin,

HMGB1, S100A4, S100A8, S100A9, and IL-33 (Hernandez *et al.*, 2016). These DAMPs act as ligands for receptors on nearby tumor cells, dendritic cells, myofibroblasts, or mast cells. Broad downstream pro-tumor effects include tumor growth and progression, tumor regrowth in wound-healing sites such as tumor margins, and metastasis (Hernandez *et al.*, 2016). Additionally, DAMPs such as HMGB1 has been shown to be highly expressed in solid CRC tumors (Sims *et al.*, 2010). However, ATP has been shown to induce an anti-tumor immune response (Ghiringhelli *et al.*, 2009) and calreticulin has been shown to improve chemotherapy-induced tumor regression (Obeid *et al.*, 2007), and thus DAMPs are considered "double-edged" in that they can have both pro-tumor and anti-tumor effects (Hernandez *et al.*, 2016). However, data regarding hypoxia-necrosis-DAMP pathways in CRC is relatively sparse, yielding an intriguing research gap (Hernandez *et al.*, 2016).

Cancer cells require high ROS levels to proliferate (Sosa *et al.*, 2013). In both normal and cancerous cells, mitochondria are the main producers of ROS, which include hydroxyl radicals, superoxides, and hydroperoxides (Tafani *et al.*, 2016). Under normoxic conditions, complexes I, II, and III of the mitochondrial electron transport chain (ETC) produce low concentrations of ROS during oxidative phosphorylation (Kondoh *et al.*, 2013; Görlach *et al.*, 2015; Hamanaka *et al.*, 2009). Alternatively, under hypoxic conditions in solid tumors, ROS levels increase, although the exact biological mechanism is currently under investigation (Tafani *et al.*, 2016). ROS levels also increase early in the tumorigenesis, such as during carcinogen exposure or chronic inflammation (Tafani *et al.*, 2016). Increases in ROS can cause mitochondrial DNA damage and mutation (Lievre *et al.*, 2005), as well as inactivation of PHD-2, which would otherwise inactivate HIF-1α. Thus, ROS increase activation of HIF-1α, which, as described

previously, drives gene expression that contribute to CRC progression and malignancy (Semenza, 2010).

In summary, hypoxic conditions promote non-angiogenic CRC tumor progression by maintaining cancer cell stemness (Vadde *et al.*, 2017), inducing release of damage-associated molecular patterns (DAMPs)(Tafani *et al.*, 2016), and increasing production of reactive oxygen species (ROS) (Tafani *et al.*, 2016). However, the most prominent effect of CRC tumor hypoxia is angiogenesis, which will be described in the following section.

1.1.2 Angiogenesis in colorectal cancer

The most well-known and studied effect of hypoxia is angiogenesis. As previously stated, HIF-1α is activated during hypoxia and translocates to the nucleus where it dimerizes with HIF-1β. This dimerized complex, also known as HIF-α/Arnt, undergoes posttranslational modification and binds to hypoxia response elements (HREs) of target gene promoters and enhancers with the sequence G/ACGTG (Krock *et al.*, 2011). HIF upregulates a variety of pro-angiogenic proteins including fibroblast growth factor (FGF)(Korc *et al.*, 2009), vascular endothelial growth factor (VEGF) (Duff *et al.*, 2006), angiopoietin-1 and 2(Ellis *et al.*, 2002), platelet-derived growth factor (PDGF) (Manzat Saplacan *et al.*, 2017), as well as the angiogenic chemokine, monocyte chemoattractant protein-1 (CCL2 aka MCP-1)(Yoshidome *et al.*, 2009), and a variety of interleukins (Krock *et al.*, 2011). The angiogenic effects of FGF, VEGF, PDGF, angiopoietins, and interleukins are well-understood.

The less well-known effects of CCL2, and its receptor, CCR2, are briefly described here. After CCL2 is transcribed and translated by CRC cells and monocytes/macrophages, in part due to HIF-1, it binds to CCR2 on target cells which include monocytes, macrophages, memory T lymphocytes, natural killer (NK) cells, and arterial endothelial cells (Deshmane *et al.*, 2009). The

CCL2-CCR2 binding on endothelial cells causes upregulation of MCP-1-induced protein (MCPIP), which is a transcription factor for cadherins 12 (cdh12) and cadherin 19 (cdh19). It has been shown that *in vitro* knockdown of *cdh12* and *cdh19* reduced capillary formation (Niu *et al.*, 2008), although the exact biological mechanism is not fully elucidated (Roy *et al.*, 2012). Finally, CCL2 induces gene expression of HIF-1α, creating a pro-angiogenic feedback loop (Hong *et al.*, 2005). Thus, HIF-1 mediates CRC tumor angiogenesis by up-regulation of myriad pro-angiogenic growth factors, cytokines, and chemokines.

1.1.3 Clinical background: diagnostic standard for colorectal cancer

Colonoscopy is the gold standard for CRC diagnosis because of its ability to quickly examine the entire colon while simultaneously performing biopsies and polypectomies (Geiger *et al.*, 2009) (Figure 3). Colonoscopies are recommended every 10 years beginning at age 50 for average-risk individuals, although screening prevalence is only 63% for this group (Burt *et al.*, 2010; Society, 2017).

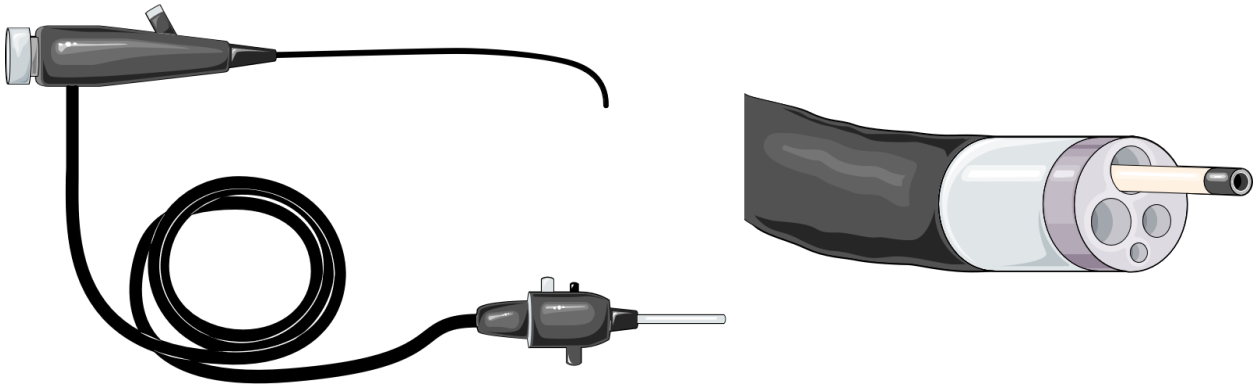

Figure 3. Colonoscopy is the gold standard for CRC diagnosis because of its ability to quickly examine the entire colon while simultaneously performing biopsies and polypectomies. *Images sourced from the Smart Servier Medical Art, which are free to share, copy, and redistribute under Create Commons License CC BY 3.0.*

Other diagnostic tests do exist, such as the fecal occult blood test (FOBT), fecal immunochemical based stool test (FIT), double-contrast barium enema (DCBE), and computed

tomography colonography (CTC), but colonoscopy is still used to confirm abnormal results in most cases (Geiger *et al.*, 2009; Society, 2017; Navarro *et al.*, 2017). Treatment for CRC is based on the Tumor, Node and Metastasis (TNM) staging system. The TNM system stages tumors I-IV (Figure 4) based on how deep the tumor has spread, how many lymph nodes contain tumor cells, and number of distant metastases (Dienstmann *et al.*, 2017). Stages I, II, III, and IV account for 28%, 27%, 26%, and 19% of cases at diagnosis, respectively, according to a 2013 meta-analysis of 132,696 patients based on data from the Surveillance, Epidemiology, and End Results Program (SEER) database (Lee *et al.*, 2013).

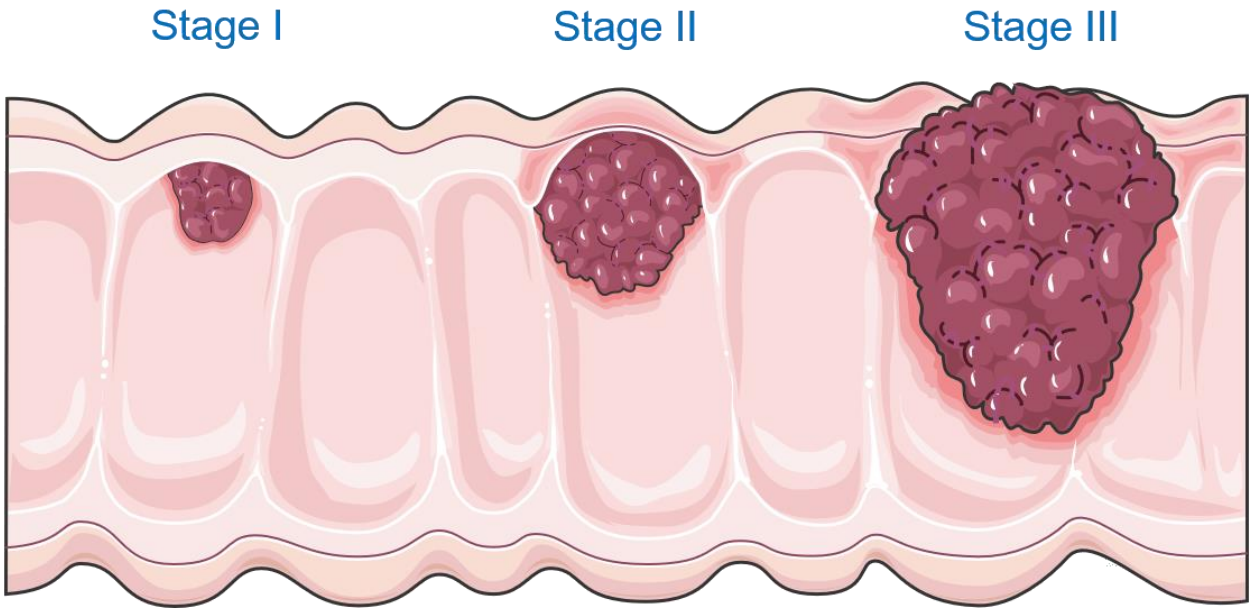

Figure 4. The TNM system stages tumors I-IV based on how deep the tumor has spread, how many lymph nodes contain tumor cells, and the number of distant metastases. *Image sourced from the Smart Servier Medical Art, which are free to share, copy, and redistribute under Create Commons License CC BY 3.0.*

However, in locally advanced CRC (stages II and III), which account for over half of patients at diagnosis, TNM staging less clearly predicts patient prognosis, so standard treatment for both stages includes colectomy with postoperative adjuvant chemotherapy (Dienstmann *et*

al., 2017; Lee *et al.*, 2013). Currently, the most clinically valuable method to classify tumors is the tumor, node, and metastasis (TNM) staging system, which is used to guide treatment.

1.1.4 Clinical background: treatment standard for colorectal cancer

In recent years, growing evidence has supported using preoperative neoadjuvant chemotherapy prior to surgical resection to achieve a complete eradication of cancer cells before surgery, or, at least, a reduction in intraoperative tumor cell shedding (Zhou *et al.*, 2013; Boland *et al.*, 2014). Such preoperative therapy typically uses a fluorouracil-based regimen, such as FOLFOX (Jeon *et al.*, 2011). A patient's response to neoadjuvant chemotherapy is a critical prognostic indicator; patients who exhibit a significant reduction in tumor burden during neoadjuvant chemotherapy are more likely to experience complete resection of the tumor during colectomy, have fewer local and distal recurrences (Zhou *et al.*, 2013), and have greater 5-year disease-free survival (Martin *et al.*, 2012). However, in patients treated with neoadjuvant chemotherapy, pathologic complete response (pCR), a complete eradication of tumor cells, and surgical downstaging still remain low (both ~20-25%) (Zhou *et al.*, 2013). Predicting which patients will respond to neoadjuvant chemotherapy, and which drugs are most appropriate, remains challenging (Wang *et al.*, 2017). Ideally, CRC preoperative treatment would be tailored to each patient based on initial therapeutic response, with the end goal of avoiding surgery if possible (Walker *et al.*, 2014). At present, in locally advanced CRC, fluorouracil-based FOLFOX chemotherapy is generally given to patients in 3-4 cycles over 6-8 weeks in the neoadjuvant setting, following by surgery and by 9-12 cycles of adjuvant chemotherapy over 18-24 weeks (Zhou *et al.*, 2013; Cheeseman *et al.*, 2008; Habr-Gama *et al.*, 2010). The current FOLFOX treatment regimen consists of 2,400 mg/m^2 of 5-FU, 400 mg/m^2 of leucovorin, and 85 mg/m^2 of oxaliplatin per cycle. Occasionally, irinotecan is given instead of oxaliplatin at a dose

of 180 mg/m^2 in the FOLFIRI treatment regimen (de Gramont *et al.*, 2000; Cheeseman *et al.*, 2008; Maindrault-Goebel *et al.*, 2000; Fuchs *et al.*, 2007; Goldberg *et al.*, 2004). Tumor therapeutic response to neoadjuvant chemotherapy is assessed using radiological techniques (CT, PET-CT, or MRI) following conclusion of neoadjuvant chemotherapy (after 1.5-2 months) and before surgery (Habr-Gama *et al.*, 2010) (Figure 5).

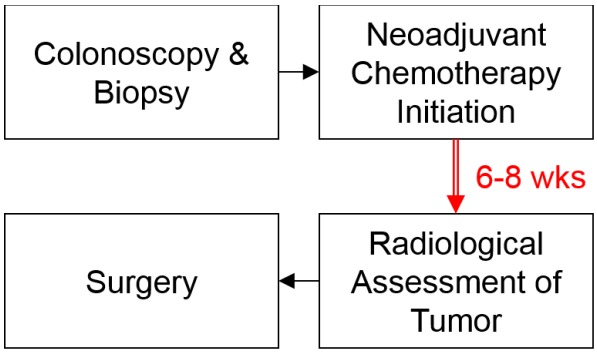

Figure 5. Tumor therapeutic response is not assessed until nearly 2 months following chemotherapy initiation

However, several studies have shown that therapeutic response can, in fact, be assessed on a scale of days, rather than months, using a variety of methods. However, most methods lack practicality as routine clinical applications (Park *et al.*, 2014). Therefore, one branch of CRC research is devoted to developing clinically-translatable methods to rapidly assess (within 72 hours following therapy initiation) whether a therapy regimen is effective on a per patient basis (Berger *et al.*, 2017; Roblyer *et al.*, 2011). A second branch is devoted to exploring immunotherapy, a broad term for any treatment that modulates the host immune system to fight cancer, to compliment neoadjuvant chemotherapy and increase rates of pCR and decrease rates of distal recurrence (Boland *et al.*, 2017; Walker *et al.*, 2014; Bouvier *et al.*, 2015; Xiang *et al.*, 2014). The research in this proposal exists at the interface between these two branches.

1.1.5 Effects of chemotherapy on colorectal cancer tumors

Fluorouracil-based chemotherapy, especially 5-fluorouracil (5-FU) used in the FOLFOX regimen (combined 5-FU, leucovorin, and oxaliplatin), has been a staple in CRC treatment for nearly 60 years (Noordhuis *et al.*, 2004; Monteil *et al.*, 2009), with leucovorin and oxaliplatin becoming standard in first-line chemotherapy in the early-to-mid 2000's after successful Phase III clinical trials (Jeon *et al.*, 2011; Wolmark *et al.*, 1999; de Gramont *et al.*, 2000; Andre *et al.*, 2003; Goldberg *et al.*, 2004). In the body, 5-FU is converted to fluorodeoxyuridine monophosphate (FdUMP). FdUMP forms a complex with thymidylate synthase (TS), an enzyme that catalyzes deoxyuridine monophosphate (dUMP) to deoxythymidine monophosphate (dTMP), which is a DNA monomer and key for DNA replication. Thus, 5-FU-mediated depletion of dTMP results in cytotoxicity and apoptosis in the rapidly growing cells in CRC (Zhang *et al.*, 2008).

1.1.6 Immunotherapy in colorectal cancer

Immunotherapy is an emerging approach to treat a variety of cancers by modulating the immune system. Although the pathogenesis of CRC is well understood, the effects of immunotherapy on the TME is less understood (Boland *et al.*, 2017). Immunotherapy, in general, can fall into one of several categories: 1) adoptive cell transfer therapy (ACT) (Rosenberg *et al.*, 2008), 2) monoclonal antibody (mAb) therapy (Weiner *et al.*, 2009), 3) immune checkpoint inhibitors (Dine *et al.*, 2017; Jacobs *et al.*, 2015), 4) cancer vaccines (Guo *et al.*, 2014), and 5) cytokine-targeted immunotherapy (Lee *et al.*, 2011; Waldmann, 2017). The immunotherapy focus of this proposal is on cytokine-targeted immunotherapy; for brevity and focus, other categories of immunotherapy are not discussed. Several mAb immunotherapy drugs are FDA approved for CRC, including nivolumab (Mehrvarz Sarshekeh *et al.*, 2018) and pembrolizumab

(Birendra *et al.*, 2017), as well as ipilimumab, which is currently under FDA priority review. Other drugs such as durvalumab and tremelimumab, also mAbs, are undergoing clinical trials (Grierson *et al.*, 2017). The mAb immunotherapy drugs have been a breakthrough for treating MSI-high metastatic CRC (Grierson *et al.*, 2017), one of several subtypes of CRC (Guinney *et al.*, 2015). However, this subtype is estimated to represent less than 20% of all CRC cases (Guinney *et al.*, 2015; Boland *et al.*, 2011). Thus, there has been renewed research interest in cytokine-targeted immunotherapy to compliment neoadjuvant chemotherapy regimens to capture a wider variety of patients (Lynch *et al.*, 2016). Whereas most cancers have, in general, benefitted from immunotherapeutics, CRC, aside from MSI-high metastatic CRC, has not (Boland *et al.*, 2017). One overarching hypothesis as to why CRC has benefitted less from immunotherapy compared to other cancers is the controversial role of tumor-associated macrophages (TAMs) in the TME (Erreni *et al.*, 2011).

1.1.7 Tumor-associated macrophage controversy in colorectal cancer

TAMs, the most abundant immune cell in the TME, also have the most substantial and pervasive effect of any immune cell in the TME (Allavena *et al.*, 2008; Chen *et al.*, 2005; Erreni *et al.*, 2011; Marech *et al.*, 2016). In CRC, TAMs have been shown to have both anti-tumor and pro-tumor functions, depending on whether they are polarized more towards an M1 (classical) or M2 (alternative) phenotype and their physical location within the tumor (Marech *et al.*, 2016). CRC cells, independent of sub-type (Lim *et al.*, 2016; Becht *et al.*, 2016), recruit circulating monocytes via chemotaxis to the TME through monocyte chemoattractant protein-1 (CCL2), a highly elevated chemokine in CRC (Marech *et al.*, 2016; Chun *et al.*, 2015; Becht *et al.*, 2016; Lim *et al.*, 2016). Monocytes differentiate into M2-polarized TAMs through a variety of cytokines and chemokines including IL-4, IL-10, IL-13, CSF-1, CSF2 (primary cytokine

responsible for monocyte-TAM differentiation), CCL2, CXCL12, TGFα, MFG-E8, and MIF produced by CRC cells, helper T-cells, regulatory T-cells, mesenchymal stem cells, and previously differentiated TAMs (Liu *et al.*, 2015). CCL2 is primarily responsible for monocyte recruitment, which leads to TAM infiltration into the TME. Broad anti-tumor functions of classically activated M1-polarized TAMs include inflammation and immune response (Funada *et al.*, 2003; Sugita *et al.*, 2002; Zhou *et al.*, 2010). On the other hand, pro-tumor functions of alternatively activated M2-polarized TAMs include tumor growth, angiogenesis, immunosuppression, and matrix remodeling (Liu *et al.*, 2015) (Figure 6).

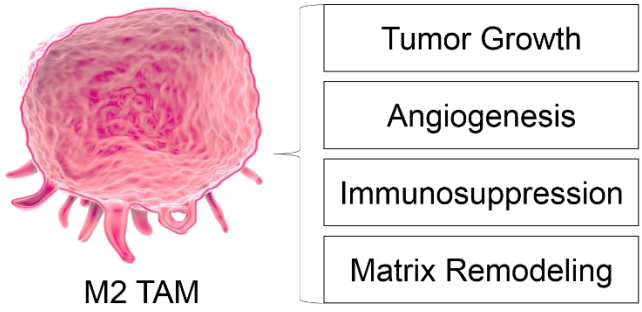

Figure 6. TAMs in CRC generally have pro-tumor functions. *Image of macrophage sourced from the Library of Science Medical Figures by somersault1824, which are free to share, copy, and redistribute under Create Commons License CC BY-NC-SA 4.0.*

For tumor growth and angiogenesis, TAMs release a variety of pro-angiogenic growth factors (GFs) including VEGF, PDGF, EGF, FGF, TGF-β, MMP9, CXCL8, IL-1, IL-6, and IL-8 (Liu *et al.*, 2015). Additionally, TAMs suppress the activity of cytotoxic ($CD8^+$) T-cells, whose otherwise elevated expression is associated with increased 5-year survival in CRC patients (Ziai *et al.*, 2018), by releasing immunosuppressive factors including IL-10, TGF-β, CCL17, CCL18, CCL22, and PGE2 (Liu *et al.*, 2015). For matrix remodeling, TAMs release a variety of proteolytic enzymes called matrix metalloproteases (MMPs) which allow for tumor expansion and release of ECM-sequestered pro-angiogenic GFs. Finally, TAMs release a variety of

cytokines such as IL-10, CXCL12, and MIF that help differentiate monocytes into TAMs (Marech *et al.*, 2016; Erreni *et al.*, 2011; Barbera-Guillem *et al.*, 2002; Burmeister *et al.*, 2017; Ucuzian *et al.*, 2011). It has recently been shown that macrophages induce resistance to 5-FU chemotherapy, and that this TAM-induced resistance may contribute to the heterogenous patient response to chemotherapy (Zhang *et al.*, 2016; Zhang *et al.*, 2008). Currently, a gap in CRC research is how cytokine-targeted immunotherapy affects tumor-associated macrophages in the colon TME. Furthermore, does altering TAM population impact tumor response to chemotherapy? If so, can this impact be quantified by clinically translatable tools on a scale of days rather than months after treatment initiation?

1.1.8 Current methods to assess tumor response to therapy

This study proposes using DRS as a tool to monitor early tumor therapeutic response to chemotherapy and CCL2-targeted immunotherapy. However, other methods to quantify therapeutic response do exist. Clinically, after initiation of neoadjuvant chemotherapy, tumor response is not assessed for nearly 2 months using radiological imaging methods (Kim *et al.*, 2015; Habr-Gama *et al.*, 2010). There are several solutions to this problem, all with advantages and disadvantages. One clinical assessment tool is quantifying carcinoembryonic antigen (CEA), a cell adhesion glycoprotein elevated in the blood of CRC patients that correlates with tumor stage. However, this test, although widely used and inexpensive, is non-specific does not sufficiently predict positive responders to therapy (Dreyer *et al.*, 2017). Many biomarkers, such as p53, Ki67, and VEGF, are under investigation to correlate with initial tumor response, but the literature shows conflicting results (Kim *et al.*, 2015). Both cancer stem cell markers (CD133, CD44, and CD24) and gene expression profiling show promising results for predicting tumor response, although it is generally agreed that these methods have several practical limitations in

clinical practice despite high potential for elucidating the complex genetic response of CRC (Kim *et al.*, 2015). On the other hand, several optical and spectroscopic methods have shown promise in assessing tumor response after neoadjuvant chemotherapy. Several diffuse spectroscopy-based studies have shown a significant increase in oxyhemoglobin, or concentration of oxygen-bound heme in blood (Stadler *et al.*, 2008), within one day after starting neoadjuvant chemotherapy (Figure 7).

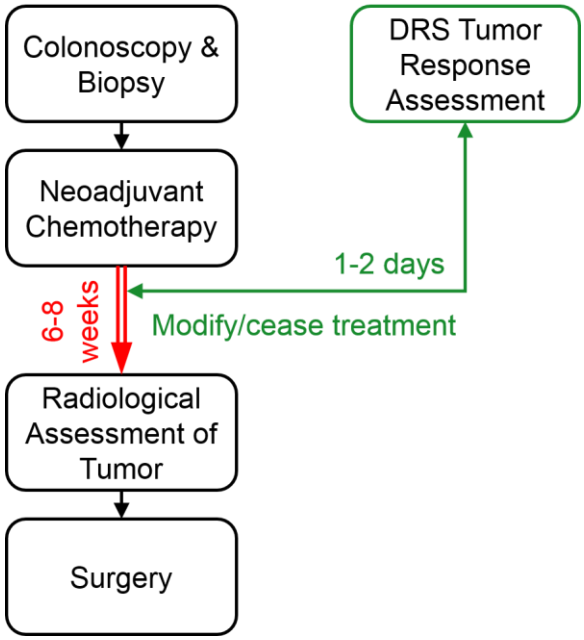

Figure 7. DRS is a clinically translatable & complimentary tool that can quantify oxy-hemoglobin flare (tumor response) to guide clinicians in modifying or ceasing treatment.

This increase, referred to as the "oxyhemoglobin flare," was shown in patients with partially or pathologically complete responding tumors but not in nonresponding patients (Roblyer *et al.*, 2011). The oxyhemoglobin flare has been extensively shown by the Tromberg group in clinical trials of locally advanced breast cancer patients receiving neoadjuvant chemotherapy (Falou *et al.*, 2012; Ueda *et al.*, 2013; Tromberg *et al.*, 2017). However, a gap in research is that the oxyhemoglobin flare has not been quantified after *combinatorial*

chemotherapy and immunotherapy, and furthermore, has not been quantified in CRC tumors. DRS is a probe-based spectroscopy tool, operating under the same principals as described in the above studies, with the ability to accurately assess oxyhemoglobin *in vivo* (Chin *et al.*, 2017; Rajaram, Gopal, *et al.*, 2010; Rajaram *et al.*, 2016; Jayanthi *et al.*, 2011; Greening, Rajaram, *et al.*, "Multimodal Imaging and Spectroscopy Fiber-Bundle Microendoscopy Platform for Non-Invasive, in Vivo Tissue Analysis," 2016; Greening, James, *et al.*, 2016; Greening, Rajaram, *et al.*, "In Vivo Measurement of Non-Keratinized Squamous Epithelium Using a Spectroscopic Microendoscope with Multiple Source-Detector Separations," 2016; Hennessy *et al.*, 2015; Glennie *et al.*, 2015; Yu *et al.*, 2014; Glennie *et al.*, 2014; Karsten *et al.*, 2013; Spliethoff *et al.*, 2014). In the past decade, there have been 6 clinical trials using DRS in CRC (Jermyn *et al.*, 2017; Tanis, Evers, *et al.*, 2016; Spliethoff *et al.*, 2016; Tanis, Spliethoff, *et al.*, 2016; Wang *et al.*, 2009; Douplik *et al.*, 2010). However, all trials focus on early cancer diagnostics and intraoperative surgical guidance, rather than tracking tissue response to therapy. Thus, our group believes that non-invasively quantifying the oxyhemoglobin flare following initiation of chemotherapy and cytokine-targeted immunotherapy via DRS is worth exploring.

1.1.9 Significance of clinical health problem

At present, there have been no studies correlating tumor perfusion response (via clinically translatable DRS) with biological correlates, such as TAMs and associated cytokines, in the TME following combinatorial cytokine-targeted immunotherapy and chemotherapy in a mouse model of CRC. We expect that DRS can potentially be used in the clinic to monitor the oxyhemoglobin flare in colon tumors of patients in response to neoadjuvant therapy initiation (Fig. X). We have built and validated a DRS platform that can monitor the oxyhemoglobin flare in response to therapy initiation in a mouse model of CRC. We note that, although we have

claimed DRS is potentially clinically translatable (i.e. fits through the biopsy port of a standard colonoscope with minimal interference with established clinical workflow), the specific DRS platform used in this study is *not* translatable since we hope to quantify daily perfusion metrics in mouse subcutaneous tumor allografts, which necessarily require a larger probe size.

1.1.10 Research perspectives of diffuse reflectance spectroscopy

DRS has been received favorably in the clinical management of certain cancers such as breast and skin cancer, pioneered in part by the Tromberg and Tunnell groups, respectively (Tromberg *et al.*, 2017; Ueda *et al.*, 2013; Roblyer *et al.*, 2011; Shah *et al.*, 2004; Hennessy *et al.*, 2015; Bish *et al.*, 2014; Sharma *et al.*, 2014; Bish *et al.*, 2011; Rajaram, Reichenberg, *et al.*, 2010; Rajaram, Aramil, *et al.*, 2010). Adoptability in CRC has been milder, although the Richards-Kortum group has done a lot of work with microendoscopy imaging systems compatible with the biopsy port of standard colonoscopes (Parikh *et al.*, 2014; Chang *et al.*, 2013) or upper GI endoscopes (Muldoon *et al.*, 2011; Muldoon *et al.*, 2010; Muldoon *et al.*, 2008; Muldoon *et al.*, 2007; Pierce, Schwarz, *et al.*, 2012; Pavlova *et al.*, 2009; Schwarz *et al.*, 2008). DRS systems, which can be of comparable physical size to microendoscopes, have also been integrated with colonoscopes in clinical research studies (Schols *et al.*, 2015). In fact, future studies in the Translational Biophotonics and Imaging Laboratory at the University of Arkansas will explore DRS in a colonoscope in an orthotopic mouse model of CRC. Although physically feasible, clinical adoptability of DRS (i.e. integration of DRS within standard colonoscopy workflow) is not yet scientifically justified. Therefore, one goal of my PhD work was to lay the foundation for our laboratory to be a pioneer in compiling evidence to justify using DRS in the clinical management of CRC. In addition to DRS, long-term clinical prospects of cytokine-targeted immunotherapy are promising. Neutralizing antibodies for specific cytokines involved

in pro-tumor pathways have shown therapeutic activity in both murine models and in several human cancers. Several research groups are engineering innovative targeted cytokine delivery approaches to reduce systemic toxicity. Overall, cytokine-targeted immunotherapy will continue to be an active cancer research field (Lee *et al.*, 2011; Waldmann, 2017). This research capitalizes on this prospect and will help clarify how blocking of several key intercellular communication pathways affects certain aspects of the colon TME and tumor therapeutic response.

1.1.11 Murine subcutaneous allograft model of colorectal cancer

In the studies reported in this dissertation, Balb/c mice were subcutaneously injected with CT26 cells in sterile saline (Figure 8). CT26 cells are colon carcinoma cells derived from the Balb/c mouse strain. CT26 cells were originally induced in 1975 via N-nitroso-N-methylurethane-(NNMU) and are an undifferentiated cell line (Ojo-Amaize *et al.*, 2007). The CT26 cell line is currently one of the most common models of murine CRC. As such, Balb/c mice were chosen as the host organism since CT26 cells were originally derived from this mouse strain (Castle *et al.*, 2014). A 2014 genomic report verified that subcutaneous CT26 tumor allografts in Balb/c mice have gene expression profiles similar to sporadic, undifferentiated, and metastatic human CRC (Castle *et al.*, 2014) and are a valid model for an *in vivo* CRC test system.

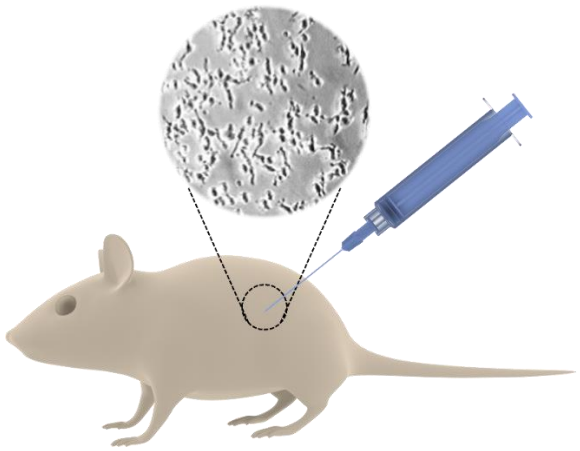

Figure 8. Balb/c mice were the model organization for the studies presented here. CT26 cells were injected subcutaneously into the left flank to form colon tumor allografts. *Image of mouse and syringe sourced from the Library of Science Medical Figures by somersault1824, which are free to share, copy, and redistribute under Create Commons License BY-NC-SA 4.0.*

1.2 Engineering focus: diffuse reflectance spectroscopy

1.2.1 Introduction to diffuse reflectance spectroscopy platforms

In this dissertation, we have engineered three DRS systems (Figure 9); however, only two systems were used for data collection in this dissertation. The first system, described in detail in Chapter 2 and briefly in Chapter 3, combines DRS with fiber-based high-resolution microendoscopy (HRME) (Figure 9, acf). This system was used for initial feasibility testing to investigate a combined DRS-HRME system and was tested on various *in vitro* and human *in vivo* platforms. Additionally, a novel third modality was included, diffuse reflectance intensity mapping (DRIM), although this modality was only briefly explored in Chapter 2. The second system, described in detail in Chapters 4-6, is a uni-modal DRS system that was optimized to quantify tissue optical parameters in subcutaneous colon tumors in mice (Figure 9, abe). This system was designed to test the feasibility of using DRS as a method to quantify tumor therapeutic response to chemotherapy and immunotherapy. A third DRS system, described briefly in the overall discussion (Chapter 7), is a combined DRS-HRME system optimized to fit

within the biopsy port of a small animal colonoscope to test the feasibility of using combined DRS-HRME as a method to monitor tumor therapeutic response in orthotopic murine colorectal tumors (Figure 9, adg). The engineering of this third system was pioneered by Ariel Mundo of the Translational Biophotonics and Imaging Laboratory (Muldoon Lab), while I served as a technical advisor based on my previous DRS experience.

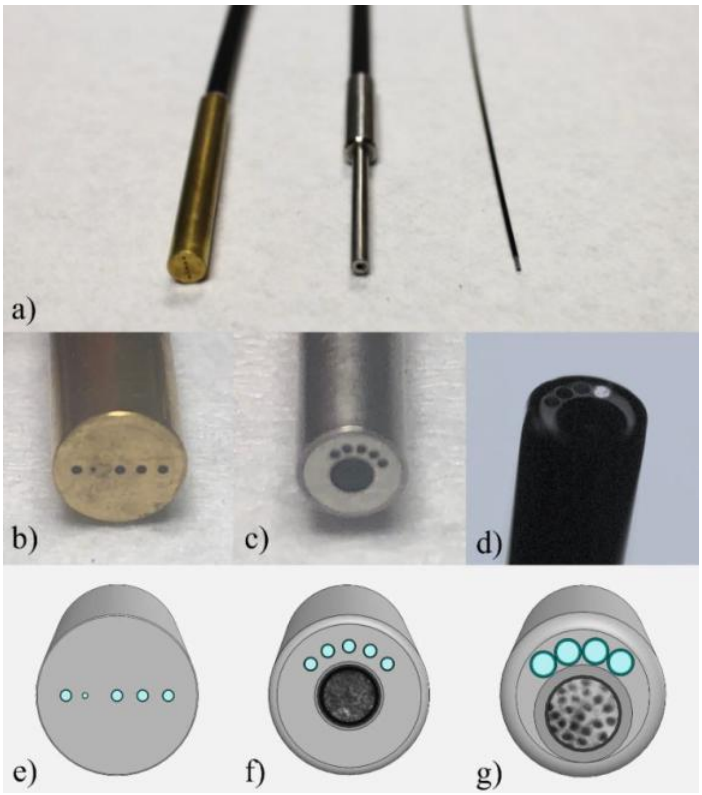

Figure 9. In this dissertation, we have engineered three DRS systems (a). The first system (c, f) was used for initial feasibility testing to investigate a combined DRS-HRME system and was tested on various *in vitro* and human *in vivo* platforms. The second system (b, e) was designed to test the feasibility of using DRS as a method to quantify tumor therapeutic response to chemotherapy and immunotherapy in the Balb/c-CT26 subcutaneous model of CRC. The third system (d, g) is a combined DRS-HRME system optimized to fit within the biopsy port of a small animal colonoscope to test the feasibility of using combined DRS-HRME as a method to monitor tumor therapeutic response in orthotopic murine colorectal tumors. Photo and 3D renderings of probe taken and created by the author.

1.2.2 High-resolution microendoscopy

HRME will be briefly described here since it is used as an imaging modality for two of the three DRS systems. HRME is a non-invasive diagnostic imaging technique that provides sub-cellular resolution images of tissue *in vivo*. Tissue samples are topically stained with a fluorescent contrast agent like proflavine, an acridine-derive fluorescent dye that intercalates DNA. Proflavine highlights cell nuclei with appropriate excitation light to allow visualization of morphological features (Muldoon *et al.*, 2007; Pierce, Guan, *et al.*, 2012; Pierce *et al.*, 2011; Quinn *et al.*, 2012; Chang *et al.*, 2013; Keahey *et al.*, 2015; Parikh *et al.*, 2014; Prieto *et al.*, 2015). Other contrast agents, such as benzoporphyrin-derivative monoacid ring A (BPD-MA) and fluorescein, have also been investigated for similar purposes (Pierce *et al.*, 2011). Generally, excitation light is delivered to the specimen though a coherent image fiber consisting of tens of thousands of individual fibers. The image fiber is placed in direct contact with tissue to excite fluorescent contrast agent and resultant fluorescence is collected by the same image fiber. Lateral and axial resolution are approximately 4 and 20 μm, respectively, with variable fields-of-view depending on the diameter of the image fiber and any distal optics. The primary advantages of HRME are low cost and portability, making this technique clinically translatable (Muldoon *et al.*, 2007; Muldoon *et al.*, 2011; Parikh *et al.*, 2014; Chang *et al.*, 2013; Quinn *et al.*, 2012; Pierce, Guan, *et al.*, 2012; Keahey *et al.*, 2015; Pierce *et al.*, 2011). Development of these systems has led to clinical studies in the upper and lower gastrointestinal tracts (Muldoon *et al.*, 2007; Muldoon *et al.*, 2011; Parikh *et al.*, 2014; Chang *et al.*, 2013) and cervix (Quinn *et al.*, 2012; Pierce, Guan, *et al.*, 2012; Keahey *et al.*, 2015). However, a limitation of HRME is insufficient depth resolution, minimizing effectiveness in detecting dysplastic changes in the sub-epithelial microenvironment. Only cells on the topmost 20 μm can be visualized and thus some

information is lost that would normally be apparent with histopathological analysis (Keahey *et al.*, 2015; Muldoon *et al.*, 2007; Muldoon *et al.*, 2011). While other microendoscopy methods, such as laser scanning confocal systems, are able to perform axial optical sectioning to resolve cellular structures below the surface, these systems require the use of complex galvanometer or microelectromechanical (MEMS)-based approaches to raster scan the excitation source across the surface of the tissue (Rivera *et al.*, 2011; Piyawattanametha *et al.*, 2010; Chen *et al.*, 2015). Fiber bundle microendoscopy, as described in this manuscript, does not include these features in favor of increased robustness and decreased cost. An additional limitation of HRME is its inability to quantify changes in tissue scattering and absorption (Muldoon *et al.*, 2007; Pierce, Guan, *et al.*, 2012; Pierce *et al.*, 2011; Quinn *et al.*, 2012; Chang *et al.*, 2013; Keahey *et al.*, 2015; Parikh *et al.*, 2014). Thus, HRME techniques could benefit from additional quantitative and depth sensitive modalities.

1.2.3 Diffuse reflectance spectroscopy

Recent work has described DRS, which uses short source-detector separations (SDS) (less than 1 mm) to non-invasively interrogate deeper within epithelia and quantify optical properties (Kanick *et al.*, 2014; Kanick *et al.*, 2009; Hennessy *et al.*, 2014; Jayanthi *et al.*, 2011; Zonios *et al.*, 1999; Marin *et al.*, 2005; Rajaram, Reichenberg, *et al.*, 2010). Optical properties depend on tissue morphology and can provide a means to quantify dysplastic changes (Jayanthi *et al.*, 2011). More specifically, broadband DRS has been used in multiple clinical studies including quantifying hemoglobin absorption to distinguish between different grades of oral cancer (Jayanthi *et al.*, 2011), distinguishing between adenomatous colon polyps and normal tissue (Zonios *et al.*, 1999), diagnosing cervical dysplasia *in vivo* (Marin *et al.*, 2005), and quantifying changes associated with non-melanoma skin cancer (Rajaram, Reichenberg, *et al.*,

2010). These studies have shown that DRS can be a useful, non-invasive method to quantify the health of small volumes of tissue although the ability to resolve fine cellular detail with spectroscopy is non-existent (Rajaram, Reichenberg*, et al.*, 2010; Marin *et al.*, 2005; Zonios *et al.*, 1999; Jayanthi *et al.*, 2011). DRS is used in this study because it can indicate tumor perfusion, which is affected by treatment with chemotherapy and immunotherapy. Alteration of the monocyte and TAM population in the colon TME via cytokine-targeted immunotherapy is hypothesized to alter downstream pro-angiogenic signals (Liu *et al.*, 2015). As tumors grow, they require an adequate oxygen supply, nutrients, and the ability to remove waste such as CO_2, catabolites, and other toxins (Cuenod *et al.*, 2013). Angiogenesis is a normal process of new blood vessel formation from already existing nearby blood vessels, and is utilized by tumors to meet their growing metabolic demands (Nishida *et al.*, 2006; Dighe *et al.*, 2012). Angiogenesis is known to increase tumor perfusion, defined as blood flow through the tumor's circulatory network (Cuenod *et al.*, 2013). Functional changes in angiogenesis-induced perfusion occur prior to structural/morphological changes, such as tumor growth (Cuenod *et al.*, 2013; Hu *et al.*, 2007). It is well known that tumor perfusion is a strong predictor of therapeutic response to chemotherapy. Delivery of cytotoxic drugs, such as 5-FU, and availability of oxygen are critical factors in inducing apoptosis of colon tumor cells (Turley *et al.*, 2012). DRS is a probe-based technique that can measure bulk tumor perfusion. DRS has several advantages including ability to quantify the functional oxyhemoglobin flare (as a quantifier of early perfusion) and tissue optical properties, non-invasiveness, depth-sensitivity, potential for clinical translation, ease-of-implementation in the laboratory, and scalability (physical size) for different tissue types in question. Because of the inherent scalability and adaptability of DRS, each DRS system and probe must be extensively calibrated to extract accurate perfusion metrics. This aim focuses on

validating a DRS platform for *in vivo* assessment of tissue perfusion and quantification of tissue optical properties, all of which may be affected by chemo- and/or immunotherapy-induced changes to the TME. Fundamental tissue optical properties are the reduced scattering coefficient (μ_s'), which depends on light scattering from cell nuclei, lipid membranes of cells and organelles, keratin (in skin), and collagenous, elastic, and reticular fibers (Lister *et al.*, 2012; Arifler *et al.*, 2007; Kumka *et al.*, 2012; Sandell *et al.*, 2011), and absorption coefficient (μ_a), which depends on hemoglobin concentration ([Hb]) and oxygen saturation (SaO_2) (Prahl, 2015; Greening, James, *et al.*, 2016; Rajaram, Reichenberg, *et al.*, 2010; Rajaram, Aramil, *et al.*, 2010; Rajaram, Gopal, *et al.*, 2010; Rajaram *et al.*, 2008). The μ_a also relies on melanin, fat, and water, although these physiological parameters are not quantified in this study (Spliethoff *et al.*, 2014; Prahl, 2015). A mobile, all-inclusive spectroscopy suite, which integrates with all three custom DRS probes, was created to monitor *in vivo* tissue properties (Figure 10).

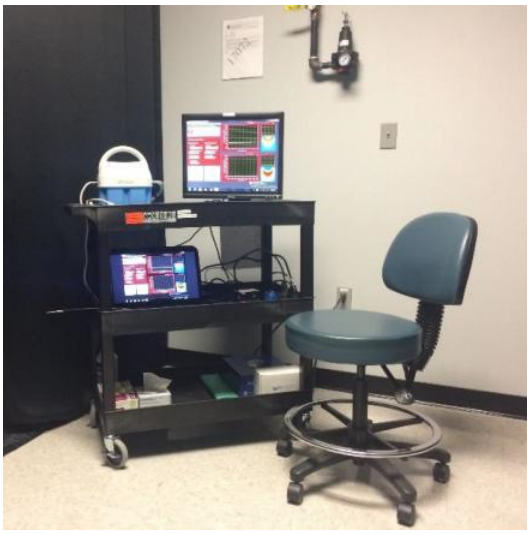

Figure 10. DRS setup for *in vivo* measurements on tissue or tissue-simulating phantoms. Photo taken by the author.

Bulk, volume-averaged tumor perfusion was optically quantified by DRS-derived oxyhemoglobin (product of total hemoglobin concentration and tissue oxygen saturation). The

post-processing DRS software to quantify μ_s' and μ_a is based on the damped least-squares fitting method, in which a curve is iterated to "best-fit" the raw spectra. Based on the best-fit curve, μ_s' and μ_a experimental values are extracted. Once μ_a is accurately quantified, THC and StO_2 of *in vivo* tissue can be derived (process described in detail in Chapters 2 and 4).

1.3 Diffuse reflectance physics

1.3.1 Turbid media

DRS is one a simple and widely used technique for non-invasively studying biological tissues. All biological tissues, including colorectal and CRC tissue, are considered turbid media (Zonios *et al.*, 2011). But what is exactly meant by the term, turbid media? Turbid media is any medium which has significant scattering due to randomly distributed optical nonuniformities. A light wave/photon contacting or passing through the turbid media will change direction based on the index of refraction throughout the medium (Figure 11). A photon will continue scattering throughout the turbid media until it is absorbed by an absorber or is transmitted or diffusely reflected from the media. Light propagation through biological tissues can indicate the structural and functional makeup of the tissue due to scattering, absorption, and fluorescence events; however, light propagation through turbid media is a challenging problem (Romanov *et al.*, 2012).

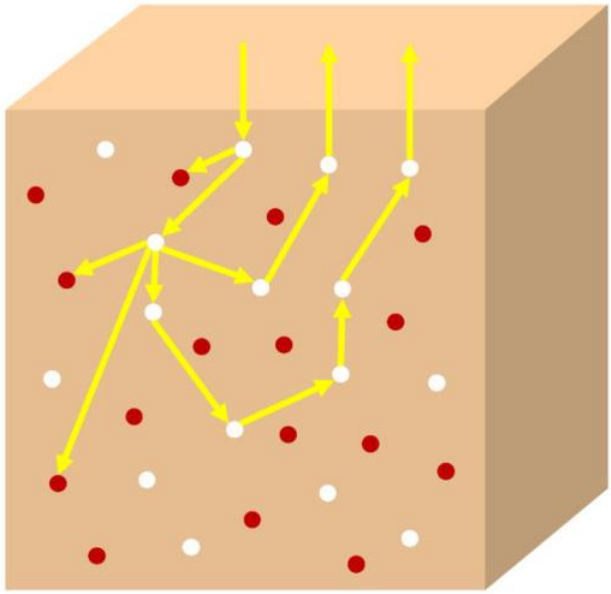

Figure 11. An oversimplification of the movement of photons through turbid media. Photons can be scattered by scattering agents (white circles) or absorbed by absorbing agents (red circles). Image created by the author.

Light propagation in tissue can be fully described by the radiative transport equation (RTE). The RTE states that the total radiance for photons traveling in a specific direction through time and space is equal to the sum of all sources that affect (increase or decrease) radiance. Radiance is defined as the quantity of photons per unit volume. A more detailed description of the RTE can be found in numerous sources (Liemert *et al.*, 2012; Liemert *et al.*, 2014; Wilson *et al.*, 2011). The RTE has been successfully used to model photon transport in turbid media. However, the RTE is mathematically and computationally intensive, and because of this, research has sought to create simpler models that approximate the RTE (Liemert *et al.*, 2014; Liemert *et al.*, 2012; Wilson *et al.*, 2011; Kim *et al.*, 2006; Kim, 2004; Kim *et al.*, 2003).

One such simplification used in biological tissues is the diffuse approximation. The diffusion approximation is a method that has been used to determine μ_s' and μ_a in tissue (Wilson *et al.*, 2011; Reif *et al.*, 2007; Gibson *et al.*, 2005; Kim, 2004; Kim *et al.*, 2003). However, the diffusion approximation is only valid in turbid media if the following requirements are met: 1)

the μ_s' must be much greater than the μ_a, and 2) large source-detector separations must exist (Reif *et al.*, 2007). Some sources have also claimed that the diffusion approximation is not valid in media that exhibit anisotropic scattering (Gibson *et al.*, 2005). These requirements ensure that any collected photons have traveled through large volumes of tissue. In turn, this ensures that extracted optical properties represent an accurate average of the real optical properties. However, in many cases, investigators used small endoscopy devices, to sample thin tissues with a small sampling depth. This is the case for dysplasia or cancers that are confined to the epithelium, which is only between 100-500 μm thick (Rajaram *et al.*, 2008).

Therefore, a distinction must be made between what is meant by the diffuse regime, in which the diffusion approximation is valid, and the sub-diffuse regime, in which the diffusion approximation is not valid (Reif *et al.*, 2007; Subramanian *et al.*, 2007; Turzhitsky, Rogers, *et al.*, 2010; Turzhitsky, Radosevich, *et al.*, 2010; Bosschaart *et al.*, 2011; Kanick *et al.*, 2014). For many of the cases listed here, the validity of the diffusion approximation begins to fail for one of two reasons. The first reason is that μ_s' is not much greater than μ_a (Reif *et al.*, 2007; Turzhitsky, Radosevich, *et al.*, 2010; Turzhitsky, Rogers, *et al.*, 2010; Subramanian *et al.*, 2007; Bosschaart *et al.*, 2011). The μ_s' is considered "not much greater" than the μ_a when albedo is less than 0.9 (Rajaram *et al.*, 2008). The second reason the diffusion approximation begins to fail is the use of small source-detector separations common to small endoscopic probes. A source-detector separation is considered "small" if it is less than approximately one reduced mean free path (Rajaram *et al.*, 2008; Subramanian *et al.*, 2007; Bosschaart *et al.*, 2011; Kanick *et al.*, 2014). Therefore, although most "diffuse reflectance spectroscopy" is really "sub-diffuse reflectance spectroscopy", the term "sub-diffuse" will not be used for clarity.

1.3.2 Light scattering in turbid media

There are two primary types of scattering: Rayleigh scattering and Mie scattering (Figure 12). Simply, Rayleigh scattering refers to scattering by particles much smaller than the wavelength of light. Mie scattering refers to scattering by particles larger or of comparable size to the wavelength of light. However, it is more correct to say that all scattering is Mie scattering, and Rayleigh scattering is the Rayleigh limit of Mie scattering (Jacques, 2013). Biological tissue typically exhibits Mie scattering. In biological tissue, organelles such as mitochondria and cell nuclei are the primary scattering agents (Mourant *et al.*, 1998). Striations in collagen fibrils are also responsible for scattering (Arifler *et al.*, 2007). The magnitude of scattering is typically quantified with μ_s', which can be measured with DRS.

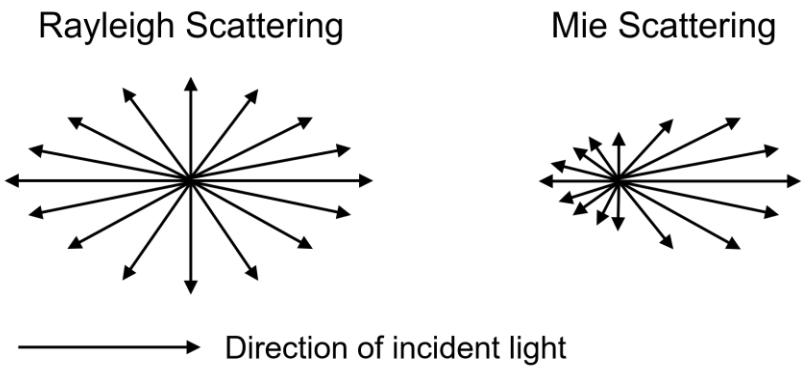

Figure 12. Rayleigh and Mie scattering in biological tissue (a turbid media). Mie scattering is the name for scattering by a sphere of any size, whereas Rayleigh scattering is a type of Mie scattering in which the scattering agents are much smaller than the wavelength of light (Jacques, 2013). Image created by the author.

1.3.3 Light absorption in turbid media

In addition to μ_s', DRS can also measure μ_a. The μ_a depends on the concentration of absorbing agents in the biological tissue. In living systems, there are 5 primary absorbers spanning the ultraviolet to near-infrared spectrum (approximately between 300-2000 nm):

melanin, oxygenated hemoglobin, deoxygenated hemoglobin, fat, and water. The normalized μ_a of these 5 absorbers are shown in Figure 13 (Prahl, 2015).

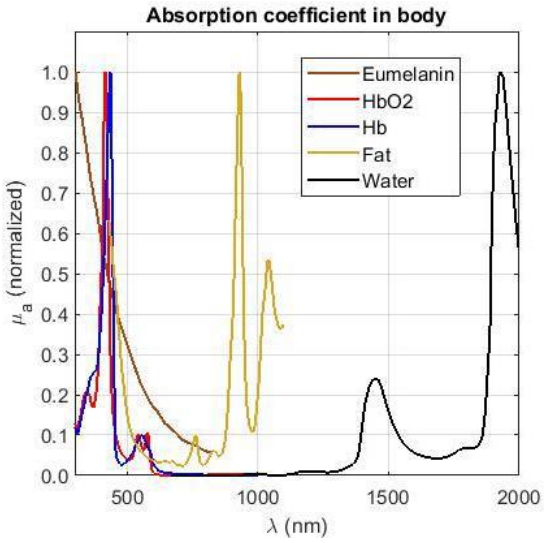

Figure 13. Normalized absorption coefficients of melanin, oxygenated hemoglobin, deoxygenated hemoglobin, fat, and water in biological tissues. Graph created by the author using data by Scott Prahl (Prahl, 2015).

Our studies report absorption in the visible and very near-infrared spectrum (~450 to 800 nm). Therefore, in the following studies for this dissertation, water is not looked at because absorption is negligible below 1400 nm. Melanin is not analyzed since albino mice (Balb/c) were used as the test subjects. Additionally, some studies were done in the oral mucosa of health human volunteers – oral mucosa does not contain melanin. Finally, fat was not analyzed because, although fat does contribute slightly to absorption in the visible to near-infrared spectrum, it is negligible compared to the two primary absorbers, oxygenated and deoxygenated hemoglobin. Figure 14 shows the absolute μ_a of oxygenated and deoxygenated hemoglobin in whole blood compared to the μ_a of fat (Prahl, 2015; Greening, James, *et al.*, 2016; Greening, James, *et al.*, 2015; Greening *et al.*, 2018; Greening, Powless, *et al.*, 2015).

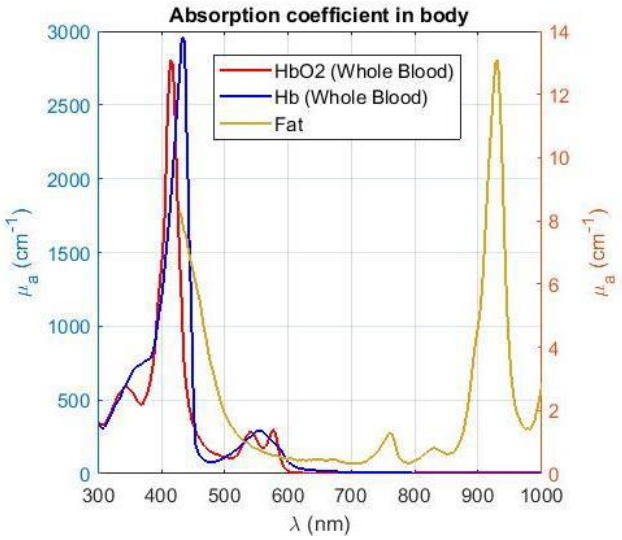

Figure 14. Absorption coefficients of melanin, oxygenated hemoglobin, and deoxygenated hemoglobin below 1000 nm. Graph created by the author using data by Scott Prahl (Prahl, 2015).

1.4 Concluding remarks to introduction

Chapters 2 and 3 represent specific aims 1 and 2, respectively. Aim 3, on the other hand, is longer, and consists of chapters 4, 5, and 6. The following aims were designed to address the investigation and optimization of using DRS as a technique to monitor *in vivo* tissue health and tumor therapeutic response, specifically in murine colon cancer.

1.5 Specific Aims

The overall health focus of this dissertation is CRC. Murine subcutaneous allografts were used as a model for CRC. Specifically, for my dissertation work, I looked at murine subcutaneous CRC allografts as a model for CRC from two angles. First, can DRS be used as a platform to monitor tumor therapeutic response in this CRC tumor model? Second, does treatment with standard chemotherapy and macrophage-targeted immunotherapy alter the TME? Combining these two angles (Figure 1), do these TME alterations correlate with DRS data?

Before DRS was implemented in the scientific investigation of therapy response in murine subcutaneous CRC allografts, the first step (Aim 1) was to engineer and characterize a

DRS probe for *in vivo* tissue analysis. The second step (Aim 2) was to design tissue-simulating phantoms with tunable optical properties to test the sensitivity of our probe to phantom-based, sub-surface optical heterogeneities. Additionally, this phantom design sparked a non-DRS-based collaboration with Boston University who used these phantoms to improve longitudinal preclinical tumor imaging in the spatial frequency domain (Tabassum *et al.*, 2018). The third step (Aim 3) was to develop the murine subcutaneous CRC allografts, optimize probe design for subcutaneous tumor allografts, test isoflurane anesthesia as a potential confounding variable, and implement DRS in a longitudinal study on treating mice with chemotherapy and macrophage-targeted immunotherapy to see how this therapy would affect DRS results.

<u>Specific Aim 1</u>: Design and characterization of broadband diffuse reflectance spectroscopy probes for *in vivo* tissue analysis

Publications:

- Greening GJ, Powless AJ, Hutcheson JA, James HM, Dierks MK, Rajaram N, Muldoon TJ, "Fiber-bundle microendoscopy with sub-diffuse reflectance spectroscopy and intensity mapping for multimodal optical biopsy of stratified epithelium," Biomedical Optics Express, 6(12), (2015).
- Greening GJ, James HM, Dierks MK, Vongkittiargorn N, Osterholm SM, Rajaram N, Muldoon TJ. "Towards monitoring dysplastic progression in the oral cavity using a hybrid fiber-bundle imaging and spectroscopy probe," Scientific Reports, 6(26734), (2016).
- Greening GJ, Rajaram N, Muldoon TJ. "Multimodal imaging and spectroscopy fiber-bundle microendoscopy platform for non-invasive in vivo tissue analysis," Journal of Visualized Experiments, 116, (2016).

Background: Early detection of structural or functional changes in dysplastic epithelia is crucial for improving long-term patient care. Recent work has explored non-invasive or minimally invasive optical biopsy techniques for diagnosing early dysplasia, such as HRME, a method to resolve sub-cellular features of apical epithelia, as well as DRS, a method that evaluates bulk health of a small volume of tissue. It is possible that the high-resolution imaging modality may be beneficial in providing image data of later stage moderate and severe dysplasia while the DRS modality may be sensitive to tissue optical changes associated with early dysplasia.

Objective: Develop and validate a quantitative hybrid imaging and spectroscopy microendoscope to monitor dysplastic progression within epithelial tissues. Co-registration of both techniques is important because this technique can be potentially used to not only detect dysplasia using two different modalities, but also to monitor personalized response of sub-surface dysplastic lesions to anti-tumor therapy at multiple source-detector separations.

Central Hypothesis: High-resolution microendoscopy and DRS can be combined within a single optical probe to co-register image and spectral data of *in vivo* epithelia.

Significance: With this multimodal system, epithelial morphological data can be correlated with quantitative spectroscopy data of the subsurface microenvironment, including associated optical properties. This multimodal microendoscopy approach encompasses both structural and spectroscopic reporters of perfusion within the tissue microenvironment and can potentially be used to monitor tumor response to therapy. This hybrid imaging and spectroscopy platform may be capable of collecting a wealth of information about the structural and functional properties of tissue at various imaging sites in *ex vivo* and *in vivo* models. The potential of this technique to be coupled to the biopsy port of a conventional endoscope makes further clinical translation and complimentary optical biopsy in the oral cavity and other epithelial tissues feasible.

<u>Specific Aim 2</u>: Characterization of poly(dimethylsiloxane)-based tissue-simulating phantoms with tunable reduced scattering and absorption coefficients with applications for diffuse reflectance spectroscopy

Publications:

- Greening GJ, Istfan R, Higgins LM, Balachandran K, Roblyer D, Pierce MC, Muldoon TJ, "Characterization of thin poly (dimethylsiloxane)-based tissue simulating phantoms with tunablereduced scattering and absorption coefficients at visible and near infrared wavelength," Journal of Biomedical Optics, 19(11), (2014).
- Greening GJ, James HM, Muldoon TJ. "Optical Phantoms: Diffuse and sub-diffuse imaging and spectroscopy validation," SPIE Spotlights, (2015).
- Tabassum S, Pera V, Greening GJ, Muldoon TJ, Roblyer D. "Two-layer inverse model for improved longitudinal preclinical tumor imaging in the spatial frequency domain," Journal of Biomedical Optics, 23(7), (2018).

Background: Optical phantoms are used in the development of various imaging systems. For certain applications, the development of thin phantoms that simulate physical size and optical properties of tissue is important.

Objective: Here, we demonstrate a method for producing thin phantom layers with tunable optical properties using poly(dimethylsiloxane) (PDMS) as a substrate material at six discrete wavelengths (591, 631, 659, 691, 731, and 851 nm) at varying concentrations of titanium dioxide and nigrosin.

Central Hypothesis: Thin, PDMS-based optical phantoms can accurately simulate the geometry and optical properties of target epithelia, and can be used to tst the sensitivity of various imaging and spectroscopy equipment to heterogeneities.

Significance: From the presented data, we provide lookup tables to determine appropriate concentrations of scattering and absorbing agents to be used in the design of PDMS-based phantoms with specific optical coefficients. In addition, heterogeneous phantoms, mimicking the layered features of certain tissue types, may be fabricated from multiple stacked layers, each with custom optical properties. These thin, tunable PDMS optical phantoms can simulate many tissue types and have broad imaging calibration applications in endoscopy, diffuse optical spectroscopic imaging (DOSI), or optical coherence tomography (OCT), among others.

<u>Specific Aim 3</u>: Optical property quantification of subcutaneous murine colon carcinoma tumors in response to chemotherapy and macrophage-targeted immunotherapy measured using diffuse reflectance spectroscopy

Publications:

- Greening GJ, Mundo AI, Rajaram N, Muldoon TJ. "Sampling depth of a diffuse reflectance spectroscopy probe for in vivo physiologic quantification of murine subcutaneous tumor allografts," Journal of Biomedical Optics, 23(8), (2018).
- Greening GJ, Miller KP, Spainhour CR, Cato MD, Muldoon TJ. "Effects of isoflurane anesthesia on physiological parameters in murine subcutaneous tumor allografts measured via diffuse reflectance spectroscopy," Biomedical Optics Express, 9(6), (2018).
- Greening GJ, Bess SN, Muldoon TJ. "Immunohistochemistry staining for tumor-associated macrophage polarization in murine subcutaneous colon tumor allografts," Bio-101, 3106, (2018).

Background: (1) DRS is a probe-based spectral biopsy technique used in cancer studies to quantify tissue reduced scattering (μ_s') and absorption (μ_a) coefficients and vary in source-detector separation (SDS) to fine tune sampling depth. In subcutaneous murine tumor allografts

or xenografts, a key design requirement is ensuring the source light interrogates past the skin layer into the tumor without significantly sacrificing signal-to-noise ratio (target of ≥ 15 dB). Once this has been verified, DRS can be used in cancer allograft or xenograft studies, such as those subject to chemotherapy and/or immunotherapy regimens. (2) Immunotherapy in colorectal cancer (CRC) describes therapy that regulates specific immune checkpoints, and when used in combination with chemotherapy, can improve prognosis. One specific immune checkpoint is recruitment of circulating monocytes, which differentiate into tumor-associated macrophages (TAMs) and promote angiogenesis and tumor progression. Thus, immunotherapeutic strategies blocking monocyte recruitment may play an anti-tumor role. Vascularization can be non-invasively assessed via DRS, which quantifies metrics such as hemoglobin concentration and oxygenation in a localized tumor volume. However, there have been no studies investigating the efficacy of DRS in evaluating therapeutic response of combined immunotherapy and chemotherapy.

Objecive: (1) Design a DRS probe with four SDSs (0.75, 2.00, 3.00, and 4.00 mm) to interrogate increasing tissue volumes between 450-900 nm. The goal was to quantify percent errors in extracting μ_a and μ_s', and to quantify sampling depth into subcutaneous Balb/c-CT26 colon tumor allografts. Using an optical phantom-based experimental method, lookup-tables were constructed relating μ_a, μ_s', diffuse reflectance, and sampling depth. (2) Examine whether blockade of monocyte recruitment via anti-CCL2 (macrophage chemoattractant protein-1) leads to enhanced sensitivity of 5-FU (5-fluorouracil) therapy in a CT26-Balb/c mouse model of CRC, and whether this effect can be quantified via DRS.

Central Hypothesis: The oxyhemoglobin flare has not been quantified after combinatorial chemotherapy and immunotherapy, and furthermore, has not been quantified in colon cancer

tumors. Can DRS be used to quantify the therapy-induced oxyhemoglobin flare in a mouse model of colon cancer? The central hypothesis is that tumors treated with immunotherapy will have increased tumor therapeutic response to chemotherapy, as measured via tumor size and DRS-derived metrics.

Significance: This work shows that the DRS probe can accurately extract optical properties, and the resultant physiological parameters such as total hemoglobin concentration and tissue oxygen saturation, from sufficient depth within subcutaneous Balb/c-CT26 colon tumor allografts. Methods described here can be generalized for other murine tumor models.

References

Allavena, P., *et al.* "The Inflammatory Micro-Environment in Tumor Progression: The Role of Tumor-Associated Macrophages." *Critical Reviews in Oncology/Hematology* 66 (2008): 1-9.

Andre, T., *et al.* "Semimonthly Versus Monthly Regimen of Fluorouracil and Leucovorin Administered for 24 or 36 Weeks as Adjuvant Therapy in Stage Ii and Iii Colon Cancer: Results of a Randomized Trial." *J Clin Oncol* 21.15 (2003): 2896-903.

Arifler, D., *et al.* "Light Scattering from Collagen Fiber Networks: Micro-Optical Properties of Normal and Neoplastic Stroma." *Biophys J* 92.9 (2007): 3260-74.

Arifler, D., *et al.* "Light Scattering from Collagen Fiber Networks: Micro-Optical Properties of Normal and Neoplastic Stroma." *Biophysical Journal* 92 (2007): 3260-74.

Baek, S. K. "Laterality: Right-Sided and Left-Sided Colon Cancer." *Ann Coloproctol* 33.6 (2017): 205-6.

Barbera-Guillem, E., *et al.* "Vascular Endothelial Growth Factor Secretion by Tumor-Infiltrating Macrophages Essentially Supports Tumor Angiogenesis, and Igg Immune Complexes Potentiate the Process." *Cancer Research* 62.23 (2002): 7042-9.

Becht, E., *et al.* "Immune and Stromal Classification of Colorectal Cancer Is Associated with Molecular Subtypes and Relevant for Precision Immunotherapy." *Clincal Cancer Research* 22.16 (2016): 4057-66.

Berger, A.W., *et al.* "Treatment Monitoring in Metastatic Colorectal Cancer Patients by Quantification and Kras Genotyping of Circulating Cell-Free DNA." *PLoS One* 12.3 (2017).

Birendra, K.C., *et al.* "Advances in Immunotherapy in the Treatment of Colorectal Cancer." *American Journal of Hematology/Oncology* 13.7 (2017): 4-8.

Bish, S.F., *et al.* "Development of a Noncontact Diffuse Optical Spectroscopy Probe for Measuring Tissue Optical Properties." *Journal of Biomedical Optics* 16.12 (2011): 120505.

Bish, S.F., *et al.* "Handheld Diffuse Reflectance Spectral Imaging (Drsi) for in-Vivo Characterization of Skin." *Biomedical Optics Express* 5.2 (2014): 573-86.

Boland, C.R., and A. Goel. "Microsatellite Instability in Colorectal Cancer." *Gastroenterology* 138.6 (2011): 2073-87.

Boland, P.M., and M. Fakih. "The Emerging Role of Neoadjuvant Chemotherapy for Rectal Cancer." *Journal of Gastrointestinal Oncology* 5.5 (2014): 362-73.

Boland, P.M., and W.W. Ma. "Immunotherapy for Colorectal Cancer." *Cancers* 9.5 (2017).

Bosschaart, N., *et al.* "Optical Properties of Neonatal Skin Measured in Vivo as a Function of Age and Skin Pigmentation." *Journal of Biomedical Optics* 16.9 (2011).

Bouvier, A.M., *et al.* "Incidence and Patterns of Late Recurrences in Colon Cancer Patients." *International Journal of Cancer* 137.9 (2015).

Burmeister, K., *et al.* "Vascular Endothelial Growth Factor a Amplification in Colorectal Cancer Is Associated with Reduced M1 and M2 Macrophages and Diminished Pd-1-Expressing Lymphocytes." *PLoS One* 12.4 (2017).

Burt, R.W., *et al.* "Nccn Clinical Practice Guidelines in Oncology. Colorectal Cancer Screening." *Journal of the National Comprehensive Cancer Network* 8.1 (2010): 8-61.

Castle, J. C., *et al.* "Immunomic, Genomic and Transcriptomic Characterization of Ct26 Colorectal Carcinoma." *BMC Genomics* 15.1 (2014): 190.

Cejudo-Martin, P., and R. S. Johnson. "A New Notch in the Hif Belt: How Hypoxia Impacts Differentiation." *Dev Cell* 9.5 (2005): 575-6.

Chang, S.S., *et al.* "High Resolution Microendoscopy for Classification of Colorectal Polyps." *Endoscopy* 45.7 (2013): 553-9.

Cheeseman, S.L., *et al.* "A 'Modified De Gramont' Regimen of Fluorouracil, Alone and with Oxaliplatin, for Advanced Colorectal Cancer." *British Journal of Cancer* 87.4 (2008): 393-9.

Chen, J.J., *et al.* "Tumor-Associated Macrophages: The Double-Edged Sword in Cancer Progression." *Journal of Clinical Oncology* 23.5 (2005): 953-64.

Chen, X., *et al.* "Multimodal Nonlinear Endo-Microscopy Probe Design for High Resolution, Label-Free Intraoperative Imaging." *Biomedical Optics Express* 6.7 (2015): 2283-93.

Chin, L.C.L., *et al.* "Early Biomarker for Radiation-Induced Wounds: Day One Post-Irradiation Assessment Using Hemoglobin Concentration Measured from Diffuse Optical Reflectance Spectroscopy." *Biomedical Optics Express* 8.3 (2017): 1682-8.

Chun, E., *et al.* "Ccl2 Promotes Colorectal Carcinogenesis by Enhancing Polymorphonuclear Myeloid-Derived Suppressor Cell Population and Function." *Cell Reports* 12.2 (2015): 244-57.

Covello, K. L., *et al.* "Hif-2α Regulates Oct-4: Effects of Hypoxiaon Stem Cell Function, Embryonic Development, and Tumor Growth." *Genes Dev* 20.5 (2006): 557-70.

Cuenod, C.A., and D. Balvay. "Perfusion and Vascular Permeability: Basic Concepts and Measurement in Dce-Ct and Dce-Mri." *Diagnostics and Interventional Imaging* 94.12 (2013): 1187-204.

de Gramont, A., *et al.* "Leucovorin and Fluorouracil with or without Oxaliplatin as First-Line Treatment in Advanced Colorectal Cancer." *J Clin Oncol* 18.16 (2000): 2938-47.

Deshmane, S.L., *et al.* "Monocyte Chemoattractant Protein-1 (Mcp-1): An Overview." *Journal of Interferon & Cytokine Research* 29.6 (2009): 313-26.

Dienstmann, R., *et al.* "Prediction of Overall Survival in Stage Ii and Iii Colon Cancer Beyond Tnm System: A Retrospective, Pooled Biomarker Study." *Annals of Oncology* 28.5 (2017): 1023-31.

Dighe, S., *et al.* "Perfusion Ct to Assess Angiogenesis in Colon Cancer: Technical Limitations and Practical Challenges." *The British Journal of Radiology* 85.1018 (2012): e814-25.

Dine, J., *et al.* "Immune Checkpoint Inhibitors: An Innovation in Immunotherapy for the Treatment and Management of Patients with Cancer." *Asia-Pacific Journal of Oncology Nursing* 4.2 (2017): 127-35.

Douplik, A., *et al.* "Assessment of Photobleaching During Endoscopic Autofluorescence Imaging of the Lower Gi Tract." *Lasers in Surgery and Medicine* 42.3 (2010): 224-31.

Dreyer, S.B., *et al.* "The Pretreatment Systemic Inflammatory Response Is an Important Determinant of Poor Pathologic Response for Patients Undergoing Neoadjuvant Therapy for Rectal Cancer." *Annals of Surgical Oncology* 24.5 (2017): 1295-303.

Duff, S. E., *et al.* "Vascular Endothelial Growth Factors and Receptors in Colorectal Cancer: Implications for Anti-Angiogenic Therapy." *Eur J Cancer* 42.1 (2006): 112-7.

Eales, K. L., *et al.* "Hypoxia and Metabolic Adaptation of Cancer Cells." *Oncogenesis* 5 (2016): e190.

Ellis, L. M., *et al.* "Angiopoietins and Their Role in Colon Cancer Angiogenesis." *Oncology (Williston Park)* 16.4 Suppl 3 (2002): 31-5.

Eppensteiner, J., *et al.* "Immunothrombotic Activity of Damage-Associated Molecular Patterns and Extracellular Vesicles in Secondary Organ Failure Induced by Trauma and Sterile Insults." *Front Immunol* 9 (2018): 190.

Erreni, M., *et al.* "Tumor-Associated Macrophages (Tam) and Inflammation in Colorectal Cancer." *Cancer Microenviornment* 4 (2011): 141-54.

Esplin, E. D., and M. P. Snyder. "Genomic Era Diagnosis and Management of Hereditary and Sporadic Colon Cancer." *World J Clin Oncol* 5.5 (2014): 1036-47.

Falou, O., *et al.* "Diffuse Optical Spectroscopy Evaluation of Treatment Response in Women with Locally Advanced Breast Cancer Receiving Neoadjuvant Chemotherapy." *Translational Oncology* 5.4 (2012): 238-46.

Fleming, M., *et al.* "Colorectal Carcinoma: Pathologic Aspects." *J Gastrointest Oncol* 3.3 (2012): 153-73.

Fuchs, C. S., *et al.* "Randomized, Controlled Trial of Irinotecan Plus Infusional, Bolus, or Oral Fluoropyrimidines in First-Line Treatment of Metastatic Colorectal Cancer: Results from the Bicc-C Study." *J Clin Oncol* 25.30 (2007): 4779-86.

Funada, Y., *et al.* "Prognostic Significance of Cd8+ T Cell and Macrophage Peritumoral Infiltration in Colorectal Cancer." *Oncology Reports* 10.2 (2003): 309-13.

Geiger, T.M., and R. Ricciardi. "Screening Options and Recommendations for Colorectal Cancer." *Clinics in Colon and Rectal Surgery* 22.4 (2009): 209-17.

Ghiringhelli, F., *et al.* "Activation of the Nlrp3 Inflammasome in Dendritic Cells Induces Il-1beta-Dependent Adaptive Immunity against Tumors." *Nat Med* 15.10 (2009): 1170-8.

Gibson, A.P., *et al.* "Recent Advances in Diffuse Optical Imaging." *Physics in Medicine and Biology* 50 (2005).

Glennie, D.L., *et al.* "Modeling Changes in the Hemoglobin Concentration of Skin with Total Diffuse Reflectance Spectroscopy." *Journal of Biomedical Optics* 20.3 (2015): 035002.

Glennie, D.L., *et al.* "Inexpensive Diffuse Reflectance Spectroscopy System for Measuring Changes in Tissue Optical Properties." *Journal of Biomedical Optics* 19.10 (2014): 105005.

Goldberg, R. M., *et al.* "A Randomized Controlled Trial of Fluorouracil Plus Leucovorin, Irinotecan, and Oxaliplatin Combinations in Patients with Previously Untreated Metastatic Colorectal Cancer." *J Clin Oncol* 22.1 (2004): 23-30.

Görlach, A., *et al.* "Reactive Oxygen Species, Nutrition, Hypoxia and Diseases: Problems Solved?" *Redox Biol* 6 (2015): 372-85.

Greening, G.J., *et al.* "Towards Monitoring Dysplastic Progression in the Oral Cavity Using a Hybrid Fiber-Bundle Imaging and Spectroscopy Probe." *Scientific Reports* 6.26734 (2016).

Greening, G.J., *et al.* Optical Phantoms: Diffuse and Sub-Diffuse Imaging and Spectroscopy Validation. Bellingham, Washington: SPIE Spotlights, 2015.

Greening, G.J., *et al.* "Sampling Depth of a Diffuse Reflectance Spectroscopy Probe for in-Vivo Physiological Quantification of Murine Subcutaneous Tumor Allografts." *Journal of Biomedical Optics* 23.8 (2018).

Greening, G.J., *et al.* "Design and Validation of a Diffuse Reflectance and Spectroscopic Microendoscope with Poly(Dimethylsiloxane)-Based Phantoms." *Proceedings of SPIE* 9332 (2015).

Greening, G.J., *et al.* "In Vivo Measurement of Non-Keratinized Squamous Epithelium Using a Spectroscopic Microendoscope with Multiple Source-Detector Separations." *Proceedings of SPIE* 9715 (2016).

---. "Multimodal Imaging and Spectroscopy Fiber-Bundle Microendoscopy Platform for Non-Invasive, in Vivo Tissue Analysis." *Journal of Visualized Experiments* 116 (2016).

Grierson, P., *et al.* "Immunotherapy in Gastrointestinal Cancers." *Journal of Gastrointestinal Oncology* 8.3 (2017): 474-84.

Guinney, J., *et al.* "The Consensus Molecular Subtypes of Colorectal Cancer." *Nature Medicine* 21.11 (2015): 1350-6.

Guo, C., *et al.* "Therapeutic Cancer Vaccines: Past, Present and Future." *Advances in Cancer Research* 119 (2014): 421-75.

Habr-Gama, A., *et al.* "Complete Clinical Response after Neoadjuvant Chemoradiation Therapy for Distal Rectal Cancer: Characterization of Clinical and Endoscopic Findings for Standardization." *Diseases of the Colon & Rectum* 53.12 (2010): 1692-8.

Hamanaka, R. B., and N. S. Chandel. "Mitochondrial Reactive Oxygen Species Regulate Hypoxic Signaling." *Curr Opin Cell Biol* 21.6 (2009): 894-9.

Hennessy, R., *et al.* "Effect of Probe Geometry and Optical Properties on the Sampling Depth for Diffuse Reflectance Spectroscopy." *Journal of Biomedical Optics* 19.10 (2014): 107002.

Hennessy, R., *et al.* "Impact of One-Layer Assumption on Diffuse Reflectance Spectroscopy of Skin." *Journal of Biomedical Optics* 20.2 (2015): 27001.

Hernandez, C., *et al.* "Damage-Associated Molecular Patterns in Cancer: A Double-Edged Sword." *Oncogene* 35.46 (2016): 5931-41.

Hinck, L., and I. Näthke. "Changes in Cell and Tissue Organization in Cancer of the Breast and Colon." *Curr Opin Cell Biol* 0 (2014): 87-95.

Hong, K. H., *et al.* "Monocyte Chemoattractant Protein-1-Induced Angiogenesis Is Mediated by Vascular Endothelial Growth Factor-A." *Blood* 105.4 (2005): 1405-7.

Hu, H.J., *et al.* "Mri Measurements of Tumor Size and Pharmacokinetic Parameters as Early Predictors of Response in Breast Cancer Patients Undergoing Neoadjuvant Anthracycline Chemotherapy." *Journal of Magnetic Resonance Imaging* 36.3 (2007): 615-23.

Hussain, M., *et al.* "Right-Sided and Left-Sided Colon Cancers Are Two Distinct Disease Entities: An Analysis of 200 Cases in Pakistan." *Asian Pac J Cancer Prev* 17.5 (2016): 2545-8.

Jacobs, J., *et al.* "Immune Checkpoint Modulation in Colorectal Cancer: What's New and What to Expect." *Journal of Immunology Research* 2015 (2015).

Jacques, S.L. "Optical Properties of Biological Tissues: A Review." *Physics in Medicine and Biology* 58.11 (2013).

Jasperson, K. W., *et al.* "Hereditary and Familial Colon Cancer." *Gastroenterology* 138.6 (2010): 2044-58.

Jayanthi, J.L., *et al.* "Diffuse Reflectance Spectroscopy: Diagnostic Accuracy of a Non-Invasive Screening Technique for Early Detection of Malignant Changes in the Oral Cavity." *BMJ Open* (2011).

Jeon, H.J., *et al.* "Adjuvant Chemotherapy Using the Folfox Regimen in Colon Cancer." *Journal of the Korean Society of Coloproctology* 27.3 (2011): 140-6.

Jermyn, M., *et al.* "Highly Accurate Detection of Cancer in Situ with Intraoperative, Label-Free, Multimodal Optical Spectroscopy." *Cancer Research* 77.14 (2017): 3942-50.

Kanick, S.C., *et al.* "Sub-Diffusive Scattering Parameter Maps Recovered Using Wide-Field High-Frequency Structured Light Imaging." *Biomedical Optics Express* 5.10 (2014): 3376-90.

Kanick, S.C., *et al.* "Monte Carlo Analysis of Single Fiber Reflectance Spectroscopy: Photon Path Length and Sampling Depth." *Physics in Medicine and Biology* 54.22 (2009): 6991-7008.

Karsten, A.E., *et al.* "Diffuse Reflectance Spectroscopy as a Tool to Measure the Absorption Coefficient in Skin: South African Skin Phototypes." *Photochemistry and Photobiology* 89.1 (2013): 227-33.

Keahey, P.A., *et al.* "Optimizing Modulation Frequency for Structured Illumination in a Fiber-Optic Microendoscope to Image Nuclear Morphometry in Columnar Epithelium." *Biomedical Optics Express* 6.3 (2015): 870-80.

Kim, A.D. "Transport Theory for Light Propagation in Biological Tissue." *Journal of the Optical Society of America: Optics, Image Science, and Vision* 21.5 (2004).

Kim, A.D., *et al.* "Estimating Optical Properties in Layered Tissues by Use of the Born Approximation of the Radiative Transport Equation." *Optics Letters* 15.31 (2006).

Kim, A.D., and J.B. Keller. "Light Propagation in Biological Tissue." *Journal of the Optical Society of America: Optics, Image Science, and Vision* 20.1 (2003).

Kim, N.K., and H. Hur. "New Perspectives on Predictive Biomarkers of Tumor Response and Their Clinical Application in Preoperative Chemoradiation Therapy for Rectal Cancer." *Yonsei Medical Journal* 56.6 (2015): 1461-77.

Kondoh, M., *et al.* "Hypoxia-Induced Reactive Oxygen Species Cause Chromosomal Abnormalities in Endothelial Cells in the Tumor Microenvironment." *PLoS One* 8.11 (2013): e80349.

Korc, M., and R. E. Friesel. "The Role of Fibroblast Growth Factors in Tumor Growth." *Curr Cancer Drug Targets* 9.5 (2009): 639-51.

Krock, B. L., *et al.* "Hypoxia-Induced Angiogenesis: Good and Evil." *Genes Cancer* 2.12 (2011): 1117-33.

Kumka, M., and J. Bonar. "Fascia: A Morphological Description and Classification System Based on a Literature Review." *The Journal of the Canadian Chiropractic Association* 56.3 (2012): 179-91.

Land, W. G. "The Role of Damage-Associated Molecular Patterns (Damps) in Human Diseases: Part Ii: Damps as Diagnostics, Prognostics and Therapeutics in Clinical Medicine." *Sultan Qaboos Univ Med J* 15.2 (2015): e157-70.

Lathia, J. D., and H. Liu. "Overview of Cancer Stem Cells and Stemness for Community Oncologists." *Target Oncol* 12.4 (2017): 387-99.

Lee, S., and K. Margolin. "Cytokines in Cancer Immunotherapy." *Cancers* 3.4 (2011): 3856-93.

Lee, Y.C., *et al.* "Differences in Survival between Colon and Rectal Cancer from Seer Data." *PLoS ONe* 8.11 (2013).

Levin, T.R. "Colorectal Cancer Screening: 80% by 2018. Colonoscopists Simply Cannot Do It Alone." *Gastrointestinal Endoscopy* 83.3 (2016).

Liemert, A., and A. Kienle. "Explicit Solutions of the Radiative Transport Equation in the P3 Approximation." *Medical Physics* 41.11 (2014).

---. "Light Transport in Three-Dimensional Semi-Infinite Scattering Media." *Journal of the Optical Society of America: Optics, Image Science, and Vision* 29.7 (2012).

Lievre, A., *et al.* "Clinical Value of Mitochondrial Mutations in Colorectal Cancer." *J Clin Oncol* 23.15 (2005): 3517-25.

Lim, D. R., *et al.* "Comparison of Oncological Outcomes of Right-Sided Colon Cancer Versus Left-Sided Colon Cancer after Curative Resection: Which Side Is Better Outcome?" *Medicine (Baltimore)* 96.42 (2017).

Lim, S.Y., *et al.* "Targeting the Ccl2-Ccr2 Signaling Axis in Cancer Metastasis." *Oncotarget* 7.19 (2016): 18697-710.

Lister, T., *et al.* "Optical Properties of Human Skin." *Journal of Biomedical Optics* 17.9 (2012).

Liu, Y., and X. Cao. "The Origin and Function of Tumor-Associated Macrophages." *Cellular & Molecular Immunology* 12.1 (2015): 1-4.

Luo, Z., *et al.* "Colon Cancer Treatment Costs for Medicare and Dually Eligible Beneficiaries " *Health Care Financing Review* 31.1 (2009): 35-50.

Lynch, D., and A. Murphy. "The Emerging Role of Immunotherapy in Colorectal Cancer." *Annals of Translational Medicine* 4.16 (2016): 305.

Maindrault-Goebel, F., *et al.* "Evaluation of Oxaliplatin Dose Intensity in Bimonthly Leucovorin and 48-Hour 5-Fluorouracil Continuous Infusion Regimens (Folfox) in Pretreated Metastatic Colorectal Cancer. Oncology Multidisciplinary Research Group (Gercor)." *Ann Oncol* 11.11 (2000): 1477-83.

Mansour, R. N., *et al.* "Evaluation of Hypoxia Inducible Factor-1 Alpha Gene Expression in Colorectal Cancer Stages of Iranian Patients." *J Cancer Res Ther* 12.4 (2016): 1313-17.

Manzat Saplacan, R. M., *et al.* "The Role of Pdgfs and Pdgfrs in Colorectal Cancer." *Mediators Inflamm* 2017 (2017): 4708076.

Marech, I., *et al.* "Tumour-Associated Macrophages Correlate with Microvascular Bed Extension in Colorectal Cancer Patients." *Journal of Cellular and Molecular Medicine* 20.7 (2016): 1373-80.

Marin, N.M., *et al.* "Diffuse Reflectance Patterns in Cervical Spectroscopy." *Gynecologic Oncology* 99.3 (2005): 116-20.

Marley, A.R., and H. Nan. "Epidemiology of Colorectal Cancer." *International Journal of Molecular Epidemiology and Genetics* 7.3 (2016): 105-14.

Martin, S.T., *et al.* "Systematic Review and Meta-Analysis of Outcomes Following Pathological Complete Response to Neoadjuvant Chemoradiotherapy for Rectal Cancer." *The British Journal of Surgery* 99.7 (2012): 918-28.

Maxwell, P. H., *et al.* "The Pvhl-Hif-1 System. A Key Mediator of Oxygen Homeostasis." *Adv Exp Med Biol* 502 (2001): 365-76.

Mehrvarz Sarshekeh, M., *et al.* "Nivolumab in the Treatment of Microsatellite Instability High Metastatic Colorectal Cancer." *Future Oncology* (2018).

Mik, M., *et al.* "Right- and Left-Sided Colon Cancer – Clinical and Pathological Differences of the Disease Entity in One Organ." *Arch Med Sci* 13.1 (2017): 157-62.

Monteil, J., *et al.* "Chemotherapy Response Evaluation in Metastatic Colorectal Cancer with Fdg Pet/Ct and Ct Scans." *Anticancer Research* 29.7 (2009): 2563-8.

Mourant, J.R., *et al.* "Mechanisms of Light Scattering from Biological Cells Relevant to Noninvasive Optical-Tissue Diagnostics." *Applied Optics* 37.16 (1998): 3586-93.

Muldoon, T.J., *et al.* "High-Resolution Imaging in Barrett's Esophagus: A Novel, Low-Cost Endoscopic Microscope." *Gastrointestinal Endoscopy* 68.4 (2008): 737-44.

Muldoon, T.J., *et al.* "Subcellular-Resolution Molecular Imaging within Living Tissue by Fiber Microendoscopy." *Optics Express* 15.25 (2007): 16413-23.

Muldoon, T.J., *et al.* "Noninvasive Imaging of Oral Neoplasia with a High-Resolution Fiber-Optic Microendoscope." *Head & Neck* 34.3 (2011): 305-12.

Muldoon, T.J., *et al.* "Evaluation of Quantitative Image Analysis Criteria for the High-Resolution Microendoscopic Detection of Neoplasia in Barrett's Esophagus." *Journal of Biomedical Optics* 15.2 (2010): 026027.

Mundade, R., *et al.* "Genetic Pathways, Prevention, and Treatment of Sporadic Colorectal Cancer." *Oncoscience* 1.6 (2014): 400-6.

Navarro, M., *et al.* "Colorectal Cancer Population Screening Programs Worldwide in 2016: An Update." *World Journal of Gastroenterology* 23.20 (2017): 3632-42.

Nishida, N., *et al.* "Angiogenesis in Cancer." *Vascular Health and Risk Management* 2.3 (2006): 213-9.

Niu, J., *et al.* "Monocyte Chemotactic Protein (Mcp)-1 Promotes Angiogenesis Via a Novel Transcription Factor, Mcp-1-Induced Protein (Mcpip)." *J Biol Chem* 283.21 (2008): 14542-51.

Noordhuis, P., *et al.* "5-Fluorouracil Incorporation into Rna and DNA in Relation to Thymidylate Synthase Inhibition of Human Colorectal Cancers." *Annals of Oncology* 15.7 (2004): 1025-32.

Obeid, M., *et al.* "Calreticulin Exposure Dictates the Immunogenicity of Cancer Cell Death." *Nature Medicine* 13.1 (2007): 54-61.

Ojo-Amaize, E. A., *et al.* "Hypoestoxide Inhibits Tumor Growth in the Mouse Ct26 Colon Tumor Model." *World J Gastroenterol* 13.34 (2007): 4586-8.

Parikh, N., *et al.* "In Vivo Diagnostic Accuracy of High Resolution Microendoscopy in Differentiating Neoplastic from Non-Neoplastic Colorectal Polyps: A Prospective Study." *The American Journal of Gastroenterology* 109.1 (2014): 68-75.

Park, I.J., and C.S. Yu. "Current Issues in Locally Advanced Colorectal Cancer Treated by Preoperative Chemoradiotherapy." *World Journal of Gastroenterology* 20.8 (2014): 2023-9.

Pavlova, I., *et al.* "Fluorescence Spectroscopy of Oral Tissue: Monte Carlo Modeling with Site-Specific Tissue Properties." *Journal of Biomedical Optics* 14.1 (2009).

Pierce, M.C., *et al.* "A Pilot Study of Low-Cost, High-Resolution Microendoscopy as a Tool for Identifying Women with Cervical Precancer." *Cancer Prevention Research* 5.11 (2012): 1273-9.

Pierce, M.C., *et al.* "Accuracy of in Vivo Multi-Modal Optical Imaging for Detection of Oral Neoplasia." *Cancer Prevention Research* 5.6 (2012): 801-9.

Pierce, M.C., *et al.* "High-Resolution Fiber-Optic Microendoscopy for in Situ Cellular Imaging." *Journal of Visualized Experiments* 47 (2011).

Piyawattanametha, W., and T.D. Wang. "Mems-Based Dual Axes Confocal Microendoscopy." *IEEE Journal of Selected Topics in Quantum Electronics* 16.4 (2010): 804–14.

Prahl, S. "Optical Absorption of Hemoglobin." *Optical Properties Spectra*. Oregon Medical Laser Center 2015. Web.

Prieto, S.P., *et al.* "Proflavine Hemisulfate as a Fluorescent Contrast Agent for Point-of-Care Cytology." *PLOS One* 10.5 (2015): e0125598.

Qin, Q., *et al.* "Comparison of 627 Patients with Right- and Left-Sided Colon Cancer in China: Differences in Clinicopathology, Recurrence, and Survival." *Chronic Dis Transl Med* 3.1 (2017): 51-9.

Quinn, M.K., *et al.* "High-Resolution Microendoscopy for the Detection of Cervical Neoplasia in Low-Resource Settings." *PLOS One* 7.9 (2012).

Rajaram, N., *et al.* "Design and Validation of a Clinical Instrument for Spectral Diagnosis of Cutaneous Malignancy." *Applied Optics* 49.2 (2010): 142-52.

Rajaram, N., *et al.* "Experimental Validation of the Effects of Microvasculature Pigment Packaging on in Vivo Diffuse Reflectance Spectroscopy." *Lasers in Surgery and Medicine* 42.7 (2010): 680-8.

Rajaram, N., *et al.* "Optical Spectroscopy of Tumor Oxygenation and Metabolism in Preclinical Head and Neck Tumors That Fail Radiation Therapy." *Molecular Cancer Research* 14.1 (2016).

Rajaram, N., *et al.* "Lookup Table-Based Inverse Model for Determining Optical Properties of Turbid Media." *Journal of Biomedical Optics* 13.5 (2008): 050501.

Rajaram, N., *et al.* "Pilot Clinical Study for Quantitative Spectral Diagnosis of Non-Melanoma Skin Cancer." *Lasers in Surgery and Medicine* 42.10 (2010): 716-27.

Reif, R., *et al.* "Analytical Model of Light Reflectance for Extraction of the Optical Properties in Small Volumes of Turbid Media." *Applied Optics* 46.29 (2007).

Rivera, D.R., *et al.* "Compact and Flexible Raster Scanning Multiphoton Endoscope Capable of Imaging Unstained Tissue." *PNAS* 108.43 (2011): 17598-603.

Roblyer, D., *et al.* "Optical Imaging of Breast Cancer Oxyhemoglobin Flare Correlates with Neoadjuvant Chemotherapy Response One Day after Starting Treatment." *PNAS* 108.35 (2011): 14626-31.

Romanov, O.G., *et al.* "Modeling of Light Propagation in Turbid Media: Application to Biological Tissues." *Nonlinear phenomena in complex systems* 15.4 (2012).

Rosenberg, S.A., *et al.* "Adoptive Cell Transfer: A Clinical Path to Effective Cancer Immunotherapy." *Nature Reviews Cancer* 8.4 (2008): 299-308.

Roy, A., and P. E. Kolattukudy. "Monocyte Chemotactic Protein-Induced Protein (Mcpip) Promotes Inflammatory Angiogenesis Via Sequential Induction of Oxidative Stress, Endoplasmic Reticulum Stress and Autophagy." *Cell Signal* 24.11 (2012): 2123-31.

Sandell, J.L., and T.C. Zhu. "A Review of in-Vivo Optical Properties of Human Tissues and Its Impact on Pdt." *Journal of Biophotonics* 4.11 (2011): 773-87.

Santoyo-Ramos, P., *et al.* "Hypoxia-Inducible Factors Modulate the Stemness and Malignancy of Colon Cancer Cells by Playing Opposite Roles in Canonical Wnt Signaling." *PLoS One* 9.11 (2014).

Schols, R.M., *et al.* "Automated Spectroscopic Tissue Classification in Colorectal Surgery." *Surgical Innovation* 22.6 (2015): 557-67.

Schwarz, R.A., *et al.* "Autofluorescence and Diffuse Reflectance Spectroscopy of Oral Epithelial Tissue Using a Depth-Sensitive Fiber-Optic Probe." *Applied Optics* 47.6 (2008): 825-34.

Semenza, G. L. "Defining the Role of Hypoxia-Inducible Factor 1 in Cancer Biology and Therapeutics." *Oncogene* 29.5 (2010): 625-34.

Shah, N., *et al.* "The Role of Diffuse Optical Spectroscopy in the Clinical Management of Breast Cancer." *disease Markers* 19.3 (2004): 95-105.

Sharma, M., *et al.* "Design and Characterization of a Novel Multimodal Fiber-Optic Probe and Spectroscopy System for Skin Cancer Applications." *Review of Scientfic Instruments* 85 (2014): 083101.

Siegel, R.L., *et al.* "Cancer Statistics, 2018." *A Cancer Journal for Clinicians* 68.1 (2018): 7-30.

Sims, G. P., *et al.* "Hmgb1 and Rage in Inflammation and Cancer." *Annu Rev Immunol* 28 (2010): 367-88.

Society, American Cancer. "Colorectal Cancer Facts & Figures 2017-2019." (2017). Web.

Sosa, V., *et al.* "Oxidative Stress and Cancer: An Overview." *Ageing Res Rev* 12.1 (2013): 376-90.

Spliethoff, J.W., *et al.* "In Vivo Characterization of Colorectal Metastases in Human Liver Using Diffuse Reflectance Spectroscopy: Toward Guidance in Oncological Procedures." *Journal of Biomedical Optics* 21.9 (2016): 10.1117/1.JBO.21.9.097004.

Spliethoff, J.W., *et al.* "Monitoring of Tumor Response to Cisplatin Using Optical Spectroscopy." *Translational Oncology* 7.2 (2014): 230-9.

Stadler, A.M., *et al.* "Hemoglobin Dynamics in Red Blood Cells: Correlation to Body Temperature." *Biophysical Journal* 95.11 (2008): 5449-61.

Stigliano, V., *et al.* "Early-Onset Colorectal Cancer: A Sporadic or Inherited Disease?" *World J Gastroenterol* 20.35 (2014): 12420-30.

Subramanian, H., *et al.* "Penetration Depth of Low-Coherence Enhanced Backscattered Light in Subdiffusion Regime." *Physical Review E: Statistical, Nonlinear, and Soft Matter Physics* 75.4 (2007): 041914.

Sugita, J., *et al.* "Close Association between Fas Ligand (Fasl; Cd95l)-Positive Tumor-Associated Macrophages and Apoptotic Cancer Cells Along Invasive Margin of Colorectal Carcinoma: A Proposal on Tumor-Host Interactions." *Japanese Journal of Cancer Research* 93.3 (2002): 320-8.

Tabassum, S., *et al.* "Two-Layer Inverse Model for Improved Longitudinal Preclinical Tumor Imaging in the Spatial Frequency Domain." *J Biomed Opt* 23.7 (2018): 1-12.

Tafani, M., *et al.* "The Interplay of Reactive Oxygen Species, Hypoxia, Inflammation, and Sirtuins in Cancer Initiation and Progression." *Oxidative Medicine and Cellular Longevity* 2016.3907147 (2016).

Tanis, E., *et al.* "In Vivo Tumor Identification of Colorectal Liver Metastases with Diffuse Reflectance and Fluorescence Spectroscopy." *Lasers in Surgery and Medicine* 48.9 (2016): 820-27.

Tanis, E., *et al.* "Real-Time in Vivo Assessment of Radiofrequency Ablation of Human Colorectal Liver Metastases Using Diffuse Reflectance Spectroscopy." *European Journal of Surgical Oncology* 42.2 (2016): 251-9.

Tromberg, B.J., *et al.* "Predicting Responses to Neoadjuvant Chemotherapy in Breast Cancer: Acrin 6691 Trial of Diffuse Optical Spectroscopic Imaging (Dosi)." *Cancer Research* 76.20 (2017): 5933-44.

Turley, R.S., *et al.* "Bevacizumab-Induced Alterations in Vascular Permeability and Drug Delivery: A Novel Approach to Augment Regional Chemotherapy for in-Transit Melanoma." *Clinical Cancer Research* 18.12 (2012): 3328-39.

Turzhitsky, V., *et al.* "A Predictive Model of Backscattering at Subdiffusion Length Scales." *Biomedical Optics Express* 1.3 (2010): 1034-46.

Turzhitsky, V., *et al.* "Characterization of Light Transport in Scattering Media at Sub-Diffusion Length Scales with Low-Coherence Enhanced Backscattering." *IEEE Journal of Selected Topics in Quantum Electronics* 16.3 (2010): 619-26.

Ucuzian, A.A., *et al.* "Molecular Mediators of Angiogenesis." *Journal of Burn Care and Research* 31.1 (2011).

Ueda, S., *et al.* "Baseline Tumor Oxygen Saturation Correlates with a Pathologic Complete Response in Breast Cancer Patients Undergoing Neoadjuvant Chemotherapy." *Cancer Research* 72.17 (2013): 4318-28.

Ulivi, P., *et al.* "Relationship between Hypoxia and Response to Antiangiogenic Therapy in Metastatic Colorectal Cancer." *Oncotarget* 7.29 (2016): 46678-91.

Vadde, R., *et al.* "Role of Hypoxia-Inducible Factors (Hif) in the Maintenance of Stemness and Malignancy of Colorectal Cancer." *Crit Rev Oncol Hematol* 113 (2017): 22-27.

Waldmann, T.A. "Cytokines in Cancer Immunotherapy." *Cold Spring Harbor Perspectives in Biology* a028472 (2017).

Walker, A.S., *et al.* "Future Directions for Monitoring Treatment Response in Colorectal Cancer." *Journal of Cancer* 5.1 (2014): 44-57.

Wang, H.W., *et al.* "Diffuse Reflectance Spectroscopy Detects Increased Hemoglobin Concentration and Decreased Oxygenation During Colon Carcinogenesis from Normal to Malignant Tumors " *Optics Express* 17.4 (2009): 825-34.

Wang, J., *et al.* "Notch Signaling in Cancer Stem Cells." *Adv Exp Med Biol* 727 (2012): 174-85.

Wang, K., *et al.* "Long-Term Postoperative Survival Prediction in Patients with Colorectal Liver Metastasis." *Oncotarget* 8.45 (2017): 79927-34.

Weiner, L.M., *et al.* "Monoclonal Antibodies for Cancer Immunotherapy." *The Lancet* 373.9668 (2009): 1033-40.

Wilson, R.H., and M.A. Mycek. "Models of Light Propagation in Human Tissue Applied to Cancer Diagnostics." *Technology in Cancer Research and Treatment* 10.2 (2011).

Wolmark, N., *et al.* "Clinical Trial to Assess the Relative Efficacy of Fluorouracil and Leucovorin, Fluorouracil and Levamisole, and Fluorouracil, Leucovorin, and Levamisole in Patients with Dukes' B and C Carcinoma of the Colon: Results from National Surgical Adjuvant Breast and Bowel Project C-04." *J Clin Oncol* 17.11 (1999): 3553-9.

Xiang, B., *et al.* "Colorectal Cancer Immunotherapy." *Discovery Medicine* 15.84 (2014): 301-8.

Xue, X., *et al.* "Hypoxia-Inducible Factor-2alpha Activation Promotes Colorectal Cancer Progression by Dysregulating Iron Homeostasis." *Cancer Res* 72.9 (2012): 2285-93.

Yabroff, K.R., *et al.* "Economic Burden of Cancer in the Us: Estimates, Projections, and Future Research." *Cancer Epidemiology, Biomarkers & Prevention* 20.10 (2011): 2006-14.

Yabroff, K.R., *et al.* "Projections of the Costs Associated with Colorectal Cancer Care in the United States, 2000–2020." *Health Economics* 17.8 (2007).

Yamagishi, H., *et al.* "Molecular Pathogenesis of Sporadic Colorectal Cancers." *Chin J Cancer* 35 (2016).

Yoshidome, H., *et al.* "Significance of Monocyte Chemoattractant Protein-1 in Angiogenesis and Survival in Colorectal Liver Metastases." *Int J Oncol* 34.4 (2009): 923-30.

Yu, B., *et al.* "Diffuse Reflectance Spectroscopy of Epithelial Tissue with a Smart Fiber-Optic Probe." *Biomedical Optics Express* 5.3 (2014): 675-89.

Zhang, N., *et al.* "5-Fluorouracil: Mechanisms of Resistance and Reversal Strategies." *Molecules* 13.8 (2008): 1551-69.

Zhang, X., *et al.* "Macrophages Induce Resistance to 5-Fluorouracil Chemotherapy in Colorectal Cancer through the Release of Putrescine." *Cancer Letters* 381.2 (2016): 305-13.

Zhou, H., *et al.* "Expression of Oct-4 Is Significantly Associated with the Development and Prognosis of Colorectal Cancer." *Oncol Lett* 10.2 (2015): 691-6.

Zhou, Q., *et al.* "The Density of Macrophages in the Invasive Front Is Inversely Correlated to Liver Metastasis in Colon Cancer." *Journal of Translational Medicine* 8.13 (2010): 1-9.

Zhou, Z., *et al.* "Preoperative Chemotherapy for Locally Advanced Resectable Colon Cancer - a New Treatment Paradigm in Colon Cancer?" *Annals of Translational Medicine* 1.2 (2013): 11.

Ziai, J., *et al.* "Cd8+ T Cell Infiltration in Breast and Colon Cancer: A Histologic and Statistical Analysis." *PloS One* 13.1 (2018).

Zonios, G., and A. Dimou. "Modeling Diffuse Reflectance from Homogeneous Semi-Infinite Turbid Media for Biological Tissue Applications: A Monte Carlo Study." *Biomed Opt Express* 2.12 (2011): 3284-94.

Zonios, G., *et al.* "Diffuse Reflectance Spectroscopy of Human Adenomatous Colon Polyps in Vivo." *Applied Optics* 38.31 (1999): 6628-37.

Chapter 2 (Specific Aim 1): Design and characterization of broadband diffuse reflectance spectroscopy probes for *in vivo* tissue analysis

2.1 Introduction

Several recent non-invasive translational endoscopy-based techniques have aimed at improving cancer detection and monitoring tumor therapeutic response in both oral intraepithelial dysplasia and colon carcinoma.

Intraepithelial dysplastic progression within the oral mucosa is a dynamic process that typically arises at the basement membrane and is classified into stages based on how far it has spread towards the upper epithelial layers (Zhu and Liu, 2011; Speight, 2007; Warnakulasuriya *et al.*, 2008; Bouquot *et al.*, 2006). For example, mild dysplasia occurs in the basal epithelial layers, directly above the basement membrane. As dysplasia progresses upwards towards the apical epithelial surface, the stages are characterized as moderate and severe (or carcinoma *in-situ*), respectively (Speight, 2007; Warnakulasuriya *et al.*, 2008; Bouquot *et al.*, 2006). These stages are not considered invasive cancer since they have not yet penetrated the basement membrane and metastasized, although the severity of dysplasia increases this risk (Speight, 2007; Bouquot *et al.*, 2006). It has been found that <5%, 3-15%, and >15% of patients with mild, moderate, and severe dysplasia, respectively, progressed to carcinoma (Speight, 2007; Bouquot *et al.*, 2006). Oral squamous cell carcinoma (OSCC) is the most common form of this carcinoma in the oral cavity and patients diagnosed with OSCC have a 5-year survival rate of less than 60-70% and this number decreases in developing countries (Speight, 2007; Davies *et al.*, 2015; Cheng *et al.*, 2015; Muldoon *et al.*, 2011). This is because primary detection of dysplastic malignancies typically occurs upon visual inspection by non-specialized dentists, who then refer

patients to specialists (Davies *et al.*, 2015; Brailo, 2015; Brocklehurst *et al.*, 2015). Diagnoses at this point are often late-stage (Brailo, 2015). Therefore, detection of oral dysplasia at its various stages via affordable, available, and non-invasive techniques is crucial in limiting the number of cases that progress to OSCC.

Gastrointestinal dysplasia is an abnormal but non-invasive proliferation of cells in the gastrointestinal epithelium that, when diagnosed, is assumed to progress to carcinoma (Sharma, 2013; Speight, 2007). In the oral cavity and esophagus, dysplasia can potentially become squamous cell carcinoma (SCC) or adenocarcinoma, cancer of the stratified squamous epithelium or columnar glandular cells, respectively (Speight, 2007). Most adenocarcinomas arise from dysplastic changes associated with Barrett's esophagus, although SCC is more prevalent in the upper digestive tract worldwide (Zhang, 2013). In the colorectal region, dysplasia can form adenomatous polyps which become invasive upon penetration into the submucosa (Harpaz and Polydorides, 2010; Ponz de Leon and Di Gregorio, 2001). Dysplasia can also arise in the epithelia of other organs. For example, cervical dysplasia, which can be either squamous or columnar in origin, leads to increased risk of cervical cancer (Arends *et al.*, 1998). Conventional practice for diagnosing dysplasia in the lumen of the gastrointestinal tract is endoscopy-guided biopsy with wide-field, broadband illumination followed by histological examination by a pathologist using hematoxylin and eosin (H&E) staining (Hwang and Shroyer, 2012; Dacosta *et al.*, 2002; Muldoon *et al.*, 2011). However, diagnosis in this way may be subject to sampling errors and is subjective to the experience of the pathologist, potentially limiting reproducibility (Appelman, 2005; Dacosta *et al.*, 2002; Muldoon *et al.*, 2011).

One such technique aimed at improving cancer detection and monitoring tumor therapeutic response is high-resolution microendoscopy, which can provide clinicians rapid,

high-resolution visualization of tissue architecture and histology when compared to that of the naked eye alone. These techniques provide a step towards point-of-care "optical biopsy," potentially reducing the number of biopsies performed each year (Muldoon *et al.*, 2011; Shukla *et al.*, 2011). Preclinical and clinical studies using high-resolution microendoscopy techniques have been demonstrated in various body organs including the oral cavity (Muldoon *et al.*, 2011; Pierce, Schwarz, *et al.*, 2012), esophagus (Hur *et al.*, 2015; Muldoon *et al.*, 2008; Muldoon *et al.*, 2010; Shin *et al.*, 2015), lower gastrointestinal tract (Carns *et al.*, 2013; Chang *et al.*, 2013; Elahi *et al.*, 2011; Louie *et al.*, 2014; Parikh *et al.*, 2014; Prieto, Powless, Lai, *et al.*, 2015), cervix (Pierce, Guan, *et al.*, 2012; Quinn *et al.*, 2012), ear (Campbell *et al.*, 2010; Levy *et al.*, 2013; Monfared *et al.*, 2006), and liver and pancreas (Regunathan *et al.*, 2012). Furthermore, several studies have developed high-resolution imaging techniques compatible with the biopsy port of conventional white-light endoscopes, making it more attractive for clinicians to adopt these new techniques (Muldoon *et al.*, 2008; Shukla *et al.*, 2011; Louie *et al.*, 2014). Work has also been performed in quantifying high-resolution microendoscopy image data, but for the most part this remains a qualitative screening technique (Muldoon *et al.*, 2010; Shin *et al.*, 2015; Prieto, Powless, Lai, *et al.*, 2015; Ishijimi *et al.*, 2015). The advantages of high-resolution microendoscopy are low cost, portability, and instantaneous imaging of tissue architecture. However, a drawback of high-resolution microendoscopy is lack of depth sectioning, meaning it can only resolve tissue architecture at the apical epithelial surface. More complex instrumentation does exist to overcome this drawback, including laser scanning confocal systems, but this instrumentation requires galvanometers or microelectromechanical (MEMS)-based technology to do so. Additionally, information gathered by these more complex depth-sensitive technologies are primarily qualitative (Greening, James, Powless, *et al.*, 2015; Rivera *et*

al., 2011; Chen *et al.*, 2015; Piyawattanametha and Wang, 2010). High-resolution microendoscopy can thus benefit from additional depth sensitive modalities since mild and moderate dysplasia are often sub-epithelial surface phenomena, but relatively simple and quantitative techniques are desirable.

One depth sensitive technique that has demonstrated diagnostic efficacy is diffuse reflectance spectroscopy (DRS), a well-established method capable of non-invasively quantifying volume-averaged tissue optical parameters using simple probe designs (Glennie *et al.*, 2014; Rajaram, Aramil, *et al.*, 2010; Rajaram, Gopal, *et al.*, 2010; Rajaram, Reichenberg, *et al.*, 2010; Bish *et al.*, 2014; Karsten *et al.*, "Diffuse Reflectance Spectroscopy as a Tool to Measure the Absorption Coefficient in Skin: South African Skin Phototypes," 2013; Hennessy *et al.*, 2013), Raw DRS data is given in terms of reflectance, that is, the percentage of light recovered from a detection fiber to light delivered by a source fiber. Studies have shown that volume-averaged optical properties, such as reduced scattering coefficient (μ_s') and absorption coefficient (μ_a) can be determined from *in vivo* samples (Rajaram, Aramil, *et al.*, 2010; Karsten *et al.*, "Diffuse Reflectance Spectroscopy as a Tool to Measure the Absorption Coefficient in Skin: South African Skin Phototypes," 2013; Rajaram *et al.*, 2008; Karsten *et al.*, "Diffuse Reflectance Spectroscopy as a Tool to Measure the Absorption Coefficient in Skin: System Calibration," 2013; Vishwanath *et al.*, 2011; Yu *et al.*, 2008; Yu *et al.*, 2010; Bish *et al.*, 2011; Pimenta *et al.*, 2012; Nichols *et al.*, 2015). It should be noted that these extracted values are based on the delivery and collection of light throughout an often inhomogeneous layered media, such as tissue, and extracted optical properties thus represent volume averaged, rather than axially resolved, values. Several *in vivo* DRS studies have extracted other clinically relevant optical parameters including blood volume fraction, hemoglobin concentration, oxygen

saturation, mean blood vessel diameter, nicotinamide adenine dinucleotide (NADH) concentration, and tissue thickness (Rajaram, Aramil, *et al.*, 2010; Rajaram, Gopal, *et al.*, 2010; Rajaram, Reichenberg, *et al.*, 2010; Bish *et al.*, 2014; Lim *et al.*, 2011; Nichols *et al.*, 2012; Sharma *et al.*, 2014; Sharma *et al.*, 2013; Hennessy *et al.*, 2015). Furthermore, DRS is an appealing non-invasive screening technique because it is sensitive to optical changes beneath the apical tissue layer (Glennie *et al.*, 2014; Rajaram, Aramil, *et al.*, 2010; Rajaram, Gopal, *et al.*, 2010; Rajaram, Reichenberg, *et al.*, 2010; Bish *et al.*, 2014; Karsten *et al.*, "Diffuse Reflectance Spectroscopy as a Tool to Measure the Absorption Coefficient in Skin: South African Skin Phototypes," 2013; Hennessy *et al.*, 2013; Rajaram *et al.*, 2008; Karsten *et al.*, "Diffuse Reflectance Spectroscopy as a Tool to Measure the Absorption Coefficient in Skin: System Calibration," 2013; Vishwanath *et al.*, 2011; Yu *et al.*, 2008; Yu *et al.*, 2010; Bish *et al.*, 2011; Pimenta *et al.*, 2012; Nichols *et al.*, 2015; Lim *et al.*, 2011; Nichols *et al.*, 2012; Sharma *et al.*, 2013; Sharma *et al.*, 2014; Hennessy *et al.*, 2015). However, a drawback of DRS is inability to spatially resolve tissue architecture.

We have recently reported on a probe-based technique that combines high-resolution microendoscopy imaging, and DRS (Rajaram *et al.*, 2008; Durduran *et al.*, 2010; Dehghani *et al.*, 2009; Subramanian *et al.*, 2007; Turzhitsky, Radosevich, *et al.*, 2010; Turzhitsky, Rogers, *et al.*, 2010). This hybrid fiber-bundle spectroscopy and imaging probe is capable of co-registering qualitative high-resolution images of tissue surface microarchitecture with complimentary quantitative and depth-sensitive spectral data (Greening, James, Powless, *et al.*, 2015; Greening, Powless, *et al.*, 2015). Furthermore, our design uses two SDSs (shallow and deep channels) to collect data at two different sampling depths with the goal of sampling different tissue volumes. Therefore, the high-resolution imaging modality may be beneficial in providing image data of

later stage moderate and severe dysplasia while the DRS modality may be sensitive to tissue optical changes associated with early dysplasia arising at the basement membrane (Greening, James, Powless, *et al.*, 2015).

In this manuscript, we validate the DRS portion of the quantitative hybrid imaging and spectroscopy microendoscope and present a pilot phantom and pre-clinical study to extract *in vivo* optical parameters of the human oral mucosa. First, a set of calibration phantoms was used to generate reflectance lookup tables (LUT) describing the relationship between reflectance and optical properties (μ_s' and μ_a) for the DRS modality (Rajaram *et al.*, 2008). Then, to validate the LUT, the probe and LUT-based inverse model was used to extract μ_s' and μ_a from a set of hemoglobin-based validation phantoms with known μ_s' and μ_a (Rajaram *et al.*, 2008). Extracted optical properties were compared to theoretical values and reported as percent errors. Next, we quantify sampling depth for the shallow and deep SDSs of the DRS modality and validate results using the same calibration and validation phantoms (Hennessy *et al.*, 2014). Following this, we present a simple phantom study simulating the physical layered progression from healthy tissue to severe dysplasia to show how reflectance changes with an optically scattering heterogeneity buried at various depths (Zhu and Liu, 2011; Bouquot *et al.*, 2006; Speight, 2007). Finally, the LUT-based inverse model was demonstrated on *in vivo* human oral mucosa from thirteen healthy volunteers in a laboratory setting to determine volume-averaged scattering exponent, hemoglobin concentration, oxygen saturation, and sampling depth. The extracted *in vivo* quantitative optical parameters were compared to an *in vivo* high-resolution image of healthy, non-keratinized oral tissue. These studies validate our hybrid fiber-bundle imaging and spectroscopy technique and demonstrate the translational potential to a clinical setting. This technique can potentially be used

to for diagnostic purposes as well as dynamically monitoring personalized tumor response to therapy.

2.2 Rationale

This multimodal instrumentation and associated technique is the first combination of these modalities within a single probe, although other combined structural/functional techniques do exist that combine different modalities. For example, hyperspectral imaging combines wide-field imaging with quantitative hemoglobin and melanin properties (Ghassemi *et al.*, 2014; Vasefi *et al.*, 2014), and other techniques have been developed that combine optical coherence tomography (OCT) with analysis of tissue protein expression (Winkler *et al.*, 2010), to name a few. This article reports on a compact and easy-to-implement instrumentation setup that uses a general fiber-optic probe which can be optimized for various purposes including endoscopic use in the lower gastrointestinal tract and esophagus or as a handheld probe for use in the oral cavity and external skin placement (Greening, James, Powless, *et al.*, 2015; Bish *et al.*, 2014).

The hardware for this instrumentation requires both custom data acquisition and post-processing code to acquire diffuse reflectance spectra and then extract the resulting volume-averaged tissue physiological parameters including THC, [Mel], and StO_2. The custom data acquisition code was built to allow the simultaneous acquisition from a camera (for high-resolution fluorescence microscopy) and a spectrometer (for diffuse reflectance spectroscopy). Drivers are often available from the manufacturers' websites to allow integration with a variety of programming languages. The custom post-processing code imports *a priori* absorption values of *in vivo* THC and [Mel](Prahl, 1999) and then utilizes a previously developed nonlinear optimization fitting process that creates a fitted curve of the spectra (Rajaram, Aramil, *et al.*, 2010). The fitted curve is built by minimizing the χ^2 value between itself and the raw spectra and

determining the tissue physiological parameters (THC, [Mel], and StO_2) from the fitted curve and with the lowest χ^2 value (Rajaram, Aramil, *et al.*, 2010). The code can be modified to include absorption from other chromophores as well, such as the exogenous pyranine ink used here, so that target physiological parameters are unaffected.

Physiological indicators of tissue health, such as THC, [Mel], and StO_2, can be used as reports of tumor response to therapy or as indicators of local vascularization and angiogenesis (Hennessy *et al.*, 2015; Chang *et al.*, 2009). Including a high-resolution fluorescence microendoscopy modality helps guide probe placement and provides investigators with a more complete picture of the relationship between epithelial tissue structure and function. In this article, construction and application of the multimodal microendoscope is described (Greening, James, Powless, *et al.*, 2015).

2.3 Materials and Methods

2.3.1 Fiber-Optic Probe Design

The custom fiber-optic probe (Myriad Fiber Imaging, USA) used for this trimodal microendoscopy technique uses five 200/220 µm core/cladding, 0.22 NA multimode fibers (Molex Inc., USA) surrounding a 1 mm Fujikura image fiber (Myriad Fiber Imaging, USA) for a total of six fibers. The central 1 mm image fiber contains approximately 50,000 individual fiber elements 4.5 µm in diameter with center-to-center spacing of approximately 4.5 µm. The center-to-center separation between any one of the 200 µm fibers and the image fiber is 864 µm. Therefore, the closest edge of the image fiber to the center of any 200 µm fiber is approximately 350 µm. Similarly, the farthest edge of the image fiber to the center of any 200 µm fiber is approximately 1,350 µm. The centers of each of the 200 µm fibers are separated by 25°. Based on this geometry, center-to-center SDS between adjacent 200 µm fibers with respect to the

leftmost fiber are 374, 730, 1,051, and 1,323 µm. For the purposes of this paper, only the first two SDSs (374 and 730 µm) were used for DRS measurements. The total length of the fiber-optic probe is 4 ft. in which the distal 2 ft. of the fiber-optic probe consists of a single probe tip 3 mm in diameter and the proximal 2 ft. of the fiber-optic probe, nearest the optical instrumentation, splits into six individual fibers corresponding to each fiber within the bundle. Each of the six fibers ends in an SMA905 connector and can be readily coupled to the microendoscopy instrumentation. Figure 1 shows the details of the fiber-optic probe (Greening, Powless, *et al.*, 2015). Figure 2 shows the details of the hybrid fiber-bundle imaging and spectroscopy system including the proximal instrumentation such as the imaging hardware, spectroscopy hardware, and the optical fiber switch.

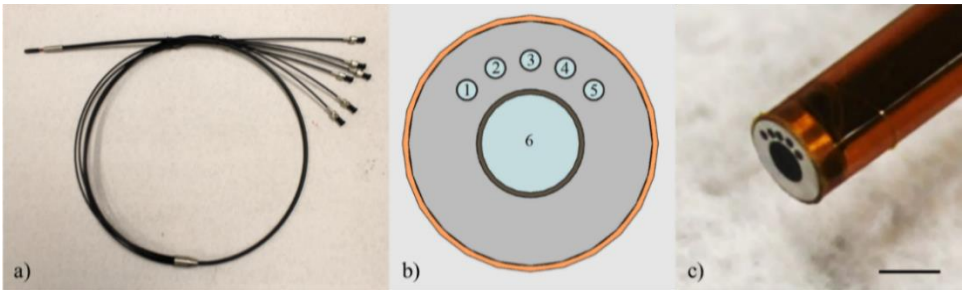

Figure 1. Fiber-optic probe showing **(a)** the full length (4 ft.) of the probe with the single bundle at the distal end and splitting into six individual bundles at the proximal end, **(b)** a schematic of the probe tip with the central 1 mm image fiber (#6) surrounded by five 200 µm multimode fibers (#1-5) separated by 25º. SDS between fiber #1 and the four adjacent fibers (#2-5) are 374, 730, 1051, and 1323 µm, respectively, and **(c)** close-up of the distal end of the fiber-optic probe (scale bar = 2 mm).

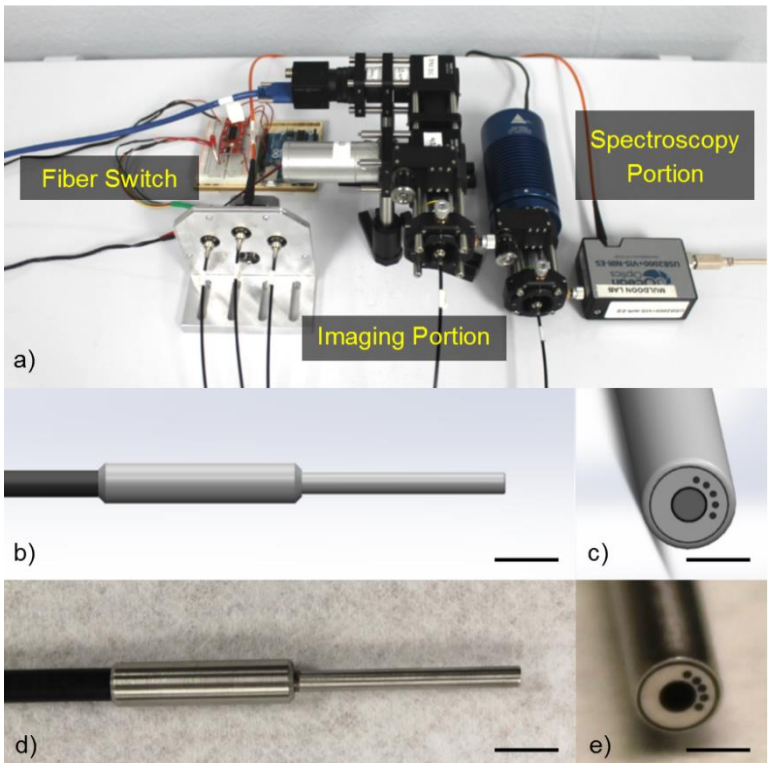

Figure 2. Representation of the hybrid fiber-bundle imaging and spectroscopy system showing (a) the major instrumentation components including (from left to right) fiber switch, imaging portion, and spectroscopy portion, (b) a SolidWorks representation of the distal probe (scale bar = 1 cm) showing the (c) en face view of the central 1 mm-diameter image fiber and 5 surrounding 200 μm multimode fibers (scale bar = 2.5 mm), (d) distal probe (scale bar = 1 cm), and (e) en face view of the distal probe tip (scale bar = 2.5 mm).

2.3.2 Instrumentation Design

Three light sources, corresponding to the three optical modes of the instrumentation, are delivered to the sample via the custom fiber-optic probe: an LED light source (Philips, USA) centered at 455 nm (20 nm FWHM), a broadband tungsten-halogen white light source (Ocean Optics, USA), and a 635 nm laser (Thorlabs, USA).

For the first mode (high-resolution, image fiber-based fluorescence imaging), light from the 455 nm LED passes through a 460 nm short pass excitation filter (Chroma Technology Corp., USA) and is directed into the back aperture of a 10X/0.30 NA infinity-corrected objective lens (Olympus Corp., Japan) using a 475 nm cut-off dichroic mirror (Chroma Technology Corp.,

USA). 455 nm excitation light passes through the 1 mm image fiber to the distal end of the probe, illuminating the sample with 1 mW of power. Samples fluorescently stained with proflavine excite in this wavelength range and emit light centered at approximately 515 nm which is collected by the image fiber (Prieto, Powless, Boice, *et al.*, 2015). Emission light passes through the 475 nm dichroic mirror and is reflected by a second dichroic mirror with a cut-off wavelength of 590 nm (Chroma Technology Corp., USA). This reflected emission light (centered at 515 nm) then passes through a 525/40 nm emission bandpass filter (Chroma Technology Corp., USA), a 50 mm tube lens (Thorlabs), and into an 8-bit, Flea3 USB 3.0 monochrome CMOS camera (Point Grey, Canada) (Greening, Powless, *et al.*, 2015; Muldoon *et al.*, 2007; Muldoon *et al.*, 2011; Pierce, Guan, *et al.*, 2012; Pierce *et al.*, 2011; Quinn *et al.*, 2012; Chang *et al.*, 2013; Keahey *et al.*, 2015; Parikh *et al.*, 2014). The CMOS camera thus provides magnified apical cell morphological data from the 1 mm-diameter field-of-view (FOV).

For the second mode (broadband DRS), broadband light (450-750 nm) from the tungsten-halogen lamp is coupled into one 200 μm fiber (fiber #1 from Figure 1) of the fiber-optic probe to deliver white light to the sample. The wavelength range is limited by the output of the tungsten-halogen source lamp. Sub-diffusely reflected light is collected by two adjacent 200 μm fibers (fiber #2 and #3 from Figure 1) with corresponding center-to-center SDS of 374 and 730 μm and delivered to a single visible-to-near infrared spectrometer (Ocean Optics, USA) with a spectral resolution of 0.36 nm. A custom designed motorized optical fiber switch allows the spectrometer to sequentially acquire from each collection fiber (Greening, Powless, *et al.*, 2015).

For the third mode (DRIM), the 635 nm laser is coupled into one 200 μm fiber (fiber #5 from Figure 1) of the fiber-optic probe to deliver light to the sample. Within the sample, laser light undergoes multiple scattering events and emitted light is collected by the central 1 mm

image fiber (Kanick *et al.*, 2014; Turzhitsky, Radosevich, *et al.*, 2010). This emitted 635 nm light passes through both the 475 and 590 nm cut-off dichroic mirrors before being reflected by a 1-inch aluminum mirror (Thorlabs, USA). The collected 635 nm light then passes through a 610 nm long pass emission filter (Chroma Technology Corp., USA), a 50 mm tube lens (Thorlabs, USA), and into a second 8-bit, Flea3 USB 3.0 monochrome CMOS camera (Point Grey, Canada). A second camera is necessary so the resultant 2D sub-diffuse reflectance image maps have the same FOV and image area as the apical cell morphological data and thus can be directly compared. Both CMOS cameras presented here have a sensor array of 2080 x 1552 pixels 2.5 µm wide, a corresponding sensor size of 5.2 x 3.9 mm, and a dynamic range of 62.9 dB (Greening, Powless, *et al.*, 2015).

All modalities of the instrumentation are controlled with custom LabVIEW software (National Instruments, USA). Figure 3 shows a schematic of the fiber-bundle microendoscopy system along with images of the physical bench-top instrumentation.

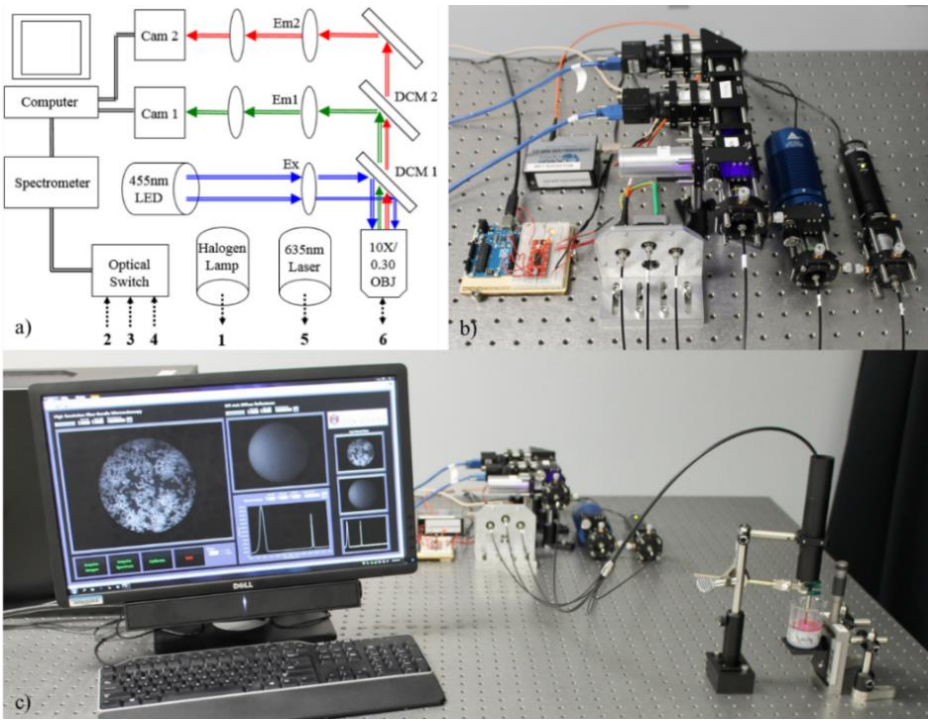

Figure 3. The trimodal microendoscope showing **(a)** a schematic illustrating major components. 455 nm light passes through a 460 nm short pass excitation filter (Ex). Emitted signal passes through a 10X objective, 475 nm dichroic mirror (DCM1), 525/40 nm emission filter (Em1), and into a camera (Cam 1). 635 nm DRIM signal passes through the objective lens, 475 (DCM1) and 590 nm dichroic mirrors (DCM2), 610 long pass filter (Em2), and into a camera (Cam 2). An optical fiber switch delivers reflected broadband light from the tungsten halogen lamp to a spectrometer. Finally, **(b)** shows a close-up of the optical components and **(c)** shows the optical components and custom LabVIEW software acquiring data from a hybrid cell phantom.

2.3.3 Assembly of the High-Resolution Fluorescence Microendoscopy Modality

Note: The outlined steps for assembly of the high-resolution fluorescence microendoscopy modality can be visualized in Figure 4.

1.1) Place a 470 nm dichroic mirror inside a 30 mm cage cube.

1.1.1) Obtain a 30 mm cage cube and remove the dichroic filter mount.

1.1.2) Place a 470 nm dichroic mirror in the dichroic filter mount.

1.1.3) Re-insert and secure the dichroic filter mount back inside the cage cube.

1.2) Attach cage assembly rods to the 30 mm cage cube.

1.2.1) Secure four 1.5 in. cage assembly rods to the front of the cage cube.

1.2.2) Secure four 3.0 in. cage assembly rods to the right side of the cage cube.

1.2.3) Secure two 2.0 in. cage assembly rods diagonally on the left side of the cage cube.

1.3) Build a cage plate/lens tube assembly.

1.3.1) Obtain a 1.0 in. threaded 30 mm cage plate and attach a stress free retaining ring to the inside of the cage plate using the provided threading.

1.3.2) Screw in a 1.0 in. lens tube to the stress-free retaining ring.

1.3.3) Attach a second 1.0 in. threaded 30 mm cage plate to the 1.0 in. lens tube and adjust the standard retaining rings so that the two cage plates are flush.

1.4) Slide the 1.0 in. cage plate/lens tube assembly onto the left side of the 30 mm cage cube.

1.5) Build the right-angle mirror mount assembly.

1.5.1) Obtain a right-angle mirror mount and a 1.0 in. UV-enhanced aluminum mirror.

1.5.2) Place the 1.0 in. UV-enhanced aluminum mirror into the mirror mount and tighten.

1.5.3) Secure four 2.0 in. cage assembly rods to the front of mirror mount

1.5.4) Secure two 2.0 in. cage assembly rods diagonally on the right side of the cage cube.

1.6) Connect the right-angle mirror mount assembly onto the left side of the 1.0 in. cage plate/lens tube assembly by placing the opposing cage assembly rods through the respective openings of the 30 mm cage plate.

1.7) Thread a z-axis translation mount through the 3.0 in. cage assembly rods on the right side of the assembly.

1.8) Attach a 10X achromatic objective lens to the z-axis translation mount.

1.9) Build a 1.0 in. fiber adaptor plate/xy-axis translation lens mount assembly.

1.9.1) Obtain an xy-axis translation mount and an 1.0 in. fiber adaptor plate.

1.9.2) Secure the 1.0 in. fiber adaptor plate into the xy-axis translation lens mount.

1.10) Slide the 1.0 in. fiber adaptor/xy-axis translation lens mount assembly in front of the objective lens.

1.11) Obtain two 0.5 in. long, 1.0 in. diameter lens tubes, one 440/40 nm bandpass filter (excitation filter) and one 525/36 nm bandpass filter (emission filter).

1.12) Place each filter inside a 0.5 in. long, 1.0 in. diameter lens tube, such that the arrow on the outside of the filter is facing the side of the lens tube with the external threads.

1.13) Attach the filters to the assembly.

1.13.1) Obtain two standard retaining rings.

1.13.2) Secure the filters inside the 0.5 in. long, 1.0 in. diameter lens tubes with the standard retaining rings.

1.13.3) Screw in the lens tube with the excitation filter to the front of the 30 mm cage cube and screw in the lens tube with the emission filter to the right-angle mirror mount.

1.13.4) Screw in the 0.5 in. lens tube with the emission filter to the front of the right-angle mirror mount.

1.14) Obtain two 1.0 in. threaded 30 mm cage plates and place them in front of the 0.5 in. long, 1.0 in. diameter lens tubes containing the filters.

1.15) Using epoxy or strong adhesive, attach a 455 nm LED to the cage plate connected to the excitation filter.

1.16) Obtain one 0.5 in. long, 1.0 in. diameter lens tube and a 1.0 in. achromatic doublet tube lens with focal length of 50 mm.

1.17) Place the tube lens inside the lens tube such that the arrow on the outside of lens is facing the side of the lens tube with the external threads.

1.18) Screw in the tube lens to the assembly.

1.18.1) Obtain one standard retaining ring.

1.18.2) Secure the lens inside the 0.5 in. long, 1.0 in. diameter lens tube with the standard retaining ring.

1.18.3) Attach the lens tube with the tube lens to the left-most cage plate.

1.19) Place a 30 mm cage plate in front of the 0.5 in. long, 1.0 in. diameter lens tube containing the tube lens.

1.20) Attach a stress-free retaining ring to the inside of the 30 mm cage plate.

1.21) Attach a USB monochrome camera to the cage plate with the stress-free retaining ring.

1.22) Construct the optical post mounting devices.

1.22.1) Obtain four 0.5 in. post holders, four 0.5 in. optical posts, and four mounting bases.

1.22.2) Secure the 0.5 in. optical posts inside the 0.5 in. post holders.

1.23.3) Secure the 0.5 in. post holders onto the mounting bases.

1.23) Screw in the four optical post mounting devices to the screw holes located under the 30 mm cage cube, the right-angle mirror mount, the cage plate connected to the LED, and the cage plate connected to the camera.

1.24) Screw in the four the optical post mounting devices to either an optical breadboard or optical table to finish construction of the high-resolution fluorescence microendoscopy modality.

Figure 4. Assembly of the high-resolution fluorescence microendoscopy modality. The high-resolution fluorescence microendoscopy modality can be constructed by building a shell of 1.0 in. diameter-sized components, with special care taken in handling the dichroic mirror, objective lens, excitation/emission filters, and tube lens. Glass surfaces of these components must be carefully handled using lens paper.

2.3.4 Assembly of the Diffuse Reflectance Spectroscopy Modality

Note: The outlined steps for assembly of the sub-diffuse reflectance spectroscopy modality can be visualized in Figure 5.

2.1) Obtain a tungsten-halogen light source and, using epoxy or a strong adhesive, secure a 1.0 in. threaded 30 mm cage plate onto the front.

2.2) Secure four 3.0 in. cage assembly rods to the cage plate.

2.3) Attach a z-axis translation mount to the cage assembly rods.

2.4) Screw in a 20X achromatic objective lens to the z-axis translation mount.

2.5) Build a fiber adaptor plate/xy-axis translation lens mount assembly.

2.5.1) Obtain an xy-axis translation mount and an 1.0 in. fiber adaptor plate.

2.5.2) Secure the fiber adaptor plate into the xy-axis translation lens mount.

2.6) Slide the 1.0 in. fiber adaptor/xy-translation mount assembly in front of the objective lens.

2.7) Build the motor arm assembly.

2.7.1) Obtain the custom-built aluminum motor arm and one SMA fiber adaptor plate.

2.7.2) Screw in the fiber adaptor plate (with external threading) into the aluminum motor arm (with internal threading).

2.7.3) Attach the custom-built aluminum motor arm adaptor to the motor arm with four #4-40 0.5 in. screws.

2.8) Build the motor/motor arm/motor housing assembly.

2.8.1) Obtain the custom-built aluminum motor housing and the 400-step stepper motor.

2.8.2) Line up the screw holes on the stepper motor and motor housing and then secure with four #4-40 0.5 in. screws.

2.8.3) Feed the rotating motor rod of the stepper motor through the opening of the motor arm assembly and tighten the locking screw on the aluminum motor arm adaptor.

2.9) Build the optical switch assembly.

2.9.1) Obtain the custom-built aluminum optical switch and three 1.0 in. fiber adaptor plates.

2.9.2) Thread the adaptor plates into the threaded holes in the optical switch.

2.9.3) Attach the custom-built aluminum optical switch face-plate onto the optical switch with four #4-40 0.5 in. screws.

2.10) Attach the motor/motor arm/motor housing assembly to the optical switch by feeding the rotating motor rod of the stepper motor through the central hole of the optical switch.

2.11) Obtain an electric circuit board and stepper motor driver, and then place the stepper motor driver across the central groove of the breadboard.

2.12) Observe the electrical connection schematic (Figure 5, 2.12) for the stepper motor driver, 12V power supply, and stepper motor.

2.13) Connect the stepper motor driver, 12V power supply, and stepper motor as specified in the circuit diagram (Figure 3, 2.12) to complete construction of the motorized optical switch.

2.14) Screw in the optical switch components and tungsten-halogen light source to an optical breadboard or optical table near the previously constructed (Figure 4, 1.24) high-resolution fluorescence microendoscopy assembly.

2.15) Attach one end of a 550 μm, 0.22 NA patch cable to the 1.0 in. fiber adaptor plate of the motor arm assembly.

2.16) Attach the other end of the 550 μm, 0.22 NA patch cable to the fiber connector of the USB spectrometer.

2.17) Screw in the five distal probe cables to the respective 1.0 in. fiber adaptor plates on the instrumentation to finish completion of the multimodal high-resolution imaging and sub-diffuse reflectance spectroscopy fiber-bundle microendoscope.

2.17.1) Screw in the central 1 mm-diameter image fiber cable to the 1.0 in. fiber adaptor plate mentioned in step 1.9.2.

2.17.2) Screw in the leftmost 200 μm multimode fiber cable to the 1.0 in. fiber adaptor plate mentioned in step 2.6.

2.17.3) Screw in the 2nd 200 μm multimode fiber cable to the leftmost 1.0 in. fiber adaptor attached to the tungsten-halogen lamp mentioned in step 2.9.2.

2.17.4) Screw in the 3rd 200 μm multimode fiber cable to the middle 1.0 in. fiber adaptor plate mentioned in step 2.9.2.

2.17.5) Screw in the 4th 200 μm multimode fiber cable to the rightmost 1.0 in. fiber adaptor plate mentioned in step 2.9.2.

Figure 5. Assembly of the sub-diffuse reflectance spectroscopy modality. The sub-diffuse reflectance spectroscopy modality can be constructed using a basic tungsten-halogen lamp coupled to an objective lens to focus light through the 200 μm multimode delivery fiber, and a spectrometer. Additionally, a custom-built motorized optical switch can be constructed within the lamp-fiber-spectrometer path to switch between each SDS. Investigators using multiple spectrometers to acquire from multiple SDSs can bypass the optical switch component.

2.3.5 Characterization of the High-Resolution Microendoscopy Modality

The instrumentation was characterized to determine the following specifications: 1) spatial resolution, 2) magnification, 3) percent of maximum field-of-view, and 4) sampling frequency. These values were determined with three objective/tube lenses with focal lengths of 50, 100, and 150 mm. For each lens, a 10X/0.30 NA infinity-corrected objective lens was used. Next, the ability of the DRS modality to extract optical properties (absorption and reduced scattering coefficients) was quantified using a lookup table (LUT) approach (Rajaram *et al.*, 2008; Rajaram, Aramil, *et al.*, 2010) Finally, sampling depth was determined for the broadband DRS modality (Hennessy *et al.*, 2014).

First, spatial resolution and maximum field-of-view (FOV) was determined by the geometry of the fiber-optic probe. The image fiber consists of approximately 50,000 individual 4.5 μm-diameter fiber elements with center-to-center spacing of 4.5 μm. The probe is placed in direct contact with a sample; therefore, the optimal spatial resolution that can be achieved is 4.5 μm. In addition, the maximum FOV was approximately 0.8 mm^2, which was determined by the diameter (≈ 1 mm) of the image fiber. Depending on the objective/tube lens configuration, values for magnification, percent-of-maximum FOV, and sampling frequency vary.

A positive 1951 USAF resolution test target was back-illuminated with a white LED and imaged at group 3/element 3 (linewidth = 49.50 μm) with three tube lenses (focal lengths = 50, 100, and 150 mm). The number of image sensor pixels per micron within the images was then computed. This number was multiplied by the width of the individual pixels (2.5 μm/pixel) to obtain magnification. Percent of maximum FOV was determined by dividing the sampled area projected onto the image sensor by the maximum FOV (0.8 mm^2). Finally, sampling frequency was determined by multiplying the individual fiber element diameter (4.5 μm) by the number of

pixels per micron within the images. Equations for obtaining spatial resolution, magnification, percent of maximum FOV, and sampling frequency are shown below as Eq. (1), Eq. (2), Eq. (3), and Eq. (4), respectively. In the following equations, *R* is spatial resolution, *D* is diameter of individual fiber elements (4.5 μm), *M* is magnification, *N* is the number of pixels per micron, *W* is pixel width (2.5 μm), *FOV* is percent of maximum field-of-view, *A* is area, and *F* is sampling frequency.

$$R(\mu m) = D_{fibers}\left(\frac{\mu m}{fiber}\right) \cdot fiber \tag{1}$$

$$M = N_{pixel}\left(\frac{pixel}{\mu m}\right) \cdot W_{pixel}\left(\frac{\mu m}{pixel}\right) \tag{2}$$

$$FOV(\%) = \frac{A_{sample}(\mu m^2)}{A_{maximum}(\mu m^2)} \tag{3}$$

$$F_{sampling} = D_{fiber}\left(\frac{\mu m}{fiber}\right) \cdot N_{pixel}\left(\frac{pixel}{\mu m}\right) \tag{4}$$

2.3.6 Generation of and validation of lookup tables for volume-averaged optical property extraction

The second objective of this study was to use the DRS modality to extract volume-averaged optical parameters. To accomplish this, reflectance lookup tables (LUTs) were generated describing the relationship between absolute reflectance and optical properties (μ_s' and μ_a) for the two SDSs (374 and 730 μm). The target ranges of the LUTs were μ_s' and μ_a between 5-26 cm^{-1} and 0-10 cm^{-1}, respectively. These LUTs required calibration phantoms of similar order of magnitude as biological tissue (Rajaram *et al.*, 2008; Sandell and Zhu, 2011).

Calibration phantoms were constructed to exceed the target range using deionized water as the solvent (Rajaram *et al.*, 2008). The scattering agent was 1.0 μm-diameter polystyrene

microspheres (07310-15, Polysciences, USA) and the associated μ_s' range (3-31 cm^{-1}) was calculated using Mie theory (Nichols *et al.*, 2012; Sharma *et al.*, 2014; Fu *et al.*, 2010). The absorbing agent was a combination of yellow, red, and blue food dye (McCormick & Company, USA), in ratio of 20:6:2, which contained propylene glycol, Yellow 5, Red 40, Red 3, Blue 1, and 0.1% propylparaben. The μ_a range (0-47 cm^{-1}) was calculated by measuring the dye solution in deionized water using a spectrophotometer (5102-00, PerkinElmer, USA) and Beer's Law. All calibration phantoms were homogenous so μ_s' and μ_a were identical throughout the phantom volume.

A total of 12 liquid calibration phantoms was created which was sufficient to build the LUTs. Six of the 12 phantoms were considered "scattering-only" and contained only deionized water and polystyrene microspheres without dye. Deionized water and polystyrene microspheres were gently mixed inside 7 mL scintillation vials (66022-300, VWR, USA) to yield six μ_s' ranges of 3.0-4.9, 4.4-7.1, 6.4-10.2, 9.2-14.7, 13.2-21.2, and 19.5-31.0 cm^{-1}. These values were chosen so there was sufficient overlap between the maximum μ_s' value of one phantom at 450 nm and the minimum μ_s' value of another phantom at 750 nm. Sufficient overlap was determined such that the minimum μ_s' value of one phantom was no greater than 90% of the maximum μ_s' value of the proceeding phantom. This ensured the six scattering-only phantoms spanned a continuous μ_s' range. Eq. 5 expresses this relationship in which *n* is the phantom number.

$$\mu'_{s,min,phantom(n)} \leq 0.9 \cdot \mu'_{s,max,phantom(n-1)}, \quad (5)$$

The remaining six phantoms contained both polystyrene microspheres and the dye combination. Deionized water, polystyrene microspheres, and dye were gently mixed inside 7 mL scintillation vials to yield a continuous μ_s' range of 3-31 cm^{-1} and continuous μ_a range of 0-

47 cm^{-1}. The wavelength-dependent variations in μ_s' and μ_a provide the wide range of scattering and absorbing values.

To generate the reflectance LUTs, the probe was placed in each phantom so it was completely submerged at a distance of 2 cm from the bottom of the 7 mL scintillation vial. Broadband DRS data (450-750 nm) were recorded at each SDS (374 and 730 μm) with an integration time of 400 ms. Five spectra were averaged for all measurements. Spectra were converted to absolute reflectance values by calibrating with a Spectralon® 20% diffuse reflectance standard (SRS-20-010, Labsphere, USA) which was spectrally flat between 200-2600 nm. A custom, 3D printed probe holder was used to fix the distance between the probe tip and the Spectralon® 20% diffuse reflectance standard to acquire maximum reflectance at each SDS (Figure 6 and 7).

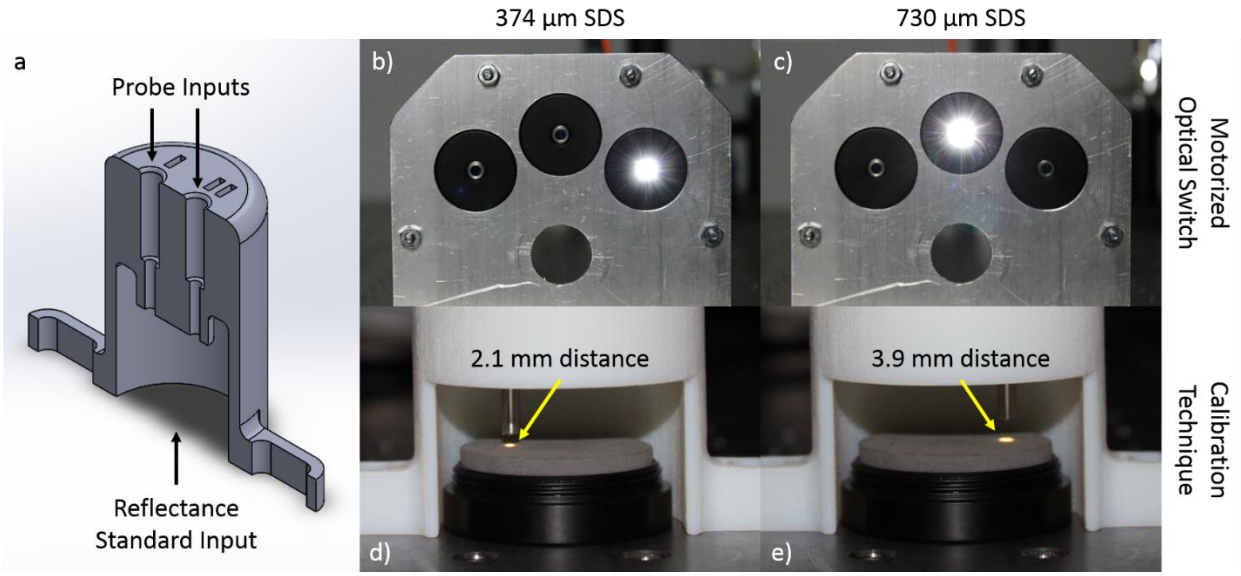

Figure 6. Calibration of the sub-diffuse reflectance spectroscopy modality. For experimental calibration, the fiber-optic probe tip must be placed at different perpendicular distances from the 20% diffuse reflectance standard depending on the SDS. To consistently achieve these perpendicular distances across all experiments, a calibration standard device was designed (device cross section shown in (a)) to hold the probe at exact distances from the 20% diffuse reflectance standard. In this specific fiber-optic probe setup, light from the tungsten-halogen lamp is shown through the optical switch at source-detector separations of (b) 374 µm and (c) 730 µm (with motor and motor arm removed from the optical path for clarity). Distances of (d) 2.1 mm for the 374 µm SDS, and (e) 3.9 mm for the 730 µm SDS are required for calibration.

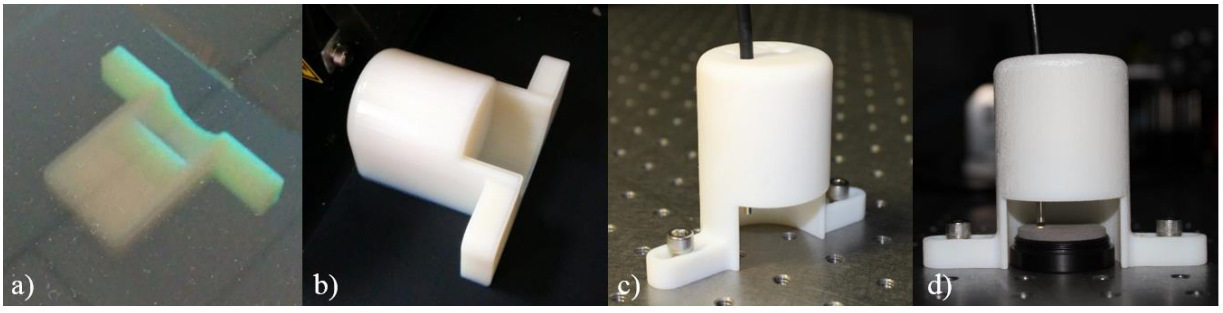

Figure 7. The final design, including during 3D printing

All spectra were corrected for background noise (Glennie *et al.*, 2014; Rajaram, Aramil, *et al.*, 2010; Rajaram *et al.*, 2008; Nichols *et al.*, 2015; Nichols *et al.*, 2012). After acquiring absolute reflectance spectra at a resolution of 0.35 nm, the LUTs relating reflectance (R) to μ_s' and μ_a were generated using MATLAB. Raw data from the 12 calibration phantoms (C.P. #1-12)

was interpolated to generate a color-mapped mesh with an optical property resolution of 0.02 cm^{-1}. The reflectance LUTs were interpolated in the target μ_s' and μ_a ranges of 5-26 cm^{-1} and 0-10 cm^{-1}, respectively.

To validate the reflectance LUTs, a set of liquid validation phantoms with known optical properties was built of similar order of magnitude as biological tissue (Sandell and Zhu, 2011; Rajaram *et al.*, 2008). Validation phantoms were constructed in a similar manner to calibration phantoms, but contained bovine hemoglobin (H2625, Sigma-Aldrich, USA), rather than food dye, as the absorbing agent. The μ_s' was calculated using Mie theory and μ_a was calculated by measuring a solution of bovine hemoglobin in deionized water using a spectrophotometer (5102-00, PerkinElmer, USA) and Beer's Law. It was necessary to validate the LUTs using a different absorber and different scattering ranges than those used to generate the LUTs so that the interpolated range of the LUTs were tested. All validation phantoms were homogenous so μ_s' and μ_a were identical throughout the phantom volume.

A 3 x 3 (9 total) set of validation phantoms was created, corresponding to three μ_s' ranges and three μ_a ranges. Deionized water, polystyrene microspheres and diluted bovine hemoglobin were gently mixed inside 7 mL scintillation vials. This yielded μ_s' values from 5-26 cm^{-1} and μ_a values from 0-10 cm^{-1} to validate 100% of the reflectance LUTs. Figure 8 shows the μ_s' and μ_a for the calibration phantoms (C.P. 1-12) and validation phantoms (V.P. 1-9).

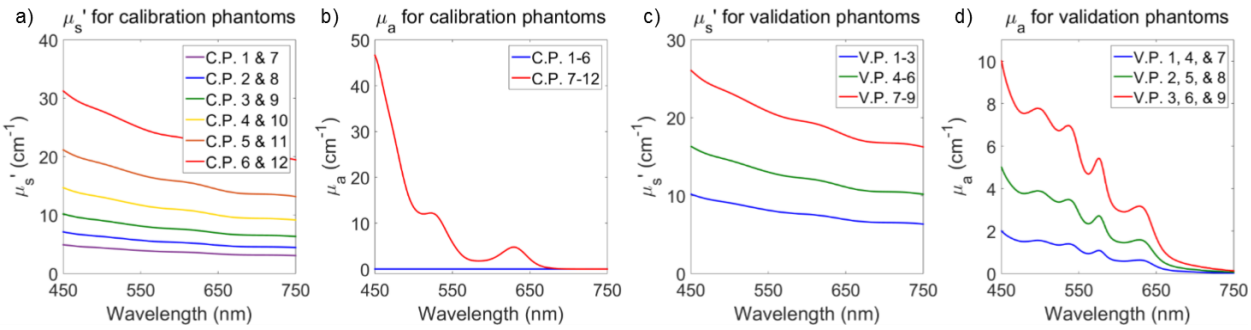

Figure 8. Comparison of the optical properties of the (a, b) 6x2 (12 total) calibration phantoms (C.P.) and the (c, d) 3x3 (9 total) validation phantoms (V.P.). Calibration phantoms were made with polystyrene microspheres and a combination of yellow, red, and blue dye and the validation phantoms were made with polystyrene microspheres and bovine hemoglobin as the scattering and absorbing agents, respectively. Calibration phantoms had μ_s' spanning 3-31 cm^{-1} and μ_a spanning 0-47 cm^{-1} and the validation phantoms had a μ_s' spanning 5-26 cm^{-1} and μ_a spanning 0-10 cm^{-1} to validate the target LUT range.

Broadband DRS data on validation phantoms were collected in the same method as the calibration phantoms. The LUT-based inverse model was used to extract μ_s' and μ_a from the validation phantoms. Theoretical optical properties of the validation phantoms were compared to extracted optical properties and reported as percent errors. To quantify percent errors, the LUT-based inverse model extracted μ_s' and μ_a for the 3x3 validation phantoms at a spectral resolution of 0.35 nm and percent errors were calculated using Eq. 6 and Eq. 7,

$$Error_{\%,\mu_s'} = \left| \frac{\mu'_{s,extracted} - \mu'_{s,theoretical}}{\mu'_{s,theoretical}} \right| \cdot 100\% \quad (6)$$

$$Error_{\%,\mu_a} = \left| \frac{\mu_{a,extracted} - \mu_{a,theoretical}}{\mu_{a,theoretical}} \right| \cdot 100\%, \quad (7)$$

2.3.7 Generation of and validation of lookup tables for sampling depth quantification

The third objective of this study was to determine the sampling depth of the DRS modality. To accomplish this, sampling depth lookup tables (LUTs) were generated describing the relationship between sampling depth and volume-averaged optical properties (μ_s' and μ_a) for

the two SDSs (374 and 730 μm). The target ranges of the sampling depth LUTs were μ_s' and μ_a between 5-26 cm^{-1} and 0-10 cm^{-1}, respectively. The same calibration phantoms as described previously were used to generate the sampling depth LUTs.

A highly absorbing phantom layer ($\mu_a \geq 100$ cm^{-1} for all wavelengths between 450-750 nm) was created in a 5 mL beaker using 6.5% w/w India Ink in PDMS (Hennessy *et al.*, 2014; Di Ninni *et al.*, 2010). Contributions from specular reflection were proven negligible by placing the probe in contact with the absorbing layer and acquiring DRS data between distances of 0-2 mm in 50 μm increments (Hennessy *et al.*, 2014).

Next, the six dye-containing calibration phantoms (Figure 8, C.P. 7-12) were placed on top of the highly absorbing layer within the beaker. Spectra (450-750 nm) at each SDS were taken by varying the distance of the probe-tip and absorbing layer between 0-2 mm in 50 μm increments (Hennessy *et al.*, 2014). Sampling depth is been defined as the depth reached by 50% of photons (Hennessy *et al.*, 2014). At a certain probe-absorbing layer distance (around 2 mm), there were no significant changes in signal intensity, meaning that nearly 100% of incident photons were not reaching the highly absorbing layer. Figure 9 shows how sampling depth was quantified for the DRS modality in representative data (Hennessy *et al.*, 2014). As the probe is translated away from the absorbing layer, as shown in Figure 9(a), reflectance increases until plateauing as shown in Figure 9(b). A depth (x-axis) can then be identified that correlates with the 50% cutoff point (y-axis) which is defined as the sampling depth as shown in Figure 9(c) (Hennessy *et al.*, 2014).

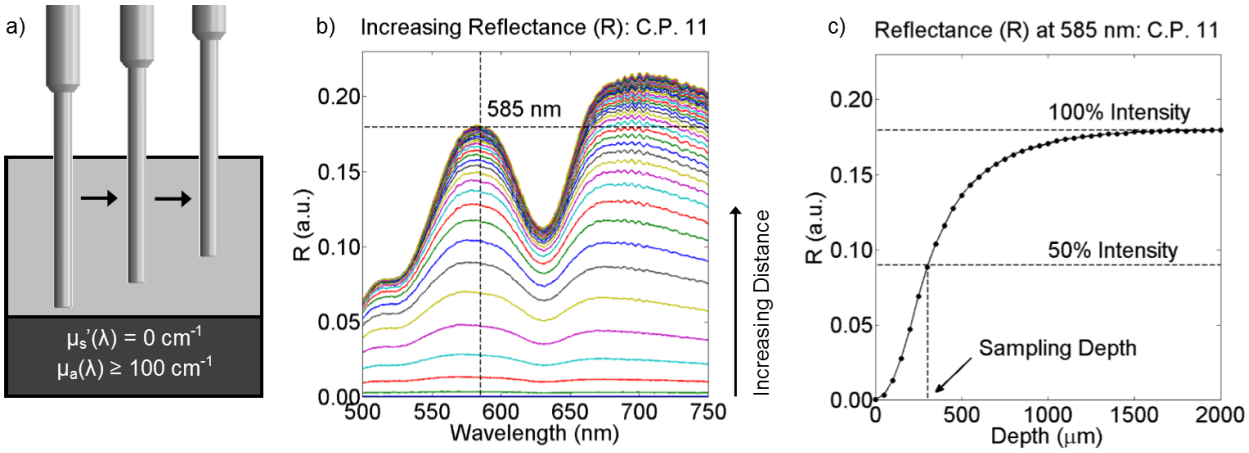

Figure 9. The probe is placed (a) in contact with the highly absorbing ($\mu_a \geq 100$ cm^{-1} for 450-750 nm) inside a 5 mL beaker and translated upwards in 50 µm increments to (b) acquire DRS data from a calibration phantom (C.P. 11) at a 374 µm SDS. (c) Representative data from the 374 µm SDS shows the percentage of photons not reaching the highly absorbing layer as a function of depth for C.P. 11 at 585 nm. Sampling depth is defined as the depth reached by 50% of photons.

The process from Figure 3 was repeated for all wavelengths at a spectral resolution of 0.35 nm for the 6 calibration phantoms (C.P. 7-12). Raw data was interpolated in MATLAB to generate a color-mapped mesh with a maximum optical property resolution of 0.02 cm^{-1}. The sampling depth LUTs were interpolated in a target μ_s' range of 5-26 cm^{-1} and μ_a range of 0-10 cm^{-1}.

To validate sampling depth, spectra (450-750 nm) at each SDS of the previously described validation phantoms were acquired by varying the distance of the probe-tip and absorbing layer between 0-2 mm in 50 µm increments. To quantify percent errors, sampling depths of the validation phantoms were compared to the sampling depths (D) from the calibration phantoms. Percent errors were calculated using Eq. 8,

$$Error_{\%,D} = \left| \frac{D_{calibration} - D_{validation}}{D_{validation}} \right| \cdot 100\% \quad (8)$$

2.3.8 Hybrid Cell Phantoms

To demonstrate the three modalities, two hybrid cell phantoms were constructed using PDMS as a substrate material and titanium dioxide (Sigma Aldrich, USA) and nigrosin (Sigma Aldrich, USA) as the scattering and absorbing agents, respectively (Greening *et al.*, 2014). Both phantoms consisted of a 2.5 cm thick layer containing a scattering concentration of 8.0 mg/g TiO_2/PDMS and absorbing concentration of 5.0 µL/g 1% w/v distilled nigrosin/PDMS. The second phantom consisted of an additional 500 µm thin absorbing layer which had had a scattering concentration of 8.0 mg/g TiO_2/PDMS and absorbing concentration of 10.0 µL/g 1% w/v distilled nigrosin/PDMS (Greening *et al.*, 2014).

After curing, hybrid cell phantoms were autoclaved, and MDA-MB-468 breast adenocarcinoma cells were cultured on top. MDA-MB-468 breast adenocarcinoma cells (ATCC, USA) were cultured up to the fourth passage in Dulbecco's Modified Eagle Medium (DMEM) (ATCC, USA) containing 10% fetal bovine serum (ATCC, USA) and 5% antibiotics (Sigma Aldrich, USA) at 37°C in 5% CO_2. 24 hours after passaging, 200,000 cells in 4 mL DMEM were seeded onto the phantoms. Each phantom was then transferred to the fiber-optic probe tip. A 0.01% w/v solution (1 mL) of proflavine in saline was added to the cell culture media to provide fluorescent contrast of the nuclei (Prieto, Powless, Boice, *et al.*, 2015). The 455 nm LED and 635 nm laser provided optical powers at the sample plane of 1.00 mW and 0.25 mW, respectively. Both high-resolution fluorescence and DRIM data were collected simultaneously. DRIM data were quantified by using a MATLAB script to compute a line plot through the center of the image circle and plotting intensity over continuous SDS between 400 and 1,300 µm. Ten raw DRIM images were averaged. Immediately following this, the tungsten-halogen lamp delivered 0.35 mW of power at the sample plane. Broadband DRS measurements were then acquired at

both tested SDSs of 374 and 730 µm. For this experiment, both cameras were set to an exposure time of 150 ms and gain of 10 dB. The spectrometer had an integration time of 0.5 s and boxcar width (Kiisk, 2014) of 3. Three spectra were averaged at each SDS for both hybrid phantoms.

The hypothesis for this experiment was that there would be no discernable difference between high-resolution image data of cultured MDA-MB-468 breast adenocarcinoma cells between the two phantoms, but differences would be seen in the reflectance intensities for DRIM and DRS data due to the underlying absorbing layer. Table 1 shows specifications for all phantom layers.

Table 1. Specifications for non-biological components of hybrid tissue-simulating phantoms

Phantom Number	1 (single-layer)		2 (double-layer)	
Layer	Bottom	Top	Bottom	Top
Thickness (mm)	25	0	25	0.5
[Scattering] (mg/g TiO_2/PDMS)	8.0	0	8.0	8.0
Estimated μ_s' (cm^{-1})	10.0	0	10.0	10.0
[Absorption] (µL/g dist. Nigrosin/PDMS)	5.0	0	5.0	10.0
Estimated μ_a (cm^{-1})	1.0	0	1.0	2.0

2.3.9 In vivo human melanocytic nevus

The trimodal technique was tested on a selected benign melanocytic nevus and adjacent normal skin from a healthy Caucasian volunteer. All procedures were approved by the University of Arkansas Institutional Review Board (IRB #15-09-149). A benign melanocytic nevi was chosen as a demonstration because of its similar cellular arrangement to surrounding normal tissue. Contributions from melanin cannot be discerned using high-resolution fluorescence imaging, but these highly absorbing contributions become apparent when using the integrated sub-diffuse reflectance modalities, DRIM and DRS (Zonios *et al.*, 2008; Tseng *et al.*, 2009).

Highlighter ink, which contains the fluorescence compound, pyranine, was applied to the skin instead of proflavine. Excitation of pyranine was accomplished using the 455 nm LED as the excitation source, similar to proflavine. However, unlike proflavine, pyranine does not

intercalate DNA and thus preferentially stains cell membranes rather than nuclei. The probe tip was placed in direct contact with the skin surface while the 455 nm LED, 635 nm laser, and tungsten-halogen lamp provided optical powers of 1.00 mW, 0.25 mW, and 0.35 mW, respectively. Both high-resolution fluorescence imaging and DRIM data were collected with an exposure time of 150 ms and gain of 10 dB whereas broadband DRS data used an integration time of 500 ms and boxcar width of 3 (Kiisk, 2014). Ten high-resolution fluorescence images, ten DRIM data, and three DRS data were acquired from each site. The best qualitative high-resolution fluorescence image was selected while ten DRIM and three DRS data were averaged together. After acquisition, the LUT-based inverse model was used to extract μ_s' and μ_a (@ 630 nm) from the *in vivo* DRS data of the melanocytic nevus and adjacent normal skin tissue (Rajaram, Gopal, *et al.*, 2010; Rajaram *et al.*, 2008; Rajaram, Reichenberg, *et al.*, 2010; Rajaram, Aramil, *et al.*, 2010).

The hypothesis for this experiment was that there would be no discernable difference between high-resolution image data between the keratinocytes of the benign melanocytic nevus and surrounding tissue, but differences would be seen in the reflectance intensities for DRIM and DRS data due to increases in melanin concentration.

2.3.10 Ex vivo murine colon tissue

As a demonstration of the technique in a murine model, a 16-week old wild-type (C57BL/6J) mouse (Jackson Laboratories, USA) was housed in a room with a 16:8-hour light-dark cycle and had access to standard rodent food **(**8640 Teklad 22/5 Rodent Diet**,** Harlan Sprague Dawley Inc., USA) and water ad libitum. Seven days prior to data collection, the mouse was switched to a 50/50 mix of standard rodent food and purified food (AIN-93G Purified Diet, Harlan Sprague Dawley Inc., USA). The mouse was switched to 100% purified food four days

prior to data collection and no food 24 hours prior. All procedures were approved by the University of Arkansas Institutional Animal Care and Use Committee (IACUC, #15009) (Moser *et al.*, 1990; Su *et al.*, 1992; Karim and Huso, 2013).

A 1 cm^2 square section of colonic tissue (4-5 cm from anus) was isolated. A segment of this tissue site was immediately placed in 10% formalin for 24 hours for fixation prior to H&E staining. The 4-5 cm section was placed lumen-side up on a solid PDMS-based phantom. An underlying PDMS-based phantom was used to eliminate transmitted light because of the thinness of tissue (≈ 200 μm thick) (Lim *et al.*, 2011; Shangguan *et al.*, 1998; Simpson *et al.*, 1998). The phantom had a refractive index of 1.4 to match that of tissue to avoid artifacts due to Fresnel reflection and contained 1% w/v nigrosin/EtOH (5.0 μL/g PDMS, $\mu_a \approx 1.0$ cm^{-1} at 635nm) and TiO_2 (8.0 mg/g PDMS, $\mu_s' \approx 10$ cm^{-1} at 635nm) to approximate the optical coefficients of colonic tissue at 635 nm (Pogue and Patterson, 2006; Siegman, 2010; Sandell and Zhu, 2011; Bashkatov *et al.*, 2014; Wei *et al.*, 2005; Wall and Barton, 2014).

Cold PBS at 4°C was used to keep tissue moist throughout data collection which took place within an hour after time of death. A 4°C, 0.01% w/v solution (1 mL) of proflavine in saline was topically applied to the tissue sample immediately prior to data collection. The 455 nm LED, 635 nm laser, and tungsten-halogen lamp provided optical powers at the sample plane of 1.00 mW, 0.25 mW, and 0.35 mW, respectively. High-resolution fluorescence imaging and DRIM data were collected with an exposure time of 150 ms and gain of 10 dB whereas broadband DRS data used an integration time of 500 ms and boxcar width of 3 (Kiisk, 2014).

Ten high-resolution fluorescence images, ten DRIM data, and three DRS data were acquired from the colon section. The best qualitative high-resolution fluorescence image was selected for comparison to H&E while the ten DRIM and three DRS data were averaged.

2.3.11 In vivo assessment of oral structural and optical properties

The final objective of this study was to extract optical parameters from *in vivo* oral mucosa and elucidate the differences of the optical parameters for each SDS (374 and 730 μm). The multimodal technique was demonstrated in the inner lip of thirteen healthy volunteers, with no history of tobacco use, between the ages of 18-35. Institutional Review Board approval (IRB #15-09-149) was obtained from the Human Subjects Research program at the University of Arkansas for all aspects of this study. The methods described were carried out in accordance with the approved guidelines, and informed consent was obtained from all participants.

Extracting optical parameters required two steps. First, *in vivo* data acquisition was carried out with custom LabVIEW software (Greening, James, Powless, *et al.*, 2015). The probe was directly placed in contact with the inner lip and broadband DRS were acquired at both SDSs (374 and 730 μm). The tungsten-halogen lamp delivered 0.35 mW of power at the probe tip for 500 ms. Additionally, in one volunteer, a single high-resolution fluorescence image was taken using topical proflavine (0.01% w/v in saline) as a contrast agent with an exposure of 100 ms and gain of 5 dB, thus demonstrating the capability of the probe to sequentially and non-invasively extract image and optical property data. Second, for post-processing, raw broadband DRS data was imported into custom MATLAB software which was integrated with the LUT-based inverse model and sampling depth LUT to extract optical parameters. The use of this post-processing algorithm to extract optical parameters has been previously described (Rajaram, Reichenberg, *et al.*, 2010; Rajaram, Gopal, *et al.*, 2010; Rajaram, Aramil, *et al.*, 2010).

The optical parameters extracted in this study were volume-averaged scattering exponent (B), hemoglobin concentration (THC), and oxygen saturation (StO_2). Sampling depth was also quantified which is a function of the underlying optical parameters (Rajaram, Gopal, *et al.*, 2010;

Rajaram *et al.*, 2008; Sharma *et al.*, 2013; Hennessy *et al.*, 2014). The scattering exponent relates to the size of a tissue's scattering particles, and thus can provide reasoning for changes in scattering when comparing groups within the same SDS (Mourant *et al.*, 1998). Hemoglobin concentration and oxygen saturation are commonly derived measurements in optical spectroscopy to assess angiogenesis, and since blood vessel density has been shown to increase as oral tissue progresses from normal to dysplastic, extracting these parameters was important (Mourant *et al.*, 2014). These optical parameters and their relation to μ_s' and μ_a are given in Eq. 9 and Eq. 10. The μ_s' was calculated based on Eq. 9,

$$\mu_s'(\lambda) = \mu_s'(\lambda_0) \cdot \left(\frac{\lambda}{\lambda_0}\right)^{-B} \tag{9}$$

where $\mu_s'(\lambda)$ is the reduced scattering coefficient (cm^{-1}) at any wavelength, λ is a wavelength (nm), λ_0 is 630 nm, and B is the scattering exponent (Sharma *et al.*, 2013). The μ_a was calculated based on Eq. 10,

$$\mu_a(\lambda) = 2.303 \cdot [Hb] \cdot \left(\frac{1}{MW}\right) \cdot \left[\alpha\left(\varepsilon_{Hb_{oxy}}\right) + (1-\alpha)\left(\varepsilon_{Hb_{deoxy}}\right)\right] \tag{10}$$

where μ_a is the absorption coefficient (cm^{-1}) , THC is the bulk tissue hemoglobin concentration mg/mL), MW is the gram molecular weight of hemoglobin which is assumed to be 64,500 g/mole (Prahl, 1999), α is the bulk tissue oxygen saturation, and ε is the molar extinction coefficient ($cm^{-1}M^{-1}$) of oxygenated hemoglobin (Hb_{oxy}) and deoxygenated hemoglobin (Hb_{de-oxy}). Some groups have also included a packaging correction factor when calculating μ_a for sampling wavelengths below 450 nm, but this was shown to have no impact on the LUT-based inverse model fits presented here since spectra were taken between 500-750 nm (Rajaram, Gopal, *et al.*, 2010).

Figure 10 shows the experimental setup with the instrumentation, hybrid fiber-bundle probe, and post-processing software. For this experiment, it was hypothesized that the 730 μm SDS would yield reduced B values due longer SDSs having greater reflectance from longer wavelengths. Alternatively, the 730 μm SDS should yield greater THC values because of increased sampling into the sub-epithelia, where the blood vessels exist (Sharma *et al.*, 2013; Chang *et al.*, 2009). StO_2 was expected to be comparable when sampling at different depths since changes in StO_2 have been shown to not be depth dependent (Bezemer *et al.*, 2009). Finally, we expected increased sampling depth for the longer SDS (Hennessy *et al.*, 2014; Sharma *et al.*, 2013). Results from this study were expected to show the value of including two different sub-diffuse reflectance spectroscopy SDSs along with a high-resolution fluorescence imaging capability.

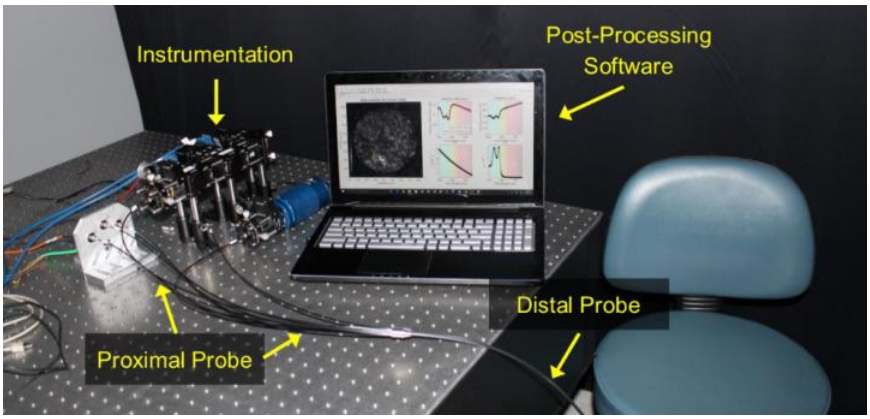

Figure 10. An image of the experimental setup showing the optical instrumentation, post-processing software based in MATLAB showing a high-resolution fluorescence image of the inner lip, LUT-based inverse model fit of raw reflectance data, sampling depth, μ_s', and μ_a from one volunteer (image center), and the proximal and distal hybrid fiber-bundle probe.

2.4 Results

2.4.1 Characterization of the High-Resolution Microendoscopy Modality

Figure 11 shows images taken of a positive 1951 USAF resolution test target at group 3/element 3 (linewidth = 49.50 µm). These images were used to quantify spatial resolution, magnification, percent maximum FOV, and sampling frequency, listed in Table 2. The 50 mm tube lens (Figure 11(a)) was chosen for use with the 10X/0.30 NA infinity-corrected objective lens for data collection because of the desirable percent maximum FOV (%) and sampling frequency (pixels/fiber element) which were 100% and 5.4, respectively. This configuration maximizes the field-of-view while satisfying the Nyquist sampling requirement.

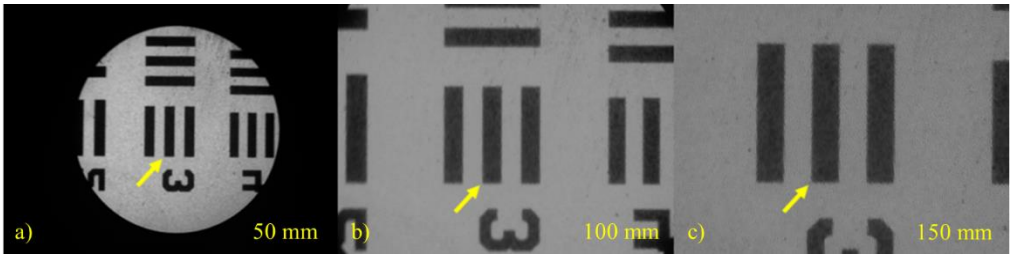

Figure 11. Images of group 3/element 3 (linewidth = 49.50 µm) of a positive 1951 USAF resolution test target taken with a 10X/0.30 NA infinity-corrected objective lens and tube lenses with focal lengths of **(a)** 50 mm, **(b)** 100 mm, and **(c)** 150 mm. The yellow arrow points to the same target on each image.

Table 2. System specifications for the high-resolution modality with different tube lenses

Focal Length of Tube Lens	**50 mm**	**100 mm**	**150 mm**
Spatial Resolution [µm]	4.5	4.5	4.5
Image sensor pixels/µm [pixels/µm]	1.21	2.65	3.61
Magnification on CCD sensor	3.0	6.6	9.0
Percent of Maximum FOV	100%	56%	30%
Sampling Frequency [pixels/fiber]	5.4	11.9	16.2

2.4.2 Generation of and validation of lookup tables for volume-averaged optical property extraction

Figure 12 (a, b) shows the reflectance LUTs (μ_s' = 5-26 cm^{-1} and μ_a = 0-10 cm^{-1}) overlaid with the respective reflectance data from the dye-based calibration phantoms. Similarly, Figure 12 (d, e) shows the reflectance LUTs overlaid with the respective data from the bovine

hemoglobin-based validation phantoms. Validation phantom data that perfectly overlays the LUT would indicate a 0% error; however, minor errors do exist. Additionally, Figure 12 (c, f) shows a ratio of the 730 to 374 µm SDS LUTs. The mean ratio is 1.14, with a standard deviation of 0.27, indicating a variable reflectance ratio as μ_s' and μ_a vary. Notice that at high reduced mean free paths (low μ_s' and μ_a) in Figure 12 (c, f), the reflectance ratio is at a maximum of 1.69, and at low reduced mean free paths (high μ_s' and μ_a), the reflectance ratio is at a minimum of 0.58. This trend supports the observation that longer SDSs are more sensitive to lower scattering values, especially at longer wavelengths. Similarly, shorter SDSs are more sensitive to higher scattering values. Thus, this reflectance ratio trend supports the validity of our LUTs.

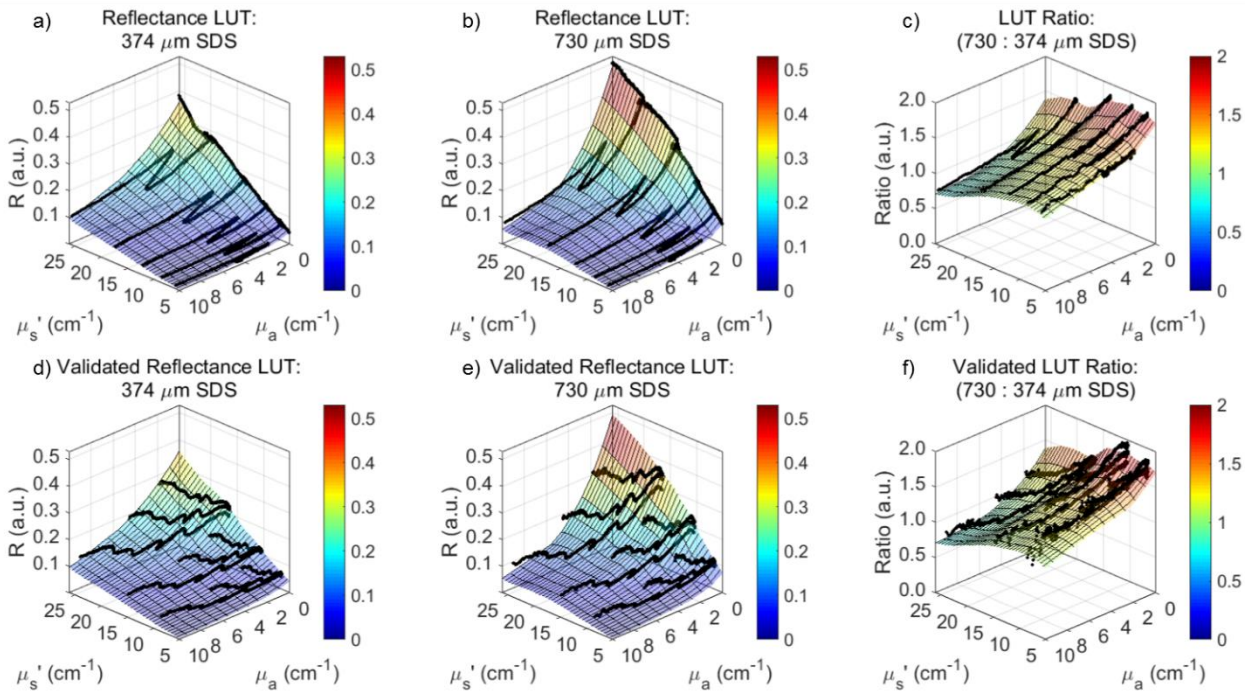

Figure 12. 100% (μ_s' = 5-26 cm^{-1}, μ_a = 0-10 cm^{-1}) of both reflectance LUTs were validated with acceptable percent errors less than 10%. Following validation, optical properties can be reliably extracted from samples with unknown optical properties using the LUT-based inverse model. (a, b) Reflectance LUTs were interpolated with raw data from calibration phantoms and (c) shows a ratio of the 730 µm SDS to 374 µm SDS LUTs. (d, e) Reflectance LUTs were validated with raw data from the bovine hemoglobin-based validation phantoms and (f) shows the validated ratio of the 730 µm SDS to 374 µm SDS LUTs.

The LUT-based inverse model correctly estimated μ_s' of the validation phantoms with average percent errors of 1.6% and 2.5% for the 374 and 730 μm SDS, respectively. Minimum and maximum percent errors for μ_s' extraction were 0.1% and 5.3% for the 374 μm SDS and 1.2% and 11.4% for the 730 μm SDS, respectively. Additionally, the LUT-based inverse model correctly estimated μ_a of the validation phantoms with average percent errors of 4.2% and 7.2% for the 374 and 730 μm SDS, respectively. Minimum and maximum percent errors for μ_a extraction were 2.1% and 18.4% for the 374 μm SDS and 0.1% and 22.1% for the 730 μm SDS, respectively.

Average percent errors were comparable to similar studies (< 10%) and considered acceptable (Rajaram, Aramil, *et al.*, 2010; Rajaram, Gopal, *et al.*, 2010; Rajaram *et al.*, 2008; Rajaram, Reichenberg, *et al.*, 2010; Vishwanath *et al.*, 2011; Yu *et al.*, 2010; Yu *et al.*, 2008; Nichols *et al.*, 2012; Sharma *et al.*, 2013; Sharma *et al.*, 2014). Thus, 100% of the optical property range of the LUTs were validated, and could be used to reliably extract volume-averaged optical properties from unknown samples. Figure 13 shows the ability of the reflectance LUTs to extract accurate μ_s' and μ_a.

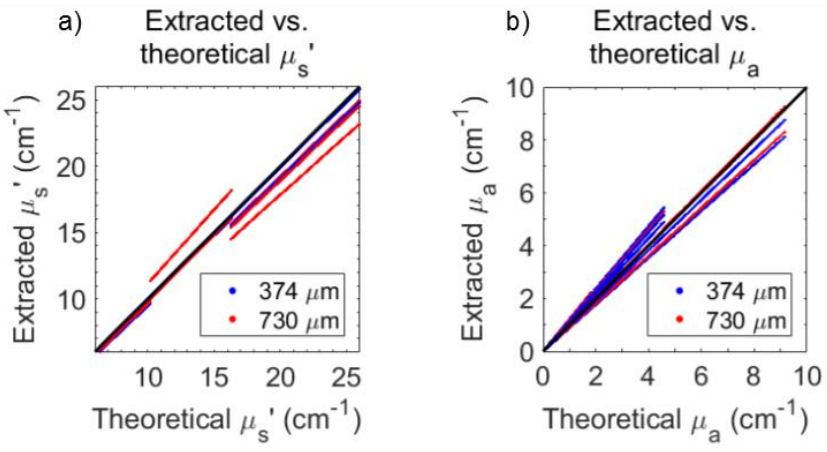

Figure 13. The LUT-based inverse model correctly estimated μ_s' with average percent errors of 1.6% and 2.5% for the 374 and 730 µm SDS, respectively, and correctly estimated μ_a with average percent errors of 4.2% and 7.2% for the 374 and 730 µm SDS, respectively. The ability to extract optical properties is shown with a perfect fit line.

2.4.3 Generation of and validation of lookup tables for sampling depth quantification

Sampling depth ranged between 240 to 530 µm and 300 to 680 µm for the 374 and 730 µm SDSs, respectively (Figure 14). In both cases, maximum sampling depth occurred when μ_s' and μ_a were 0 cm^{-1} and minimum sampling depth occurred at the maximum μ_s' (26 cm^{-1}) and maximum μ_a (10 cm^{-1}) in the target range of the LUTs. After validation with hemoglobin-based validation phantoms, sampling depth was estimated with average percent errors of 1.9% and 1.6% for the 374 and 730 µm SDS, respectively. Minimum and maximum percent errors for μ_s' extraction were 1.8% and 5.3% for the 374 µm SDS and 1.1% and 2.1% for the 730 µm SDS, respectively. Average percent errors, all under 2%, were considered acceptable in this study. Additionally, the ratio of sampling depths for the 730 to 374 µm SDS were calculated for the entire LUT range (Figure 14 (c, f)). On average, the sampling depth ratio was 1.20 with a standard deviation of 0.08, and relatively flat as expected. This indicates the sampling depth of the longer SDS is approximately 1.2x that of the shorter SDS across all wavelengths.

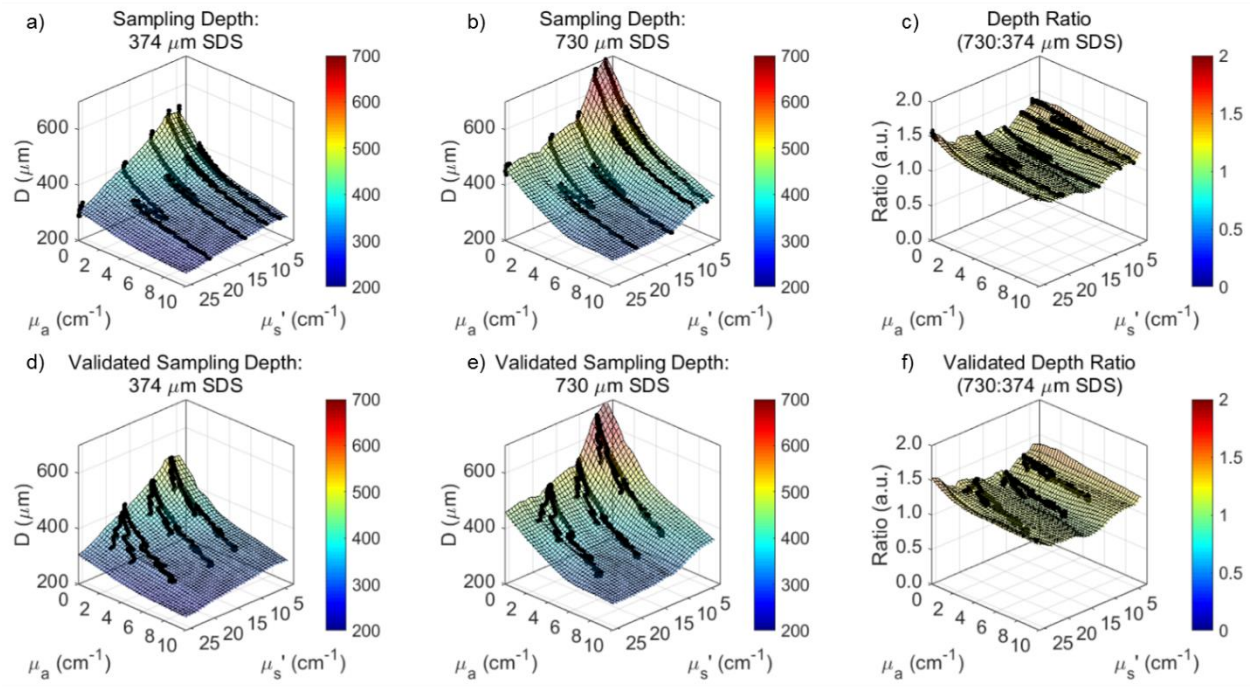

Figure 14. 100% (μ_s' = 5-26 cm^{-1}, μ_a = 0-10 cm^{-1}) of both sampling depth LUTs were validated with acceptable percent errors much less than 10%. (a, b) Sampling depth LUTs were interpolated with raw data from calibration phantoms and (c) shows a ratio (1.2x) of the 730 µm SDS to 374 µm SDS sampling depths. (d, e) Sampling depths LUTs were validated with raw data from the bovine hemoglobin-based validation phantoms and (f) shows the validated ratio of the 730 µm SDS to 374 µm SDS sampling depths.

2.4.4 Hybrid Cell Phantoms

A representation of the hybrid cell phantoms are shown in Figure 15(a, d). Sample data from the high-resolution, fiber-based fluorescence imaging modality are shown for both hybrid cell phantoms in Figure 15(b, e). DRIM data are shown in Figure 15(c, f) and the quantification of these maps is shown in Figure 15(g). DRIM data were quantified by using a MATLAB script to take a line plot through the center of the image circle and plotting intensity (in pixel values) over continuous SDS between 400 and 1,300 µm. Finally, broadband DRS data for both SDSs (374 and 730 µm) from both hybrid cell phantoms are shown in Figure 15(h, i).

Our hypothesis was supported. There was no discernable difference between high-resolution image data of cultured breast adenocarcinoma cells between the two phantoms, but clear differences were seen in reflectance for the DRIM and DRS data. DRIM data shows greater signal closer to the 635 nm source delivery fiber, and intensity is markedly reduced for the double-layer phantom containing the more highly absorbing underlying layer. The overall shape of the DRIM profiles remains similar between samples, as expected. The shape of DRIM profiles are similar to those predicted by established Monte Carlo models of reflectance (Martinelli *et al.*, 2011). For the DRS data, intensity changes are due to increases in nigrosin concentration, which have a flat absorption spectra across the tested wavelengths (Greening *et al.*, 2014). Also note that for the 730 μm SDS, there are increased reflectance contributions from longer wavelengths when compared to the 374 μm SDS, consistent with the 730 μm SDS sampling a greater depth range (Hennessy *et al.*, 2014).

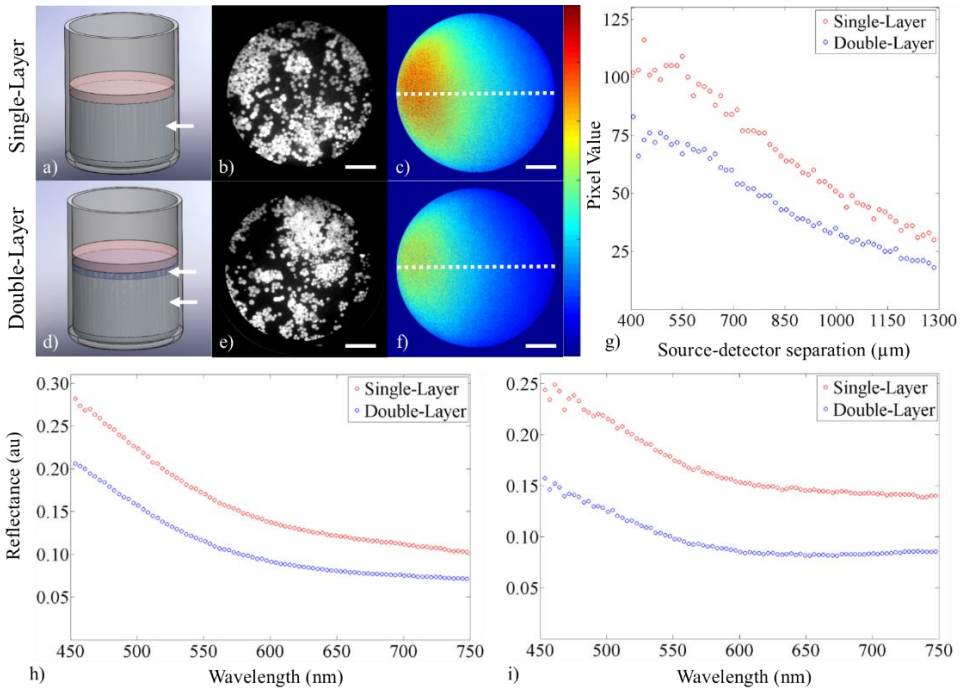

Figure 15. Demonstration of the three modalities showing data from the hybrid cell phantoms containing **(a-c)** one or **(d-f)** two layers. The figure shows **(a, d)** a SolidWorks representation of the single and double layer hybrid cell phantoms (with white arrows pointing at layers), **(b, e)** enhanced high-resolution fluorescence images after topical staining of MDA-MB-468 breast adenocarcinoma cells with proflavine (scale bar = 225 µm), **(c, f)** DRIM data (scale bar = 225 µm, color bar = 0-130), **(g)** quantification of the DRIM data taken across the face of the image fiber (400-1,300 µm SDS from laser source), **(h)** broadband DRS data (374 µm SDS), and **(i)** broadband DRS data (730 µm SDS).

2.4.5 In vivo human melanocytic nevus

For the healthy skin tissue and adjacent melanocytic nevus, data were collected for all three modalities, shown in Figure 16. A DSLR image of both tissue sites is shown in Figure 16(a, d) alongside the high-resolution fluorescence image (Figure 16(b, e)), DRIM data (Figure 16(c, f, g)), and broadband DRS at both SDSs of 374 and 730 µm (Figure 16(h, i)).

Our hypothesis was supported. There were no discernable differences between high-resolution image data between the keratinocytes of the benign melanocytic nevus and

surrounding tissue. In addition, differences were seen in DRIM and DRS modalities due to increased melanin concentration, contributing to increased μ_a (Jacques, 2015).

Keratinocyte morphology can be distinguished in both sites in the high-resolution fluorescence images. Nuclei are not visualized in Fig 16(b, e) because pyranine-derived ink does not intercalate DNA, and thus only the cell membranes boundaries are visualized.

Next, a comparison of DRIM data shows markedly different reflectance intensities across the face of the image fiber. The overall shape of the DRIM profiles remains similar between samples, as expected. The shape of DRIM profiles are similar to those predicted by established Monte Carlo models of reflectance (Martinelli *et al.,* 2011). Finally, *in vivo* broadband DRS data was fit using the validated LUT-based model approach as previously described. Raw data (dots) and model fits (lines) are plotted together in Figure 16(h, i). DRS data shows Q-bands of hemoglobin at 542 and 577 nm for surrounding healthy tissue, although these Q-bands are masked by melanin contributions in the benign melanocytic nevus. The appearance of the Q-bands in the reflectance spectra indicated that our instrument was sampling into the vascularized dermis (Prahl, 1999).

Next, the LUT-based model extracted μ_s' and μ_a from the normal skin and melanocytic nevus for both SDSs (374 and 730 μm). All listed optical properties were referenced at 630 nm. For normal skin, μ_s' was estimated at 16.0 and 11.6 cm^{-1} while μ_a was estimated at 0.9 cm^{-1} for both the 374 and 730 μm SDS, respectively. For the melanocytic nevus, μ_s' was estimated at 23.9 and 28.0 cm^{-1} while μ_a was estimated at 13.8 and 12.3 cm^{-1} for the 374 and 730 μm SDS, respectively. These values for normal skin, as well as the relative increase in both μ_s' and μ_a for the melanocytic nevus, are consistent with previously published results (Tseng *et al.,* 2009; van

Leeuwen-van Zaane *et al.*, 2013; Rajaram, Reichenberg, *et al.*, 2010; Meglinski and Matcher, 2002; Garcia-Uribe *et al.*, 2011).

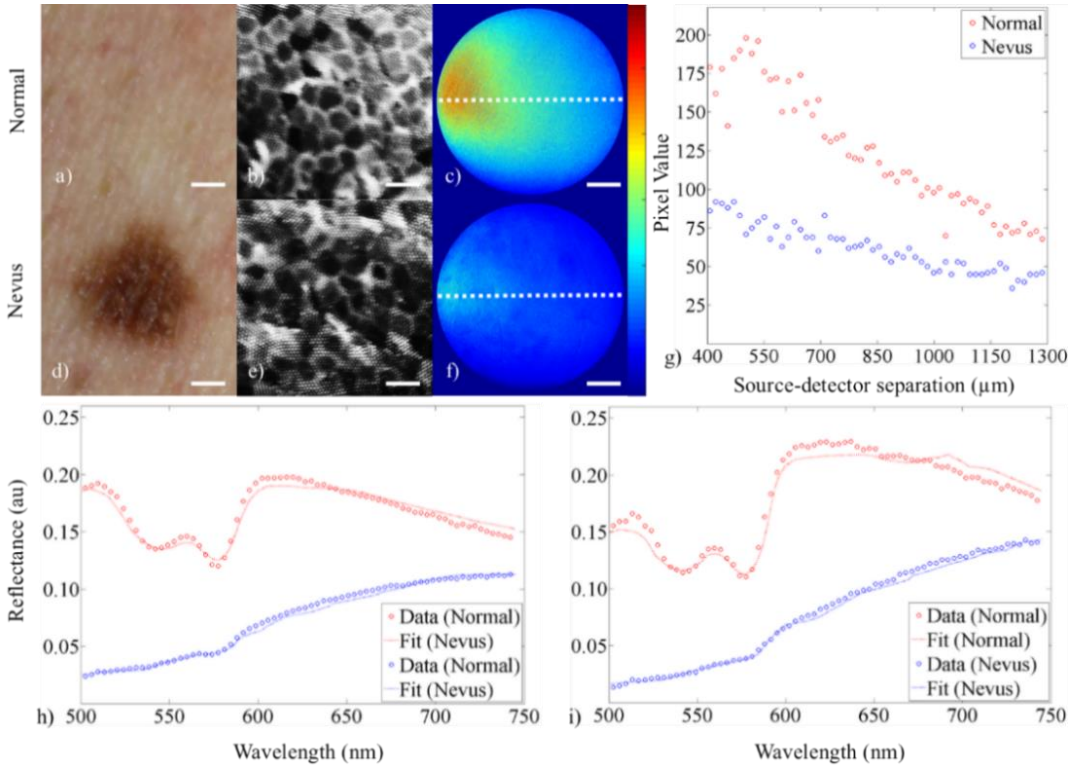

Figure 16. Demonstration of technique showing data from **(a-c)** human healthy skin tissue and **(d-f)** adjacent melanocytic nevus. The figure shows **(a, d)** a digital image of the healthy skin and adjacent melanocytic nevus (scale bar = 1 mm), **(b, e)** cropped and enhanced high-resolution fluorescence images after topical staining with pyranine-derived highlighter ink (scale bar = 50 µm), **(c, f)** DRIM data (scale bar = 225 µm, color bar = 0-225), **(g)** quantification of the DRIM data taken across the face of the image fiber (400-1,300 µm SDS from 635 nm laser source), **(h)** broadband DRS data (374 µm SDS), and **(i)** broadband DRS data (730 µm SDS). Raw data are shown as dots and the LUT-based inverse model fits are shown as a curve.

2.4.6 Ex vivo murine colon tissue

For the healthy (C57BL/6J) mouse, data was collected for all three modalities, shown in Figure 17. A DSLR image of the resected piece of colon is shown in Figure 17(a) alongside the associated histology (Figure 17(b)) and high-resolution fluorescence image (Figure 17(c)), DRIM (Figure 17(d)), and broadband DRS at both SDSs of 374 and 730 µm (Figure 17(f, g)).

For the DRIM data, a line plot was taken through the center of each intensity map (Figure 17(d)) to create a plot of intensity as a function of SDS between 400 and 1,300 μm, shown in Figure 17(e).

Note the ability to clearly resolve glandular structure in the murine colon alongside spatially resolved sub-diffuse reflectance intensity. For the DRIM data, the overall shape is similar to previous results presented here with a shape similar to that predicted by Monte Carlo models of reflectance (Martinelli *et al.*, 2011). The Soret bands due to hemoglobin can be clearly distinguished from the DRS data. The Q-bands (542 and 577 nm) are less apparent, most likely due to contributions from the underlying phantom layer. Also note that for the 730 μm SDS, there was increased reflectance contributions from longer wavelengths when compared to the 374 μm SDS. This data demonstrates that data can be acquired from murine colon tissue. Future studies will forego the use of an underlying phantom in *in vivo* studies to elucidate the effectiveness of the DRIM and DRS modalities within a larger sample size.

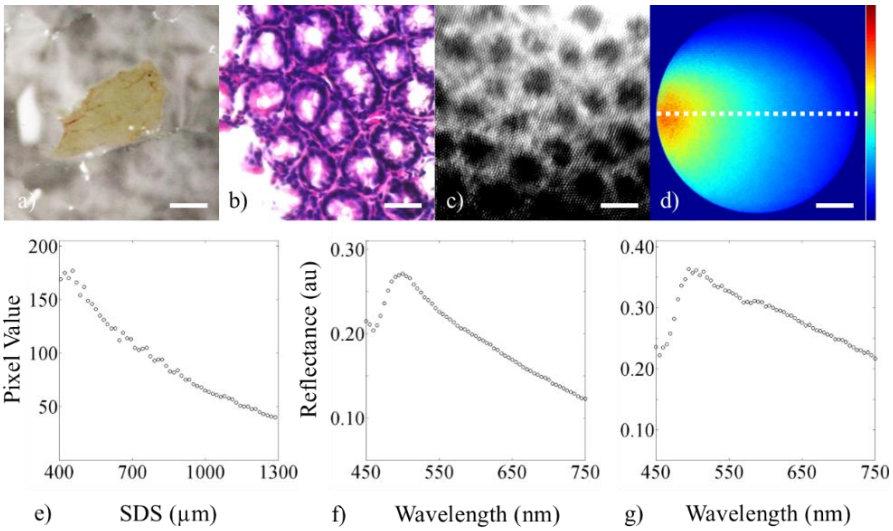

Figure 17. Demonstration of the three modalities showing data from a 16-week old wild-type (C57BL/6J) male mouse. The figure shows **(a)** digital image of the 4-5 cm colon tissue (lumen side facing up, scale bar = 5 mm), **(b)** histology of an adjacent section (scale bar = 50 μm), **(c)** cropped and enhanced high-resolution fluorescence image after topical staining with 0.01% w/v proflavine (scale bar = 50 μm), **(d)** DRIM data (scale bar = 225 μm, color bar = 0-200), **(e)** quantification of the DRIM data taken across the face of the image fiber (400-1,300 μm SDS from 635 nm laser source), **(f)** broadband DRS data (374 μm SDS), and **(g)** broadband DRS data (730 μm SDS).

2.4.7 In vivo *assessment of oral structural and optical properties*

Thirteen volunteers underwent data collection in the oral mucosa via the hybrid imaging and spectroscopy microendoscope (Figure 18). One high-resolution fluorescence image is presented in Figure 18 (a) which shows the 1 mm-diameter image circle of the image fiber in direct contact with proflavine-stained oral mucosa. Individual cell nuclei appear as distinct white spots in the image. Figure 18 (b) shows representative absolute reflectance data from both the 374 and 730 μm SDS from a single volunteer. Reflectance is presented as black dots and the LUT-based inverse model (Figure 12) and an established hemoglobin absorption spectrum (Prahl, 1999) was used to fit the data via custom post-processing software based in MATLAB. The fitted reflectance is a function of the volume-averaged optical parameters, B, THC, and StO_2 (Eq. 9 and Eq. 10). These values are presented as averages with standard deviations from the 13

volunteers in Figure 18 (d-f) and Table 1. Sampling depth was quantified and presented in Figure 10 (c) after μ_s' and μ_a were determined using the LUT-based inverse model (Figure 13).

The 730 μm SDS typically demonstrates increased reflectance values, especially at wavelengths greater than 600 nm, indicating a greater contribution from the red and near-infrared region at larger source-detector separations. This phenomenon was responsible for the decreased B values at the longer SDS of 0.48 compared to 0.80 of the shorter SDS as shown in Figure 18 (d). Average THC was significantly different at 2.39 and 2.91 mg/mL for the 374 and 730 μm SDS, respectively (Fig 18 (e)). These values support our hypothesis and demonstrate increased THC for the longer SDS compared to the shorter SDS. Average StO_2 was not significantly different at 94.1% and 91.7% for the 374 and 730 μm SDS, respectively (Figure 18 (f)), supporting our hypothesis that oxygen saturation does not significantly vary with sampling depth. Finally, sampling depth ranged between 355 and 447 μm for the 374 μm SDS and between 435 and 563 μm for the 730 μm SDS, with the sampling depth minima occurring at the first Q-band of hemoglobin at 542 nm and the sampling depth maxima occurring at the furthest tested wavelength at 750 nm. Complete paired t-test statistics for optical parameters are shown in Table 3.

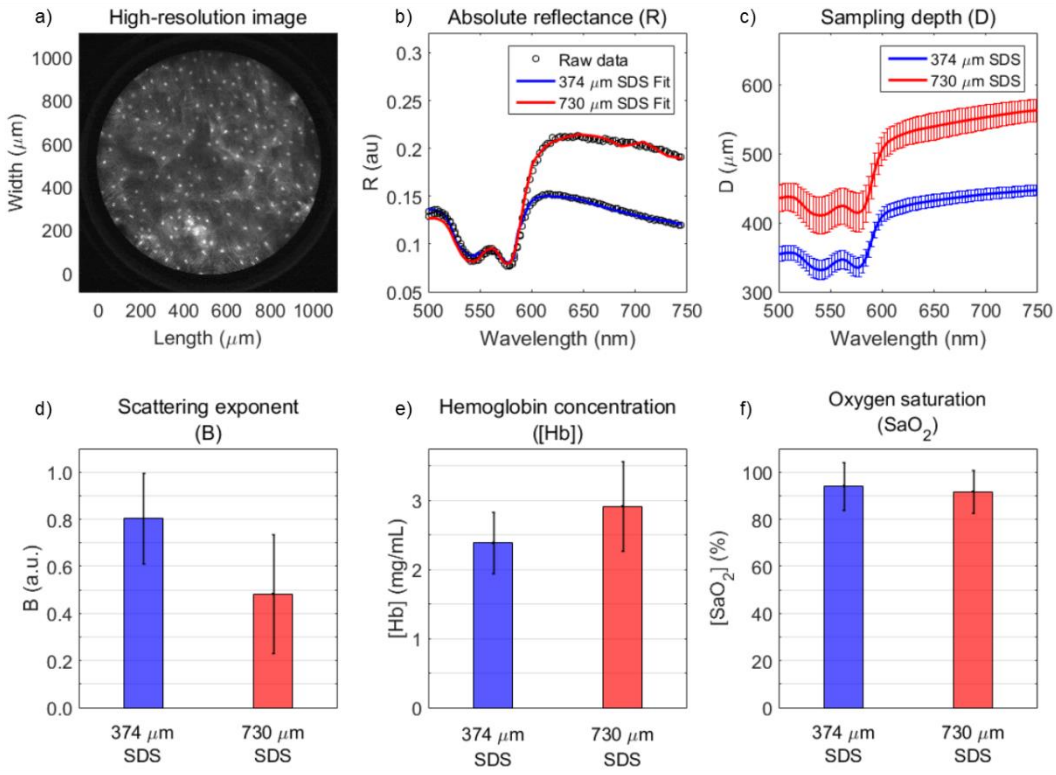

Figure 18. Comparison of qualitative and quantitative data acquired by the hybrid imaging and spectroscopy technique from 13 healthy volunteers showing (a) a high-resolution fluorescence image of apical oral mucosa from the inner lip of one volunteer (scale bar = 200 μm), (b) representative absolute reflectance profiles showing reflectance data and the overlaid LUT-based inverse model fits from the same volunteer from (a), (c) average sampling depths for each SDS, (d) scattering exponent (B), (e) hemoglobin concentration (THC), and (f) oxygen saturation (StO_2). Error bars from (c-f) represent standard deviation.

Table 3. Paired t-test statistics for extracted *in vivo* oral optical properties from LUT-based inverse model

Optical Property	374 μm SDS (n=13)		730 μm SDS (n=13)		P-Value	Significance (Y/N), α=0.01
	Mean	Std. Dev.	Mean	Std. Dev.		
B	0.80	0.19	0.48	0.25	$8.8x10^{-4}$	Y
THC (mg/mL)	2.39	0.44	2.91	0.65	$8.8x10^{-3}$	Y
StO_2 (%)	94.1	10.0	91.7	9.10	$4.6x10^{-1}$	N

2.5 Discussion

We have demonstrated a hybrid spectroscopy and imaging probe capable of acquiring qualitative and quantitative data by combining high-resolution microendoscopy and broadband DRS. High-resolution fiber-bundle microendoscopy provides a highly resolved and magnified

image of apical epithelial architecture in a small 1 mm-diameter field-of-view while DRS provides quantitative optical parameters of tissue in approximately the same image region (Figure 1 and 2). By combining these two modalities, we can co-register qualitative image data and quantitative spectral data within a single probe. Co-registration is important because this technique can be potentially used to not only detect dysplasia using two different modalities, but also to monitor personalized response of sub-surface dysplastic lesions to anti-tumor therapy at two different source-detector separations.

We characterized our technique in terms of spatial resolution, magnification, field-of-view, sampling frequency, optical property extraction, and sampling depth (Figure 11-13, Table 2). The technique was demonstrated in optical phantoms containing cultured MDA-MB-468 breast adenocarcinoma cells (Figure 15, Table 1), an *in vivo* human melanocytic nevus of the skin (Figure 16), and *ex vivo* murine colon epithelial tissue (Figure 17). The validated LUT-based inverse model was used to extract tissue optical properties of the *in vivo* human melanocytic nevus and surrounding healthy skin tissue.

High-resolution fluorescence imaging, using a coherent fiber bundle image fiber, was chosen as the first modality because of its established success in diagnosis of dysplasia in various endoscopically accessible organs. This modality can provide highly-resolved qualitative data regarding structure and morphology of the apical layers of epithelial tissue. However, alone, it lacks the capability of providing functional information and imaging deeply into tissue. To overcome this limitation, broadband DRS was chosen as a second modality to provide quantitative functional, rather than structural, information at various sampling depth ranges in tissue. Thus, these modalities have great complimentary potential. A third modality, DRIM, was developed to provide 2D, spatially-resolved image maps of sub-diffuse reflectance intensity of

the same image area and field-of-view as the high-resolution fluorescence imaging modality. These additionally modalities, DRS and DRIM, can collect information below the surface, which wasn't possible with conventional end-on fiber bundle microendoscopy (Gu *et al.*, 2014; Muldoon *et al.*, 2007; Pierce, Guan, *et al.*, 2012; Pierce *et al.*, 2011; Quinn *et al.*, 2012; Chang *et al.*, 2013; Keahey *et al.*, 2015; Parikh *et al.*, 2014; Kanick *et al.*, 2014; Kanick *et al.*, 2009; Hennessy *et al.*, 2014; Jayanthi *et al.*, 2011; Zonios *et al.*, 1999; Marin *et al.*, 2005; Greening, Powless, *et al.*, 2015; Rajaram, Aramil, *et al.*, 2010; Rajaram, Gopal, *et al.*, 2010; Rajaram *et al.*, 2008; Rajaram, Reichenberg, *et al.*, 2010).

Other techniques have attempted to address similar technical limitations. For example, high-resolution imaging techniques have been coupled with wide-field autofluorescence imaging, such as with the commercially available VELscope, to increase field-of-view while increasing diagnostic specificity in dysplastic lesions (Pierce, Schwarz, *et al.*, 2012). However, no functional depth-sensitive information is acquired. Several clinically available systems capable of providing highly resolved morphological information at varying depths are the Pentax ISC-1000 confocal endomicroscopy system (Pentax/Hoya, Japan and Optiscan Pty Ltd, Australia), and the Cellvizio system (Mauna Kea Technology, France), which have the capability of being coupled to conventional video endoscopes for combined widefield and confocal imaging (Jabbour *et al.*, 2012). These commercial systems have significantly increased sensitivity and specific in cancer diagnostics, but still lack the quantitative features that make spectroscopy attractive. Additionally, the scanning optics necessary for such confocal systems can be costly to miniaturize (Jabbour *et al.*, 2012). Our instrumentation design eliminates the need for scanning optics in favor of simple optics that combine high-resolution probe-based

fluorescence imaging with additional spectroscopy and reflectance modalities that can be potentially miniaturized for clinical use.

In this study, we designed two sets of liquid phantoms (Figure 8) to generate and validate a LUT-based inverse model that was used to extract material optical parameters from raw DRS data for each SDS (Figure 12). As of the current report, the LUTs are valid for μ_s' between 5-26 cm^{-1} and μ_a between 0-10 cm^{-1}. These ranges of optical properties are sufficient to acquire accurate DRS data for many tissue types between 500-750 nm. Furthermore, our calibration and validation methods were optimized until all average percent errors were below 10% (Figure 12 and 7), a benchmark error value comparable to many similar studies (Rajaram, Aramil, *et al.*, 2010; Rajaram, Gopal, *et al.*, 2010; Rajaram *et al.*, 2008; Rajaram, Reichenberg, *et al.*, 2010; Bish *et al.*, 2011; Bish *et al.*, 2014; Sharma *et al.*, 2013; Sharma *et al.*, 2014; Nichols *et al.*, 2012; Nichols *et al.*, 2015; Yu *et al.*, 2008; Yu *et al.*, 2010; Vishwanath *et al.*, 2011; Hennessy *et al.*, 2013).

In the same set of calibration phantoms (Figure 8), sampling depth was determined for each SDS (Hennessy *et al.*, 2014). A demonstration of calculating sampling depth was presented (Figure 9) and an empirical relationship was determined for sampling depth as a function of μ_a and μ_s' (Figure 14). Sampling depths were comparable to a similar study by Hennessy et al (Hennessy *et al.*, 2014).

Next, the bench-top technique was applied to *in vivo* oral mucosa by collecting DRS data from the inner lip of 13 healthy volunteers (Figure 10). The LUT-based inverse model was used to extract the wavelength-dependent B, THC, and StO_2 values from all 13 volunteers (Figure 18). The representative reflectance data demonstrates increased reflectance for the 730 μm SDS compared to the 374 μm SDS at wavelengths greater than approximately 600 nm, consistent with

previous findings (Greening, James, Powless, *et al.*, 2015; Mirabal *et al.*, 2002). It is well known that longer SDSs penetrate deeper into tissue, and thus longer wavelengths will dominate reflectance for longer SDSs (Sharma *et al.*, 2013; Hennessy *et al.*, 2014; Mirabal *et al.*, 2002). This phenomenon is apparent when analyzing the scattering exponent (B). At longer separations, B values decrease because of greater reflectance from longer wavelengths.

The extracted absorption-based optical properties, THC and StO_2, were comparable to other studies (Amelink *et al.*, 2011; Rajaram, Gopal, *et al.*, 2010). The longer 730 μm SDS extracted greater THC compared to the shorter 374 μm SDS. This supports our hypothesis that the longer SDS sampled deeper into the tissue vasculature, although it is clear the vasculature is still being sampled with the 374 μm SDS (Prahl, 1999; Sharma *et al.*, 2013; Chang *et al.*, 2009). This penetration into the vasculature was expected since sampling depth in the short SDS was greater than 300 μm, which exceeds the non-vascularized epithelial thickness of the oral cavity (Greening, James and Muldoon, 2015). We anticipate the standard deviations for THC and StO_2 values (Figure 18 and Table 3) to be most likely due to variations in the pressure applied between the probe tip and volunteer's inner lip. It has been shown that probe-pressure variations among measurements can induce large errors in THC and StO_2, so future studies will seek to develop a real-time probe-pressure monitoring system similar in concept to those reported in other studies (Yu *et al.*, 2014).

The study presented here was an extensive validation of the quantitative spectroscopy modality of this technique. Since this technique has been validated, its ability to monitor tissue health in response to anti-tumor therapy can be further evaluated in pre-clinical and clinical studies. Additionally, future studies will explore quantitative measures regarding the high-resolution fluorescence imaging modality, such as automated nuclear-to-cytoplasmic ratio and

cells-per-area calculations and co-register these values with DRS extracted optical parameters. Since this hybrid imaging and spectroscopy technique lacks a widefield imaging modality, future trials will explore designing probes with identical probe-tip geometries that are compatible with conventional endoscopes.

The multimodal high-resolution imaging and sub-diffuse reflectance spectroscopy fiber-bundle microendoscope reported here can be optimized and used by investigators for a variety of applications including endoscopic or handheld use for human or animal studies. It thus provides a flexible method for visualizing *in vivo* apical tissue micro-architecture alongside measurements of hemoglobin concentration, melanin concentration, and tissue oxygen saturation from two different tissue depths. This article describes the specifications for the fiber-optic probe, outlined a protocol for assembling the high-resolution imaging system and sub-diffuse reflectance imaging system, and shown its application in human tissues *in vivo*, using pyranine ink as the fluorescent contrast agent for tissue visualization. Other inks, such as proflavine or fluorescein, can be used instead of pyranine ink with appropriate approval (Chang *et al.*, 2013; Muldoon *et al.*, 2011; Greening, James, Powless, *et al.*, 2015; Prieto, Powless, Boice, *et al.*, 2015; Muldoon *et al.*, 2010).

Any probe feature may be modified from this design. For the high-resolution fluorescence microendoscopy modality, the 1 mm-diameter image fiber consisted of 50,000 individual core fibers with 4.5 μm spacing, resulting in a constant sub-cellular spatial resolution of 4.5 μm. Investigators wanting a different sized image fiber to obtain a smaller or larger field-of-view can find these image fibers readily available with diameters between 0.14 and 1.40 mm. A tube lens with focal length of 50 mm was chosen such that the CMOS sensor captured the full 1-mm field-of-view from the image fiber. When keeping the objective lens constant, increasing

the focal length of the tube lens will increase magnification and sampling frequency but decrease field-of-view (Greening, James, Powless, *et al.*, 2015). Thus, the magnification of the objective lens, focal length of the tube lens, size of the image sensor, and size of the image fiber can and should be optimized depending on need. Finally, filters and excitation light source may be modified depending on the excitation/emission spectra of fluorescent dyes (Muldoon *et al.*, 2010; Chang *et al.*, 2013; Prieto, Powless, Boice, *et al.*, 2015; Muldoon *et al.*, 2011). In addition to modifying the probe and high-resolution fluorescence microendoscopy instrumentation, the sub-diffuse reflectance spectroscopy instrumentation can be modified.

For the sub-diffuse reflectance spectroscopy modality, different sized multimode fibers can be used at each SDS. Smaller diameter multimode fibers will be able to deliver and collect light over a smaller area, but it is recommended to use an array of identically spaced fibers to increase signal-to-noise if fiber diameters less than 200 μm are used. Investigators analyzing skin or oral tissue may benefit from an overall larger probe to increase field-of-view and signal-to-noise, but in narrower luminous organs, such as the esophagus or gastrointestinal tract, investigators will face added constraints regarding probe size, especially for compatibility with the biopsy port of conventional endoscopes (Parikh *et al.*, 2014). Other spectroscopy components that may be modified include the broadband light source and motorized optical switch. A tungsten-halogen lamp was chosen in this case, although other light sources can and have been used in other studies, including xenon arc lamps and LEDs, which may increase signal-to-noise and lower integration times (Rajaram, Reichenberg, *et al.*, 2010; Yu *et al.*, 2014; Bish *et al.*, 2014). The motorized optical switch presented here was custom built to handle up to three SDSs, but can be modified to include more or less inputs. It should be noted that the motorized optical switch does add an additional optical component between the broadband light source and

spectrometer, decreasing signal-to-noise. The switch may not be necessary for investigators with multiple spectrometers that acquire data simultaneously, but including an optical switch component ultimately reduces instrumentation cost by approximately $3,000USD per SDS.

Construction of the instrumentation (Figure 4 and 5) is fairly straightforward. The most critical step in this protocol is the calibration of the sub-diffuse reflectance spectroscopy modality (Figure 6 and 7). Calibration must be completed immediately prior to spectral data collection. Once calibration has been completed, ensure no pieces of the instruments are shut off or re-calibration may be necessary. Proper calibration is necessary to obtain accurate reflectance spectra, and thus obtain accurate values for underlying melanin concentration, hemoglobin concentration, and tissue oxygen saturation from an unknown sample. Conveniently, most investigators use similar calibration techniques which have been well described (Greening, James, Powless, *et al.*, 2015; Rajaram, Gopal, *et al.*, 2010; Rajaram, Reichenberg, *et al.*, 2010; Nichols *et al.*, 2012). Information regarding software requirements for converting reflectance spectra into optical parameters can be found elsewhere (Rajaram *et al.*, 2008; Greening, James and Muldoon, 2015; Greening, James, Powless, *et al.*, 2015).

In regard to troubleshooting, spectra resulting in poor fits (average percent errors greater than 10% between raw data and fitted data) will yield unreliable values for the three tissue physiological parameters (THC, [Mel], and StO_2) presented here. Poor fits are most likely the result of either movement between the probe and skin site during data acquisition, narrow boundary conditions in the post-processing code, or unreliable *a priori* values of THC and [Mel] (Prahl, 1999; Greening, James, Powless, *et al.*, 2015; Rajaram *et al.*, 2008; Greening, James and Muldoon, 2015). Improvements in these three common error occurrences should fix the accurate fitting of sub-diffuse reflectance spectra. Thus, data collection can be improved by reducing

spectrometer integration time to reduce motion artifacts within the spectra. Additionally, boundary conditions represent the range of possible computational output values for THC, [Mel], and StO_2 following post-processing. In these studies, boundary conditions were 0-10 mg/mL for THC (Prahl, 1999; Rajaram, Aramil, *et al.*, 2010), 0-40 mg/mL for [Mel] (Karsten and Smit, 2012; Glennie *et al.*, 2015), and 0-100% for StO_2 (Lim *et al.*, 2011), which are based on values from previous studies (Prahl, 1999; Karsten and Smit, 2012; Lim *et al.*, 2011; Rajaram, Aramil, *et al.*, 2010; Glennie *et al.*, 2015). If measuring tissue without melanin, the lower and upper bounds for [Mel] can both simply be set to 0 mg/mL. Finally, it is recommended to use established *a priori* absorbance values for hemoglobin and melanin published by Prahl et al (Prahl, 1999). These simple improvements should fix the accurate fitting of sub-diffuse reflectance spectra, and if questions remain, spectra can be validated with phantoms with known optical properties (reduced scattering and absorption coefficients).

The primary limitation to this multimodal imaging and spectroscopy fiber-bundle microendoscopy platform is the lack of a widefield imaging modality. The high-resolution fluorescence microendoscopy modality has a circular field-of-view that is 1 mm in diameter, making it difficult to rapidly scan a large area of tissue. One computational method to overcome this limitation is image mosaicking, a technique used to provide a broader field-of-view by stacking adjacent micro-scale images into a single, larger image map (Prieto, Powless, Lai, *et al.*, 2015). Such image mosaicking has been previously demonstrated by Prieto et al. to investigate colonic image features (Prieto, Powless, Lai, *et al.*, 2015). An instrumentation modification to overcome this limitation would be making the probe compatible with the biopsy port of a conventional endoscope, such as the probe presented by Parikh et al. to investigate colorectal

neoplasia (Parikh *et al.*, 2014). This feature combines the advantages of a wide field-of-view with micro-scale imaging of high-resolution fluorescence microendoscopy (Parikh *et al.*, 2014).

Overall, this technique was demonstrated on *in vivo* human skin and shows the value of co-registering high-resolution tissue micro-architectural images with the underlying melanin concentration, hemoglobin concentration, and tissue oxygen saturation. This technique can be used by researchers wishing to investigate the link between structural and functional tissue abnormalities *in vivo* or analyzing tissue functional changes in the absence of observable structural changes. Future studies will investigate the viability of this technique in various epithelial disease states.

2.6 Conclusion

We have developed a hybrid spectroscopy and imaging technique comprising of a conventional fluorescence fiber-bundle microendoscopy platform coupled with a series of off-axis broadband spectroscopy (DRS) channels. Since dysplasia can initially arise near the epithelial basement membrane, collecting structural and functional information from deeper within the tissue microenvironment is critical for many applications, including detection of early dysplasia, analysis of tumorigenesis, and monitoring of therapeutic response. As a result, this hybrid imaging and spectroscopy platform may be capable of collecting a wealth of information about the structural and functional properties of tissue at various imaging sites in *ex vivo* and *in vivo* models. Finally, the potential of this technique to be coupled to the biopsy port of a conventional endoscope makes further clinical translation and complimentary optical biopsy in the oral cavity and other epithelial tissues feasible.

2.7 Acknowledgements

This material is based on work supported by the National Institutes of Health (1R03-CA182052, 1R15-CA202662), the National Science Foundation Graduate Research Fellowship Program (G.G., DGE-1450079), the Arkansas Biosciences Institute, and the University of Arkansas Doctoral Academy Fellowship. Any opinions, findings, and conclusions or recommendations expressed in this material are those of the authors and do not necessarily reflect the views of the acknowledged funding agencies.

References

Amelink, A., *et al.* "Non-Invasive Measurement of the Microvascular Properties of Non-Dysplastic and Dysplastic Oral Leukoplakias by Use of Optical Spectroscopy." *Oral Oncology* 47.12 (2011): 1165-70.

Appelman, H.D. "What Is Dysplasia in the Gastrointestinal Tract?" *Archives of Pathology & Laboratory Medicine* 129.2 (2005): 170-3.

Arends, M.J., *et al.* "Aetiology, Pathogenesis, and Pathology of Cervical Neoplasia." *Journal of Clinical Pathology* 51.2 (1998): 96-103.

Bashkatov, A.N., *et al.* "Optical Properties of Human Colon Tissues in the 350 – 2500 Nm Spectral Range." *Quantum Electronics* 44.8 (2014): 779-84.

Bezemer, R., *et al.* "Simultaneous Multi-Depth Assessment of Tissue Oxygen Saturation in Thenar and Forearm Using near-Infrared Spectroscopy During a Simple Cardiovascular Challenge." *Critical Care* 13.5 (2009).

Bish, S.F., *et al.* "Development of a Noncontact Diffuse Optical Spectroscopy Probe for Measuring Tissue Optical Properties." *Journal of Biomedical Optics* 16.12 (2011): 120505.

Bish, S.F., *et al.* "Handheld Diffuse Reflectance Spectral Imaging (Drsi) for in-Vivo Characterization of Skin." *Biomedical Optics Express* 5.2 (2014): 573-86.

Bouquot, J.E., *et al.* "Epithelial Dysplasia of the Oral Mucosa—Diagnosticproblems and Prognostic Features." *Current Diagnostic Pathology* 12 (2006): 11-21.

Brailo, V. "Dentist and Early Detection of Oral Carcinoma." *Acta Medica Croatica* 69.1 (2015): 45-48.

Brocklehurst, P., *et al.* "Comparative Accuracy of Different Members of the Dental Team in Detecting Malignant and Non-Malignant Oral Lesions." *British Dental Journal* 218.9 (2015): 525-29.

Campbell, A.P., *et al.* "Flexible Cochlear Microendoscopy in the Gerbil." *Laryngoscope* 120.8 (2010).

Carns, J., *et al.* "Optical Molecular Imaging in the Gastrointestinal Tract." *Gastrointestinal Endoscopy Clinics of North America* 23.3 (2013).

Chang, S.S., *et al.* "High Resolution Microendoscopy for Classification of Colorectal Polyps." *Endoscopy* 45.7 (2013): 553-9.

Chang, V.T., *et al.* "Quantitative Physiology of the Precancerous Cervix in Vivo through Optical Spectroscopy." *Neoplasia* 11.4 (2009): 325-32.

Chen, X., *et al.* "Multimodal Nonlinear Endo-Microscopy Probe Design for High Resolution, Label-Free Intraoperative Imaging." *Biomedical Optics Express* 6.7 (2015): 2283-93.

Cheng, Y.S., *et al.* "Updates Regarding Diagnostic Adjuncts for Oral Squamous Cell Carcinoma." *Texas Dental Journal* 132.8 (2015): 538-49.

Dacosta, R.S., *et al.* "New Optical Technologies for Earlier Endoscopic Diagnosis of Premalignant Gastrointestinal Lesions." *Journal of Gastroenterology and Hepatology* 17 (2002).

Davies, K., *et al.* "Point of Care Optical Diagnostic Technologies for the Detection of Oral and Oropharyngeal Squamous Cell Carcinoma." *The Surgeon* 13.6 (2015): 321-29.

Dehghani, H., *et al.* "Numerical Modelling and Image Reconstruction in Diffuse Optical Tomography." *Philosophical Transactions of the Royal Society A* 367 (2009).

Di Ninni, P., *et al.* "The Use of India Ink in Tissue-Simulating Phantoms." *Optics Express* 18.26 (2010): 26854-65.

Durduran, T., *et al.* "Diffuse Optics for Tissue Monitoring and Tomography." *Reports on Progress in Physics* 73.7 (2010): 076701.

Elahi, S.F., *et al.* "Targeted Imaging of Colorectal Dysplasia in Living Mice with Fluorescence Microendoscopy." *Biomedical Optics Express* 2.4 (2011): 981–86.

Fu, H.L., *et al.* "A Low-Cost, Portable, and Quantitative Spectral Imaging System for Application to Biological Tissues." *Optics Express* 18.12 (2010): 12630-45.

Garcia-Uribe, A., *et al.* "In-Vivo Characterization of Optical Properties of Pigmented Skin Lesions Including Melanoma Using Oblique Incidence Diffuse Reflectance Spectrometry." *Journal of Biomedical Optics* 16.2 (2011).

Ghassemi, P., *et al.* "A Polarized Multispectral Imaging System for Quantitative Assessment of Hypertrophic Scars." *Biomedical Optics Express* 5.10 (2014): 3337–54.

Glennie, D.L., *et al.* "Modeling Changes in the Hemoglobin Concentration of Skin with Total Diffuse Reflectance Spectroscopy." *Journal of Biomedical Optics* 20.3 (2015): 035002.

Glennie, D.L., *et al.* "Inexpensive Diffuse Reflectance Spectroscopy System for Measuring Changes in Tissue Optical Properties." *Journal of Biomedical Optics* 19.10 (2014): 105005.

Greening, G.J., *et al.* "Characterization of Thin Poly (Dimethylsiloxane)-Based Tissue Simulating Phantoms with Tunable Reduced Scattering and Absorption Coefficients at Visible and Nearinfrared Wavelength." *Journal of Biomedical Optics* 19.11 (2014): 115002.

Greening, G.J., *et al.* Optical Phantoms: Diffuse and Sub-Diffuse Imaging and Spectroscopy Validation. Bellingham, Washington: SPIE Spotlights, 2015.

Greening, G.J., *et al.* "Fiber-Bundle Microendoscopy with Sub-Diffuse Reflectance Spectroscopy and Intensity Mapping for Multimodal Optical Biopsy of Stratified Epithelium." *Biomedical Optics Express* 6.12 (2015): 4934-50.

Greening, G.J., *et al.* "Design and Validation of a Diffuse Reflectance and Spectroscopic Microendoscope with Poly(Dimethylsiloxane)-Based Phantoms." *Proceedings of SPIE* 9332 (2015).

Gu, M., *et al.* "Fibre-Optical Microendoscopy." *Journal of Microscopy* 254.1 (2014): 13-8.

Harpaz, N., and A.D. Polydorides. "Colorectal Dysplasia in Chronic Inflammatory Bowel Disease: Pathology, Clinical Implications, and Pathogenesis." *Archives of Pathology & Laboratory Medicine* 134.6 (2010): 876-95.

Hennessy, R., *et al.* "Effect of Probe Geometry and Optical Properties on the Sampling Depth for Diffuse Reflectance Spectroscopy." *Journal of Biomedical Optics* 19.10 (2014): 107002.

Hennessy, R., *et al.* "Monte Carlo Lookup Table-Based Inverse Model for Extracting Optical Properties from Tissue-Simulation Phantoms Using Diffuse Reflectance Spectroscopy." *Journal of Biomedical Optics* 18.3 (2013): 037003.

Hennessy, R., *et al.* "Impact of One-Layer Assumption on Diffuse Reflectance Spectroscopy of Skin." *Journal of Biomedical Optics* 20.2 (2015): 27001.

Hur, C., *et al.* "High-Resolution Microendoscopy for Esophageal Cancer Screening in China: A Cost-Effectiveness Analysis." *World Journal of Gastroenterology* 21.18 (2015): 5513-23.

Hwang, S.J., and K.R. Shroyer. "Biomarkers of Cervical Dysplasia and Carcinoma." *Journal of Oncology* (2012).

Ishijimi, A., *et al.* "Automated Frame Selection Process for High-Resolution Microendoscopy." *Journal of Biomedical Optics* 20.4 (2015): 46014.

Jabbour, J.M., *et al.* "Confocal Endomicroscopy: Instrumentation and Medical Applications." *Annals of Biomedical Engineering* 40.2 (2012).

Jacques, S.L. *Optical Absorption of Melanin*2015. Print.

Jayanthi, J.L., *et al.* "Diffuse Reflectance Spectroscopy: Diagnostic Accuracy of a Non-Invasive Screening Technique for Early Detection of Malignant Changes in the Oral Cavity." *BMJ Open* (2011).

Kanick, S.C., *et al.* "Sub-Diffusive Scattering Parameter Maps Recovered Using Wide-Field High-Frequency Structured Light Imaging." *Biomedical Optics Express* 5.10 (2014): 3376-90.

Kanick, S.C., *et al.* "Monte Carlo Analysis of Single Fiber Reflectance Spectroscopy: Photon Path Length and Sampling Depth." *Physics in Medicine and Biology* 54.22 (2009): 6991-7008.

Karim, B.O., and D.L. Huso. "Mouse Models for Colorectal Cancer." *American Journal of Cancer Research* 3.3 (2013): 240-50.

Karsten, A.E., *et al.* "Diffuse Reflectance Spectroscopy as a Tool to Measure the Absorption Coefficient in Skin: South African Skin Phototypes." *Photochemistry and Photobiology* 89.1 (2013): 227-33.

Karsten, A.E., *et al*. "Diffuse Reflectance Spectroscopy as a Tool to Measure the Absorption Coefficient in Skin: System Calibration." *Lasers in Surgery and Medicine* 28.2 (2013): 437-44.

Karsten, A.E., and J.E. Smit. "Modeling and Verification of Melanin Concentration on Human Skin Type." *Photochemistry and Photobiology* 88.2 (2012): 469-74.

Keahey, P.A., *et al.* "Optimizing Modulation Frequency for Structured Illumination in a Fiber-Optic Microendoscope to Image Nuclear Morphometry in Columnar Epithelium." *Biomedical Optics Express* 6.3 (2015): 870-80.

Kiisk, V. "An Educational Spectrograph Using a Digital Camera as a Training Aid for Physics Students." *European Journal of Physics* 35.3 (2014).

Levy, L.L., *et al.* "Optical Imaging with a High Resolution Microendoscope to Identify Cholesteatoma of the Middle Ear." *Laryngoscope* 123.4 (2013): 1016-20.

Lim, L., *et al.* "Probe Pressure Effects on Human Skin Diffuse Reflectance and Fluorescence Spectroscopy Measurements." *Journal of Biomedical Optics* 16.1 (2011): 011012.

Louie, J.S., *et al.* "Applications and Advancements in the Use of High-Resolution Microendoscopy for Detection of Gastrointestinal Neoplasia." *Clinical Gastroenterology and Hepatology* 12.11 (2014): 1789-92.

Marin, N.M., *et al.* "Diffuse Reflectance Patterns in Cervical Spectroscopy." *Gynecologic Oncology* 99.3 (2005): 116-20.

Martinelli, M., *et al.* "Analysis of Single Monte Carlo Methods for Prediction of Reflectance from Turbid Media." *Optics Express* 19.20 (2011).

Meglinski, I.V., and S.J. Matcher. "Quantitative Assessment of Skin Layers Absorption and Skin Reflectance Spectra Simulation in the Visible and near-Infrared Spectral Regions." *Physiological Measurement* 23.4 (2002).

Mirabal, Y.N., *et al.* "Reflectance Spectroscopy for in Vivo Detection of Cervical Precancer." *Journal of Biomedical Optics* 7.4 (2002): 587-94.

Monfared, A., *et al.* "In Vivo Imaging of Mammalian Cochlear Blood Flow Using Fluorescence Microendoscopy." *Otology & Neurotology* 27.2 (2006): 144-52.

Moser, A.R., *et al.* "A Dominant Mutation That Predisposes to Multiple Intestinal Neoplasia in the Mouse." *Science* 247.4940 (1990): 322-4.

Mourant, J.R., *et al.* "Mechanisms of Light Scattering from Biological Cells Relevant to Noninvasive Optical-Tissue Diagnostics." *Applied Optics* 37.16 (1998): 3586-93.

Mourant, J.R., *et al.* "Hemoglobin Parameters from Diffuse Reflectance Data." *Jouornal of Biomedical Optics* 19.3 (2014).

Muldoon, T.J., *et al.* "High-Resolution Imaging in Barrett's Esophagus: A Novel, Low-Cost Endoscopic Microscope." *Gastrointestinal Endoscopy* 68.4 (2008): 737-44.

Muldoon, T.J., *et al.* "Subcellular-Resolution Molecular Imaging within Living Tissue by Fiber Microendoscopy." *Optics Express* 15.25 (2007): 16413-23.

Muldoon, T.J., *et al.* "Noninvasive Imaging of Oral Neoplasia with a High-Resolution Fiber-Optic Microendoscope." *Head & Neck* 34.3 (2011): 305-12.

Muldoon, T.J., *et al.* "Evaluation of Quantitative Image Analysis Criteria for the High-Resolution Microendoscopic Detection of Neoplasia in Barrett's Esophagus." *Journal of Biomedical Optics* 15.2 (2010): 026027.

Nichols, B.S., *et al.* "Performance of a Lookup Table-Based Approach for Measuring Tissue Optical Properties with Diffuse Optical Spectroscopy." *Journal of Biomedical Optics* 17.5 (2012): 057001.

Nichols, B.S., *et al.* "A Quantitative Diffuse Reflectance Imaging (Qdri) System for Compresensive Surveillance of the Morphological Landscape in Breast Tumor Margins." *PLOS One* 10.6 (2015): e0127525.

Parikh, N., *et al.* "In Vivo Diagnostic Accuracy of High Resolution Microendoscopy in Differentiating Neoplastic from Non-Neoplastic Colorectal Polyps: A Prospective Study." *The American Journal of Gastroenterology* 109.1 (2014): 68-75.

Pierce, M.C., *et al.* "A Pilot Study of Low-Cost, High-Resolution Microendoscopy as a Tool for Identifying Women with Cervical Precancer." *Cancer Prevention Research* 5.11 (2012): 1273-9.

Pierce, M.C., *et al.* "Accuracy of in Vivo Multi-Modal Optical Imaging for Detection of Oral Neoplasia." *Cancer Prevention Research* 5.6 (2012): 801-9.

Pierce, M.C., *et al.* "High-Resolution Fiber-Optic Microendoscopy for in Situ Cellular Imaging." *Journal of Visualized Experiments* 47 (2011).

Pimenta, S., *et al.* "Optical Microsystem for Analysis of Diffuse Reflectance and Fluorescence Signals Applied to Early Gastrointestinal Cancer Detection." *Sensors* 15.2 (2012): 3138-53.

Piyawattanametha, W., and T.D. Wang. "Mems-Based Dual Axes Confocal Microendoscopy." *IEEE Journal of Selected Topics in Quantum Electronics* 16.4 (2010): 804–14.

Pogue, B.W., and M.S. Patterson. "Review of Tissue Simulating Phantoms for Optical Spectroscopy, Imaging and Dosimetry." *Journal of Biomedical Optics* 11.4 (2006).

Ponz de Leon, M., and C. Di Gregorio. "Pathology of Colorectal Cancer." *Digestive and Liver Disease* 33.4 (2001): 372-88.

Prahl, S.A. "Optical Absorption of Hemoglobin." 1999. Web. January 1, 2016.

Prieto, S.P., *et al.* "Proflavine Hemisulfate as a Fluorescent Contrast Agent for Point-of-Care Cytology." *PLOS One* 10.5 (2015): e0125598.

Prieto, S.P., *et al.* "Qualitative and Quantitative Comparison of Colonic Microendoscopy Image Features to Histopathology." *Proceedings of SPIE* 9328 (2015).

Quinn, M.K., *et al.* "High-Resolution Microendoscopy for the Detection of Cervical Neoplasia in Low-Resource Settings." *PLOS One* 7.9 (2012).

Rajaram, N., *et al.* "Design and Validation of a Clinical Instrument for Spectral Diagnosis of Cutaneous Malignancy." *Applied Optics* 49.2 (2010): 142-52.

Rajaram, N., *et al.* "Experimental Validation of the Effects of Microvasculature Pigment Packaging on in Vivo Diffuse Reflectance Spectroscopy." *Lasers in Surgery and Medicine* 42.7 (2010): 680-8.

Rajaram, N., *et al.* "Lookup Table-Based Inverse Model for Determining Optical Properties of Turbid Media." *Journal of Biomedical Optics* 13.5 (2008): 050501.

Rajaram, N., *et al.* "Pilot Clinical Study for Quantitative Spectral Diagnosis of Non-Melanoma Skin Cancer." *Lasers in Surgery and Medicine* 42.10 (2010): 716-27.

Regunathan, R., *et al.* "Feasibility and Preliminary Accuracy of High-Resolution Imaging of the Liver and Pancreas Using Fns Compatible Microendoscopy." *Gastrointestinal Endoscopy* 76.2 (2012): 293-300.

Rivera, D.R., *et al.* "Compact and Flexible Raster Scanning Multiphoton Endoscope Capable of Imaging Unstained Tissue." *PNAS* 108.43 (2011): 17598-603.

Sandell, J.L., and T.C. Zhu. "A Review of in-Vivo Optical Properties of Human Tissues and Its Impact on Pdt." *Journal of Biophotonics* 4.11 (2011): 773-87.

Shangguan, H., *et al.* "Pressure Effects on Soft Tissues Monitored by Changes in Tissue Optical Properties." *SPIE Proceedings of Laser-Tissue Interaction IX* 3254 (1998): 366-71.

Sharma, M., *et al.* "Verification of a Two-Layer Inverse Monte Carlo Absorption Model Using Multiple Source-Detector Separation Diffuse Reflectance Spectroscopy." *Biomedical Optics Express* 5.1 (2013): 40–53.

Sharma, M., *et al.* "Design and Characterization of a Novel Multimodal Fiber-Optic Probe and Spectroscopy System for Skin Cancer Applications." *Review of Scientfic Instruments* 85 (2014): 083101.

Sharma, P. "Gastrointestinal Dysplasia." *Pathology* 45.3 (2013): 273-85.

Shin, D., *et al.* "Quantitative Analysis of High-Resolution Microendoscopic Images for Diagnosis of Esophageal Squamous Cell Carcinoma." *Clinical Gastroenterology and Hepatology* 13 (2015): 272-79.

Shukla, R., *et al.* "Endoscopic Imaging: How Far Are We from Real-Time Histology?" *World Journal of Gastroenterology* 3.10 (2011): 183-94.

Siegman, A. "Fresnel Reflection, Lenserf Reflection and Evanescent Gain." *Optics and Photonics News* 21.1 (2010): 38-45.

Simpson, C.R., *et al.* "Near-Infrared Optical Properties of Ex Vivo Human Skin and Subcutaneous Tissues Measured Using the Monte Carlo Inversion Technique." *Physics in Medicine and Biology* 43.9 (1998).

Speight, P.M. "Update on Oral Epithelial Dysplasia and Progression to Cancer." *Head and Neck Pathology* 1.1 (2007): 61-6.

Su, L.K., *et al.* "Multiple Intestinal Neoplasia Caused by a Mutation in the Murine Homolog of the Apc Gene." *Science* 256.5057 (1992): 668-70.

Subramanian, H., *et al.* "Penetration Depth of Low-Coherence Enhanced Backscattered Light in Subdiffusion Regime." *Physical Review E: Statistical, Nonlinear, and Soft Matter Physics* 75.4 (2007): 041914.

Tseng, S., *et al.* "Chromophore Concentrations, Absorption and Scattering Properties of Human Skin in-Vivo." *Optics Express* 17.17 (2009).

Turzhitsky, V., *et al.* "A Predictive Model of Backscattering at Subdiffusion Length Scales." *Biomedical Optics Express* 1.3 (2010): 1034-46.

Turzhitsky, V., *et al.* "Characterization of Light Transport in Scattering Media at Sub-Diffusion Length Scales with Low-Coherence Enhanced Backscattering." *IEEE Journal of Selected Topics in Quantum Electronics* 16.3 (2010): 619-26.

van Leeuwen-van Zaane, F., *et al.* "In Vivo Quantification of the Scattering Properties of Tissue Using Multi-Diameter Single Fiber Reflectance Spectroscopy." *Biomedical Optics Express* 4.5 (2013).

Vasefi, F., *et al.* "Polarization-Sensitive Hyperspectral Imaging in Vivo: A Multimode Dermoscope for Skin Analysis." *Scientific Reports* 4.4924 (2014).

Vishwanath, K., *et al.* "Portable, Fiber-Based, Diffuse Reflection Spectroscopy (Drs) Systems for Estimating Tissue Optical Properties." *Applied Spectroscopy* 62.2 (2011): 206-15.

Wall, R.A., and J.K. Barton. "Oblique Incidence Reflectometry: Optical Models and Measurements Using a Side-Viewing Gradient Index Lens-Based Endoscopic Imaging System." *Journal of Biomedical Optics* 19.6 (2014).

Warnakulasuriya, S., *et al.* "Oral Epithelial Dysplasia Classification Systems: Predictive Value, Utility, Weaknesses and Scope for Improvement." *Journal of Oral Pathology & Medicine* 37.3 (2008): 127-33.

Wei, H.J., *et al.* "Differences in Optical Properties between Healthy and Pathological Human Colon Tissues Using a Ti:Sapphire Laser: An in Vitro Study Using the Monte Carlo Inversion Technique." *Journal of Biomedical Optics* 10.4 (2005).

Winkler, A.M., *et al.* "Quantitative Tool for Rapid Disease Mapping Using Optical Coherence Tomography Images of Azoxymethane-Treated Mouse Colon." *Journal of Biomedical Optics* 15.4 (2010): 041512.

Yu, B., *et al.* "Instrument Independent Diffuse Reflectance Spectroscopy." *Journal of Biomedical Optics* 16.1 (2010): 011010.

Yu, B., *et al.* "Cost-Effective Diffuse Reflectance Spectroscopy Device for Quantifying Tissue Absorption and Scattering in Vivo." *Journal of Biomedical Optics* 13.6 (2008): 060505.

Yu, B., *et al.* "Diffuse Reflectance Spectroscopy of Epithelial Tissue with a Smart Fiber-Optic Probe." *Biomedical Optics Express* 5.3 (2014): 675-89.

Zhang, Y. "Epidemiology of Esophageal Cancer." *World Journal of Gastroenterology* 19.34 (2013): 5598-606.

Zhu, C., and Q. Liu. "Validity of the Semi-Infinite Tumor Model in Diffuse Reflectance Spectroscopy for Epithelial Cancer Diagnosis: A Monte Carlo Study " *Optics Express* 19.18 (2011): 17799-812.

Zonios, G., *et al.* "Melanin Absorption Spectroscopy: New Method for Noninvasive Skin Investigation and Melanoma Detection." *Journal of Biomedical Optics* 13.1 (2008).

Zonios, G., *et al.* "Diffuse Reflectance Spectroscopy of Human Adenomatous Colon Polyps in Vivo." *Applied Optics* 38.31 (1999): 6628-37.

<u>Chapter 3 (Specific Aim 2)</u>: Characterization of poly(dimethylsiloxane)-based tissue-simulating phantoms with tunable reduced scattering and absorption coefficients with applications for diffuse reflectance spectroscopy

3.1 Introduction

The translation of novel optical imaging techniques from a basic laboratory setting to a clinical setting requires substantial calibration and validation, which is often performed on tissue-simulating materials known as phantoms. Tissue-simulating phantoms have several broad applications in regard to imaging systems including optimizing software and hardware, gathering preclinical data in advance of clinical trials, and are necessary for providing proof of reproducibility between trials of certain optical imaging techniques (de Bruin *et al.*, 2010; Saager *et al.*, 2010; Cerussi *et al.*, 2012). For example, optical coherence tomography (OCT) may use phantoms to determine vital instrumentation characteristics including axial and lateral resolution and point spread function (Gu *et al.*, 2012; Agrawal *et al.*, 2013). Diffuse Optical Spectroscopic Imaging (DOSI) techniques may use phantoms for initial calibration and stability measurements between trials (Cerussi *et al.*, 2012). Features of phantoms that are viewed as especially important include precise control of phantom geometry, the ability to easily modify and quantify scattering and absorption properties across commonly used wavelengths, stability over time, a comparable refractive index to human tissue, and the ability to introduce thin layers of different optical properties to simulate heterogeneities commonly seen in tissue (de Bruin *et al.*, 2010; Saager *et al.*, 2010; Cerussi *et al.*, 2012; Moffitt *et al.*, 2006; Pogue *et al.*, 2006). These heterogeneities may represent layers of different cell types as seen in the interface between the

dermis and epidermis of the skin, or as malignant morphological changes in a single tissue type as a result of disease (de Bruin *et al.*, 2010).

Optical phantoms are a widely used tool to validate optical instrumentation. In essence, phantoms are "false-tissues" made of various materials and can be liquid, solid, or gelatinous. Generally, phantoms are made to either simulate a tissue's optical, mechanical, chemical, or physical properties, or a combination of these. These structures are typically comprised of a base substrate material which can be doped with certain additives that give the material specific optical, mechanical, or chemical properties. Additionally, depending on the substrate material used and desired geometry, optical phantoms can be molded into a variety of shapes and sizes for different applications (Pogue *et al.*, 2006; Greening *et al.*, 2014; Lamouche *et al.*, 2012).

This chapter opens with a review of optical phantoms as validation tools for imaging and spectroscopy platforms, with a majority of the discussed optical instrumentation being probe-based. This will provide insight into the use of optical phantoms within the context of current biomedical optics research. Following this, the "diffuse" and "sub-diffuse" scattering regimes governing light transport through tissue will be addressed. Distinguishing between the "diffuse" and "sub-diffuse" scattering regimes is important for several reasons including 1) generating design requirements for probe-based instrumentation, especially for determining appropriate source-detector separations in spectroscopy probes, 2) evaluating the accuracy of computational or numerical models of light transport, and 3) understanding the optical properties of target human tissues and designing optical phantoms to mimic such tissues. Finally, this chapter concludes with a tutorial on how to construct thin, solid, multilayer tissue-simulating phantoms using a spin-coating technique for a variety of applications, and a tutorial on how to construct liquid phantoms to build a lookup table (LUT) inverse model to extract optical properties using

diffuse or sub-diffuse reflectance spectroscopy.

3.2 Phantoms in Probe-Based Optical Systems

Each subtype of optical phantom discussed in this section will be described based on their intended application, substrate material, scattering and absorbing agents, corresponding reduced scattering coefficients (μ_s') and absorption coefficients (μ_a), and experimental design. Additionally, the probe and/or detector used to acquire data will be briefly described. Optical phantoms for validating instrumentation in high-resolution microendoscopy, hyperspectral imaging, diffuse optical tomography, reflectance spectroscopy, fluorescence spectroscopy, and Raman spectroscopy will be discussed.

3.2.1 High-resolution microendoscopy

High-resolution microendoscopy is a non-invasive, imaging technique that couples a light source to a small image fiber probe. The probe is placed in contact with an exogenously stained sample, is excited via an illumination source, and then fluorescence emission travels back through the probe, distal optics, and into an image sensor to provide high-resolution, spatially resolved images of tissue morphology. Contrast may be provided by a variety of exogenous tissue stains. Various high-resolution microendoscopy techniques have been explored to reduce signal contributions from outside the focal plane, including two-photon and confocal microendoscopic systems, as well as structured illumination (SI). Optical phantoms are a useful tool in high-resolution microendoscopy to investigate imaging parameters or for a demonstration of technique prior to imaging *ex vivo* or *in vivo* tissue samples (Bedard *et al.*, 2012; S. S. Chang *et al.*, 2013; Campbell *et al.*, 2010; Muldoon *et al.*, 2008; Muldoon *et al.*, 2007; Muldoon *et al.*, 2011; Kyrish *et al.*, 2013; Louie *et al.*, 2014; Parikh *et al.*, 2014; Prieto *et al.*, 2015; Pierce, Guan, *et al.*, 2012; Pierce, Schwarz, *et al.*, 2012; Pierce *et al.*, 2011; Quinn *et al.*, 2012; Shin *et*

al., 2015; Shukla *et al.*, 2011; Koucky *et al.*, 2013; Gu *et al.*, 2010; Shahmoon *et al.*, 2013; Keahey *et al.*, 2015; Maitland *et al.*, 2006; Makhlouf *et al.*, 2011; Rogers *et al.*, 2008). Figure 1 shows a simple schematic of high-resolution microendoscopy instrumentation. Note that some of the specific research discussed in the following paragraphs employs modified instrumentation.

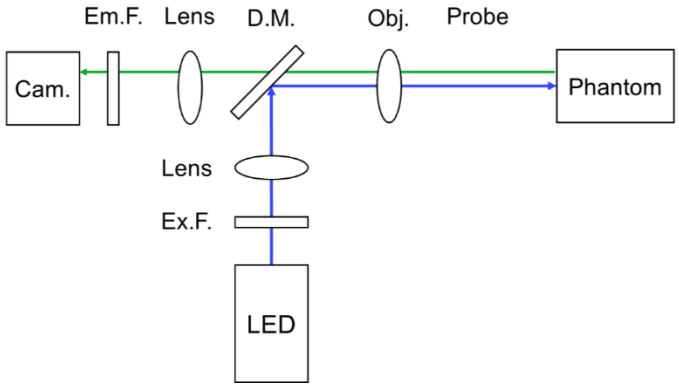

Figure 1. Simple schematic of high-resolution microendoscopy instrumentation showing an LED delivering light through an excitation filter (Ex.F.), lens (Lens), dichroic mirror (D.M.), and objective lens (Obj.) through a probe to a phantom. Fluorescence emission light travels through the probe, objective (Obj.), dichroic mirror (D.M.), tube lens (T.L.), emission filter (Em.F.), and camera (Cam.).

One common technique for optical phantom creation is constructing cell-based phantoms using buffered collagen type I from rat tail tendons as a substrate material. For this technique, collagen type I is added to a pellet of target epithelial cells cultured via conventional *in vitro* methods, such as human cervical adenocarcinoma cells, cervical squamous cell carcinoma, or oral squamous cell carcinoma. This mixture is transferred to a well plate and allowed to culture until the collagen-cell matrix forms a gel with a desired thickness. The resultant gel is densely packed with collagen and epithelial cells throughout (Gu *et al.*, 2010; Maitland *et al.*, 2006; Rogers *et al.*, 2008; Sokolov *et al.*, 2003). Studies have modified this technique with various cell types and exogenous contrast agents for high-resolution microendoscopic imaging. One study used a non-linear, probe-based microendoscope to investigate a collagen-based optical phantom containing human cervical adenocarcinoma (HeLa) cells for targeted photothermal therapy

microsurgery. The HeLa cells were labeled with transferrin-conjugated gold nanorods and mixed with propidium iodide. The probe was placed in gentle contact with the phantom surface and a near infrared (NIR) laser irradiated the phantom at the nanorod peak absorption (790 nm) from 0-252 μm in depth at 4 μm increments to induce HeLa cell necrosis. Then, a 740 nm laser was used to image the propidium iodide, which was used to stain necrotic cell death. In this way, the HeLa cell-based phantom's response to photothermal therapy could be quantified (Gu *et al.*, 2010). In another case, collage type I was infused with human cervical squamous cell carcinoma (SiHa) cells to demonstrate the imaging and video capture capabilities of a single fiber reflectance confocal microendoscope (SFCM) with a 140 μm x 100 μm field-of-view (FOV). For this system, the probe was placed in contact with the SiHa cell-based phantom surface and a 635 nm laser diode and micro-electro-mechanical system (MEMS) scanning device were used to raster scan the full FOV (Maitland *et al.*, 2006). As another demonstration of a separate high-resolution imaging device, optical phantoms were created using collagen type I as the substrate material with suspended human oral squamous cell carcinoma cells (1483 line). The cell-based collagen phantom was labeled with 10 nM streptavidin-coated quantum dots,(Stanisavljevic *et al.*, 2015) small semiconductor materials whose fluorescent properties are governed by their size, and gold nanoparticles, and then fixed in 10% formalin to preserve the phantom's structure. For imaging of fluorescent contrast agents within the collagen-based phantom, the probe contained a multimode fiber coupled to a 450 nm LED with a circular 250 μm-diameter FOV (Rogers *et al.*, 2008; Sokolov *et al.*, 2003). In addition to cells, other groups use fluorescent beads to characterize or demonstrate their high-resolution microendoscopy systems.

Three-dimensional phantoms can be created using water and agar, instead of collagen, as the substrate material and Intralipid, a soybean oil emulsion, as the scattering agent.

Microendoscopy studies typically use this design to study the effects of out-of-plane scattering, which can decrease image contrast (Koucky *et al.*, 2013; Keahey *et al.*, 2015). One confocal-based microendoscopy study built agar-based phantoms with 14.8 μm-diameter green fluorescent beads as the fluorescent agent. Intralipid was added at increasing concentrations from 0%, 0.5%, and 2.0% to create non-scattering, low-scattering, and high-scattering phantoms molded into a petri dish. At 520 nm, the low and high scattering phantoms had a μ_s' of 10.8 and 25.4 cm^{-1}. The 3D phantoms were imaged by placing a 455 nm LED-coupled probe in contact with the phantom and exciting fluorescence from the beads. Additionally, the phantom was imaged with the objective lens only to acquire in-focus images of beads at various depths within the phantom (Koucky *et al.*, 2013). Another similar microendoscopy study, using structured illumination, constructed optical phantoms using agar and deionized water as the substrate material and Intralipid as the scattering agent. Fluorescent polystyrene microspheres were used as the fluorescent agent. The phantom was constructed to simulate the optical properties of cervical columnar epithelium and was imaged by placing the 455 nm LED-coupled probe in gentle contact with the phantom surface to acquire images with and without structured illumination for comparison (Keahey *et al.*, 2015).

Thus far, the explored experimental setups have revolved around using a probe in contact with the phantom surface, although one technique uses microendoscopy submerged within a blood-mimicking liquid phantom (Shahmoon *et al.*, 2013). The purpose of this technique is to quantify hemoglobin concentration using a microendoscopy imaging probe. A liquid phantom was created with a mixture of water as the substrate material, and Intralipid and human hemoglobin and Intralipid as the scattering and absorbing agents, respectively, to mimic human blood. The mixture was flowed through a 400 μm-diameter channel within a solid phantom block

made of polyurethane and titanium dioxide (TiO_2). Different oxygenation levels of hemoglobin were used to test the instrument's capability of monitoring hemoglobin concentration. A 532 nm laser-coupled probe was submerged within the flow channel to illuminate the liquid hemoglobin phantom to quantify the difference between absorbance intensities to indicate hemoglobin concentration (Shahmoon *et al.*, 2013).

As demonstrated, optical phantom use in microendoscopy has myriad applications, including but not limited to demonstration of imaging technique, photothermal therapy, and investigating methods to reduce out-of-focus light (Koucky *et al.*, 2013; Gu *et al.*, 2010; Shahmoon *et al.*, 2013; Keahey *et al.*, 2015; Maitland *et al.*, 2006; Rogers *et al.*, 2008; Makhlouf *et al.*, 2011).

3.2.2 Hyperspectral imaging

Hyperspectral imaging is a non-invasive hybrid technique that combines spectroscopy and imaging. A two-dimensional (2D) detector array is used to collect images of a region of interest. The novelty of hyperspectral imaging is that each pixel on the 2D detector array also collects a spectrum that can potentially span the entire UV-NIR region. This generates what is known as a hypercube, a 3D dataset containing spectral and spatial information. Since hyperspectral imaging produces spectra at each pixel, optical properties at each pixel can often be quantified using LUT inverse models, Monte Carlo (MC) inverse models, or diffusion models (Lu *et al.*, 2014; Bish *et al.*, 2014; Lue *et al.*, 2012; Xu *et al.*, 2012; Tseng *et al.*, 2011; Zonios *et al.*, 1999). Figure 2 shows a simple schematic of hyperspectral imaging instrumentation. Note that some of the specific research discussed in the following paragraphs employs modified instrumentation.

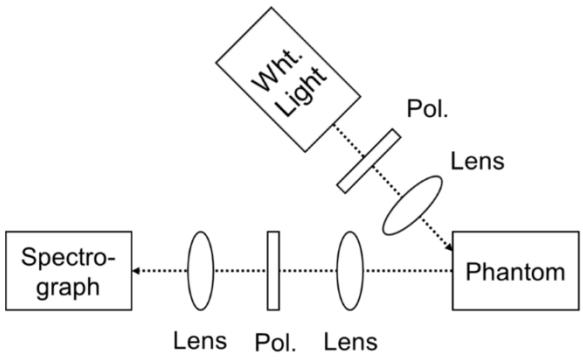

Figure 2. Simple schematic of hyperspectral imaging instrumentation showing a source (Wht. Light) delivering broadband light through a polarizer (Pol.) and lens (Lens) to a phantom. Emitted light from the phantom passes through a lens (Lens), polarizer (Pol.), and another lens (Lens) into a spectrograph.

Water-based liquid phantoms are the most common medium for phantom construction in hyperspectral imaging. One study developed two sets of optical phantoms to test the accuracy of a LUT-based inverse model in estimating μ_s' and total hemoglobin concentration (THC) using a handheld hyperspectral imaging system. The first set of water-based liquid phantoms were constructed inside a container and polystyrene microspheres and red food dye were added to simulate scattering and absorbing properties, respectively. Hyperspectral images were taken of the phantoms and spectra from each pixel were used to create a LUT of reflectance as a function of μ_s' and absorber concentration. Accuracy of the LUT was validated on a second set of water-based phantoms containing polystyrene microspheres and human lyophilized powder and was shown to be accurate with μ_s' values between 10 to 30 cm^{-1} and THC between 0 to 3 mg/mL. Following validation, the hyperspectral imaging system was tested on *in vivo* skin (Bish *et al.*, 2014).

A similar study acquired hyperspectral images of optical phantoms to validate the ability of an MC inverse model, rather than a LUT inverse model, to extract tissue optical properties. Three liquid phantoms were prepared inside a clear cylinder 10 mm in diameter and 200 mm in height using polystyrene microspheres and red ink as the scattering and absorbing agents,

respectively. Ranges of μ_s' were from ~10 to 20 cm^{-1} and ranges of μ_a were from ~0 to 4 cm^{-1}. A fiber bundle containing an image-fiber coupled to a hyperspectral imaging camera and off-axis broadband source fiber was dipped into the liquid phantoms to acquire spatially-resolved diffuse reflectance spectra. These spectra were compared to simulated reflectance spectra from MC models (Tseng *et al.*, 2011). In addition to using inverse models such as LUT and MC models, diffusion models have also been developed to extract a sample's optical properties with low errors.

The diffusion model can be applied in a similar mechanism to LUT and MC inverse models, in which phantoms with known optical properties are created and actual spectral data is compared to spectral data predicted by the diffusion model. For example, one group developed hyperspectral instrumentation to delineate tumor margins during surgery by quantifying optical properties, specifically THC. To quantify THC *in vivo*, 15 liquid-based phantoms were first prepared with 2% Intralipid as the scattering agent, and either hemoglobin or blood as the absorbing agent. Liquid phantoms with known THC were pipetted into a container until the liquid was 2.5 mm deep and diffuse reflectance spectra were acquired from each pixel of the hyperspectral scanner. The diffusion model was shown to be accurate for extracting THC from ~0 to 6 mg/mL. Following phantom validation testing, the scanner was used to delineate tumor margins in resected, diseased breast tissue (Lue *et al.*, 2012; Zonios *et al.*, 1999). Building phantoms is an important step for instrumentation and model validation. However, there is a need for readily available phantoms for investigators to use to cut down on the time and research costs required to build such validation tools (Xu *et al.*, 2012).

To address this need for standardization, digital tissue phantoms (DTPs) have recently been developed that could potentially be accessed by investigators and medical device

manufacturers around the world for their validation needs. The DNP was specifically created for hyperspectral imaging applications to measure oxygenation in chronic ischemic wounds. The DTP was built by acquiring hyperspectral data cubes from a biological system and digitally reproducing the cube. The liquid phantoms for DNP construction were made using phosphate buffered saline (PBS) as a substrate material, powdered milk solution as the scattering agent, and 4% porcine whole blood and India ink as the absorbing agents, yielding a μ_s' of 6.0 cm^{-1} at 690 nm. The hyperspectral data cube was acquired with a hyperspectral linear camera at 240 wavelengths between 380 and 885 nm at phantom oxygenation levels between 4-96% (Xu *et al.*, 2012).

The primary objective for constructing phantoms for hyperspectral imaging is to validate a model's ability to extract optical properties of phantoms with known values. Additionally, work has been done to standardize and digitize this technique for hyperspectral imaging applications (Lu *et al.*, 2014; Bish *et al.*, 2014; Lue *et al.*, 2012; Xu *et al.*, 2012; Tseng *et al.*, 2011; Zonios *et al.*, 1999).

3.2.3 Diffuse optical tomography

Diffuse optical tomography (DOT) is a non-invasive imaging technique that aims to quantify optical properties of tissues using various image reconstruction algorithms. Far red and near-infrared light, encompassing the spectral region between 650-1000 nm, is delivered to tissue and collected. Light in this range can penetrate several centimeters into a sample because of the low μ_a of water, lipids, and hemoglobin. Collected light is used to construct tomographic maps of tissue optical properties using various image reconstruction algorithms (Dehghani *et al.*, 2009; Mora *et al.*, 2015; Gonzalez-Rodriguez *et al.*, 2015; Bi *et al.*, 2015; Wu *et al.*, 2014; Saikia *et al.*, 2014; Valim *et al.*, 2013; Ansari *et al.*, 2014; Guggenheim *et al.*, 2013; Puszka *et al.*, 2013;

Sharikova *et al.*, 2014; Tavakoli *et al.*, 2011). Figure 3 shows a simple schematic of DOT instrumentation. Note that some of the specific research discussed in the following paragraphs employs modified instrumentation.

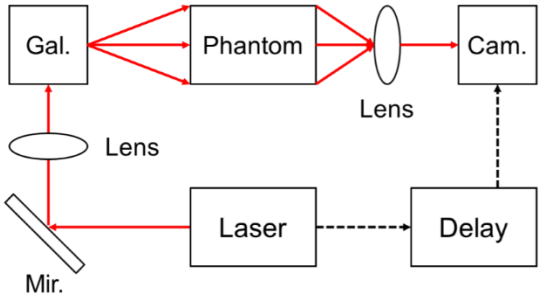

Figure 3. Simple schematic of diffuse optical tomography instrumentation showing a laser delivering light to a mirror (Mir.) and lens (Lens) and is raster scanned across a phantom using a mirror galvanometer (Gal.). Emitted light is delivered to a lens (Lens) and image sensor (Cam.) which is controlled with a delay mechanism (Delay).

Most optical phantom studies for DOT involve validating an image reconstruction algorithm within optical phantoms containing heterogeneities to investigate the instrument's ability to detect or delineate these inclusions. For the DOT phantom studies presented here, heterogeneities are solids that are contained within a surrounding bulk solid or liquid substrate material. For example, one study constructed breast-tissue mimicking phantoms with known optical properties (μ_s' = 1.14 cm^{-1}, μ_a = 0.07 cm^{-1} at 780 nm). Optical phantoms were constructed using agarose as the substrate material to create a gel-based phantom with 10% Intralipid as the scatterer and India ink as the absorber. Cylindrical heterogeneities (0.7 cm in diameter) simulating the optical properties of malignant breast tissue (μ_s' = 1.92 cm^{-1}, μ_a = 0.15 cm^{-1} at 780 nm) were placed inside the normal phantoms at varying locations and the image reconstruction algorithm was used to identify and delineate the inclusion (Ansari *et al.*, 2014). Similarly, DOT image reconstruction algorithms have been demonstrated in cylindrical gel-based optical phantoms with TiO_2 as the scatter and whole porcine blood as the absorber. Within this

cylindrical phantom, a 25 mm-diameter hole was drilled 10 mm from the phantom's edge which was filled with a 0.75% Intralipid and 4% porcine blood. This created a heterogeneity that contained an approximately 2:1 ratio of total hemoglobin compared to the background phantom. Six wavelengths between 649-850 nm were used to acquire images, and the DOT image reconstruction algorithm was subsequently applied (Dehghani *et al.*, 2009).

Solid optical phantoms with heterogeneities are also beneficial for small animal imaging using DOT. For example, phantoms can be designed to simulate the size and optical properties of a whole mouse. This mouse-simulating phantom was designed to be of similar size to a mouse and was made in a 25 mm-diameter, 50 mm-long cylinder. The phantom was built with a spatially homogenous solid plastic as the substrate material with varying μ_s' between 16.3 and 17.9 cm^{-1} and μ_a between 0.07 and 0.12 cm^{-1} within a spectral range of 500 to 850 nm. Two 6 mm-diameter holes were drilled in the phantom in which either inclusions or background-matching rods could be added. Images were collected of the phantom under different illumination patterns and the reconstruction algorithm was applied to produce an reconstructed image of the inclusion rods (Guggenheim *et al.*, 2013).

Other groups have explored their DOT instrument's capability to resolve solid inclusions within a surrounding liquid phantom. For example, time-resolved DOT at short source-detector separations was investigated using a liquid phantom built inside a 17 cm (length), 10 cm (width), and 7 cm (height) container. The liquid phantom was made using water, Intralipid and black ink, corresponding to a μ_s' and μ_a were 10 cm^{-1} and 0.1 cm^{-1} of 820 nm. Inside the container was a solid, resin-based cylinder doped with TiO_2 and black ink that served as an inclusion to measure depth sensitivity. At 820 nm, the cylinder's μ_s' and μ_a were 10 cm^{-1} and 0.6 cm^{-1}. NIR spectral measurements were taken with an 820 nm light source at 6 source-detector separations between 5

and 15 mm and a reconstruction algorithm was applied (Puszka *et al.*, 2013). Similarly, a prostate-simulating optical phantom with μ_s' of 7 cm^{-1} and μ_a of 0.3 cm^{-1} was created inside container. Two solid PVC-based inclusions were added to the liquid phantom. The first inclusion had a μ_s' of 15 cm^{-1} and μ_a of 0.5 cm^{-1} and the second had a μ_s' of 15 cm^{-1} and μ_a of 0.9 cm^{-1}. A robotically-controlled DOT platform and custom reconstruction algorithm, based on the steady-state light diffuse equation, was used to reconstruct images of the inclusions within the prostate-simulating phantoms (Sharikova *et al.*, 2014). In another study, a bulk liquid phantom was made to simulate healthy breast tissue. The breast tissue-simulating phantom was constructed with 0.8% Intralipid to yield a μ_s' range from 6.9 to 7.8 cm^{-1} and a near-negligible μ_a range from 0.02 to 0.03 cm^{-1} at 780 nm. A low-contrast breast lesion phantom was made using a solid plastisol, a suspension of polyvinyl chloride (PVC), as the substrate material to have μ_s' and μ_a of 5.6 cm^{-1} and 0.075 cm^{-1}. Additionally, a high-contrast breast lesion phantom was made, also using solid plastisol, to have μ_s' and μ_a of 6.53 cm^{-1} and 0.158 cm^{-1}. These low and high-contrast heterogeneities were submerged at different depths with the background Intralipid-based phantom and measurements were taken with a handheld DOT system and post-processed using the depth-correction algorithm (Tavakoli *et al.*, 2011).

As discussed here, optical phantoms for DOT applications usually have some type of optical or mechanical inclusion that can be detected after an image reconstruction algorithm has been applied to DOT-acquired data (Dehghani *et al.*, 2009; Ansari *et al.*, 2014; Tavakoli *et al.*, 2011; Sharikova *et al.*, 2014; Puszka *et al.*, 2013; Guggenheim *et al.*, 2013).

3.2.4 Diffuse reflectance spectroscopy

Diffuse reflectance spectroscopy is a non-invasive spectroscopic technique in which a light source, typically a broadband source, is coupled to a fiber-optic cable embedded within a

small probe. Light is delivered to tissue by placing the probe in contact or near-contact with the tissue surface. Light reflects back into an adjacent, embedded fiber-optic cable that delivers reflected light to a spectrometer to recover tissue spectra. Models, such as LUT, MC, and diffusion models can be used in conjunction with the tissue reflectance spectra to extract the tissue's optical properties, similar to techniques discussed with hyperspectral imaging (Alerstam *et al.*, 2008; Baran, Fenn, *et al.*, 2013; Bender *et al.*, 2009; Bosschaart *et al.*, 2011; Bremmer *et al.*, 2011; Bremmer *et al.*, 2013; Bydlon *et al.*, 2010; Chang *et al.*, 2011; Dhar *et al.*, 2012; Fu *et al.*, 2010; Sharma *et al.*, 2014; Nichols *et al.*, 2012; Glennie *et al.*, 2014; Rajaram *et al.*, 2008; Rajaram, Aramil, *et al.*, 2010; Rajaram, Reichenberg, *et al.*, 2010; Rajaram, Gopal, *et al.*, 2010). Figure 4 shows a simple schematic of reflectance spectroscopy instrumentation. Note that some of the specific research discussed in the following paragraphs employs modified instrumentation.

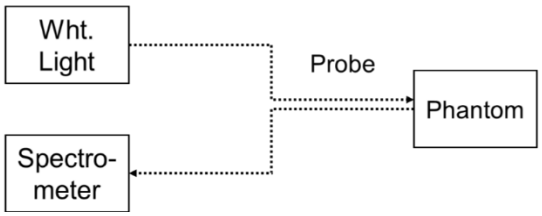

Figure 4. Simple schematic of reflectance spectroscopy instrumentation showing a broadband source (Wht. Light) delivering light through a probe to a phantom. Emitted light from the phantom passes through the probe into a spectrometer.

The most common types of phantoms used in reflectance spectroscopy are water-based liquid phantoms. Water-based phantom make it easy and convenient to build and validate LUTs for the purpose of optical property extraction. In one study, a discrete matrix of optical phantoms made with polystyrene beads and India ink was created to span a wide range of known μ_s' (4-47 cm^{-1}) and μ_a (0-25 cm^{-1}). A diffuse reflectance spectra was acquired from each phantom in the matrix and these reflectance values were interpolated to generate a topographic LUT describing the relationship between reflectance, μ_a, and μ_s' in three-dimensional (3D) space. The

topographic LUT was validated on a second set of optical phantoms made with polystyrene beads and red food dye with μ_s' between ~5-35 cm^{-1} and μ_a between ~0-25 cm^{-1}. The validated LUT was used to extract optical properties from cancerous skin tissue.(Sharma *et al.*, 2014) Another similar LUT study investigated broadband diffuse reflectance spectra between 350-750 nm for phantoms made with water, polystyrene microspheres and India ink to span a wide range of known μ_s' (2-71 cm^{-1}) and μ_a (0-53 cm^{-1}). The LUT was validated on a second set of tissue simulating phantoms made with water, polystyrene microspheres as the scatterer and powdered hemoglobin as the absorber (Rajaram, Reichenberg, *et al.*, 2010). The LUT was used to extract *in vivo* optical properties from a malignant basal cell carcinoma. Another method for optical property extraction are computational models, such as MC-based inverse models.

One study validated an MC-based inverse model by constructing optical phantoms in a 3 liter container using deionized water as the substrate material, 20% Intralipid as the scattering agent, and either manganese meso-tetra porphine (MnTPPS) or isolated human erythrocytes as the absorber. The probe, consisting of one delivery fiber and six surrounding collection fibers, was dipped into the phantoms 3 cm below the surface to simulate an infinite homogenous medium. Optical property extraction was shown to be valid between a μ_s' range from ~15 to 30 cm^{-1} and a μ_a range from ~0.1 to 1.3 cm^{-1}. Additionally, oxygen partial pressure of the erythrocyte-based phantoms were monitored using an oxygen-sensitive microelectrode (Baran, Fenn, *et al.*, 2013). Another group limited their study to using breast tissue-simulating phantoms to evaluate the robustness of their inverse MC model for optical property extraction. The optical phantom was made using deionized water as the substrate material and polystyrene microspheres and powered hemoglobin and/or crocin as the scatterer and absorber, respectively. Powdered hemoglobin was used to simulate blood and crocin was used to simulate beta-carotene, the most

common absorbers in breast tissue. The μ_s' and μ_a ranged from ~5-25 cm^{-1} and ~0-3 cm^{-1}, respectively, while THC ranged from 0-30 μM and [crocin] ranged from 0-500 μM. Multiple probe geometries were explored for wavelength ranges between 350-600 nm (Bender *et al.*, 2009). A similar study used an MC inverse model to extract μ_s' between 3-10 cm^{-1}, THC between 40-80 μM, and [crocin] between 0-400 μM from a breast-tissue mimicking phantom (Bydlon *et al.*, 2010). This technique for evaluating MC inverse models in breast tissue-mimicking phantoms has also been translated to other tissue types, including cervical epithelium. Cervical epithelia-mimicking phantoms, made with distilled water as the substrate material and polystyrene microspheres and lyophilized human hemoglobin, were used to test the accuracy of an MC model so that it could be used in low-resource settings. The μ_s' and μ_a ranged from 8.4 to 10.4 cm^{-1} and 0.04 to 0.39 cm^{-1} over a range of 450-600 nm, respectively. The probe consisted of 6 illumination fibers surrounding a single collection fiber and was submerged within the liquid cervical-simulating phantoms for measurements and the MC inverse model extracted the optical properties (Chang *et al.*, 2011).

In addition to LUT and MC models, diffusion models have been shown to be accurate in neonatal skin-simulating phantoms. These phantoms were made with water as the substrate material and 1.5% Intralipid and non-scattering, magenta dye as the scattering and absorbing agents, respectively. This corresponded to a μ_s' range of 3 to 37 cm^{-1} and a μ_a range of 0 to 27 cm^{-1}. These neonatal skin phantoms allowed the investigators to assess their ability to extract optical properties using the steady state diffusion approximation to the photon transport equation and determine instrumentation probing depth. The probe consisted of one illumination fiber and four collection fibers coupled to an imaging spectrograph and was submersed at varying distances (0-5 mm in 100 μm steps) from the bottom a blackened container holding a neonatal

skin-simulating phantom. Following phantom measurements, the investigators assessed the optical properties of neonatal skin *in vivo* (Bosschaart *et al.*, 2011).

Reflectance spectroscopy is primarily concerned with using their probe-based instrumentation and model to non-invasively extract optical properties from *in vivo* tissue. In order to do this, the technique must be validated on phantoms with known optical properties (Chang *et al.*, 2011; Rajaram *et al.*, 2008; Sharma *et al.*, 2014; Baran, Fenn, *et al.*, 2013; Bender *et al.*, 2009; Bosschaart *et al.*, 2011; Bydlon *et al.*, 2010).

3.2.5 Fluorescence spectroscopy

Fluorescence spectroscopy is a non-invasive probe-based spectroscopy technique that uses one or several excitation wavelengths to excite endogenous tissue fluorescence. A monochromatic excitation source is coupled to a flexible, fiber-optic cable(s) embedded in a probe. When the probe is in contact with tissue, the fluorescent molecule of interest is excited with a wavelength within the molecule's absorption spectrum. The molecule will absorb this energy, rise to an excited state, and then relaxes back down to ground state by emitting a photon of a longer wavelength. Fluorescent signal is recovered by one or more adjacent fiber-optic probes coupled to a detector such as a spectrometer. Phantoms in fluorescence spectroscopy are generally used to test instrumentation response for detecting fluorescence in the presence of background scattering and absorbing agents (Ramanujam, 2000; Choi *et al.*, 2011; Kanick, Davis, *et al.*, 2014; Du Le *et al.*, 2014; Gamm *et al.*, 2014; Baran and Foster, 2013; Croce *et al.*, 2014; C. Y. Chang *et al.*, 2013; Liu *et al.*, 2011). Figure 5 shows a simple schematic of fluorescence spectroscopy instrumentation. Note that some of the specific research discussed in the following paragraphs employs modified instrumentation.

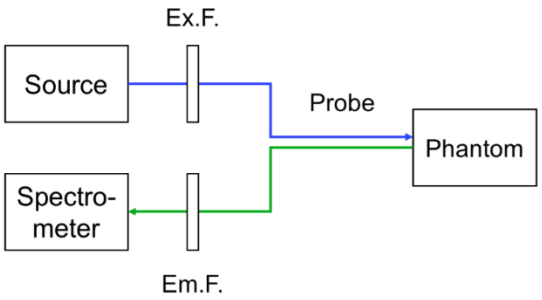

Figure 5. Simple schematic of fluorescence spectroscopy instrumentation showing a source delivering light through an excitation filter (Ex.F.) through a probe to a phantom. Emitted light from the phantom passes through the probe and emission filter (Em.F.) into a spectrometer.

Optical phantoms have been developed to measure the minimum concentration of added fluorophore that could be detected in the presence of background scattering, absorbing, and autofluorescence. One set of phantoms was built using water as the substrate material with 1% Intralipid, 1% bovine whole blood, and protoporphyrin IX (PpIX) as the scattering, absorption, and fluorescent agents, respectively. 5% Tween 20 was also mixed to prevent aggregation of the additives. Resultant μ_s' was between 10 – 50 cm^{-1} and blood volume fraction was between 0.5 – 2.5%. PpIX was added in 16 increasing concentrations between 0.1 and 4000 nM. The lower limit of PpIX detection was shown to be 1.95 or 250 nM for 405 nm or 639 nm, respectively (Kanick, Davis, *et al.*, 2014). Another group designed similar optical phantoms using deionized water as the substrate material, diluted 20% Intralipid as the scatterer, and manganese meso-tetra porphine (MnTPPS) (2-12 μM) as the absorber to simulate hemoglobin absorption. Instead of PpIX, doxorubicin hydrochloride (1.5-50 μM) was used as the fluorescence agent. Fluorescence spectra of these liquid phantoms were collected via a 0.8 mm epi-illumination probe coupled to a 488 nm laser to recover intrinsic fluorescence and other optical properties (Baran and Foster, 2013). These intrinsic fluorescence spectra were fit using a modified inverse MC model. Modified inverse MC models have been used in other cases to accurately estimate fluorophore

contribution in the presence of increasing non-fluorescent absorber. To validate this absorption-corrected MC model, optical phantoms were created using PBS as the substrate material and 20% Intralipid as the scatterer, yielding μ_s' between 0.05 and 65.8 cm^{-1} at 405 nm. Fluorescein, with a negligible μ_a, was added as the fluorescence agent at a constant 1 μM concentration. Finally, increasing concentration of isolated human red blood cells were added as the absorber (μ_a = 0-26 cm^{-1} at 405 nm) to demonstrate that fluorescence spectra can be corrected for absorption using the custom, empirical MC model (Gamm *et al.*, 2014).

Thus far, methods of fluorescence spectroscopy have been explored that include an exogenous fluorophore within their optical phantom design, such as PpIX, doxorubicin hydrochloride, and fluorescein, to test probe sensitivity or validate MC models. Fluorescence spectroscopy research has also explored the endogenous fluorescence of optical phantoms containing no exogenous fluorophores. This research hoped to determine whether common scattering agents, such as Intralipid and polystyrene microspheres, contributed to background fluorescence in the 350-650 nm wavelength range. For this study, Intralipid-based phantoms were made at concentrations of 0.25%, 0.5%, 1%, 1.5%, 2%, 3%, and 5% in deionized water within 12 mL test tubes. Additionally, polystyrene microsphere-based phantoms were made at *w/v* concentrations of 0.72%, 0.4%, and 0.2%. Fluorescence measurements were made using a 355 nm laser coupled to a 600 μm fiber for illumination and detection. With this knowledge of endogenous fluorescence from Intralipid and polystyrene microspheres, correction factors could be added to models to correctly extract optical properties and fluorescence from optical phantoms (Du Le *et al.*, 2014).

Additionally, optical phantoms can be designed, not only to validate modified MC models, but to test the depth sensitivity of a fluorescence spectroscopy probe. Depth sensitivity

can be quantified by creating a two-layer phantom model. In one study, two 300 μm thick phantom layers were constructed using water and agarose powder as the substrate material mixed with different types of quantum dots (Qdot) (Stanisavljevic *et al.*, 2015). The bottom layer was mixed with Qdot 655 and molded into a 13 mm-diameter cylinder, 300 μm thick. The top layer was mixed with varying concentrations of Qdot 565 and was molded on top of the bottom layer. Both layers had negligible scattering and absorption. A 405 nm laser diode was coupled to a non-contact probe and fluorescent signal from the phantoms was detected by a broadband spectrometer via an integrated collection fiber to quantify detection of the bottom layer (Choi *et al.*, 2011).

Optical phantoms in fluorescence spectroscopy are often used to validate MC inverse models, similar to those presented for reflectance spectroscopy, with modifications that account for fluorescence of added fluorophores. Additionally, fluorescence-based optical phantoms are used to test instrument sensitivity to fluorophore concentration or depth-sensitivity (Choi *et al.*, 2011; Kanick, Davis, *et al.*, 2014; Du Le *et al.*, 2014; Gamm *et al.*, 2014; Baran and Foster, 2013).

3.2.6 Raman spectroscopy

Raman spectroscopy is a non-invasive spectroscopy technique based on the principal of inelastic scattering. A monochromatic source injects light into the sample and target molecules within the sample absorb energy, generating molecule-specific vibrations. Therefore, emitted light from tissue undergoes a frequency shift compared to the excitation light due to the induced vibrational state. This shift is called a Raman shift (Kourkoumelis *et al.*, 2015; Agenant *et al.*, 2014; Esmonde-White *et al.*, 2011; Okagbare *et al.*, "Fluorocarbon Fiber-Optic Raman Probe for Non-Invasive Raman Spectroscopy," 2012; Demers *et al.*, 2012; Chen *et al.*, 2014; Barman *et*

al., 2009; Srinivasan *et al.*, 2008; Stone *et al.*, 2008; Okagbare *et al.*, 2010; Okagbare *et al.*, "Polymer-Capped Fiber Optic Raman Probe for Non-Invasive Raman Spectroscopy," 2012). Figure 6 shows a simple schematic of Raman spectroscopy instrumentation. Note that some of the specific research discussed in the following paragraphs employs modified instrumentation.

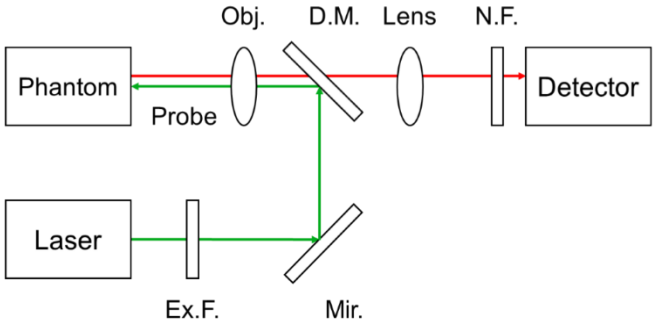

Figure 6. Simple schematic of Raman spectroscopy instrumentation showing a laser source delivering light through an excitation filter (Ex.F.), mirror (Mir.), dichroic mirror (D.M.), and objective lens (Obj.) through a probe to a phantom. Emitted light passes through the probe, objective lens (Obj.), dichroic mirror (D.M.), lens (Lens), and notch filter (N.F.) to a detector.

Optical phantoms for Raman spectroscopy are typically solid phantoms that are used to simulate the optical and geometric properties of a tissue type, such as cartilage and bone. Additionally, phantoms have been created for other purposes such as quantifying Raman spectroscopy probe sampling depth and detecting blood analytes in liquid phantoms.

One such phantom is an optical phantom that simulates a rat tibia. The rat tibia phantoms were made using a solid gelatin material as the substrate using a silicone rubber mold. The gelatin was doped with Intralipid as the scattering agent and hemoglobin as the absorber. Additionally, hydroxyapatite was added to simulate the chemical makeup of rat tibia. An 830 nm laser coupled to an illumination fiber bundle provided light to the sample and similar collection fibers delivered Raman signal to a spectrograph (Okagbare *et al.*, "Fluorocarbon Fiber-Optic Raman Probe for Non-Invasive Raman Spectroscopy," 2012; Okagbare *et al.*, "Polymer-Capped Fiber Optic Raman Probe for Non-Invasive Raman Spectroscopy," 2012; Okagbare *et al.*, 2010).

A similar study constructed a cylindrical rat leg-simulating phantom (27 mm diameter) using agar and water as the substrate material to create a gel. Scattering and absorption were controlled using 1% Intralipid and 0.01% India ink to yield μ_s' of 10 cm^{-1} and μ_a of 0.1 cm^{-1} at 830 nm. Teflon rods, simulating bone, at different sizes (5 and 12.5 mm diameter) were inserted into the agar-based phantom. Raman collection fibers were placed around the surface to collect Raman signal to assess the ability of creating tomographic maps of different regions within the phantom (Demers *et al.*, 2012). Bone-simulating phantoms, such as these presented, have been modified to test another hypothesis that Raman spectroscopy of subchondral bone is attenuated due to optical scattering of surrounding cartilage. To test this hypothesis, a bone-simulating optical phantom was made by dissolving gelatin in PBS. A 5 mm thick bone layer was created with 0.2 g/mL hydroxyapatite and 10% *v/v* Liposyn II. On top of the bone layer, a 6 mm thick cartilage layer was created with 3 mg/mL chondroitin sulfate at 0%, 10%, or 20%. The bone layer was cast in a Petri dish and the cartilage layer was cast on the same Petri dish once the bone layer had cured. The investigators took Raman spectra using 830 nm excitation laser coupled to a single, hand-held probe (Esmonde-White *et al.*, 2011). Two-layer phantoms can also be used to quantify depth sensitivity in Raman spectroscopy probes.

To quantify depth sensitivity, one study built a two-layer phantom in which the top layer consisted of 20% Intralipid in water with variable thicknesses. Thickness was controlled based on the volume of solution residing above the bottom layer, which was a 170 μm thick polyethylene terephthalate (PET) slide to mimic stromal tissue. The top layer thickness was increased from 0 to 1,500 μm in 50 μm increments until signal from the bottom layer was negligible. Both a superficial and non-superficial Raman probe were compared, and depth sensitivity was 200 and 300 μm, respectively (Agenant *et al.*, 2014).

Presented here are liquid phantoms used in Raman spectroscopy to demonstrate a method to detect blood analytes within the phantom. The optical phantoms were made using distilled water as the substrate material with Intralipid (μ_s' = 24-130 cm^{-1} at 830 nm) and India ink (μ_a = 0.08-1.3 cm^{-1} at 830 nm) serving as the primer scattering and absorbing agents. Additionally, the blood analytes, glucose and creatinine, were pipetted into the solution at concentrations ranging from 4-30 mM, spanning the range from hypoglycemic to hyperglycemic levels in humans. Aliquots of this solution were placed in a fused silica cuvette for Raman spectroscopic analysis to predict a phantoms' analyte concentration based on a custom calibration model (Barman *et al.*, 2009).

Raman spectroscopy is a broadly applicable to many subfields in biomedicine and many investigators demonstrate their technique or characterize their instrumentation using tissue-mimicking optical phantoms (Demers *et al.*, 2012; Okagbare *et al.*, 2010; Okagbare *et al.*, "Polymer-Capped Fiber Optic Raman Probe for Non-Invasive Raman Spectroscopy," 2012; Esmonde-White *et al.*, 2011; Agenant *et al.*, 2014; Barman *et al.*, 2009; Okagbare *et al.*, "Fluorocarbon Fiber-Optic Raman Probe for Non-Invasive Raman Spectroscopy," 2012).

3.3 Requirements for small endoscopic instrumentation

The major objective of the probe-based methods outlined in the previous sections are to non-invasively characterize tissue based on its qualitative appearance or optical properties, most prevalent being μ_s' and μ_a, among others. Optical phantoms provide a necessary step in evaluating parameters of these non-invasive or minimally invasive imaging and spectroscopy techniques. However, before such research goals can be realized, an understanding of several key aspects is necessary. First, it is vital to understand the type of tissue one hopes to work with, including its size and mechanical, chemical, and optical properties. Second, it is useful to

understand the models describing how light propagation through these tissues is typically understood. Therefore, in this next section, the biology of common epithelial structures is described in terms of size and optical properties, which are important for designing optical phantoms that mimic these tissues. Next, the sub-diffuse scattering regime will be described, a common physical regime within optical imaging when using small spectroscopy probes with small source-detector separations.

3.3.1 Sub-diffuse scattering regime

Light propagation in tissue can be fully described by the radiative transport equation (RTE). The RTE states that the total radiance for photons traveling in a specific direction through time and space is equal to the sum of all sources that affect (increase or decrease) radiance. Radiance is defined as the quantity of photons per unit volume. A more detailed description of the RTE can be found in numerous sources (Liemert *et al.*, 2012; Liemert *et al.*, 2014; Wilson *et al.*, 2011). The RTE has been successfully used to model photon transport in turbid media, such as tissue or tissue-simulating phantoms. However, the RTE is mathematically and computationally intensive, and because of this, research has sought to create simpler models that approximate the RTE (Liemert *et al.*, 2014; Liemert *et al.*, 2012; Wilson *et al.*, 2011; Kim *et al.*, 2006; Kim, 2004; Kim *et al.*, 2003).

One such simplification used in biological tissues is the diffuse approximation. The diffusion approximation is a method that has been used to determine μ_s' and μ_a in tissue (Wilson *et al.*, 2011; Reif *et al.*, 2007; Gibson *et al.*, 2005; Kim, 2004; Kim *et al.*, 2003). However, the diffusion approximation is only valid in turbid media if the following requirements are met: 1) the μ_s' must be much greater than the μ_a, and 2) large source-detector separations must exist (Reif *et al.*, 2007). Some sources have also claimed that the diffusion approximation is not valid

in media that exhibit anisotropic scattering (Gibson *et al.*, 2005). These requirements ensure that any collected photons have traveled through large volumes of tissue. In turn, this ensures that extracted optical properties represent an accurate average of the real optical properties. However, in many cases, investigators are interested in using small endoscopy devices, as mentioned in the previous section, to sample thin tissues with a small sampling depth. This is the case for dysplasia or cancers that are confined to the epithelium, which is only between 100-500 μm thick (Rajaram *et al.*, 2008).

Therefore, a distinction must be made between what is meant by the diffuse regime, in which the diffusion approximation is valid, and the sub-diffuse regime, in which the diffusion approximation is not valid (Reif *et al.*, 2007; Subramanian *et al.*, 2007; Turzhitsky, Rogers, *et al.*, 2010; Turzhitsky, Radosevich, *et al.*, 2010; Bosschaart *et al.*, 2011; Kanick, McClatchy, *et al.*, 2014). For many of the cases listed here, the validity of the diffusion approximation begins to fail for one of two reasons. The first reason is that μ_s' is not much greater than μ_a (Reif *et al.*, 2007; Turzhitsky, Radosevich, *et al.*, 2010; Turzhitsky, Rogers, *et al.*, 2010; Subramanian *et al.*, 2007; Bosschaart *et al.*, 2011). The μ_s' is considered "not much greater" than the μ_a when albedo is less than 0.9 (Rajaram *et al.*, 2008). Albedo is defined by Eq. 1,

$$A = \frac{(\mu_s')}{(\mu_s' - \mu_a)} \tag{1}$$

where A is the albedo [unitless], μ_s' is the reduced scattering coefficient [cm^{-1}] and μ_a is the absorption coefficient [cm^{-1}] (Rajaram *et al.*, 2008; Bish *et al.*, 2014; Bremmer *et al.*, 2011). The second reason the diffusion approximation begins to fail is the use of small source-detector separations common to small endoscopic probes. A source-detector separation is considered "small" if it is less than approximately one reduced mean free path (Rajaram *et al.*, 2008;

Subramanian *et al.*, 2007; Bosschaart *et al.*, 2011; Kanick, McClatchy, *et al.*, 2014). The reduced mean free path is defined by Eq. 2,

$$MFP_{reduced} = \frac{1}{(\mu_s' + \mu_a)} \quad (2)$$

where $MFP_{reduced}$ is the reduced mean free path (cm), μ_s' is the reduced scattering coefficient [cm^{-1}], and μ_a is the absorption coefficient [cm^{-1}] (Rajaram *et al.*, 2008; Bosschaart *et al.*, 2011). Consider the case in which an investigator is using a spectroscopy probe to non-invasively quantify the optical properties of skin at 630 nm. Skin tends to have a μ_s' of approximately 20 cm^{-1} and μ_a of approximately 0.4 cm^{-1} at 630 nm, although there is a wide range associated with skin optical properties (Sandell *et al.*, 2011). If this were the case, the albedo and reduced mean free path would be 0.98 and 490 μm, respectively. This theoretical value for albedo satisfies the requirements for the diffusion approximation. However, if an investigator is using source-detector separations less than 490 μm which is often the case, the diffusion approximation may begin to fail. In such a situation, we define the volume of tissue being probed to be in the "sub-diffuse scattering regime" rather than the "diffuse scattering regime" (Rajaram *et al.*, 2008; Turzhitsky, Radosevich, *et al.*, 2010; Turzhitsky, Rogers, *et al.*, 2010; Subramanian *et al.*, 2007).

The reason this distinction is important is that light in the sub-diffuse transport regime requires modified model-based interpretations. Mathematical models that describe light transport in the sub-diffuse regime require additional knowledge of the first and second Legendre moments, which is based on backscattering probability (Kanick, McClatchy, *et al.*, 2014). Figure 7 shows a three-dimensional, color-mapped representation of albedo and reduced mean free path as a function of μ_s' and μ_a for visualization. Albedo increases with higher μ_s' and lower μ_a. The reduced mean free path increases with lower μ_s' and μ_a values. Both three-dimensional graphs

are shown for μ_s' between 5-40 cm^{-1} and μ_a between 0-40 cm^{-1}.

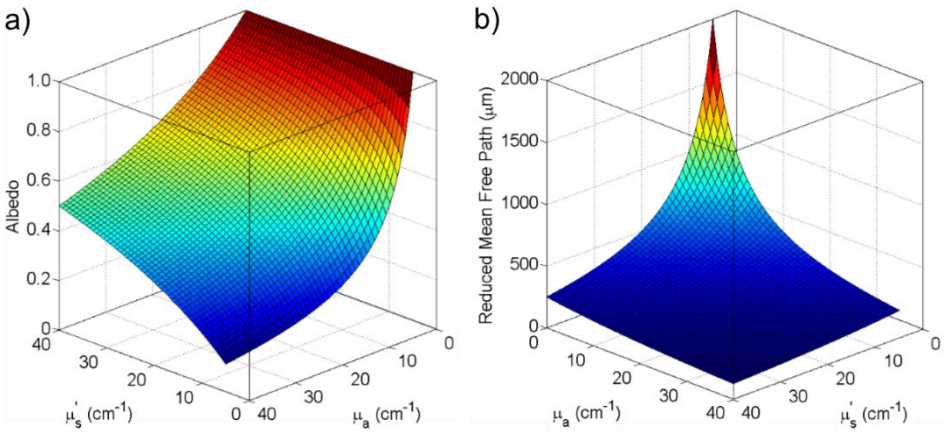

Figure 7. This figure shows the relationship between μ_s' and μ_a and the (a) albedo and (b) reduced mean free path of tissue. Notice that increasing μ_s' and decreasing μ_a increases albedo. For the diffusion approximation to be valid, albedo must be greater than 0.9. For tissues with albedo less than 0.9, optical imaging and spectroscopy occurs in the sub-diffuse regime. Alternatively, notice that decreasing μ_s' and μ_a increases the reduced mean free path of tissue. For the diffuse approximation (and thus the diffuse regime) to be valid, source-detector separations for spectroscopy probes must be greater than one reduced mean free path.

3.3.2 Geometry and optical properties of epithelial tissue

We next present a review of the geometry and optical properties of several types of epithelial tissues that are often the target of analysis in imaging and spectroscopy systems. Tissue thickness, albedo and reduced mean free path will be provided to correlate with the previous section. This section aims to 1) provide an organized set of relevant information regarding epithelial tissues, 2) guide the design of imaging and spectroscopy probes, and 3) facilitate an understanding of the basic optic and geometric parameters defining the "diffuse regime" and "sub-diffuse regime". Understanding how the diffuse and sub-diffuse regimes are affected by tissue properties such as albedo and reduced mean free path and a probe's source-detector separation can facilitate design of tissue-mimicking optical phantoms.

3.4 Considerations for thin tissue-simulating PDMS phantoms

When considering optical imaging techniques, a primary feature of phantom development is the control of optical properties (reduced scattering and absorption coefficients) to mimic human tissue (Pogue *et al.*, 2006; Ayers *et al.*, 2008). Optical properties of myriad human tissues have previously been characterized and can provide a guideline for phantom design (Sandell *et al.*, 2011). In addition, some applications are required to probe deep layers of tissues, such as the basement membrane or submucosa, which can exist up to 800 or more microns below the apical surface (Liu *et al.*, 2006; Harris *et al.*, 1992). In such cases, modulation of the phantom geometry on the scale of tens to hundreds of microns is crucial in phantom development (de Bruin *et al.*, 2010; Chang *et al.*, 2012; Koschwanez *et al.*, 2009; Guimarães *et al.*, 2007). Therefore, the ability to reproducibly create thin tissue-like phantoms with tunable optical properties may be beneficial for a wide range of optical image techniques (de Bruin *et al.*, 2010; Cerussi *et al.*, 2012; Pogue *et al.*, 2006; Ayers *et al.*, 2008).

Many other groups have attempted to address this need for their applications. Bruin et al. demonstrated a method to produce 50 μm thick phantoms by curing PDMS between two glass plates. These phantoms contained either silicon or titanium dioxide as the scattering agent and ABS 551, a green dye, as the absorber (de Bruin *et al.*, 2010). Saager et al. demonstrated a method to produce 90 μm thick phantoms by curing PDMS in a custom well plate using titanium dioxide as the scattering agent and either coffee, nigrosin, or India ink as the absorber (Saager *et al.*, 2010). Finally, Bae et al. demonstrated a method to use a spin coater to spin epoxy down to ultra-thin (5 μm) layers. India ink was used as the absorber (Bae *et al.*, 2013). Although these methods provided rigorous validation of tissue-simulating phantoms, all have specific limitations which we seek to address. Bruin et al. reported their optical properties only in terms of the

attenuation coefficient (μ_t) instead of the more conventional reduced scattering (μ'_s) and absorption (μ_a) coefficients commonly used to quantify tissue optical properties (de Bruin *et al.*, 2010). Saager et al. thoroughly reported on the wavelength dependence of their phantoms but do not provide information on the dependence of these optical properties on the concentrations of absorbing and scattering agents (Saager *et al.*, 2010). Finally, Bae et al. introduced a spin coating technique to produce ultra-thin layers. The resulting multi-layered phantoms with included heterogeneities were permanent, meaning thin layers cannot be easily interchanged (Bae *et al.*, 2013).[15] We seek to combine various aspects of the phantom design procedures briefly reviewed here to create unique tissue-simulating optical phantoms (de Bruin *et al.*, 2010; Saager *et al.*, 2010; Bae *et al.*, 2013).

We introduce a method to produce thin, interchangeable phantom layers with tunable optical properties using poly(dimethylsiloxane) (PDMS), an optically clear, silicone-based elastomer, to simulate epithelium (Pogue *et al.*, 2006; Ayers *et al.*, 2008; Sandell *et al.*, 2011; Liu *et al.*, 2006).[9-12] PDMS was chosen because of its durability, optical stability over time, comparable refractive index to human tissue (1.4), and the easy manipulation of both layer thickness and optical properties through the addition of scattering and absorbing agents (de Bruin *et al.*, 2010; Cerussi *et al.*, 2012; Pogue *et al.*, 2006).

Phantom thickness was controlled by spinning uncured PDMS on a clean, non-patterned silicon wafer in a spin coater, in which the spin speed (100 to 1000 rpm) was manipulated to reproducibly create thin PDMS optical phantoms between 115 and 880 microns (Bae *et al.*, 2013; Koschwanez *et al.*, 2009). Thicker phantoms were constructed by pouring uncured PDMS into a mold. Preparing phantom layers in the range of 100 to 300 microns is especially important to model many tissue types, such as the skin, gingivae, esophagus, and cervix, among others (de

Bruin *et al.*, 2010; Harris *et al.*, 1992; Guimarães *et al.*, 2007; Rocha *et al.*, 2010; Baxi *et al.*, 2014).

Phantom optical properties were controlled by introducing varying concentrations of titanium dioxide and alcohol-soluble nigrosin as the scattering and absorbing agents, respectively (de Bruin *et al.*, 2010; Pogue *et al.*, 2006; Ayers *et al.*, 2008; Sandell *et al.*, 2011; Liu *et al.*, 2006). The reduced scattering and absorption coefficients of PDMS-based phantoms with increasing concentrations of titanium dioxide and alcohol-soluble nigrosin were quantified by spatial frequency domain imaging (SFDI) at six discrete wavelengths (591, 631, 659, 691, 731, and 851 nm) across the visible to near-infrared spectrum (Cuccia *et al.*, 2009; Cuccia *et al.*, 2005). Optical characterization with SFDI outside this wavelength range was unreliable (data not shown). Based on the data presented here, lookup tables have been provided that list appropriate concentrations of titanium dioxide and alcohol-soluble nigrosin to use based on desired reduced scattering and absorption coefficients. These lookup tables may be useful for researchers interested in developing similar phantoms for their specific imaging applications.

Once phantoms were characterized, individual thin phantom layers were stacked to create thicker, multi-layer phantoms, which can model an optically heterogeneous tissue of interest (Saager *et al.*, 2010; Agrawal *et al.*, 2013; Chang *et al.*, 2012). Using SFDI, optical properties of multi-layer phantoms were compared to single-layer phantoms with identical concentrations of titanium dioxide and alcohol-soluble nigrosin for validation. Furthermore, multi-layered phantoms were imaged using OCT B-scanning for validation and qualitative purposes.

3.5 Materials and methods

3.5.1 Design of thin PDMS-based optical phantom layers for thickness characterization

For each thin phantom, 6.5 ± 0.1 grams of PDMS (Sylgard 184 Silicone Elastomer Kit, Dow Corning, USA) elastomer base was dispensed into an ARE-100 conditioning mixer cup (Intertronics, UK). Next, the curing agent was dispensed into a 7 mL scintillation vial (VWR, USA) based on a 10:1 ratio of base to curing agent. Titanium dioxide (Sigma-Aldrich, USA) and alcohol-soluble nigrosin (Sigma-Aldrich, USA, SKU: 211680-25G) were used to control the reduced scattering coefficient (μ'_s) and absorption coefficient (μ_a), respectively. Titanium dioxide (TiO_2) was weighed and dispensed into the 7 mL scintillation vial containing the curing agent. Next, a 1% w/v solution of nigrosin in ethanol was prepared and added to the scintillation vial. The mixture in the scintillation vial was mixed for one minute on a vortex mixer (VWR, USA) to disperse large particles of TiO_2. Following this, the scintillation vial was placed in a Model 3510 sonicator (Branson Ultrasonics Corporation, USA) for 30 minutes to disperse small particles of TiO_2 and nigrosin emulsions in the curing agent solvent. The process of vortexing for one minute and sonicating for 30 minutes was repeated a total of five times to ensure uniform scattering and absorption throughout.

The mixture of curing agent, TiO_2, and 1% w/v nigrosin/EtOH was then dispensed into the mixing cup containing the PDMS elastomer base. This final mixture was thoroughly mixed and degassed for three cycles in an ARE-100 conditioning mixer (Intertronics, UK) for a total of 12 minutes. Immediately following mixing and conditioning in the ARE-100 conditioning mixer, the uncured mixture was placed in an oven at 70°C for three minutes to initiate curing. The PDMS mixture was removed from the oven and slowly poured onto the center of a 10 cm silicon wafer (University Wafer, USA) within a G3P-8 Spin Coater (SCS Spin Coating Systems, USA).

The spin coater was optimized to accelerate to its peak speed in four seconds, spin at maximum speed for 20 seconds, and then decelerate to zero RPM in four seconds. Once the spin coater reaches zero RPM, the silicon wafer, containing a thin film of partially cured PDMS mixture, was removed and placed in an oven at 70°C for two hours to complete curing.

Thin phantoms were created at spin speeds of 100, 200, 300, 400, 500, 700 and 1000 RPM, with three trials of each. Each phantom at a particular spin coater speed was sampled six times for a total of 18 thickness measurements at each speed, shown in Figure 2. Thickness was quantified by analyzing transmittance images of PDMS phantom layers. A transverse cut was made in each phantom and imaged using a wide-field microscope with a Nikon Plan Fluor 10X, 0.30 NA objective and Nikon DS-Fi2 camera. Calibration of image scale was performed with a positive USAF 1951 resolution target. Images were analyzed using the MATLAB Image Analysis Toolbox (Mathworks, USA).

3.5.2 Design of PDMS-based optical phantoms for characterization of reduced scattering and absorption coefficients

The μ'_s and μ_a of phantoms containing varying amounts of TiO_2 and 1% w/v nigrosin/EtOH were quantified with spatial frequency domain imaging (SFDI) (Cuccia *et al.*, 2005; Cuccia *et al.*, 2009). For analysis with SFDI, thicker phantoms (2.5 cm thick) were built using an ARE-100 conditioning mixer cup (Intertronics, UK) as a mold. Construction of thick phantoms followed the same procedure as the construction of thin phantoms up until the point the spin coater was introduced. Instead of using a spin coater to spin partially cured PDMS into a thin layer, completely mixed PDMS was placed in an oven at 70°C for two hours to complete curing. 16 phantoms were created using this technique. Eight phantoms (#1-8 in Table 1) contained a constant amount of 1% w/v nigrosin/EtOH solution with increasing concentration of

TiO_2 in PDMS elastomer base to manipulate μ'_s. Nine phantoms (#1 and 9-16 in Table 1) contained a constant amount of TiO_2 with increasing concentration of 1% w/v nigrosin/EtOH solution in PDMS elastomer base to manipulate μ_a. As an example, since 50 grams of PDMS elastomer base were used to create Phantom #5, 0.25 grams of TiO_2 and 25 μL of 1% w/v nigrosin/EtOH were added. Table 1 shows the breakdown of each phantom created for the quantification of optical properties by SFDI. In addition, Figure 8 shows an aerial view of all 16 phantoms represented in Table 1. Figures 12-15 provide analysis on the resulting μ'_s and μ_a.

Table 1. Amounts of titanium dioxide (scattering agent) and nigrosin/ethanol solution (absorbing agent) per thick (2.5 cm) "semi-infinite" phantom quantified by SFDI

Phantom Number	**TiO_2 [g/g]**	**1% w/v Nigrosin/EtOH [μL/g]**
1	0.001	0.5
2	0.002	0.5
3	0.003	0.5
4	0.004	0.5
5	0.005	0.5
6	0.006	0.5
7	0.007	0.5
8	0.008	0.5
9	0.001	1.0
10	0.001	2.0
11	0.001	3.0
12	0.001	4.0
13	0.001	5.0
14	0.001	7.0
15	0.001	10.0
16	0.001	40.0

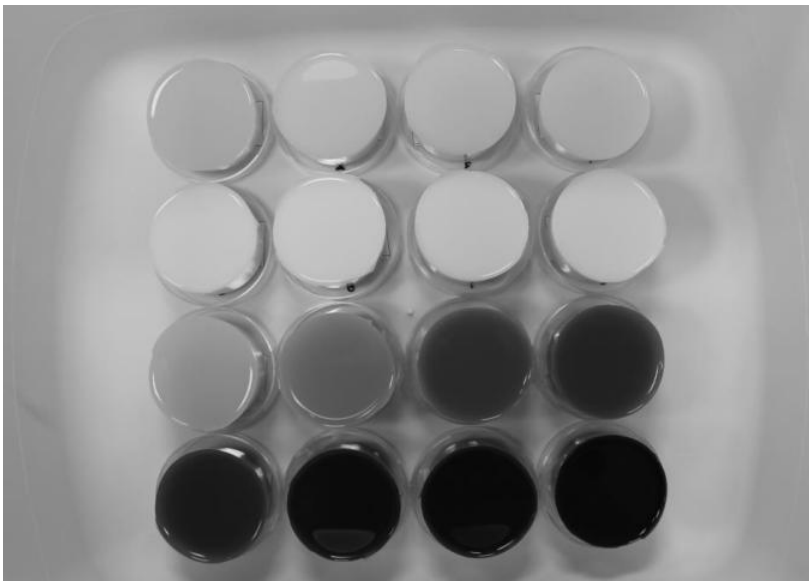

Figure 8. Aerial view of the 16 phantoms used in the SFDI characterization of μ'_s and μ_a, corresponding to Table 1. Phantoms used in this study are #1-4 (1st row), #5-8 (2nd row), #9-12 (3rd row), and #13-16 (4th row).

3.5.3 Construction of multi-layer phantoms for inclusion of heterogeneities

One multi-layer phantom was constructed, quantified by SFDI, and compared to a single-layer, "semi-infinite" control phantom with identical concentrations of optical agents (Cuccia *et al.*, 2005; Cuccia *et al.*, 2009). The primary concern during construction of multi-layer phantoms was the formation of air pockets between two adjacent layers. One possible technique to avoid air pocket formation was directly spinning uncured PDMS over an existing base layer to build multi-layer tissue-simulating phantoms. While this method can successfully eliminate air pocket formation, it was not be suitable for creating thin layers that were easily interchangeable (Bae *et al.*, 2013). Instead, our method allowed for thin PDMS layers to readily be stacked and removed, creating diverse sets of multi-layer phantoms for various optical imaging purposes. First, two 2.5 cm thick "semi-infinite" phantom layers were molded and cured in an ARE-100 conditioning mixer cup (Intertronics, UK), containing 0.002g TiO_2 and 2.0 µL 1% w/v nigrosin/EtOH per gram PDMS elastomer base. Then, using the described spin coating method, two 200-micron

layers were constructed, containing exactly the same concentrations of optical agents. After the two 200-micron layers finished curing, they were carefully peeled off the silicon wafer. The layers were cut using a scalpel into approximately 3 cm^2 squares. Each thin-layer square was placed into a 70% ethanol/DI water solution and sonicated for 10 minutes to remove dust and other surface contaminants. Following this, two drops of ethanol were placed on one of the 2.5 cm "semi-infinite" base layers. One 200-micron layer was placed directly on top of the ethanol drops so that no visible air bubbles remained. This two-layer phantom was placed in an oven at 70°C for three minutes to allow evaporation of the ethanol, creating two adjacent layers without air pockets. These steps were repeated for the second 200-micron layer on the same multi-layered phantom (Phantom #18 in Table 2). To the second 2.5 cm "semi-infinite" base layer, no thin layers were added (Phantom #17 in Table 2). Table 2 shows the geometric specifications of the two phantoms.

Table 2. Thickness specifications for single-layer and multi-layer control phantoms (for all layers: 0.002g TiO_2 and 2.0 µL 1% w/v Nigrosin/EtOH in PDMS elastomer base)

Thickness [µm]	Phantom #17 (single-layer)	Phantom #18 (multi-layer)
Top Layer	N/A	200
Middle Layer	N/A	200
Bottom Layer	25,000	25,000

Both phantoms were subjected to SFDI analysis to quantify μ'_s and μ_a at the six discrete wavelengths shown in Figure 16 and 17. This analysis served to validate the process of creating multi-layer phantoms without air pocket formation. In addition, SFDI analysis on multi-layered phantoms served to validate that thin (<880 µm) and thick (2.5 cm) phantoms layers with identical concentrations of optical agents have comparable optical properties. Because all layers contain identical concentrations of TiO_2 and 1% w/v nigrosin/EtOH, μ'_s and μ_a should be identical for both single-layer and multi-layer phantoms (Figure 16 and 17).

Additionally, one more three-layer multi-layer phantom was constructed and imaged

using an OCT B-scan for qualitative purposes. First, one 2.5 cm thick phantom layer was molded and cured in an ARE-100 conditioning mixer cup (Intertronics, UK), containing 0.002 g titanium dioxide and 2.0 µL 1% w/v nigrosin/EtOH per g PDMS elastomer base. Then, using the described spin coating method, two 200-micron layers were constructed. The first 200-µm layer contained 0.006 g TiO_2 and 2.0 µL 1% w/v nigrosin/EtOH per g PDMS elastomer base, tripling the scattering agent concentration while keeping the absorbing agent concentration constant. The second 200-micron layer contained 0.002g TiO_2 and 2.0 µL 1% w/v nigrosin/EtOH per g PDMS elastomer base (identical to the base layer). The first (optically different) thin layer was placed between the base layer and second (optically identical) thin layer to produce a heterogeneous multi-layer phantom that was imaged by an OCT B-scanning technique. These phantom images are compared to various types of human epithelium (skin and oral mucosa) in Figure 18. Table 3 shows the geometric and optical specifications of the heterogeneous multi-layer phantom for this comparative study using OCT. Optical coherence tomography (OCT) imaging was performed on a custom-built spectral-domain OCT platform with a center wavelength of 1325 nm, axial resolution of 8.0 µm (in air), lateral resolution of 22.5 µm, and maximum imaging depth of 3.0 mm (in air) (Higgins *et al.*, 2014). For phantom imaging (Figure 18), OCT cross-sections (B-scans) contained 500 A-lines acquired over a 5 mm scan width. B-scan images were generated by standard SD-OCT processing (spectrometer wavelength calibration, interpolation to evenly spaced samples in k-space, and Fourier transformation) (Higgins *et al.*, 2014). The OCT system used here operates at 1325 nm, further out into the near-infrared range than our SFDI system was capable of testing (591-851 nm). The majority of OCT imaging of tissues (including the epithelial tissues in which our phantoms seek to mimic) is done in the 1325 nm region (Higgins *et al.*, 2014). Therefore, OCT B-scans were used for comparative purposes and not to

characterize optical properties of phantoms.

Table 3. Thickness and optical concentration specifications for multi-layer phantom imaged by an OCT B-scanning technique

Phantom #19	Layer 1	Layer 2	Layer 3
Thickness [μm]	25,000	200	200
TiO_2 [g/g]	0.002	0.006	0.002
1 w/v% Nigrosin/EtOH [uL/g]	2	2	2

3.5.4 Semi-infinite phantom model of dysplastic progression

Once optical property extraction and sampling depth were validated, we tested the capabilities of the DRS modality of the hybrid fiber-bundle in a dysplasia-mimicking phantom model (Zhu *et al.*, 2011). Figure 9 (a-c) shows a simplified representation of dysplastic progression starting at the basement membrane and proliferating upwards into surrounding healthy tissue (Speight, 2007; Warnakulasuriya *et al.*, 2008). Early dysplasia is known to significantly increase epithelial scattering by nearly two-fold (Arifler *et al.*, 2003; Collier *et al.*, 2003; Clark *et al.*, 2004). To simulate this phenomenon, three solid scattering-only phantoms, shown in Figure 9 (d-f), were created (Zhu *et al.*, 2011). Since scattering contributes much more to reflectance intensity compared to absorption, the μ_a was held constant at 0 cm^{-1} (Clark *et al.*, 2004). Additionally, the phantom "epithelia" was made to be 300 μm thick to approximately simulate the thickness of oral mucosa (Greening *et al.*, 2015). With the understanding that the 374 and 730 μm SDSs sample different depths, it was expected that the 374 μm SDS may be more sensitive to shallower, epithelial-confined scattering changes associated with early dysplasia.

The three phantom models have a semi-infinite geometry, a common geometry used in various models of photon transport in tissues with sub-surface optical heterogeneities (Zhu *et al.*, 2011). The semi-infinite geometry requires an optically thick base layer (bottom gray layer in Figure 9 (d-f)) that can be considered infinitely thick in the *z* direction since no photons penetrate

through this layer. In this experiment, the semi-infinite base layer was 1 cm thick. Additionally, all layers can be considered infinite in the *x* and *y* directions since no photons penetrate laterally outside this plane (Zhu *et al.*, 2011).

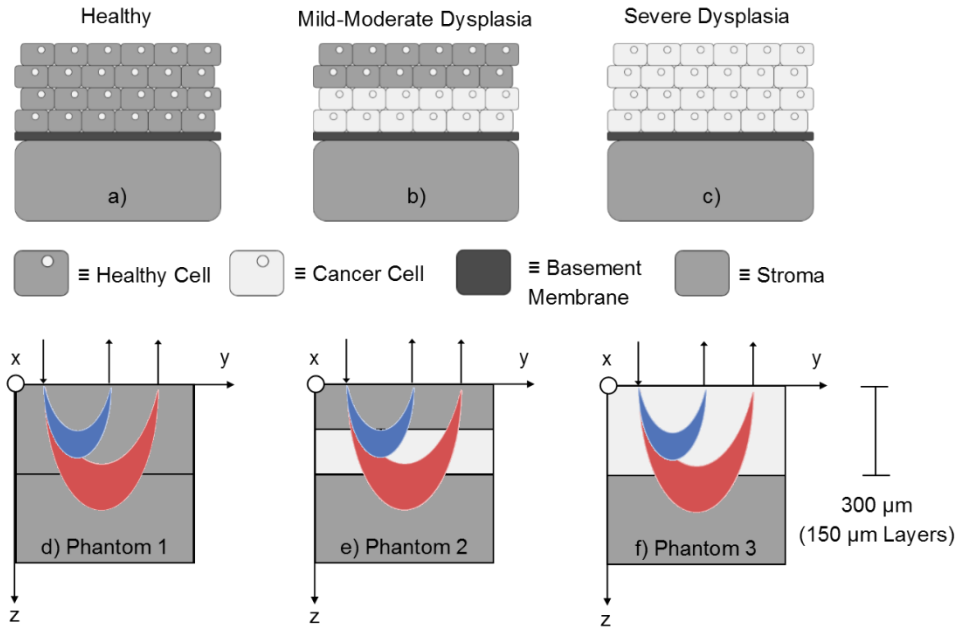

Figure 9. A simplified representation of dysplastic proliferation arising at the basement membrane in the oral cavity (a-c) showing normal cells (gray with nuclei), dysplastic cells (light gray with nuclei), basement membrane (dark gray), and the stroma (gray). The associated dysplasia-mimicking phantom models (d-f) simulate this progression. Two SDSs (374 and 730 µm) deliver and collect broadband light at different depths (detected photons shown here as blue and red crescents, respectively). Each of thin phantom layers was 150 µm thick for a total phantom thickness of 300 µm to simulate the thickness of oral epithelium.

Phantoms were created using poly(dimethylsiloxane) (PDMS) as the substrate material, and titanium dioxide (TiO_2) as the scattering agent. PDMS was used because of its optical clarity (μ_s' and $\mu_a = 0$ cm^{-1} between 500-750 nm), comparable refractive index to human tissue (~1.4), optical stability over time, physical durability, and ability to form multilayer geometries (Greening *et al.*, 2014). Since μ_s' contributes to reflectance intensity much more than μ_a, no absorbing agent was used (Clark *et al.*, 2004).

The semi-infinite layer and 150 μm thick healthy tissue-mimicking layers were designed with 0.25% w/w TiO_2 in PDMS (2.5 mg TiO_2 per 1.0 g PDMS) to yield a μ_s' of ~7 cm^{-1} at 630 nm which is comparable to healthy tissue (Chang *et al.*, 2009; Greening *et al.*, 2014). The 150 μm thick dysplasia-mimicking layers were designed with 0.50% w/w TiO_2 in PDMS (5.0 mg per 1.0 g PDMS) to yield a μ_s' of ~14 cm^{-1} at 630 nm (Greening *et al.*, 2014; Chang *et al.*, 2009). This represented a two-fold increase in scattering which is representative of the increased scattering ratio of dysplastic to healthy epithelial tissue (Collier *et al.*, 2003; Clark *et al.*, 2004; Arifler *et al.*, 2003). For each geometry in Figure 9, two 150 μm layers were stacked to generate the desired phantom (Greening *et al.*, 2014; Greening *et al.*, 2015). The total phantom "epithelial" thickness was thus 300 μm, not including the "stromal" semi-infinite base layer, which was 1 cm thick. All thin phantom layers were created using a previously described spin coating technique (Greening *et al.*, 2015; Greening *et al.*, 2014).

The volume-averaged μ_s' was extracted between 500-750 nm for each phantom. Ten DRS measurements were averaged for each geometry (Phantoms 1-3) and SDS with an integration time of 500 ms. We hypothesized that the 374 μm SDS would show larger deviations in volume-averaged μ_s' compared to the 730 μm SDS because the changes in scattering were confined to the upper 300 μm of the phantom. The 730 μm would be sampling significantly more into the underlying "stromal" semi-infinite layer, in which μ_s' was held constant for this experiment. Results from this study were expected to indicate that the shorter SDS would be more sensitive to scattering changes associated with dysplastic epithelium.

3.5.5 Collaboration with the Boston University Department of Biomedical Engineering: Two-Layer Tissue-Simulating Optical Phantoms

The following section was directly adapted from Syeda Tabassum, Vivian Pera and

Darren Roblyer from Boston University, with whom we provided tissue-simulating PDMS phantoms for their experiments (Tabassum *et al.*, 2018).

A set of two-layer solid silicone phantoms was fabricated to optically simulate subcutaneous tumors in a mouse with a range of optical properties. These phantoms were used to test the accuracy of Gardner LUT inversion algorithms. The phantoms consisted of a thin skin layer above a tumor layer. Four different two-layer phantoms were fabricated, all of which used the same skin layer. In all phantoms, silicone was used as the base solvent, nigrosin as the absorber, and titanium dioxide as the scatterer. The optical properties of the phantoms were adjusted by varying the amount of absorber and scatterer during fabrication as previously described (Ayers *et al.*, 2008; Tabassum *et al.*, 2018).

The thin upper layer phantom was made by adapting a previously described technique (Saager *et al.*, 2010). First, an aluminum phantom mold was fabricated by machining a well that was 330 μm in depth and 1.5 in. × 1.5 in. in the lateral dimensions using a computer-controlled milling machine (SV-2414S-M, Sharp Industries). After the phantom ingredients were mixed together, the liquid mixture was poured into the aluminum mold. A microtome blade was used to draw and spread the mixture evenly across the well, and the edges of the blade remained in contact with the top surface of the mold at all times. The phantom was then left to cure, uncovered, overnight. During curing, the silicone layer was observed to shrink in the center of the well. Once cured, the thin silicone layer was removed from the mold and cut to the size of 100 × 100 to remove the uneven and thicker edge. The thickness of the phantom was confirmed using caliper measurements by confining the thin layer between two microscope slide coverslips for stability and consistency. Because the top layer phantom was too thin for accurate optical property measurements with diffuse imaging techniques, a much larger, 2.5-cm thick

homogeneous phantom was made from the same batch of material and SFDI was used to extract the optical properties (Tabassum *et al.*, 2018).

Similarly, for the bottom (tumor) layer, four homogeneous phantoms were fabricated in collaboration with Dr. Muldoon's group (Greening *et al.*, 2014) and measured with SFDI. The thickness of each phantom was 2.5 cm, and the μa and μ0s values of each phantom were targeted to span known mouse tumor optical properties. The skin layer and tumor layer phantoms were stacked to create the two-layer phantoms. First, the thin skin layer phantom was cleaned using an alcohol wipe. Then a small amount of ethanol was poured on a thick tumor layer phantom, and the thin layer was directly placed on top of the tumor layer, making sure that no visible air bubbles remained. The two-layer phantom was left under the chemical hood overnight to allow the ethanol to evaporate without leaving any air pockets between the layers. An example of one of the two-layer phantoms is shown in Figure 10(c). The procedure was repeated 4 times to generate the four two-layer phantoms (Tabassum *et al.*, 2018).

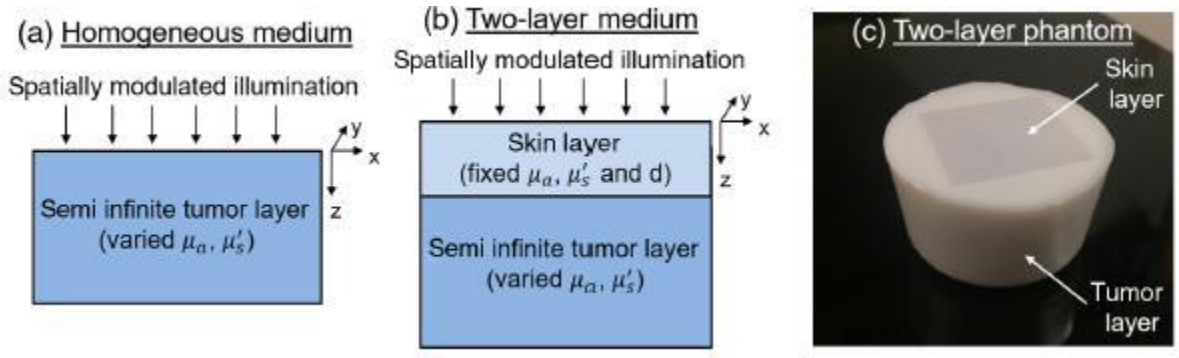

Figure 10. (a) Schematic of tissue model for the homogenous case, (b) schematic of the tissue model for the two-layer case, and (c) an example of a custom-made two-layer silicone phantom used to validate the accuracy of the resulting two-layer inverse algorithm (Tabassum *et al.*, 2018).

3.6 Results

3.6.1 Characterization of thickness of thin PDMS-based optical phantoms

Figure 11 shows the relationship between the primary, maximum 20-second spin speed and resulting thickness of PDMS layers. Seven different spin speeds were used (100, 200, 300, 400, 500, 700, and 1000 rpm) to characterize the resulting thickness (between 115 and 880 µm) of thin PDMS-based phantoms.

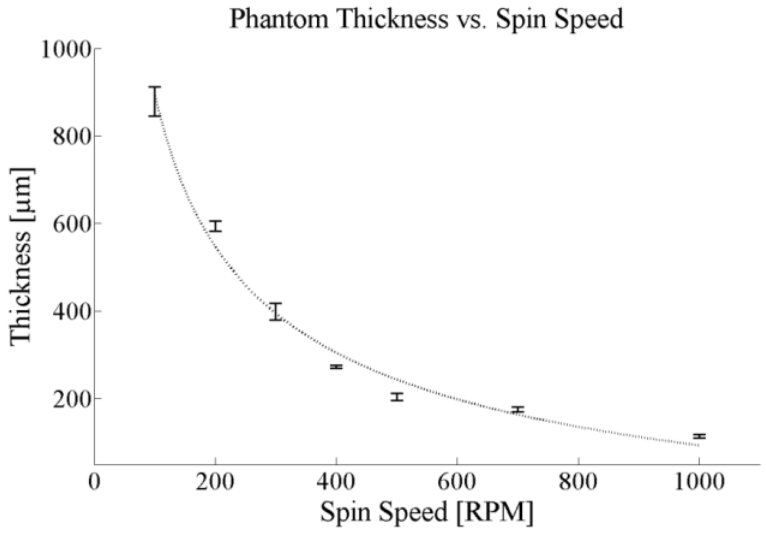

Figure 11. Relationship between thickness of thin-layer phantoms and maximum 20-second spin speed of a spin coater. Here, phantoms were constructed between approximately 115 and 880 µm. The R^2 value for the curve of best fit is 0.988. Best fit lines were generated by the MATLAB curve-fitting toolbox (power fit).

3.6.2 Characterization of reduced scattering coefficient of PDMS-based optical phantoms

Figure 12 shows the relationship between TiO_2 (scattering agent) in PDMS elastomer base [g/g] and the resulting μ'_s [cm^{-1}] for six discrete wavelengths [nm] measured by SFDI (591, 621, 659, 691, 731, and 851 nm). Eight phantoms (#1-8 in Table 1) were used in this study which contained a constant amount of 1% w/v nigrosin/Et/OH (absorbing agent) and increasing concentration of TiO_2 in PDMS elastomer base [g/g].

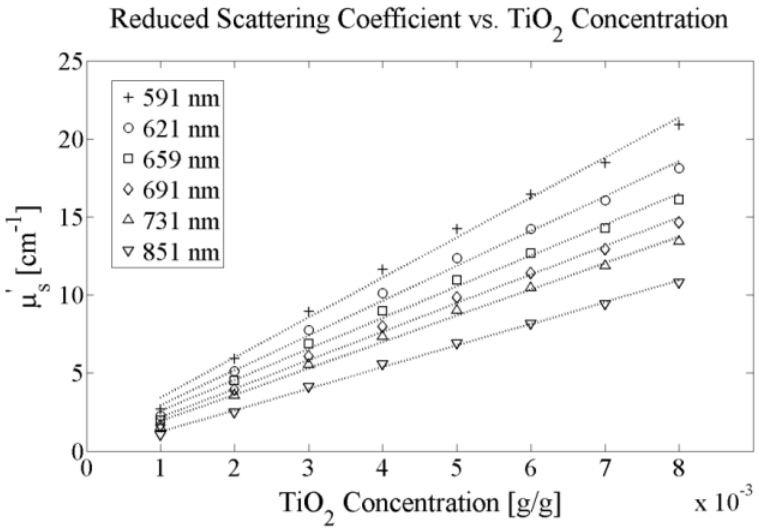

Figure 12. Relationship between μ'_s [cm^{-1}] and TiO_2 concentration in PDMS elastomer base [g/g] measured at six discrete wavelengths (591, 621, 659, 691, 731, and 851 nm) using spatial frequency domain imaging (SFDI) analysis. Here, μ'_s values range between approximately 1 and 21 cm^{-1}. R^2 values for best fit lines from 591 to 851 nm are 0.994, 0.994, 0.994, 0.995, 0.995, and 0.998, respectively. Best fit lines were generated by the MATLAB curve-fitting toolbox (linear fit).

In addition, μ'_s was measured at increasing 1% w/v nigrosin/EtOH concentrations in PDMS elastomer base to determine if increasing the chosen absorbing agent would affect the bulk scattering properties. Figure 13 shows the relationship between 1 w/v% of nigrosin/EtOH concentration and the resulting μ'_s [cm^{-1}]. Results from Phantom #16 are not shown in Figure 4. The phantoms used in this experiment (#1, 9-15 in Table 1) all contained identical concentrations of the chosen scattering agent, TiO_2 (0.001 g/g).

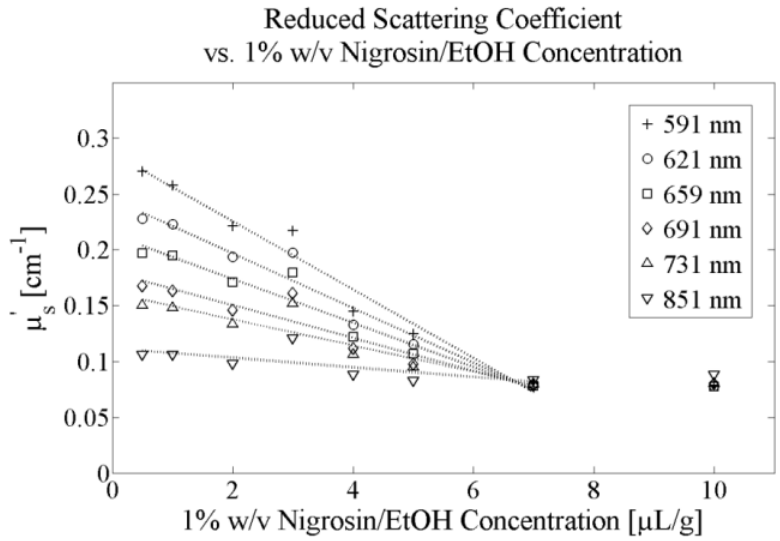

Figure 13. Relationship between μ'_s [cm^{-1}] and 1% w/v nigrosin/EtOH concentrations in PDMS elastomer base [μL/g] measured at six discrete wavelengths (591, 621, 659, 691, 731, and 851 nm) using spatial frequency domain imaging (SFDI) analysis. Best fit lines were generated by the MATLAB curve-fitting toolbox (linear fit).

3.6.3 Characterization of absorption coefficient of PDMS-based optical phantoms

Figure 14 shows the relationship between 1 w/v% of nigrosin/EtOH (absorbing agent) in PDMS elastomer base [μL/g] and the resulting μ_a [cm^{-1}] for six discrete wavelengths measured by SFDI (591, 621 ,659, 691, 731, and 851 nm). Nine phantoms (#1 and 9-16 in Table 1) were used in this study which contained a constant amount of TiO_2 (scattering agent) and increasing 1% w/v nigrosin/EtOH concentration in PDMS elastomer base.

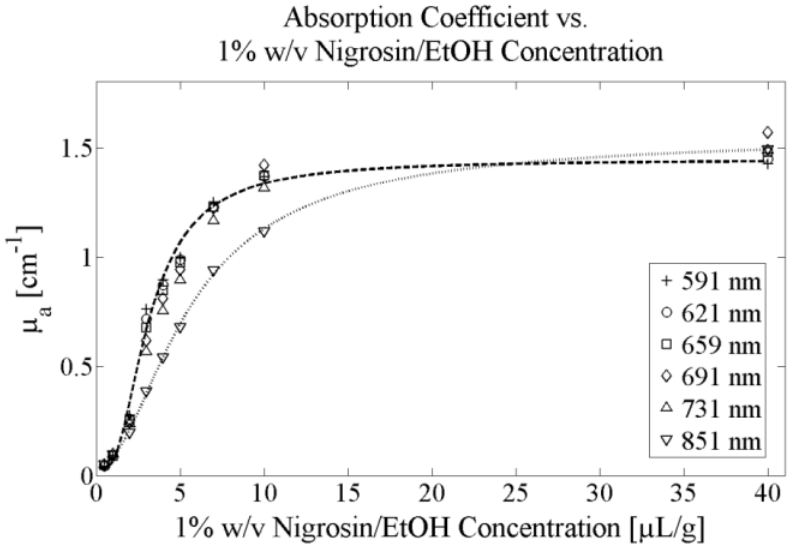

Figure 14. Relationship between μ_a [cm^{-1}] and 1% w/v nigrosin/EtOH concentration in PDMS elastomer base [μL/g] measured at six discrete wavelengths (591, 621, 659, 691, 731, and 851 nm) using spatial frequency domain imaging (SFDI) analysis. Here, μ_a values range between approximately 0 and 1.5 cm^{-1}. Best fit curves, generated by the MATLAB curve-fitting toolbox (power fit), are shown for the 591 nm (dashed) and 851 nm (dotted) wavelengths, respectively.

In addition, μ_a was measured at increasing TiO_2 concentrations in PDMS elastomer base to determine if increasing the chosen scattering agent would affect the bulk absorbing properties. Figure 15 shows the relationship between TiO_2 concentration and the resulting μ_a [cm^{-1}]. Eight phantoms (#1-8 in Table 1) were used in this study which contained identical concentrations of the chosen absorbing agent, 1% w/v nigrosin/EtOH (0.5 μL/g).

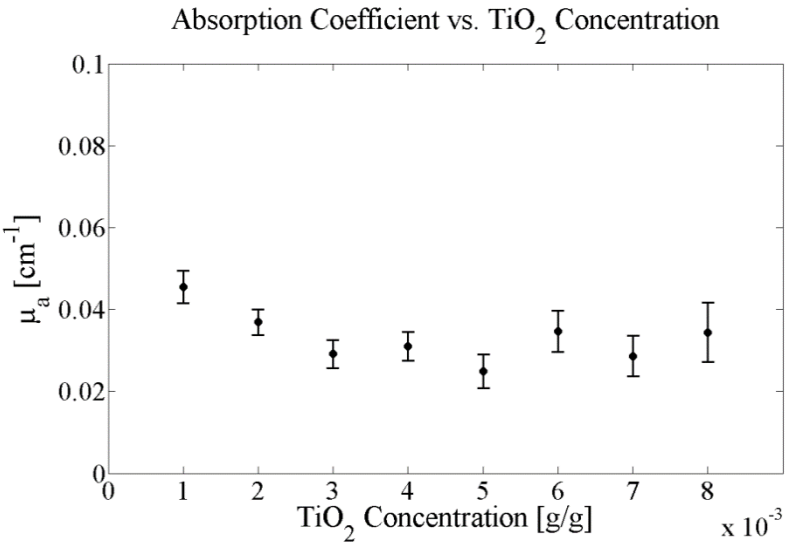

Figure 15. Relationship between μ_a [cm^{-1}] and TiO_2 concentration in PDMS elastomer base [g/g] measured at six discrete wavelengths (591, 621, 659, 691, 731, and 851 nm) using spatial frequency domain imaging (SFDI) analysis.

3.6.4 Validation of multi-layer PDMS-based optical phantoms

For the two phantoms specified in Table 2 (Phantom # 17 and 18), μ'_s [cm^{-1}] and μ_a [cm^{-1}] were quantified with SFDI (Cuccia *et al.*, 2005; Cuccia *et al.*, 2009). Phantom #17 (square data points in Figure 16 and 17) consisted of only one thick 2.5 cm base layer, containing 0.002 g TiO_2 and 2.0 µL 1% w/v nigrosin/EtOH per gram PDMS elastomer base. Phantom #18 (diamond data points in Figure 16 and 17) consisted of one thick 2.5 cm base layer with two overlying 200-µm layers, all containing 0.002 g TiO_2 and 2.0 µL 1% w/v nigrosin/EtOH per gram PDMS elastomer base. This experiment attempted to validate the creation of multi-layer phantoms by comparing the overall optical properties (μ'_s and μ_a) of a single-layer and multi-layer phantoms with all layers containing identical concentrations of scattering and absorbing agents. Figure 16 shows the relationship between the wavelength and resulting μ'_s while Figure 17 shows the relationship between the wavelength and resulting μ_a for the single-layer (Phantom #17) and multi-layer (Phantom #18) phantoms specified in Table 2.

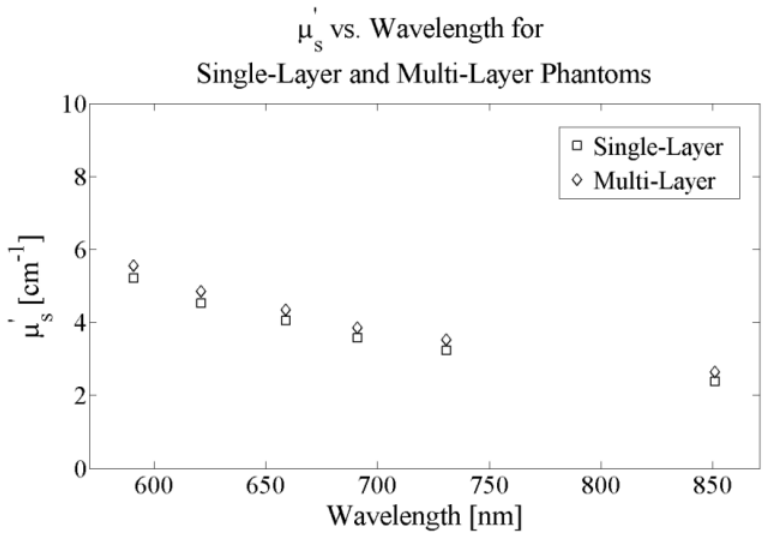

Figure 16. Comparison of μ'_s [cm^{-1}] between a single-layer and multi-layer phantom with identical concentrations of scattering and absorbing agents measured at six discrete wavelengths (591, 621, 659, 691, 731, and 851 nm) using spatial frequency domain imaging (SFDI) analysis. Average aggregate error was 7.7%.

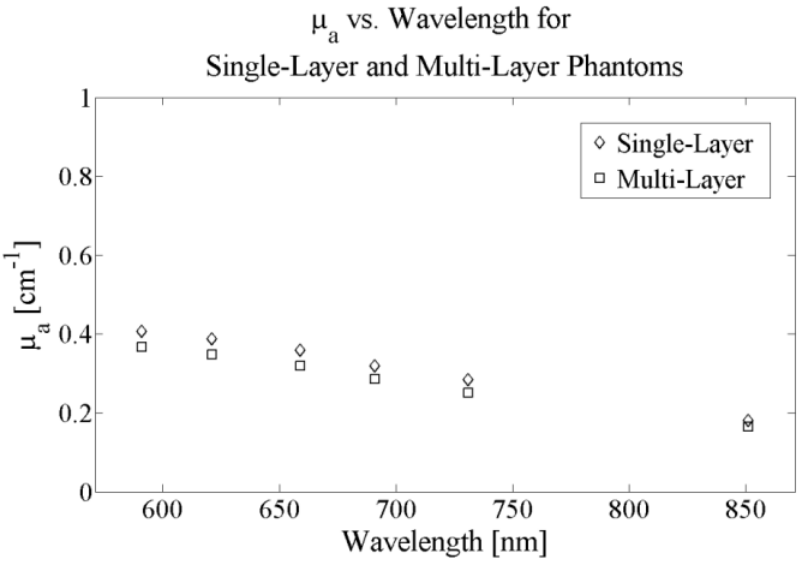

Figure 17. Comparison of μ_a [cm^{-1}] between a single-layer and multi-layer phantom with identical concentrations of scattering and absorbing agents measured at six discrete wavelengths (591, 621, 659, 691, 731, and 851 nm) using spatial frequency domain imaging (SFDI) analysis. Average aggregate error was 10.9%.

Figure 18 represents an OCT B-scan comparison between multi-layered phantoms and several types of human epithelium from a normal volunteer (fingertip epithelium, wrist epithelium, and oral mucosa).

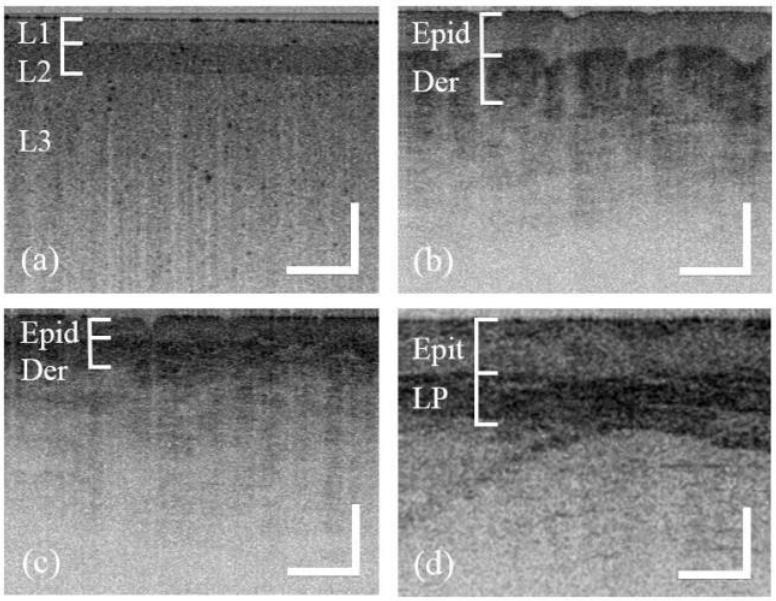

Figure 18. Images of multi-layered PDMS-based phantoms compared to OCT B-scans of various human epithelium. (a) OCT B-scan of a three-layer phantom. Thickness in layers 1 and 2 (L1 and L2) were approximately 200 μm, respectively. TiO_2 concentration in layers 1, 2, and 3 (L3) were 0.002, 0.006, and 0.002 [g/g], respectively. 1 w/v% nigrosin/EtOH concentration was 2.0 μL/g in all layers. The comparative images show OCT B-scans from a normal volunteer of the (b) fingertip showing the epidermis (Epid) and dermis (Der), (c) wrist showing the epidermis (Epid) and dermis (Der), and (d) oral mucosa showing the epithelium (Epit) and lamina propria (LP) Scale bars represents 500 μm.

3.6.5 Lookup Tables for Optical Properties of Solid PDMS-Based Phantoms

The following lookup tables can be used as a guideline to determine approximate concentrations of the studied absorbing agent (1% w/v Nigrosin/Ethanol) and scattering agent (Titanium dioxide) given a desired absorption coefficient (μ_a) and reduced scattering coefficient (μ'_s) at a specific wavelength when designing PDMS-based tissue-simulating phantoms. Six lookup tables are included, corresponding to the six wavelengths (591, 631, 659, 691, 731, and 851 nm) used in this study. It should be noted that individual concentrations listed in this table

were not explicitly measured. Instead, the individual concentrations listed here were acquired based on empirical mathematical models fitting the presented data. While the tables do fit the presented data, extensive validation of these tables was not performed. Therefore, optical properties should always be independently validated.

To use these lookup tables, first choose a desired μ_a to obtain the correct concentration of 1% w/v nigrosin/EtOH in PDMS elastomer base [μL/g]. Then, choose a desired μ'_s and line up this row with the column corresponding to the chosen μ_a to obtain the correct concentration of TiO_2 in PDMS elastomer base [g/g].

Table 4. Lookup table to determine the required concentrations of absorbing and scattering agents from desired absorption and reduced scattering coefficients at 591 nm (Greening *et al.*, 2014).

Absorption Coefficient μ_a [cm^{-1}]														
Concentration of 1% w/v Nigrosin/EtOH to PDMS elastomer base [µL/g]														
	0.1	**0.2**	**0.3**	**0.4**	**0.5**	**0.6**	**0.7**	**0.8**	**0.9**	**1.0**	**1.1**	**1.2**	**1.3**	**1.4**
	1.0	1.3	1.7	2.1	2.4	2.8	3.1	3.5	4.1	4.9	5.8	6.6	7.1	13.9
Reduced Scattering Coefficient μ'_s [cm^{-1}]														
Concentration of Titanium Dioxide to PDMS elastomer base [g/g] x10-3														
1	0.1	0.1	0.1	0.2	0.2	0.2	0.2	0.3	0.3	0.5	0.6	0.9	1.1	1.1
2	0.5	0.5	0.6	0.6	0.7	0.7	0.8	0.9	1.0	1.2	1.6	2.2	2.6	2.6
3	0.9	1.0	1.0	1.1	1.2	1.3	1.3	1.4	1.7	2.0	2.6	3.4	4.0	4.0
4	1.3	1.4	1.5	1.6	1.7	1.8	1.9	2.0	2.3	2.8	3.5	4.7	5.5	5.5
5	1.7	1.8	1.9	2.0	2.2	2.3	2.4	2.6	3.0	3.6	4.5	5.9	7.0	7.0
6	2.2	2.3	2.4	2.5	2.7	2.8	3.0	3.2	3.6	4.4	5.4	7.2	8.4	8.4
7	2.6	2.7	2.8	3.0	3.2	3.3	3.5	3.8	4.3	5.1	6.4	8.4	9.9	9.9
8	3.0	3.1	3.3	3.5	3.6	3.9	4.1	4.4	4.9	5.9	7.4	9.7	11.3	11.3
9	3.4	3.5	3.7	3.9	4.1	4.4	4.7	5.0	5.6	6.7	8.3	10.9	12.8	12.8
10	3.8	4.0	4.2	4.4	4.6	4.9	5.2	5.5	6.2	7.5	9.3	12.2	14.2	14.2
11	4.2	4.4	4.6	4.9	5.1	5.4	5.8	6.1	6.9	8.2	10.2	13.4	15.7	15.7
12	4.6	4.8	5.1	5.3	5.6	5.9	6.3	6.7	7.5	9.0	11.2	14.7	17.1	17.1
13	5.0	5.3	5.5	5.8	6.1	6.5	6.9	7.3	8.2	9.8	12.1	15.9	18.6	18.6
14	5.4	5.7	6.0	6.3	6.6	7.0	7.4	7.9	8.8	10.6	13.1	17.2	20.0	20.0
15	5.8	6.1	6.4	6.7	7.1	7.5	8.0	8.5	9.5	11.3	14.1	18.4	21.5	21.5
16	6.3	6.5	6.9	7.2	7.6	8.0	8.5	9.0	10.2	12.1	15.0	19.7	22.9	22.9
17	6.7	7.0	7.3	7.7	8.1	8.6	9.1	9.6	10.8	12.9	16.0	20.9	24.4	24.4
18	7.1	7.4	7.8	8.2	8.6	9.1	9.6	10.2	11.5	13.7	16.9	22.2	25.8	25.8
19	7.5	7.8	8.2	8.6	9.1	9.6	10.2	10.8	12.1	14.5	17.9	23.4	27.3	27.3
20	7.9	8.3	8.7	9.1	9.6	10.1	10.7	11.4	12.8	15.2	18.8	24.7	28.7	28.7

Table 5. Lookup table to determine the required concentrations of absorbing and scattering agents from desired absorption and reduced scattering coefficients at 631 nm (Greening *et al.*, 2014).

Absorption Coefficient μ_a [cm^{-1}]														
Concentration of 1% w/v Nigrosin/EtOH to PDMS elastomer base [µL/g]														
	0.1	**0.2**	**0.3**	**0.4**	**0.5**	**0.6**	**0.7**	**0.8**	**0.9**	**1.0**	**1.1**	**1.2**	**1.3**	**1.4**
	1.0	1.4	1.7	2.1	2.5	2.9	3.2	3.6	4.2	5.1	5.9	6.8	7.3	14.5
Reduced Scattering Coefficient μ'_s [cm^{-1}]														
Concentration of Titanium Dioxide to PDMS elastomer base [g/g] x10-3														
1	0.2	0.2	0.2	0.2	0.3	0.3	0.3	0.4	0.4	0.6	0.7	1.0	1.1	1.1
2	0.7	0.7	0.7	0.8	0.8	0.9	1.0	1.0	1.2	1.4	1.8	2.3	2.5	2.5
3	1.1	1.2	1.3	1.3	1.4	1.5	1.6	1.7	1.9	2.3	2.8	3.6	3.9	3.9
4	1.6	1.7	1.8	1.9	2.0	2.1	2.2	2.4	2.6	3.1	3.8	4.9	5.3	5.3
5	2.1	2.2	2.3	2.4	2.5	2.7	2.8	3.0	3.4	4.0	4.9	6.2	6.7	6.7
6	2.5	2.7	2.8	2.9	3.1	3.3	3.5	3.7	4.1	4.8	5.9	7.5	8.1	8.1
7	3.0	3.1	3.3	3.5	3.7	3.9	4.1	4.3	4.8	5.7	6.9	8.8	9.5	9.5
8	3.5	3.6	3.8	4.0	4.2	4.4	4.7	5.0	5.6	6.6	8.0	10.1	10.9	10.9
9	3.9	4.1	4.3	4.5	4.8	5.0	5.3	5.7	6.3	7.4	9.0	11.4	12.3	12.3
10	4.4	4.6	4.8	5.1	5.3	5.6	6.0	6.3	7.0	8.3	10.0	12.7	13.7	13.7
11	4.9	5.1	5.3	5.6	5.9	6.2	6.6	7.0	7.8	9.1	11.1	14.0	15.1	15.1
12	5.4	5.6	5.9	6.1	6.5	6.8	7.2	7.6	8.5	10.0	12.1	15.3	16.4	16.4
13	5.8	6.1	6.4	6.7	7.0	7.4	7.8	8.3	9.2	10.8	13.1	16.6	17.8	17.8
14	6.3	6.6	6.9	7.2	7.6	8.0	8.4	9.0	10.0	11.7	14.1	17.9	19.2	19.2
15	6.8	7.1	7.4	7.8	8.2	8.6	9.1	9.6	10.7	12.6	15.2	19.1	20.6	20.6
16	7.2	7.6	7.9	8.3	8.7	9.2	9.7	10.3	11.4	13.4	16.2	20.4	22.0	22.0
17	7.7	8.0	8.4	8.8	9.3	9.8	10.3	10.9	12.2	14.3	17.2	21.7	23.4	23.4
18	8.2	8.5	8.9	9.4	9.8	10.4	10.9	11.6	12.9	15.1	18.3	23.0	24.8	24.8
19	8.6	9.0	9.4	9.9	10.4	11.0	11.6	12.3	13.6	16.0	19.3	24.3	26.2	26.2
20	9.1	9.5	10.0	10.4	11.0	11.5	12.2	12.9	14.4	16.8	20.3	25.6	27.6	27.6

Table 6. Lookup table to determine the required concentrations of absorbing and scattering agents from desired absorption and reduced scattering coefficients at 659 nm (Greening *et al.*, 2014).

Absorption Coefficient μ_a [cm^{-1}]														
Concentration of 1% w/v Nigrosin/EtOH to PDMS elastomer base [µL/g]														
	0.1	**0.2**	**0.3**	**0.4**	**0.5**	**0.6**	**0.7**	**0.8**	**0.9**	**1.0**	**1.1**	**1.2**	**1.3**	**1.4**
	1.0	1.4	1.8	2.2	2.6	3.0	3.3	3.7	4.4	5.2	6.0	6.8	7.5	12.6
Reduced Scattering Coefficient μ'_s [cm^{-1}]														
Concentration of Titanium Dioxide to PDMS elastomer base [g/g] x10-3														
1	0.3	0.3	0.3	0.3	0.4	0.4	0.4	0.5	0.5	0.7	0.8	1.0	1.1	1.1
2	0.8	0.8	0.9	0.9	1.0	1.1	1.1	1.2	1.4	1.6	1.9	2.3	2.4	2.4
3	1.3	1.4	1.5	1.5	1.6	1.7	1.8	1.9	2.2	2.5	2.9	3.6	3.8	3.8
4	1.8	1.9	2.0	2.1	2.2	2.4	2.5	2.6	3.0	3.4	4.0	4.8	5.1	5.1
5	2.4	2.5	2.6	2.7	2.9	3.0	3.2	3.4	3.8	4.3	5.1	6.1	6.5	6.5
6	2.9	3.0	3.2	3.3	3.5	3.7	3.9	4.1	4.6	5.3	6.1	7.4	7.8	7.8
7	3.4	3.6	3.7	3.9	4.1	4.3	4.6	4.8	5.4	6.2	7.2	8.7	9.2	9.2
8	3.9	4.1	4.3	4.5	4.7	5.0	5.3	5.6	6.2	7.1	8.3	9.9	10.5	10.5
9	4.5	4.7	4.9	5.1	5.4	5.6	5.9	6.3	7.0	8.0	9.4	11.2	11.9	11.9
10	5.0	5.2	5.4	5.7	6.0	6.3	6.6	7.0	7.8	8.9	10.4	12.5	13.2	13.2
11	5.5	5.8	6.0	6.3	6.6	6.9	7.3	7.7	8.6	9.8	11.5	13.8	14.6	14.6
12	6.0	6.3	6.6	6.9	7.2	7.6	8.0	8.5	9.4	10.8	12.6	15.0	15.9	15.9
13	6.6	6.8	7.2	7.5	7.9	8.3	8.7	9.2	10.2	11.7	13.6	16.3	17.3	17.3
14	7.1	7.4	7.7	8.1	8.5	8.9	9.4	9.9	11.0	12.6	14.7	17.6	18.6	18.6
15	7.6	7.9	8.3	8.7	9.1	9.6	10.1	10.6	11.8	13.5	15.8	18.9	20.0	20.0
16	8.1	8.5	8.9	9.3	9.7	10.2	10.8	11.4	12.6	14.4	16.8	20.1	21.3	21.3
17	8.7	9.0	9.4	9.9	10.3	10.9	11.5	12.1	13.4	15.4	17.9	21.4	22.7	22.7
18	9.2	9.6	10.0	10.5	11.0	11.5	12.1	12.8	14.2	16.3	19.0	22.7	24.0	24.0
19	9.7	10.1	10.6	11.1	11.6	12.2	12.8	13.6	15.0	17.2	20.0	24.0	25.4	25.4
20	10.2	10.7	11.1	11.7	12.2	12.8	13.5	14.3	15.9	18.1	21.1	25.2	26.7	26.7

Table 7. Lookup table to determine the required concentrations of absorbing and scattering agents from desired absorption and reduced scattering coefficients at 691 nm (Greening *et al.*, 2014).

Absorption Coefficient μ_a [cm^{-1}]														
Concentration of 1% w/v Nigrosin/EtOH to PDMS elastomer base [µL/g]														
	0.1	**0.2**	**0.3**	**0.4**	**0.5**	**0.6**	**0.7**	**0.8**	**0.9**	**1.0**	**1.1**	**1.2**	**1.3**	**1.4**
	1.0	1.4	1.8	2.3	2.7	3.1	3.5	3.9	4.7	5.4	6.1	6.8	7.3	9.1
Reduced Scattering Coefficient μ'_s [cm^{-1}]														
Concentration of Titanium Dioxide to PDMS elastomer base [g/g] x10-3														
1	0.4	0.4	0.5	0.5	0.5	0.5	0.6	0.6	0.7	0.8	0.9	1.0	1.1	1.1
2	1.0	1.0	1.1	1.1	1.2	1.2	1.3	1.4	1.5	1.7	1.9	2.2	2.3	2.3
3	1.6	1.6	1.7	1.8	1.9	1.9	2.0	2.2	2.4	2.6	3.0	3.4	3.5	3.5
4	2.1	2.2	2.3	2.4	2.5	2.6	2.8	2.9	3.2	3.6	4.0	4.6	4.7	4.7
5	2.7	2.8	2.9	3.0	3.2	3.3	3.5	3.7	4.1	4.5	5.0	5.7	5.9	5.9
6	3.3	3.4	3.5	3.7	3.9	4.0	4.2	4.5	4.9	5.4	6.1	6.9	7.2	7.2
7	3.8	4.0	4.1	4.3	4.5	4.7	5.0	5.2	5.7	6.4	7.1	8.1	8.4	8.4
8	4.4	4.6	4.8	5.0	5.2	5.4	5.7	6.0	6.6	7.3	8.2	9.3	9.6	9.6
9	5.0	5.2	5.4	5.6	5.9	6.1	6.4	6.8	7.4	8.2	9.2	10.4	10.8	10.8
10	5.5	5.7	6.0	6.2	6.5	6.8	7.2	7.5	8.3	9.2	10.2	11.6	12.0	12.0
11	6.1	6.3	6.6	6.9	7.2	7.5	7.9	8.3	9.1	10.1	11.3	12.8	13.2	13.2
12	6.7	6.9	7.2	7.5	7.9	8.2	8.6	9.1	10.0	11.0	12.3	14.0	14.5	14.5
13	7.2	7.5	7.8	8.2	8.5	8.9	9.4	9.8	10.8	12.0	13.4	15.2	15.7	15.7
14	7.8	8.1	8.4	8.8	9.2	9.6	10.1	10.6	11.6	12.9	14.4	16.3	16.9	16.9
15	8.4	8.7	9.0	9.4	9.9	10.3	10.8	11.4	12.5	13.8	15.4	17.5	18.1	18.1
16	8.9	9.3	9.7	10.1	10.5	11.0	11.6	12.1	13.3	14.7	16.5	18.7	19.3	19.3
17	9.5	9.9	10.3	10.7	11.2	11.7	12.3	12.9	14.2	15.7	17.5	19.9	20.6	20.6
18	10.1	10.5	10.9	11.4	11.9	12.4	13.0	13.7	15.0	16.6	18.6	21.0	21.8	21.8
19	10.6	11.0	11.5	12.0	12.5	13.1	13.7	14.5	15.9	17.5	19.6	22.2	23.0	23.0
20	11.2	11.6	12.1	12.6	13.2	13.8	14.5	15.2	16.7	18.5	20.6	23.4	24.2	24.2

Table 8. Lookup table to determine the required concentrations of absorbing and scattering agents from desired absorption and reduced scattering coefficients at 731 nm (Greening *et al.*, 2014).

Absorption Coefficient μ_a [cm^{-1}]														
Concentration of 1% w/v Nigrosin/EtOH to PDMS elastomer base [µL/g]														
	0.1	**0.2**	**0.3**	**0.4**	**0.5**	**0.6**	**0.7**	**0.8**	**0.9**	**1.0**	**1.1**	**1.2**	**1.3**	**1.4**
	1.0	1.5	1.9	2.4	2.8	3.3	3.8	4.3	5.1	5.8	6.5	7.3	9.3	17.3
Reduced Scattering Coefficient μ'_s [cm^{-1}]														
Concentration of Titanium Dioxide to PDMS elastomer base [g/g] x10-3														
1	0.5	0.5	0.5	0.6	0.6	0.6	0.7	0.7	0.8	0.9	1.0	1.0	1.0	1.0
2	1.1	1.2	1.2	1.3	1.3	1.4	1.4	1.5	1.7	1.8	2.0	2.2	2.2	2.2
3	1.7	1.8	1.9	1.9	2.0	2.1	2.2	2.4	2.6	2.8	3.1	3.4	3.4	3.4
4	2.3	2.4	2.5	2.6	2.7	2.9	3.0	3.2	3.5	3.8	4.2	4.5	4.5	4.5
5	2.9	3.1	3.2	3.3	3.5	3.6	3.8	4.0	4.4	4.8	5.3	5.7	5.7	5.7
6	3.6	3.7	3.8	4.0	4.2	4.4	4.6	4.9	5.3	5.8	6.4	6.8	6.8	6.8
7	4.2	4.3	4.5	4.7	4.9	5.1	5.4	5.7	6.2	6.8	7.5	8.0	8.0	8.0
8	4.8	5.0	5.2	5.4	5.6	5.9	6.1	6.5	7.1	7.7	8.5	9.2	9.2	9.2
9	5.4	5.6	5.8	6.1	6.3	6.6	6.9	7.4	8.0	8.7	9.6	10.3	10.3	10.3
10	6.0	6.2	6.5	6.8	7.0	7.4	7.7	8.2	8.9	9.7	10.7	11.5	11.5	11.5
11	6.6	6.9	7.1	7.4	7.8	8.1	8.5	9.0	9.8	10.7	11.8	12.6	12.6	12.6
12	7.2	7.5	7.8	8.1	8.5	8.9	9.3	9.9	10.7	11.7	12.9	13.8	13.8	13.8
13	7.9	8.1	8.5	8.8	9.2	9.6	10.1	10.7	11.6	12.7	13.9	15.0	15.0	15.0
14	8.5	8.8	9.1	9.5	9.9	10.4	10.8	11.5	12.5	13.6	15.0	16.1	16.1	16.1
15	9.1	9.4	9.8	10.2	10.6	11.1	11.6	12.3	13.4	14.6	16.1	17.3	17.3	17.3
16	9.7	10.1	10.5	10.9	11.3	11.9	12.4	13.2	14.3	15.6	17.2	18.4	18.4	18.4
17	10.3	10.7	11.1	11.6	12.1	12.6	13.2	14.0	15.2	16.6	18.3	19.6	19.6	19.6
18	10.9	11.3	11.8	12.3	12.8	13.3	14.0	14.8	16.1	17.6	19.4	20.8	20.8	20.8
19	11.5	12.0	12.4	12.9	13.5	14.1	14.8	15.7	17.0	18.6	20.4	21.9	21.9	21.9
20	12.1	12.6	13.1	13.6	14.2	14.8	15.5	16.5	17.9	19.5	21.5	23.1	23.1	23.1

Table 9. Lookup table to determine the required concentrations of absorbing and scattering agents from desired absorption and reduced scattering coefficients at 851 nm (Greening *et al.*, 2014).

Absorption Coefficient μ_a [cm^{-1}]														
Concentration of 1% w/v Nigrosin/EtOH to PDMS elastomer base [µL/g]														
	0.1	**0.2**	**0.3**	**0.4**	**0.5**	**0.6**	**0.7**	**0.8**	**0.9**	**1.0**	**1.1**	**1.2**	**1.3**	**1.4**
	1.0	1.7	2.4	3.1	3.8	4.4	5.2	5.9	6.7	7.7	9.6	12.9	18.4	27.4
Reduced Scattering Coefficient μ'_s [cm^{-1}]														
Concentration of Titanium Dioxide to PDMS elastomer base [g/g] x10-3														
1	0.6	0.6	0.7	0.7	0.7	0.7	0.8	0.8	0.8	0.8	0.8	0.8	0.8	0.8
2	1.4	1.4	1.4	1.5	1.5	1.6	1.6	1.7	1.8	1.8	1.8	1.8	1.8	1.8
3	2.1	2.1	2.2	2.3	2.4	2.4	2.5	2.6	2.7	2.8	2.8	2.8	2.8	2.8
4	2.8	2.9	3.0	3.1	3.2	3.3	3.4	3.5	3.7	3.7	3.7	3.7	3.7	3.7
5	3.6	3.7	3.8	3.9	4.0	4.1	4.3	4.4	4.6	4.7	4.7	4.7	4.7	4.7
6	4.3	4.4	4.5	4.7	4.8	5.0	5.2	5.4	5.6	5.7	5.7	5.7	5.7	5.7
7	5.0	5.2	5.3	5.5	5.7	5.8	6.0	6.3	6.5	6.6	6.6	6.6	6.6	6.6
8	5.8	5.9	6.1	6.3	6.5	6.7	6.9	7.2	7.5	7.6	7.6	7.6	7.6	7.6
9	6.5	6.7	6.9	7.1	7.3	7.5	7.8	8.1	8.4	8.6	8.6	8.6	8.6	8.6
10	7.2	7.4	7.7	7.9	8.1	8.4	8.7	9.0	9.4	9.5	9.5	9.5	9.5	9.5
11	8.0	8.2	8.4	8.7	9.0	9.2	9.6	9.9	10.3	10.5	10.5	10.5	10.5	10.5
12	8.7	9.0	9.2	9.5	9.8	10.1	10.4	10.8	11.3	11.4	11.4	11.4	11.4	11.4
13	9.4	9.7	10.0	10.3	10.6	10.9	11.3	11.7	12.2	12.4	12.4	12.4	12.4	12.4
14	10.2	10.5	10.8	11.1	11.4	11.8	12.2	12.7	13.2	13.4	13.4	13.4	13.4	13.4
15	10.9	11.2	11.6	11.9	12.3	12.6	13.1	13.6	14.1	14.3	14.3	14.3	14.3	14.3
16	11.6	12.0	12.3	12.7	13.1	13.5	14.0	14.5	15.1	15.3	15.3	15.3	15.3	15.3
17	12.4	12.7	13.1	13.5	13.9	14.3	14.8	15.4	16.0	16.3	16.3	16.3	16.3	16.3
18	13.1	13.5	13.9	14.3	14.7	15.2	15.7	16.3	17.0	17.2	17.2	17.2	17.2	17.2
19	13.9	14.2	14.7	15.1	15.6	16.0	16.6	17.2	17.9	18.2	18.2	18.2	18.2	18.2
20	14.6	15.0	15.4	15.9	16.4	16.9	17.5	18.1	18.8	19.2	19.2	19.2	19.2	19.2

3.6.6 Extraction of sampling depth from semi-infinite phantom model of dysplastic progression

Three different phantom geometries, simulating the progression from healthy tissue to severe dysplasia, underwent DRS evaluation using both SDSs (374 and 730 µm). Figure 19 shows that the extracted μ_s' for phantom 1 (blue line) was approximately 7 cm^{-1} at 630 nm, as expected from the phantom generation protocol (Greening *et al.*, 2014). As the higher scattering (μ_s' = 14 cm^{-1}) layers proliferated upwards towards the probe tip (phantoms 2 and 3), an increase in volume-averaged μ_s' occurred for both SDSs, although more so for the shorter SDS, as expected. For the shorter SDS, there was a significant increase in volume-averaged μ_s' from phantoms 1 to 2 and 2 to 3. However, for the longer SDS, there was only a significant increase in

volume-averaged μ_s' from phantoms 2 to 3. This indicates the 374 μm SDS is more sensitive to scattering heterogeneities at upper layers compared to the 730 μm SDS.

This phenomenon is further quantified in Table 10 by the percent increase in volume-averaged μ_s' at 630 nm for Phantoms 1-3 for each SDS. The data indicates that the μ_s' percent increase for the 374 μm SDS is significantly greater compared to the 730 μm SDS. This is because the shorter SDS has a decreased sampling depth, and therefore scattering is mostly affected by more superficial heterogeneities, as seen in early dysplasia, compared to the longer SDS. However, it is important to note that the 374 μm SDS still does not exclusively sample the upper layers, as indicated by the fact that the volume-averaged μ_s' of phantom 3 (300 μm thick heterogeneity) is approximately 9 cm^{-1} rather than 14 cm^{-1} at the reference 630 nm. Additionally, sampling depth of the 374 μm SDS at a μ_s' of 14 cm^{-1} is ~400 μm, indicating a sampling depth deeper than the 300 μm scattering heterogeneity. These results demonstrate the value of including a shorter SDS for detection of more superficial scattering changes. The value of including an additional longer SDS was shown in the following section describing *in vivo* results from healthy human oral mucosa.

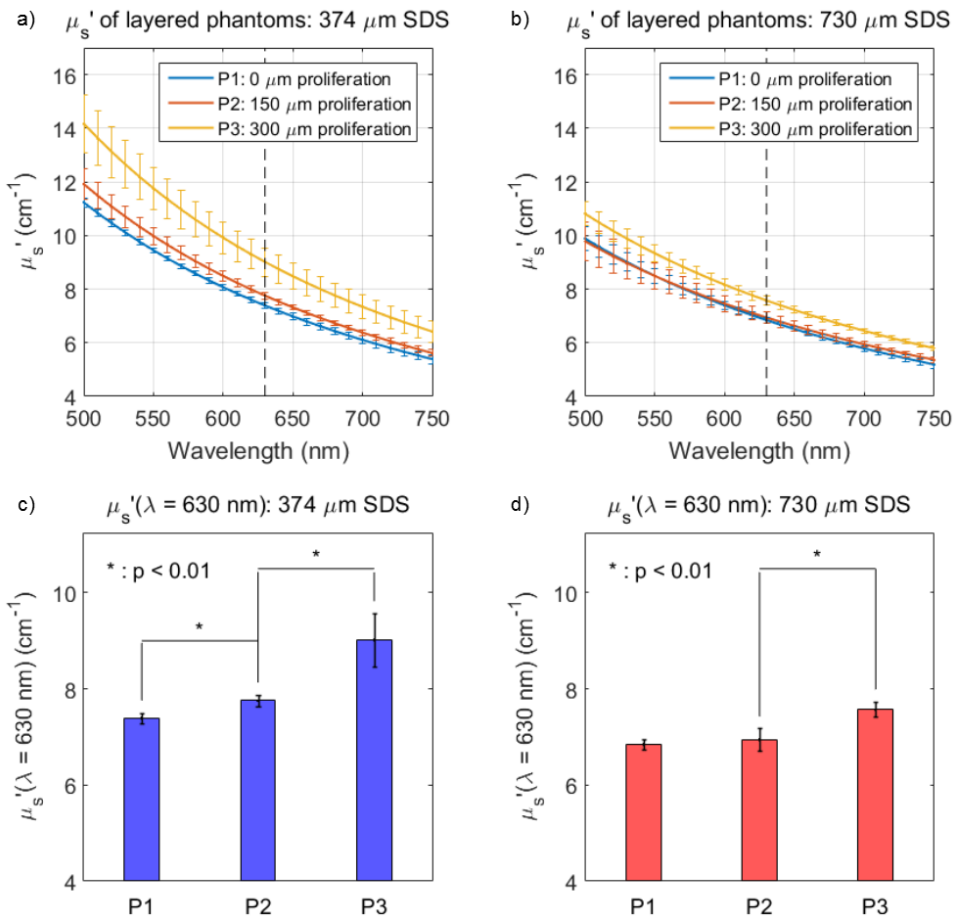

Figure 19. The volume-averaged μ_s' (a, b) increased as the proliferating scattering heterogeneity moved upwards towards the phantom surface (going from P1 to P3) showing a vertical line at 630 nm, in which percent increase in volume-averaged μ_s' was measured from. There was a significantly greater μ_s' increase in these values for the 374 µm SDS compared to the 730 µm SDS, indicating that the shorter SDS is more sensitive to superficial scattering changes associated with early epithelial dysplasia.

Table 10. Paired t-test statistics for percent increases in μ_s' (λ = 630 nm) for dysplasia-mimicking phantom model

Phantom Comparison	374 µm SDS (n=10)		730 µm SDS (n=10)		P-Value	Significance (Y/N), α=0.01
	Mean	Std. Dev.	Mean	Std. Dev.		
P1 to P2 (%)	4.97	0.40	1.42	1.93	$1.7\text{x}10^{-4}$	Y
P2 to P3 (%)	16.18	5.95	9.19	1.54	$4.6\text{x}10^{-3}$	Y
P1 to P3 (%)	21.96	6.42	10.72	0.93	$1.2\text{x}10^{-4}$	Y

3.6.7 Collaboration with the Boston University Department of Biomedical Engineering: two-layer LUT improves the accuracy of tumor layer optical property extractions using SFDI

The following section was directly adapted from Syeda Tabassum, Vivian Pera and Darren Roblyer from Boston University, with whom we provided tissue-simulating PDMS phantoms for their experiments (Tabassum *et al.*, 2018).

Experimental measurements were conducted to determine if the Gardner two-layer LUT inversion algorithm improves the accuracy of tumor layer optical property extractions compared to the Gardner homogeneous LUT. This accuracy test utilized the four two-layer phantoms described in Section 3.5.5. Each of the two-layer phantoms used the same top (skin) layer. The measured thickness of the skin layer was 310 μm at its center, which is within 0.8% of the skin layer thickness defined in the MC simulations used to generate the Gardner two-layer LUT. Absorption of the skin layer was 0.0936 mm−1 at 659 nm, which is within 2.52% of the MC absorption parameter, and the μ0s value was 0.780 mm−1 at 659 nm, which is within 0.063% of the MC value. For the tumor layer, four different pairs of optical properties were utilized, spanning a range of optical properties observed in our prior work, in which we monitored PC3/2G7 mouse xenografts over 45 days using SFDI (Tabassum *et al.*, 2016). These pairs are labeled as tumor 1 through tumor 4 in Figure 10. The optical property pairs, reported at 659 nm, are as follows: for tumor 1: μa ¼ 0.0244 mm−1 and μ0 s ¼ 2.054 mm−1; tumor 2: μa ¼ 0.002 mm−1 and μ0s ¼ 2.314 mm−1; tumor 3: μa ¼ 0.0039 mm−1 and μ0s ¼ 0.714 mm−1; and tumor 4: μa ¼ 0.0301 mm−1 and μ0s ¼ 0.676 mm−1.

Each two-layer phantom was measured with SFDI, and the bottom (tumor) layer optical properties were extracted using both the Gardner homogeneous and Gardner two-layer LUTs. Since these phantoms have flat surfaces, no corrections for height or angle were implemented.

The absolute differences between the measured and true μa for the tumor layer are shown in Figures 10(a) and 10(b). The absolute differences between the measured and true μ0s for the tumor layer are shown in Figures 5(c) and 5(d). In both cases, Figures 10(b) and 10(d) recapitulates the data in Figures 10(a) and 10(c) but with a zoomed-in y-axis to allow visualization of the small error values obtained for some phantoms. In the worst-case, the μa and μ0 s extraction errors were 20.33% and 10.87% for the two-layer LUT.

In all cases, the error in tumor layer optical property extraction is substantially lower for the two-layer LUT versus the homogeneous LUT. This effect is not as pronounced in μ0s for tumors 3 and 4, as μ0s values in these tumors are very similar to that of the skin layer (μ0 s ¼ 0.78 mm−1). Note that the decrease in error by the two-layer LUT is between 7 and 256 times for μa and between 2 and 24 times for μ0s. Taken together, these results confirm that the two-layer LUT provides a better estimate of the true tumor layer optical properties than the homogeneous LUT (Tabassum *et al.*, 2018).

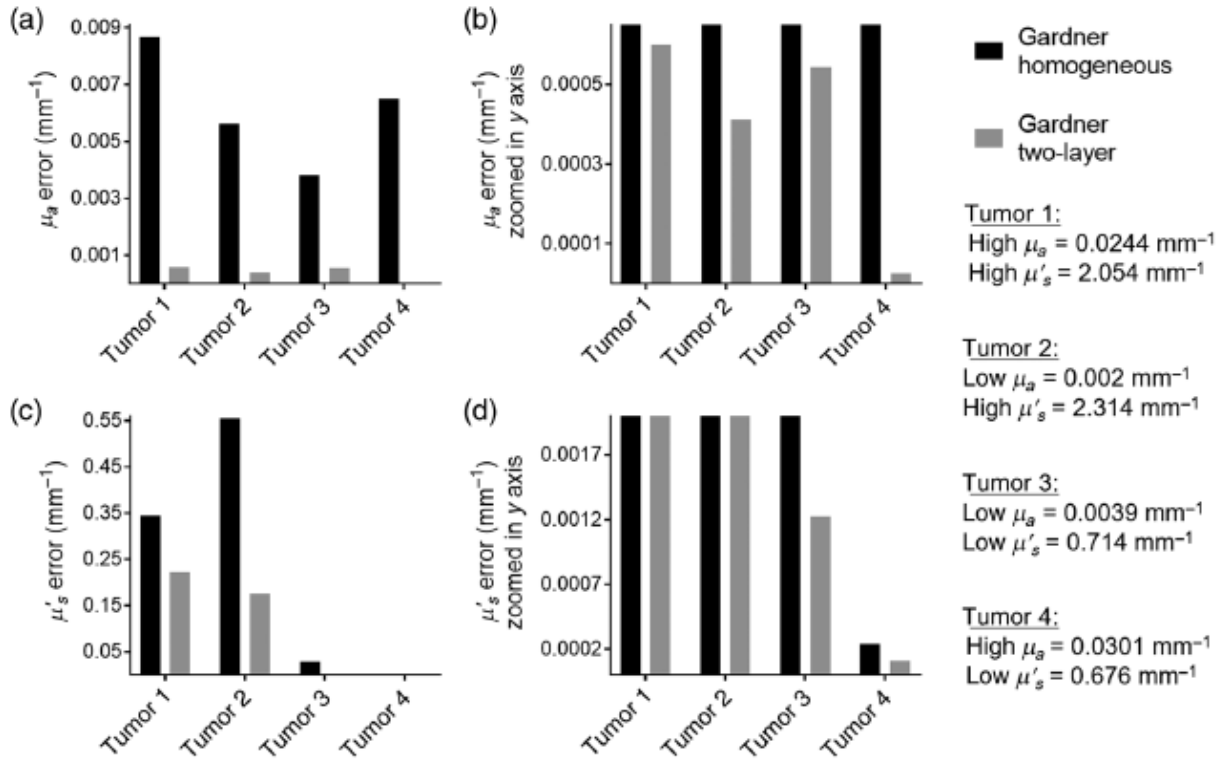

Figure 20. Comparisons in bottom (tumor) layer optical property extraction errors for the Gardner homogeneous and Gardner two-layer LUT inversion algorithms. Diffuse reflectance measurements of four two-layer tissue-simulating optical phantoms were made with SFDI, and both inversion models were used to extract the bottom (tumor) layer optical properties (labeled as tumors 1 to 4). (a) The absolute extraction error compared with the known tumor layer μa. (b) The same data but with a zoomed-in y-axis so that small extraction errors can be visualized. (c) Absolute errors in tumor layer μ0s extractions and (d) the same data with a zoomed-in y-axis. Optical properties were measured at 659 nm (Tabassum *et al.*, 2018).

3.7 How-to guide: solid phantoms as tools for simulating epithelial structure

Presented in this section is a tutorial for constructing solid phantoms. These phantoms can be used to simulate thin epithelial tissue 100's of microns thick. Thin layers can be stacked to mimic the geometry of layered epithelia, such as in the epidermis and dermis of skin. Different types of scattering and absorbing agents can be added to the solid phantoms to mimic an array of μ_s' and μ_a. Furthermore, these solid optical phantoms can easily be molded into a variety of thicker shapes and inclusions/heterogeneities can be added for various purposes. Therefore, these

phantoms are a robust, multipurpose tool for a variety of imaging and spectroscopy applications.

3.7.1 Constructing the PDMS-based mix

The substrate material used to construct the following optical phantoms is polydimethylsiloxane (PDMS), a thermoset polymer. PDMS-based phantoms have been used by investigators for various purposes including epithelial tissue simulation (Greening *et al.*, 2014; Wang *et al.*, 2011), retina-simulating phantoms (Fogli *et al.*, 2014), aorta models (Schlicht *et al.*, 2013), and other soft tissues (Avigo *et al.*, 2015) for various imaging purposes.

To construct these PDMS-based phantoms, an aliquot of PDMS elastomer base (Sylgard® 184 Silicone Elastomer Base) is poured into a plastic mixing cup. Depending on the application, less volume of elastomer base is needed for thinner layers (~150-300 μm) versus slightly thicker layers (300+ μm). After dispensing the PDMS elastomer base, the scattering and absorbing agents can be added. Scattering agents can be a variety of substances, such as TiO_2 or polystyrene microspheres. Absorbing agents can also be a variety of substances including dyes and inks. The examples for this tutorial will use TiO_2 (14021, Sigma Aldrich, USA) and water-soluble nigrosin (N4763, Sigma Aldrich, USA) as the scattering and absorbing agents, respectively. Before adding the curing agent, it is important to thoroughly mix the elastomer base and optical agents. Mixing can be done by hand or in an appropriate automated mixing machine. Once mixed, the appropriate amount of curing agent (Sylgard® 184 Silicone Elastomer Curing Agent) should be added to the mix. The amount of curing agent needed is a 1:10 mass-to-mass ratio of curing agent to elastomer base (Greening *et al.*, 2014). It is recommended to use a reliable micropipette to add in the appropriate amount of curing agent to the mix. Immediately following addition of curing agent, the curing process will begin. Therefore, it is imperative to mix the curing agent into the PDMS elastomer base immediately either by hand or with an

automated mixing machine. Some mixing machines contain a “degassing” feature, in which the recovered mixed product is free of air bubbles. If mixing the elastomer base, curing agent, and scattering and absorbing agents by hand, the resultant mix must be fully degassed using a vacuum for at least 90-120 minutes. Furthermore, the PDMS must always be vacuumed to create a spatially homogenous solution free of air bubbles after dispensing into a mold.

Curing PDMS at room temperature takes between 48-72 hours. Curing can be accelerated by placing the fully mixed and degassed solution into an oven. Placing the mix inside an oven at 70°C will cure the mix in 2 hours. Furthermore, if needed, curing can be halted by placing the mix in a sub-0°C freezer.

Figure 21 shows the process for creating bulk PDMS-based phantoms, including the viscous, pre-cured PDMS elastomer base, the addition of TiO_2 as the scattering agent and water soluble nigrosin as the absorbing agent.

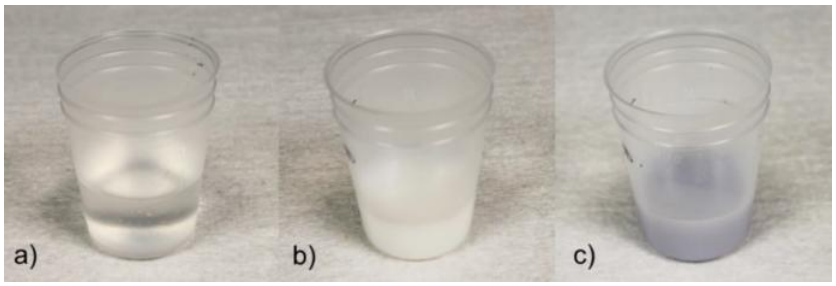

Figure 21. A demonstration of the process to create PDMS-based phantoms with TiO_2 and water-soluble nigrosin. The figure shows (a) PDMS elastomer base with no mixed components, (b) TiO_2 mixed in the PDMS elastomer base, and (c), water-soluble nigrosin mixed in the PDMS elastomer base.

Since PDMS is a viscous polymer prior to curing into a permanent solid polymer, it can be molded into a variety of shapes and sizes. Figure 22 shows an example of a PDMS-based phantom, containing TiO_2 and water-soluble nigrosin, molded into a cylinder 28 mm in diameter and 50 mm in height. The cylinder had a μ_s’ of 4.75 cm^{-1} and μ_a of 0.25 cm^{-1} at a reference of 633 nm. One 6.35-diameter hole was drilled into the top of the phantom 30 mm deep. The drilled

hole was filled with PDMS-based phantom mix with a μ_s' of 4.75 cm^{-1} and μ_a of 5.0 cm^{-1}, so that scattering was constant, and absorption was increased by a factor of 20. This demonstration shows that heterogeneities or inclusions can be added to a solid-PDMS phantom to potentially simulate a variety of tissue types for different imaging or spectroscopic applications.

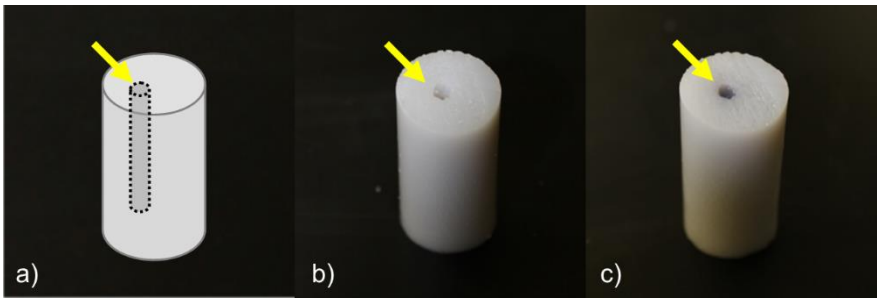

Figure 22. PDMS-based phantoms molded into three-dimensional structures. The figure shows (a) PDMS molded into the shape of a finger, (b) a PDMS optical phantom with 5 mm-diameter holes drilled 5 cm deep for the addition of optical inclusions, and (c) a block of PDMS containing TiO_2 and water-soluble nigrosin that can be used as a "semi-infinite" layer in which thin PDMS phantom layers can be stacked.

3.7.2 Spin coating technique for creation of thin phantoms

In addition to using PDMS to create bulk tissue phantoms, thin phantoms, down to approximately 100 μm or thinner, can also be constructed (Greening *et al.*, 2014; Koschwanez *et al.*, 2009). These thin phantoms can be stacked to create semi-permanent multilayer phantoms. These multilayer phantoms are semi-permanent because each individual layer is optically stable over time, but each layer can be switched out for additional layers. This gives investigators the freedom to mix and match stable layers of varying optical properties and thicknesses.

Optical properties of these PDMS-based phantoms are controlled with the addition of scattering and absorbing agents. The scattering properties can be controlled by obtaining a LUT showing μ_s' as a function of scattering agent concentration, other empirical methods presented in literature, or Mie Theory. The absorbing properties can be controlled by evaluating the μ_a of dilute solutions of the absorbing agent using a spectrophotometer and Beer's Law.

Layer thickness is controlled using a custom spin coating technique. Immediately after the PDMS-reagent mixture has completed the mixing and degassing steps outlined in the previous section, a quarter-sized amount is transferred to an unmodified silicon wafer. These wafers are 500 microns in depth, with a diameter of 100 millimeters. The wafer is then placed within a spin coating machine and spun at an appropriate rotational speed (RPM) to yield the desired layer thickness. For our purposes, the spin coater spins the silicon wafer at maximum speed for 20 seconds, with a 2 second acceleration and deceleration period. Immediately after curing, the still-viscous spun layer of PDMS is transferred to a 70°C oven where it is allowed to complete the curing process for 2 hours. Several groups have used spin coating methods to produce thin phantom layers and their specific target thicknesses can be found elsewhere (Koschwanez *et al.*, 2009; Greening *et al.*, 2014).

For this tutorial, it is important to note the parameters that affect layer thickness using a spin coater. First, maximum speed affects layer thickness. The faster the silicon wafer spins the PDMS mix, the thinner the resultant layer. Second, duration of speed affects layer thickness. A shorter spin duration increases layer thickness whereas a longer spin duration decreases layer thickness. Third, the temperature of the PDMS mix prior to mixing affects resultant layer thickness. Since PDMS is a thermoset, the higher the temperature prior to spinning, the thicker the layer since the polymer will begin to resist mechanical forces throughout curing. A colder pre-spun mix will result in thinner layers. Fourth, the post-spinning curing temperature will affect thickness. Since the PDMS will not have fully cured after spinning, it will continue to slightly settle and spread out post-spinning. Therefore, the higher the temperature post spinning, the thicker the resultant layer. Fifth, additives to the PDMS mix will affect layer thickness. One group has shown that adding in a type of alcohol results in thinner layers when holding all other

variables constant (Koschwanez *et al.*, 2009). Additionally, adding in varying amounts of scattering and absorbing agents may affect resultant thickness, although this has not been extensively investigated at this time. The next few factors are timing factors, since the curing process is time sensitive. In all cases, increased time between steps results in thicker layers. These factors include the time between mixing the curing agent with the elastomer base and spinning with the spin coater, and the time between mixing with the spin coater and placing in the oven to finalize the curing process.

The spin coating method for creating phantoms is extremely useful and important. It is, for this process, what allows there to be multiple layer thicknesses to simulate different depths within epithelial tissues. It also allows for a simple way of creating multi-layer phantoms to quickly and easily vary a simulation of different depths within epithelial tissues by stacking a pre-made, set number of individual thin phantoms (Greening *et al.*, 2014).

Figure 23 shows the process of creating thin PDMS-based phantoms. The uncured viscous PDMS-phantom mix, with μ_s' of 4.75 cm^{-1} and μ_a of 0.25 cm^{-1} at a reference of 633 nm, is poured onto a silicon wafer. The silicon wafer is placed into a spin coating machine which spins the uncured PDMS at a user-specified speed. The uncured PDMS spreads out, becoming thinner. The uncured, thinned PDMS-phantom is then placed in an oven to finish curing, and afterwards a piece can be cut to various geometries. In this example, the resultant cured phantom was 300 μm and approximately 2 cm^2.

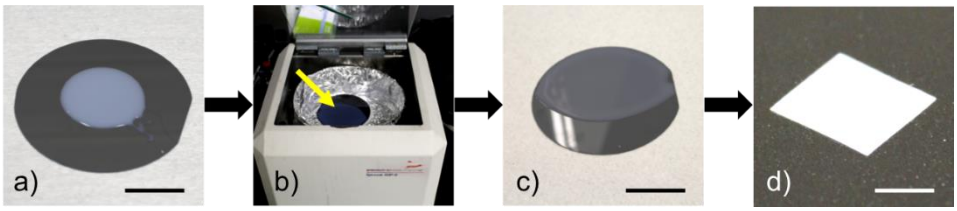

Figure 23. The process of creating thin PDMS-based optical phantoms. The figure shows the (a) silicon wafer with uncured the uncured PDMS mix (scale bar =3 cm), (b) silicon wafer inside the spin coating machine, (c) uncured PDMS mix after being spun down in the spin coating machine (scale bar =3 cm), and (d) cured 300 μm thick phantom cut to a 2 cm^2 square with μ_s' of 4.75 cm^{-1} and μ_a of 0.25 cm^{-1} at a reference of 633 nm to simulate Caucasian epidermal tissue (scale bar = 7.5 mm).

Figure 24 shows more examples of thin PDMS-based optical phantoms. Figure 24(a) shows three 270 μm thick phantoms with increasing concentration of TiO_2, corresponding to μ_s' values of 4.6, 8.2, and 21.5 cm^{-1} and a μ_a of 0 cm^{-1} at 633 nm. Figure5(b) shows an image of a large base phantom layer with μ_s' and μ_a of 4.75 cm^{-1} and 0.25 cm^{-1} at 633 nm. One top of this base layer are four optically heterogeneous 100 μm-thick PDMS-based phantoms with μ_s' and μ_a of 4.75 cm^{-1} and 5.00 cm^{-1} at 633 nm. To demonstrate the ability to create semi-permanent multilayer phantoms, the four optical heterogeneous layers have either zero, one, two, or three 100 μm-thick layers that have identical optical properties to the base layer (μ_s' = 4.75 cm^{-1} and μ_a = 0.25 cm^{-1} at 633 nm). This demonstrates the ability of thin PDMS-based phantom layers to be stacked in various arrangements to create multilayer phantoms with optical heterogeneities. In this case, the optical heterogeneities had a 20x increase in absorption for demonstrative purposes, although in real tissue, heterogeneities may not be as optically different (Greening *et al.*, 2014; Salomatina *et al.*, 2006).

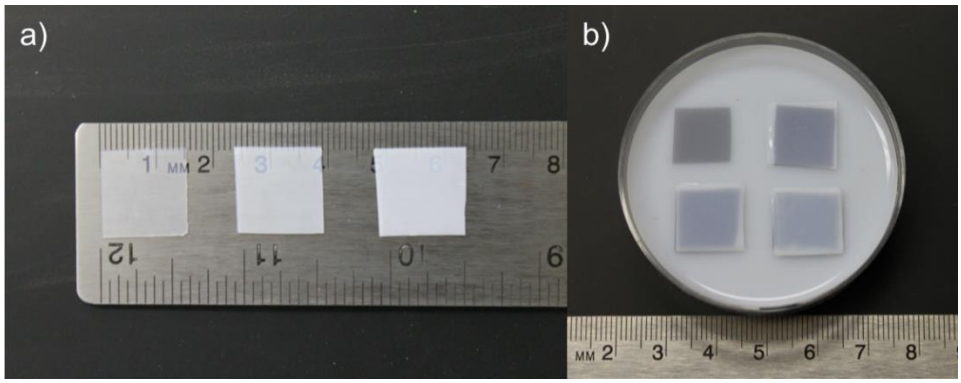

Figure 24. This figure shows (a) three non-absorbing 270 μm thick phantom layers, each approximately 1.5 cm^2, with increasing μ_s' (4.6, 8.2, and 21.5 cm^{-1}) due to increased concentrations of titanium dioxide (TiO_2) and μ_a = 0 cm^{-1}, and (b) a 6 cm-diameter "semi-infinite" layer (μ_s' = 4.75 cm^{-1}, μ_a = 0.25 cm^{-1} at 633 nm) with various thin stacked phantoms on top. At each quadrant, there exists a highly absorbing inclusion (μ_s' = 4.75 cm^{-1}, μ_a = 5.00 cm^{-1} at 633 nm) with either 0, 1, 2, or 3 overlying 100 μm thick layers with optical properties (μ_s' = 4.75 cm^{-1}, μ_a = 0.25 cm^{-1} at 633 nm) matching that of the underlying "semi-infinite" layer.

3.8 Discussion

3.8.1 PDMS as a substrate material

We have demonstrated a reproducible method for creating thin PDMS-based phantoms with tunable thickness and optical properties (reduced scattering and absorption coefficients) (de Bruin *et al.*, 2010; Saager *et al.*, 2010; Pogue *et al.*, 2006; Ayers *et al.*, 2008; Sandell *et al.*, 2011; Liu *et al.*, 2006; Bae *et al.*, 2013). PDMS, a silicone based polymer, was chosen as the substrate material due to its relatively long optical stability when compared to other commonly used substrates (de Bruin *et al.*, 2010; Pogue *et al.*, 2006). Bruin et al. demonstrated that optical properties of PDMS-based phantoms using TiO_2 as a scattering agent remained stable over a six month testing period (de Bruin *et al.*, 2010). Pogue et al. reports that silicone-based phantoms with TiO_2 and various inks should have an optical stability of at least one year (Pogue *et al.*, 2006). Furthermore, PDMS is optically clear, easily moldable, and has a comparable refractive index (1.4) to human tissue (de Bruin *et al.*, 2010; Saager *et al.*, 2010; Pogue *et al.*, 2006).

3.8.2 Spin coating to produce individual thin layers

We demonstrated an ability to create both thin phantom layers (between 115 and 880 μm) and thick phantom layers (approximately 2.5 cm thick). Thick phantoms could be made at other thicknesses as well by varying the volume dispensed into the ARE-100 conditioning mixer cup (Intertronics, UK) mold.

To create thin phantom layers, a spin coating technique was used to spin partially cured PDMS down to reproducible thicknesses as shown in Figure 11 (Bae *et al.*, 2013; Koschwanez *et al.*, 2009). Koschwanez et al. have previously outlined a spin coating technique to create multi-layered PDMS phantoms by spinning uncured PDMS over an already cured layer. However, their thin phantoms ranged between 2 and 30 μm, much thinner than our intended range (100-300 μm) for mimicking epithelial tissue thickness (Harris *et al.*, 1992; Chang *et al.*, 2012; Guimarães *et al.*, 2007; Rocha *et al.*, 2010). Furthermore, our method allowed for thin layers to be used interchangeably and non-permanently to rapidly test multiple configurations. In our studies, the relationship between the maximum 20 second spin speed of the spin coater and the resulting thickness of cured, individual PDMS layers containing varying amounts of TiO_2 and 1% w/v nigrosin/EtOH can be seen in Figure 11. Spin speeds of 100 rpm produced phantoms with an average thickness of 880 μm and standard deviation of 34 μm. Spin speeds of 1000 μm produced phantoms with an average thickness of 115 μm and standard deviation of 4 μm. As spin speed increased, thickness decreased, and standard deviation tended to decrease. For researchers interested in using this technique, the following inverse equation (Eq. 3), based on data presented here, can be used as a guideline to estimate the necessary spin speed [rpm] given a desired thickness with relative accuracy,

$$s = 115{,}900 \cdot (t^{-0.9985}) - 15.09 \quad (3)$$

where *t* is the desired thickness [μm] and *s* is the resulting spin speed [rpm]. The R^2 value for this equation is 0.988 for the data presented in this manuscript. This equation (Eq. 3) was generated by the MATLAB curve fitting toolbox using a 2-term power model.

One consideration when using this spin coating technique is the potential non-uniformity of absorbing and scattering agents within the PDMS material. Heterogeneities in these materials may result at increasing radial distances due to the rotational acceleration of the spin coater (Saager *et al.*, 2010). This may also mean that thin phantoms of identical concentrations of optical agents, but different thicknesses may have slightly different optical properties. Since SFDI required thick phantoms (> 2.5 cm) for characterization, optical properties of thin layers were not explicitly measured (Cuccia *et al.*, 2009). However, from data presented in Figure 16 and 17, we are reasonably confident that thin layers have bulk scattering and absorbing properties comparable to the thicker layers characterized by SFDI. To definitively validate thin layer uniformity, methods capable of characterizing optical properties of thin layers, such as integrating spheres and Inverse Adding-Doubling (IAD) methods, must be further explored (Prahl *et al.*, 1993; Pickering *et al.*, 1993). Another limitation to this procedure was creating phantoms with a lower limit of approximately 115 μm. While thinner layers could potentially be produced using our spin coating technique, such thin layers were increasingly difficult to work with by hand and could no longer be considered interchangeable with regards to creating multilayered phantoms. Therefore, applications in need of phantoms thinner than 115 μm, such as retinal imaging, may benefit from other spin coating techniques such as those presented by Bae et al. or Koschwanez et al. that can produce much thinner layers (Bae *et al.*, 2013; Chang *et al.*, 2012; Baxi *et al.*, 2014).

3.8.3 Alcohol-soluble nigrosin as an absorbing agent

The absorption coefficient (μ_a) of PDMS phantoms was manipulated by using alcohol-soluble nigrosin as the absorbing agent (Saager *et al.*, 2010; Liu *et al.*, 2006). A 1% w/v solution of nigrosin/ethanol was prepared and added to phantoms at increasing concentrations as seen in Figure 14. Figure 15 shows that μ_a was independent of TiO_2 concentrations. However, μ_a was shown to be wavelength dependent when using 1% w/v nigrosin/EtOH for the absorbing agent. This can be seen in Figure 14 in the difference between the best fit curves for the 591 nm (dashed) and 851 nm (dotted) wavelengths, respectively. As wavelength increased, μ_a tended to decrease. This observation is comparable to results on similar phantoms created by Saager et al (Saager *et al.*, 2010). In addition, μ_a was strongly dependent on concentration of 1% w/v nigrosin/EtOH as expected. Figure 14 shows that a more linear region exists between 1% w/v nigrosin/EtOH concentrations from 0 to 7 µL/g PDMS elastomer base, corresponding to μ_a values between approximately 0 and 0.9-1.2 cm^{-1} depending on the measured wavelengths. Increases in μ_a began to level off for 1% w/v nigrosin/EtOH concentrations between 7 to 40 µL/g PDMS elastomer base, corresponding to μ_a values between approximately 0.9-1.2 and 1.5 cm^{-1}.

Just as in the case of the previous thickness-spin speed relationship (Eq. 3), a useful inverse equation would be one that estimates the necessary concentration of 1% w/v nigrosin/EtOH in PDMS given a desired μ_a. Because μ_a was shown to be dependent on both absorbing concentration and wavelength, a simple inverse equation was not found. Instead, the relationship between absorbing agent concentration and desired μ_a was modeled by a piecewise function for each of the six studied wavelengths (591, 631, 659, 691, 731, and 851 nm). This set of equations, generated by the MATLAB curve-fitting toolbox, was used to create the lookup tables found in the appendix. However, it should be noted that these equations and corresponding

lookup tables, generated from our limited sample size of 16 PDMS-based phantoms (Table 1), should just be used as guidelines. Exact μ_a values cannot be accurately predicted due to our lack of extensive validation testing so optical properties should always be independently validated.

One of the major drawbacks to using alcohol-soluble nigrosin as the absorber was its hydrophilic nature. The alcohol-soluble nigrosin did not mix easily with the silicone base material used to produce PDMS. To account for this, Bisaillon et al. and Bruin et al. both suggest mixing hexane with PDMS (de Bruin *et al.*, 2010; Bisaillon *et al.*, 2008). However, Koschwanez et al. suggested that adding hexane swells the PDMS substrate, and instead mixed tert-butyl alcohol with PDMS (Koschwanez *et al.*, 2009). Using a certain percent tert-butyl alcohol within the PDMS substrate may aid in more efficient mixing of alcohol-soluble nigrosin and should be explored in future studies. If this is to be done, however, new thickness-spin speed curves (see Figure 11) would need to be generated between 100 and 1000 rpm for tert-butyl alcohol infused PDMS (Koschwanez *et al.*, 2009). However, our described procedure accounted for mixing difficulties by thoroughly mixing 1% w/v nigrosin/EtOH in PDMS with a sonicator, vortex mixer, and an ARE-100 conditioning mixer. Another limitation for the phantoms presented here was a characteristic peak in absorption in the 870-930 nm range when using nigrosin-silicone based tissue phantoms (Saager *et al.*, 2010). Because our SFDI analysis only covered a wavelength range up to 851 nm, this phenomenon was not observed. Therefore, for our purposes, the procedure presented here to manipulate μ_a using alcohol-soluble nigrosin is sufficient. Finally, other absorbing agents such as whole blood, inks, dyes, or fluorophores may be investigated either as the single absorber or in combination with each other in the outlined procedure for phantom construction (Saager *et al.*, 2010; Pogue *et al.*, 2006).

3.8.4 Titanium dioxide as a scattering agent

The reduced scattering coefficient (μ'_s) of PDMS phantoms was manipulated by using titanium dioxide (TiO_2) as the scattering agent (Saager *et al.*, 2010). The μ'_s of PDMS phantoms was shown to be dependent on TiO_2 concentration (Figure 12), wavelength (Figure 12), and 1% w/v nigrosin/EtOH concentration (Figure 13). The dependence of μ'_s on scattering agent concentration and wavelength has been demonstrated in previous phantom studies (de Bruin *et al.*, 2010; Saager *et al.*, 2010). Depending on the wavelength, Figure 12 shows that phantoms were produced with reduced scattering coefficients between approximately 1 and 20 cm^{-1}. However, Figure 13 shows that as 1% w/v nigrosin/EtOH concentration increased, μ'_s decreased in phantoms with identical concentrations of TiO_2 (Phantoms #1, 9-15 in Table 1). Furthermore, the decline of μ'_s due to increased concentration of 1% w/v nigrosin/EtOH was greater at lower wavelengths (591 and 621 nm) when compared to higher wavelengths (731 and 851 nm). Furthermore, in Figure 13, once a certain concentration of 1% w/v nigrosin/EtOH was reached (around 7 μL/g), further changes in wavelength and concentration did not affect μ'_s.

The roughly linear relationship between μ'_s and absorbing agent concentration over the tested wavelengths (Figure 13) implies there may exist an empirically determined correction factor that could account for all variables (TiO_2 concentration, wavelength, and 1% w/v nigrosin/EtOH concentration) that affect μ'_s. Thus, given a desired wavelength, μ_a, and μ'_s, the necessary TiO_2 concentration was analytically determined. Therefore, for researchers interested in manipulating μ'_s within PDMS phantoms, the provided lookup tables can predict TiO_2 concentration based on data presented in this paper. Of note, however, in Figure 13, the phenomenon that increasing 1% w/v nigrosin/EtOH concentration reduced μ'_s was only observed in phantoms with minimal TiO_2 concentration (0.001 g TiO_2/g PDMS elastomer base). Further

studies will need to be completed to validate the lookup tables presented here and determine whether this phenomenon is prevalent in phantoms with much higher TiO_2 concentrations, such as 0.007 or 0.008 g TiO_2/g PDMS elastomer base. It should also be noted that the lookup tables assume a linear relationship in μ'_s and TiO_2 concentration beyond the tested limits (0.001 – 0.008 g/g). Further SFDI analysis will be needed to validate these values within the lookup table.

Finally, it is possible to expand this approach by using scattering agents other than TiO_2. Scattering materials such as polystyrene beads, silicon dioxide, aluminum oxide powders or other types of microspheres have been successfully demonstrated by other investigators and could potentially be applied using our spin coater approach (de Bruin *et al.*, 2010; Pogue *et al.*, 2006; Kanick *et al.*, 2012; Passos *et al.*, 2005).

3.8.5 Multi-layered phantoms to simulate heterogeneities

Generally, the purpose of multi-layered phantoms is to introduce geometrical and optical heterogeneities in phantoms to simulate the layered structure of epithelial tissue (de Bruin *et al.*, 2010; Pogue *et al.*, 2006). A multi-layered phantom (Table 2, Phantom #18) with two thin layers (200 µm) was compared to a control phantom (Table 2, Phantom #17) with identical concentrations of optical agents. The μ'_s and μ_a for the two phantoms were compared in Figure 16 and 17. Only slight differences were present between the two phantoms across the six measured wavelengths. Figure 16, comparing μ'_s, shows an average aggregate error of 7.7%. Figure 17, comparing μ_a, shows an average aggregate error 10.9%. We believe these differences were due to random error in dispensing the precise amounts of TiO_2 and 1% w/v nigrosin/EtOH solution rather than being due to air pockets between layers. This assumption was further validated in Figure 18, which compares multi-layered phantoms to human epithelium using an OCT B-scan technique. OCT instrumentation, operating at 1325 nm (outside the wavelength

range of our SFDI equipment), was used for comparative purposes and was not meant to validate optical properties of phantoms. The multi-layered phantom (Figure 18) shows no visible air pockets between adjacent layers. These validations give us good reason to believe that creating PDMS-based multi-layered phantoms using our procedure can serve as appropriate models of various epithelium. In addition to providing evidence for the absence of air pockets, B-scans in Figure 18 were used for visually comparing thicknesses of phantoms to several types of epithelium (Higgins *et al.*, 2014).

The comparative images shown in Figure 18 as well as the data from Figure 11 show that the thickness of individual PDMS layers accurately modeled the thickness of several types of human epithelium (skin from the finger or wrist and oral mucosa). In addition, we believe that the phantom procedure presented here could potentially model the thickness of other epithelial tissue types, such as tongue and gingivae (100-200 μm thick, cervical epithelium (180 μm thick), and esophageal epithelium (250 μm thick) (Harris *et al.*, 1992; Guimarães *et al.*, 2007; Rocha *et al.*, 2010).

3.9 Conclusion

To design these phantoms, lookup tables (Tables 4-9) have been provided to guide researchers in selecting the appropriate concentrations of scattering and absorbing agents (TiO_2 and 1% w/v Nigrosin/EtOH). Thick or thin (between 115 and 880 μm) phantoms can be created by either directly molding uncured PDMS or by using the described spin coating technique. Eq. 3 provides guidance in selecting an appropriate spin speed based on a desired phantom layer thickness. Thick and thin layers can be combined to form multi-layered phantoms to simulate optical heterogeneities seen in tissue (Figure 16-18). In addition, individual thin layers may be used interchangeably to test multiple configurations (Saager *et al.*, 2010). These PDMS-based

tissue-simulating phantoms may be used by researchers as optically stable calibration devices for various optical imaging techniques including, but not limited to, optical coherence tomography (OCT), diffuse optical spectroscopic imaging (DOSI), endoscopy, or microendoscopy (de Bruin *et al.*, 2010; Saager *et al.*, 2010; Cerussi *et al.*, 2012; Pogue *et al.*, 2006; Higgins *et al.*, 2014). Using the provided lookup tables, these phantoms have the potential to mimic the optical properties of common types of epithelium including breast, skin, colon, oral, cervical, and esophagus, among others (Sandell *et al.*, 2011; Harris *et al.*, 1992; Guimarães *et al.*, 2007; Rocha *et al.*, 2010).

A semi-infinite phantom model was used to simulate dysplastic progression in the oral mucosa (Figure 9) (Zhu *et al.*, 2011; Speight, 2007; Warnakulasuriya *et al.*, 2008). Results confirmed that the longer 374 μm SDS was more sensitive to the scattering heterogeneity at superficial layers (Figure 19), where epithelial dysplasia is known to have a profound effect on the scattering properties in such layers (Collier *et al.*, 2003; Clark *et al.*, 2004; Arifler *et al.*, 2003). These experiments demonstrate the potential for monitoring scattering changes associated with early epithelial dysplasia which is often confined above the basement membrane (Warnakulasuriya *et al.*, 2008; Zhu *et al.*, 2011; Speight, 2007; Bouquot *et al.*, 2006).

3.10 Acknowledgements

This material is based on work supported by the National Institutes of Health (1R15CA202662-01), the National Science Foundation Graduate Research Fellowship Program (G.G., DGE-1450079), the Arkansas Biosciences Institute, and the University of Arkansas Doctoral Academy Fellowship. Any opinions, findings, and conclusions or recommendations expressed in this material are those of the authors and do not necessarily reflect the views of the acknowledged funding agencies. I wish to thank Haley James for her contribution to our SPIE

Spotlights eBook discussing phantom design in optical systems. Additionally, I wish to thank Raeff Istfan and Darren Roblyer from Boston University and Laura Higgin and Mark Pierce from Rutgers University for their contributions to this chapter.

3.11 Disclosures

The authors declare that there are no conflicts of interest related to this chapter.

References

Agenant, M., *et al.* "Clinical Superficial Raman Probe Aimed for Epithelial Tumor Detection: Phantom Model Results." *Biomedical Optics Express* 5.4 (2014).

Agrawal, A., *et al.* "Multilayer Thin-Film Phantoms for Axial Contrast Transfer Function Measurement in Optical Coherence Tomography." *Biomed Opt Express* 4.7 (2013): 1166-75.

Alerstam, E., *et al.* "Improved Accuracy in Time-Resolved Diffuse Reflectance Spectroscopy." *Optics Express* 16.14 (2008).

Ansari, M.A., *et al.* "Difuse Optical Tomography: Image Reconstruction and Verification." *Journal of Lasers in Medical Sciences* 5.1 (2014).

Arifler, D., *et al.* "Light Scattering from Normal and Dysplastic Cervical Cells at Different Epithelial Depths: Finite-Difference Time-Domain Modeling with a Perfectly Matched Layer Boundary Condition." *Journal of Biomedical Optics* 8.3 (2003): 484-94.

Avigo, C., *et al.* "Organosilicon Phantom for Photoacoustic Imaging." *Journal of Biomedical Optics* 20.4 (2015).

Fabrication and Characterization of Silicone-Based Tissue Phantoms with Tunable Optical Properties in the Visible and near Infrared Domain. SPIE BiOS. 2008. SPIE. Print.

Bae, Y., *et al.* "Fabrication of a Thin-Layer Solid Optical Tissue Phantom by a Spin-Coating Method: Pilot Study." *J Biomed Opt* 18.2 (2013): 25006.

Baran, T.M., *et al.* "Determination of Optical Properties by Interstitial White Light Spectroscopy Using a Custom Fiber Optic Probe." *Journal of Biomedical Optics* 18.10 (2013).

Baran, T.M., and T.H. Foster. "Recovery of Intrinsic Fluorescence from Single-Point Interstitial Measurements for Quantification of Doxorubicin Concentration." *Lasers in Surgery and Medicine* 45.8 (2013).

Barman, I., *et al.* "Turbidity Corrected Raman Spectroscopy for Blood Analyte Detection." *Analytical Chemistry* 81.11 (2009).

Baxi, J., *et al.* "Retina-Simulating Phantom for Optical Coherence Tomography." *J Biomed Opt* 19.2 (2014): 21106.

Bedard, N., *et al.* "Real-Time Video Mosaicing with a High-Resolution Microendoscope." *Biomedical Optics Express* 3.10 (2012).

Bender, J.E., *et al.* "A Robust Monte Carlo Model for the Extraction of Biological Absorption and Scattering in Vivo." *IEEE Transactions on Biomedical Engineering* 56.4 (2009).

Bi, B., *et al.* "Image Reconstruction for Diffuse Optical Tomography Based on Radiative Transfer Equation." *Computational and Mathematical Methods in Medicine* 2015 (2015).

Bisaillon, C. E., *et al.* "Deformable and Durable Phantoms with Controlled Density of Scatterers." *Phys Med Biol* 53.13 (2008): N237-47.

Bish, S.F., *et al.* "Handheld Diffuse Reflectance Spectral Imaging (Drsi) for in-Vivo Characterization of Skin." *Biomedical Optics Express* 5.2 (2014): 573-86.

Bosschaart, N., *et al.* "Optical Properties of Neonatal Skin Measured in Vivo as a Function of Age and Skin Pigmentation." *Journal of Biomedical Optics* 16.9 (2011).

Bouquot, J.E., *et al.* "Epithelial Dysplasia of the Oral Mucosa—Diagnosticproblems and Prognostic Features." *Current Diagnostic Pathology* 12 (2006): 11-21.

Bremmer, R.H., *et al.* "Non-Contact Spectroscopic Determination of Large Blood Volume Fractions in Turbid Media." *Biomedical Optics Express* 2.2 (2011).

Bremmer, R.H., *et al.* "Diffuse Reflectance Relations Based on Diffusion Dipole Theory for Large Absorption and Reduced Scattering." *Journal of Biomedical Optics* 18.8 (2013).

Bydlon, T.M., *et al.* "Performance Metrics of an Optical Spectral Imaging System for Intra-Operative Assessment of Breast Tumor Margins." *Optics Express* 18.8 (2010).

Campbell, A.P., *et al.* "Flexible Cochlear Microendoscopy in the Gerbil." *Laryngoscope* 120.8 (2010).

Cerussi, A. E., *et al.* "Tissue Phantoms in Multicenter Clinical Trials for Diffuse Optical Technologies." *Biomed Opt Express* 3.5 (2012): 966-71.

Chang, C.Y., *et al.* "Fluorescence Intrinsic Characterization of Excitation-Emission Matrix Using Multi-Dimensional Ensemble Empirical Mode Decomposition." *International Journal of Molecular Sciences* 14.11 (2013).

Chang, R. C., *et al.* "Fabrication and Characterization of a Multilayered Optical Tissue Model with Embedded Scattering Microspheres in Polymeric Materials." *Biomed Opt Express* 3.6 (2012): 1326-39.

Chang, S.S., *et al.* "High Resolution Microendoscopy for Classification of Colorectal Polyps." *Endoscopy* 45.7 (2013): 553-9.

Chang, V.T., *et al.* "Quantitative Physiology of the Precancerous Cervix in Vivo through Optical Spectroscopy." *Neoplasia* 11.4 (2009): 325-32.

Chang, V.T., *et al.* "Towards a Field-Compatible Optical Spectroscopic Device for Cervical Cancer Screning in Resource-Limited Settings: Effects of Calibration and Pressure." *Optics Express* 19.19 (2011).

Chen, S., *et al.* "Recovery of Raman Spectra with Low Signal-to-Noise Ratio Using Wiener Estimation." *Optics Express* 22.10 (2014).

Choi, H.Y., *et al.* "Microlensed Dual-Fiber Probe for Depth-Resolved Fluorescence Measurements." *Optics Express* 19.15 (2011).

Clark, A.L., *et al.* "Detection and Diagnosis of Oral Neoplasia with an Optical Coherence Microscope." *Journal of Biomedical Optics* 9.6 (2004): 1271-80.

Collier, T., *et al.* "Determination of Epithelial Tissue Scattering Coefficient Using Confocal Microscopy." *IEEE Journal of Selected Topics in Quantum Electronics* 9.2 (2003): 307-13.

Croce, A.C., and G. Bottiroli. "Autofluorescence Spectroscopy and Imaging: A Tool for Biomedical Research and Diagnosis." *European Journal of Histochemistry* 58.4 (2014).

Cuccia, D. J., *et al.* "Modulated Imaging: Quantitative Analysis and Tomography of Turbid Media in the Spatial-Frequency Domain." *Opt Lett* 30.11 (2005): 1354-6.

Cuccia, D.J., *et al.* "Quantitation and Mapping of Tissue Optical Properties Using Modulated Imaging." *Journal of Biomedical Optics* 14.2 (2009).

de Bruin, D.M., *et al.* "Optical Phantoms of Varying Geometry Based on Thin Building Blocks with Controlled Optical Properties." *Journal of Biomedical Optics* 15.2 (2010).

Dehghani, H., *et al.* "Numerical Modelling and Image Reconstruction in Diffuse Optical Tomography." *Philosophical Transactions of the Royal Society A* 367 (2009).

Demers, J.H., *et al.* "Multichannel Diffuse Optical Raman Tomography for Bone Characterization in Vivo: A Phantom Study." *Biomedical Optics Express* 3.9 (2012).

Dhar, S., *et al.* "A Diffuse Reflectance Spectral Imaging System for Tumor Margin Assessment Using Custom Annular Photodiode Arrays." *Biomedical Optics Express* 3.12 (2012).

Du Le, V.N., *et al.* "Measurements of Extrinsic Fluorescence in Intralipid and Polystyrene Microspheres." *Biomedical Optics Express* 5.8 (2014).

Esmonde-White, K.A., *et al.* "Fiber-Optic Raman Spectroscopy of Joint Tissues." *Analyst* 136.8 (2011).

Fogli, G., *et al.* "New Eye Phantom for Ophthalmic Surgery." *Journal of Biomedical Optics* 19.6 (2014).

Fu, H.L., *et al.* "A Low-Cost, Portable, and Quantitative Spectral Imaging System for Application to Biological Tissues." *Optics Express* 18.12 (2010): 12630-45.

Gamm, U.A., *et al.* "Extraction of Intrinsic Fluorescence from Single Fiber Fluorescence Measurements on a Turbid Medium: Experimenal Validation." *Biomedical Optics Express* 5.6 (2014).

Gibson, A.P., *et al.* "Recent Advances in Diffuse Optical Imaging." *Physics in Medicine and Biology* 50 (2005).

Glennie, D.L., *et al.* "Inexpensive Diffuse Reflectance Spectroscopy System for Measuring Changes in Tissue Optical Properties." *Journal of Biomedical Optics* 19.10 (2014): 105005.

Gonzalez-Rodriguez, P., and A.D. Kim. "Diffuse Optical Tomography Using the One-Way Radiative Transfer Equation." *Biomedical Optics Express* 6.6 (2015).

Greening, G.J., *et al.* "Characterization of Thin Poly (Dimethylsiloxane)-Based Tissue Simulating Phantoms with Tunable Reduced Scattering and Absorption Coefficients at Visible and Nearinfrared Wavelength." *Journal of Biomedical Optics* 19.11 (2014): 115002.

Greening, G.J., *et al.* Optical Phantoms: Diffuse and Sub-Diffuse Imaging and Spectroscopy Validation. Bellingham, Washington: SPIE Spotlights, 2015.

Gu, M., *et al.* "Cancer-Cell Microsurgury Using Nonlinear Optical Endomicroscopy." *Journal of Biomedical Optics Letters* 15.5 (2010).

Gu, R. Y., *et al.* "Variable-Sized Bar Targets for Characterizing Three-Dimensional Resolution in Oct." *Biomed Opt Express* 3.9 (2012): 2317-25.

Guggenheim, J.A., *et al.* "Multi-Modal Molecular Diffuse Optical Tomography System for Small Animal Imaging." *Measurement Science and Technology* 24.10 (2013).

Guimarães, J.V., *et al.* "Thickness of the Cervical Epithelium of Autopsied Patients with Acquired Immunodeficiency Syndrome." *Annals of Diagnostic Pathology* 11.4 (2007).

Harris, D., and J. R. Robinson. "Drug Delivery Via the Mucous Membranes of the Oral Cavity." *J Pharm Sci* 81.1 (1992): 1-10.

Higgins, L. M., and M. C. Pierce. "Design and Characterization of a Handheld Multimodal Imaging Device for the Assessment of Oral Epithelial Lesions." *J Biomed Opt* 19.8 (2014): 086004.

Kanick, S. C., *et al.* "Scattering Phase Function Spectrum Makes Reflectance Spectrum Measured from Intralipid Phantoms and Tissue Sensitive to the Device Detection Geometry." *Biomed Opt Express* 3.5 (2012): 1086-100.

Kanick, S.C., *et al.* "Dual-Channel Red/Blue Fluorescence Dosimetry with Broadband Reflectance Spectroscopic Correction Measures Protoporphyrin Ix Production During Photodynamic Therapy of Actinic Keratosis." *Journal of Biomedical Optics* 19.7 (2014).

Kanick, S.C., *et al.* "Sub-Diffusive Scattering Parameter Maps Recovered Using Wide-Field High-Frequency Structured Light Imaging." *Biomedical Optics Express* 5.10 (2014): 3376-90.

Keahey, P.A., *et al.* "Optimizing Modulation Frequency for Structured Illumination in a Fiber-Optic Microendoscope to Image Nuclear Morphometry in Columnar Epithelium." *Biomedical Optics Express* 6.3 (2015): 870-80.

Kim, A.D. "Transport Theory for Light Propagation in Biological Tissue." *Journal of the Optical Society of America: Optics, Image Science, and Vision* 21.5 (2004).

Kim, A.D., *et al.* "Estimating Optical Properties in Layered Tissues by Use of the Born Approximation of the Radiative Transport Equation." *Optics Letters* 15.31 (2006).

Kim, A.D., and J.B. Keller. "Light Propagation in Biological Tissue." *Journal of the Optical Society of America: Optics, Image Science, and Vision* 20.1 (2003).

Koschwanez, J.H., *et al.* "Thin Pdms Films Using Long Spin Times or Tert-Butyl Alcohol as a Solvent." *PLOS One* 4.2 (2009).

Koucky, M.H., and M.C. Pierce. "Axial Response of High-Resolution Microendoscopy in Scattering Media." *Biomedical Optics Express* 4.10 (2013).

Kourkoumelis, N., *et al.* "Advances in the in Vivo Raman Spectrosscopy of Malignant Skin Tumors Using Portable Instrumentation." *International Journal of Molecular Sciences* 16 (2015).

Kyrish, M., *et al.* "Needle-Based Fluorescence Endomicroscopy Via Structured Illumination with a Plastic, Achromatic Objective." *Journal of Biomedical Optics* 18.9 (2013).

Lamouche, G., *et al.* "Review of Tissue Simulating Phantoms with Controllable Optical, Mechanical and Structural Properties for Use in Optical Coherence Tomography." *Biomedical Optics Express* 3.6 (2012).

Liemert, A., and A. Kienle. "Explicit Solutions of the Radiative Transport Equation in the P3 Approximation." *Medical Physics* 41.11 (2014).

---. "Light Transport in Three-Dimensional Semi-Infinite Scattering Media." *Journal of the Optical Society of America: Optics, Image Science, and Vision* 29.7 (2012).

Liu, Q., *et al.* "Compact Point-Detection Fluorescence Spectroscopy System for Quantifying Intrinsic Fluorescence Redox Ratio in Brain Cancer Diagnostics." *Journal of Biomedical Optics* 16.3 (2011).

Liu, Q., and N. Ramanujam. "Sequential Estimation of Optical Properties of a Two-Layered Epithelial Tissue Model from Depth-Resolved Ultraviolet-Visible Diffuse Reflectance Spectra." *Appl Opt* 45.19 (2006): 4776-90.

Louie, J.S., *et al.* "Applications and Advancements in the Use of High-Resolution Microendoscopy for Detection of Gastrointestinal Neoplasia." *Clinical Gastroenterology and Hepatology* 12.11 (2014): 1789-92.

Lu, G., and G. Fei. "Medical Hyperspectral Imaging: A Review." *Journal of Biomedical Optics* 19.1 (2014).

Lue, N., *et al.* "Portable Optical Fiber Probe-Based Spectroscopic Scanner for Rapid Cancer Diagnosis: A New Tool for Intraoperative Margin Assessment." *PLOS One* 7.1 (2012).

Maitland, K.C., *et al.* "Single Fiber Confocal Microscope with a Two-Axis Gimbaled Mems Scanner for Cellular Imaging." *Optics Express* 14.19 (2006).

Makhlouf, H., *et al.* "Dual Modality Fluorescence Confocal and Spectral-Domain Optical Coherence Tomography Microendoscope." *Biomedical Optics Express* 2.3 (2011).

Moffitt, T., *et al.* "Preparation and Characterization of Polyurethane Optical Phantoms." *J Biomed Opt* 11.4 (2006): 041103.

Mora, A.D., *et al.* "Towards Next-Generation Time-Domain Diffuse Optics for Extreme Depth Penetration and Sensitivity." *Biomedical Optics Express* 6.5 (2015).

Muldoon, T.J., *et al.* "High-Resolution Imaging in Barrett's Esophagus: A Novel, Low-Cost Endoscopic Microscope." *Gastrointestinal Endoscopy* 68.4 (2008): 737-44.

Muldoon, T.J., *et al.* "Subcellular-Resolution Molecular Imaging within Living Tissue by Fiber Microendoscopy." *Optics Express* 15.25 (2007): 16413-23.

Muldoon, T.J., *et al.* "Noninvasive Imaging of Oral Neoplasia with a High-Resolution Fiber-Optic Microendoscope." *Head & Neck* 34.3 (2011): 305-12.

Nichols, B.S., *et al.* "Performance of a Lookup Table-Based Approach for Measuring Tissue Optical Properties with Diffuse Optical Spectroscopy." *Journal of Biomedical Optics* 17.5 (2012): 057001.

Okagbare, P.I., *et al.* "Development of Non-Invasive Raman Spectroscopy for in-Vivo Evaluation of Bone Graft Osseointegration in a Rat Model." *Analyst* 135.12 (2010).

Okagbare, P.I., and M.D. Morris. "Fluorocarbon Fiber-Optic Raman Probe for Non-Invasive Raman Spectroscopy." *Applied Spectroscopy* 66.6 (2012).

---. "Polymer-Capped Fiber Optic Raman Probe for Non-Invasive Raman Spectroscopy." *Analyst* 137.1 (2012).

Parikh, N., *et al.* "In Vivo Diagnostic Accuracy of High Resolution Microendoscopy in Differentiating Neoplastic from Non-Neoplastic Colorectal Polyps: A Prospective Study." *The American Journal of Gastroenterology* 109.1 (2014): 68-75.

Passos, D., *et al.* "Tissue Phantom for Optical Diagnostics Based on a Suspension of Microspheres with a Fractal Size Distribution." *J Biomed Opt* 10.6 (2005): 064036.

Pickering, J. W., *et al.* "Double-Integrating-Sphere System for Measuring the Optical Properties of Tissue." *Appl Opt* 32.4 (1993): 399-410.

Pierce, M.C., *et al.* "A Pilot Study of Low-Cost, High-Resolution Microendoscopy as a Tool for Identifying Women with Cervical Precancer." *Cancer Prevention Research* 5.11 (2012): 1273-9.

Pierce, M.C., *et al.* "Accuracy of in Vivo Multi-Modal Optical Imaging for Detection of Oral Neoplasia." *Cancer Prevention Research* 5.6 (2012).

Pierce, M.C., *et al.* "High-Resolution Fiber-Optic Microendoscopy for in Situ Cellular Imaging." *Journal of Visualized Experiments* 47 (2011).

Pogue, B.W., and M.S. Patterson. "Review of Tissue Simulating Phantoms for Optical Spectroscopy, Imaging and Dosimetry." *Journal of Biomedical Optics* 11.4 (2006).

Prahl, S. A., *et al.* "Determining the Optical Properties of Turbid Mediaby Using the Adding-Doubling Method." *Appl Opt* 32.4 (1993): 559-68.

Prieto, S.P., *et al.* "Qualitative and Quantitative Comparison of Colonic Microendoscopy Image Features to Histopathology." *Proceedings of SPIE* 9328 (2015).

Puszka, A., *et al.* "Time-Resolved Diffuse Optical Tomography Using Fast-Gated Single-Phton Avalanche Diodes." *Biomedical Optics Express* 4.8 (2013).

Quinn, M.K., *et al.* "High-Resolution Microendoscopy for the Detection of Cervical Neoplasia in Low-Resource Settings." *PLOS One* 7.9 (2012).

Rajaram, N., *et al.* "Design and Validation of a Clinical Instrument for Spectral Diagnosis of Cutaneous Malignancy." *Applied Optics* 49.2 (2010): 142-52.

Rajaram, N., *et al.* "Experimental Validation of the Effects of Microvasculature Pigment Packaging on in Vivo Diffuse Reflectance Spectroscopy." *Lasers in Surgery and Medicine* 42.7 (2010): 680-8.

Rajaram, N., *et al.* "Lookup Table-Based Inverse Model for Determining Optical Properties of Turbid Media." *Journal of Biomedical Optics* 13.5 (2008): 050501.

Rajaram, N., *et al.* "Pilot Clinical Study for Quantitative Spectral Diagnosis of Non-Melanoma Skin Cancer." *Lasers in Surgery and Medicine* 42.10 (2010): 716-27.

Ramanujam, N. "Fluorescence Spectroscopy of Neoplastic and Non-Neoplastic Tissues." *Neoplasia* 2.1-2 (2000).

Reif, R., *et al.* "Analytical Model of Light Reflectance for Extraction of the Optical Properties in Small Volumes of Turbid Media." *Applied Optics* 46.29 (2007).

Rocha, L. , *et al.* "Esophageal Epithelium of Women with Aids: Thickness and Local Immunity." *Pathology - Research and Practice* 206.4 (2010).

Rogers, J.D., *et al.* "Imaging Performance of a Miniature Integrated Microendoscope." *Journal of Biomedical Optics* 13.5 (2008).

Saager, R.B., *et al.* "Multi-Layer Silicone Phantoms for the Evaluation of Quantitative Optical Techniques in Skin Imaging." *Proceedings of SPIE* 7567 (2010).

Saikia, M.J., *et al.* "High-Speed Gpu-Based Fully Three-Dimensional Diffuse Optical Tomographic System." *International Journal of Biomedical Imaging* 2014 (2014).

Salomatina, E., *et al.* "Optical Properties of Normal and Cancerous Human Skin in the Visible and near-Infrared Spectral Range." *Journal of Biomedical Optics* 11.6 (2006).

Sandell, J.L., and T.C. Zhu. "A Review of in-Vivo Optical Properties of Human Tissues and Its Impact on Pdt." *Journal of Biophotonics* 4.11 (2011): 773-87.

Schlicht, M.S., *et al.* "Experimental Foundation for in Vivo Measurement of the Elasticity of the Aorta in Computed Tomography Angiography." *European Journal of Vascular and Endovascular Surgery* 46.4 (2013).

Shahmoon, A., *et al.* "In Vivo Minimally Invasive Interstitial Multi-Functional Microendoscopy." *Scientific Reports* 3 (2013).

Sharikova, A.V., *et al.* "Diffuse Optical Tomography Using Multichannel Robotic Platform for Interstitial Pdt." *Proceedings of SPIE* 8931 (2014).

Sharma, M., *et al.* "Design and Characterization of a Novel Multimodal Fiber-Optic Probe and Spectroscopy System for Skin Cancer Applications." *Review of Scientfic Instruments* 85 (2014): 083101.

Shin, D., *et al.* "Quantitative Analysis of High-Resolution Microendoscopic Images for Diagnosis of Esophageal Squamous Cell Carcinoma." *Clinical Gastroenterology and Hepatology* 13 (2015): 272-79.

Shukla, R., *et al.* "Endoscopic Imaging: How Far Are We from Real-Time Histology?" *World Journal of Gastroenterology* 3.10 (2011): 183-94.

Sokolov, K., *et al.* "Real Time Vital Imaging of Pre-Cancer Using Anti-Egfr Antibodies Conjugated to Gold Nanoparticles." *Cancer Research* 63 (2003).

Speight, P.M. "Update on Oral Epithelial Dysplasia and Progression to Cancer." *Head and Neck Pathology* 1.1 (2007): 61-6.

Srinivasan, S., *et al.* "Image-Guided Raman Spectroscopic Recovery of Canine Cortical Bone Contrast in Situ." *Optics Express* 16.16 (2008).

Stanisavljevic, M., *et al.* "Quantum Dots-Fluorescence Resonance Energy Transfer-Based Nanosensors and Their Application." *Biosensors and Bioelectronics* 74 (2015).

Stone, N., and P. Matousek. "Advanced Transmission Raman Spectroscopy: A Promising Tool for Breast Disease Diagnosis." *Cancer Research* 68.11 (2008).

Subramanian, H., *et al.* "Penetration Depth of Low-Coherence Enhanced Backscattered Light in Subdiffusion Regime." *Physical Review E: Statistical, Nonlinear, and Soft Matter Physics* 75.4 (2007): 041914.

Tabassum, S., *et al.* "Two-Layer Inverse Model for Improved Longitudinal Preclinical Tumor Imaging in the Spatial Frequency Domain." *J Biomed Opt* 23.7 (2018): 1-12.

Tabassum, S., *et al.* "Feasibility of Spatial Frequency Domain Imaging (Sfdi) for Optically Characterizing a Preclinical Oncology Model." *Biomed Opt Express* 7.10 (2016): 4154-70.

Tavakoli, B., and Q. Zhu. "Depth-Correction Algorithm That Improves Optical Quantification of Large Breast Lesions Imaged by Diffuse Optical Tomography." *Journal of Biomedical Optics* 16.5 (2011).

Tseng, T., *et al.* "Quantification of the Optical Properties of Two-Layered Turbid Media by Simultaneously Analyzing the Spectral and Spatial Information of Steady-State Diffuse Reflectance Spectroscopy." *Biomedical Optics Express* 2.4 (2011).

Turzhitsky, V., *et al.* "A Predictive Model of Backscattering at Subdiffusion Length Scales." *Biomedical Optics Express* 1.3 (2010): 1034-46.

Turzhitsky, V., *et al.* "Characterization of Light Transport in Scattering Media at Sub-Diffusion Length Scales with Low-Coherence Enhanced Backscattering." *IEEE Journal of Selected Topics in Quantum Electronics* 16.3 (2010): 619-26.

Valim, N., *et al.* "The Effect of Temporal Impulse Response on Experimental Reduction of Photon Scatter in Time-Resolved Diffuse Optical Tomography." *Physics in Medicine and Biology* 58.2 (2013).

Wang, T., *et al.* "Comparison of Pulsed Photothermal Radiometry, Optical Coherence Tomography and Ultrasound for Melanoma Thickness Measurement in Pdms Tissue Phantoms." *Journal of Biophotonics* 4.5 (2011).

Warnakulasuriya, S., *et al.* "Oral Epithelial Dysplasia Classification Systems: Predictive Value, Utility, Weaknesses and Scope for Improvement." *Journal of Oral Pathology & Medicine* 37.3 (2008): 127-33.

Wilson, R.H., and M.A. Mycek. "Models of Light Propagation in Human Tissue Applied to Cancer Diagnostics." *Technology in Cancer Research and Treatment* 10.2 (2011).

Wu, X., *et al.* "Quantitative Evaluation of Atlas-Based High-Density Diffuse Optical Tomography for Imaging of the Human Visual Cortex." *Biomedical Optics Express* 5.11 (2014).

Xu, R.X., *et al.* "Developing Digital Tissue Phantoms for Hyperspectral Imaging of Ischemic Wounds." *Biomedical Optics Express* 3.6 (2012).

Zhu, C., and Q. Liu. "Validity of the Semi-Infinite Tumor Model in Diffuse Reflectance Spectroscopy for Epithelial Cancer Diagnosis: A Monte Carlo Study " *Optics Express* 19.18 (2011): 17799-812.

Zonios, G., *et al.* "Diffuse Reflectance Spectroscopy of Human Adenomatous Colon Polyps in Vivo." *Applied Optics* 38.31 (1999): 6628-37.

Chapter 4 (Specific Aim 3): Sampling depth of a diffuse reflectance spectroscopy probe for *in vivo* physiologic quantification of murine subcutaneous tumor allografts

4.1 Introduction

Diffuse reflectance spectroscopy (DRS) is a non-invasive, spectral biopsy technique that is used to indirectly estimate tissue optical properties and differentiate tissue types (Valdés *et al.*, 2017; Baltussen *et al.*, 2017). The fundamental tissue optical properties are reduced scattering coefficient (μ_s') and absorption coefficient (μ_a) (Novikova, 2017). The μ_s' morphologically depends on the size, density, and orientation of scattering particles in tissue, such as the cell membrane, cell nuclei, mitochondria, lysosomes, and collagen fibers, among others (Sandell *et al.*, 2011; Arifler *et al.*, 2007). In amelanotic tissues, the μ_a in the visible and near infrared spectral range functionally depends on total hemoglobin concentration and tissue oxygen saturation (Novikova, 2017). Changes in these fundamental optical properties have been shown to occur in neoplastic and cancerous tissue because of angiogenesis, degradation of stromal collagen, and altered morphology of epithelial cells (Arifler *et al.*, 2007; Arifler *et al.*, 2003; Lister *et al.*, 2012). Therefore, DRS has shown promise for early cancer diagnostics, tracking tissue response to therapy, and in intraoperative surgical guidance (Yu *et al.*, 2014; Valdés *et al.*, 2017; Baltussen *et al.*, 2017; Spliethoff *et al.*, 2016; Spliethoff *et al.*, 2014; Lin *et al.*, 2000; Hu *et al.*, 2016).

Spliethoff et al. used DRS to track changes in optical parameters over time in a mouse xenograft model of hereditary breast cancer in response to cisplatin chemotherapy. They showed that treated tumors had increased StO_2 compared to non-treated tumors, and concluded that DRS provided valuable functional tissue information that correlated well with tumor treatment

response (Spliethoff *et al.*, 2014). This group also evaluated their fiber-optic needle-based DRS system on human lung cancer patients undergoing a diagnostic image-guided transthoracic needle biopsy procedure, and concluded that spectroscopic guidance enabled more accurate needle positioning for lung biopsies (Spliethoff *et al.*, 2016). DRS has also been clinically applied to neurosurgery, in which Lin et al. performed DRS measurements on *in vitro* brain tumors and developed a discrimination algorithm, primarily based on scattering from white matter, with a sensitivity and specificity of 96% and 93%, respectively (Lin *et al.*, 2000). Recently, Hu et al. used DRS to measure tissue hypoxia in a subcutaneous mouse xenograft model of human pharynx squamous cell carcinoma treated with radiation and found that higher doses of radiation yielded a quicker increase in tumor oxygenation (Hu *et al.*, 2016).

DRS probes vary greatly in terms physical geometry and sampling depth depending on the tissue-of-interest. Physical geometry can differ in terms of probe length, probe tip diameter, number and type of integrated optical fibers, and degree of invasiveness. For example, most DRS probes contact the tissue surface and are considered non-invasive but contact probes have limited sampling depth. Some groups have overcome this sampling depth limitation by creating minimally invasive, fiber-optic needle-based DRS systems (Spliethoff *et al.*, 2014). However, these systems sacrifice non-invasiveness and may induce bleeding at the tip of the needle, potentially affecting accuracy when quantifying total hemoglobin content. In non-invasive, contact-based DRS systems, sampling depth depends on source-detector separation (SDS), or the distance between the optical fibers delivering and collecting light. In general, as SDS increases, sampling depth increases-due to the increased overall path length travel of the remitted photons at a cost of progressively decreasing signal-to-noise ratio (Kanick *et al.*, 2009; Hennessy *et al.*, 2014; Hennessy *et al.*, 2013). Thus, sampling depth can be fine-tuned to collect light primarily

from specific tissue layers, such as epithelial, stromal, or subcutaneous tumor layers. Therefore, a relationship between raw diffuse reflectance, μ_s', μ_a, and sampling depth must be established for each SDS channel.

Specifically, DRS can be used in subcutaneous murine tumors, which are used for a variety of research purposes including investigating the effects of potential therapies (He, Tian, Li, *et al.*, 2015). The central research question in this paper is: How can a DRS probe be optimally designed for evaluating tissue physiological parameters in subcutaneous murine tumors? At present, there have been no studies simultaneously quantifying wavelength- and SDS-dependent sampling depth in DRS probes with multiple channels to sample murine subcutaneous tumor allografts. The present study fills this knowledge gap by elaborating on methods to quantify wavelength-dependent sampling depth and demonstrating our capability to quantify physiologically-relevant parameters such as total hemoglobin concentration (THC) and tissue oxygen saturation (StO_2), in subcutaneous murine tumors models. Experimental methods presented here are scalable for a variety of application-specific constraints, such as using small SDSs for endoscopically-deployable probes within the sub-diffuse regime, where the diffuse approximation is limited (Kanick *et al.*, 2014).

A DRS probe was designed to interrogate subcutaneous murine tumors at increasing sampling depths and quantify the associated optical properties. The relationship between diffuse reflectance, μ_s', μ_a, and SDS was experimentally established by measuring a set of tissue-simulating calibration phantoms to create lookup tables (LUTs). Then, the LUT was used as an inverse model to fit measured spectral data and extract optical properties (Greening, James, *et al.*, 2016; Greening, James, Powless, *et al.*, 2015; Greening, Rajaram, *et al.*, 2016). DRS data at each SDS represents a weighted average of physiological parameters collected at increasing

depths. Therefore, a one-layer inverse experimental model was chosen to quantity volume-averaged, rather than layer-specific, physiological parameters without assuming precise thickness of overlying skin layers (Sharma *et al.*, 2013). The accuracy of the probe in extracting optical properties was determined using a second set of hemoglobin-based tissue-simulating phantoms. Following this, the relationship between sampling depth, μ_s', μ_a, and SDS was experimentally established by detecting an embedded, highly-absorbing, optical heterogeneity within tissue-simulating phantoms at incremental distances. Finally, the DRS technique was applied to a Balb/c murine allograft model of CT26 colon carcinoma as a model for subcutaneous mouse tumors. The μ_s', μ_a, THC, StO_2, and sampling depths were compared for normal and tumor tissue. The central hypothesis was that this probe would simultaneously sample the overlying epithelial skin layer as well as the subcutaneous Balb/c-CT26 tumor and accurately extract physiologically-relevant optical parameters from each.

4.2 Materials and methods

4.2.1 Instrumentation

The DRS probe (FiberTech Optica, Kitchener, ON, Canada) consists of a brass ferrule tip 6.35 mm in diameter and 50 mm in length (Figure 1). Five multimode optical fibers (NA = 0.22 ± 0.02, high-OH for wavelength range 190-1200 nm) are arranged in a slit line along the tip of the brass ferrule, with one fiber serving as the source fiber and the remaining four fibers serving as the detector fibers. SDSs are 0.75, 2.00, 3.00, and 4.00 mm. These optical fibers were included to sample into the subcutaneous murine tumor at increasing sampling depths The source fiber, as well as the 2.00, 3.00, and 4.00 SDS fibers (FiberTech Optica, SUV400/440PI) consist of a 400/440 μm ± 2% silica core/cladding with a 470 μm ± 5% polyimide jacket. The 0.75 mm SDS fiber (FiberTech Optica, SUV200/220PI) consists of a 200/220 μm ± 2% silica

core/cladding with a 245 μm ± 5% polyimide jacket.

The total length of the DRS probe is 1.00 m. The distal (common) end of the probe, is 0.67 m long, and fibers are secured within a 4.8 mm outer diameter black PVC coating monocoil. The proximal (legs) end of the probe is 0.33 m in length, and each individual fiber is secured within a 3.0 mm outer diameter black PVC monocoil terminating in Subminiature version A (SMA) connectors, reinforced with strain relief, to be attached to the lamp or spectrometers.

A 20W tungsten-halogen lamp (Ocean Optics, HL-2000-HP) provided broadband light (360-2400 nm) to the 400-μm core source fiber. One spectrometer (Ocean Optics, USB2000+VIS-NIR-ES) with a Sony ILX511B 2048-element linear silicon CCD array collected diffusely reflected light from the 0.75 and 2.00 mm SDSs. A second spectrometer (Ocean Optics, FLAME-S) with a Sony ILX511B 2048-element linear silicon CCD array collected diffusely reflected light from the 3.00 and 4.00 mm SDSs. The spectral resolution of the system (Eq. 1) was calculated by

$$R_{spectral}(nm) = \left[\frac{Range_{spectral}(nm)}{Elements_{pixel}(pixels)}\right] \times R_{pixel}(pixels) \quad (1)$$

where $R_{spectral}$ is the spectral resolution in nm, $Range_{spectral}$ is the spectral range which equaled 667 nm based on each spectrometer having a grating of 600 lines/nm, $Elements_{pixel}$ is the number of pixel elements which equaled 2048, and R_{pixel} is the pixel resolution which equaled 6.5 pixels based on a 50 μm diameter laser cut slit within the round SMA connector (Ocean Optics, INTSMA-KIT). This resulted in a spectral resolution of 2.1 nm. No binning was performed.

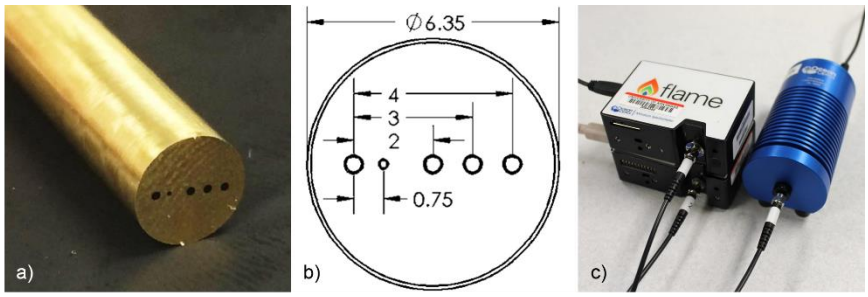

Figure 1. The diffuse reflectance spectroscopy probe showing (a) distal optics, (b) dimenstions of the optical fibers within the probe tip, and (c) proximal optics showing several legs of the DRS probe, spectrometers and lamp.

4.2.2 Animal model

The study was approved by the University of Arkansas Institutional Animal Care and Use Committee (IACUC #18060). CT26 (ATCC®, CRL-2638™), a murine colon carcinoma cell line derived from the Balb/c mouse strain, was maintained in Roswell Park Memorial Institute (RPMI)-1640 medium (ATCC®, 30-2001™) supplemented with 10% fetal bovine serum (ATCC®, 30-2020), 1% antibiotic antimycotic solution (Sigma-Aldrich, A5955-100ML), and 0.2% amphotericin B/gentamicin (Thermo Fisher Scientific, R015010). Third passage (P3) CT26 cells were used throughout the study (Castle *et al.*, 2014).

Ten female Balb/c mice were (strain: 000651, The Jackson Laboratory, ME, USA) aged nine weeks were housed in groups of three in three cages in the Small Animal Facility at the University of Arkansas. The facility was maintained at 23°C ± 1°C and 40-60% humidity on a 12:12 hour light-dark cycle. Food (8640, Teklad) and water was provided *ad libitum*. All nine mice acclimated for seven days after arrival prior to the study start. After one week of acclimation, the left flanks of the 10-week old Balb/c mice were shaved, and Nair was applied for one minute to locally remove hair. Then, $1x10^5$ CT26 cells in sterile saline were injected subcutaneously into the left flank (Zhang *et al.*, 2013; Tongu *et al.*, 2015; Malvicini *et al.*, 2011).

Tumor allografts grew until they reached a volume of 200 mm^3, after which the tumor underwent DRS measurements.

4.2.3 Tumor allograft geometry

After performing DRS measurements of Balb/c-CT26 tumor allografts at a volume of 200 ± 50 mm^3, mice were euthanized via cervical dislocation under 4.0% isoflurane and 1 L/min oxygen. Tumors were dissected, placed in OCT and flash frozen in isopentane in liquid nitrogen, and stored at -80°C for up to one week. Tumors cut into 6-μm sections using a cryostat (Leica Biosystems CM1860) and stained with hematoxylin (VWR 100504-404) and eosin (VWR 10143-130) (H&E). H&E-stained tissue sections were imaged with a microscope (Nikon Eclipse Ci) with a 4X/0.25 NA objective and field-of-view (FOV) of 2.9 x 2.2 mm. Tumors often exceeded this FOV (i.e. a perfectly spherical tumor at a volume of 200 mm^3 would have a diameter of ~7.4 mm). Therefore, images were taken of the entire tumor cross section and stitched together using a commercial panoramic image stitching software (Microsoft, Image Composite Editor) (Figure 2). Thickness of the epidermis, dermis/hypodermis, and fascia were calculated from H&E images calibrated to a 1951 USAF resolution test target (Thorlabs, R1DS1P). All nine CT26 tumors were measured to determine average and standard deviation. Calculating tissue thickness overlying the subcutaneous tumor was important to determine which layers were sampled by each SDS of the DRS probe (Figure 2).

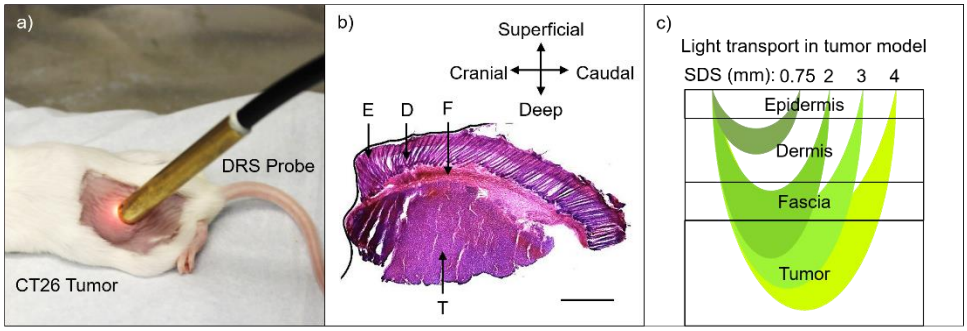

Figure 2. The subcutanous Balb/c-CT26 colon tumor allograft showing (a) the DRS probe in contact with the tumor (b) an H&E-stained transverse section of tumor with overlying tissue layers (scale bar = 1 mm, E=epidermis, D=dermis, F=fascia, T=tumor), and (c) a representation of light transport through the murine subcutaneous tumor allograft at each of the four SDSs (0.75, 2.00, 3.00, and 4.00)

4.2.4 Optical phantoms

To establish a relationship between optical properties, diffuse reflectance, and sampling depth in the LUT model, liquid calibration phantoms were generated with known μ_s' and μ_a. Calibration phantoms were constructed using distilled water as the solvent. The scattering agent was 1.00 µm-diameter polystyrene microspheres (07310-15, Polysciences, USA) and the associated μ_s' was calculated using Mie theory. The absorbing agent was teal India ink (11BY, Salis International, USA). The μ_a was calculated by measuring a diluted solution of teal India ink in distilled water using a spectrophotometer (5102-00, PerkinElmer, USA) and the Beer-Lambert Law (Greening, James, *et al.*, 2016; Greening, Rajaram, *et al.*, 2016; Greening, James and Muldoon, 2015; Greening, James, Powless, *et al.*, 2015).

A 5 x 3 (15 total) set of calibration phantoms was created, corresponding to five scattering ranges and three absorbing ranges (Figure 3). Five of the 15 phantoms were considered "scattering-only" and contained only polystyrene microspheres without India ink. Distilled water and polystyrene microspheres were mixed inside 7 mL scintillation vials (66022-300, VWR, USA) to yield a μ_s' of 2.7, 3.8, 5.4, 7.6, and 10.9 cm^{-1} at a reference of 630 nm to span a μ_s' range of 2-15 cm^{-1} from 450-900 nm. The remaining ten calibration phantoms

contained both polystyrene spheres and teal India Ink. Five of the 12 phantoms had a peak μ_a of 3.0 cm^{-1} at 632 cm^{-1} and the final five phantoms had a peak μ_a of 10 cm^{-1} at 632 cm^{-1}. Thus, calibration phantoms spanned a μ_s' range of 2-15 cm^{-1} and a μ_a range of 0-10 cm^{-1} from 450-900 nm. These ranges span the optical property range of interest for subcutaneous Balb/c-CT26 tumor allografts (Sabino *et al.*, 2016; Spliethoff *et al.*, 2014; Honda *et al.*, 2011).

To validate the relationship between optical properties and diffuse reflectance in the LUT model, liquid validation phantoms were generated with known μ_s' and μ_a. Using these validation phantoms, accuracy of the LUT model could be established by comparing known μ_s' and μ_a (expected values) to the μ_s' and μ_a generated by the LUT model (experimental). Validation phantoms were constructed similar to calibration phantoms, but used bovine hemoglobin (H2625, Sigma-Aldrich, USA) as the absorbing agent. Bovine hemoglobin was used to better simulate biological tissue absorption.

A 3 x 3 (9 total) set of validation phantoms was created, corresponding to three scattering ranges and three absorbing ranges (Figure 3). Polystyrene microspheres were added such that phantoms yielded a μ_s' of 5.2, 8.5, and 13.5 cm^{-1} at a reference of 630 nm to span a μ_s' range of 4-19 cm^{-1} from 450-900 nm. Bovine hemoglobin was added such that phantoms yielded a μ_a of 0-1.8 cm^{-1}, 0-3.6 cm^{-1}, and 0-8.1 cm^{-1}, respectively.

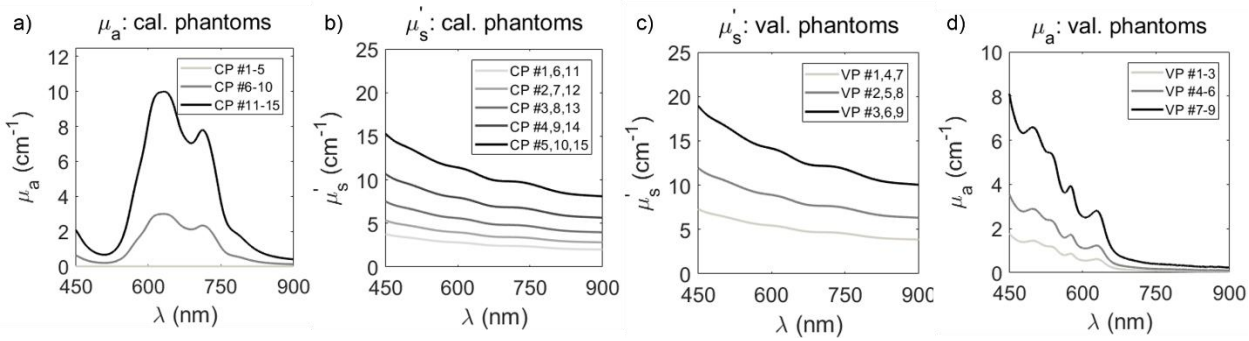

Figure 3. Calibration phantoms were made with distilled water, polystyrene microspheres, and teal India ink to span μ_s' and μ_a ranges between (a) 2-15 cm^{-1} and (b) 0-10 cm^{-1}, respectively, while validation phantoms were made with distilled water, polystyrene microspheres, and bovine hemoglobin to span μ_s' and μ_a ranges between (c) 4-19 cm^{-1} and (d) 0-8 cm^{-1}, respectively.

4.2.5 Lookup tables for diffuse reflectance

The DRS probe was placed in each liquid calibration phantom, so it was completely submerged at 2 cm from the bottom of the 7 mL scintillation vial. Broadband DRS data (450-900 nm) were recorded at each SDS (0.75, 2.00, 3.00, and 4.00 mm) with integration times of 100, 200, 300, and 400 ms, respectively, to yield a signal-to-noise ratio (SNR) of at least 15 dB. Five spectra were averaged for all measurements. Spectra were converted to absolute diffuse reflectance values (Sharma *et al.*, 2013) by calibrating with a Spectralon® 20% diffuse reflectance standard (SRS-20-010, Labsphere, USA), which accounts for the spectral shape and daily intensity fluctuations of the halogen lamp. Diffuse reflectance calibration (Eq. 2) was calculated by

$$R(\lambda) = \frac{I_{sample}(\lambda) - I_{background}(\lambda)}{\left[I_{std}(\lambda) - I_{background}(\lambda)\right] \times 100/R_{std}} \quad (2)$$

where $R(\lambda)$ is absolute diffuse reflectance, $I_{sample}(\lambda)$ is the intensity of the raw, uncorrected spectra from phantoms or tissue, $I_{background}(\lambda)$ is the inherent background noise (spectra collected without excitation from the light source), $I_{std}(\lambda)$ is the spectral intensity of the

Spectralon® 20% diffuse reflectance standard, and $100/R_{std}$ accounts for the reflectance level (20%) of the Spectralon® diffuse reflectance standard. All intensity measurements per SDS were acquired with equal integration time.

LUTs were generated for each SDS by plotting absolute diffuse reflectance (R) against μ_s' and μ_a and then interpolating between raw data points to create a smooth mesh for μ_s' between 4-12 cm^{-1} and μ_a between 0-8 cm^{-1} (Figure 4). This optical property range accounts for all expected μ_s' and μ_a in murine tissue in the wavelength range of interest (450-900 nm) (Sabino *et al.*, 2016).

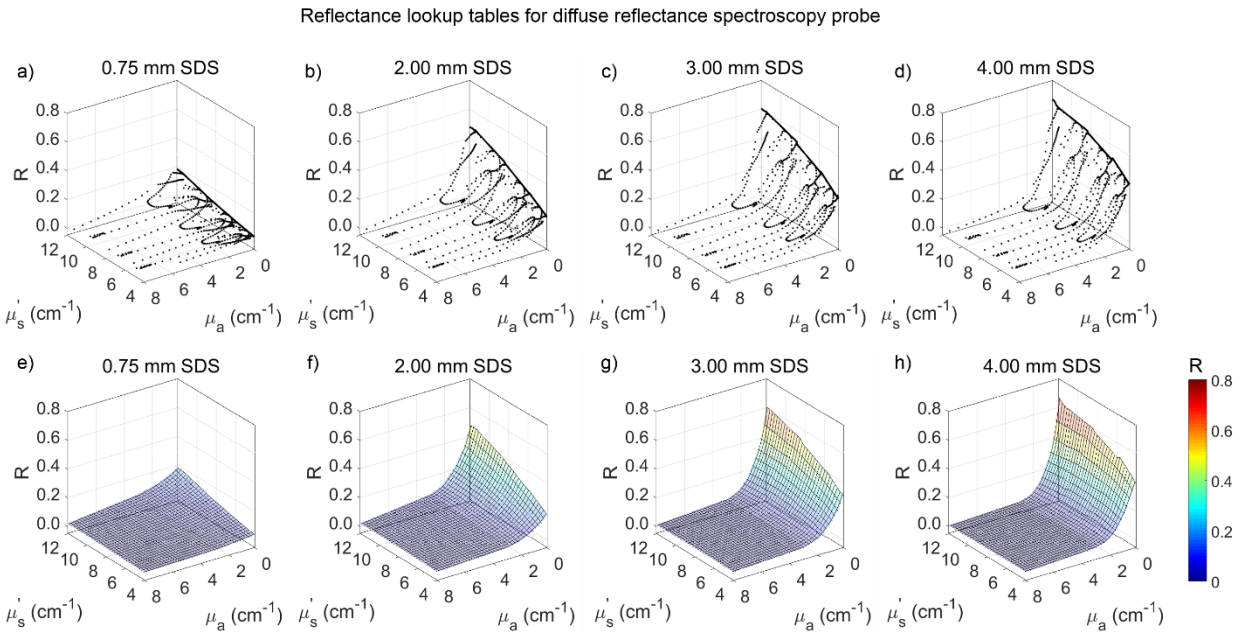

Figure 4. (a-d) LUTs were created for each SDS (0.75, 2.00, 3.00, and 4.00 mm) using diffuse reflectance spectra from calibration phantoms which were then (e-h) interpolated to create a continuous mesh for μ_s' values between 4-12 cm^{-1} and μ_a values between 0-8 cm^{-1}.

4.2.6 Validation of lookup table inverse model

Once LUTs were constructed (Figure 4), the accuracy of the LUTs needed to be quantified. In other words, for a single spectrum, how closely do the experimental optical properties (determined by the LUT model) match the expected optical properties?

The DRS probe was placed in each liquid bovine Hb-based validation phantom, so it was completely submerged 2 cm from the bottom of the 7 mL scintillation vial. Broadband DRS data (450-900 nm) were recorded at each SDS (0.75, 2.00, 3.00, and 4.00 mm) with integration times of 100, 200, 300, and 400 ms, respectively, to yield an SNR of at least 15 dB. Five spectra were averaged for all measurements. Spectra were converted to absolute diffuse reflectance values by calibrating with a Spectralon® 20% diffuse reflectance standard and background noise subtraction as previously described.

Experimental μ_s' and μ_a were calculated using the damped least-squares nonlinear fitting method, appropriate for least squares curve fitting. This method will be henceforth referred to as the LUT inverse model fit and was based on the constraining equation for μ_s' (Eq. 3) and μ_a (Eq. 4). The constraining equation for μ_s' is

$$\mu_s'(\lambda) = \mu_s'(\lambda_0) \times \left[\frac{\lambda}{\lambda_o}\right]^{-B} \quad (3)$$

where $\mu_s'(\lambda)$ is the reduced scattering coefficient, $\mu_s'(\lambda_0)$ is the reduced scattering coefficient at a reference of 630 nm, λ is all wavelengths, λ_0 is 630 nm, and B is the scattering exponent, which relates to the size of tissue scatterers; smaller values of B correspond to larger scatterer sizes (Greening, James, *et al.*, 2016; Zonios *et al.*, 2008). Zonios et al. describes an in-depth method to calculate spherical scatterer diameter based on B, which can range between 0.2 and 4.0 in tissue (Zonios *et al.*, 2008). On the other hand, the constraining equation for μ_a is

$$\mu_a(\lambda) = C \times \mu_{a,stock}(\lambda) \quad (4)$$

where $\mu_a(\lambda)$ is the absorption coefficient, $\mu_{a,\,stock}(\lambda)$ is the absorption coefficient of the bovine-Hb stock solution, and C is the volume fraction of bovine-Hb stock solution in the phantom. The μ_a of the bovine-Hb stock solution was determined via a spectrophotometer and the Beer-Lambert Law. These constraining equations required initial and boundary conditions, listed in Table 1.

Bounds for μ_s' at 630 nm were set based on the μ_s' limits of the calibration phantoms used to create the LUTs. Bounds for B were set to exceed values commonly observed (~0.9-1.2) in tissue (Semeniak, 2017). Bounds for C were set to be the minimum and maximum values for volume fraction (Greening *et al.*, 2018). Initial conditions did not affect outcomes as long as they were between the lower and upper bounds. Initial and boundary conditions were constant for all validation phantoms and for all SDSs.

Table 1. Boundary conditions for quantifying optical properties of validation phantoms

Variable	Lower Bound	Upper Bound
μ_s' (λ_0)	2.0 cm^{-1}	15.0 cm^{-1}
B	0.0	4.0
C	0.0%	100%

After initial conditions were set, the LUT inverse model fit performed up to $1x10^4$ iterations until the sum of squares (χ^2) was minimized (Sharma *et al.*, 2013) between the fitted reflectance and measured reflectance. All phantom DRS spectra underwent a final quality control step. If χ^2 was greater than 5%, data was discarded (Figure 5).

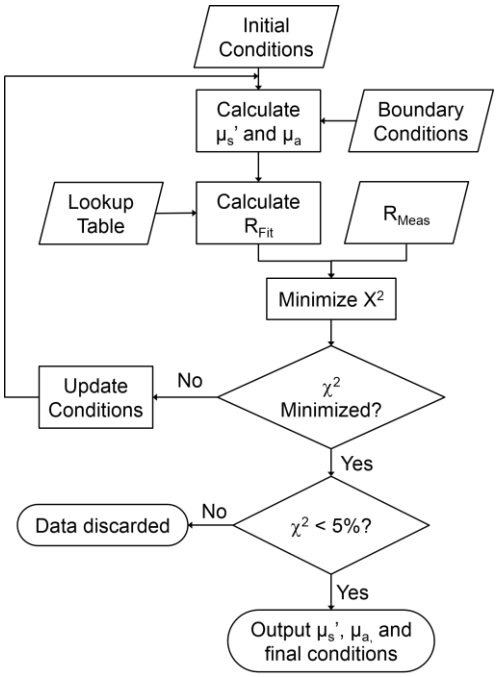

Figure 5. The LUT inverse model of diffuse reflectance fit is based on the damped least-squares nonlinear fitting method, with the goal of outputting μ_s' and μ_a, as well as contributing parameters from the constraining equations such as scattering exponent and absorber concentration.

Percent errors for μ_s' and μ_a were calculated by comparing the expected optical properties derived from Mie Theory and the Beer-Lambert Law to experimental optical properties derived from the LUT inverse model fit. Average percent error was then calculated by averaging the percent error at each wavelength (450-900 nm) for each validation phantom (9 phantoms). Percent errors were always positive values; thus, overestimating and underestimating optical properties produced positive errors that did not cancel out. The LUT was considered accurate when average percent errors for μ_s' and μ_a were each less than 10%, a standard cutoff across literature (Vishwanath *et al.*, 2011; Yu *et al.*, 2008; Yu *et al.*, 2010; Bish *et al.*, 2011; Greening, James, *et al.*, 2016; Greening, Rajaram, *et al.*, 2016).

4.2.7 Optical properties from Balb/c-CT26 tumor allografts

After validation of the LUTs, spectra were collected from Balb/c-CT26 tumor allografts

200 ± 50 mm^3 in diameter (n=9), as well as immediately adjacent tissue from the same mouse. Mice were not anesthetized during data collection. The DRS probe was placed in direct contact with the tissue. Broadband DRS data (450-900 nm) were recorded at each SDS (0.75, 2.00, 3.00, and 4.00 mm) with integration times of 100, 200, 300, and 400 ms, respectively, to yield an SNR of at least 15 dB. Five spectra were averaged for all measurements. Spectra were converted to absolute diffuse reflectance values by calibrating with a Spectralon® 20% diffuse reflectance standard and background noise subtraction as previously described.

The optical properties were quantified in a similar manner to validation phantoms, using the LUT inverse model fit based on the damped least-squares nonlinear fitting method (Nichols *et al.*, 2012). Quantifying *in vivo* μ_s' relied on the same constraining equation as validation phantoms (Eq. 3). Next, assuming hemoglobin as the only *in vivo* absorber from 450-900 nm, the constraining equation (Eq. 5) for μ_a was expressed as

$$\mu_{a,i}(\lambda) = THC \times \left[\alpha\varepsilon_{HbO_2}(\lambda) + (1-\alpha)\varepsilon_{Hb}(\lambda)\right] \quad (5)$$

where, $\mu_{a,i}$ is the initial tissue absorption coefficient, *THC* is the total hemoglobin concentration in tissue, α is the tissue oxygen saturation (StO_2), and $\varepsilon_{HbO_2}(\lambda)$ and $\varepsilon_{Hb}(\lambda)$ are the extinction coefficients of oxyhemoglobin and deoxyhemoglobin, respectively. Next, the final version of the constraining equation for μ_a (Eq. 6) incorporated the standard pigment-packaging correction factor, described in depth by Rajaram et al. (Rajaram, Gopal, *et al.*, 2010). The corrected absorption equation is expressed as

$$\mu_{a,f}(\lambda) = \mu_{a,i}(\lambda) \times \left[\frac{1 - e^{-2\cdot\mu_{a,bl}(\lambda)\cdot r_{vess}}}{2\cdot\mu_{a,bl}(\lambda)\cdot r_{vess}}\right] \quad (6)$$

where $\mu_{a,f}$ is the final tissue absorption coefficient, $\mu_{a,i}$ is the initial absorption coefficient, $\mu_{a,bl}$ is the absorption coefficient of whole blood assuming a hemoglobin concentration of 150 mg/mL, and r_{vess} is the average blood vessel radius in the sampled tissue. Including the pigment-

packaging correction factor accounts for hemoglobin in tissue being confined to blood vessels, which is a small fraction of the total volume sampled by light. This phenomenon differs from the homogenous tissue-simulating phantoms. However, like the homogenous tissue-simulating phantoms, the constraining equations for in vivo measurements of Balb/c-CT26 allografts required initial and boundary conditions, listed in Table 2. Bounds for μ_s' at 630 nm were set based on the μ_s' limits of the calibration phantoms used to create the LUTs. Bounds for B were set to exceed values commonly observed (~0.9-1.2) in tissue *(Semeniak, 2017)*. Bounds for THC were set such that the maximum could not exceed the hemoglobin concentration found in whole blood (150 mg/mL). Bounds for StO_2 were set such that the maximum could not exceed the StO_2 found in fully oxygenated tissue (100%). For r_{vess}, average capillary radius is approximately 2.5 μm *(Potter et al., 1983)*, whereas average arteriole radius is approximately 10-15 μm *(Burrows et al., 1981)*. Bounds for r_{vess} were set to significantly exceed these averages. Initial conditions (Figure 5) did not affect outcomes as long as they were between the lower and upper bounds. Initial and boundary conditions were constant for all in vivo measurements and for all SDSs.

Table 2. Boundary conditions for quantifying optical properties of Balb/c-CT26 tissue

Variable	Lower Bound	Upper Bound
μ_s' (λ_0)	2.0 cm^{-1}	15.0 cm^{-1}
B	0.0	4.0
THC	0 mg/mL	150 mg/mL
StO_2	0.0%	100%
r_{vess}	0 μm	100 μm

After initial conditions were set, the LUT inverse model fit performed up to $1x10^4$ iterations until the sum of squares (χ^2) was minimized between the fitted reflectance and measured reflectance. Using the constraining equations for in vivo tissue, μ_s' at 630 nm, THC, and StO_2 were quantified as a function of tissue type (normal vs. tumor) and SDS. Optical properties were compared between normal and tumor tissue for each SDS. The significance

threshold was set at 0.05. All in vivo DRS spectra underwent a final quality control step. If χ^2 was greater than 5%, data was discarded (Figure 5). Artifacts due to mouse movement during data collection could potentially cause a high χ^2 between the fitted reflectance and measured reflectance. Significance of optical properties between tissue type (healthy and tumor) and SDS (0.75, 2.00, 3.00, 4.00) was determined using two-way mixed ANOVA. The significance level was set at 0.05.

4.2.8 Sampling depth of DRS probe into tissue

The next goal was to quantify sampling depth for each SDS as a function of μ_s' and μ_a. In other words, once μ_s' and μ_a have been quantified via the LUT inverse model, at what depth into tissue are these optical properties being measured?

To quantify sampling depth, a 5 x 3 (15 total) set of calibration phantoms were constructed (Greening, James, *et al.*, 2016). Each of these phantoms was placed into a 5 mL beaker (Figure 6) with a highly absorbing ($\mu_a > 100$ cm^{-1}) black phantom layer, made with (poly)-dimethylsiloxane (PDMS) and black India ink at the bottom. It was assumed that any photon contacting this layer would be attenuated. The μ_a of the black layer was calculated using a spectrophotometer and the Beer-Lambert Law. Additionally, the black layer contained no scattering agent. Contributions from specular reflection at the interface between the black layer and calibration phantoms were negligible (data not shown) since there is a minimal mismatch between the PDMS and liquid phantoms (Greening, James, *et al.*, 2016; Hennessy *et al.*, 2014).

The probe was placed in direct contact with the black layer (Figure 6(a-d)). Using a mechanical translation stage equipped with a micrometer scale (LNR25M, Thorlabs, USA), the probe was raised from the black layer in 50 μm increments from 0 to 3 mm. DRS measurements, from 450-900 nm, were taken at each 50 μm step at each SDS of 0.75, 2.00, 3.00, and 4.00 mm

at integration times of 100, 200, 300, and 400 ms, respectively, to yield an SNR of at least 15 dB. Since the optical properties of the calibration phantoms were known, a relationship was established between μ_s', μ_a, and reflectance at various sampling depths. As the probe increased in distance from the black layer, reflectance increased, then leveled (Figure 6(e)). At each wavelength, the probe was most sensitive to changes in optical properties when 50% of photons reached the black layer (Figure 6(f)). When this process was repeated at each wavelength, a relationship between sampling depth and wavelength was established (Figure 6 (g)). Therefore, sampling depth(λ) was defined at the most sensitive 50-μm increment.

Three-dimensional plots were generated for each SDS by plotting sampling depth (D) against μ_s' and μ_a and then interpolating between raw data points to create a smooth mesh for μ_s' between 4-12 cm^{-1} and μ_a between 0-8 cm^{-1}. This optical property range accounts for all expected μ_s' and μ_a in murine tissue in the wavelength range of interest (450-900 nm). Once optical properties were calculated using the LUT inverse model, sampling depth was quantified. Significance of sampling depth between tissue type (healthy and tumor) and SDS (0.75, 2.00, 3.00, 4.00) was determined using two-way mixed ANOVA. The significance level was set at 0.05.

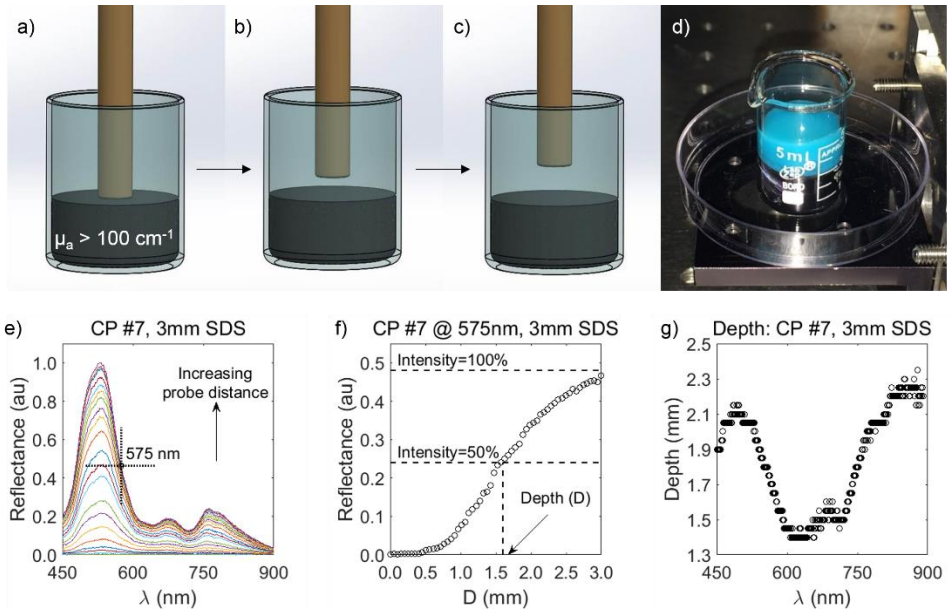

Figure 6. Sampling depth was quantified by (a-d) taking DRS measurements of calibration phantoms at 50 μm increments between 0-3 mm from a highly absorbing (μ_a > 100 cm^{-1}) phantom layer. (e) Reflectance (R) increased as distance between the probe and black layer increased, shown for calibration phantom #7 at the 3.00 mm SDS as an example. (f) Sampling depth (D) was defined when the SDS is most sensitive to the black layer, which occurs when 50% of photons reach the black layer. (g) Sampling depth (D) was then quantified at the 50 μm increment at each wavelength.

4.3 Results

4.3.1 Tumor allograft geometry by tissue type

Tumors were dissected, cut into 6 μm sections, and H&E stained. Three primary tissue types were visualized above the subcutaneous tumor (Figure 7): the epidermis, dermis/hypodermis, and fascia. In female Balb/c-CT26 tumor allografts (n=9), the epidermis was 0.22 ± 0.05 mm thick, the base of the dermis was 0.71 ± 0.11 mm from the surface, and the base of the fascia was 1.00 ± 0.15 mm from the surface.

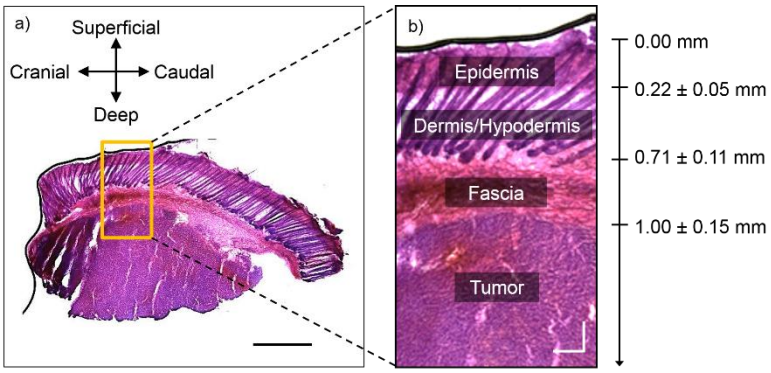

Figure 7. To acquire optical properties from the subcutaneous tumor, broadband light from the DRS probe needed to penetrate past the fascia, located 1.00 ± 0.15 mm from the surface. Values are mean ± SD. (scale bar = 1 mm)

4.3.2 Validation of lookup table inverse model

The reflectance from each validation phantom at each SDS, with known μ_s' and μ_a, was plotted against the LUT created from the calibration phantoms (Figure 8). Percent errors were acceptable if less than 10% for both μ_s' and μ_a.

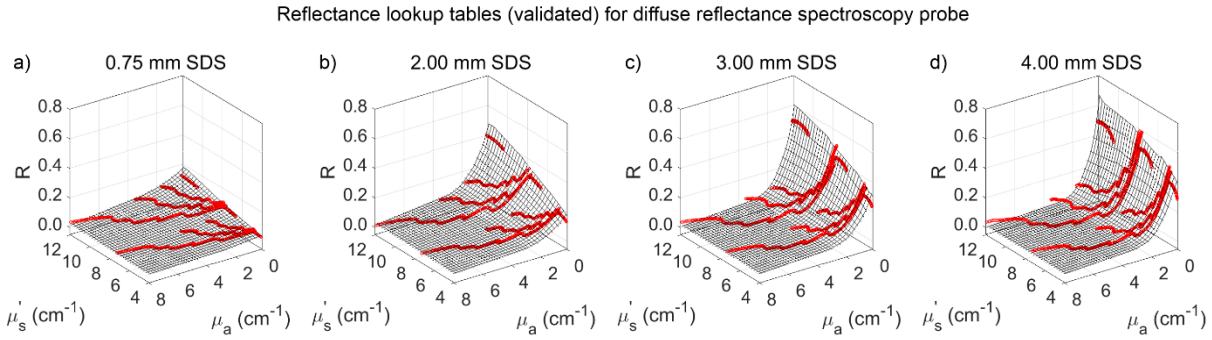

Figure 8. Reflectance from bovine Hb-based validation phantoms (red) was plotted against the LUTs (grayscale grid) for each SDS of a) 0.75 mm, b) 2.00 mm, c) 3.00 mm, and d) 4.00 mm.

Average percent errors for μ_s' were 2.9%, 4.7%, 2.2%, and 2.8% for the 0.75, 2.00, 3.00, and 4.00 mm SDSs, respectively. Average percent errors for μ_a were 9.1%, 9.6%, 9.6%, and 9.2% for the 0.75, 2.00, 3.00, and 4.00 mm SDSs, respectively. Thus, all percent errors were below 10% (Figure 9).

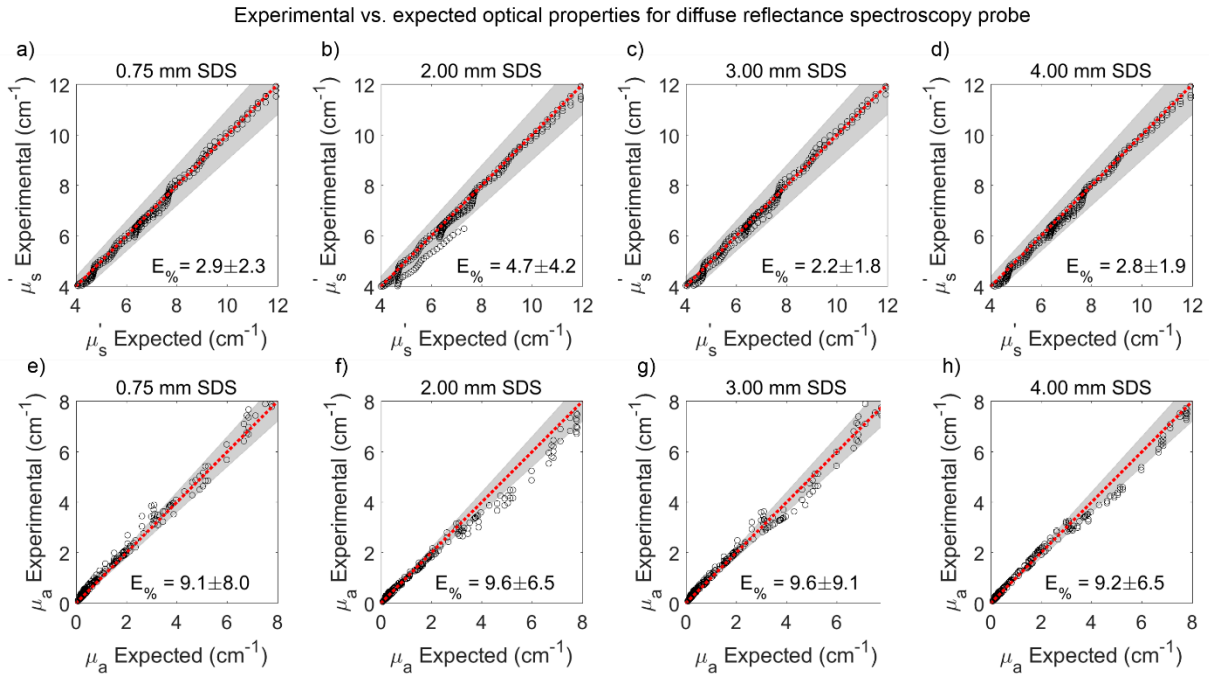

Figure 9. Percent errors for comparing experimental optical properties (from LUT inverse model fit) and expected (known) optical properties were below 10% for all SDS of (a,e) 0.75 mm, (b,f) 2.00 mm, (c,g) 3.00 mm, and (d,h) 4.00 mm. The LUT inverse model fit more accurately extracted (a-d) μ_s' (percent errors < 5%) compared to (e-h) μ_a. Black dots represent raw data. Red lines indicate a perfect fit with 0% error. Gray background represents the acceptable 10% error.

4.3.3 Sampling depth in Balb/c-CT26 allografts

Following DRS measurements of calibration phantoms overlying a highly absorbing PDMS layer, three-dimensional plots were generated for each SDS by plotting sampling depth (D) against μ_s' and μ_a and then interpolating between raw data points to create a smooth mesh. Sampling depths were valid for μ_s' between 4-12 cm^{-1} and μ_a between 0-8 cm^{-1} (Figure 10). Lowest sampling depth occurred at highest optical properties (μ_s' = 12 cm^{-1}, μ_a = 8 cm^{-1}) and highest sampling depth occurred at lowest optical properties (μ_s' = 4 cm^{-1}, μ_a = 0 cm^{-1}). Based on this, sampling depths ranged between 0.37 to 1.10 mm, 0.72 to 1.76 mm, 0.92 to 2.08 mm, and 1.16 to 2.25 mm for the 0.75, 2.00, 3.00, and 4.00 mm SDSs, respectively, indicating sampling depth increased as SDS increased. Subcutaneous tumors were located 1.00 ± 0.15 mm or deeper

below the skin surface; thus, broadband light from the DRS probe needed to penetrate at least 1.15 mm into tissue to sample tumor optical properties. With regards to the colormap in Figure 10, red coloring indicates sampling depth ≤ 1.15 mm, which was the average thickness, plus one standard deviation, of the overlying skin and fascia of the subcutaneous Balb/c-CT26 tumor. Yellow coloring indicates sampling depth between 1.15 and 1.45 mm, with peak yellow occurring at 1.30 mm, which was the average thickness, plus two standard deviations. Green coloring indicates sampling depth ≥ 1.45 mm, which was the average thickness plus three standard deviations. Thus, yellow and green coloring represent optical properties in which tumor tissue was sampled.

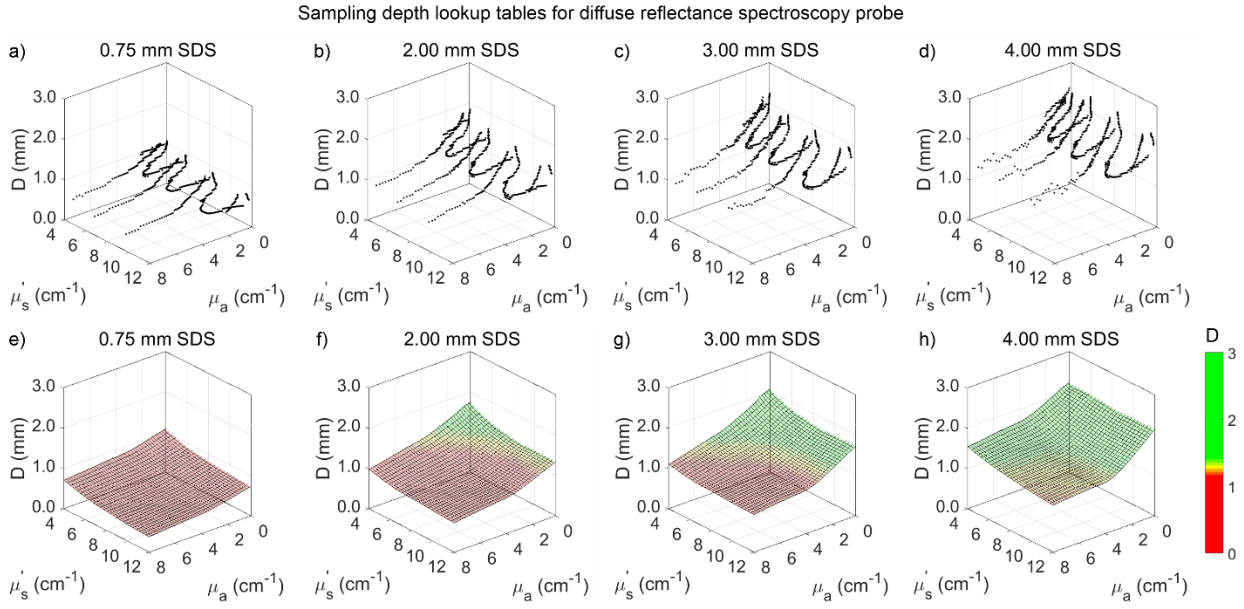

Figure 10. Raw sampling depth data (a-d) was plotted for each SDS and then (e-h) interpolated into a mesh. Sampling depth increased as SDS increased.

4.3.4 Balb/c-CT26 allograft wavelength-dependent optical properties

Next, DRS measurements were collected from Balb/c-CT26 tumor allografts (n=9) 200 ± 50 mm^3 in diameter, as well as immediately adjacent normal flank tissue from the same mouse. The LUT inverse model fit analyzed the spectra to output $\mu_s'(\lambda)$ and $\mu_a(\lambda)$ (Figure 11). Based on

the relationship between μ_s', μ_a, and sampling depth (Figure 10), sampling depth was quantified as a function of wavelength. In general, as SDS increased, $\mu_s'(\lambda)$ decreased, $\mu_a(\lambda)$ increased, and sampling depth increased for both normal and tumor tissue.

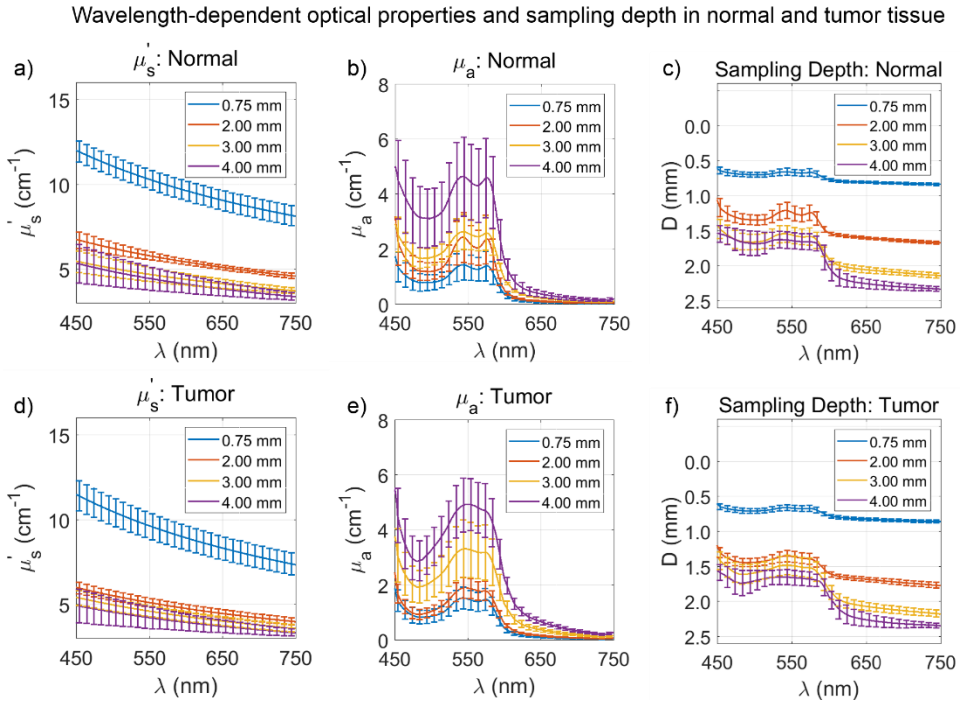

Figure 11. Average optical properties and sampling depth for (a-c) normal Balb/c flank tissue and (d-f) subcutaneous Balb/c-CT26 tumor allografts showing (a, d) μ_s', (b, e) μ_a, and (c, f) sampling depth. As SDS increased, μ_s' decreased, μ_a increased, and sampling depth increased for both tissue types. Values are mean ± SD.

4.3.5 Balb/c-Ct26 allograft DRS-derived physiological parameters

After comparing wavelength-dependent optical properties as a function of SDS, key physiological optical parameters were extracted and compared for normal and tumor tissue (Figure 12).

The μ_s' at 630 nm decreased as SDS increased (Figure 12(a)), as observed in Figure 11. For the 0.75, 3.00, and 4.00 mm SDSs, differences in μ_s' were insignificant between normal and tumor tissue. In the 2.00 mm SDS, μ_s' was significantly lower in tumor tissue ($p=0.02$) compared

to normal tissue, but only by 0.49 cm^{-1}.

The THC, measured in mg/mL, increased as SDS increased (Figure 12(b)). This was also indicated by the observed increased $\mu_a(\lambda)$ magnitude observed in Figure 11. For the 0.75, 2.00, and 4.00 mm SDSs, differences in THC were insignificant between normal and tumor tissue. In the 3.00 mm SDS, THC was significantly lower in normal tissue ($p=0.03$) compared to tumor tissue, but only by 0.64 mg/mL. The THC rose from approximately 1.4 mg/mL in the 0.75 mm SDS to approximately 6.8 mg/mL in the 4.00 mm SDS for both tissue types.

The StO_2 remained constant as SDS increased in normal tissue (Figure 12(c)). However, StO_2 decreased as SDS increased in tumor tissue, indicating increasing hypoxia at increased depths within the tumor microenvironment. The StO_2 quantified by the short 0.75 mm SDS was significantly higher ($p<0.01$) than the StO_2 quantified by all longer SDSs. Furthermore, there was no significant difference in StO_2 between normal and tumor tissue in the 0.75 mm SDS. However, tumor tissue expressed significantly decreased StO_2 compared to normal tissue for SDSs of 2.00, 3.00, and 4.00 mm.

In Figure 12(d), sampling depth was quantified at the first Q-band of hemoglobin at 542 nm, where the lowest sampling depth would occur. In normal tissue, sampling depth was 0.66±0.04, 1.22±0.11, 1.55±0.12, and 1.64±0.12 mm at 542 nm for the 0.75, 2.00, 3.00, and 4.00 mm SDSs, respectively. In tumor tissue, sampling depth was 0.66±0.03, 1.30±0.09, 1.49±0.14, and 1.65±0.05 mm at 542 nm for the 0.75, 2.00, 3.00, and 4.00 mm SDSs, respectively. There was no significant difference ($p > 0.05$) comparing sampling depth in normal vs. tumor tissue. For both normal and tumor tissue, sampling depth increased significantly ($p<0.01$) at longer SDSs of 2.00, 3.00, and 4.00 mm compared to the shorter 0.75 mm SDS.

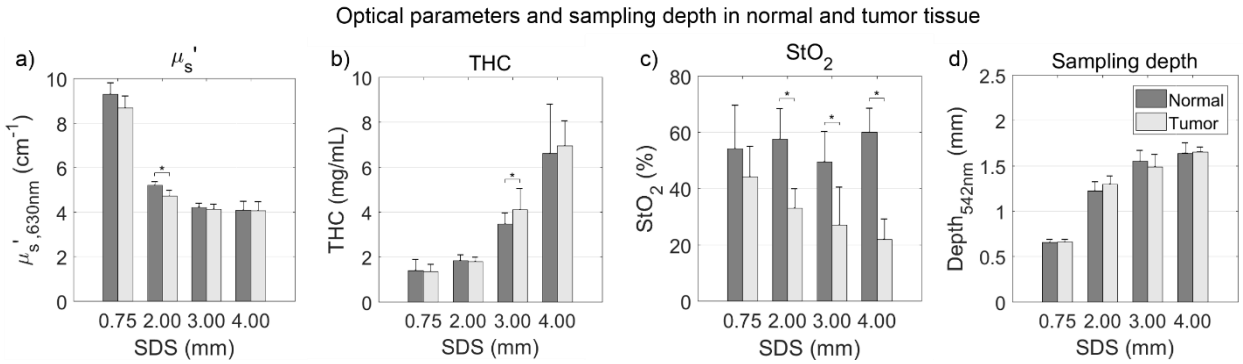

Figure 12. Average (a) μ_s' at 630 nm, (b) THC, (c), StO_2, and (d) sampling depth for normal (dark gray) and tumor (light gray) tissue. The μ_s' was comparable between normal and tumor tissue and decreased as SDS increased. The THC was comparable between normal and tumor tissue and increased as SDS increased. The StO_2 in tumor tissue was significantly decreased compared to normal tissue for SDSs longer than 0.75 mm. Additionally, StO_2 decreased as SDS decreased. The sampling depth was comparable between normal and tumor tissue and increased as SDS increased. Values are mean ± SD. Significance is indicated by *($p<0.05$).

4.4 Discussion

A diffuse reflectance spectroscopy (DRS) probe was designed to acquire optical properties of subcutaneous murine tumor allografts and was applied specifically in Balb/c-CT26 colon tumor allografts. In this paper, a complete validation of the DRS probe in this context was presented. Raw data from DRS is reflectance intensity as a function of wavelength. This paper explicitly describes a method to post-process raw spectra into the associated optical properties, μ_s' and μ_a, physiological perfusion parameters including THC and StO_2, and sampling depth (Hennessy *et al.*, 2014; Rajaram *et al.*, 2008). The central hypothesis was that this DRS probe would simultaneously sample the overlying epithelial skin layer as well as the subcutaneous tumor allograft by including multiple discrete source-detector separations (SDSs) and extract optical parameters from increasing depths (He, Tian and He, 2015; Hennessy *et al.*, 2014). DRS data at each SDS represents a weighted average of physiological parameters collected from increasing sampling depths. In the female Balb/c-CT26 colon tumor allograft model, the skin,

consisting of the epidermis, dermis, and hypodermis was 0.71 ± 0.11 mm thick, and the underlying fascia resulted in 1.00 ± 0.15 mm of total tissue above the underlying subcutaneous tumor. These values are expected to vary based on mouse strain, subcutaneous tumor location, sex, and age, and should be independently confirmed by investigators performing similar studies (Azzi *et al.*, 2005; Calabro *et al.*, 2011; Sabino *et al.*, 2016). Thus, the DRS probe needed to sufficiently sample beyond the 1.00 mm skin layer and into the subcutaneous tumor.

A lookup-table (LUT)-based inverse model, an established method, was chosen as the method to relate diffuse reflectance with μ_s' and μ_a (Rajaram *et al.*, 2008; Greening, James, Powless, *et al.*, 2015; Greening, James, *et al.*, 2016; Nichols *et al.*, 2012). Other methods exist to perform this task such as Monte Carlo-based simulations (Hennessy *et al.*, 2014; Hennessy *et al.*, 2013; Zhong *et al.*, 2014), but the LUT-based inverse model was chosen because it is based on experimental values that necessarily account for our specific system response (Nichols *et al.*, 2012). To generate a LUT, a set of calibration phantoms with known optical properties was used. As of the current report, the LUTs for each SDS are valid for μ_s' between 4-12 cm^{-1} at 630 nm and for μ_a between 0-8 cm^{-1}. This optical property range effectively encompasses expected optical properties found in murine skin and subcutaneous tumors between 450-900 nm (Sabino *et al.*, 2016). This wavelength range was chosen because of the absorption properties of hemoglobin, with specific absorption peaks (Q-bands) at 542 and 576 nm that indicate THC and StO_2 and negligible absorption ($\mu_a < 0.5$ cm^{-1} for both oxygenated and deoxygenated hemoglobin in whole blood) between 600-900 nm (Prahl, 2015). Therefore, reflectance in the 600-900 nm wavelength range necessarily indicates μ_s' (Sharma *et al.*, 2013). It is common in literature to report μ_s' at a reference of 630 nm, so this convention was used here (Sharma *et al.*, 2013; Rajaram, Aramil, *et al.*, 2010; Rajaram, Gopal, *et al.*, 2010; Hennessy *et al.*, 2015).

Since the LUTs were generated with dye-based calibration phantoms, a set of bovine hemoglobin-based phantoms, which more closely simulate physiological conditions, with known optical properties was used to validate the LUTs (Greening, James, *et al.*, 2016). Within the LUT optical property range, it was shown that average percent errors for extracting μ_s' and μ_a were below 10% for all SDSs, indicating it is reasonable to assume that measured tissue optical properties and physiological perfusion metrics are accurate within 10%. Average percent errors below 10% are considered acceptable and are comparable to many other DRS studies (Vishwanath *et al.*, 2011; Yu *et al.*, 2008; Yu *et al.*, 2010; Bish *et al.*, 2011). However, it was not uncommon for percent errors in several experimental optical property observations to exceed 10% (Figure 9). Despite this, there was no relationship between percent error and magnitude of μ_s' and μ_a, indicating that while some *in vivo* measurements of murine tissue may indeed exceed 10%, on average the percent errors will be within 10% regardless of magnitude of μ_s' and μ_a. Additionally, percent errors did not significantly change with respect to SDS. Since SDS is related to sampling depth (Hennessy *et al.*, 2014), this indicates that measuring optical properties of deeper tumor tissue was no less accurate than measuring optical properties of shallower skin tissue. It should be noted that average percent errors for extracting μ_a were greater (~9%) compared to extracting μ_s' (~3%), a common observation in existing literature (Rajaram, Aramil, *et al.*, 2010). Finally, since LUT validation was performed with bovine hemoglobin-based phantoms, it was extraneous to perform additional validation via Monte Carlo simulations.

Once the relationship between diffuse reflectance, μ_s' and μ_a was established and validated, the same set of calibration phantoms was used to establish a relationship between sampling depth, μ_s' and μ_a. As of the current report, the sampling depth relationship for each SDS are valid for μ_s' between 4-12 cm^{-1} at 630 nm and for μ_a between 0-8 cm^{-1}. We employed a

method to quantify sampling depth similar to that pioneered by Hennessey et al. (Hennessy *et al.*, 2014), in which sampling depth as a function of wavelength was quantified based on the depth at which the SDS was most sensitive to an optical heterogeneity (Figure 6). It is important to note that, even at lower and higher depths, the probe was still sensitive to the optical heterogeneity (Figure 6(f)), similar to other studies (Hennessy *et al.*, 2014). This shows that stating the probe has a single sampling depth at specific optical properties is an oversimplification. Instead, the depth sampled by our DRS probe represents a wide range, a phenomenon described explicitly by Kanick et al. (Kanick *et al.*, 2009). However, for simplicity, we report sampling depth as a single value at which the SDS was most sensitive to the heterogeneity. Figure 10 shows that sampling depth increased with increasing SDS, and decreased with increasing μ_s' and μ_a, as expected (Hennessy *et al.*, 2014; Kanick *et al.*, 2009).

There was a decrease in sampling depth at the Soret band (< 500 nm) and Q-bands (542 and 576 nm) of hemoglobin. It is these peaks that most heavily influence extracted THC and StO_2 in the LUT inverse model. Thus, even though sampling depth is higher at longer wavelengths, we explicitly report sampling depth at the first Q-band of hemoglobin, where sampling depth is lowest in our wavelength range (450-900 nm). From Figure 12(d), we can conclude that the 0.75 mm SDS only samples the skin layer since its sampling depth was 0.66±0.04 mm and 0.66±0.03 mm for normal and tumor tissue, respectively, shallower than the 1.00 ± 0.15 mm normal tissue above the subcutaneous tumor. Further evidence for the 0.75 mm SDS sampling only the overlying skin layer is shown from Figure 12(a-c), in which there were insignificant differences between normal vs. tumor tissue with respect to μ_s', THC, and StO_2. The tumor begins to be sampled at the 2.00, 3.00, and 4.00 mm SDSs, indicated by the sampling depths at the first Q-band to be 1.30±0.09, 1.49±0.14, and 1.65±0.05 mm, respectively. As such,

since the subcutaneous tumor is relatively hypoxic (Shay *et al.*, 2014), there was a significant difference in StO_2 between normal and tumor tissue at these sampling depths (Figure 12(c)). Furthermore, in tumor tissue, StO_2 decreased steadily from 44±11% to 22±7% as SDS increased. It is important to note that the observed decreasing StO_2 with increasing sampling depth does not necessarily indicate the tumor was more hypoxic at increased depths but is most likely due to more overall tumor tissue contributing to the volume-averaged physiological parameters. It is common for DRS-derived StO_2 of keratinized epithelia, such as the skin, to be much less than 100% (Spliethoff *et al.*, 2014). DRS studies reporting in non-keratinized epithelia tend to extract much higher StO_2 values upwards of 95% (Greening, James, *et al.*, 2016). Additionally, the StO_2 presented in this study does not necessarily correlate to arterial oxygen saturation, which would be more accurately measured using pulse oximetry (Bashkatov *et al.*, 2014). Interestingly, μ_s' and THC were mostly comparable between normal and tumor tissue, indicating StO_2 may be a key physiological parameter to evaluate murine tissue health via DRS, a sentiment held by other research groups (Spliethoff *et al.*, 2014; Spliethoff *et al.*, 2016; Sircan-Kucuksayan *et al.*, 2015).

Figures 11 and 12 show that increasing sampling depth resulted in decreased μ_s' and increased μ_a in both normal and tumor tissue. In the skin, scattering from the epidermis (0 to 0.22 mm) is primarily caused by keratin, a filamentous protein, as well as cell nuclei and lipid membranes. In the dermis and hypodermis, (0.22 to 0.71 mm) scattering is primarily caused by collagen, which accounts for approximately 25% of the dermal volume, other cellular constituents (Lister *et al.*, 2012; Arifler *et al.*, 2007; Arifler *et al.*, 2003), and lipids confined to adipocytes in the hypodermis. In the superficial fascia (0.71 to 1.00 mm), an areolar connective tissue (Arifler *et al.*, 2007; Kumka *et al.*, 2012), scattering is primarily caused by collagenous, elastic, and reticular fibers. Finally, scattering in the CT26 cell layer (an epithelial cell type) is

caused by cellular constituents. Measurements in similar tissue in literature have suggested that epithelial tumors have lower light scattering (Collier *et al.*, 2003) compared to skin, whose scattering properties are dominated by the dermis (Lister *et al.*, 2012), although a direct comparison of μ_s' between subcutaneous CT26 allografts and skin has not been exclusively studied. The μ_s' presented here were comparable to other studies (Sabino *et al.*, 2016). On the other hand, increased μ_a, associated with increased THC, increased with sampling depth. The epidermis contains no blood vessels, which are situated in deeper dermal layers (Sabino *et al.*, 2016). In Balb/c mice, which are albino, hemoglobin is the only significant absorber. It is important to note that the observed increasing THC with increasing sampling depth does not necessarily indicate higher THC in the tumor but is most likely due to reduced contribution of the epidermis to the volume-averaged optical properties of the subcutaneous tumor model. The μ_a and THC presented here were comparable to other studies (Lister *et al.*, 2012; Rajaram, Reichenberg, *et al.*, 2010; Bremmer *et al.*, 2011; Sabino *et al.*, 2016).

This work has several limitations. First, contact-based, non-invasive DRS cannot sample into the center of a subcutaneous tumor 200 ± 50 mm^3 in diameter. Sampling into the tumor center may be difficult even for small tumors, since even at the 4.00 mm SDS, sampling depth only reached 1.65±0.05 mm Therefore, considering the spatial heterogeneity of the tumor microenvironment (Yuan, 2016), DRS may not provide representative data for the entire tumor. Spliethoff et al. overcame this limitation by using a minimally-invasive biopsy needle with integrated optical fibers for intratumoral DRS measurements in subcutaneous murine xenografts (Spliethoff *et al.*, 2014). Secondly, extracted optical properties are volume-averaged, meaning that fine spatial resolution of μ_s' and μ_a is lost (Kanick *et al.*, 2009; Saager *et al.*, 2011). Moreover, even at long SDSs designed to sample deeper into the subcutaneous tumor allograft,

extracted optical properties are a volume-averaged measurement of both tumor and skin. To overcome this limitation, the 0.75 mm SDS was integrated into the DRS probe design to simultaneously and exclusively sample overlying skin. This way, fluctuations in optical properties and physiological parameters over time could be attributed to either changes in the tumor itself, or changes in the skin, and assumptions could be limited. Saager et al. mitigated this volume-average limitation by implementing a depth-resolved quantification based on a two-layer Monte Carlo model (Saager *et al.*, 2011). Additionally, due to the thin nature of skin, we expect overall optical contributions on tumor physiological parameters to be relatively small (Muldoon *et al.*, 2012). Finally, future work must correlate DRS-derived perfusion metrics with immunohistochemical analysis. For example, pimonidazole is a dye that stains for hypoxia (Aguilera *et al.*, 2014), and can be used to correlate end-point hypoxic fraction of tumor sections with *in-vivo* StO_2 measurements via DRS.

4.5 Conclusion

Diffuse reflectance spectroscopy is a non-invasive spectral biopsy tool that has shown promise in early cancer diagnostics, tracking tissue response to therapy, and in intraoperative surgical guidance. This paper provides an outline for a general method for quantifying tissue optical properties, as well as physiologically relevant perfusion parameters, such as hemoglobin concentration and tissue oxygen saturation, that can be used by investigators hoping to implement diffuse reflectance spectroscopy for cancer research. Experimental methods presented here are scalable for smaller probe sizes (within the sub-diffuse regime) for endoscopically-deployable spectroscopy probes, where the diffuse approximation is limited.

4.6 Acknowledgements

This material is based on work supported by the National Institutes of Health (1R15CA202662-01), the National Science Foundation Graduate Research Fellowship Program (G.G., DGE-1450079), the Arkansas Biosciences Institute, and the University of Arkansas Doctoral Academy Fellowship. Any opinions, findings, and conclusions or recommendations expressed in this material are those of the authors and do not necessarily reflect the views of the acknowledged funding agencies. I wish to thank Ariel Mundo for his valuable insight into this project, Dr. Narasimhan Rajaram for his guidance in experimental design, and of course Dr. Timothy Muldoon for his mentorship.

4.7 Disclosures

The authors declare that there are no conflicts of interest related to this chapter.

References

Aguilera, K.Y., and R.A. Brekken. "Hypoxia Studies with Pimonidazole in Vivo." *Bio-protocol* 4.19 (2014).

Arifler, D., *et al.* "Light Scattering from Normal and Dysplastic Cervical Cells at Different Epithelial Depths: Finite-Difference Time-Domain Modeling with a Perfectly Matched Layer Boundary Condition." *Journal of Biomedical Optics* 8.3 (2003): 484-94.

Arifler, D., *et al.* "Light Scattering from Collagen Fiber Networks: Micro-Optical Properties of Normal and Neoplastic Stroma." *Biophysical Journal* 92.9 (2007): 3260-74.

---. "Light Scattering from Collagen Fiber Networks: Micro-Optical Properties of Normal and Neoplastic Stroma." *Biophysical Journal* 92 (2007): 3260-74.

Azzi, L., *et al.* "Gender Differences in Mouse Skin Morphology and Specific Effects of Sex Steroids and Dehydroepiandrosterone." *Journal of Investigative Dermatology* 124.1 (2005): 22-7.

Baltussen, E.J.M., *et al.* "Diffuse Reflectance Spectroscopy as a Tool for Real-Time Tissue Assessment During Colorectal Cancer Surgery." *Journal of Biomedical Optics* 22.10 (2017): 1-6.

Bashkatov, A.N., *et al.* "Optical Properties of Human Colon Tissues in the 350 – 2500 Nm Spectral Range." *Quantum Electronics* 44.8 (2014): 779-84.

Bish, S.F., *et al.* "Development of a Noncontact Diffuse Optical Spectroscopy Probe for Measuring Tissue Optical Properties." *Journal of Biomedical Optics* 16.12 (2011): 120505.

Bremmer, R.H., *et al.* "Non-Contact Spectroscopic Determination of Large Blood Volume Fractions in Turbid Media." *Biomedical Optics Express* 2.2 (2011).

Burrows, M. E., and P. C. Johnson. "Diameter, Wall Tension, and Flow in Mesenteric Arterioles During Autoregulation." *Am J Physiol* 241.6 (1981): H829-37.

Calabro, K., *et al.* "Gender Variations in the Optical Properties of Skin in Murine Animal Models." *Journal of Biomedical Optics* 16.1 (2011).

Castle, J. C., *et al.* "Immunomic, Genomic and Transcriptomic Characterization of Ct26 Colorectal Carcinoma." *BMC Genomics* 15.1 (2014).

Collier, T., *et al.* "Determination of Epithelial Tissue Scattering Coefficient Using Confocal Microscopy." *IEEE Journal of Selected Topics in Quantum Electronics* 9.2 (2003): 307-13.

Greening, G.J., *et al.* "Towards Monitoring Dysplastic Progression in the Oral Cavity Using a Hybrid Fiber-Bundle Imaging and Spectroscopy Probe." *Scientific Reports* 6.26734 (2016).

Greening, G.J., *et al.* Optical Phantoms: Diffuse and Sub-Diffuse Imaging and Spectroscopy Validation. Bellingham, Washington: SPIE Spotlights, 2015.

Greening, G.J., *et al.* "Fiber-Bundle Microendoscopy with Sub-Diffuse Reflectance Spectroscopy and Intensity Mapping for Multimodal Optical Biopsy of Stratified Epithelium." *Biomedical Optics Express* 6.12 (2015): 4934-50.

Greening, G.J., *et al.* "In Vivo Measurement of Non-Keratinized Squamous Epithelium Using a Spectroscopic Microendoscope with Multiple Source-Detector Separations." *Proceedings of SPIE* 9715 (2016).

Greening, Gage J., *et al.* "Effects of Isoflurane Anesthesia on Physiological Parameters in Murine Subcutaneous Tumor Allografts Measured Via Diffuse Reflectance Spectroscopy." *Biomedical Optics Express* 9.6 (2018): 2871-86.

He, L., *et al.* "Mouse Models of Liver Cancer: Progress and Recommendations." *Oncotarget* 6.27 (2015): 23306-22.

He, L., *et al.* "Mouse Models of Liver Cancer: Progress and Recommendations." *Oncotarget* 6.27 (2015): 23306-22.

Hennessy, R., *et al.* "Effect of Probe Geometry and Optical Properties on the Sampling Depth for Diffuse Reflectance Spectroscopy." *Journal of Biomedical Optics* 19.10 (2014): 107002.

Hennessy, R., *et al.* "Monte Carlo Lookup Table-Based Inverse Model for Extracting Optical Properties from Tissue-Simulation Phantoms Using Diffuse Reflectance Spectroscopy." *Journal of Biomedical Optics* 18.3 (2013): 037003.

Hennessy, R., *et al.* "Impact of One-Layer Assumption on Diffuse Reflectance Spectroscopy of Skin." *Journal of Biomedical Optics* 20.2 (2015): 27001.

Honda, N., *et al.* "Determination of the Tumor Tissue Optical Properties During and after Photodynamic Therapy Using Inverse Monte Carlo Method and Double Integrating Sphere between 350 and 1000 Nm." *Journal of Biomedical Optics* 16.5 (2011).

Hu, F., *et al.* "Oxygen and Perfusion Kinetics in Response to Fractionated Radiation Therapy in Fadu Head and Neck Cancer Xenografts Are Related to Treatment Outcome." *International Journal of Radiation Oncology* 96.2 (2016): 462-9.

Kanick, S.C., *et al.* "Sub-Diffusive Scattering Parameter Maps Recovered Using Wide-Field High-Frequency Structured Light Imaging." *Biomedical Optics Express* 5.10 (2014): 3376-90.

Kanick, S.C., *et al.* "Monte Carlo Analysis of Single Fiber Reflectance Spectroscopy: Photon Path Length and Sampling Depth." *Physics in Medicine and Biology* 54.22 (2009): 6991-7008.

Kumka, M., and J. Bonar. "Fascia: A Morphological Description and Classification System Based on a Literature Review." *The Journal of the Canadian Chiropractic Association* 56.3 (2012): 179-91.

Lin, W.C., *et al.* "Brain Tumor Demarcation Using Optical Spectroscopy; an in Vitro Study." *Journal of Biomedical Optics* 5.2 (2000): 214-20.

Lister, T., *et al.* "Optical Properties of Human Skin." *Journal of Biomedical Optics* 17.9 (2012).

Malvicini, M., *et al.* "Reversal of Gastrointestinal Carcinoma-Induced Immunosuppression and Induction of Antitumoural Immunity by a Combination of Cyclophosphamide and Gene Transfer of Il-12." *Molecular Oncology* 5.3 (2011): 242-55.

Muldoon, T.J., *et al.* "Analysis of Skin Lesions Using Laminar Optical Tomography." *Biomedical Optics Express* 3.7 (2012): 1701-12.

Nichols, B.S., *et al.* "Performance of a Lookup Table-Based Approach for Measuring Tissue Optical Properties with Diffuse Optical Spectroscopy." *Journal of Biomedical Optics* 17.5 (2012): 057001.

Novikova, T. "Optical Techniques for Cervical Neoplasia Detection." *Beilstein Journal of Nanotechnology* 8 (2017): 1844-62.

Potter, R. F., and A. C. Groom. "Capillary Diameter and Geometry in Cardiac and Skeletal Muscle Studied by Means of Corrosion Casts." *Microvasc Res* 25.1 (1983): 68-84.

Prahl, S. "Optical Absorption of Hemoglobin." *Optical Properties Spectra*. Oregon Medical Laser Center 2015. Web.

Rajaram, N., *et al.* "Design and Validation of a Clinical Instrument for Spectral Diagnosis of Cutaneous Malignancy." *Applied Optics* 49.2 (2010): 142-52.

Rajaram, N., *et al.* "Experimental Validation of the Effects of Microvasculature Pigment Packaging on in Vivo Diffuse Reflectance Spectroscopy." *Lasers in Surgery and Medicine* 42.7 (2010): 680-8.

Rajaram, N., *et al.* "Lookup Table-Based Inverse Model for Determining Optical Properties of Turbid Media." *Journal of Biomedical Optics* 13.5 (2008): 050501.

Rajaram, N., *et al.* "Pilot Clinical Study for Quantitative Spectral Diagnosis of Non-Melanoma Skin Cancer." *Lasers in Surgery and Medicine* 42.10 (2010): 716-27.

Saager, R.B., *et al.* "Method for Depth-Resolved Quantitation of Optical Properties in Layered Media Using Spatially Modulated Quantitative Spectroscopy." *Journal of Biomedical Optics* 16.7 (2011).

Sabino, C.P., *et al.* "The Optical Properties of Mouse Skin in the Visible and near Infrared Spectral Regions." *Journal of Photochemistry and Photobiology B* 160 (2016): 72-78.

Sandell, J.L., and T.C. Zhu. "A Review of in-Vivo Optical Properties of Human Tissues and Its Impact on Pdt." *Journal of Biophotonics* 4.11 (2011): 773-87.

Semeniak, D. "Sensitivity of Diffuse Reflectance Spectroscopy to Dose- and Depth-Dependent Changes in Tumor Oxygenation after Radiation Therapy." University of Arkansas, 2017. Print.

Sharma, M., *et al.* "Verification of a Two-Layer Inverse Monte Carlo Absorption Model Using Multiple Source-Detector Separation Diffuse Reflectance Spectroscopy." *Biomedical Optics Express* 5.1 (2013): 40–53.

Shay, J.E.S., *et al.* "Inhibition of Hypoxia-Inducible Factors Limits Tumor Progression in a Mouse Model of Colorectal Cancer." *Carcinogenesis* 35.5 (2014): 1067-77.

Sircan-Kucuksayan, A., *et al.* "Diffuse Reflectance Spectroscopy for the Measurement of Tissue Oxygen Saturation." *Physiological Measurement* 36.12 (2015): 2461-9.

Spliethoff, J.W., *et al.* "Monitoring of Tumor Response to Cisplatin Using Optical Spectroscopy." *Translational Oncology* 7.2 (2014): 230-9.

Spliethoff, J.W., *et al.* "Real-Time in Vivo Tissue Characterization with Diffuse Reflectance Spectroscopy During Transthoracic Lung Biopsy: A Clinical Feasibility Study." *Clinical Cancer Research* 22.2 (2016): 357-65.

Tongu, M., *et al.* "Intermittent Chemotherapy Can Retain the Therapeutic Potential of Anti-Cd137 Antibody During the Late Tumor-Bearing State." *Cancer Science* 106.1 (2015): 9-17.

Valdés, P.A., *et al.* "Optical Technologies for Intraoperative Neurosurgical Guidance." *Neurosurgical Focus* 40.3 (2017).

Vishwanath, K., *et al.* "Portable, Fiber-Based, Diffuse Reflection Spectroscopy (Drs) Systems for Estimating Tissue Optical Properties." *Applied Spectroscopy* 62.2 (2011): 206-15.

Yu, B., *et al.* "Instrument Independent Diffuse Reflectance Spectroscopy." *Journal of Biomedical Optics* 16.1 (2010): 011010.

Yu, B., *et al.* "Cost-Effective Diffuse Reflectance Spectroscopy Device for Quantifying Tissue Absorption and Scattering in Vivo." *Journal of Biomedical Optics* 13.6 (2008): 060505.

Yu, B., *et al.* "Diffuse Reflectance Spectroscopy of Epithelial Tissue with a Smart Fiber-Optic Probe." *Biomedical Optics Express* 5.3 (2014): 675-89.

Yuan, Y. "Spatial Heterogeneity in the Tumor Microenvironment." *Cold Spring Harbor Perspectives in Medicine* 6.8 (2016).

Zhang, Y., *et al.* "Development and Characterization of a Reliable Mouse Model of Colorectal Cancer Metastasis to the Liver." *Clinical & Experimental Metastasis* 30.7 (2013).

Zhong, X., *et al.* "Lookup-Table-Based Inverse Model for Human Skin Reflectance Spectroscopy: Two-Layered Monte Carlo Simulations and Experiments." *Biomedical Optics Express* 22.1 (2014).

Zonios, G., and A. Dimou. "Light Scattering Spectroscopy of Human Skin *in Vivo*." *Optics Express* 17.3 (2008): 1256-67.

<u>Chapter 5 (Specific Aim 3)</u>: Effects of isoflurane anesthesia on physiological parameters in murine tumor allografts measured via diffuse reflectance spectroscopy

5.1 Introduction

Diffuse reflectance spectroscopy (DRS) is a non-invasive method which can be used to quantify volumetric total hemoglobin concentration (THC), tissue oxygen saturation (StO_2), and tissue scattering at or within accessible tissue sites (Rajaram *et al.*, 2010; Glennie *et al.*, 2015; Yu *et al.*, 2014; Glennie *et al.*, 2014; Chin *et al.*, 2017; Fong *et al.*, 2017; Greening, James and Muldoon, 2015; Greening *et al.*, 2016; Hennessy *et al.*, 2014; Karsten *et al.*, 2013). This technique has been adapted for studies of tumor perfusion and response to therapy, since THC and StO_2 can be used to differentiate therapeutic responders from non-responders over the course of treatment (Yu *et al.*, 2017; Thong *et al.*, 2017; Schaafsma *et al.*, 2015). DRS is widely used in murine studies in which subcutaneous or orthotopic tumor models are treated with anti-cancer agents or radiation therapy and tumor perfusion is monitored longitudinally over time (Turley *et al.*, 2012; Spliethoff *et al.*, 2014; Hu *et al.*, 2016; Vishwanath, Klein, *et al.*, 2009; Palmer *et al.*, 2009). For example, Turley et al. used a handheld DRS probe to show that Bevacizumab, an anti-VEGF monoclonal antibody, decreased oxyhemoglobin (THC * StO_2) in melanoma tumor xenografts over a 7-day study (Turley *et al.*, 2012). Spliethoff et al. used DRS to show that cisplatin, a chemotherapy drug, caused an increase in tumor StO_2 in an orthotopic model of mammary tumors over a 7-day study (Spliethoff *et al.*, 2014). Finally, Hu et al. used DRS to show that oxygenation kinetics of pharynx squamous cell carcinoma xenografts changed prior to tumor volume changes in response to radiation therapy (Hu *et al.*, 2016). These studies indicate

that DRS provides clinically relevant, quantitative, and functional information that can be used to monitor tumor response to various types of chemotherapy, radiation therapy, or immunotherapy.

Anesthesia is typically used in murine studies because it reduces the animals' stress, enables easy manipulation of the mice, allows for injections of cancer cells and anti-cancer agents, and allows for accompanying surgical procedures. Anesthetic agents used in mouse studies can be delivered via inhalational (isoflurane or sevoflurane) or injected (pentobarbital or ketamine/xylazine) routes (Gargiulo *et al.*, 2012). According to the American Veterinary Medical Association (AVMA), the Institute for Laboratory Animal Research (ILAR), and the Cornell University Institutional Animal Care and Use Committee (IACUC), the most common and recommended anesthesia technique for mice is inhaled isoflurane, a halogenated anesthetic gas supplemented with either 21% (i.e. room air equivalent) or 100% oxygen (O_2) (Gargiulo *et al.*, 2012; Leary *et al.*, 2013; Bliss, 2017). The minimum alveolar concentration (MAC), which is the anesthesia required to prevent movement in response to surgical stimuli in 50% of subjects, is 1.4% for mice under isoflurane anesthesia (Gargiulo *et al.*, 2012). Therefore, the most common practice in DRS studies is placing mice in an induction chamber where anesthesia is quickly induced at 3.0-5.0% isoflurane, and then transferred to a nose cone where anesthesia is maintained at 1.5-3.0% isoflurane, with a constant gas flow rate of 1 L/min (Leung *et al.*, 2015; Spliethoff *et al.*, 2014; Turley *et al.*, 2012; Hu *et al.*, 2016; Vishwanath, Klein, *et al.*, 2009; Gargiulo *et al.*, 2012; Wang *et al.*, 2004; Vishwanath, Yuan, *et al.*, 2009; Guoqiang *et al.*, 2005). Isoflurane is a respiratory and myocardial depressant, which causes increased partial pressure of carbon dioxide and bicarbonate levels in arterial blood (Cesarovic *et al.*, 2010; Thal *et al.*, 2007). Thus, even in the presence of O_2 delivery via nose cone, isoflurane results in tissue O_2 desaturation, which may be a confounding variable when studying tissue perfusion of

subcutaneous murine models in response to therapy. Additionally, some therapies, such as chemotherapy or immunotherapy, depend on adequate tissue perfusion and O_2 saturation to be effective (Ueda *et al.*, 2013). DRS can quantify these perfusion metrics and help understand if limitations exist for emerging cancer therapies (Huang *et al.*, 2013). However, there have been no studies analyzing the effects of isoflurane anesthesia on DRS-derived physiological parameters of murine tissue.

The present study fills this knowledge gap by monitoring DRS-derived physiological parameters of murine tissue while mice were under various anesthesia conditions. Physiological parameters studied include THC, StO_2, tissue oxyhemoglobin (HbO_2), and reduced scattering coefficient (μ_s'). It should be noted that DRS quantifies average StO_2 sampled by light, rather than arterial oxygen saturation (SaO_2), venous oxygen saturation (SvO_2), or peripheral oxygen saturation (SpO_2) (Teng *et al.*, 2008; Sircan-Kucuksayan *et al.*, 2015). StO_2 linearly correlates with the average of SaO_2 and SvO_2; thus, StO_2 values are significantly lower than SaO_2 (Hueber *et al.*, 2001). HbO_2 is the product of THC and StO_2, and describes the concentration of O_2-bound hemoglobin in circulation (Chung *et al.*, 2010; Lee *et al.*, 2007). This study was divided into four aims: 1) examine the effects of isoflurane anesthesia on DRS-derived physiological parameters of normal immunocompetent mouse tissue, 2) determine optimal anesthetic conditions for performing DRS while adhering to AVMA and IACUC standards (Gargiulo *et al.*, 2012; Bliss, 2017; Leary *et al.*, 2013), 3) characterize the time-dependent response of physiological parameters while maintaining mice on 1.5% isoflurane after induction with either 1.5% or 4.0% isoflurane, and 4) validate findings in a subcutaneous murine allograft model of colon carcinoma. An allograft model of colon carcinoma was chosen because they are well-established models in literature but are understudied regarding DRS. For the first aim, physiological

parameters were quantified after manipulating two variables including metabolic gas type (O_2 vs. medical air) and isoflurane concentration (1.5% to 4.0%). For the second aim, optimal anesthetic conditions were determined based on least significant differences between control (no-anesthesia) and experimental groups. For the third aim, mice were anesthetically induced with either 4.0% isoflurane for one minute or 1.5% isoflurane for four minutes. Following induction, mice were transferred to a nose cone and maintained on 1.5% isoflurane for 15 minutes to determine how initial induction conditions affect physiological properties over time. Physiological parameters were monitored via DRS every minute. Finally, for the fourth aim, an allograft model of murine colon carcinoma was used to demonstrate expected changes in DRS-derived tumor physiological parameters during isoflurane anesthesia.

The central hypothesis was that DRS can accurately monitor physiological changes associated with isoflurane anesthesia. Specially, isoflurane anesthesia was expected to yield experimentally-induced low StO_2 and HbO_2, but insignificant changes in THC and μ_s', for both normal and subcutaneous tumor sites. Optimal anesthesia conditions were expected to occur at the lowest tested isoflurane concentration (1.5%) with 100% O_2. Furthermore, StO_2 and HbO_2 were expected to change over time in response to anesthesia. This work aims to guide investigators in eliminating, limiting, or managing anesthesia-induced physiological changes in DRS studies in mouse models.

5.2 Materials and methods

5.2.1 Murine models

The study was approved by the University of Arkansas Institutional Animal Care and Use Committee (IACUC #18060). Fifteen female Balb/c mice (strain: 000651, The Jackson Laboratory, ME, USA) aged nine weeks were purchased. Balb/c mice were housed in groups of

three in five cages at 23°C ± 1°C and 50% ± 10% humidity on a 12:12 hour light-dark cycle. Food (8640, Teklad) and water was provided *ad libitum*. All 15 mice acclimated for seven days, including daily handling (2 minutes) for adaptation to future measurements, after arrival prior to the start of the study. After one week of acclimation, left flanks of the 10-week old Balb/c mice were shaved and Nair® depilatory was applied for one minute to locally remove fur.

5.2.2 Cell line for allograft model of colon carcinoma

Five of the 15 Balb/c mice were randomly selected for tumor allotransplantation. CT26 (ATCC®, CRL-2638™), a colon carcinoma cell line derived from the Balb/c mouse strain, was maintained in Roswell Park Memorial Institute (RPMI)-1640 medium (ATCC®, 30-2001™) supplemented with 10% fetal bovine serum (ATCC®, 30-2020), 1% antibiotic antimycotic solution (Sigma-Aldrich, A5955-100ML), and 0.2% amphotericin B/gentamicin (Thermo Fisher Scientific, R015010) at 37°C and 5% CO_2. CT26 cells were brought to the third passage (P3). Then, $1x10^5$ CT26 cells in sterile saline were injected subcutaneously into the left flank. Tumor allografts grew until they reached a volume of 100 mm^3, measured via $V = (L \cdot W^2)/2$, which took 14.4 ± 2.2 days, upon which tumor underwent DRS measurements. Then, tumor allografts continued to grow until they reached 500 mm^3, approximately 18.1 ± 1.2 days following implantation, upon which additional DRS measurements were taken to compare physiological parameters at different tumor sizes in response to isoflurane anesthesia. For controls, adjacent healthy flank tissue was measured.

5.2.3 Diffuse reflectance spectroscopy instrumentation

The custom, handheld DRS probe (FiberTech Optica, Kitchener, ON, Canada) was used in direct contact with tissue to perform all spectroscopy measurements. The brass probe tip is cylindrical with a diameter of 6.35 mm. The probe includes a 400 μm-core source fiber

(FiberTech Optica, SUV400/440PI, 0.22 ± 0.02 NA) which delivers broadband light (450-900 nm) from a 20W tungsten-halogen lamp (Ocean Optics, HL-2000 HP) into tissue, and an adjacent 400-μm core detector fiber (FiberTech Optica, SUV400/440PI, 0.22 ± 0.02 NA) which transfers diffusely reflected light to a spectrometer (Ocean Optics, FLAME-S) with an optical resolution of 2.1 nm. The center-to-center source-detector separation (SDS) between these two optical fibers was 3.00 mm. All DRS measurements were performed in a dark environment.

The four physiological parameters were quantified by inputting raw DRS spectra into an experimental lookup-table (LUT)-based post-processing software with *a priori* values for oxygenated and deoxygenated hemoglobin extinction coefficients (Greening *et al.*, 2016; Prahl, 2015; Greening, James, Powless, *et al.*, 2015). The software performed an iterative model fit, based on a standard damped least-squares nonlinear fitting method, on raw DRS data to quantify THC, StO_2, HbO_2, and μ_s' (Greening *et al.*, 2016). Additionally, the chi-squared (X^2) value indicated goodness-of-fit between the model fit and raw DRS data; for this study, if X^2 values exceeded 1.0, data was rejected and re-acquired as this was likely due to user-induced movement artifacts during data collection (i.e. discarding data taken with small air gaps between probe and skin). Finally, the software is based on a fitting range (i.e. boundary conditions) for all four physiological parameters, as shown in table 1. Lower and upper bounds were set to encompass a wide range of potential physiological parameters in murine skin and tumor tissue (Sabino *et al.*, 2016; Prahl, 1999). The wavelength range used to fit the data was between 450 to 900 nm.

Table 1. Boundary conditions for quantifying *in vivo* physiological parameters

Physiological parameter	Lower Bound	Upper Bound
THC	0 mg/mL	150 mg/mL
StO_2	0%	100%
HbO_2	0 mg/mL	150 mg/mL
μ_s' (750 nm)	3 cm^{-1}	^{12} m^{-1}

5.2.4 Controlling for confounding variables in mouse diffuse reflectance spectroscopy

Positioning of the mice during DRS measurements could potentially affect results by changing venous blood distribution. Therefore, for DRS measurements of mice under isoflurane anesthesia, mice were placed in the prone position. For DRS measurements of non-anesthetized mice, mice sat in the operator's hand. Thus, the tumor and adjacent healthy skin were identically oriented during measurements in both anesthesia and non-anesthesia cases.

Next, the method of restraining non-anesthetized animals during measurements could affect results by increasing stress leading to altered hemodynamic and tissue blood volume levels (Sikora *et al.*, 2016; Zhao *et al.*, 2011). Mice were restrained by holding the base of the tail between index and middle fingers and allowing the mouse to rest in the palm, or, for the anesthesia conditions, in the prone position with a nose cone delivering isoflurane and metabolic gas. Stress was accounted for in two ways. First, all mice were handled daily for 2 minutes during the 7-day acclimation period to allow the mouse to adapt to DRS measurement procedures and provide reproducible results (Zhao *et al.*, 2011). Additionally, mouse respiration rate was monitored during experiments. During DRS measurements of anesthetized animals, respiration rate was monitored visually by an operator not performing measurements. Safe respiration rate under anesthesia is 55-70 breaths per minute (Ewald *et al.*, 2011). During DRS measurements of non-anesthetized animals, breath rate was not to exceed 150 breaths per minute (BPM) or a 10% increase from baseline prior to handling (Ewald *et al.*, 2011). If BPM did not fall within these stress-related criteria, DRS measurements were not taken.

Finally, previous research has shown that absorption due to THC and StO_2 decreases with both increasing probe-tissue pressure and time since the probe may physically compress blood out of the tissue site and impede the sampled tissue site from receiving replacement oxygenated

blood (Lim *et al.*, 2011). Although probe-pressure effects were not directly measured in this study, probe-pressure effects have been shown to be nearly negligible (< 5% error) within a range of probe-skin pressures between 9 to 152 mN/mm^2 (1.3 to 22.0 PSI) using a similar 6.35 mm-diameter DRS probe in short (< 2 s) contact durations. Normal probe-skin pressure tends to be less than 9 mN/mm^2, and, for our setup, a contact time less than 1 s, justifying the non-use of an integrated pressure sensor (Lim *et al.*, 2011).

5.2.5 Effect of isoflurane concentration on physiological tissue parameters

The aim of this experiment was to examine the effect of inhaled isoflurane anesthesia physiological parameters of murine tissue, measured by DRS, and determine optimal anesthetic conditions for DRS.

The normal, exposed left flank of Balb/c mice (n=10) underwent DRS with varying anesthesia conditions. The control group received no anesthesia. Subsequent groups received isoflurane anesthesia (Henry Schein Animal Health, 1169567762) using a tabletop laboratory animal anesthesia system (VWR, 89012-492). Metabolic gas was varied between pure O_2 (100% O_2, Airgas, OX USP200) and medical air (21% O_2, Airgas, AI USP200), with a constant flow rate of 1 L/min. Isoflurane concentration was varied between 1.5%, 2.0%, 3.0%, and 4.0%. Mice were induced and maintained on the same isoflurane concentration. Concentrations below 1.5% were not tested because such concentrations would be below the MAC value (1.4%) for isoflurane in mice (Gargiulo *et al.*, 2012). Isoflurane concentrations above 4.0% were not tested since higher values are usually only used for isoflurane-induced euthanasia according to AVMA (Leary *et al.*, 2013). Furthermore, investigators generally do not exceed 4.0% isoflurane during anesthetic induction (Turley *et al.*, 2012; Spliethoff *et al.*, 2014; Hu *et al.*, 2016; Vishwanath,

Klein, *et al.*, 2009; Gargiulo *et al.*, 2012; Leung *et al.*, 2015; Wang *et al.*, 2004; Vishwanath, Yuan, *et al.*, 2009; Guoqiang *et al.*, 2005).

Mice were placed in a 2L induction chamber with an input connected to the isoflurane-gas mix and output connected to a disposable charcoal filter (VWR, 89012-608) housed in an externally ventilating chemical fume hood. Mice were anesthetically induced until they had no pedal reflex (firm toe pinch). Mice were then transferred to a second independent anesthesia circuit consisting of a 9 mm-diameter nose cone with an input connected to the isoflurane-gas mix and output connected to a disposable charcoal filter. To maintain body temperature, mice were placed on a water-based warming pad (Stryker, #TP12E) controlled by a warming pump (Stryker, #TP700) set to 42°C (107°F), as recommended by the Cornell University IACUC (Bliss, 2017).

The DRS probe was placed in direct contact with the exposed skin of the left flank. DRS measurements were taken with an integration time of 75 ms, and the probe was in direct contact with skin for less than 1 s to mitigate probe-pressure effects. Ten DRS measurements were averaged over the course of 30 seconds per mouse, with the probe being completely removed from the skin between each data take. Total time under anesthesia was less than 5 minutes in all cases. Paired t-tests were used to compare groups since each mouse was subject to all groups. Figure 1 shows the experimental setup.

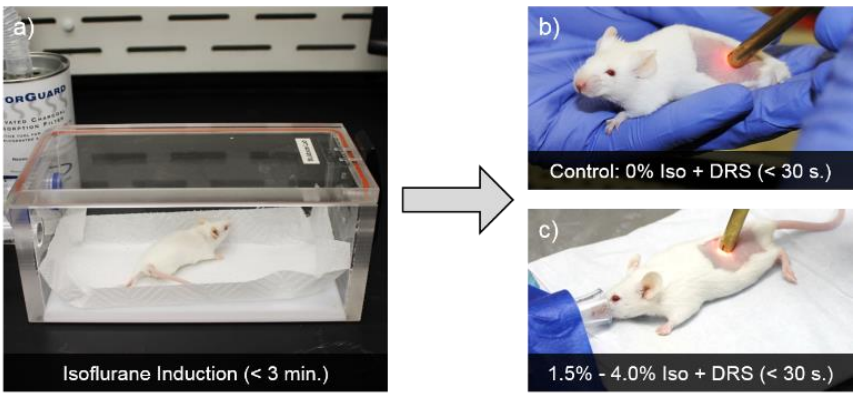

Figure 1. Balb/c mice in experimental groups underwent isoflurane induction for less than 3 minutes, depending on concentration (1.5%, 2.0%, 3.0%, or 4.0%), using either 1 L/min of 100% or 21% O_2 (a). Then, mice underwent less than 30 seconds of 10 consecutive DRS measurements on healthy tissue of the exposed left flank in either control (b), or experimental (1.5%, 2.0%, 3.0%, or 4.0% isoflurane) groups (c). During maintenance, mice were maintained on a warming pad.

5.2.6 Temporal effects of isoflurane anesthesia on physiological tissue parameters

The aim of this experiment was to characterize the time-dependent physiological parameter response while maintaining the mouse on 1.5% isoflurane after isoflurane induction.

DRS measurements were taken on left flank of conscious mice (n=10) every minute for five minutes with no isoflurane anesthesia as a baseline. Mice were restrained within the palm of the hand gently holding the tail, held no more than three inches above the work surface.

Then, mice were placed into the 2L induction chamber supplied with either 4.0% isoflurane for one minute or 1.5% isoflurane for four minutes with 1 L/min O_2. No DRS measurements occurred during induction. Mice were then transferred to a nose cone and maintained on 1.5% isoflurane and 1 L/min O_2 for 15 minutes, with DRS measurements taken every minute. A maximum of 15 minutes was chosen since it takes approximately 10-15 minutes for mice to fully respond to a change in isoflurane concentration (Ewald *et al.*, 2011). Therefore, to control for intergroup and intragroup variation, DRS measurements must occur only after the mouse has presumably fully responded to such change. Throughout DRS measurements under

anesthesia, mice were maintained on a water-based warming pad (Stryker, #TP12E) controlled by a warming pump (Stryker, #TP700) set to 42°C (107°F).

Following 15 minutes of isoflurane maintenance, mice were removed from anesthesia and DRS measurements were taken every minute for 5 minutes. DRS measurements were taken with an integration time of 75 ms. Figure 2 visualizes the experimental set-up.

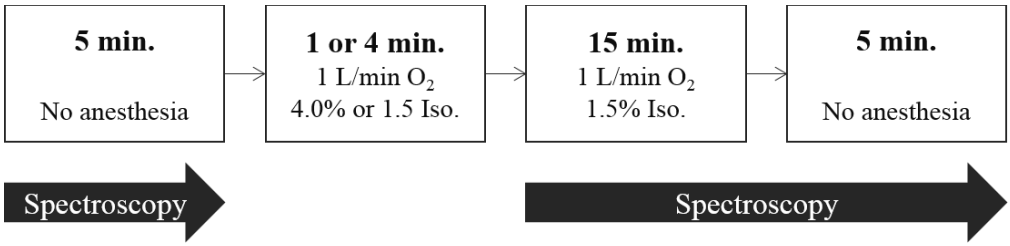

Figure 2. Conscious Balb/c mice underwent DRS for 5 minutes. Then, mice were anesthetically induced for 1 or 4 minutes with 4.0% or 1.5% isoflurane (Iso), respectively, and 1 L/min O_2. Following induction, mice were transferred to a nose cone and underwent DRS for 15 minutes at 1.5% isoflurane and 1 L/min O_2. Finally, mice were removed from the nose cone and the left flank underwent DRS for 5 minutes.

For each mouse, physiological parameters (THC, StO_2, HbO_2, and μ_s') were normalized to the highest value over the 25-minute data acquisition period. Then, normalized values of all mice were averaged as a function of time. Both normalized and non-normalized data are presented.

5.2.7 Physiological parameters of CT26 colon carcinoma allografts

A second cohort of Balb/c mice (n=5) with CT26 murine colon carcinoma allografts underwent DRS as a representative model of subcutaneous tumor allografts. Measurements with (1.5% isoflurane and 1 L/min O_2) and without anesthesia were performed on allografts at volumes of 100 mm^3 and 500 mm^3 and an immediately adjacent normal site. Mice were placed in the 2L induction chamber (1.5% isoflurane and 1 L/min O_2) until loss of pedal reflex and transferred to the nose cone. Ten DRS measurements were averaged per site at an integration

time of 75 ms per spectra to minimize motion artifacts. Figure 3 visualizes the experimental set-up.

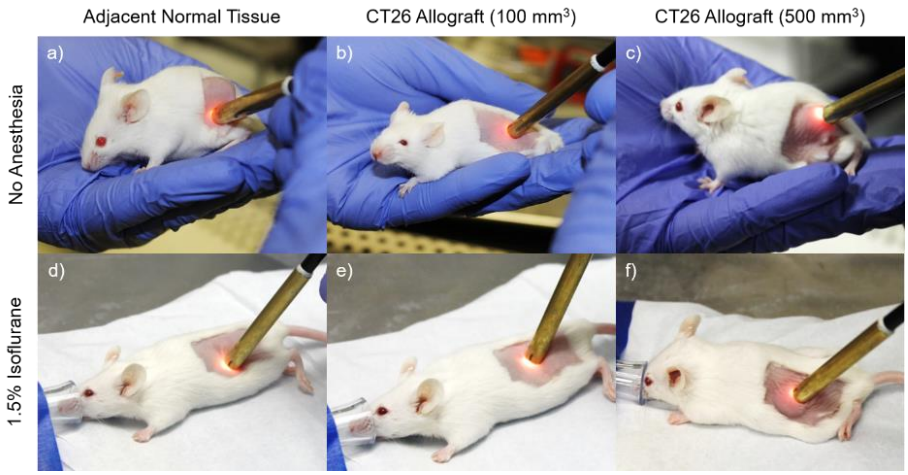

Figure 3. DRS was performed on Balb/c mouse (10 weeks old) to quantify physiological parameters (THC, StO_2, HbO_2, and μ_s') in subcutaneous CT26 tumor allografts at a volume of 100 mm^3 (b, e), 500 mm^3 (c, f), and adjacent normal tissue (a, d) both with (d, e, f) and without isoflurane anesthesia (a, b, c). Anesthesia was constant at 1.5% isoflurane and 1 L/min O_2.

5.3 Results

5.3.1 Effect of isoflurane concentration on physiological tissue parameters

The left flank of Balb/c mice (n=10) underwent DRS measurements while varying isoflurane concentration between 0.0% (control, no anesthesia) and 4.0%, and varying metabolic gas between 21% O_2 and 100% O_2.

For THC (Figure 4a), there were no significant differences between using O_2 or air. However, there was a significant decrease in THC compared to control as isoflurane exceeds 2.0% ($p < 0.01$). At 4.0% isoflurane, THC dropped to 68% ($p < 0.01$) and 67% ($p < 0.01$) compared to the control in O_2 and air, respectively.

For StO_2 (Figure 14b), there were no significant differences between using O_2 or air, although average values for StO_2 tended to be higher when using O_2. Unlike THC, StO_2 decreases rapidly, even at the minimum 1.5% isoflurane. For example, at 1.5% isoflurane with

air, StO_2 decreased to 87% ($p = 0.028$) compared to the control. StO_2 continued to decrease within both O_2 and air groups ($p < 0.01$) up to 3.0% isoflurane. Then, between 3.0% and 4.0% isoflurane, StO_2 stabilized to ~8-15% compared to the control.

For HbO_2 (Figure 14c), despite there being no significant differences between using O_2 or air for THC and StO_2, there was a significant difference in HbO_2 between using O_2 and air at 1.5% isoflurane ($p = 0.04$), suggesting that O_2 is the preferred metabolic gas compared to air with regards to DRS-derived physiological parameters. Most notably, there were significant differences between using 1.5% isoflurane and the control for both O_2 (88%, $p = 0.043$) and air (69%, $p < 0.01$) groups. This finding suggests that even at the lowest isoflurane concentration (1.5%) above the MAC value (1.4%) for mice, DRS-derived HbO_2 values were affected.

For μ_s' (Figure 14d), there were no significant differences between using O_2 or air. Additionally, μ_s' was unaffected by changes in isoflurane concentration. These findings suggest that all anesthesia conditions affect at least one of the tested physiological parameters. However, 1.5% isoflurane and 1 L/min O_2 most closely mimicked ideal no-anesthesia conditions.

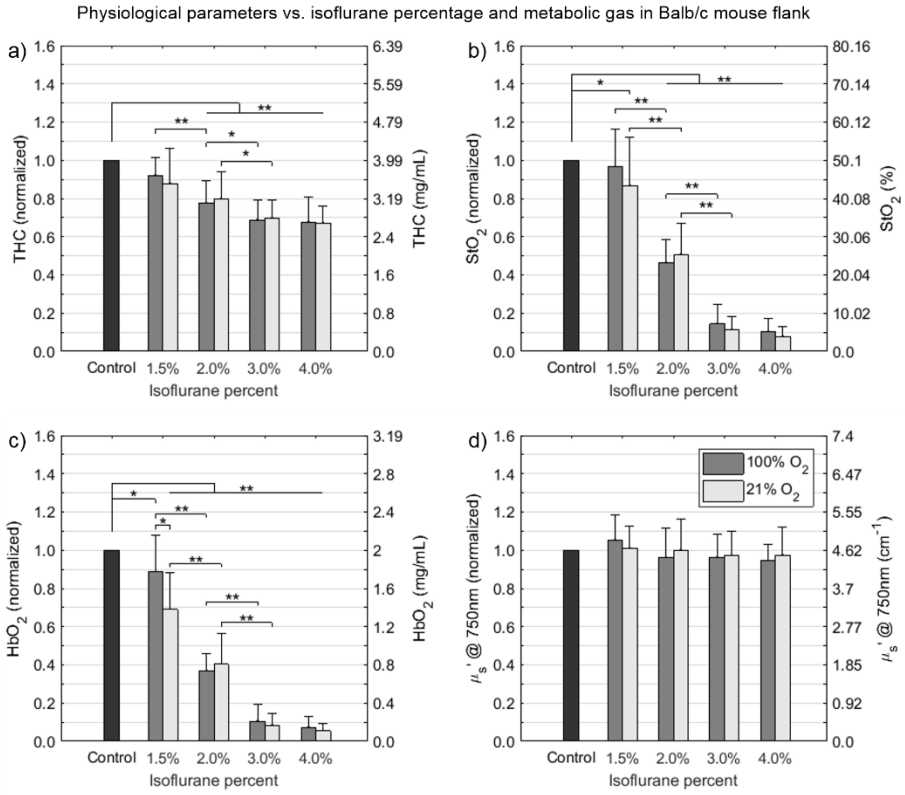

Figure 4. Physiological parameters of THC (a), StO_2 (b), HbO_2 (c), and μ_s' (d) of the normal left flank of Balb/c mice (n=10) was compared for isoflurane concentration (1.5% to 4.0%) and either 100% O_2 (dark gray) or 21% O_2 (light gray). THC (a) and StO_2 (b) were only affected by isoflurane concentration. HbO_2 (c) was affected by both isoflurane concentration and metabolic gas. Finally, μ_s' (d) was unaffected by increases in isoflurane concentration and metabolic gas. Even at low isoflurane concentrations (1.5%), physiological parameters were affected. Based on these results, O_2 is the preferred metabolic gas over air, and 1.5% isoflurane is most appropriate when applicable. Control indicates measurements from non-anesthetized mice. Values are means ± SD. Significance is indicated by *($p<0.05$) and ** ($p<0.01$).

5.3.2 Temporal effects of isoflurane anesthesia on physiological tissue parameters

DRS measurements were taken on Balb/c mice (n=10) every minute for five minutes with no isoflurane anesthesia as a baseline. During these five minutes, all physiological parameters remained stable. After one or four minutes with 4.0% or 1.5% isoflurane, respectively, and 1 L/min O_2, mice were transferred to a nose cone with 1.5% isoflurane and 1 L/min O_2.

For both 4.0% and 1.5% isoflurane induction condition, THC (Figure 5a) decreased from approximately 3.7 mg/mL to 2.8-3.2 mg/mL and remained relatively stable throughout the 15-minute duration. During the 5-minute recovery period, THC showed a slight rise to approximately 3.4 mg/mL. For StO_2, on the other hand (Figure 5b), the induction period resulted in a decrease from approximately 50% to 31% and 7% for the 1.5% and 4.0% isoflurane induction conditions, respectively. For the 4.0% isoflurane condition, StO_2 increased over time during the maintenance period, but not dramatically, having reached a final value of just 11% at the end of 15 minutes. On the other hand, for the 1.5% isoflurane condition, StO_2 continued to decrease to 51% for 6 months, then rose back to 22% at the end of 15 minutes, indicating that, as expected, physiological changes occur more slowly in mice anesthetized with 1.5% isoflurane. Similarly, HbO_2 (Figure 5c), as anticipated, demonstrated similar trends to StO_2.

Finally, μ_s' (Figure 4d) was unaffected by isoflurane anesthesia. Following maintenance with 1.5% isoflurane and 1 L/min O_2, mice were removed from isoflurane for a "recovery" period and DRS data was collected for an additional five minutes. Mice generally regained consciousness within one minute and full movement within two minutes, after which mice were gently restrained in the palm of the hand with the tail held secure between index and middle finger no more than three inches above the work surface. THC, StO_2, and HbO_2 increased within the five minutes; however, none reached 100% of the baseline values within the five-minute recovery period. On the other hand, μ_s' remained constant during the 5 minutes of recovery.

From these experiments, physiological parameters were affected by anesthetic induction with both 1.5% and 4.0% isoflurane. It cannot be assumed, once 1.5% isoflurane maintenance begins, that physiological parameters are representative. THC, StO_2, and HbO_2 did not recover to

the baseline values by the end of 15 minutes, nor did these physiological parameters fully recover after the five-minute recovery period.

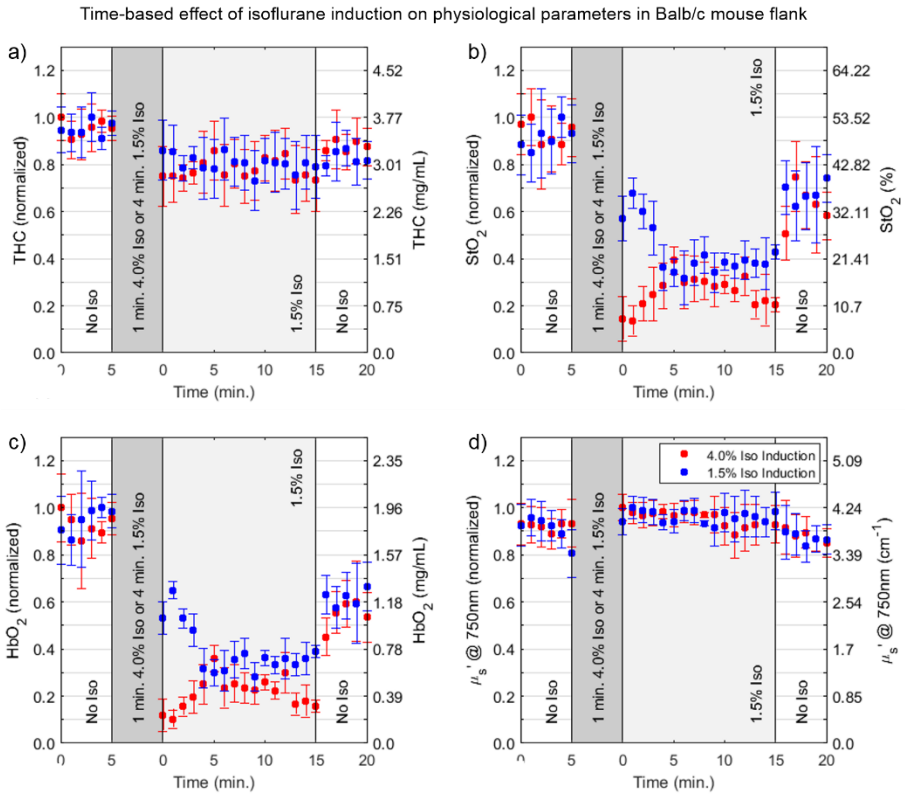

Figure 5. Temporal effects of 1.5% and 4.0% isoflurane anesthesia induction on physiological parameters of THC (a), StO_2 (b), HbO_2 (c), and μ_s' (d) of the normal left flank of Balb/c mice (n=10). The μ_s' (d) was unaffected by induction, maintenance, and recovery periods. Other physiological parameters all showed an initial decrease after induction, with a slight increase by the end of the 15-minute maintenance period, but not back to baseline values. Based on these results, it is clear than any isoflurane induction concentration influences DRS-derived physiological parameters. Values are means ± SD.

5.3.3 Physiological parameters of CT26 colon carcinoma allografts

Colon carcinoma murine CT26 allografts in Balb/c mice at volumes of 100 mm^3 and 500 mm^3 were compared with adjacent normal tissue with (1.5% isoflurane and 1 L/min O_2) and without isoflurane anesthesia to quantify physiological parameters (Figure 6). All mice were induced with 1.5% isoflurane for four minutes to avoid the effects of 4.0% isoflurane seen in Figure 4.

For adjacent tissue locations (no tumor), there was significant reduction in physiological parameters for the anesthesia condition compared to the no anesthesia condition for THC ($p < 0.01$), StO_2 ($p = 0.04$), and HbO_2 ($p = 0.02$). However, overall trends within the anesthesia and no anesthesia groups were similar, with insignificant reductions in physiological parameters when using 1.5% isoflurane and 1 L/min O_2. Additionally, as tumor size increased, StO_2 and HbO_2 decreased while THC increased and μ_s' remained constant. Further comparisons across and within groups were visually expressed in Figure 6.

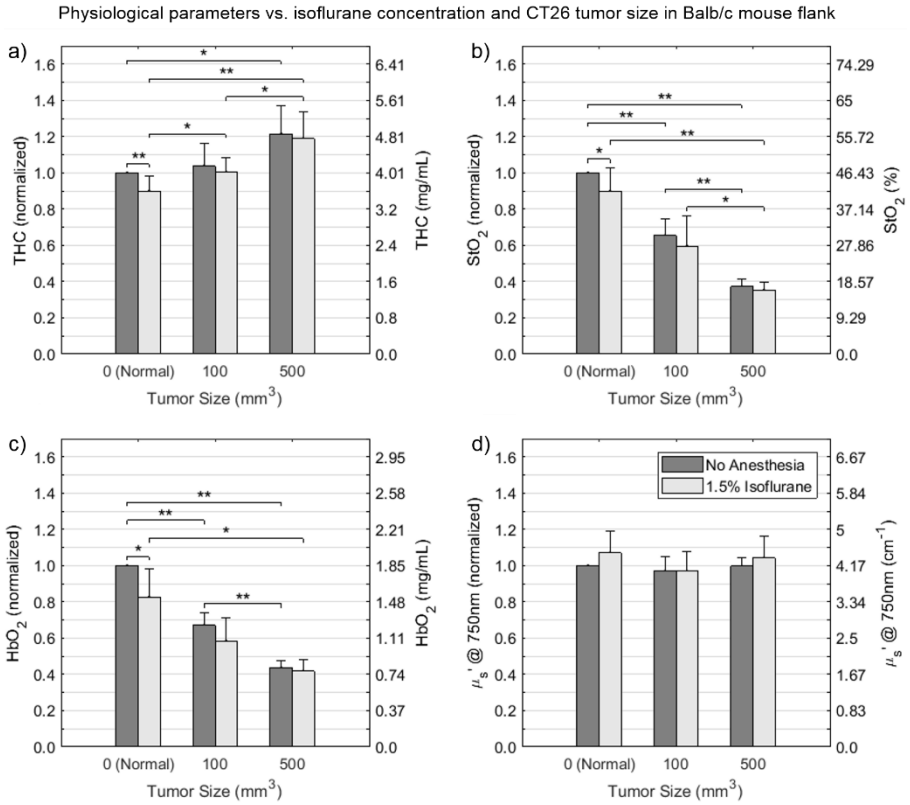

Figure 6. Comparison of the physiological parameters, THC, StO_2, HbO_2, and μ_s' of subcutaneous CT26 tumor allografts and adjacent normal tissue both with (light gray) and without (dark gray) isoflurane anesthesia. Similar to previous findings, THC, StO_2, and HbO_2 were reduced when comparing the no-anesthesia and 1.5% isoflurane conditions in adjacent normal tissue. Results demonstrate that isoflurane anesthesia causes experimentally-reduced HbO_2 values, and that StO_2 and HbO_2 decreased with increasing allograft tumor volumes, whereas THC increased and μ_s' remained constant. Values are means ± SD. Significance is indicated by *($p<0.05$) and ** ($p<0.01$).

5.4 Discussion

Isoflurane anesthesia is a known respiratory and myocardial depressant, causing increased serum carbon dioxide and bicarbonate levels, and decreased arterial pressure. Despite this, isoflurane is commonly applied as an anesthetic agent in studies investigating volumetric perfusion of murine tissue, which is the aim of many DRS-based studies. To better understand the effects of isoflurane anesthesia on DRS-derived physiological parameters, the present study monitored murine THC, StO_2, HbO_2, and μ_s' using DRS under various anesthesia conditions. Understanding the effects of isoflurane anesthesia on these tissue physiological parameters will help guide investigators in DRS experimental design.

In this study, increasing isoflurane concentration significantly decreased THC, StO_2, and HbO_2 while having no effect on μ_s' (Figs. 4-6). Of all four DRS-derived physiological parameters, StO_2 was most influenced by changes in isoflurane concentration. Furthermore, using 100% O_2, rather than 21% O_2, resulted in closer approximation to no-anesthesia controls (Figure 4), a trend echoed by Gerling et al. who showed that supplying 100% O_2 led to increased StO_2 (Gerling *et al.*, 2014). Because of this, 100% O_2 was used throughout the remainder of the study.

In Figure 4b, StO_2 did not decrease (50% to 48%, $p = 0.32$) when comparing the no-anesthesia control to the 1.5% isoflurane condition. However, StO_2 drastically decreased from 48% to 6% when increasing isoflurane from 1.5% to 4.0% in normal tissue. StO_2 values of ~6% have been observed in similar spectroscopy studies of mice tissue during anesthesia (Spliethoff *et al.*, 2014). StO_2 linearly correlates with the average of SaO_2 and SvO_2; thus, StO_2 values are significantly lower than SaO_2 (Hueber *et al.*, 2001), which can be measured via pulse oximetry (Al-Samir *et al.*, 2016). Decreased StO_2 is primarily caused by isoflurane-induced decreased

mean arterial blood pressure (MAP) (Oshita *et al.*, 1989). Szczesny et al. measured MAP of mice under increasing isoflurane concentrations, and showed that MAP decreased from 80 mmHg to below 40 mmHg as isoflurane concentration was increased from 1.0% to 4.0% (Szczesny *et al.*, 2004). Constantinides et al. echoed this trend, showing that MAP decreased from 85 mmHg to 73 mmHg when increasing isoflurane concentration from 1.0% to 2.0% with 100% O_2. Additionally, this research showed that MAP decreased from 92 mmHg to 84 mmHg when decreasing O_2 from 100% to 21% with 1.5% isoflurane (Constantinides *et al.*, 2012).

To our knowledge, no other studies report StO_2 (as low as 6% in Figure 14b) at high (4.0%) concentrations of isoflurane, since many studies state they DRS acquisition during isoflurane maintenance of 1.5%. However, this statement paints an incomplete picture. This report is important because the most common anesthetic practice in DRS studies is placing mice in an induction chamber where anesthesia is induced at ~4.0% isoflurane (Gargiulo *et al.*, 2012). This isoflurane concentration can have long-lasting effects on blood physiology, even when mice are transferred to a nose cone where isoflurane is maintained at 1.5% (Figure 5). Therefore, we show that isoflurane induction, not just maintenance, highly affects DRS-derived StO_2 (Figure 5). We recommend 1.5% isoflurane with 100% O_2 for both induction and maintenance, despite increased time to loss of pedal reflex.

Of note are conflicting results from a study by Farzam et al. In this study, mice were anesthetized and maintained on 3.5% and 2.0% isoflurane, respectively, and StO_2 values were ~75% in orthotopic renal cell carcinoma tumors (Farzam *et al.*, 2017), a stark increase from our StO_2 of 22% at 2.0% isoflurane (Figure 4b). However, this study analyzed an orthotopic, rather than subcutaneous, tumor model of a different cell line. In a more comparable study, Rajaram et al. reported StO_2 values near 30% under similar isoflurane conditions (1.5%) and wavelength

ranges (350 to 850 nm) of murine skin at a comparable SDS (2.5 mm) (Rajaram *et al.*, 2015). The wavelength range used to fit data and SDS are paramount when comparing between studies.

Unlike hemodynamic physiological parameters, the μ_s' was unaffected by changes in isoflurane concentration and O_2 levels. Tissue scattering is primarily caused by local density of lipid membranes from cellular tissues, mitochondria, lysosomes, and collagenous tissue like the skin (Jacques, 2013), which was the primary tissue type interrogated in this experiment. These scattering structures are unaffected by isoflurane conditions, resulting in stable μ_s'.

Based on these results, isoflurane anesthesia should be carefully considered when performing DRS studies to quantify THC, StO_2, and HbO_2; however, some invasive and minimally invasive studies cannot eliminate the anesthesia use. For example, Spliethoff et al. used a 21G optical needle probe to perform deep intratumoral DRS measurements to overcome sampling depth limitations with mice under anesthesia (Spliethoff *et al.*, 2014). Westerkamp et al. performed postmortem DRS on liver tissue following hepatectomy (Westerkamp *et al.*, 2015). Finally, Palmer et al. performed DRS on 4T1 mammary tumor allografts while concurrently measuring the partial pressure of O_2 using an OxyLite sensor, which required anesthesia (Palmer *et al.*, 2009). Thus, it is not always applicable to perform live DRS with no anesthesia; 100% O_2 with minimal isoflurane (1.5%) is recommended in these cases. Using a minimum of 1.5% isoflurane for induction over a four-minute period also drastically decreased StO_2 and HbO_2, although changes were slower to occur compared to 4.0% isoflurane induction (Figure 5). If anesthesia is needed when measuring *in vivo* physiological parameters via DRS, it may be more representative to slowly induce anesthesia with 1.5% isoflurane rather than rapidly inducing anesthesia with 4.0% isoflurane and lowering concentration for anesthesia maintenance.

Finally, THC, StO_2, HbO_2, and μ_s' of Balb/c-CT26 colon tumor were measured via DRS. Figure 6a indicates that increased tumor volume correlates to increased THC. Across Figs. 4-6, we report THC of 2.8 to 4.0 mg/mL in normal tissue and 4.0 to 4.8 mg/mL in subcutaneous CT26 tumor allografts under 1.5% isoflurane anesthesia, comparable to a study by Spliethoff et al (Spliethoff *et al.*, 2014) in similar conditions. Increased tumor THC is due to increased tumor microvasculature coupled with increased ratio of deoxyhemoglobin to oxyhemoglobin. This trend of increased tumor THC is well known (Quincy Brown *et al.*, 2009; Wang *et al.*, 2009). Figure 16b shows that StO_2 of tumors with volumes of 500 mm^3 was ~14%, both with and without 1.5% isoflurane. This low StO_2 value is similar to a study by Spliethoff et al., which reported slightly lower StO_2 values of 2-6% in larger mammary xenograft tumors (up to 800 mm^3) using 1.5% isoflurane anesthesia (Spliethoff *et al.*, 2014). Rich et al. reported similar StO_2 values of 5-15% in head and neck cancer xenograft tumors, measured using photoacoustic imaging (Rich *et al.*, 2016). Finally, Rajaram et al. reported DRS-derived StO_2 around 20% for mammary xenografts at 1.5% isoflurane anesthesia (Rajaram *et al.*, 2015). The Rajaram study also reported a ~1.5x decrease in StO_2 of 100 mm^3 mammary tumor xenografts compared to normal tissue, whereas this present study reports a ~1.6x decrease (Figure 6b) in StO_2 of 100 mm^3 colon tumor allografts compared to normal tissue. The comparable StO_2 values in these studies lend support to our results. HbO_2 in Figure 6c demonstrates similar trends as StO_2. In Figure 6d, μ_s' was unaffected by tumor size and isoflurane, similar to Figs. 4 and 5.

Additionally, in tumors, there were insignificant decreases in THC, StO_2, and HbO_2 when using 1.5% isoflurane compared to a no-anesthesia control, suggesting it may be appropriate to monitor percent changes in physiological parameters over time. In longitudinal treatment studies, accompanying non-endpoint procedures such as chemotherapy, radiation therapy,

immunotherapy, or other treatment or observation procedures requiring anesthesia should ideally be performed after DRS measurements have concluded.

One limitation of this study is the focus on non-invasive DRS of readily accessible murine tissue, such as skin and subcutaneous tumor allografts, which only requires contact between the probe and skin directly overlying the tumor. Additionally, DRS was the only technique used to quantify THC, StO_2, HbO_2, and μ_s' and cannot provide insights into tumor vascular heterogeneity (Kwong *et al.*, 2016; Greening *et al.*, 2016; Valdés *et al.*, 2016; Mourant *et al.*, 2014). Other optical techniques exist to quantify these parameters including diffuse optical imaging (DOI) (Kwong *et al.*, 2016), hyperspectral imaging (Hendargo *et al.*, 2015), and near infrared spectroscopy (NIRS), which extends the wavelength range of DRS into the near infrared to quantify additional endogenous chromophores such as fat and water (Kawaguchi *et al.*, 2017; Chen *et al.*, 2015; Kondepati *et al.*, 2008; Spliethoff *et al.*, 2014). For example, DOI combined with magnetic resonance imaging can differentiate tumors with low and high vascular heterogeneity, and hyperspectral imaging can quantify vascular O_2 supply and blood flow in rodent models. These spectral and imaging techniques would benefit from an in-depth analysis at how anesthetic drugs affect results. Next, DRS-derived physiological parameters were only quantified in response to isoflurane anesthesia. Despite being the most common type of anesthetic used in DRS-based mouse studies, other anesthesia drugs exist including sevoflurane, Pentobarbital, and ketamine/xylazine (Gargiulo *et al.*, 2012). Finally, further tests with additional cell lines for murine subcutaneous allografts or xenografts will generalize results. An allograft model of colon carcinoma (Balb/c-CT26) was chosen because they are well-established models in literature but are understudied regarding DRS. Results compare well with other allograft/xenograft tumors in terms of physiological parameters (THC, StO_2, HbO_2, and μ_s').

The findings presented here suggest that DRS is a valid tool to dynamically monitor changes in physiological parameters. These findings indicate that DRS has the potential to help investigators understand if limitations exist for certain cancer therapies that directly depend on tumor O_2 consumption and help guide investigators in managing anesthesia-induced physiological changes in DRS studies of murine subcutaneous tumor allografts. Future studies analyzing DRS-derived physiological parameters in response to these drugs will increase the generalization of our findings.

5.5 Conclusion

Diffuse reflectance spectroscopy can be effectively used to monitor dynamic fluctuations in tissue physiological parameters, such as total hemoglobin concentration, tissue oxygen saturation, oxyhemoglobin, and tissue scattering, and is an attractive tool for monitoring tumor response to therapy. Additionally, diffuse reflectance spectroscopy has the potential to help investigators understand if limitations exist for certain cancer therapies, such as chemotherapy or PDT, that directly depend on oxygen consumption and well-perfused tumors. Investigators using this tool should understand the dynamic effects of isoflurane concentration on resulting physiologic values. We show that isoflurane induction, not just maintenance, highly affect hemodynamic parameters. Alternative methods to diffuse reflectance spectroscopy, such as pulse oximetry, should be considered when monitoring arterial, rather than tissue, oxygen saturation, during anesthesia.

5.6 Funding

This material is based on work supported by the National Institutes of Health (1R15CA202662-01), the National Science Foundation Graduate Research Fellowship Program (G.G., DGE-1450079), the Arkansas Biosciences Institute, and the University of Arkansas

Doctoral Academy Fellowship. Any opinions, findings, and conclusions or recommendations expressed in this material are those of the authors and do not necessarily reflect the views of the acknowledged funding agencies.

5.7 Acknowledgements

We thank the entire team of the Translational Biophotonics and Imaging Laboratory for continued constructive support for this study and Dr. Narasimhan Rajaram for guidance in the spectroscopy setup and data post-processing.

5.8 Disclosures

The authors declare that there are no conflicts of interest related to this chapter.

References

Al-Samir, S., *et al.* "Maximal Oxygen Consumption Is Reduced in Aquaporin-1 Knockout Mice." *Frontiers in Physiology* 7.347 (2016).

Bliss, S. "Rodent Anesthesia (Animal Care and Use Procedure 101.02)." Cornell University Institutional Animal Care and Use Committee 2017. Web2017.

Cesarovic, N., *et al.* "Isoflurane and Sevoflurane Provide Equally Effective Anaesthesia in Laboratory Mice." *Laboratory Animals* 44 (2010): 329-36.

Chen, H., *et al.* "Near-Infrared Spectroscopy as a Diagnostic Tool for Distinguishing between Normal and Maligant Colorectal Tissues." *BioMed Research International* 472197 (2015).

Chin, L.C.L., *et al.* "Early Biomarker for Radiation-Induced Wounds: Day One Post-Irradiation Assessment Using Hemoglobin Concentration Measured from Diffuse Optical Reflectance Spectroscopy." *Biomedical Optics Express* 8.3 (2017): 1682-8.

Chung, S.H., *et al.* "Non-Invasive Tissue Temperature Measurements Based on Quantitative Diffuse Optical Spectroscopy (Dos) of Water." *Physics in Medicine & Biology* 55.13 (2010): 3753-65.

Constantinides, C., *et al.* "Effects of Isoflurane Anesthesia on the Cardiovascular Function of the C57bl/6 Mouse." *Institute for Laboratory Animal Research Journal* 52.3 (2012).

Ewald, A.J., *et al.* "Monitoring of Vital Signs for Long-Term Survival of Mice under Anesthesia." *Cold Spring Harbor Protocols* 2 (2011).

Farzam, P., *et al.* "Pre-Clinical Longitudinal Monitoring of Hemodynamic Response to Anti-Vascular Chemotherapy by Hybrid Diffuse Optics." *Biomedical Optics Express* 8.5 (2017): 2563-82.

Fong, C.J., *et al.* "Assessment of Infantile Hemangiomas Using a Handheld Wireless Diffuse Optical Spectroscopic Device." *Pediatric Dermatology* 34.4 (2017): 386-91.

Gargiulo, S., *et al.* "Mice Anesthesia, Analgesia, and Care, Part I: Anesthetic Considerations in Preclinical Research." *Institute for Laboratory Animal Research Journal* 53.1 (2012).

Gerling, M., *et al.* "Real-Time Assessment of Tissue Hypoxia in Vivo with Combined Photoacoustics and High-Frequency Ultrasound." *Theranostics* 4.6 (2014): 604-13.

Glennie, D.L., *et al.* "Modeling Changes in the Hemoglobin Concentration of Skin with Total Diffuse Reflectance Spectroscopy." *Journal of Biomedical Optics* 20.3 (2015): 035002.

Glennie, D.L., *et al.* "Inexpensive Diffuse Reflectance Spectroscopy System for Measuring Changes in Tissue Optical Properties." *Journal of Biomedical Optics* 19.10 (2014): 105005.

Greening, G.J., *et al.* "Towards Monitoring Dysplastic Progression in the Oral Cavity Using a Hybrid Fiber-Bundle Imaging and Spectroscopy Probe." *Scientific Reports* 6.26734 (2016).

Greening, G.J., *et al.* Optical Phantoms: Diffuse and Sub-Diffuse Imaging and Spectroscopy Validation. Bellingham, Washington: SPIE Spotlights, 2015.

Greening, G.J., *et al.* "Fiber-Bundle Microendoscopy with Sub-Diffuse Reflectance Spectroscopy and Intensity Mapping for Multimodal Optical Biopsy of Stratified Epithelium." *Biomedical Optics Express* 6.12 (2015): 4934-50.

Guoqiang, Y., *et al.* "Noninvasive Monitoring of Murine Tumor Blood Flow During and after Photodynamic Therapy Provides Early Assessment of Therapeutic Efficacy." *Clinical Cancer Research* 11.9 (2005): 3543-52.

Hendargo, H.C., *et al.* "Snap-Shot Multispectral Imaging of Vascular Dynamics in a Mouse Window-Chamber Model." *Optics Letters* 40.14 (2015): 3292-5.

Hennessy, R., *et al.* "Effect of Probe Geometry and Optical Properties on the Sampling Depth for Diffuse Reflectance Spectroscopy." *Journal of Biomedical Optics* 19.10 (2014): 107002.

Hu, F., *et al.* "Oxygen and Perfusion Kinetics in Response to Fractionated Radiation Therapy in Fadu Head and Neck Cancer Xenografts Are Related to Treatment Outcome." *International Journal of Radiation Oncology* 96.2 (2016): 462-9.

Huang, Y., *et al.* "Vascular Normalization as an Emerging Strategy to Enhance Cancer Immunotherapy." *Cancer Research* 73.10 (2013): 2943-8.

Hueber, D.M., *et al.* "Non-Invasive and Quantitative near-Infrared Haemoglobin Spectrometry in the Piglet Brain During Hypoxic Stress, Using a Frequency-Domain Multidistance Instrument." *Physics in Medicine and Biology* 46 (2001): 41-62.

Jacques, S.L. "Optical Properties of Biological Tissues: A Review." *Physics in Medicine and Biology* 58.11 (2013).

Karsten, A.E., *et al.* "Diffuse Reflectance Spectroscopy as a Tool to Measure the Absorption Coefficient in Skin: South African Skin Phototypes." *Photochemistry and Photobiology* 89.1 (2013): 227-33.

Kawaguchi, F., *et al.* "Liposome-Encapsulated Hemoglobin Improves Tumor Oxygenation as Detected by near-Infrared Spectroscopy in Colon Carcinoma in Mice." *Artificial Organs* 41.4 (2017): 327-35.

Kondepati, V.R., *et al.* "Recent Applications of near-Infrared Spectroscopy in Cancer Diagnosis and Therapy." *Analytical and Bioanalytical Chemistry* 390.1 (2008): 125-39.

Kwong, T.C., *et al.* "Differentiation of Tumor Vasculature Heterogeneity Levels in Small Animals Based on Total Hemoglobin Concentration Using Magnetic Resonance-Guided Diffuse Optical Tomography in Vivo." *Applied Optics* 55.21 (2016): 5479-87.

Leary, S., *et al. Avma Guidelines for the Euthanasia of Animals: 2013 Edition*. Ed. Association, American Veterinary Medical. 2013.Web.

Lee, J., *et al.* "Hemoglobin Measurement Patterns During Noninvasive Diffuse Optical Spectroscopy Monitoring of Hypovolemic Shock and Fluid Replacement." *Journal of Biomedical Optics* 12.2 (2007).

Leung, H.M., and A.F. Gmitro. "Fluorescence and Reflectance Spectral Imaging System for a Murine Mammary Window Chamber Model." *Biomedical Optics Express* 6.8 (2015): 2887-94.

Lim, L., *et al.* "Probe Pressure Effects on Human Skin Diffuse Reflectance and Fluorescence Spectroscopy Measurements." *Journal of Biomedical Optics* 16.1 (2011): 011012.

Mourant, J.R., *et al.* "Hemoglobin Parameters from Diffuse Reflectance Data." *Jouornal of Biomedical Optics* 19.3 (2014).

Oshita, S., *et al.* "Correlation between Arterial Blood Pressure and Oxygenation in Tetralogy of Fallot." *Journal of Cardiothoracic and Vascular Anesthesia* 3.5 (1989): 597-600.

Palmer, G.M., *et al.* "Quantitative Diffuse Reflectance and Fluorescence Spectroscopy: A Tool to Monitor Tumor Physiology in Vivo." *Journal of Biomedical Optics* 14.2 (2009).

Prahl, S. "Optical Absorption of Hemoglobin." *Optical Properties Spectra*. Oregon Medical Laser Center 2015. Web.

Prahl, S.A. "Optical Absorption of Hemoglobin." 1999. Web. January 1, 2016.

Quincy Brown, J., *et al.* "Quantitative Optical Spectroscopy: A Robust Tool for Direct Measurement of Breast Cancer Vascular Oxygenation and Total Hemoglobin Content in Vivo." *Cancer Research* 69.7 (2009): 2919-26.

Rajaram, N., *et al.* "Design and Validation of a Clinical Instrument for Spectral Diagnosis of Cutaneous Malignancy." *Applied Optics* 49.2 (2010): 142-52.

Rajaram, N., *et al.* "Non-Invasive, Simultaneous Quantification of Vascular Oxygenation and Glucose Uptake in Tissue." *PLoS One* 10.1 (2015).

Rich, L.J., and M. Seshadri. "Photoacoustic Monitoring of Tumor and Normal Tissue Response to Radiation." *Scientific Reports* 6.21237 (2016).

Sabino, C.P., *et al.* "The Optical Properties of Mouse Skin in the Visible and near Infrared Spectral Regions." *Journal of Photochemistry and Photobiology B* 160 (2016): 72-78.

Schaafsma, B.E., *et al.* "Optical Mammography Using Diffuse Optical Spectroscopy for Monitoring Tumor Response to Neoadjuvant Chemotherapy in Women with Locally Advanced Breast Cancer." *Clinical Cancer Research* 21.3 (2015): 577-84.

Sikora, M., *et al.* "Repeated Restraint Stress Produces Acute and Chronic Changes in Hemodynamic Parameters in Rats." *Stress* 19.6 (2016): 621-9.

Sircan-Kucuksayan, A., *et al.* "Diffuse Reflectance Spectroscopy for the Measurement of Tissue Oxygen Saturation." *Physiological Measurement* 36.12 (2015): 2461-9.

Spliethoff, J.W., *et al.* "Monitoring of Tumor Response to Cisplatin Using Optical Spectroscopy." *Translational Oncology* 7.2 (2014): 230-9.

Szczesny, G., *et al.* "Long-Term Anaesthesia Using Inhalatory Isoflurane in Different Strains of Mice—the Haemodynamic Effects." *Laboratory Animals* 38.1 (2004): 64-9.

Teng, Y., *et al.* "Non-Invasive Measurement and Validation of Tissue Oxygen Saturation Covered with Overlying Tissues." *ScienceDirect* 18 (2008): 1083-8.

Thal, S.C., and N. Plesnila. "Non-Invasive Intraoperative Monitoring of Blood Pressure and Arterial Pco2 During Surgical Anesthesia in Mice." *Journal of Neuroscience Methods* 159.2 (2007): 261-7.

Thong, P., *et al.* "Early Assessment of Tumor Response to Photodynamic Therapy Using Combined Diffuse Optical and Diffuse Correlation Spectroscopy to Predict Treatment Outcome." *Oncotarget* 8.12 (2017): 19902-13.

Turley, R.S., *et al.* "Bevacizumab-Induced Alterations in Vascular Permeability and Drug Delivery: A Novel Approach to Augment Regional Chemotherapy for in-Transit Melanoma." *Clinical Cancer Research* 18.12 (2012): 3328-39.

Ueda, S., *et al.* "Baseline Tumor Oxygen Saturation Correlates with a Pathologic Complete Response in Breast Cancer Patients Undergoing Neoadjuvant Chemotherapy." *Cancer Research* 72.17 (2013): 4318-28.

Valdés, P.A., *et al.* "Optical Technologies for Intraoperative Neurosurgical Guidance." *Neurosurgical Focus* 40.3 (2016).

Vishwanath, K., *et al.* "Quantitative Optical Spectroscopy Can Identify Long-Term Local Tumor Control in Irradiated Murine Head and Neck Xenografts." *Journal of Biomedical Optics* 14.5 (2009).

Vishwanath, K., *et al.* "Using Optical Spectroscopy to Longitudinally Monitor Physiological Changes within Solid Tumors." *Neoplasia* 11.9 (2009): 889-900.

Wang, H.W., *et al.* "Diffuse Reflectance Spectroscopy Detects Increased Hemoglobin Concentration and Decreased Oxygenation During Colon Carcinogenesis from Normal to Malignant Tumors " *Optics Express* 17.4 (2009): 825-34.

Wang, H.W., *et al.* "Treatment-Induced Changes in Tumor Oxygenation Predict Photodynamic Therapy Outcome." *Cancer Research* 64 (2004): 7553-61.

Westerkamp, A.C., *et al.* "Diffuse Reflectance Spectroscopy Accurately Quantifies Various Degrees of Liver Steatosis in Murine Models of Fatty Liver Disease." *Journal of Translational Medicine* 13.309 (2015).

Yu, B., *et al.* "Diffuse Reflectance Spectroscopy of Epithelial Tissue with a Smart Fiber-Optic Probe." *Biomedical Optics Express* 5.3 (2014): 675-89.

Yu, Y.H., *et al.* "Prediction of Neoadjuvant Chemotherapy Response Using Diffuse Optical Spectroscopy in Breast Cancer." *Clinical and Translational Oncology* (2017).

Zhao, X., *et al.* "Arterial Pressure Monitoring in Mice." *Current Protocols in Mouse Biology* 1 (2011): 105-22.

Chapter 6 (Specific Aim 3): Quantification of subcutaneous murine colon carcinoma tumors in response to chemotherapy and macrophage-targeted immunotherapy measured using diffuse reflectance spectroscopy

6.1 Introduction

Colorectal cancer (CRC) is the fourth most common cancer in the United States, accounting for 140,000 new cases and 50,000 deaths in 2018 (Siegel *et al.*, 2018). Until recently, patients with locally advanced CRC (high-risk stage II and stage III tumors) were treated via surgery followed by postoperative (adjuvant) chemotherapy. Adjuvant chemotherapy was given to ensure remaining cancer cells at tumor margins were eliminated after surgery (Jeon *et al.*, 2011; Wolmark *et al.*, 1999; de Gramont *et al.*, 2000; Andre *et al.*, 2003). Patients with stage IV CRC may also receive chemotherapy, but only for palliative, rather than curative, measures (Ronnekleiv-Kelly *et al.*, 2011). For early stage CRC patients, treatment options include polypectomy or local excision without chemotherapy or radiotherapy. Polypectomy is the removal of polyps during diagnostic colonoscopy (Horiuchi *et al.*, 2014), whereas local excision is the removal of small tumors and a portion of healthy surrounding tissue during colonoscopy (Althumairi *et al.*, 2015).

In recent years, the addition of preoperative (neoadjuvant) chemotherapy for locally advanced CRC has become clinically accepted in recent years after success in esophageal(2002) and gastric cancers (Cunningham *et al.*, 2006), and a series of clinical studies by the Fluoropyrimidine, Oxaliplatin and Targeted-Receptor pre-Operative Therapy (FOxTROT) Collaborative Group (Group, 2012). The goals of neoadjuvant chemotherapy include achieving complete eradication of cancer cells or pathological complete response (pCR) prior to surgery,

reducing intraoperative tumor cell shedding during surgery, and decreasing local recurrence rates (Van Cutsem *et al.*, 2013; Zhou *et al.*, 2013; Ludmir *et al.*, 2017). In a feasibility phase trial by the FOxTROT Collaborative Group, 150 patients with locally advanced CRC were given a combination of chemotherapy drugs either in the neoadjuvant or adjuvant setting. Patients receiving neoadjuvant chemotherapy experienced significant tumor downstaging and regression, and the FOxTROT Collaborative Group is currently conducting a further Phase III trial (Group, 2012).

At present, in locally advanced colon cancer, neoadjuvant chemotherapy is generally given to patients in 2-12 two-week cycles over 4-24 weeks (Cercek *et al.*, 2014). After assessing tumor therapeutic response after 4-6 cycles of neoadjuvant chemotherapy using techniques such as endorectal ultrasound (Cercek *et al.*, 2014), CT, PET-CT, or MRI (or a combination of these techniques), patients with locally advanced disease either receive additional neoadjuvant chemotherapy cycles or proceed to surgery. Surgery is followed by 9-12 two-week cycles of adjuvant chemotherapy over 18-24 weeks (Zhou *et al.*, 2013; Cheeseman *et al.*, 2008; Habr-Gama *et al.*, 2010). In both the neoadjuvant and adjuvant settings, the current chemotherapy regimen is FOLFOX, which is a combination of 5-fluorouracil (5-FU), leucovorin and oxaliplatin (Jeon *et al.*, 2011; Carrato, 2008). Variations of this type of chemotherapy have been a fixture in colorectal cancer treatment since the 1960's and have been optimized since (Sharp *et al.*, 1962; Nadler *et al.*, 1964).

Although there has been a steady reduction in CRC incidence and mortality since the 1970's, primarily attributed to reduction in preventable risk factors, advances in early detection (Miles *et al.*, 2015), nationwide screening initiatives (Siegel *et al.*, 2018; Levin, 2016; Bénard *et al.*, 2018; Issa *et al.*, 2017), and continued optimization of neoadjuvant and adjuvant

chemotherapy regimens (Zhou *et al.*, 2013), current treatment standards and management of CRC remains problematic (Van Cutsem *et al.*, 2013). Problems with standard CRC treatment include low 5-year survival rate (~10%) for patients presenting with metastatic CRC (mCRC) (Lynch *et al.*, 2016), non-specificity for the genetic and biological heterogeneity of CRC (Blanco-Calvo *et al.*, 2015), potential for multi-year treatment (Van Cutsem *et al.*, 2013), high recurrence rates (30-40%) of locally advanced disease even after successful therapy and curative surgery (A. S. Walker *et al.*, 2014), and chemoresistance (He *et al.*, 2017; Hammond *et al.*, 2016; Zhang *et al.*, 2017). Therefore, investigators are exploring new therapeutic techniques to overcome these barriers. One broad technique that has gained clinical traction is immunotherapy.

Immunotherapy is an emerging technique to treat CRC by stimulating or enhancing a patient's immune system to combat cancer cells without the cytotoxic drawbacks of chemotherapy (Boland *et al.*, 2017). Current immunotherapy techniques for CRC treatment include monoclonal antibody therapy, adoptive cell transfer (ACT) therapy, cancer vaccines and cell therapy (Lynch *et al.*, 2016). Among the many types of immunotherapy strategies, monoclonal antibody therapy has gained the most clinical traction for treating CRC in recent years (Noguchi *et al.*, 2013). This systematic review discusses current monoclonal antibody immunotherapy, which is divided into antibodies targeting either immune checkpoints or cytokines. Treatments discussed are either approved by the U.S. Food and Drug Administration (FDA), in clinical trials in humans, or in pre-clinical trials in animals. Finally, this review discusses emerging methods (optical and non-optical) to monitor tumor response to immunotherapy treatments in CRC patients.

6.2 Immune checkpoints in colorectal cancer

Immune checkpoints are any set of ligand-mediated inhibitory pathways that keep the

immune system in check and maintain homeostasis by regulating the duration and amplitude of immune responses (Pardoll, 2012; Lee *et al.*, 2016). Several immune checkpoints have been used as immunotherapeutic targets in CRC, including cytotoxic T-lymphocyte antigen-4 (CTLA4), programmed cell death protein-1 (PD-1), programmed cell death ligand-1 (PD-L1), tumor necrosis factor receptor (TNRF) superfamily member 9 (TNFRSF9 or CD137), and TNFRSF7 (or CD27) (Pardoll, 2012; Lynch *et al.*, 2016). Table 1 lists these CRC immune checkpoints that have been targeted by immunotherapy drugs and whether they are immunosuppressive or illicit a positive immune response.

Table 1. Immune checkpoints targeted for immunotherapy in colorectal cancer

Immune response	Immune checkpoint
Positive (anti-tumor)	CD28/B7
	CD137/CD137L
	CD27/CD70
Suppressive (pro-tumor)	CTLA4/B7
	PD-1/PD-L1

6.2.1 CTLA4

CTLA4, and its homolog, CD28, are cell surface receptors found on $CD4^+$ cells (helper T-cells) and $CD8^+$ cells (cytotoxic T-cells) (Lynch *et al.*, 2016). The ligands for CTLA4 and CD28 are the B7 proteins, B7-1 (CD80) and B7-2 (CD86), which are produced by antigen presenting cells (APCs) (Lynch *et al.*, 2016). B7 ligands are upregulated and presented on the cell surface by APCs when the APCs encounter and acquire non-self-antigens (Buchbinder *et al.*, 2016). When T-cells detect B7, along with major histocompatibility complex loaded with cognate peptide, competitive binding ensues between CD28/B7 and CTLA4/B7 to maintain T-cell homeostasis. CD28/B7 binding initiates immune stimulation by increasing T-cell proliferation whereas CTLA4/B7 binding initiates immunosuppression by competitively reducing signaling of the CD28/B7 complex (Beyersdorf *et al.*, 2015; Seidel *et al.*, 2018). Then, CTLA4 reduces the probability of future CD28/B7 binding by removing B7 proteins from the

APC surface via trans-endocytosis (Qureshi *et al.*, 2011). Thus, CTLA4/B7 interaction is involved in immune tolerance and immunosuppression, a hallmark of cancer (Passardi *et al.*, 2017). Monoclonal antibodies targeting and blocking the CTLA4 immune checkpoint pathway results in increased CD28/B7-dependent clonal expansion of T-cells and has shown promising clinical benefits (Sun *et al.*, 2016).

6.2.2 PD-1

PD-1 is a well-studied immune checkpoint, with its primary function to suppress the immune response to regulate tolerance and autoimmunity (Riley, 2009; Valentini *et al.*, 2018; Keir *et al.*, 2006). PD-1 is a cell surface receptor found on $CD4^+$ cells, $CD8^+$ cells, B-cells, natural killer (NK) cells, myeloid-derived cells, and macrophages (Valentini *et al.*, 2018; Sundar *et al.*, 2015). The primary function of PD-1 is to suppress the immune response (Riley, 2009). The ligands for PD-1 are the B7 proteins, B7-H1 (PD-L1) and B7-DC (PD-L2). PD-L2 is produced by APCs. PD-L1 is expressed by T-cells, B-cells, dendritic cells (DCs), and macrophages and is upregulated by many pro-tumor cytokines such as IL-4, IL-10 VEGF, and TNF-α produced by infiltrating immune cells (Riley, 2009; Wang *et al.*, 2017; Dong *et al.*, 2017; Sundar *et al.*, 2015). Additionally, PD-L1 is directly expressed by many types of cancer cell, including CRC and is associated with poor prognosis (O'Neil *et al.*, 2017). PD-1/PD-L1 binding results in T-cell apoptosis and reduced IL-2 (an anti-tumor cytokine) production (Valentini *et al.*, 2018). Thus, PD-1 and PD-L1 are active targets in CRC immunotherapy research with the goal of introducing monoclonal antibodies to block PD-1/PD-L1 binding and improve the anti-tumor immune response (Lynch *et al.*, 2016).

6.2.3 CD137

CD137 is a cell surface receptor expressed on activated T-cells, NK cells, and DCs (Segal *et al.*, 2017). Its primary ligand is CD137L which is expressed on APCs including DCs, activated B-cells, and macrophages. Binding of CD137L to CD137 promotes an immune response through T-cell activation and proliferation (Wang *et al.*, 2008). Thus, CD137/CD137L binding promotes polarization towards an anti-tumor environment. A study by Dimberg et al. showed a significantly lower CD137L concentration in CRC tissue compared to normal tissue., but similar concentrations of CD137 (Dimberg *et al.*, 2006).

6.2.4 CD27

CD27 is part of the TNFR family cell surface receptor expressed on NK cells, B-cells, and naïve $CD4^+$ and $CD8^+$ cells. After activation, T-cells upregulate CD27. Its ligand is CD70, which is expressed, after activation, by activated DCs, B-cells, T-cells, and NK cells.(van de Ven *et al.*, 2015) CD27/CD70 binding results in proliferation of $CD4^+$ and $CD8^+$ cells, promoting an anti-tumor environment. Therefore, agonistic antibodies for CD27, antibodies that target and activate receptor, have been developed to enhance this response and are currently in clinical trials for CRC (van de Ven *et al.*, 2015).

6.3 Immune checkpoint inhibition immunotherapy

6.3.1 FDA-approved drugs

FDA-approved CRC immunotherapy drugs for immune checkpoint inhibition include Nivolumab and Pembrolizumab.

Nivolumab is an immunoglobulin immune checkpoint inhibitor that binds to PD-1 receptors, blocking PD-1 activation and resulting in T-cell activation and immune response (Sundar *et al.*, 2015). Nivolumab was granted accelerated approval by the FDA in 2017

following an ongoing, multicenter Phase II trial (NCT02060188) (Overman *et al.*, 2017), funded by Bristol-Myers Squibb, that indicated Nivolumab was effective for CRC patients with deficient DNA mismatch repair (dMMR)/microsatellite instability high (MSI-H) disease (Smith *et al.*, 2018). dMMR/MSI-H CRC makes up approximately 12-15% of cases and is phenotypically characterized by a high quantify of tumor infiltrating lymphocytes (TILs), prevalence in the right side of the colon (proximal colon), and poor differentiation (Kawakami *et al.*, 2015). The approval of Nivolumab was particularly important since standard FOLFOX-based chemotherapy has limited benefit for dMMR/MSI-H CRC patients (Kawakami *et al.*, 2015). There are currently 39 ongoing clinical trials further exploring Nivolumab as either stand alone or combinatorial treatment for CRC.

Pembrolizumab is an IgG4-k monoclonal antibody that inhibits PD-1 binding with PD-L1 and PD-L2. This results in an upregulated immune response against CRC cells (O'Neil *et al.*, 2017). Pembrolizumab was granted accelerated approval by the FDA in 2017 as a second-line treatment for either unresectable, dMMR, or MSI-H CRC following multiple Phase II and III clinical trials (Diaz *et al.*, 2017; Le *et al.*, 2016). There are currently 52 ongoing clinical trials further exploring Pembrolizumab as either stand alone or combinatorial treatment for CRC.

6.3.2 Clinical studies

Immune checkpoint immunotherapy drugs for CRC that are currently undergoing clinical trials include Urelumab, Varlilumab, and Ipilimumab.

Urelumab is a monoclonal antibody that targets CD137 and activates CD137-expressing T-cells and NK cells, resulting in a positive immune response against cancer cells. Urelumab was developed by Bristol-Myers Squibb and is undergoing a Phase I/II clinical trial (NCT01471210) for melanoma, B-cell non-Hodgkin’s lymphoma, and solid tumors, including 10 patients with

CRC. The objectives for this ongoing study include safety, tolerability, pharmacokinetics, and immunogenicity (Segal *et al.*, 2017).

Varlilumab is an agonistic (activating) anti-CD27 monoclonal antibody that binds to CD27, mimicking the CD70 ligand, and eliciting proliferation of $CD4^+$ and $CD8^+$ cells. Following a Phase I study with 10 CRC tumors (Burris *et al.*, 2017), Varlilumab is currently undergoing a Phase II clinical trial (NCT02335918) in combination with the FDA-approved Nivolumab for several types of solid tumors, including CRC. The primary outcome measure is the objective response rate (ORR).

Ipilimumab is a receptor antagonistic for CTLA4 (Selby *et al.*, 2016) and was FDA approved in 2011 for treating melanoma (Specenier, 2016). Ipilimumab is currently undergoing multiple Phase I and Phase II clinical trials (12 active trials) for CRC (Toh *et al.*, 2016), including microsatellite-stable (MSS), mCRC (NCT03271047), and dMMR/MSI-H CRC (NCT03350126), with no published results yet at the time of this writing.

Additionally, a major area of clinical research in CRC is combinatorial therapy using one or more FDA-approved drugs. For example, there are currently 37 active clinical trials using FDA-approved Pembrolizumab in combination with experimental drugs or other FDA-approved drugs to treat CRC.

6.3.3 Pre-clinical studies

In a subcutaneous allograft model of murine CRC, mice were treated with a combination of anti-mouse CTLA4, and the chemotherapy agents ixabepilone, paclitaxel, gemcitabine, or etoposide (Jure-Kunkel *et al.*, 2013). CRC allografts showed reduced tumor growth rate in mice treated with anti-mouse CTLA4 alone, and further reduction in growth rate in combination treatment groups. 50% and 70% of mice displayed complete tumor regression after treatment

with anti-CTLA4 and either ixabepilone or paclitaxel, respectively. Additionally, activated T-cells in the TME significantly increased in response to therapy (Jure-Kunkel *et al.*, 2013). Although immune checkpoint inhibition was successful in this subcutaneous murine model of CRC, some groups prefer to implement orthotopic models since they better represent the tumor immune environment.

Zhao et al. established an orthotopic mouse model for CRC using endoscopy-guided microinjection of CT26 cells into the colon wall, and compared this to standard subcutaneous allograft models of CRC (Zhao *et al.*, 2017). Mice were treated with a combination of immune checkpoint inhibitors, anti-mouse PD1 and anti-mouse CLTA4, 1 day after tumor implantation. They found that orthotopic models were more sensitive to this checkpoint inhibition compared to subcutaneous tumor models; in fact, tumors failed to grow in treated orthotopic models, while tumor growth only slowed in subcutaneous models, confirming an earlier study by Leach et al (Leach *et al.*, 1996). Although subcutaneous models are easier to establish and represent a "worst-case scenario" in that the TME is highly immunosuppressive, orthotopic CRC mouse models better represent the human TME based on infiltration of immune cells (Zhao *et al.*, 2017).

6.3.4 Conclusion

Immune checkpoint inhibition is a promising approach for CRC treatment (Jenkins *et al.*, 2018), with several FDA-approved drugs already on the market and many more in clinical trials. Although immune checkpoint inhibition has shown success in treating CRC, the biggest challenge for investigators is identifying which patients may or not respond before treatment initiation (Jenkins *et al.*, 2018) and overcoming tumor cell resistance to this immunotherapy (Lee *et al.*, 2016). Jenkins et al. provides a comprehensive review of tumor cell resistance to immune

checkpoint inhibition (Jenkins *et al.*, 2018). This heterogeneous patient response to immune checkpoint inhibition is a strikingly similar problem to identifying responders vs. non-responders for standard first-line neoadjuvant chemotherapy in CRC (Tsuji *et al.*, 2012). The current state-of-the-art is to biopsy the tumor during colonoscopy and determine expression levels of markers such as a PD-L1 using immunohistochemistry (IHC). Patients overexpressing the target biomarker, such as PD-LI, are considered the best candidates for that immunotherapy (Patel *et al.*, 2015). In the future, investigators are looking into identifying other biomarkers and personalized gene-expression signatures to identify candidates most likely to respond to immune checkpoint inhibition (B. Li *et al.*, 2017; Tsuji *et al.*, 2012; Dunne *et al.*, 2017; Guinney *et al.*, 2015; Kather *et al.*, 2018).

6.4 Cytokines in colorectal cancer

Cytokines are small cell-signaling proteins, produced by immune cells (Akdis *et al.*, 2016), that are involved in myriad pathways in CRC (West *et al.*, 2015). Chemokines, members of a family of cytokines able to induce cellular chemotaxis, are also involved in CRC pathways (Itatani *et al.*, 2016). Thus, cytokines and chemokines, and their receptors, make attractive targets for CRC therapy, although pre-clinical and clinical research currently lags other discussed CRC immunotherapy techniques (Lynch *et al.*, 2016; Akram *et al.*, 2016). Development of cytokine-targeted immunotherapy can potentially be used as stand-alone treatment or, more likely, combinatorial treatment with either chemotherapy, radiotherapy, or other immunotherapy techniques to normalize the CRC tumor microenvironment (TME) (Klampfer, 2011).

Multiple immune cells in the TME release cytokines and chemokines including tumor-associated macrophages (TAMs), monocytes, neutrophils, cancer-associated fibroblasts (CAFs), dendritic cells, T-cells, NK cells, myeloid-derived suppressor cells (MDSCs), and mast cells

(Lynch *et al.*, 2016; Mager *et al.*, 2016). Table 1 shows an up-to-date snapshot of cytokines and chemokines involved in CRC, many of whose roles are under active investigation. Included in this table are interleukins and growth factors, which are types of cytokines (Itatani *et al.*, 2016; Mager *et al.*, 2016; Landskron *et al.*, 2014; Klampfer, 2011; Ohlsson *et al.*, 2016; Setrerrahmane *et al.*, 2017; Allen *et al.*, 2018; Manzat Saplacan *et al.*, 2017; Yuan *et al.*, 2015; Mira *et al.*, 2017; Wang *et al.*, 2016; Liu *et al.*, 2016). Chemokines and cytokines not listed may represent a research gap with regards to CRC. Several of these cytokines and chemokines have gained traction as effective immunotherapy targets for the treatment of CRC.

Table 2. Cytokines and chemokines involved in human CRC pathogenesis

	Interleukins		Growth Factors		Chemokines	
Pro-Tumor	IL-1β IL-4 IL-6 IL-8 IL-11	IL-17 IL-17A IL-22 IL-23 IL-33	VEGF TNF-α EGF HGF	FGF PDGF CSF1	CXCL1 CXCL2 CXCL5 CXCL8 CXCL12	CCL2 CCL15 CCL20 CX3CL1
Dual Role/ Controversial	IL-1 IL-9	IL-10 IL-21	TGF-β TGF-β1	TNF CSF2	CXLC9 CXCL17 CXCL10	CCL5 CCL21 CCL24
Anti-Tumor	IL-2 IL-12 IL-15	IL-17F IL-18	IFN-γ		CCL3 CCL4	CCL19

6.5 Cytokine-targeted immunotherapy

6.5.1 FDA-approved drugs

All current FDA-approved cytokine-targeted immunotherapy drugs for CRC either target vascular endothelial growth factor (VEGF), VEGF receptor (VEGFR), or epidermal growth factor (EGF) receptors (EGFR). Cytokine-targeted immunotherapy drugs targeting either VEGF or VEGFR include bevacizumab, aflibercept, and regorafenib. Drugs targeting EGRF include cetuximab and panitumumab. All five FDA-approved drugs primarily benefit mCRC patients, although many clinical trials are ongoing for other CRC subtypes in both neoadjuvant and adjuvant settings.

6.5.2 Anti-vascular endothelial growth factors (anti-VEGFs)

Bevacizumab is a monoclonal antibody VEGF-inhibitor, preventing tumor blood vessel growth. The FDA approved bevacizumab as first line treatment for mCRC in 2004 (Strickler *et al.*, 2012) and in 2006 for second-line treatment of mCRC in combination with FOLFOX4 (Cohen *et al.*, 2007), making it the first anti-VEGF drug for CRC. A phase III clinical trial by Eastern Cooperative Oncology Group (ECOG) tested bevacizumab's efficacy and safety in combination with FOLFOX4 (Giantonio *et al.*, 2007). Patients treated with the combination therapy saw a longer median overall survival of 12.9 months with a 22.2% response rate compared to an overall survival of 10.8 months and an 8.6% response rate for patients receiving standalone FOLFOX4 chemotherapy (Giantonio *et al.*, 2007). Additional studies have confirmed the benefits of bevacizumab in treating mCRC (Hurwitz *et al.*, 2004; Saltz *et al.*, 2008; Ilic *et al.*, 2016).

Six years later in 2012, aflibercept, an antiangiogenic VEGF inhibitor, was approved by the FDA as a second-line treatment for mCRC in combination with the FOLFIRI chemotherapy regimen (leucovorin calcium, fluorouracil, and irinotecan hydrochloride) (Stewart *et al.*, 2012). Aflibercept is meant to be used for mCRC patients who failed to respond to previous FOLFOX-based chemotherapy (Van Cutsem *et al.*, 2012). In a phase III clinical trial (NCT00561470), the addition of aflibercept to FOLFIRI improved overall median survival from 12.1 to 13.5 months and progression-free survival from 4.7 to 6.9 months for stage IV mCRC patients (Van Cutsem *et al.*, 2012). In an update to this same phase III clinical trial, published in 2014, investigators found that overall survival increased by 0.8 months for mCRC patients with no prior bevacizumab treatment and 1.5 months for patients with no prior bevacizumab treatment (Tabernero *et al.*, 2014).

Regorafenib is an oral kinase inhibitor that targets oncogenic and angiogenic kinases to inhibit VEGFR activation, resulting in inhibition of tumor cell proliferation and angiogenesis (Dhillon, 2018). In 2012, the FDA granted approval for regorafenib to treat mCRC patients based on the CORRECT phase III clinical trial (NCT01103323). The median overall survival was 6.4 months in patients who received regorafenib monotherapy and 5.0 months in patients who received placebo. This study did, however, note adverse events in 93% of regorafenib-treated patients (Grothey *et al.*, 2013). In 2015, the CONCUR phase III clinical (NCT01584830) became the second trial to demonstrate overall survival benefits of regorafenib (8.8 months) vs. placebo (6.3 months) for mCRC patients (Li *et al.*, 2015).

6.5.3 Anti-epidermal growth factor receptors (anti-EGFRs)

In 2004, the FDA approved the monoclonal antibody, cetuximab, to treat advanced CRC patients who have failed standard chemotherapy (Saltz *et al.*, 2007; Mesia *et al.*, 2016; Hubbard *et al.*, 2013; Cunningham *et al.*, 2004). Cetuximab targets the ligand-binding domain of EGFR, resulting in reduced tumor growth and differentiation (Lenz, 2007). A clinical trial conducted by the North Central Cancer Treatment Group (NCCTG) N0147 compared the use of FOLFIRI with and without cetuximab in stage III CRC patients with both wild-type KRAS and mutant KRAS. Combination treatment with cetuximab plus FOLFIRI showed that 5-year disease-free survival, overall survival, and time to recurrence in patients with wild-type KRAS improved from 64% to 83% (p=0.10), 76% to 87% (p=0.21), and 67% to 86% (p=0.09), respectively (Huang *et al.*, 2014). Based in part on this study, as well as the CEGOG trial,(Ocvirk *et al.*, 2010) the FDA approved cetuximab in 2012 as a first-line treatment in $KRAS^{-}/EGFR^{+}$ mCRC in combination with FOLFIRI.

In 2017, panitumumab, another EGFR inhibitor, was granted FDA approval to treat mCRC patients with wild-type RAS as a first-line treatment in combination with FOLFOX (Douillard *et al.*, 2014; Price *et al.*, 2014). A study by Leone et al. used panitumumab in combination with capecitabine plus oxaliplatin (XELOX) to study its efficacy in patients with liver only mCRC. Out of the forty-six patients, the objective response rate was 54% with two patients with complete responses and 23 with a partial response. The medial overall survival rate was observed to be 21.9 months with a median progression-free survival of 8.5 months. Overall, the combination of panitumumab with XELOX (P-XELOX) yield a high response for patients with liver only mCRC (Leone *et al.*, 2013).

6.5.4 Clinical studies

One pathway currently being studied is the IL-6/STAT3 pathway. IL-6 binds to the IL-6 receptor (IL-6R), activating the signal transducer and activator of transcription 3 (STAT3) signaling pathway. This pathway induces transcription of various genes involved in differentiation and proliferation and reduces $CD4^+$ immune responses (Kitamura *et al.*, 2017). In a phase I/II clinical trial, CRC patients with advanced solid tumors, along with other cancer patients, received IL-6 neutralizing antibodies at increasing doses. Although investigators showed increased tumor hemoglobin in response to IL-6 neutralization, colorectal tumors had a low response rate measured via RECIST criteria. Although this study indicate that stand-alone IL-6 inhibition was inadequate for advanced CRC solid tumors, investigation of IL-6/STAT3 modulation is worth further exploration (Angevin *et al.*, 2014).

IL-10 is also being explored as an immunotherapy target. A future spotlight will be on a collaborative industry-academic phase I clinical trial, which has enrolled 350 patients with various solid tumors including CRC. In this study, AM0010, a PEGylated human IL-10, will be

self-administered subcutaneously in four monthly cycles, either as a monotherapy or with chemotherapy, to test the safety, toxicity, maximum tolerated dose, anti-tumor activity, and pharmacokinetics of this cytokine-targeted immunotherapy (Bauer *et al.*, 2014). In addition to IL pathways, nimotuzumab (NCT00972465), a monoclonal antibody targeting EGFR, and imalumab (NCT02448810), a monoclonal antibody targeting macrophage inhibitory factor (MIF), are undergoing clinical trials for CRC (Xu *et al.*, 2016; Mahalingam *et al.*, 2015).

6.5.5 Pre-clinical studies

The effect of modulating cytokines and chemokines in the human CRC TME is mostly hypothesized and has not yet been rigorously tested in clinical trials. Most CRC cytokine modulation research, besides the aforementioned interleukins, exists in the pre-clinical and basic biology realms.

Two chemokine receptors, C-C chemokine receptor type 1 (CCR1) and chemokine C-C motif receptor-like 2 (CCRL2), have been recently implicated in aiding in liver metastasis (Akram *et al.*, 2016), the primary cause of death for CRC patients (Valderrama-Trevino *et al.*, 2017). Ligands for CCR1 and CCRL2 are the chemokines CCL3, CCL5, CCL7, and CCL23, and are suggested as potential targets for cytokine-targeted immunotherapy (Akram *et al.*, 2016). CCL2 and CCL24 were also found to be highly elevated (>100-fold) in CRC liver metastases compared to healthy adjacent liver tissue, implying that these chemokines could also be targets for cytokine-targeted immunotherapy (Cheadle *et al.*, 2007).

Chemokine neutralization, especially of CCL2, has gained traction in both CRC and non-CRC studies of mice (Chun *et al.*, 2015). CRC, independent of subtype (Lim *et al.*, 2016; Becht *et al.*, 2016), recruits circulating monocytes via chemotaxis to the TME primarily through the release of CCL2, also known as monocyte chemoattractant protein-1 (MCP1), a highly

elevated chemokine in CRC (Marech *et al.*, 2016; Lim *et al.*, 2016; Becht *et al.*, 2016; Chun *et al.*, 2015). In the TME, monocytes differentiate into TAMs, partially as a result of CCL2. TAMs, the most abundant immune cell in the TME, also have the most substantial and pervasive effect of any immune cell in the TME (Erreni *et al.*, 2011; Allavena *et al.*, 2008; Chen *et al.*, 2005; Marech *et al.*, 2016). In CRC, TAMs have been shown to have both anti-tumor and pro-tumor functions, depending on whether they are polarized more towards an M1 (classical) or M2 (alternative) phenotype and their physical location within the tumor (Marech *et al.*, 2016). Pro-tumor functions of alternatively activated M2-polarized TAMs include tumor growth, angiogenesis, immunosuppression, and matrix remodeling (Liu *et al.*, 2015). Additionally, CCL2 binding to its receptor, CCR2, on endothelial cells increases vascular permeability and metastatic risk (Lim *et al.*, 2016). Thus, targeting CCL2 to reduce M2-polarized, pro-tumor TAMs is an attractive ongoing cytokine-targeted immunotherapy strategy in pre-clinical settings. In mouse models, CCL2 blockade has resulted in reduced neovascularization and tumor size of orthotopic colon tumors in Balb/c mice, suggesting that CCL2 may be a promising target for treating colitis-associated colon cancer (Popivanova *et al.*, 2009). Additionally, anti-CCL2 immunotherapy prolonged survival in C57BL/6 mice with GL261 glioma (Zhu *et al.*, 2011), and reduced TAM infiltration in FVB/N mice with MCF-7 breast cancer (Svensson *et al.*, 2015). However, few cytokine-targeted immunotherapy techniques have been tested for efficacy in human CRC, although oral N-acetyl-L-cysteine (NAC) co-administered with mesalamine, an anti-inflammatory, has benefitted ulcerative colitis patients, attributed in part to the down-regulation of CCL2 and IL-8 (Guijarro *et al.*, 2008). In summary, many investigators now believe that CCL2-neutralizing immunotherapy will play an important role in early-stage CRC treatment in future clinical studies (Chun *et al.*, 2015).

Besides CCL2, other cytokines and chemokines have been explored. For example, blocking the pro-angiogenic and pro-tumor chemokine ligand 1 (CXCL1), whose gene is also known as growth-regulated oncogene-α, using an anti-CXCL1 neutralizing antibody inhibited tumor growth and angiogenesis in a mouse xenograft model of human CRC (Wang *et al.*, 2006). Blockade of IL-1β reduced tumor formation in a mouse model of colitis-associated CRC (Wang *et al.*, 2014). TNF blockade reduced CRC carcinogenesis in an AOM/DSS (colitis-induced) mouse model (Popivanova *et al.*, 2008). On the other hand, the addition of IL-15, which has anti-tumor effects in CRC (Table 3), was shown to increase the therapeutic effects of anti-PD-L1 and anti-CTLA4 treatment in a CT26 colon carcinoma mouse model (Yu *et al.*, 2010). The overarching current hypothesis is that cytokine-targeted immunotherapy, especially the blockade of pro-tumor cytokines in CRC, may enhance tumor therapeutic response in CRC tumors treated with chemotherapy, radiation, or approved checkpoint inhibitors (Mager *et al.*, 2016).

6.5.6 Conclusion

Cytokine-targeted immunotherapy research lags other discussed CRC immunotherapy methods, although further investigation is justified. The biggest challenge facing this type of therapy is determining which pharmacokinetic and pharmacodynamic variables are important navigating cytokine pathways while decreasing systemic toxicity in CRC patients. Additionally, the FDA approved drugs, cetuximab and panitumumab are ineffective in patients with RAS mutations (~23% of stage IV CRC patients). (sirisena, the pattern of KRAS mutations in metastatic, bmc res notes) Overall, cytokine therapies will likely be most effective in combination with other immunotherapies or chemo- and/or radiotherapy (Lynch *et al.*, 2016).

6.6 Assessing tumor therapeutic response

In addition to new CRC therapies being investigated, an important branch of CRC research is development of clinically-translatable methods to rapidly assess whether a therapy regimen is effective on a per patient basis (Berger *et al.*, 2017; Roblyer *et al.*, 2011). Rapid assessment of therapy can prevent unnecessary chemotherapy in both responders and non-responders (Granata *et al.*, 2015). Currently, tumors are assessed based on the widely accepted Response Evaluation Criteria in Solid Tumors (RECIST) criteria, which grades tumors as, from most desirable to least desirable, complete responders, partial responders, stable disease, or progressive disease (Eisenhauer *et al.*, 2009; Wahl *et al.*, 2009; Chung *et al.*, 2012). The overall goal of assessing tumor therapeutic response is adjusting treatment if necessary, avoiding surgery and reducing morbidity (A.S. Walker *et al.*, 2014). The standards for monitoring tumor therapeutic response to neoadjuvant therapy (chemotherapy, radiation, and/or immunotherapy) using RECIST are digital rectal examination (DRE), rigid proctoscopy, biopsy, carcinoembryonic antigen (CEA) level, and a radiological technique such as CT (A.S. Walker *et al.*, 2014), PET-CT (Petersen *et al.*, 2014), MRI (Van Cutsem *et al.*, 2016), or Diffusion-Weighted (DW)-MRI (A.S. Walker *et al.*, 2014). However, following neoadjuvant treatment initiation, assessing tumor response does not occur for approximately two months (Habr-Gama *et al.*, 2010; Van Cutsem *et al.*, 2016). Additionally, for patients showing evidence of partial or complete response after these two months of neoadjuvant treatment, they must wait an additional 1-2 months for follow-up as part of the "Wait and Watch Protocol" (A.S. Walker *et al.*, 2014). Finally, studies have shown that current radiological techniques are insufficient to identify responders with positive predictive values less than 50% (Kekelidze *et al.*, 2013). However, several research groups are investigating optical and imaging methods to rapidly assess

therapeutic response on a scale of days or weeks, rather than months.

Optical methods to monitor CRC tumor therapeutic response use light to acquire relevant clinical information. Since the CRC screening, diagnostic, and, in some cases, therapeutic standard (in early CRC stages only) is colonoscopy, investigators are aiming to create minimally-invasive endoscopy-compatible techniques. Techniques currently being evaluated, mostly in pre-clinical laboratory settings, for use in CRC include nonlinear optical imaging, fluorescence-based endoscopy, and diffuse reflectance spectroscopy.

6.6.1 Nonlinear optical imaging

Nonlinear optical imaging has been used to image freshly resected advanced rectal adenocarcinoma sections of patients who had received neoadjuvant radiochemotherapy. This *ex vivo*, label-free imaging method combined second harmonic generation (SHG) and two-photon excited fluorescence (TPEF) and showed that SHG microscopy could determine degree of fibrosis post-neoadjuvant chemoradiotherapy (L. H. Li *et al.*, 2017). Therefore, this method could potentially direct ideal operating time. Although this study was performed *ex vivo*, future miniaturization of nonlinear optical microscopy techniques as an endoscopic method has important applications in early preoperative tumor evaluation and clinical disease management. In fact, miniaturization of similar techniques have been performed in *in vivo* rat colon tissue.

A flexible multiphoton microendoscope, with a 3 mm outer diameter and 4 cm rigid length, has recently been developed by investigators out of Cornell University. This multiphoton microendoscope, the first of its kind, uses a resonant-nonresonant raster scanner to acquire *en face* images of unstained rat colon tissue at a field-of-view of 115 μm x 115 μm (Brown *et al.*, 2012). Potential clinical advantages of this research include diagnostic optical biopsy and real-time histopathological assessment of CRC tumor response to neoadjuvant chemotherapy and

antibody immunotherapy.

6.6.2 Fluorescence-based endoscopy

Fluorescence-based endoscopy is a new approach imaging modality that integrates a colonoscopy with optical imaging. This technique is a "robust method for early detection of CRC owing to its intrinsic coupling of detection with the underlying molecular-level pathology of the disease". With the use of molecular imaging, this type of optical system can detect variations in tissues unlike other system that only detect changes in structure (Sakuma *et al.*, 2015).

In a study by Mitsunaga et al., they developed a "rapid fluorescent detection method" using a "topically applied enzymatically activatable probe (gGlu-HMRG)" to detect the γ-glutamyltranspeptidase (GGT) enzyme during a colonoscopy. Expression of GGT was higher in mouse models with CRC than those without. Five minutes after topical administration, gGlu-HMRG fluorescent lesions were detected using fluorescent microscopy. Based on these results, the use of gGlu-HMRG can improve detection of colitis-associated colon cancer (CAC) with a "higher target to background ratio" compared to conventional white light colonoscopy (Mitsunaga *et al.*, 2013).

In a human study by Watanabe et al., used the PINPOINT® Endoscopic Fluorescence Imaging System intraoperatively to identify tumor sites using indocyanine green during laparoscopic surgery. Using this system, surgeons saw a tumor visibility rate of 93.8%. No adverse effects were observed during these procedures. As a result, this study provided evidence that the PINPOINT® system was able to identify colorectal tumors without adverse effects (Watanabe *et al.*, 2017).

Fluorescence-based endoscopy techniques are not only used for tumor detection, but they can also monitor tumor response to various therapies. Sakuma et al., used fluorescence-based

endoscopic imaging to investigate TF-antigen detection in CRC tumors during chemotherapy. With the use of a nanobeacon and fluorescence labeled (FL) endoscopy signals, they found that the tumors were above the signal threshold indicating a cancerous abnormality. After chemotherapy treatment with 4-paclitaxel, no tumors were detected through FL endoscopy. Based on these results, this type of imaging modality can be used to observe tumor response during chemotherapy (Sakuma *et al.*, 2015).

6.6.3 Diffuse reflectance spectroscopy

Diffuse reflectance spectroscopy (DRS) is a non-invasive or minimally-invasive technique that uses a small probe to deliver broadband light to tissue and collect the diffusely reflected light with a spectrometer (G.J. Greening *et al.*, 2018; Greening *et al.*, 2016; Dadgar *et al.*, 2018). DRS can provide relevant clinical information such as total hemoglobin content, tissue oxygen saturation, oxy- and deoxyhemoglobin, lipid and water content, and tissue scattering properties, and can thus be applied to monitoring tumor response to therapy (G.J. Greening *et al.*, 2018; Spliethoff *et al.*, 2014).

DRS has recently been used in an *ex vivo* study of resected human colon tissue to differentiate tissue type with an overall accuracy of 95%. The investigators hope to eventually apply this technology in an *in vivo* setting for real-time guidance during CRC surgery (Baltussen *et al.*, 2017). DRS has also been integrated into a fiber-optic biopsy needle to assess functional tissue properties in an *in vivo* study of lung cancer patients (Spliethoff *et al.*, 2016). This same research group also used their DRS system to monitor tumor response to chemotherapy in a murine subcutaneous mammary tumor model. The investigators found that tumors showed an increase in lipid content and tissue oxygen saturation after just 2 days of treatment, and believe this technology can someday help optimize personalized cancer treatments (Spliethoff *et al.*,

2014). Next, Schols et al. used DRS in open colorectal surgery to detect mesenteric arteries in real-time to reduce interoperative risk of iatrogenic surgery (Schols *et al.*, 2015). One of primary limitations with optical methods, such as DRS, is poor light sampling into highly scattering tissues. However, it's been shown that, at the optical properties found in colorectal tissue (Carneiro *et al.*, 2018), DRS sampling depth is greater than 0.5 mm at 630 nm at source-detector separations (< 1 mm) compatible with the biopsy port of standard colonoscopes (G.J. Greening *et al.*, 2018).

As of yet, DRS applied to CRC is in its infancy; it has only been applied to monitor tumor therapeutic response to chemotherapy in mouse models, although investigators believe DRS technology can be used to quantify volumetric tumor perfusion in response to immunotherapies, which can eventually help guide clinicians in identifying potential responders and non-responders during early therapy (G.J. Greening *et al.*, 2018).

6.7 Introduction to study

Colorectal cancer (CRC) is estimated to account for 140,050 new cancer cases annually in the United States, making it the 4th most common cancer type overall (behind breast, lung, and prostate), and resulting in 50,630 annual deaths (Siegel *et al.*, 2016). Tumor stage is determined using the MRI-based tumor, node, and metastasis (TNM) Staging System, which guides CRC treatment (Ferrari *et al.*, 2015; Dienstmann *et al.*, 2017). Locally-advanced CRC (stages II-III), which account for approximately 20% of cases, describes cancer that has spread from the site of the primary tumor to surrounding tissue or lymph nodes, but has not metastasized (Landmann *et al.*, 2005; Ferrari *et al.*, 2015; Dienstmann *et al.*, 2017). The standard of treatment for locally-advanced CRC is neoadjuvant chemoradiotherapy (CRT) using 5-fluorouracil (5-FU), followed by total mesorectal excision (TME) surgery (Boland *et al.*, 2014). Following neoadjuvant CRT,

biopsies are examined to determine pathologic response. Ideally, patients will exhibit pathologic complete response (pCR), defined as the absence of residual cancer cells in histological examination, since achieving pCR reduces distal recurrence risk (Ferrari *et al.*, 2015). For example, the 5-year distal-metastases-free survival is significantly greater (89%) for patients achieving pCR compared to those who don't (75%). However, pCR is achieved in less than 30% of cases, resulting in distal recurrence rates of 25%, which is the primary cause of CRC-related death (Ferrari *et al.*, 2015). An emerging strategy known as immunotherapy, or immunomodulation therapy, has gained clinical momentum in recent years to aid neoadjuvant CRT in reducing pre-operative tumor burden and recurrence risk (Lynch *et al.*, 2016; Yuan *et al.*, 2015; Sanchez-Castanon *et al.*, 2016).

Immunotherapy in CRC is a broad neoadjuvant therapy approach, with most strategies aimed at modulating the host immune system to inhibit checkpoints of pro-tumor pathways to increase the tumor's sensitivity to chemotherapy (Lynch *et al.*, 2016). One specific immunotherapy strategy is the blockade of CCL2/MCP-1 (monocyte chemoattractant protein-1), an elevated cytokine during CRC progression which recruits monocytes to the tumor microenvironment (Chun *et al.*, 2015). Monocytes differentiate into tumor-associated macrophages (TAMs), which have pro-tumor functions in CRC (Erreni *et al.*, 2011; Li *et al.*, 2016; Guo *et al.*, 2016; Zhang *et al.*, 2016; Kaler *et al.*, 2009; Popovic *et al.*, 2007; Herbeuval *et al.*, 2004; Guo *et al.*, 2013; Zou *et al.*, 2017; Barbera-Guillem *et al.*, 2002), although some conflicting studies have reported anti-tumor functions of TAMs at tumor margins (Funada *et al.*, 2003; Sugita *et al.*, 2002; Forssell *et al.*, 2007; Zhou *et al.*, 2010). Pro-tumor functions of TAMs include direct secretion of angiogenic growth factors (GFs) leading to an increase in vascular endothelial growth factor (VEGF) (Burmeister *et al.*, 2017; Erreni *et al.*, 2011; Barbera-Guillem

et al., 2002), as well as ECM-degrading matrix metalloproteases (MMPs) which allow for tumor expansion and release of ECM-sequestered angiogenic GFs (Erreni *et al.*, 2011; Guo *et al.*, 2013). Thus, CCL2-mediated TAM infiltration is linked to increased inflammation, angiogenesis and tumorigenesis (Guo *et al.*, 2016; McClellan *et al.*, 2012). Additionally, CCL2 has been linked to other pro-tumor/immunosuppressive functions such as inducing myeloid-derived suppressor cell (MDSC) accumulation and promoting STAT-mediated T-cell suppression of polymorphonuclear (PMN)-MDSCs (Chun *et al.*, 2015). Therefore, anti-CCL2 immunotherapy has the potential to reduce tumor burden and recurrence risk.

Recent research has explored CCL2 blockade as an immunotherapy strategy in mouse models of various cancers. Popivanova et al. showed that CCL2 blockade reduced neovascularization and colon tumor size in Balb/c mice (Popivanova *et al.*, 2009). Zhu et al. showed that administration of anti-CCL2 in combination with temozolomide chemotherapy to C57BL/6 mice with GL261 glioma significantly prolonged survival (Zhu *et al.*, 2011). Svensson et al. demonstrated that CCL2 blockade in FVB/N mice with MCF-7 breast cancer decreased TAM infiltration and reduced estrogen-stimulated cancer growth (Svensson *et al.*, 2015). Kirk et al. showed that delivering anti-CCL2 in combination with docetaxel chemotherapy to SCID mice with C4-2B prostate adenocarcinoma inhibited tumor progression (Kirk *et al.*, 2013). Finally, Zhang et al. demonstrated that TAMs directly contribute to 5-FU chemoresistance in CRC, and concluded that TAM pathways (such as CCL2) were potential immunotherapy targets to increase efficacy of 5-FU chemotherapy (Zhang *et al.*, 2016). However, no studies have combined chemotherapy with CCL2 blockade in a mouse model of CRC.

The present study uses anti-CCL2 as a neoadjuvant immunotherapy strategy (Singh *et al.*, 2014), combined with standard 5-FU chemotherapy, in Balb/c mice with subcutaneous CT26

colon carcinoma allografts. Female Balb/c mice were injected with CT26 tumor cells in the left flank, and then given the control vehicle, isotype control antibody, anti-CCL2 immunotherapy, 5-FU chemotherapy, or combination therapy (five groups). Combination therapy was expected to alter CRC tumor perfusion due to effects of chemotherapy and CCL2-mediated effects on TAMs. Therefore, during the study, tumor perfusion was longitudinally measured via non-invasive diffuse reflectance spectroscopy (DRS), a non-invasive, probe-based technique which can quantify perfusion metrics such as tissue hemoglobin content (THC), tissue oxygen saturation (StO_2), and oxyhemoglobin (HbO_2), as well as the reduced scattering coefficient (μ_s'). DRS measurements were then correlated to end-point immunohistochemistry (IHC) analysis of hypoxia (pimonidazole), angiogenesis (CD105), tumor-associated macrophage (TAM) polarization (CD80, CD68, and CD206), proliferation (Ki67), and apoptosis (CC3). This study forms two major hypotheses: 1) CCL2 blockade in the tumor microenvironment as an immunotherapy strategy will increase sensitivity of CT26 tumors to 5-FU chemotherapy, quantified by tumor size, DRS perfusion metrics, IHC analysis, and CCL2 ELISA and 2) changes in tumor perfusion will precede measurable changes in tumor size. Confirmation of these hypotheses may indicate that DRS could potentially be used to monitor early tumor response to combinatorial immunotherapy and chemotherapy.

6.8 Materials and methods

6.9.1 Cell line

CT26 (ATCC®, CRL-2638™), a murine colon carcinoma cell line derived from the Balb/c mouse strain, was maintained in Roswell Park Memorial Institute (RPMI)-1640 medium (ATCC®, 30-2001™) supplemented with 10% fetal bovine serum (ATCC®, 30-2020), 1% antibiotic antimycotic solution (Sigma-Alrich, A5955-100ML), and 0.2% amphotericin

B/gentamicin (Thermo Fisher Scientific, R015010). CT26 cells were brought to the third passage (P3).

6.8.2 Animal model

The study was approved by the University of Arkansas Institutional Animal Care and Use Committee (IACUC #17072). Eight-week-old female Balb/c mice (n=125) were obtained from The Jackson Laboratory (Bar Harbor, ME, USA). Upon arrival to the Small Animal Facility at the University of Arkansas, mice were housed in groups of three at 23°C ± 1°C and 50% ± 10% humidity with a 12:12-hour light-dark cycle and had access to water and standard rodent food ad libitum. Mice were weighed daily upon arrival. Mice underwent 2 weeks of environmental acclimation, including daily handling (2 minutes per mouse) for stress adaptation to future handling during measurements. After 2 weeks, the hair on the injection site (left flank) of the now 10-week old Balb/c mice was removed via shaving and Nair™, and then cleaned, prior to injection with CT26 cells. Then, the mice underwent subcutaneous (SQ) injection of $1x10^5$ CT26 cells into the shaved and depilated left flank (Figure 1). Tumors were allowed to grow until they reached 75 ± 5 mm^3 (day 0), as measured via $V = (L \cdot W^2)/2$, which took an average of 14 ± 4 days.

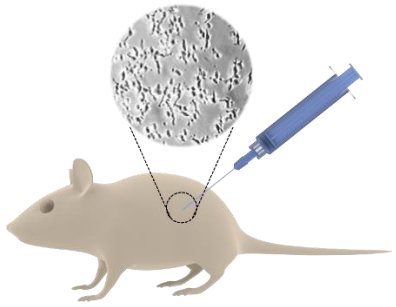

Figure 1. Balb/c mice were the model organization for the studies presented here. CT26 cells were injected subcutaneously into the left flank to form colon tumor allografts. *Image of mouse and syringe sourced from the Library of Science Medical Figures, which are free to share, copy, and redistribute under Create Commons License BY-NC-SA 4.0.*

6.8.3 Anesthesia protocol

Mice were anesthetized with isoflurane (ISO) and 1 L/min oxygen (O_2) for various procedures throughout the study. Procedures included shaving and nairing of left flank, SQ CT26 cell injection, intraperitoneal (IP) injection of therapy/control, IP injection of pimonidazole, and tumor vivisection and euthanasia. Mice undergoing DRS measurements were not anesthetized since isoflurane can depress StO_2 and HbO_2 (Gage J. Greening *et al.*, 2018). All mice were physically maintained on a water-based warming pad (Stryker, #TP700) controlled by a warming pump (Stryker, Kalamazoo, MI, #TP12E) set to 42°C. Table 3 lists the isoflurane concentration for induction and maintenance for each procedure as well as approximate anesthesia time for each.

Table 3. Isoflurane anesthesia specifications per procedure with 1 L/min O_2

Procedure	[ISO] (Induction)	Time (min)	[ISO] (Maintenance)	Time (min)
SQ Injection of CT26 Cells	3.0%	2	2.0%	2
IP Injection of Therapy/Control	3.0%	2	2.0%	1
IP Injection of Pimonidazole	2.0%	2	2.0%	1
Tumor Vivisection and Euthanasia	4.0%	1	4.0%	5

6.8.4 Control and experimental groups

For analysis of early tumor therapeutic response, 62 female Balb/c mice were randomly divided into five groups of up to 15 mice once the CT26-tumors reached 75 mm^3 (Figure 2). The first group (control, n=15) received saline injections for vehicle control. The second group (n=13) received isotype antibody control. The third group (n=10) received immunotherapy but no chemotherapy. The fourth group (n=12) received chemotherapy but no immunotherapy. The fifth group (n=12) received a combination of both chemotherapy and immunotherapy. For each group of mice, mice were euthanized on either day 1 (n=5), day 3 (n=5), or day 7 (n=5) for end-point immunohistochemical and ELISA analysis. Table 4 and Figure 2 shows the breakdown of control and experimental groups.

Table 4. Breakdown of control and experimental groups

Group	Sample Size	Saline Control	Isotype Control	Anti-CCL2 Immunotherapy	5-FU Chemotherapy
1	15	X			
2	13		X		
3	10			X	
4	11				X
5	12			X	X
Total	61				

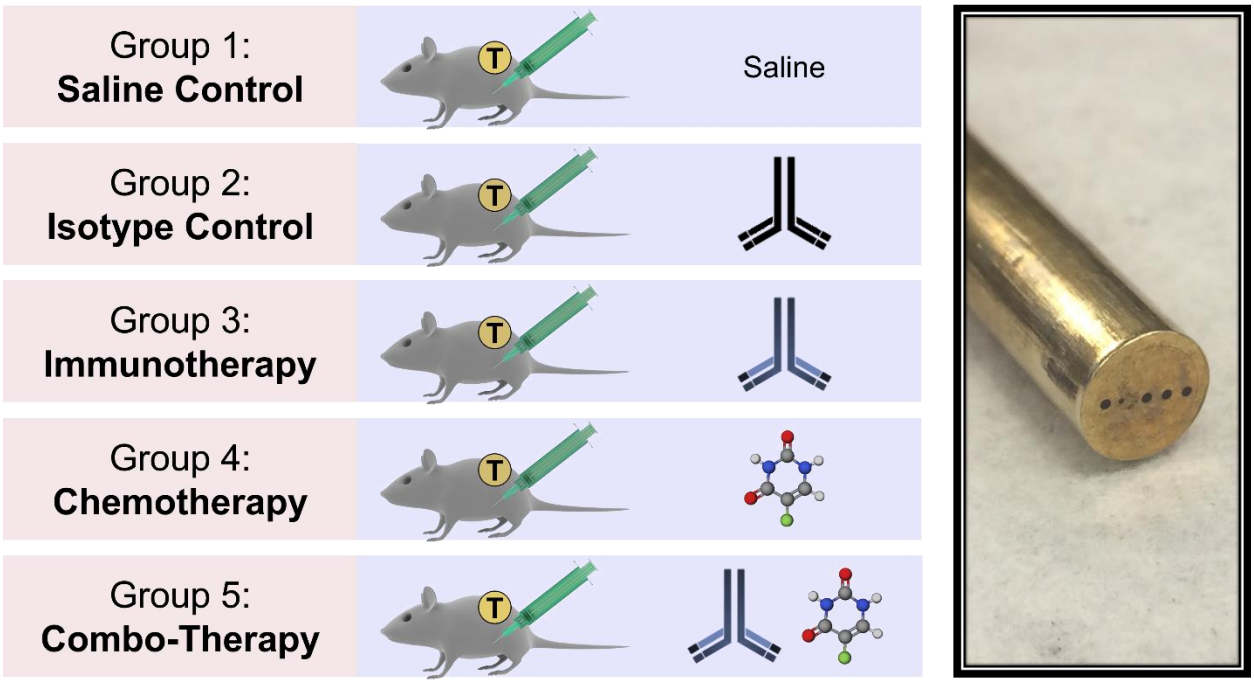

Figure 2. For analysis of early tumor therapeutic response, 62 female Balb/c mice were randomly divided into five groups of up to 15 mice once the CT26-tumors reached 75 mm^3. Then, mice were subject to either one of five therapies: saline control, isotype (antibody) control, anti-CCL2 antibody immunotherapy, 5-FU chemotherapy, or a combination of immunotherapy and chemotherapy. Tumors then underwent daily DRS measurements. *Image of mouse, syringe and antibodies sourced from the Library of Science Medical Figures, which are free to share, copy, and redistribute under Create Commons License BY-NC-SA 4.0.*

6.8.5 Chemotherapy

5-Fluorouracil (5-FU), purchased from Sigma-Aldrich (St. Louis, MO, USA), is an antitumor chemotherapy agent that induces p53-dependent apoptosis and decreases proliferation (Balmer *et al.*, 2014). 5-FU powder (Sigma Aldrich, #F6627-10G) was diluted in DMSO at 40 mg/mL and stored at -20°C for a maximum of two months before injection. A second dilution of

5-FU/DMSO was then created in sterile saline (VWR, Radnor, PA, #89167-774) to bring the 5-FU concentration to 20 mg/mL. On the day of 5-FU injection, aliquots of 20 mg/mL 5-FU+DMSO in sterile saline were further diluted to 3 mg/mL 5-FU/saline in sterile microcentrifuge tubes (VWR, #20170-038), and brought to 37.3°C. Using a 28G insulin syringe (VWR, #BD329410), mice in groups 4 and 5 received daily intraperitoneal (IP) administration of 5-FU at a concentration of 15 mg/kg/dose (Wu *et al.*, 2016) starting at day 0 (tumor = 75 mm^3) until day 6 (140 mg/kg/week). This resulted in an average injection of 300 µg 5-FU in 100 µL vehicle, based on average mouse weight of approximately 20 g at time of injection.

A daily 5-FU dosage of 15 mg/kg was chosen to approximate average 5-FU dosage in humans. In the standard FOLFOX6 CRC chemotherapy treatment, 5-FU is given every 2 weeks at 2.4 g/m^2, and repeated in 4-6 courses in the neoadjuvant settings (Fang *et al.*, 2016). The average body surface area (BSA) in cancer patients is approximately 1.8 m^2 (Sacco *et al.*, 2010) and the average body weight of adult humans in North America is approximately 80 kg (Walpole *et al.*, 2012). Based on FDA guidelines, to convert human dose (mg/m^2) to mouse dose (mg/kg), the human dose is multiplied by 12.3 and divided by 3 (Nair *et al.*, 2016). Based on this information, 5-FU dose in mice can be solved as shown in Equation 1.

$$\left[\frac{2{,}400\ mg\ 5FU}{m^2 \cdot 2\ week\ dose}\right] \cdot \left[\frac{1.8\ m^2}{80\ kg}\right] \cdot \left[\frac{12.3}{3}\right] \cdot \left[\frac{One\ 2\ week\ dose}{14\ daily\ doses}\right] = 15.8\ \frac{mg\ 5FU}{kg} \qquad (1)$$

6.8.6 Immunotherapy

Anti-CCL2 (2H5), purchased from Bio X Cell (West Lebanon, NH, USA), is a monoclonal antibody that neutralizes murine CCL2 (monocyte chemoattractant protein-1), and has been demonstrated as an *in vivo* immunotherapy agent (Singh *et al.*, 2014; Palframan *et al.*, 2001). Anti-CCL2 (Bio X Cell, 2H5, #BE0185) was shipped at 7.4 mg/mL in PBS and stored at 4°C for a maximum of two months before injection. On the day of anti-CCL2 injection, aliquots

of 7.4 mg/mL anti-CCL2/PBS solution were diluted with sterile saline (VWR, #89167-774) to 1 mg/mL anti-CCL2/saline in sterile microcentrifuge tubes (VWR, #20170-038), and brought to 37.3°C. Using a 28G insulin syringe (VWR, #BD329410), mice in groups 3 and 5 received IP administration of anti-CCL2 at a concentration of 4.0 mg/kg/dose (Zhu *et al.*, 2011; Singh *et al.*, 2014) given every other day on days 0 (tumor = 75 mm^3), 2, 4, and 6 (16 mg/kg/week). This resulted in an average injection of 80 µg anti-CCL2 (2H5) in 100 µL vehicle, based on average mouse weight of 20 g at time of injection. The isotype control antibody, polyclonal Armenian hamster IgG (Bio X Cell, #BE0091), was made in an identical manner to anti-CCL2 and mice were dosed at the same concentration, schedule, and method.

6.8.7 Diffuse reflectance spectroscopy

The purpose of DRS was to non-invasively quantify *in vivo* THC, StO_2, and HbO_2, and μ_s' of subcutaneous CT26 tumors (Figure 3).

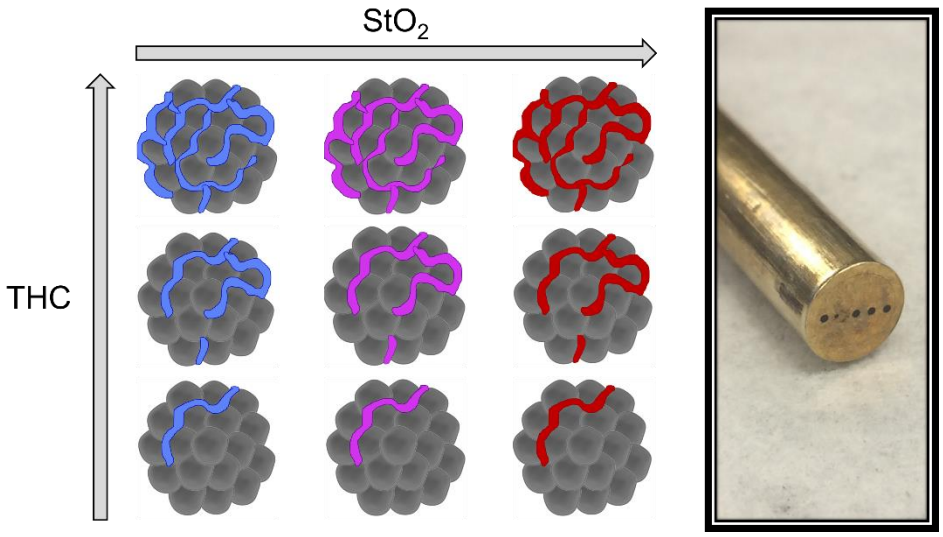

Figure 3. DRS can quantify StO_2, THC, and μ_s'. The HbO_2 can be calculated by the product of StO_2 and THC. Thus, DRS can be used as a metric to determine low (blue) vs. high (red) oxygenation and low (less vessels) vs. high (more vessels) hemoglobin content. *Image of cell sourced from the Library of Science Medical Figures by somersault1824, which are free to share, copy, and redistribute under Create Commons License BY-NC-SA 4.0.*

6.8.7.1 Diffuse reflectance spectroscopy probe

This probe was described in Chapter 4. The DRS probe (FiberTech Optica, Kitchener, ON, Canada) was 1.0 m in total length, with the split position located 0.67 m from the common (distal) end. Five individual optical fibers (one source and four detectors) were integrated within the distal brass ferrule (6.35 mm diameter x 50 mm long). All fibers were arranged linearly in a slit line, resulting in source-detector separations (SDS) of 0.75, 2.00, 3.00, and 4.00 mm. Each optical fiber consisted of a high-OH silica core, a silica cladding, and polyimide jacket optimized for a wavelength range of 190-1200 nm, which exceeded the desired wavelength range of 450-750 nm used in this study. The source fiber, as well as the 2.00, 3.00, and 4.00 SDS fibers (FiberTech Optica, SUV400/440PI) consisted of a 400/440 ± µm ± 2% silica core/cladding with a 470 µm ± 5% polyimide jacket. The 0.75 mm SDS fiber (FiberTech Optica, SUV200/220PI) consisted of a 200/220 µm ± 2% silica core/cladding with a 245 µm ± 5% polyimide jacket.

These optical fibers were included to sample into the subcutaneous murine CT26 tumor at multiple sampling depths to quantify THC, StO_2, and HbO_2, and μ_s'.

Probe sheathing consisted of black PVC coated monocoil (4.8 mm OD, 0.67 length) at the common end and black PVC furcation tubing (3.0 mm OD, 0.33 length) for the individual legs originating at the breakout joint. The five individual optical fibers within the furcation tubing terminated at standard SMA connectors, reinforced with strain relief.

6.8.7.2 Diffuse reflectance spectroscopy instrumentation

A 20W tungsten-halogen lamp (Ocean Optics, HL-2000-HP) provided broadband light (360-2400 nm) to the 400 μm core source fiber. A spectrometer (Ocean Optics, FLAME-S) with a Sony ILX511B linear silicon CCD array (2,048 pixel elements) collected diffusely reflected light from the 2 and 3 mm SDSs. The spectrometer had a grating of 600 lines/mm and grating spectral range of 667 nm. Next, the spectrometer was fit with a 50 μm diameter laser cut slit within the round SMA connector (Ocean Optics, INTSMA-KIT), yielding a pixel resolution of 6.5 pixels. This resulted in an optical resolution of 2.1 nm, as calculated from Equation 2.

$$Optical\ Resolution\ (nm) = \left[\frac{Spectral\ Range\ (nm)}{Pixel\ Elements\ (pixels)}\right] \cdot [Pixel\ Res.\ (pixels)] \qquad (2)$$

6.8.7.3 Diffuse reflectance spectroscopy measurements

All mice (n=62) underwent DRS measurements starting at day 0 (tumor = 75 mm^3) prior to therapy or control. The hair on the skin at the tumor site was removed via shaving and Nair™, and then cleaned, 24 hours prior to the first DRS measurement. In this study, only the 3.00 mm SDS was used. The 3.00 mm SDS provided an optimal balance of signal-to-noise (> 15 dB), appropriate *in vivo* integration time (75 ms), and wavelength-dependent sampling depth (~1.3 to 2.1 mm).

In the early response groups (Table 2, n=75), DRS measurements were taken daily on days 0-7, whereas in the survival groups (Table 2, n=50), DRS measurements were taken on days 0-7, 10, 15, 20, and then in increments of 10 days thereafter until humane end-point euthanasia criteria. Additionally, a final DRS measurement was taken immediately prior to euthanasia in the survival groups.

In all cases, the DRS probe was placed on the tumor site such that the linear arrangement of optical fibers were collinear with the long axis of the tumor (cranial to caudal direction). Tumor sites for DRS measurements were kept consistent throughout the study by marking the skin with histopathology ink off the collinear axis. Data was acquired using custom LabVIEW software. The user placed the probe on the tumor site of non-anesthetized mice while spectra were collected via a foot pedal control. For each tumor, at least 10 DRS measurements were acquired at an integration time of 75 ms. Day-to-day fluctuations in light source intensity were controlled for by calibration with a Spectralon® 20% diffuse reflectance standard. Daily spectrometer dark noise was subtracted from each spectra.

Each DRS measurement resulted in a value for THC, StO_2, HbO_2, μ_s'(630 nm) and a chi-square (X^2) value. THC, StO_2, HbO_2, μ_s'(630 nm) were quantified by inputting raw DRS spectra into custom lookup-table (LUT)-based MATLAB software with *a priori* values for oxygenated and deoxygenated hemoglobin extinction coefficients (Prahl, 2015; Greening *et al.*, 2016; Greening *et al.*, 2015). The software performed an iterative model fit ($1x10^4$ iterations) to the raw DRS data to quantify THC, StO_2, HbO_2, μ_s'(630 nm). The X^2 value indicated goodness-of-fit between the model fit and raw DRS data; high X^2 values usually implied specular reflection due to user movement. Therefore, if X^2 of a spectra exceeded 10, data was discarded. THC, StO_2, HbO_2, and μ_s'(630 nm) values ($\geq$10) were averaged to yield a daily result. At the conclusion of

study (either after day 7 or at humane end-point euthanasia criteria), histopathology ink was used to indicate probe location and orientation for spatial correlation with IHC.

6.8.8 Diffuse reflectance spectroscopy and tumor volume statistics

The primary data set consisted of five metrics: tumor size, StO_2, THC, HbO_2, and μ_s' (630 nm), henceforth just referred to as μ_s', which are presented as raw scores and as normalized scores. Comparing raw scores allows seeing the range of values that should be expected for each metric. Comparing normalized scores allows us to see how metrics increase or decrease from each tumor's baseline measurement. The data set consisted of observations on 61 subjects divided between 5 treatments, as shown in Table 4. Each subject was assessed at Day 0 and subsequently for one, three, or seven successive days according to the third (approximately) of the sample to which the mouse had been assigned, respectively. On each of the days on which each subject was assessed, the assessments were expressed in 5 raw score metrics and in 5 normalized metrics. This resulted in a data set consisting of 16 subjects who were assessed only on the first day after the baseline, 23 who were assessed on each of the three days following the baseline, and 22 who were assessed on each of the seven days following the baseline. Three sets of analyses were conducted on these data. Each will be described below along with statistical procedures used to conduct the analyses.

6.8.8.1 Comparisons of days 1, 3, and 7 to Day 0 within treatment by metric

These analyses compared subjects' scores at Days 1, 3, and 7 to their scores at Day 0, within each of the 5 treatments. Since the scores at Day 0 and at each of the other 3 days referenced the identical subjects, a repeated measures ANOVA analysis was required. The normality of the residual error scores for the raw and normalized metrics was tested using the Shapiro-Wilk test. Due to the large sample size, the rule of thumb of .90 or higher for the

Shapiro-Wilk test statistic (*W*) was used as the indicator of adequate normality in the error distribution. The *W* for the error residuals exceeded .90 for both the raw and normalized scores in 8 of the 10 cases, as shown in Table 5. The *W* statistic for the residual for the normalized HbO_2 score was within .006 of .90, which is close enough to .90 to avert any concern about any problematic effect of its slight departure from normality.

Table 5. Breakdown of control and experimental groups

Error Measure	Shapiro-Wilk		
	Statistic	***df***	***p***
Residual for Tumor Size (Raw)	.925	296	<.001
Residual for StO_2 (Raw)	.992	296	.111
Residual for THC (Raw)	.992	296	.113
Residual for HbO_2 (Raw)	.988	296	.017
Residual for $\mu_{s'}$ (Raw)	.956	296	<.001
Residual for Tumor Size (Normalized)	.906	297	<.001
Residual for StO_2 (Normalized)	.934	297	<.001
Residual for THC (Normalized)	.913	297	<.001
Residual for HbO_2 (Normalized)	.894	297	<.001
Residual for $\mu_{s'}$ (Normalized)	.794	297	<.001

The Šídák post-hoc test was used to adjust for multiple comparisons. The Šídák post-hoc test is a conservative test (Kim, 2015) assumes independence of all measurements, meaning that measurements have no connection to other measurements chances of happening. The Šídák post-hoc test protects against type 1 errors but is sensitive to type 2 errors (Lee *et al.*, 2018). A type 1 error is the rejection of the null hypothesis (false positive) whereas a type 2 error is the failure to reject a false null hypothesis (false negative) (Banerjee *et al.*, 2009). In these experiments, it was imperative to protect against type 1 errors. Additionally, the Šídák post-hoc test was appropriate since we operated under the universal null hypothesis assumption that all tests would not be significant (Armstrong, 2014). The normalized μ_s' scores manifested a much larger departure from normality, necessitating the use of the nonparametric Wilcoxon Signed Rank test to assess the differences between Day 0 and Days 1, 3, and 7 within each of the 5 treatments.

6.8.8.2 Comparisons of treatments for days 1, 3, and 7, within metrics

These analyses compared subjects' scores between the 5 treatments at Days 1, 3, and 7, within each of the 5 metrics. Since the scores on each treatment and on each of the 3 days referenced the identical subjects, a repeated measures analysis methodology was required. Since the necessary pairwise comparisons were derived from the same repeated measures ANOVA as was used for the first set of comparisons described above, the residual error scores were identical, as were the results of the Shapiro-Wilk tests for departures from normality. Again, the Šídák post-hoc test was used to adjust for multiple comparisons. Additionally, the normalized μ_s' scores were the only ones that manifested a serious departure from normality, necessitating the use of the nonparametric Wilcoxon Signed Rank test, this time for comparing all pairs of treatments on the normalized metric 5 scores within Days 1, 3, and 7.

6.8.8.3 Correlations between normalized metrics within treatments

These analyses computed the Pearson product-moment correlations between each pair of normalized metric scores within each of the five treatments. Shapiro-Wilk tests for normality were conducted for scores on all five normalized metrics within each treatment. Correlations between any pair of metrics within a treatment where one or both of the metrics had Shapiro-Wilk values below .88 were recomputed using the nonparametric Spearman's rho correlation.

6.8.9 Immunohistochemistry

Mice from each of the five groups (Table 4) were further divided into three cohorts (up to n=5) based on end-point IHC analysis. Tumors were vivisected immediately prior to euthanasia via cervical dislocation on day 1, 3, or 7 for IHC analysis. Tumors were resected following the final DRS measurement.

Tumors were oriented within the cryomolds (VWR, #25608-916) such that the cutting face would be coplanar to the light path from the DRS measurements. The cryomold was filled with optimal cutting temperature (OCT, VWR, #25608-930) and flash frozen in isopentane (VWR, #AA19387-AP) chilled in liquid nitrogen at -75°C for 15 seconds. Tissue was then stored at -80°C until sectioning. Tumors were longitudinally sectioned on Superfrost® Plus microslides (VWR, #48311-703) in 5 μm sections using a cryostat (Leica, #CM1860) at -25°C, which were then stored permanently at -80°C. Tumor tissue was stained for hypoxia, TAM-polarization, proliferation, apoptosis, and hematoxylin and eosin (H&E).

6.8.9.1 Tumor-associated macrophages

Next, tumor sections were stained to quantify TAM count and M1-M2 polarization (Barros *et al.*, 2013). Tumors were stained for CD68 (pan-macrophage), CD80 (M1 TAM marker), and CD206 (M2 TAM marker) (Peng *et al.*, 2017). Cells were considered M1-polarized TAMs if they expressed both CD68 and CD80 and M2-polarized TAMs if they expressed both CD68 and CD206. Cells expressing all markers were considered non-polarized TAMs and cells stained with only CD80 or CD206 were not considered TAMs (Barros *et al.*, 2013). For each tumor, two 5 μm tissue sections were stained for TAM analysis.

Upon removal from -80°C, slides were fixed in 0°C acetone (VWR, #BDH1101-4LP) for 10 minutes. Slides were blocked with sterile, 4% goat serum, 0.5% bovine serum albumin (BSA) (Sigma-Aldrich, #A9647-10G), 0.1% NaN_3, 0.05% Triton-X, and 0.05% Tween-20 in PBS for 2 hours at room temperature. Tumor sections were then stained with a cocktail of anti-CD80 Brilliant Violet 421 (BioLegend, #104725), anti-CD68 Alexa Fluor 488 (BioLegend, #137012), and anti-CD206 Alexa Fluor 594 (BioLegend, #141726) at dilutions of 1:20, 1:100, and 1:125, respectively, and stored in a PBS-humidified incubator for 90 minutes at room temperature.

Slides were washed 3x with PBS-t between major steps. Slides were mounted with Fluoromount-G (VWR, #100241-847) and permanently stored at 4°C in the dark.

Slides were imaged with a upright microscope (Nikon, Eclipse Ni-U), 20X/0.50NA objective lens (Nikon, CFI Plan Fluor 20X), monochrome digital camera (Nikon, DS-Qi1Mc), and PC-based camera control unit (Nikon, DS-U3). The anti-CD80, anti-CD68, and anti-CD206 stains were imaged with DAPI (Chroma Technology, 49000), FITC (Chroma Technology, SP101), and Texas Red (Chroma Technology, 41004) filter sets, respectively, at an integration time of 100 ms and gain of 1x. For each tumor, two 5 μm thick tissue sections were stained. Five high-powered fields-of-view (0.21 x 0.15 mm) were taken for each of the two sections for a total of 10 TAM FOVs per tumor. Cells per FOV were counted based on a previously published protocol. All counts were made blinded to DRS data. Total immune cells were counted over the 10 FOVs to calculate TAM count and polarization. A more in-depth look at tumor-associated macrophages, including the precise staining procedure, is as follows:

6.9 Tumor-associated macrophages

Tumor-associated macrophages (TAMs) are the most abundant immune cells in the tumor microenvironment (TME) in most cancers (Noy and Pollard, 2014), and also have the most substantial and pervasive effect of any immune cell in the TME (Allavena *et al.*, 2008; Erreni *et al.*, 2011; Chen *et al.*, 2005; Marech *et al.*, 2016). TAMs have been shown to have both anti-tumor and pro-tumor functions, depending on whether they are polarized more towards an M1 (classical) or M2 (alternative) phenotype (Chen *et al.*, 2005), respectively, and their physical location within a tumor (Marech *et al.*, 2016). In reality, M1 and M2 TAMs are the extremes of a continuum of intermediate cells which may have both anti-tumor and pro-tumor functions. Broad anti-tumor functions of classically activated M1-polarized TAMs include inflammation and

immune response (Sugita *et al.*, 2002; Funada *et al.*, 2003; Zhou *et al.*, 2010). On the other hand, pro-tumor functions of alternatively activated M2-polarized TAMs include tumor growth, angiogenesis, immunosuppression, and matrix remodeling (Liu and Cao, 2015). In most cancers, TAMs are skewed more towards the pro-tumor M2-phenotype (Yang and Zhang, 2017); therefore, TAMs have gained clinical momentum as immunotherapy targets for cancer. Currently, there are over 30 clinical trials targeting TAMs; strategies include reducing monocyte recruitment to the tumor and reprogramming M2-TAMs to M1-TAMs. Yang and Zhang provide a comprehensive review of TAM immunotherapy strategies (Yang and Zhang, 2017). Still many other groups are actively investigating TAMs in the basic science and pre-clinical realms (Cassetta *et al.*, 2016; He *et al.*, 2017; Jarosz-Biej *et al.*, 2018; Suarez-Lopez *et al.*, 2018). However, TAMs in some cancers, like colorectal cancer (CRC), simultaneously have both detrimental and beneficial effects on the patient (Zhong *et al.*, 2018).

The dual-role of TAMs in CRC has yet to be fully understood. It has recently been shown that macrophages induce resistance to fluorouracil-based chemotherapy, and that this TAM-induced resistance may contribute to the poor chemotherapy response in some CRC patients (Zhang *et al.*, 2008; Zhang *et al.*, 2016). Currently, a gap in colon cancer research is how therapy affects TAMs in the colorectal TME, and, in turn, how altering TAM population and polarization affects tumor therapeutic response. Therefore, this immunohistochemistry staining protocol was developed to stain for TAMs in murine subcutaneous colon tumor allografts, although this protocol can be used for other murine tissue. In this article, Balb/c mice were subcutaneously injected in the left flank with CT26 murine colon carcinoma cells. Tumors grew until they reached 75 mm^3. Following three days of additional tumor growth, untreated tumors were dissected, flash-frozen in isopentane and liquid nitrogen, and stored at -80 °C until

cryosectioning, and then sectioned at a thickness of 5 μm. The scope of this article is on macrophage immunohistochemistry of murine tumors, not on the tumor model itself. Therefore, this protocol can be readily modified to stain any murine tissue in allograft, xenograft, or orthotopic tumor models.

This direct immunohistochemistry staining method uses three primary-conjugated macrophage antibodies: anti-CD68, anti-CD80, and anti-CD206. CD68 is a pan-macrophage surface marker (Gordon *et al.*, 2014), CD80 is a cell surface marker for M1-type macrophages (Zhou *et al*., 2017), and CD206 is a cell surface marker for M2-type macrophages (Kigerl *et al.*, 2009). CD68, CD80, and CD206 are markers for other cell types as well but were chosen such that ($CD68^+/CD80^+$)-cells were considered M1-TAMs, ($CD68^+/CD206^+$)-cells were considered M2-TAMs, and ($CD80^+/CD206^+$)-cells were considered dendritic cells (DCs). Cells expressing all macrophage surface markers were considered to have a mixed M1-M2 phenotype (Figure 4).

With this simple and reproducible method, we are able to accurately stain for M1 and M2 macrophages. To ensure long-term relevancy and usability of this protocol, this work also provides an easy-to-follow mathematical analysis of antibody concentrations so that readers can easily modify and optimize this protocol for their specific test system. This work is relevant for investigators developing and/or testing TAM-targeting cancer immunotherapies in mice.

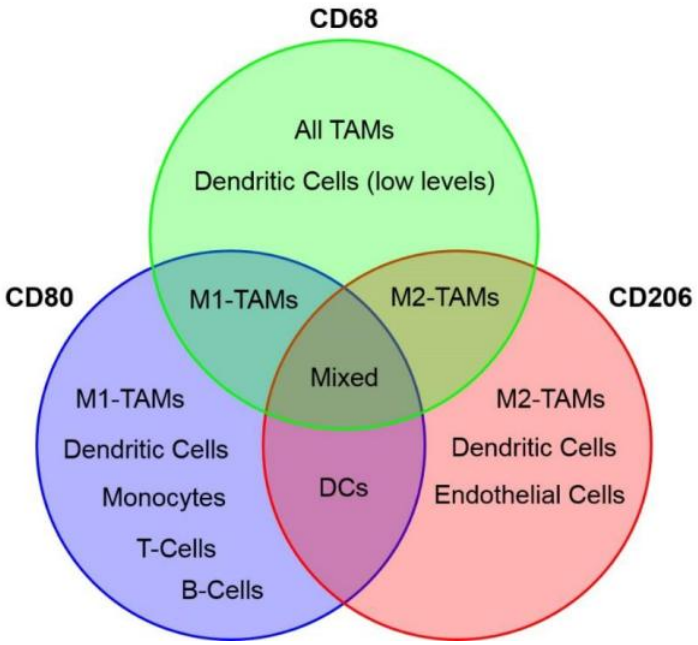

Figure 4. A double stain technique was used to distinguish M1- and M2-polarized macrophages. $CD68^+/CD80^+$ cells were considered M1 TAMs and $CD68^+/CD206^+$ cells were considered M2 TAMs. Additionally, $CD68^+/CD80^+/CD206^+$ TAMs were considered to have a mixed phenotype.

6.10.1 Materials and reagents

A. Consumables

1. Paper towel
2. Aluminum foil
3. Coverslip
4. 10 µl sterile universal Fit S^3 polymer pipette tips (VWR, catalog number: 89140-160)
5. 100 µl sterile universal Fit S^3 polymer pipette tips (VWR, catalog number: 89140-162)
6. 1,000 µl sterile universal Fit S^3 polymer pipette tips (VWR, catalog number: 89217-468)
7. SuperSpin™ microcentrifuge tubes (VWR, catalog number: 20170-038)
8. EasyDip™ slide staining rack (VWR, catalog number: CA87000-132)
9. Superfrost® plus micro slide (VWR, catalog number: 48311-703)
10. VistaVision™ cover glasses, No. 1, 22 x 50 mm (VWR, catalog number: 16004-314)

B. Animal

1. Balb/c mice (aged 10 weeks)

C. Antibodies

1. Brilliant Violet 421™ anti-mouse CD80 [stock solution concentration: 100 μg/ml, staining concentration: 5 μg/ml (1:20), storage temperature: 2-8 °C undiluted, shelf-life: ~3 years (lot-specific)] (BioLegend, catalog number: 104725)
2. Alexa Fluor® 488 anti-mouse CD68 [stock solution concentration: 500 μg/ml, staining concentration: 5 μg/ml (1:100), used at 5 μg/ml, storage temperature: 2-8 °C undiluted, shelf-life: ~3 years (lot-specific)]) (BioLegend, catalog number: 137012)
3. Alexa Fluor® 594 anti-mouse CD206 [stock solution concentration: 500 μg/ml, staining concentration: 4 μg/ml (1:125), storage temperature: 2-8 °C undiluted, shelf-life: ~3 years (lot-specific)] (BioLegend, catalog number: 141726)

D. Reagents

1. Acetone (storage temperature: -20 °C, shelf-life: 4 years) (VWR, catalog number: BDH1101-4LP)
2. Phosphate-buffered saline (PBS), 1x without Calcium and Magnesium (storage temperature: 2-8 °C, shelf-life: 3 years) (VWR, catalog number: 45000-446)
3. Triton™ X-100 (storage temperature: room temperature, shelf-life: 2 years) (Sigma Aldrich, catalog number: X100-100ML)
4. Tween® 20 (storage temperature: room temperature, shelf-life: 3 years) (Sigma-Aldrich, catalog number: P9416-100mL)
5. Goat serum (storage temperature: -20 °C, shelf-life: 2 years) (Sigma-Aldrich, catalog number: G9023-10ML)

6. Sodium azide (NaN_3) (storage temperature: room temperature) (Sigma-Aldrich, catalog number: S2002-25G)

   Note: This compound is toxic (GHS06), a health hazard (GHS08), and an environmental hazard (GHS09). It should be handled with protective clothing in a certified fume hood and disposed of at an approved waste disposal site per institutional regulations
7. Bovine serum albumin (BSA) (storage temperature: 2-8 °C, shelf-life: 1 year) (Sigma-Aldrich, catalog number: A8806-5G)
8. Universal antibody dilution buffer (storage temperature: room temperature, shelf-life: 2 years) (Sigma-Aldrich, catalog number: U3510-100ML)
9. Isopentane (storage temperature: room temperature, shelf-life: 2 years) (VWR, catalog number: AA19387-AP)
10. Liquid nitrogen (Airgas, catalog number: NI NF180LT22)
11. Quick-dry nail polish
12. Fluoromount-G® slide mounting medium (storage temperature: room temperature, shelf-life: 15 months) (VWR, catalog number: 100241-874)
13. Macrophage antibody cocktail (see Recipes)
14. Blocking solution (see Recipes)
15. PBS-T washing solution (see Recipes)

6.9.2 Equipment

1. Tweezer
2. 0.5-10 µl ergonomic high performance single-channel mechanical pipettor (VWR, catalog number: 89079-962)
3. 10-100 µl ergonomic high performance single-channel mechanical pipettor (VWR,

catalog number: 89079-968)

4. 100-1,000 µl ergonomic high performance single-channel mechanical pipettor (VWR, catalog number 89079-974)
5. Linear pipettor stand (VWR, catalog number: 40000-272)
6. 80-Place storage system (VWR, catalog number: 30128-282)
7. EasyDip™ slide staining jars, white (VWR, catalog number: CA87000-126)
8. Low temperature organic liquid filled thermometer (VWR, catalog number: 89062-908)
9. SlideTray™ 20 slide humidity chamber with black lid (VWR, catalog number: 102097-504)
10. Laboratory bench and table protector with leakproof and moisture barrier (VWR, catalog number: 89126-790)
11. -20 °C and -80 °C freezers
12. Water bath (VWR, catalog number: 89501-464)
13. Upright microscope (Nikon, model: Eclipse Ni-U)
14. Monochrome digital camera (Nikon, model: DS-Qi1Mc)
15. PC-based camera control unit (Nikon, model: DS-U3)
16. SOLA Light Engine® fluorescent lamp (Lumencor, catalog number: SOLA SM 6-LCR-SB)
17. DAPI filter set (Chroma Technology, catalog number: 49000)
18. FITC filter set (Chroma Technology, catalog number: SP101)
19. Texas red filter set (Chroma Technology, catalog number: 41004)
20. Objective lens, 20x/0.50NA (Nikon, catalog number: CFI Plan Fluor 20X)

6.9.3 Software

1. NIS-Elements F Ver4.60.00 for 64bit edition (Nikon, https://www.nikoninstruments.com/Products/Software)
2. ImageJ bundled with 64-bit Java 1.8.0_112 (National Institutes of Health and the Laboratory for Optical Computational Instrumentation, https://imagej.nih.gov/ij/download.html)

6.9.4 Procedure

The scope of this section is on macrophage immunohistochemistry of murine tumors, not on the tumor model itself; however, the tumor model is briefly described here. Five Balb/c mice (aged 10 weeks) were subcutaneously injected with 1 x 10^5 CT26 cells (passage 3) in sterile saline into the left flank until the tumors reached a volume of 75 mm^3 (Greening *et al.*, 2018a and 2018b). Three days after reaching this volume, the five untreated mice were euthanized, and the tumor was dissected for TAM analysis (Figure 5). This staining and imaging procedure works best with flash frozen tumors. Therefore, upon dissection, tumors were placed in a cryomold and covered completely in optimal cutting temperature (OCT). The cryomold with OCT and tumor was flash frozen in isopentane chilled in liquid nitrogen at -75 °C to -77 °C for at least 15 s and stored permanently in -80 °C until sectioning. The tumor was sectioned at 5 μm, although sections up to 10 μm are acceptable. Once sectioned, slides were stored for up to one month at -80 °C before staining. All antibody solutions and stained slides were handled in darkness.

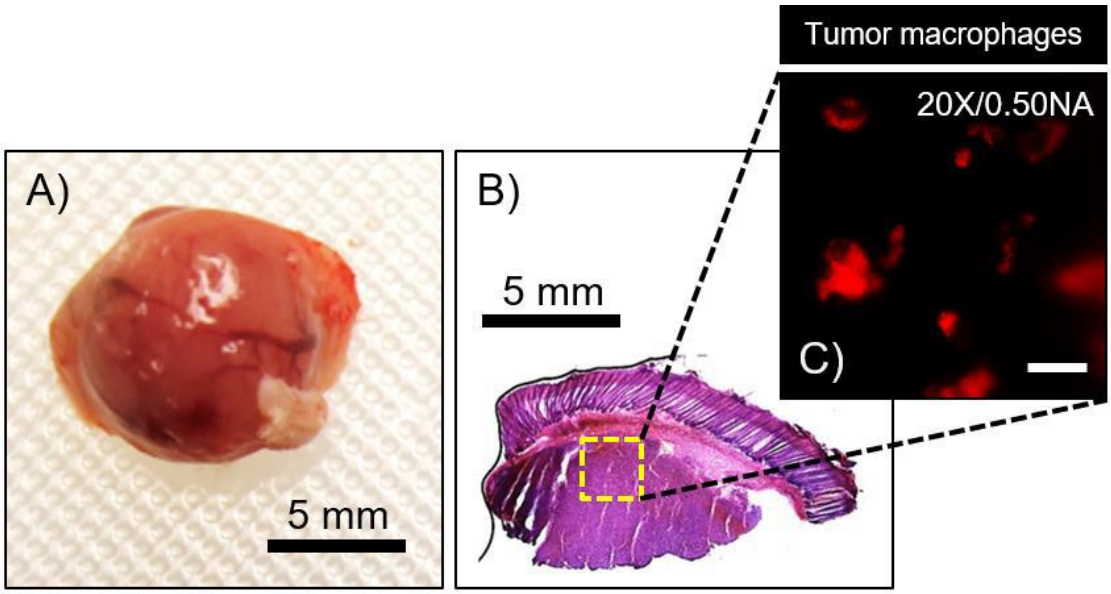

Figure 5. Murine colon tumor allografts were (a) dissected and flash frozen. Tumors were (b) sectioned at 5 µm thickness (H&E shown for clarity, yellow box not to scale). Tumor sections were (c) stained for TAMs and imaged with a 20x objective at 10 regions of interest (ROI) along the section. Scale bar = 30 µm. Images enhanced for publication.

A. Preparing slides for staining (20 min)

Note: Keep at least 90 ml of acetone stored at -20 °C for at least 1 h prior to start of procedure.

1. Remove 5 µm-thick slides from -80 °C.
2. Place all slides in -20 °C.
3. Keep the acetone for 20 min at -20 °C.
4. Prepare macrophage antibody cocktail (see Recipes).
5. Set out four EasyDip™ slide staining jars.
6. Fill 3 staining jars with 90 ml of room temperature sterile PBS-T (see Recipes).
7. Remove blocking solution aliquots (see Recipes) from 4 °C and set in 80-Place Storage System at room temperature.
8. 20 min after Step A3, remove acetone from -20 °C.

9. Fill final staining jar with 90 ml of -20 °C acetone.
10. Place low-temperature thermometer in 1st staining jar with acetone.

B. Fixation with acetone (10 min)
    1. When the acetone reaches -3 °C, remove slides from -20 °C.
    2. Place slides (up to 12) in the EasyDip™ slide staining rack.
    3. Place the staining rack (with slides) in cold acetone for 10 min.
    4. Remove from acetone and air dry for 5 s.

C. Wash with PBS-T (#1) (5 min)
    1. Place the staining rack in PBS-T (2nd staining jar) for 2 min.
    2. Dip the staining rack in PBS-T for 1 min such that each "dip" is 3 s (20 total dips).
    3. Swirl staining rack inside slide staining jar for 1 min such that each "swirl" is 1 s (60 total swirls).
    4. Keep staining rack in PBS-T unmoving for an additional 1 min.

D. Adding blocking solution (2 h)
    1. Remove staining rack from PBS-T (2nd staining jar).
    2. Remove 3 slides from the staining rack.
    3. Keep the other slides (if there are more than 3) in the staining rack and place back in PBS-T.
    4. Using a paper towel, dry the area around the tissue sections without touching the tissue sections. *Note: A hydrophobic barrier PAP pen may be used to keep reagents localized on the tissue specimen but is not required.*
    5. Add 50-100 µl (depending on size of tissue section) blocking solution to each tissue section.

6. Place slides (with blocking solution) in a dark humidified chamber at room temperature.
7. Repeat Steps D1-D6 for additional slides.
8. Incubate in the dark humidified chamber at room temperature for 60 min.
9. Reapply 50-100 µl blocking solution to each tissue section.
10. Incubate in the dark humidified chamber at room temperature for 60 min.

E. Adding macrophage antibody cocktail (2 h)

Note: The following steps must be performed in a dark room.

1. Remove macrophage antibody cocktail from 4 °C and remove aluminum foil.
2. Remove 1 slide from the dark humidified chamber.
3. Using a paper towel, dry the area around the tissue sections without touching the tissue sections.
4. Add 100 µl of macrophage antibody cocktail to each tissue section.
5. Place slide with macrophage antibody cocktail in a dark humidified chamber.
6. Repeat Steps E2-E5 for additional slides.
7. Incubate in the dark humidified chamber at room temperature for 2 h.

F. Wash with PBS-T (#2) (5 min)

Note: The following steps must be performed in a dark room.

1. Remove the dark humidified chamber from 4 °C.
2. Place all slides back in staining rack.
3. Place the staining rack in PBS-T (3rd staining jar) for 2 min.
4. Dip the staining rack in PBS-T for 1 min such that each "dip" is 3 s (20 total dips).
5. Swirl staining rack inside slide staining jar for 1 min such that each "swirl" is 1 s (60 total swirls).

6. Keep staining rack in PBS-T unmoving for an additional 1 min.

G. Wash with PBS-T (#3) (5 min)

Note: The following steps must be performed in a dark room.

1. Place the staining rack in PBS-T (4th staining jar) for 2 min.
2. Dip the staining rack in PBS-T for 1 min such that each "dip" is 3 s (20 total dips).
3. Swirl staining rack inside slide staining jar for 1 min such that each "swirl" is 1 s (60 total swirls).
4. Keep staining rack in PBS-T unmoving for an additional 1 min.

H. Mounting slides

Note: The following steps must be performed in a dark room.

1. Remove staining rack from PBS-T (4th staining jar).
2. Set all slides face-up on paper towel.
3. Using a paper towel, dry the area around the tissue sections without touching the tissue sections.
4. Add 1-2 drops of Fluoromount-G® Slide Mounting Medium to each tissue section.
5. Gently place 22 x 50 mm coverslip on each slide.
6. Using tweezers, gently press out air bubbles.
7. Wipe off any excess mounting medium.
8. Let slides sit for 5 min.
9. Apply quick-dry nail polish along the edges of the coverslip. Ensure edges are completely covered to prevent drying out of slides.
10. Leave slides to dry for 1 h.
11. Store slides permanently in the dark at 4 °C.

6.9.5 Data analysis

A. Imaging

1. Remove slides from 4 °C, but keep in the dark.
2. Place slide under a microscope.
3. Turn on fluorescent lamp, microscope, and camera.
4. Open imaging software.
5. Change the fast focus to 1,280 x 1,024 no binning.
6. Change the quality capture to 1,280 x 1,024 no binning.
7. Set the exposure to 100 ms.
8. Set the gain to 1x.
9. Switch to the 20x objective.
10. Use the DAPI filter and bring the $CD80^+$ cells into focus.
11. Image the CD80-stained cells.

    Note: In the 5 μm thick slide, some cells may be in-focus while others are out-of-focus. Starting 1 μm beneath the tissue surface, adjust the z-axis travel 1 μm between each step and take at least 4 images of the same location in the x-y plane (Figure 6).
12. Without moving tissue location, switch to the FITC filter and bring the $CD68^+$ cells into focus.
13. Image the CD68-stained cells.

    Note: See the note under step A11 (Image the CD80-stained cells).
14. Without moving tissue location, use the Texas Red filter and bring the $CD206^+$ cells into focus.
15. Image the CD206-stained cells.

Note: See the note under step A11 (Image the CD80-stained cells).

16. Switch to a new tissue location and repeat Steps A10-15.

17. Acquire images from the desired amount of tissue locations.

    Note: In this study, 10 regions-of-interests (ROI) per tumor were imaged (image area = 31,100 μm^2).

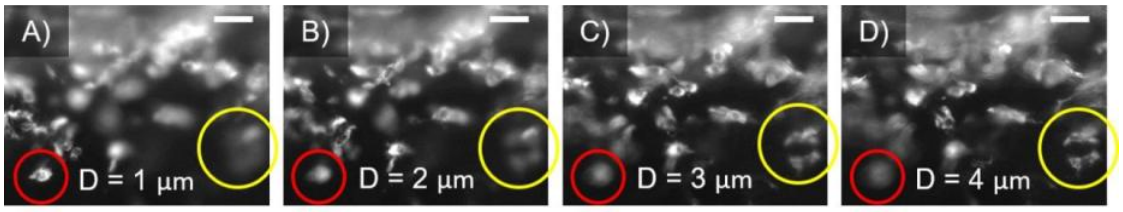

Figure 6. Multiple images in varying z-axis depths of the same x-y location may be needed for accurate TAM counting. Notice the red-circled cell starts in-focus at (A) and is out-of-focus at (D). Alternatively, notice the yellow-circled cells start off out-of-focus at (A) and are in-focus at (D). Each image (A-D) represents a 1 µm step along the z axis. Scale bars = 40 µm. 20x/0.50NA objective used for each image. Images enhanced for publication.

Note: This part of the protocol may be modified depending on tissue section thickness and desired accuracy when quantifying image-based cell counts.

B. TAM counting and polarization

1. Count $CD68^+$ cells in each ROI.
2. Count $CD80^+$ cells in each ROI.
3. Count $CD206^+$ cells in each ROI.
4. Determine the number of $CD68^+/CD80^+$ cells in each ROI. These are M1-polarized TAMs.
5. Determine the number of $CD68^+/CD206^+$ cells in each ROI. These are M2-polarized TAMs.
6. Determine the number of $CD68^+/CD80^+/CD206^+$ cells in each ROI. These are TAMs with a mixed M1/M2 phenotype (Figure 7).

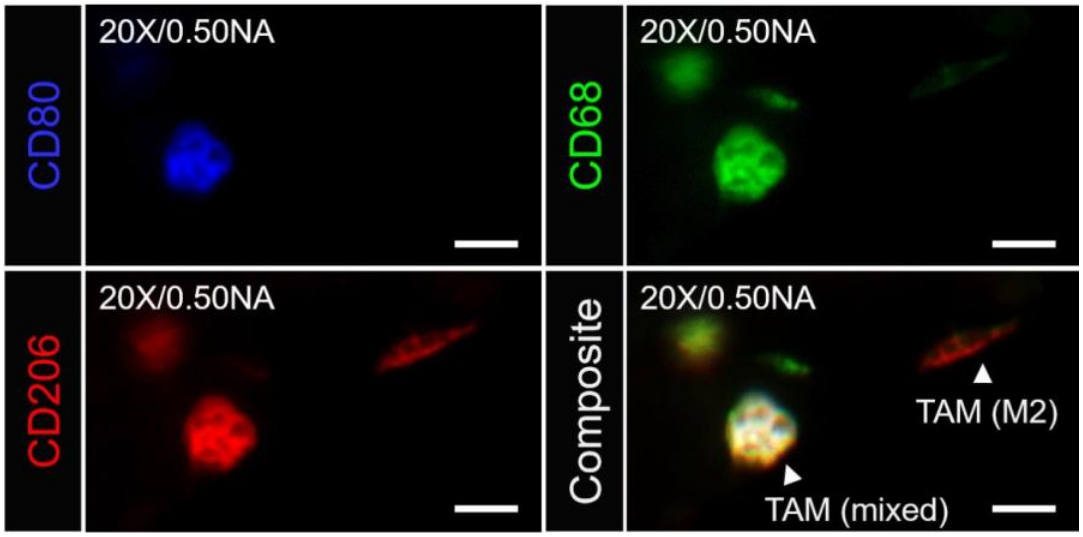

Figure 7. Image of several TAMs imaged with DAPI (for $CD80^+$), FITC (for $CD68^+$), and Texas Red (for $CD206^+$) filter sets. The composite image (ImageJ) shows a TAM with an M2 phenotype and a TAM with a mixed M1-M2 phenotype. Scale bars = 30 µm. 20x/0.50NA objective used for each image.

7. If desired, determine the number of $CD80^+/CD206^+$ cells in each ROI. There are dendritic cells.

8. Calculate the average number of M1 TAMs (included TAMs with mixed phenotype) per image area.

   $$TAM_{M1} = (CD68^+/CD80^+\ cells) + (CD68^+/CD80^+/CD206^+\ cells)$$

9. Calculate the average number of M2 TAMs (including TAMs with mixed phenotype) per image area.

   $$TAM_{M2} = (CD68^+/CD206^+\ cells) + (CD68^+/CD80^+/CD206^+\ cells)$$

10. Calculate average M1/M2 ratio per mouse (Figure 8).

    $$TAM_{ratio} = \left(\frac{TAM_{M1}}{TAM_{M2}}\right)$$

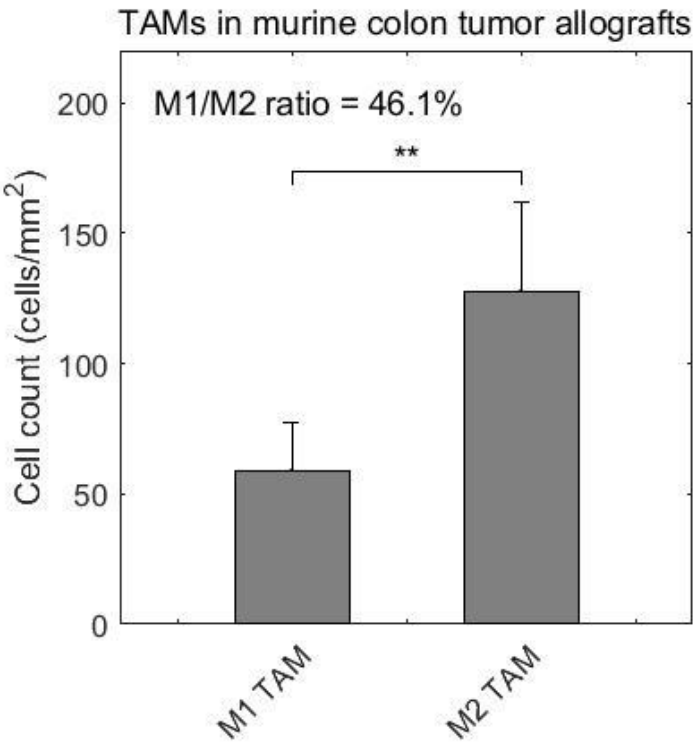

Figure 8. TAMs in subcutaneous murine colon tumor allografts. In untreated Balb/c-CT26 tumors, 3 days after the tumor reaches a volume of 75 mm^3, there is a significant difference ($P < 0.01$) between the number of M1 (58.8 ± 18.7 cells/mm^2) and M2 TAMs (127.5 ± 34.2 cells/mm^2) in the tumor, resulting in an M1/M2 ratio of 46.1%.

6.9.6 Notes on procedure

This protocol can be modified to include nuclear staining. Figure 9 shows a Balb/c-CT26 subcutaneous colon tumor allograft tissue section stained with DAPI and CD206 only.

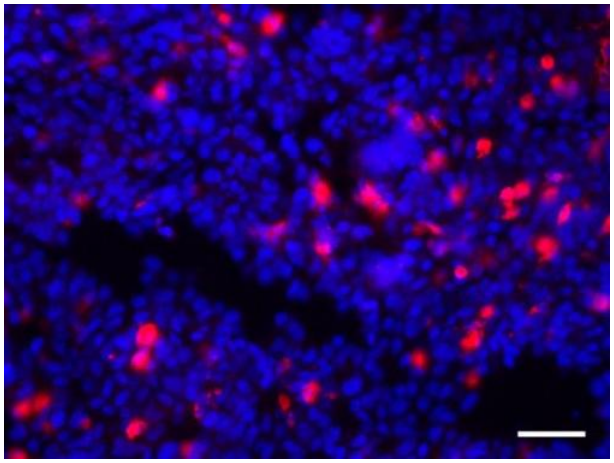

Figure 9. This staining procedure can be modified to include nuclear stains. Here, an untreated Balb/c-CT26 subcutaneous colon tumor allograft tissue section was co-stained with DAPI and Alexa Fluor® 594 anti-mouse CD206. Scale bars = 100 μm. 20x/0.50NA objective used for each image.

A limitation of this staining protocol is the absence of a reliable stain for DCs. In addition to being a commonly used pan-macrophage marker (Gordon *et al.*, 2014), CD68 can also stain for DCs at low levels in some tissues such as the lung (Yu *et al.*, 2016, Figure 1). To control for the possibility of DCs, this protocol may be modified to include a panel of DC-specific markers for murine non-lymphoid tissues on adjacent tissue sections (Yu *et al.*, 2016).

The following calculations aid in reproducibility of results and modification of the protocol for specific test systems. Stock antibody concentrations and amount of antibodies per vial are accurate up to the publication of this article and are subject to change based on manufacturer lot specifications. The desired dilution from stock were experimentally-determined in lab for the Balb/c-CT26 murine subcutaneous allograft model and may be different per specific test system. The volume of macrophage antibody cocktail represents the total volume of diluted antibody mix placed on the tissue section via micropipette before incubation at room temperature for 2 h. The average area of our tissue sections was ~50 mm^2. Thus, we recommend a macrophage antibody cocktail volume per tissue section area of ~2 $\mu l/mm^2$ (100 μl total per

section).

The following calculations determine the volume of concentrated stock antibody to add to the macrophage antibody cocktail, and how many trials can be performed with these settings.

1. Brilliant Violet 421™ anti-mouse CD80

Table 6. Constants for Brilliant Violet 421™ anti-mouse CD80 stain

Stock Antibody Concentration*	100 µg/ml
Desired Dilution from Stock*	1:20
Amount of Antibodies per Vial*	100 µg
Volume of Macrophage Antibody Cocktail per Tissue Section**	100 µl

** Values subject to change based on manufacturer specifications and recommendations*
*** Value depends on size of tissue section*

Table 7. Calculations for Brilliant Violet 421™ anti-mouse CD80 stain

Desired Volume of Stock per Trial	$\left[\frac{100\ \mu l}{1}\right] \cdot \left[\frac{1}{20}\right] = 5\ \mu l$
Desired Antibody Amount per Trial	$\left[\frac{100\ \mu l}{1}\right] \cdot \left[\frac{1}{20}\right] \cdot \left[\frac{100\ \mu g}{ml}\right] \cdot \left[\frac{1\ ml}{1000\ \mu l}\right] = 0.5\ \mu g$
Desired Antibody Concentration in Macrophage Antibody Cocktail	$\left[\frac{1}{20}\right] \cdot \left[\frac{100\ \mu g}{1\ ml}\right] = 5\ \mu g/ml$
Trials per Vial of Antibodies	$\left[\frac{100\ \mu g}{1}\right] \cdot \left[\frac{1}{0.5\ \mu g}\right] = 200$

2. Alexa Fluor® 488 anti-mouse CD68

Table 8. Constants for Alexa Fluor® 488 anti-mouse CD68 stain

Stock Antibody Concentration*	500 µg/ml
Desired Dilution from Stock*	1:100
Amount of Antibodies per Vial*	100 µg
Volume of Macrophage Antibody Cocktail per Tissue Section**	100 µl

** Values subject to change based on manufacturer specifications and recommendations*
*** Value depends on size of tissue section*

Table 9. Calculations for Alexa Fluor® 488 anti-mouse CD68 stain

Desired Volume of Stock per Trial	$\left[\frac{100\ \mu l}{1}\right] \cdot \left[\frac{1}{100}\right] = 1\ \mu l$
Desired Antibody Amount per Trial	$\left[\frac{100\ \mu l}{1}\right] \cdot \left[\frac{1}{100}\right] \cdot \left[\frac{500\ \mu g}{ml}\right] \cdot \left[\frac{1\ ml}{1000\ \mu l}\right] = 0.5\ \mu g$
Desired Antibody Concentration in Macrophage Antibody Cocktail	$\left[\frac{1}{100}\right] \cdot \left[\frac{500\ \mu g}{1\ ml}\right] = 5\ \mu g/ml$
Trials per Vial of Antibodies	$\left[\frac{100\ \mu g}{1}\right] \cdot \left[\frac{1}{0.5\ \mu g}\right] = 200$

3. Alexa Fluor® 594 anti-mouse CD206

Table 10. Constants for Alexa Fluor® 594 anti-mouse CD206 stain

Stock Antibody Concentration*	500 µg/ml
Desired Dilution from Stock*	1:125
Amount of Antibodies per Vial*	100 µg
Volume of Macrophage Antibody Cocktail per Tissue Section**	100 µl

** Values subject to change based on manufacturer specifications and recommendations*
*** Value depends on size of tissue section*

Table 11. Calculations for Alexa Fluor® 594 anti-mouse CD206 stain

Desired Volume of Stock per Trial	$\left[\frac{100\ \mu l}{1}\right] \cdot \left[\frac{1}{125}\right] = 0.8\ \mu l$
Desired Antibody Amount per Trial	$\left[\frac{100\ \mu l}{1}\right] \cdot \left[\frac{1}{125}\right] \cdot \left[\frac{500\ \mu g}{ml}\right] \cdot \left[\frac{1\ ml}{1000\ \mu l}\right] = 0.4\ \mu g$
Desired Antibody Concentration in Macrophage Antibody Cocktail	$\left[\frac{1}{125}\right] \cdot \left[\frac{500\ \mu g}{1\ ml}\right] = 4\ \mu g/ml$
Trials per Vial of Antibodies	$\left[\frac{100\ \mu g}{1}\right] \cdot \left[\frac{1}{0.4\ \mu g}\right] = 250$

6.9.7 Recipes

1. Macrophage antibody cocktail

   Note: The following steps must be prepared in the dark.

   a. Determine the number of tissue sections to be stained

   b. Add 100 µl of universal antibody dilution buffer, per number of tissue sections, to microcentrifuge tube

      Note: This volume of 100 µl/section can be changed based on the size of the specific tissue section. More than one microcentrifuge tube may be used if staining multiple tissue sections requiring > 1 ml.

   c. Add Brilliant Violet 421™ anti-mouse CD80 to universal antibody dilution buffer at 5 µg/ml (*i.e.*, 1:20 dilution from 100 µg/ml stock)

   d. Add Alexa Fluor® 488 anti-mouse CD68 to universal antibody dilution buffer at 5 µg/ml (*i.e.*, 1:100 dilution from 500 µg/ml stock)

   e. Add Alexa Fluor® 594 anti-mouse CD206 to universal antibody dilution buffer at 4 µg/ml (*i.e.*, 1:125 dilution from 500 µg/ml stock)

f. Gently and sufficiently pipette up and down to mix the macrophage antibody cocktail

g. Wrap microcentrifuge tubes with macrophage antibody cocktail with aluminum foil and store at 4 °C until ready for use

2. Blocking solution

a. Bring sterile PBS to 37 °C in a water bath

b. Bring goat serum to room temperature

Note: The following steps must be prepared in a certified biological safety cabinet.

c. Add 4% (v/v) of goat serum to PBS

d. Add 0.5% (w/v) BSA to PBS

e. Add 0.1% (w/v) NaN_3 to PBS

f. Perform sterile vacuum filtration of the blocking solution

g. Add 0.1% (v/v) Triton™ X-100 to PBS

h. Add 0.05% (v/v) Tween® 20 to PBS

i. Shake solution vigorously until Triton™ X-100 and Tween® 20 have dispersed

Note: If needed, solution can be placed in a 37 °C water bath for 5-10 min to aid dispersion.

j. Aliquot blocking solution into sterile microcentrifuge tubes

k. Store blocking solution at 4 °C (can be stored for up to 2 months)

3. PBS-T washing solution

a. Bring sterile PBS to 37 °C in a water bath

Note: The following steps must be prepared in a certified biological safety cabinet.

b. Add 0.2% (v/v) of Tween® 20 to PBS (1 ml)

c. Shake solution vigorously until Triton™ X-100 and Tween® 20 have dispersed

Note: If needed, solution can be placed in a 37 °C water bath to aid dispersion.

d. Store PBS-T washing solution at room temperature

6.10 Results

6.11.1 Repeated measures analysis of studied metrics

Figure 10 shows representative images of Balb/c-CT26 tumor size over the 7-day time course as a function of treatment regimen. After the final DRS measurement, tumors were dissected, and mice were euthanized.

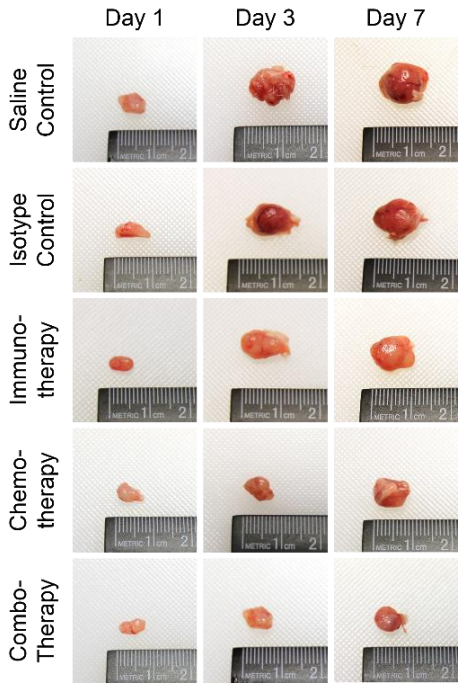

Figure 10. Tumor size of Balb/c-CT26 colon tumor allografts over time in response to controls and therapies

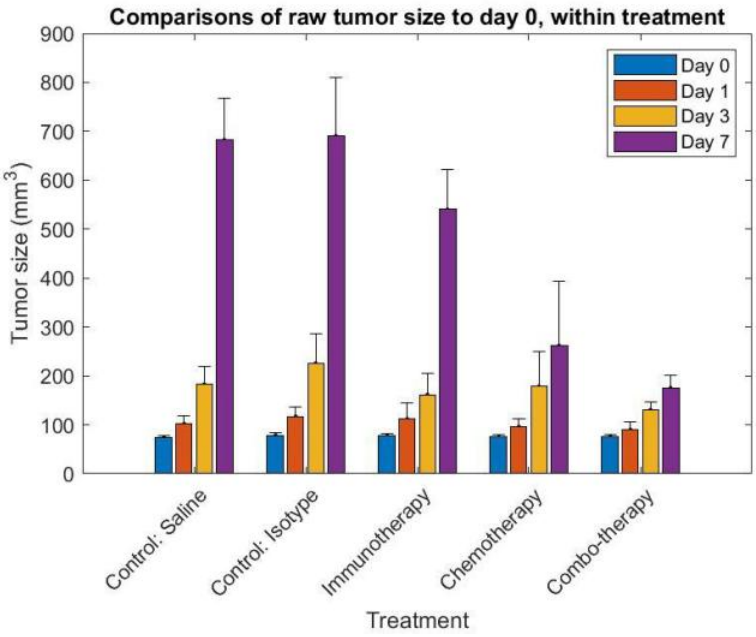

Figure 11. Raw (non-normalized) tumor size per day per treatment group. For statistical analysis, see Table 12

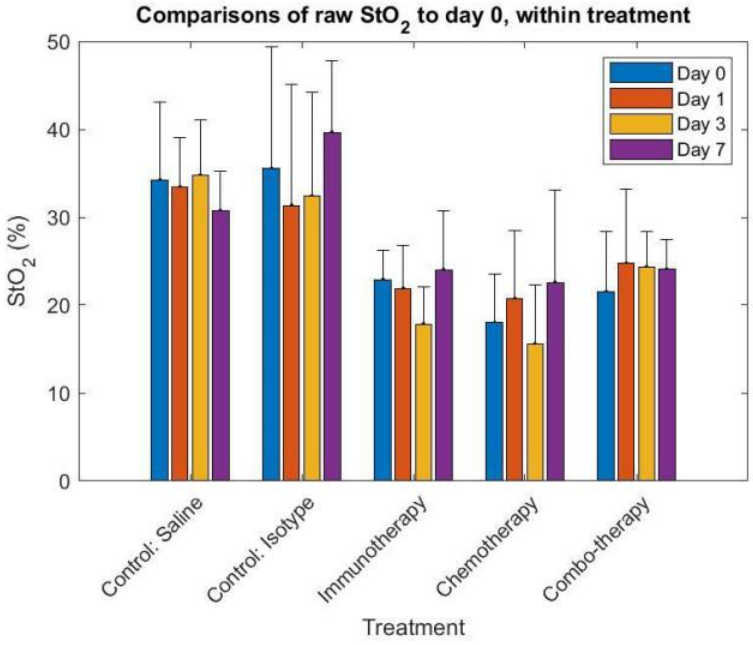

Figure 12. Raw (non-normalized) StO_2 per day per treatment group. For statistical analysis, see Table 12

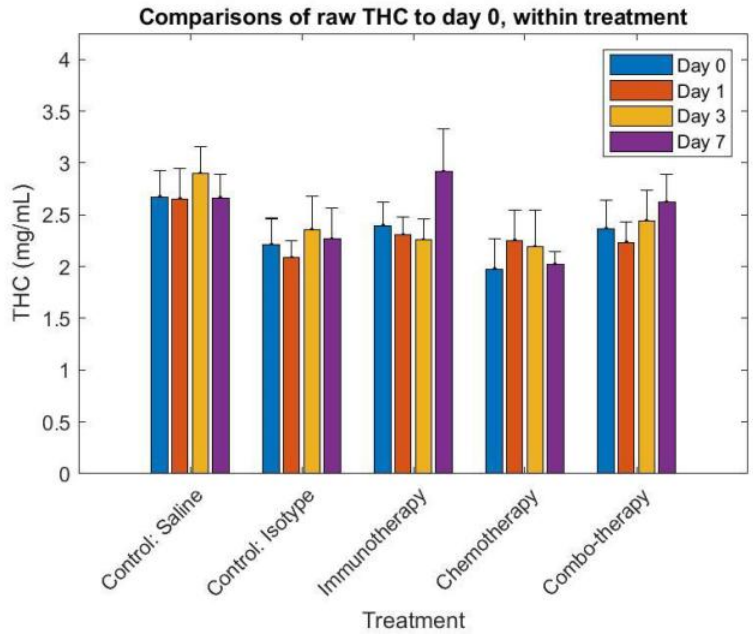

Figure 13. Raw (non-normalized) THC per day per treatment group. For statistical analysis, see Table 12

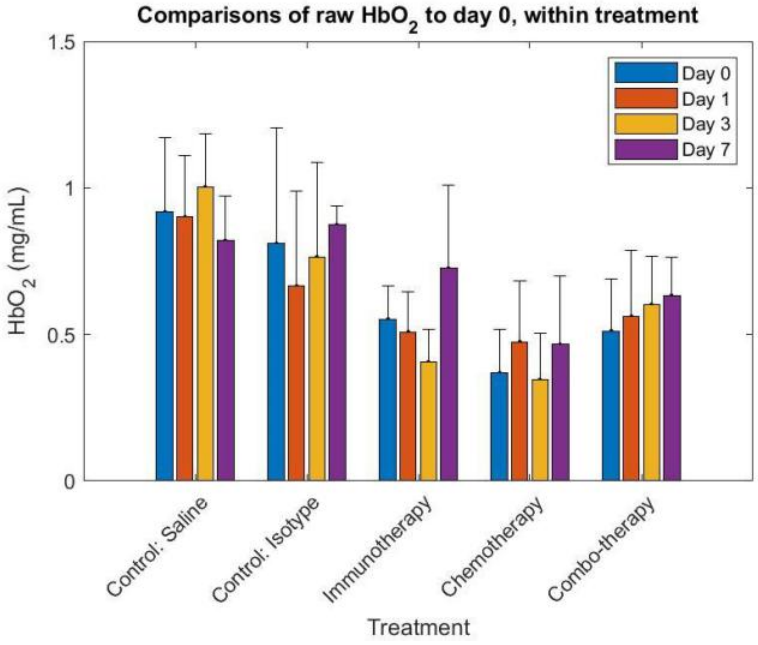

Figure 14. Raw (non-normalized) HbO_2 per day per treatment group. For statistical analysis, see Table 12

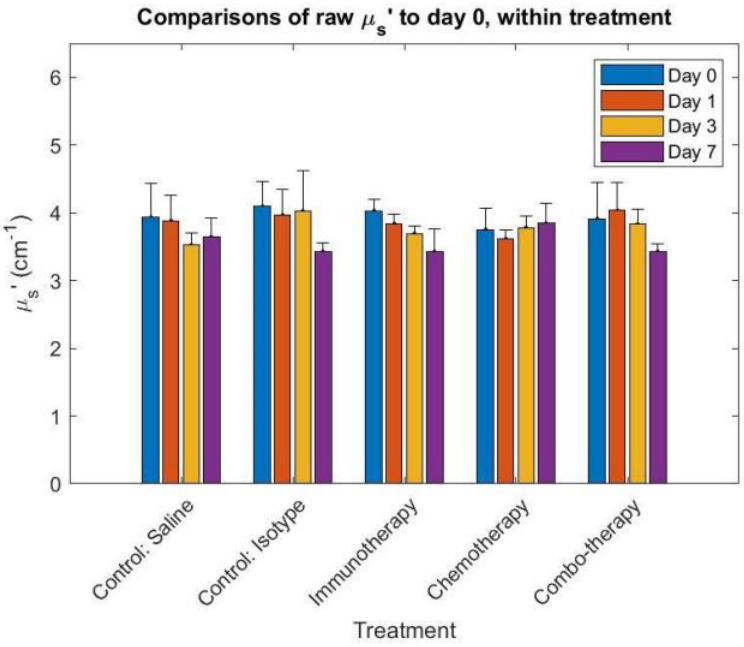

Figure 15. Raw (non-normalized) μ_s' per day per treatment group. For statistical analysis, see Table 12

Table 12. Comparisons to day 0 within treatment, within metric, raw values

Treatment	Raw Metric	Pairwise Comparisons		Mean Difference (I-J)	Std. Error	Sig.[d]	95% Confidence Interval for Difference[d]	
		(I) Day	(J) Day				Lower Bound	Upper Bound
Control: Saline	Tumor size	0	1	-27.465	17.707	.974	-83.285	28.356
			3	-108.425[a,*]	19.797	<.001	-170.834	-46.016
			7	-607.873[a,*]	25.041	<.001	-686.815	-528.931
	StO_2	0	1	.008	.031	1.000	-.089	.105
			3	-.005[a]	.034	1.000	-.113	.103
			7	.035[a]	.043	1.000	-.102	.172
	THC	0	1	.020	.106	1.000	-.316	.355
			3	-.225[a]	.119	.822	-.600	.150
			7	.009[a]	.150	1.000	-.465	.483
	HbO_2	0	1	.017	.087	1.000	-.257	.291
			3	-.086[a]	.097	1.000	-.392	.221
			7	.097[a]	.123	1.000	-.290	.485
	μ_s'	0	1	.048	.118	1.000	-.325	.420
			3	.409[a]	.132	.059	-.007	.826
			7	.286[a]	.167	.924	-.240	.813
Control: Isotype	Tumor size	0	1	-38.337[a,c]	19.020	.724	-98.298	21.624
			3	-147.328[a,*,c]	21.790	<.001	-216.022	-78.634
			7	-611.757[a,*,c]	36.832	<.001	-727.871	-495.643
	StO_2	0	1	.042[a,c]	.033	.998	-.062	.146

Table 12. Comparisons to day 0 within treatment, within metric, raw values (cont.)

Treatment	Raw Metric	Pairwise Comparisons		Mean Difference (I-J)	Std. Error	Sig.[d]	95% Confidence Interval for Difference[d]	
		(I) Day	(J) Day				Lower Bound	Upper Bound
Control: Isotype	StO_2	0	3	.031[a,c]	.038	1.000	-.088	.150
			7	-.041[a,c]	.064	1.000	-.242	.160
	THC	0	1	.128[a,c]	.114	1.000	-.232	.488
			3	-.143[a,c]	.131	1.000	-.555	.270
			7	-.053[a,c]	.221	1.000	-.750	.644
	HbO_2	0	1	.145[a,c]	.093	.974	-.150	.439
			3	.045[a,c]	.107	1.000	-.292	.383
			7	-.064[a,c]	.181	1.000	-.634	.506
	μ_s'	0	1	.126[a,c]	.127	1.000	-.275	.526
			3	.066[a,c]	.145	1.000	-.392	.525
			7	.663[a,c]	.246	.191	-.112	1.437
Immuno-Therapy	Tumor size	0	1	-34.807[a,c]	21.686	.962	-103.173	33.559
			3	-84.687[a,*,c]	21.686	.003	-153.053	-16.321
			7	-463.176[a,*,c]	26.560	.000	-546.907	-379.445
	StO_2	0	1	.010[a,c]	.038	1.000	-.108	.128
			3	.050[a,c]	.038	.996	-.068	.169
			7	-.011[a,c]	.046	1.000	-.156	.134
	THC	0	1	.092[a,c]	.130	1.000	-.319	.502
			3	.141[a,c]	.130	1.000	-.270	.552
			7	-.521[a,*,c]	.160	.035	-1.024	-.018
	HbO_2	0	1	.043[a,c]	.107	1.000	-.293	.379
			3	.146[a,c]	.107	.995	-.190	.482
			7	-.174[a,c]	.130	.997	-.585	.237
	μ_s'	0	1	.193[a,c]	.145	.997	-.263	.650
			3	.339[a,c]	.145	.434	-.118	.795
			7	.604[a,*,c]	.177	.021	.045	1.163
Chemo-Therapy	Tumor size	0	1	-20.716	22.280	1.000	-90.955	49.524
			3	-107.261[a,*]	22.644	<.001	-178.646	-35.876
			7	-186.511[a,*]	26.805	<.001	-271.013	-102.008
	StO_2	0	1	-.020	.039	1.000	-.141	.102
			3	.040[a]	.039	1.000	-.084	.164
			7	-.031[a]	.046	1.000	-.177	.115
	THC	0	1	-.255	.134	.813	-.677	.167
			3	-.192[a]	.136	.992	-.621	.237
			7	-.005[a]	.161	1.000	-.512	.503
	HbO_2	0	1	-.088	.109	1.000	-.433	.257
			3	.059[a]	.111	1.000	-.291	.410
			7	-.060[a]	.132	1.000	-.476	.355
	μ_s'	0	1	.183	.149	.999	-.285	.652

Table 12. Comparisons to day 0 within treatment, within metric, raw values (cont.)

Treatment	Raw Metric	Pairwise Comparisons		Mean Difference (I-J)	Std. Error	Sig.[d]	95% Confidence Interval for Difference[d]	
		(I) Day	(J) Day				Lower Bound	Upper Bound
Chemo-Therapy	μ_s'	0	3	.014[a]	.151	1.000	-.463	.490
			7	-.049[a]	.179	1.000	-.613	.515
Combo-Therapy	Tumor size	0	1	-14.134	19.797	1.000	-76.544	48.275
			3	-53.994[a]	23.214	.446	-127.175	19.188
			7	-99.300[a,*]	27.997	.013	-187.561	-11.040
	StO_2	0	1	-.032	.034	1.000	-.140	.076
			3	-.030[a]	.040	1.000	-.156	.097
			7	-.026[a]	.049	1.000	-.178	.127
	THC	0	1	.130	.119	1.000	-.244	.505
			3	-.081[a]	.139	1.000	-.520	.359
			7	-.256[a]	.168	.979	-.786	.274
	HbO_2	0	1	-.050	.097	1.000	-.356	.257
			3	-.094[a]	.114	1.000	-.454	.265
			7	-.121[a]	.138	1.000	-.554	.313
	μ_s'	0	1	-.122	.132	1.000	-.538	.295
			3	.096[a]	.155	1.000	-.392	.584
			7	.484[a]	.187	.248	-.105	1.073

Based on estimated marginal means

*. The mean difference is significant at the .05 level.

a. An estimate of the modified population marginal mean (J).

c. An estimate of the modified population marginal mean (I).

d. Adjustment for multiple comparisons: Sidak.

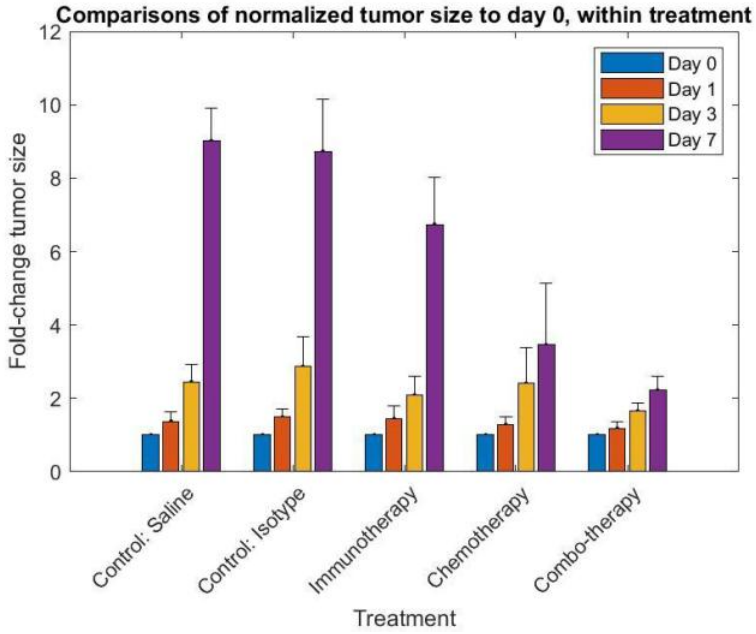

Figure 16. Normalized tumor size per day per treatment group. For statistical analysis, see Table 13

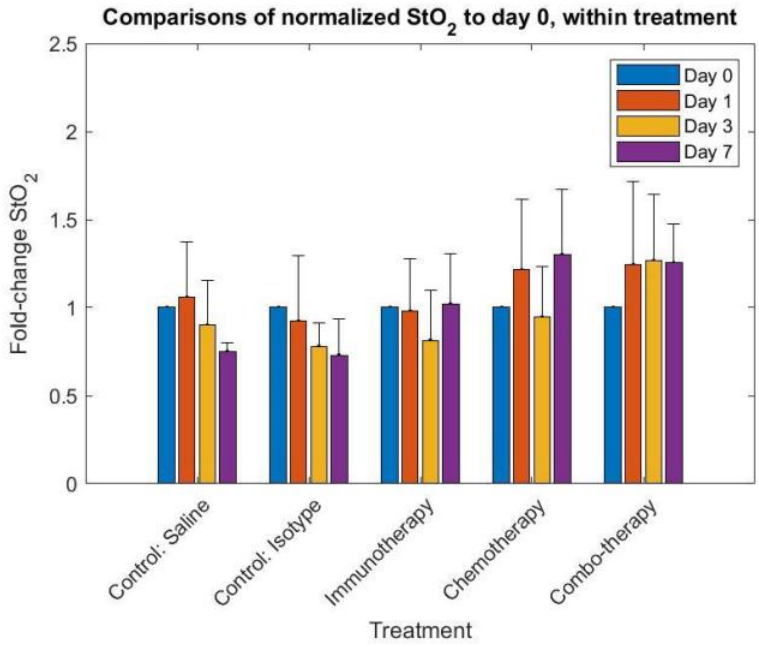

Figure 17. Normalized StO_2 per day per treatment group. For statistical analysis, see Table 13

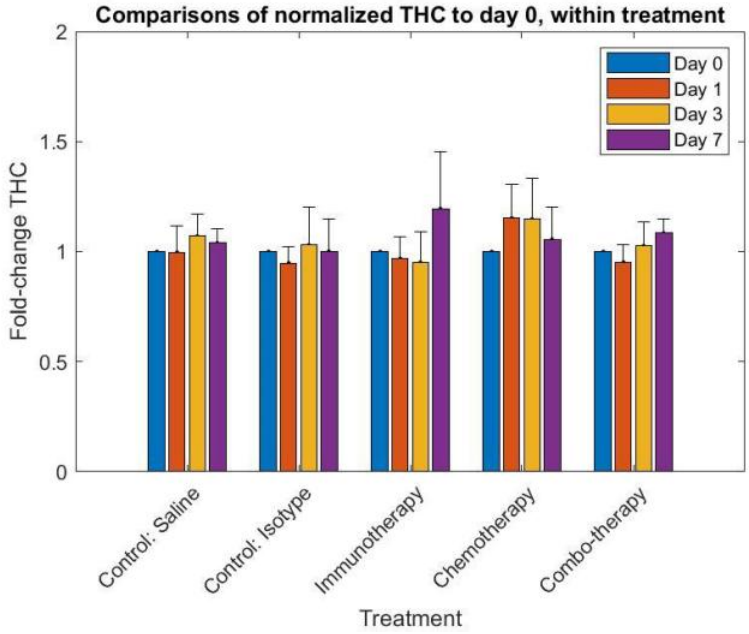

Figure 18. Normalized StO_2 per day per treatment group. For statistical analysis, see Table 13

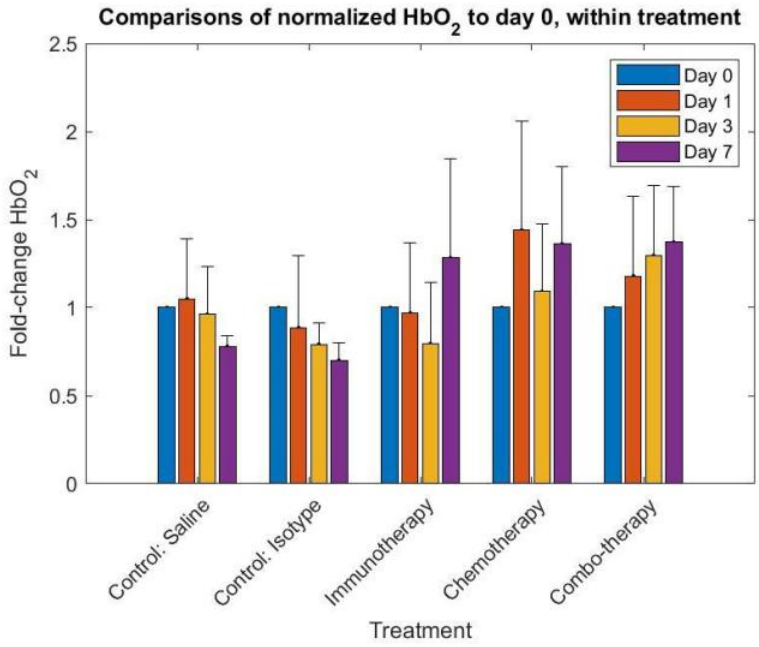

Figure 19. Normalized HbO_2 per day per treatment group. For statistical analysis, see Table 13

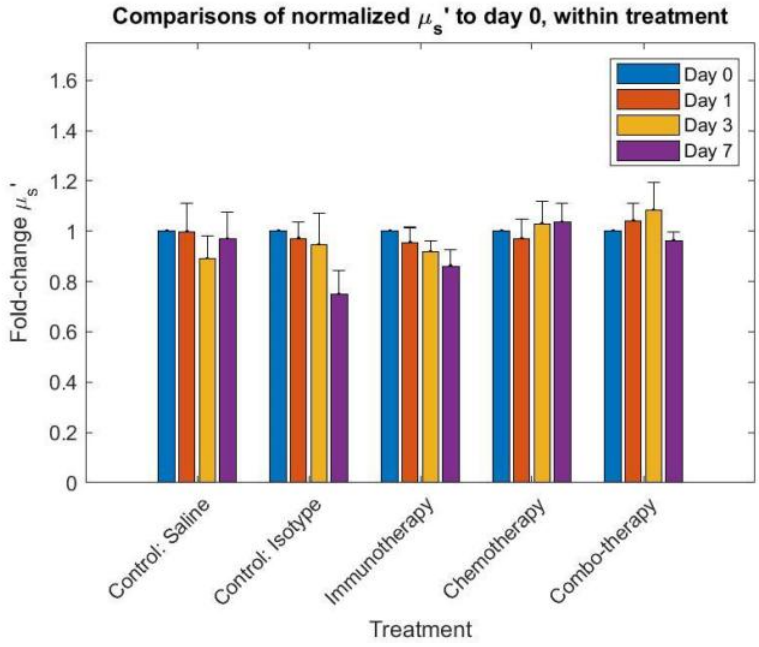

Figure 20. Normalized μ_s' per day per treatment group. For statistical analysis, see Table 13

Table 13. Comparisons to day 0 within treatment, within metric, normalized values

Treatment	Normalized Metric	Pairwise Comparisons		Mean Difference (I-J)	Std. Error	Sig.[d]	95% Confidence Interval for Difference[d]	
		(I) Day	(J) Day				Lower Bound	Upper Bound
Control: Saline	Tumor size	0	1	-.375	.234	.962	-1.112	.363
			3	-1.448[a,*]	.262	<.001	-2.272	-.623
			7	-8.020[a,*]	.331	<.001	-9.063	-6.976
	StO_2	0	1	-.058	.109	1.000	-.403	.287
			3	.100[a]	.122	1.000	-.286	.486
			7	.250[a]	.155	.960	-.238	.738
	THC	0	1	.003	.053	1.000	-.163	.168
			3	-.070[a]	.059	.999	-.255	.115
			7	-.039[a]	.074	1.000	-.273	.195
	HbO_2	0	1	-.049	.139	1.000	-.486	.388
			3	.039[a]	.155	1.000	-.450	.527
			7	.221[a]	.196	1.000	-.397	.839
	μ_s'	0	1	.003	.037	1.000	-.114	.120
			3	.111	.042	.208	-.020	.242
			7	.032	.053	1.000	-.134	.198
Control: Isotype	Tumor size	0	1	-.486[a,c]	.251	.790	-1.279	.306
			3	-1.863[a,*,c]	.288	<.001	-2.771	-.955
			7	-7.735[a,*,c]	.487	<.001	-9.270	-6.201
	StO_2	0	1	.078[a,c]	.118	1.000	-.293	.448
			3	.220[a,c]	.135	.953	-.205	.645
			7	.270[a,c]	.228	.999	-.448	.988
	THC	0	1	.052[a,c]	.056	1.000	-.126	.230
			3	-.029[a,c]	.065	1.000	-.233	.175
			7	-.001[a,c]	.109	1.000	-.345	.343
	HbO_2	0	1	.114[a,c]	.149	1.000	-.355	.583
			3	.208[a,c]	.171	.999	-.329	.746
			7	.299[a,c]	.288	1.000	-.609	1.208
	μ_s'	0	1	.029[a,c]	.040	1.000	-.097	.155
			3	.055[a,c]	.046	.999	-.089	.199
			7	.252[a,*,c]	.077	.036	.008	.496
Immuno-Therapy	Tumor size	0	1	-.444[a,c]	.287	.975	-1.347	.460
			3	-1.090[a,*,c]	.287	.005	-1.993	-.186
			7	-5.741[a,*,c]	.351	<.001	-6.848	-4.635
	StO_2	0	1	.021[a,c]	.134	1.000	-.402	.443
			3	.185[a,c]	.134	.994	-.237	.608
			7	-.020[a,c]	.164	1.000	-.538	.497
	THC	0	1	.031[a,c]	.064	1.000	-.171	.234
			3	.048[a,c]	.064	1.000	-.154	.251
			7	-.195[a,c]	.079	.325	-.444	.053

Table 13. Comparisons to day 0 within treatment, within metric, normalized values (cont.)

Treatment	Normalized Metric	Pairwise Comparisons		Mean Difference (I-J)	Std. Error	Sig.[d]	95% Confidence Interval for Difference[d]	
		(I) Day	(J) Day				Lower Bound	Upper Bound
Immuno-Therapy	HbO_2	0	1	.031[a,c]	.170	1.000	-.504	.566
			3	.205[a,c]	.170	.999	-.330	.740
			7	-.282[a,c]	.208	.996	-.938	.373
	μ_s'	0	1	.046[a,c]	.046	1.000	-.098	.189
			3	.082[a,c]	.046	.876	-.061	.226
			7	.139[a,c]	.056	.320	-.037	.315
Chemo-Therapy	Tumor size	0	1	-.280	.294	1.000	-1.208	.648
			3	-1.467[a,*]	.299	<.001	-2.411	-.524
			7	-2.453[a,*]	.354	<.001	-3.570	-1.336
	StO_2	0	1	-.169	.138	.999	-.604	.265
			3	.041[a]	.140	1.000	-.400	.482
			7	-.301[a]	.166	.872	-.823	.222
	THC	0	1	-.137	.066	.669	-.346	.071
			3	-.160[a]	.067	.402	-.372	.052
			7	-.056[a]	.080	1.000	-.307	.195
	HbO_2	0	1	-.371	.174	.626	-.920	.179
			3	-.118[a]	.177	1.000	-.676	.441
			7	-.361[a]	.210	.920	-1.023	.300
	μ_s'	0	1	.043	.047	1.000	-.104	.191
			3	-.029[a]	.048	1.000	-.179	.121
			7	-.035[a]	.056	1.000	-.212	.143
Combo-Therapy	Tumor size	0	1	-.183	.262	1.000	-1.007	.642
			3	-.447[a]	.293	.978	-1.369	.475
			7	-1.225[a,*]	.370	.030	-2.391	-.058
	StO_2	0	1	-.243	.122	.748	-.629	.143
			3	-.108[a]	.137	1.000	-.539	.323
			7	-.253[a]	.173	.988	-.799	.293
	THC	0	1	.048	.059	1.000	-.137	.233
			3	.102[a]	.066	.974	-.105	.309
			7	-.083[a]	.083	1.000	-.345	.178
	HbO_2	0	1	-.179	.155	1.000	-.668	.309
			3	-.134[a]	.173	1.000	-.680	.412
			7	-.371[a]	.219	.932	-1.062	.320
	μ_s'	0	1	-.040	.042	1.000	-.171	.091
			3	.053[a]	.047	1.000	-.094	.200
			7	.038[a]	.059	1.000	-.147	.224

Based on estimated marginal means

*. The mean difference is significant at the .05 level.

a. An estimate of the modified population marginal mean (J).

c. An estimate of the modified population marginal mean (I).
d. Adjustment for multiple comparisons: Sidak.

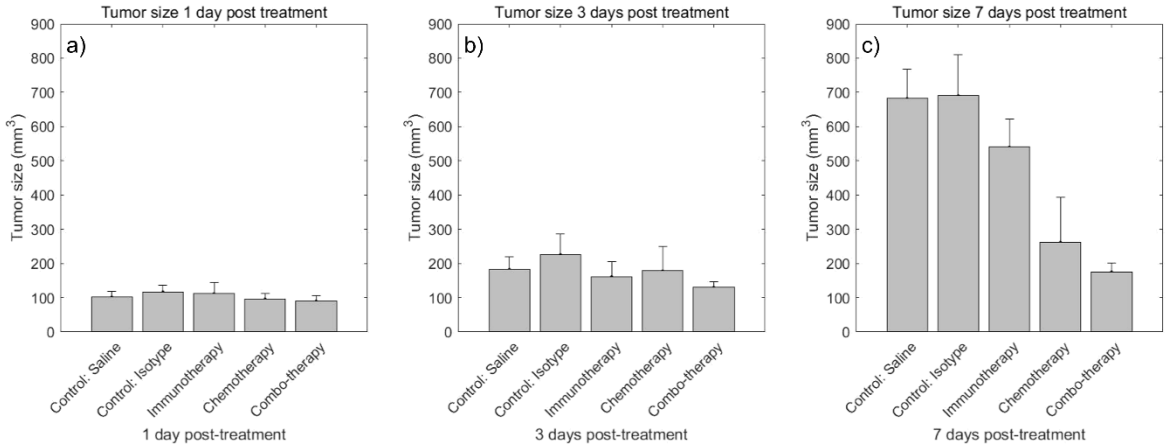

Figure 21. Comparison of treatments for days 1, 3, and 7 for raw (non-normalized) tumor size. For statistical analysis, see Table 14

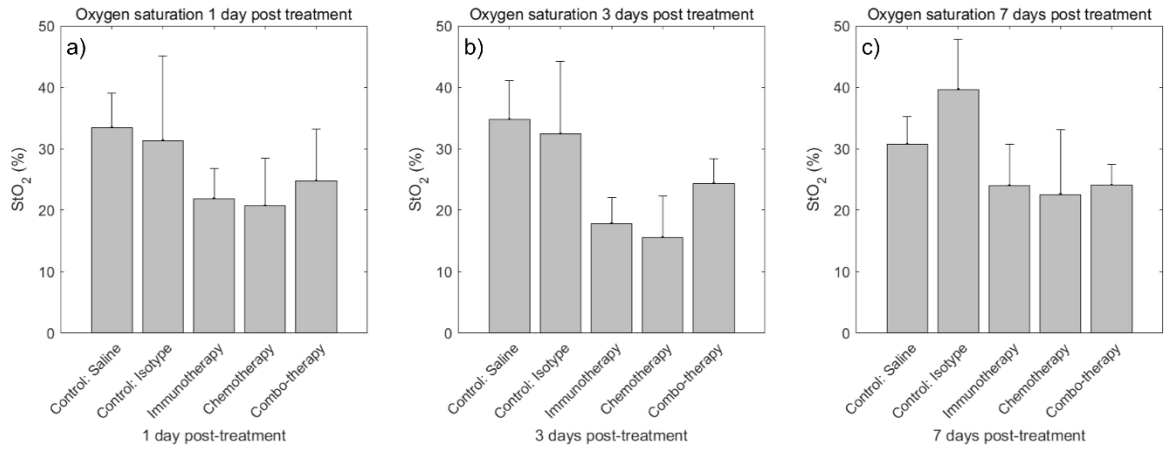

Figure 22. Comparison of treatments for days 1, 3, and 7 for raw (non-normalized) StO_2. For statistical analysis, see Table 14

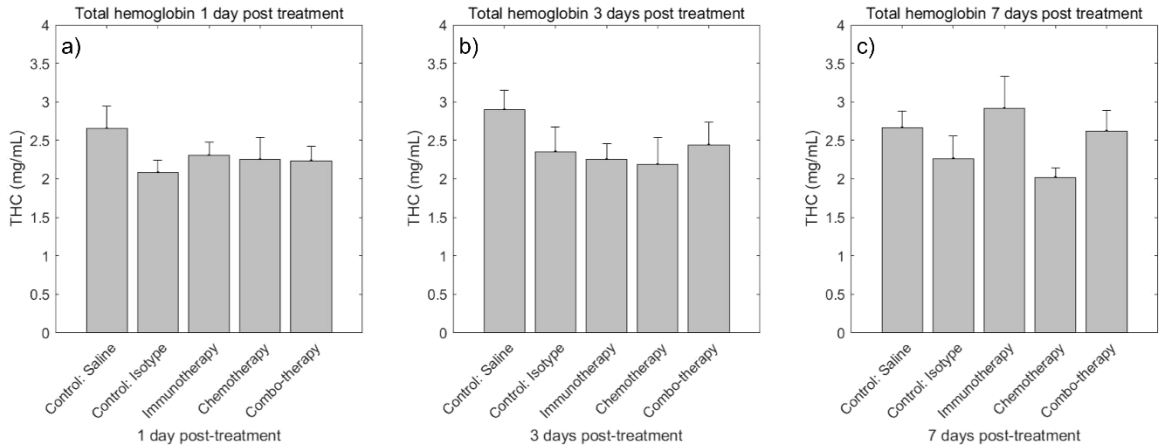

Figure 23. Comparison of treatments for days 1, 3, and 7 for raw (non-normalized) THC. For statistical analysis, see Table 14

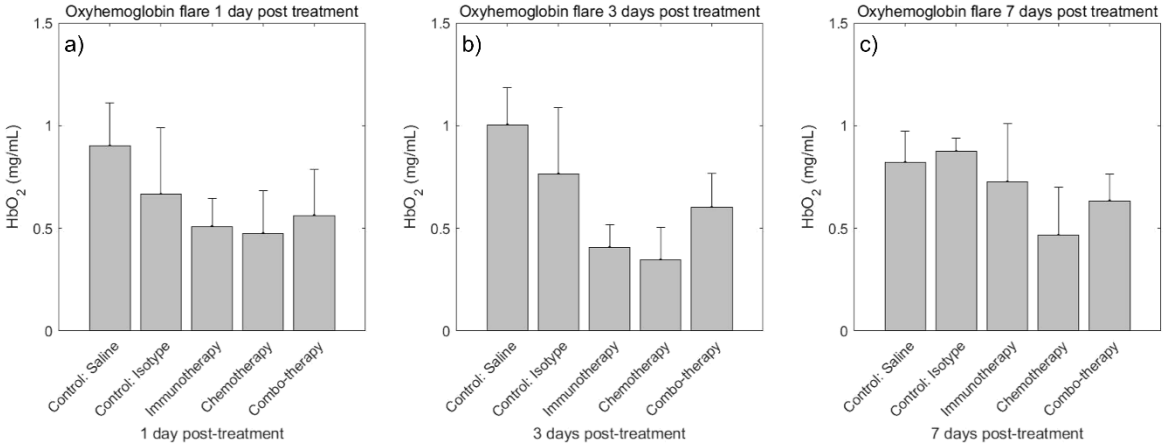

Figure 24. Comparison of treatments for days 1, 3, and 7 for raw (non-normalized) HbO_2. For statistical analysis, see Table 14

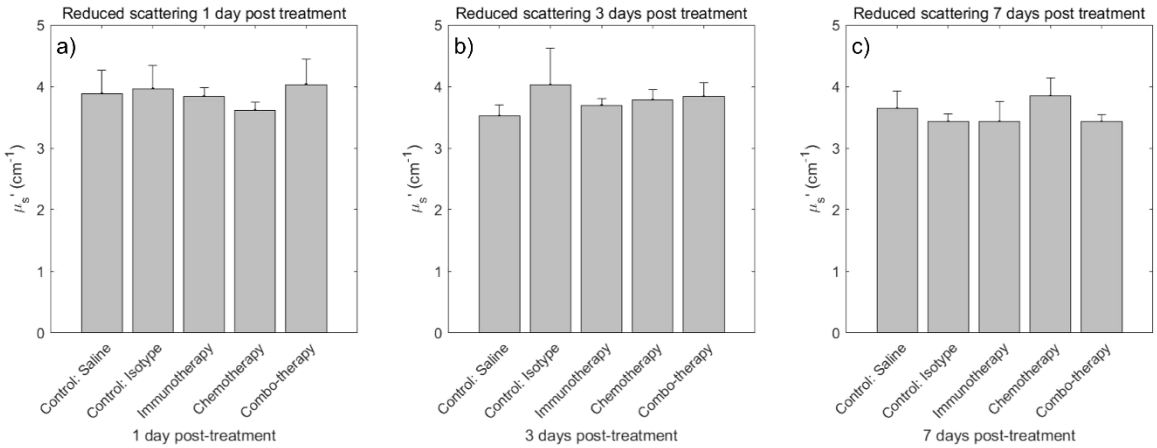

Figure 25. Comparison of treatments for days 1, 3, and 7 for raw (non-normalized) μ_s'. For statistical analysis, see Table 14

Table 14. Comparisons of treatments for days 1, 3 and 7, within metrics, raw values

Day	Raw Metric	Pairwise Comparisons		Mean Difference (I-J)	Std. Error	Sig.[d]	95% Confidence Interval for Difference[d]	
		(I) Treatment	(J) Treatment				Lower Bound	Upper Bound
1	Tumor size	Control: Saline	Control: Isotype	-15.152[a]	18.375	.995	-67.086	36.781
			Immunotherapy	-9.930[a]	19.797	1.000	-65.881	46.021
			Chemotherapy	5.771	20.124	1.000	-51.105	62.647
			Combo-therapy	11.748	18.781	.999	-41.332	64.828
		Control: Isotype	Immunotherapy	5.222[a,b]	20.397	1.000	-52.425	62.869
			Chemotherapy	20.924[b]	20.714	.977	-37.621	79.469
			Combo-therapy	26.901[b]	19.412	.839	-27.964	81.765
		Immunotherapy	Chemotherapy	15.702[b]	21.985	.998	-46.435	77.838
			Combo-therapy	21.678[b]	20.763	.971	-37.003	80.360
		Chemotherapy	Combo-therapy	5.977	21.075	1.000	-53.588	65.541
	StO_2	Control: Saline	Control: Isotype	.021	.032	.999	-.069	.111
			Immunotherapy	.115	.034	.009	.018	.212
			Chemotherapy	.120	.035	.007	.021	.219
			Combo-therapy	.087	.033	.078	-.005	.179
		Control: Isotype	Immunotherapy	.094	.035	.077	-.005	.194
			Chemotherapy	.099	.036	.060	-.002	.201
			Combo-therapy	.066	.034	.406	-.029	.161
		Immunotherapy	Chemotherapy	.005	.038	1.000	-.103	.112
			Combo-therapy	-.028	.036	.996	-.130	.073
		Chemotherapy	Combo-therapy	-.033	.037	.989	-.136	.070
	THC	Control: Saline	Control: Isotype	.570[a,*]	.110	<.001	.258	.882
			Immunotherapy	.350[a,*]	.119	.035	.014	.686
			Chemotherapy	.384[*]	.121	.017	.042	.725
			Combo-therapy	.419[*]	.113	.003	.100	.737
		Control: Isotype	Immunotherapy	-.220[a,b]	.122	.533	-.567	.126
			Chemotherapy	-.187[b]	.124	.765	-.538	.165
			Combo-therapy	-.151[b]	.117	.886	-.481	.178
		Immunotherapy	Chemotherapy	.034[b]	.132	1.000	-.339	.407
			Combo-therapy	.069[b]	.125	1.000	-.284	.421
		Chemotherapy	Combo-therapy	.035	.127	1.000	-.323	.393
	HbO_2	Control: Saline	Control: Isotype	.236[a]	.090	.092	-.019	.491
			Immunotherapy	.392[a,*]	.097	.001	.117	.667
			Chemotherapy	.408[*]	.099	.001	.129	.687
			Combo-therapy	.339[*]	.092	.003	.078	.600
		Control: Isotype	Immunotherapy	.156[a,b]	.100	.723	-.127	.439
			Chemotherapy	.172[b]	.102	.620	-.116	.460
			Combo-therapy	.103[b]	.095	.963	-.166	.373
		Immunotherapy	Chemotherapy	.016[b]	.108	1.000	-.289	.321
			Combo-therapy	-.053[b]	.102	1.000	-.341	.235

Table 14. Comparisons of treatments for days 1, 3 and 7, within metrics, raw values (cont.)

Day	Raw Metric	Pairwise Comparisons		Mean Difference (I-J)	Std. Error	Sig.[d]	95% Confidence Interval for Difference[d]	
		(I) Treatment	(J) Treatment				Lower Bound	Upper Bound
1	HbO_2	Chemotherapy	Combo-therapy	-.069	.104	.999	-.361	.224
	μ_s'	Control: Saline	Control: Isotype	-.083[a]	.123	.999	-.430	.264
			Immunotherapy	.044[a]	.132	1.000	-.330	.417
			Chemotherapy	.271	.134	.365	-.108	.651
			Combo-therapy	-.151	.125	.925	-.506	.203
		Control: Isotype	Immunotherapy	.127[a,b]	.136	.987	-.258	.512
			Chemotherapy	.355[b]	.138	.104	-.036	.745
			Combo-therapy	-.068[b]	.130	1.000	-.435	.298
		Immunotherapy	Chemotherapy	.228[b]	.147	.728	-.187	.642
			Combo-therapy	-.195[b]	.139	.825	-.587	.196
		Chemotherapy	Combo-therapy	-.423[*]	.141	.029	-.820	-.025
3	Tumor size	Control: Saline	Control: Isotype	-43.183[a,b]	23.002	.471	-108.192	21.826
			Immunotherapy	21.150[a,b]	21.686	.982	-40.141	82.441
			Chemotherapy	.186[a,b]	22.354	1.000	-62.992	63.364
			Combo-therapy	52.849[a,b]	24.043	.254	-15.103	120.802
		Control: Isotype	Immunotherapy	64.333[a,b]	23.002	.055	-.676	129.342
			Chemotherapy	43.369[a,b]	23.632	.504	-23.421	110.160
			Combo-therapy	96.033[a,b,*]	25.236	.002	24.709	167.356
		Immunotherapy	Chemotherapy	-20.964[a,b]	22.354	.986	-84.142	42.214
			Combo-therapy	31.699[a,b]	24.043	.876	-36.253	99.652
		Chemotherapy	Combo-therapy	52.663[a,b]	24.647	.290	-16.995	122.322
	StO_2	Control: Saline	Control: Isotype	.024[a,b]	.040	1.000	-.089	.136
			Immunotherapy	.169[a,b,*]	.038	<.001	.063	.275
			Chemotherapy	.193[a,b,*]	.039	<.001	.083	.302
			Combo-therapy	.103[a,b]	.042	.132	-.015	.221
		Control: Isotype	Immunotherapy	.146[a,b,*]	.040	.003	.033	.258
			Chemotherapy	.169[a,b,*]	.041	<.001	.054	.285
			Combo-therapy	.080[a,b]	.044	.517	-.044	.203
		Immunotherapy	Chemotherapy	.024[a,b]	.039	1.000	-.086	.133
			Combo-therapy	-.066[a,b]	.042	.701	-.184	.052
		Chemotherapy	Combo-therapy	-.090[a,b]	.043	.312	-.210	.031
	THC	Control: Saline	Control: Isotype	.544[a,b,*]	.138	.001	.153	.934
			Immunotherapy	.644[a,b,*]	.130	<.001	.276	1.012
			Chemotherapy	.691[a,b,*]	.134	<.001	.312	1.070
			Combo-therapy	.452[a,b,*]	.144	.020	.044	.860
		Control: Isotype	Immunotherapy	.100[a,b]	.138	.998	-.290	.490
			Chemotherapy	.147[a,b]	.142	.972	-.254	.548
			Combo-therapy	-.092[a,b]	.152	1.000	-.520	.336
		Immunotherapy	Chemotherapy	.047[a,b]	.134	1.000	-.332	.426

Table 14. Comparisons of treatments for days 1, 3 and 7, within metrics, raw values (cont.)

Day	Raw Metric	Pairwise Comparisons		Mean Difference (I-J)	Std. Error	Sig.[d]	95% Confidence Interval for Difference[d]	
		(I) Treatment	(J) Treatment				Lower Bound	Upper Bound
3	THC	Immunotherapy	Combo-therapy	-.192[a,b]	.144	.871	-.600	.216
		Chemotherapy	Combo-therapy	-.239[a,b]	.148	.680	-.657	.179
	HbO_2	Control: Saline	Control: Isotype	.239[a,b]	.113	.303	-.080	.558
			Immunotherapy	.598[a,b,*]	.107	<.001	.296	.899
			Chemotherapy	.658[a,b,*]	.110	<.001	.348	.968
			Combo-therapy	.397[a,b,*]	.118	.009	.063	.731
		Control: Isotype	Immunotherapy	.358[a,b,*]	.113	.017	.039	.678
			Chemotherapy	.419[a,b,*]	.116	.004	.091	.747
			Combo-therapy	.158[a,b]	.124	.898	-.192	.508
		Immunotherapy	Chemotherapy	.060[a,b]	.110	1.000	-.250	.371
			Combo-therapy	-.201[a,b]	.118	.614	-.534	.133
		Chemotherapy	Combo-therapy	-.261[a,b]	.121	.279	-.603	.081
	μ_s'	Control: Saline	Control: Isotype	-.504[a,b,*]	.153	.012	-.938	-.070
			Immunotherapy	-.172[a,b]	.145	.931	-.581	.237
			Chemotherapy	-.259[a,b]	.149	.582	-.681	.162
			Combo-therapy	-.295[a,b]	.160	.502	-.748	.158
		Control: Isotype	Immunotherapy	.332[a,b]	.153	.276	-.102	.765
			Chemotherapy	.245[a,b]	.158	.729	-.201	.690
			Combo-therapy	.209[a,b]	.168	.912	-.267	.685
		Immunotherapy	Chemotherapy	-.087[a,b]	.149	1.000	-.509	.335
			Combo-therapy	-.123[a,b]	.160	.997	-.576	.331
		Chemotherapy	Combo-therapy	-.036[a,b]	.164	1.000	-.501	.429
7	Tumor size	Control: Saline	Control: Isotype	-8.164[a,b]	40.571	1.000	-122.829	106.502
			Immunotherapy	142.108[a,b,*]	30.669	<.001	55.429	228.787
			Chemotherapy	420.385[a,b,*]	30.669	<.001	333.706	507.064
			Combo-therapy	506.990[a,b,*]	32.529	<.001	415.053	598.927
		Control: Isotype	Immunotherapy	150.272[a,b,*]	40.571	.003	35.607	264.938
			Chemotherapy	428.548[a,b,*]	40.571	<.001	313.883	543.214
			Combo-therapy	515.154[a,b,*]	41.995	<.001	396.464	633.844
		Immunotherapy	Chemotherapy	278.276[a,b,*]	30.669	<.001	191.597	364.955
			Combo-therapy	364.882[a,b,*]	32.529	<.001	272.945	456.819
		Chemotherapy	Combo-therapy	86.606[a,b]	32.529	.080	-5.331	178.543
	StO_2	Control: Saline	Control: Isotype	-.089[a,b]	.070	.899	-.288	.109
			Immunotherapy	.067[a,b]	.053	.902	-.083	.217
			Chemotherapy	.082[a,b]	.053	.740	-.069	.232
			Combo-therapy	.067[a,b]	.056	.934	-.093	.226
		Control: Isotype	Immunotherapy	.157[a,b]	.070	.239	-.042	.355
			Chemotherapy	.171[a,b]	.070	.147	-.028	.369
			Combo-therapy	.156[a,b]	.073	.286	-.050	.362

Table 14. Comparisons of treatments for days 1, 3 and 7, within metrics, raw values (cont.)

Day	Raw Metric	Pairwise Comparisons		Mean Difference (I-J)	Std. Error	Sig.[d]	95% Confidence Interval for Difference[d]	
		(I) Treatment	(J) Treatment				Lower Bound	Upper Bound
7	StO_2	Immunotherapy	Chemotherapy	.014[a,b]	.053	1.000	-.136	.164
			Combo-therapy	-.001[a,b]	.056	1.000	-.160	.159
		Chemotherapy	Combo-therapy	-.015[a,b]	.056	1.000	-.174	.144
	THC	Control: Saline	Control: Isotype	.400[a,b]	.244	.659	-.289	1.089
			Immunotherapy	-.252[a,b]	.184	.851	-.772	.269
			Chemotherapy	.644[a,b,*]	.184	.006	.124	1.165
			Combo-therapy	.043[a,b]	.195	1.000	-.509	.595
		Control: Isotype	Immunotherapy	-.652[a,b]	.244	.077	-1.340	.037
			Chemotherapy	.244[a,b]	.244	.978	-.444	.933
			Combo-therapy	-.357[a,b]	.252	.822	-1.070	.356
		Immunotherapy	Chemotherapy	.896[a,b,*]	.184	<.001	.375	1.416
			Combo-therapy	.295[a,b]	.195	.759	-.257	.847
		Chemotherapy	Combo-therapy	-.601[a,b,*]	.195	.023	-1.153	-.049
	HbO_2	Control: Saline	Control: Isotype	-.053[a,b]	.199	1.000	-.617	.510
			Immunotherapy	.095[a,b]	.151	.999	-.331	.520
			Chemotherapy	.355[a,b]	.151	.177	-.071	.781
			Combo-therapy	.188[a,b]	.160	.937	-.264	.639
		Control: Isotype	Immunotherapy	.148[a,b]	.199	.998	-.415	.711
			Chemotherapy	.409[a,b]	.199	.345	-.155	.972
			Combo-therapy	.241[a,b]	.206	.939	-.342	.824
		Immunotherapy	Chemotherapy	.260[a,b]	.151	.590	-.165	.686
			Combo-therapy	.093[a,b]	.160	1.000	-.359	.545
		Chemotherapy	Combo-therapy	-.168[a,b]	.160	.970	-.619	.284
	μ_s'	Control: Saline	Control: Isotype	.216[a,b]	.271	.996	-.550	.981
			Immunotherapy	.216[a,b]	.205	.968	-.362	.795
			Chemotherapy	-.199[a,b]	.205	.982	-.778	.379
			Combo-therapy	.216[a,b]	.217	.979	-.397	.830
		Control: Isotype	Immunotherapy	.001[a,b]	.271	1.000	-.765	.766
			Chemotherapy	-.415[a,b]	.271	.742	-1.180	.350
			Combo-therapy	.001[a,b]	.280	1.000	-.791	.793
		Immunotherapy	Chemotherapy	-.416[a,b]	.205	.359	-.994	.163
			Combo-therapy	-6.000E-5[a,b]	.217	1.000	-.614	.613
		Chemotherapy	Combo-therapy	.415[a,b]	.217	.443	-.198	1.029

*. The mean difference is significant at the .05 level.
a. An estimate of the modified population marginal mean (J).
c. An estimate of the modified population marginal mean (I).
d. Adjustment for multiple comparisons: Sidak.

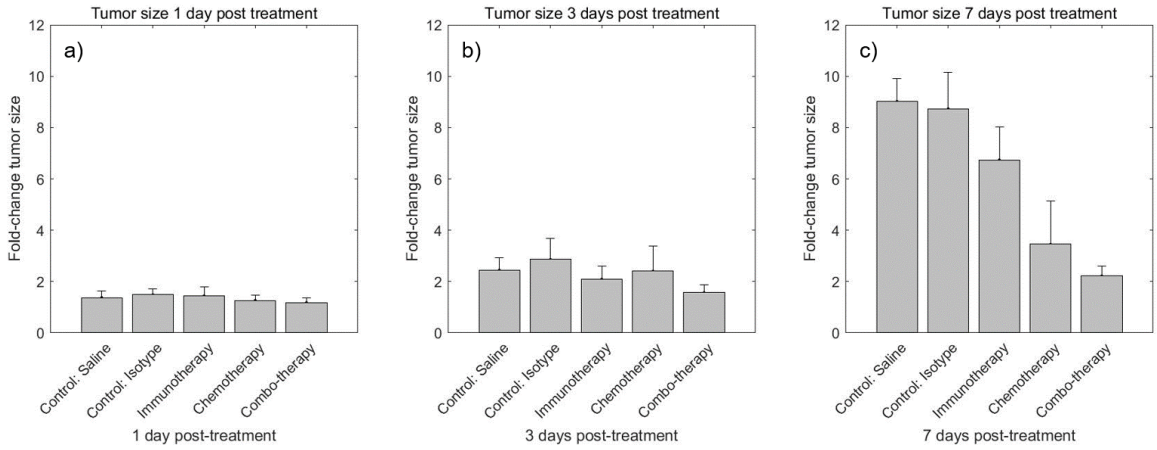

Figure 26. Comparison of treatments for days 1, 3, and 7 for normalized tumor size. For statistical analysis, see Table 15

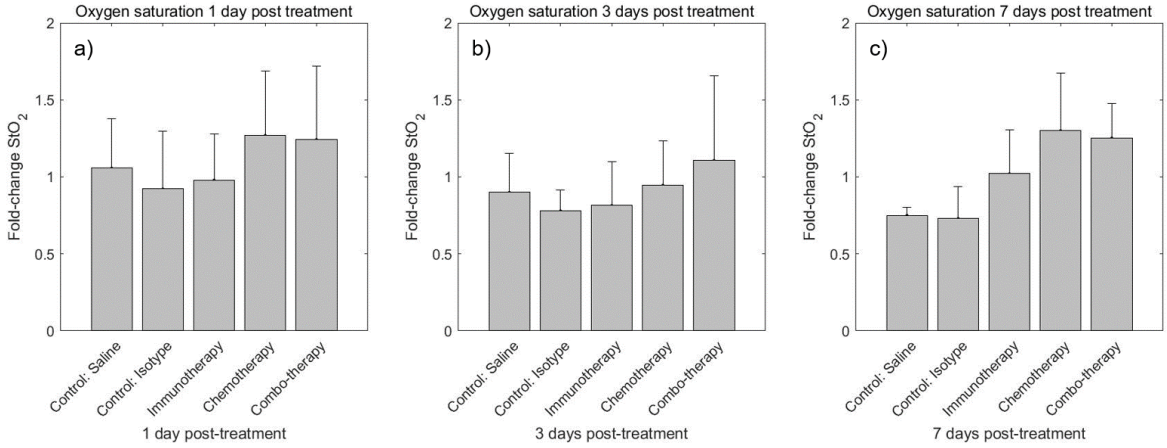

Figure 27. Comparison of treatments for days 1, 3, and 7 for normalized StO_2. For statistical analysis, see Table 15

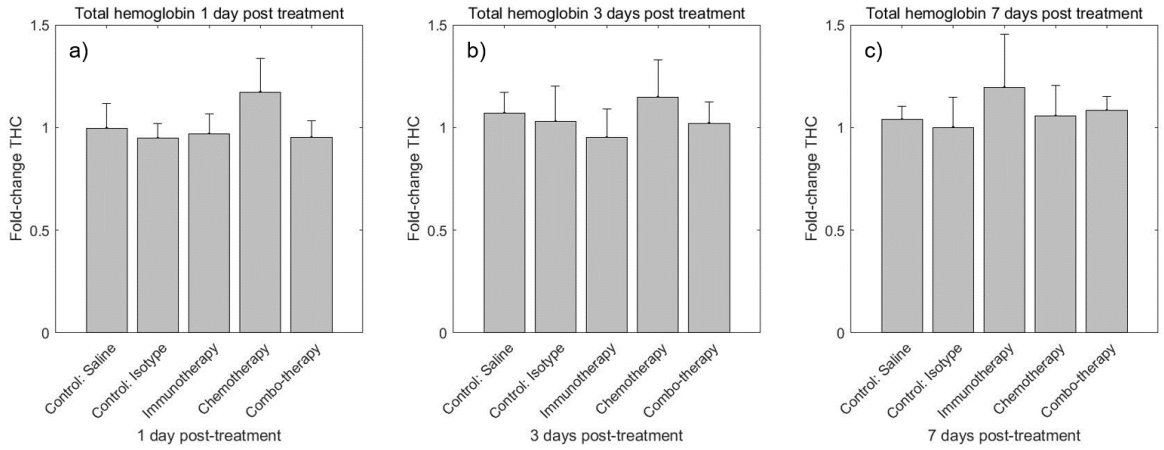

Figure 28. Comparison of treatments for days 1, 3, and 7 for normalized THC. For statistical analysis, see Table 15

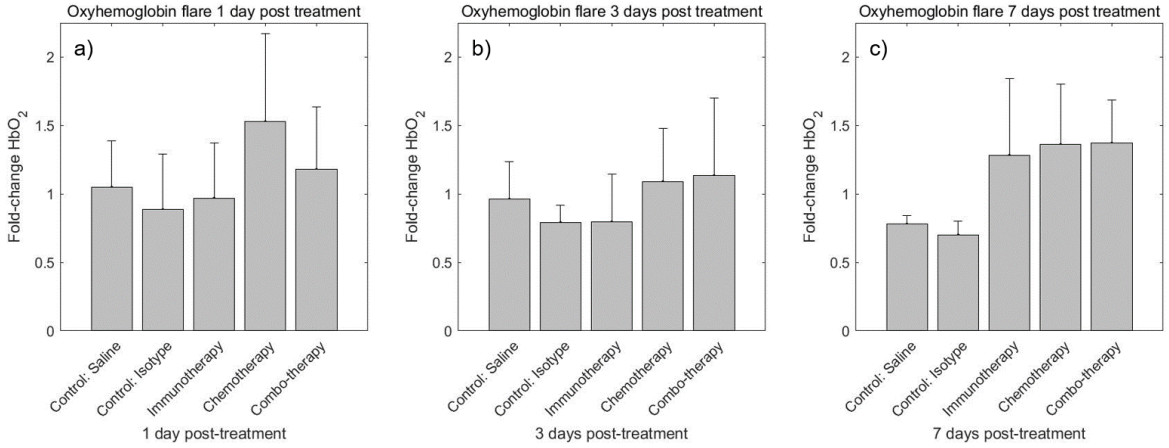

Figure 29. Comparison of treatments for days 1, 3, and 7 for normalized HbO_2. For statistical analysis, see Table 15

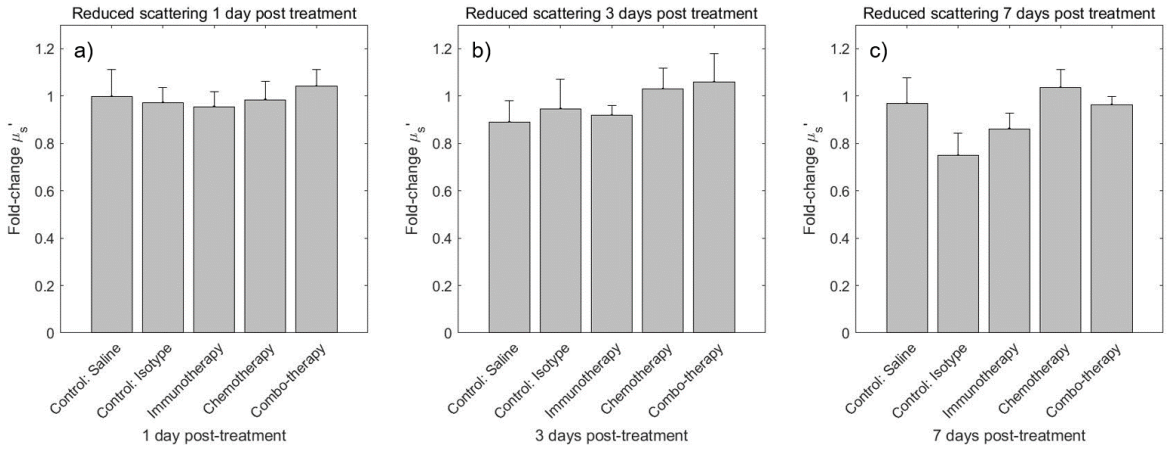

Figure 30. Comparison of treatments for days 1, 3, and 7 for normalized μ_s'. For statistical analysis, see Table 15

Table 15. Comparisons of treatments for days 1, 3 and 7, within metrics, normalized values

Day	Norm. Metric	Pairwise Comparisons		Mean Difference (I-J)	Std. Error	Sig.[d]	95% Confidence Interval for Difference[d]	
		(I) Treatment	(J) Treatment				Lower Bound	Upper Bound
1	Tumor size	Control: Saline	Control: Isotype	-.112[a]	.243	1.000	-.798	.575
			Immunotherapy	-.069[a]	.262	1.000	-.808	.670
			Chemotherapy	.095	.266	1.000	-.657	.847
			Combo-therapy	.192	.248	.997	-.509	.894
		Control: Isotype	Immunotherapy	.042[a,b]	.270	1.000	-.719	.804
			Chemotherapy	.207[b]	.274	.998	-.567	.980
			Combo-therapy	.304[b]	.257	.934	-.421	1.029
		Immunotherapy	Chemotherapy	.164[b]	.291	1.000	-.657	.985
			Combo-therapy	.261[b]	.274	.985	-.514	1.037
		Chemotherapy	Combo-therapy	.097	.279	1.000	-.690	.884
	StO_2	Control: Saline	Control: Isotype	.135[a]	.114	.931	-.186	.456
			Immunotherapy	.078[a]	.122	.999	-.268	.424
			Chemotherapy	-.112	.124	.990	-.463	.240
			Combo-therapy	-.186	.116	.693	-.514	.143
		Control: Isotype	Immunotherapy	-.057[a,b]	.126	1.000	-.413	.299
			Chemotherapy	-.247[b]	.128	.432	-.609	.115
			Combo-therapy	-.321[b]	.120	.077	-.660	.018
		Immunotherapy	Chemotherapy	-.190[b]	.136	.832	-.574	.194
			Combo-therapy	-.264[b]	.128	.341	-.627	.099
		Chemotherapy	Combo-therapy	-.074	.130	1.000	-.442	.294
	THC	Control: Saline	Control: Isotype	.049[a]	.055	.990	-.105	.203
			Immunotherapy	.029[a]	.059	1.000	-.137	.194
			Chemotherapy	-.140	.060	.179	-.309	.028
			Combo-therapy	.045	.056	.996	-.112	.203
		Control: Isotype	Immunotherapy	-.021[a,b]	.061	1.000	-.192	.150
			Chemotherapy	-.190[b,*]	.061	.022	-.363	-.016
			Combo-therapy	-.004[b]	.058	1.000	-.167	.159
		Immunotherapy	Chemotherapy	-.169[b]	.065	.098	-.353	.016
			Combo-therapy	.017[b]	.062	1.000	-.157	.191
		Chemotherapy	Combo-therapy	.185[*]	.063	.033	.009	.362
	HbO_2	Control: Saline	Control: Isotype	.163[a]	.144	.949	-.243	.570
			Immunotherapy	.080[a]	.155	1.000	-.358	.518
			Chemotherapy	-.322	.157	.350	-.767	.123
			Combo-therapy	-.130	.147	.991	-.546	.285
		Control: Isotype	Immunotherapy	-.083[a,b]	.160	1.000	-.534	.368
			Chemotherapy	-.485[b,*]	.162	.030	-.943	-.027
			Combo-therapy	-.294[b]	.152	.429	-.723	.136
		Immunotherapy	Chemotherapy	-.402[b]	.172	.186	-.888	.084
			Combo-therapy	-.211[b]	.162	.887	-.670	.249

Table 15. Comparisons of treatments for days 1, 3 and 7, within metrics, normalized values (cont.)

Day	Norm. Metric	Pairwise Comparisons		Mean Difference (I-J)	Std. Error	Sig.[d]	95% Confidence Interval for Difference[d]	
		(I) Treatment	(J) Treatment				Lower Bound	Upper Bound
1	HbO_2	Chemotherapy	Combo-therapy	.191	.165	.941	-.275	.657
	μ_s'	Control: Saline	Control: Isotype	.026[a]	.039	.999	-.083	.135
			Immunotherapy	.043[a]	.042	.974	-.075	.160
			Chemotherapy	.040	.042	.985	-.079	.160
			Combo-therapy	-.043	.040	.961	-.155	.069
		Control: Isotype	Immunotherapy	.017[a,b]	.043	1.000	-.104	.138
			Chemotherapy	.014[b]	.044	1.000	-.109	.138
			Combo-therapy	-.069[b]	.041	.620	-.184	.046
		Immunotherapy	Chemotherapy	-.002[b]	.046	1.000	-.133	.128
			Combo-therapy	-.086[b]	.044	.405	-.209	.038
		Chemotherapy	Combo-therapy	-.083	.044	.467	-.209	.042
3	Tumor size	Control: Saline	Control: Isotype	-.415[a,b]	.304	.851	-1.274	.444
			Immunotherapy	.358[a,b]	.287	.909	-.452	1.168
			Chemotherapy	-.020[a,b]	.295	1.000	-.855	.815
			Combo-therapy	1.001[a,b,*]	.304	.011	.141	1.860
		Control: Isotype	Immunotherapy	.773[a,b]	.304	.110	-.086	1.632
			Chemotherapy	.396[a,b]	.312	.901	-.487	1.278
			Combo-therapy	1.416[a,b,*]	.320	<.001	.510	2.321
		Immunotherapy	Chemotherapy	-.378[a,b]	.295	.896	-1.213	.457
			Combo-therapy	.642[a,b]	.304	.304	-.217	1.502
		Chemotherapy	Combo-therapy	1.020[a,b,*]	.312	.012	.138	1.903
	StO_2	Control: Saline	Control: Isotype	.120[a,b]	.142	.994	-.282	.522
			Immunotherapy	.085[a,b]	.134	.999	-.294	.464
			Chemotherapy	-.059[a,b]	.138	1.000	-.450	.331
			Combo-therapy	-.208[a,b]	.142	.791	-.610	.194
		Control: Isotype	Immunotherapy	-.035[a,b]	.142	1.000	-.436	.367
			Chemotherapy	-.179[a,b]	.146	.918	-.592	.234
			Combo-therapy	-.328[a,b]	.150	.260	-.752	.096
		Immunotherapy	Chemotherapy	-.145[a,b]	.138	.970	-.535	.246
			Combo-therapy	-.293[a,b]	.142	.336	-.695	.108
		Chemotherapy	Combo-therapy	-.149[a,b]	.146	.975	-.562	.264
	THC	Control: Saline	Control: Isotype	.040[a,b]	.068	1.000	-.152	.233
			Immunotherapy	.118[a,b]	.064	.505	-.064	.300
			Chemotherapy	-.090[a,b]	.066	.855	-.277	.097
			Combo-therapy	.172[a,b]	.068	.118	-.021	.365
		Control: Isotype	Immunotherapy	.078[a,b]	.068	.948	-.115	.270
			Chemotherapy	-.130[a,b]	.070	.484	-.329	.068
			Combo-therapy	.131[a,b]	.072	.512	-.072	.335

Table 15. Comparisons of treatments for days 1, 3 and 7, within metrics, normalized values (cont.)

Day	Norm. Metric	Pairwise Comparisons		Mean Difference (I-J)	Std. Error	Sig.[d]	95% Confidence Interval for Difference[d]	
		(I) Treatment	(J) Treatment				Lower Bound	Upper Bound
3	THC	Immunotherapy	Chemotherapy	-.208[a,b,*]	.066	.019	-.396	-.021
			Combo-therapy	.054[a,b]	.068	.997	-.139	.247
		Chemotherapy	Combo-therapy	.262[a,b,*]	.070	.002	.064	.460
	HbO_2	Control: Saline	Control: Isotype	.170[a,b]	.180	.986	-.339	.678
			Immunotherapy	.166[a,b]	.170	.981	-.314	.646
			Chemotherapy	-.157[a,b]	.175	.990	-.651	.338
			Combo-therapy	-.173[a,b]	.180	.984	-.681	.336
		Control: Isotype	Immunotherapy	-.003[a,b]	.180	1.000	-.512	.505
			Chemotherapy	-.326[a,b]	.185	.562	-.849	.197
			Combo-therapy	-.342[a,b]	.190	.529	-.878	.194
		Immunotherapy	Chemotherapy	-.323[a,b]	.175	.497	-.817	.172
			Combo-therapy	-.339[a,b]	.180	.467	-.848	.170
		Chemotherapy	Combo-therapy	-.016[a,b]	.185	1.000	-.539	.506
	μ_s'	Control: Saline	Control: Isotype	-.056[a,b]	.048	.943	-.193	.081
			Immunotherapy	-.028[a,b]	.046	1.000	-.157	.101
			Chemotherapy	-.140[a,b,*]	.047	.032	-.273	-.007
			Combo-therapy	-.058[a,b]	.048	.929	-.195	.079
		Control: Isotype	Immunotherapy	.027[a,b]	.048	1.000	-.109	.164
			Chemotherapy	-.084[a,b]	.050	.619	-.225	.056
			Combo-therapy	-.002[a,b]	.051	1.000	-.146	.142
		Immunotherapy	Chemotherapy	-.112[a,b]	.047	.170	-.244	.021
			Combo-therapy	-.030[a,b]	.048	1.000	-.166	.107
		Chemotherapy	Combo-therapy	.082[a,b]	.050	.652	-.058	.223
7	Tumor size	Control: Saline	Control: Isotype	.284[a,b]	.536	1.000	-1.231	1.800
			Immunotherapy	2.278[a,b,*]	.405	<.001	1.133	3.424
			Chemotherapy	5.566[a,b,*]	.405	<.001	4.421	6.712
			Combo-therapy	6.795[a,b,*]	.430	<.001	5.580	8.010
		Control: Isotype	Immunotherapy	1.994[a,b,*]	.536	.002	.479	3.509
			Chemotherapy	5.282[a,b,*]	.536	<.001	3.767	6.797
			Combo-therapy	6.511[a,b,*]	.555	<.001	4.942	8.079
		Immunotherapy	Chemotherapy	3.288[a,b,*]	.405	<.001	2.143	4.434
			Combo-therapy	4.517[a,b,*]	.430	<.001	3.302	5.731
		Chemotherapy	Combo-therapy	1.228[a,b,*]	.430	.046	.013	2.443
	StO_2	Control: Saline	Control: Isotype	.020[a,b]	.251	1.000	-.689	.729
			Immunotherapy	-.270[a,b]	.190	.816	-.806	.266
			Chemotherapy	-.550[a,b,*]	.190	.040	-1.086	-.014
			Combo-therapy	-.503[a,b]	.201	.124	-1.071	.066
		Control: Isotype	Immunotherapy	-.290[a,b]	.251	.942	-.999	.419

Table 15. Comparisons of treatments for days 1, 3 and 7, within metrics, normalized values (cont.)

Day	Norm. Metric	Pairwise Comparisons		Mean Difference (I-J)	Std. Error	Sig.[d]	95% Confidence Interval for Difference[d]	
		(I) Treatment	(J) Treatment				Lower Bound	Upper Bound
7	StO_2	Control: Isotype	Chemotherapy	-.570[a,b]	.251	.214	-1.279	.138
			Combo-therapy	-.523[a,b]	.260	.370	-1.257	.211
		Immunotherapy	Chemotherapy	-.280[a,b]	.190	.780	-.816	.256
			Combo-therapy	-.233[a,b]	.201	.943	-.801	.336
		Chemotherapy	Combo-therapy	.048[a,b]	.201	1.000	-.521	.616
	THC	Control: Saline	Control: Isotype	.038[a,b]	.120	1.000	-.302	.378
			Immunotherapy	-.156[a,b]	.091	.602	-.413	.101
			Chemotherapy	-.017[a,b]	.091	1.000	-.274	.240
			Combo-therapy	-.044[a,b]	.097	1.000	-.317	.229
		Control: Isotype	Immunotherapy	-.194[a,b]	.120	.681	-.534	.146
			Chemotherapy	-.055[a,b]	.120	1.000	-.395	.285
			Combo-therapy	-.082[a,b]	.125	.999	-.434	.270
		Immunotherapy	Chemotherapy	.139[a,b]	.091	.744	-.118	.396
			Combo-therapy	.112[a,b]	.097	.942	-.161	.385
		Chemotherapy	Combo-therapy	-.027[a,b]	.097	1.000	-.300	.245
	HbO_2	Control: Saline	Control: Isotype	.078[a,b]	.318	1.000	-.819	.976
			Immunotherapy	-.503[a,b]	.240	.315	-1.182	.175
			Chemotherapy	-.582[a,b]	.240	.149	-1.261	.096
			Combo-therapy	-.592[a,b]	.255	.190	-1.311	.127
		Control: Isotype	Immunotherapy	-.582[a,b]	.318	.507	-1.479	.316
			Chemotherapy	-.661[a,b]	.318	.324	-1.558	.236
			Combo-therapy	-.670[a,b]	.329	.352	-1.599	.258
		Immunotherapy	Chemotherapy	-.079[a,b]	.240	1.000	-.758	.599
			Combo-therapy	-.089[a,b]	.255	1.000	-.808	.631
		Chemotherapy	Combo-therapy	-.010[a,b]	.255	1.000	-.729	.710
	μ_s'	Control: Saline	Control: Isotype	.220[a,b]	.085	.101	-.021	.461
			Immunotherapy	.107[a,b]	.065	.649	-.076	.289
			Chemotherapy	-.067[a,b]	.065	.973	-.249	.116
			Combo-therapy	.006[a,b]	.068	1.000	-.187	.200
		Control: Isotype	Immunotherapy	-.113[a,b]	.085	.873	-.354	.128
			Chemotherapy	-.287[a,b,*]	.085	.009	-.528	-.045
			Combo-therapy	-.214[a,b]	.088	.152	-.463	.036
		Immunotherapy	Chemotherapy	-.173[a,b]	.065	.074	-.356	.009
			Combo-therapy	-.100[a,b]	.068	.787	-.294	.093
		Chemotherapy	Combo-therapy	.073[a,b]	.068	.966	-.120	.266

*. The mean difference is significant at the .05 level.

a. An estimate of the modified population marginal mean (J).

c. An estimate of the modified population marginal mean (I).

d. Adjustment for multiple comparisons: Sidak.

6.11.2 Correlation of spectroscopy-derived data

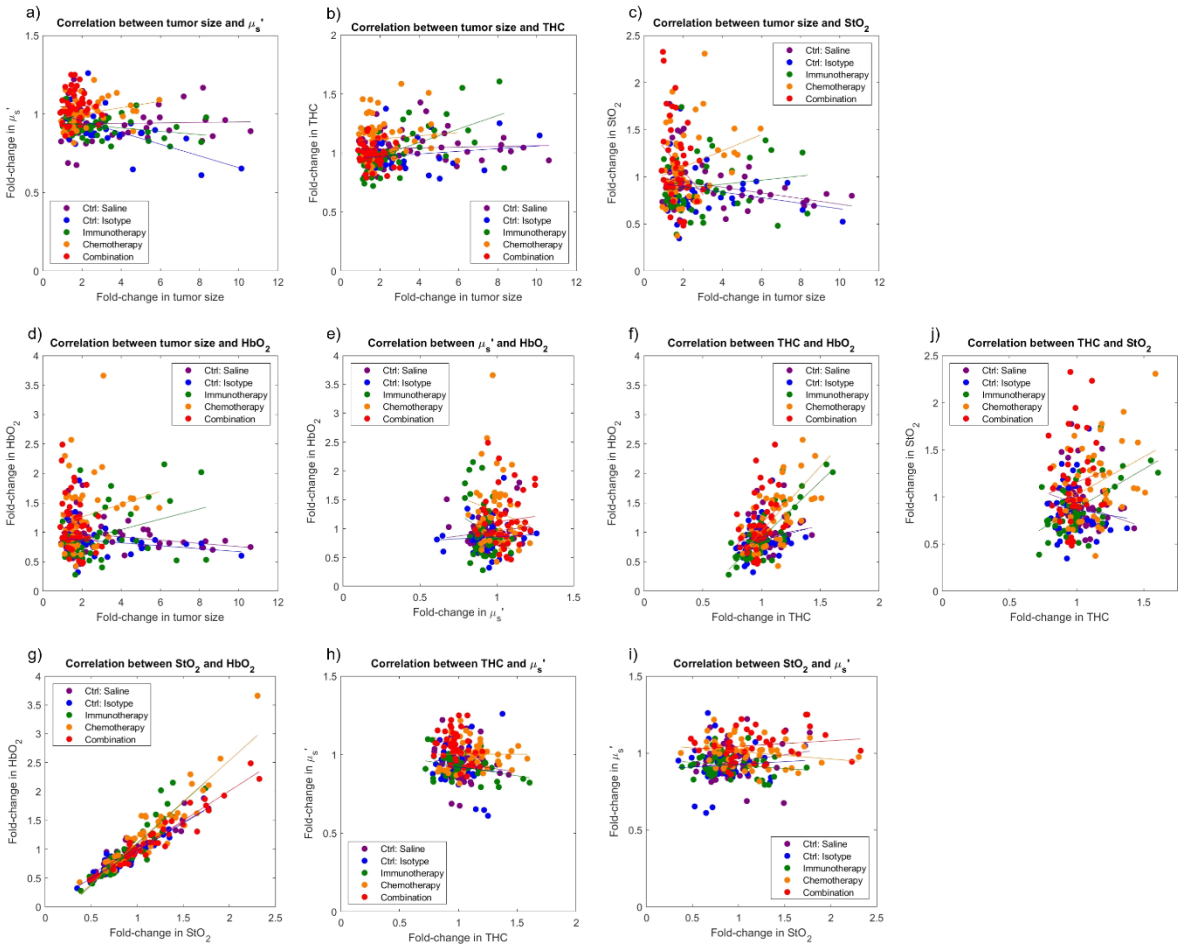

Figure 31. Correlations of normalized spectroscopy-dervied data. For statistical analysis on Pearson (parametric) and Spearman (non-parametric) correlations and significance, see Tables 16-30

Table 16. Test of normality for saline control group

		Shapiro-Wilk		
	Statistic	Statistic		Statistic
Tumor size	.771	70		.000
StO_2	.890	70		.000
THC	.925	70		.000
HbO_2	.880	70		.000
μ_s'	.968	70		.066

Table 17. Pearson correlation (parametric) of normalized metrics for saline control group

		StO_2	THC	HbO_2	μ_s'
Tumor size	Pearson Correlation	-.344**	.116	-.298*	-.074
	Sig. (2-tailed)	.003	.340	.012	.545
	N	70	70	70	70
StO_2	Pearson Correlation		-.280*	.894**	.232
	Sig. (2-tailed)		.019	.000	.053
	N		70	70	70
THC	Pearson Correlation			.168	-.162
	Sig. (2-tailed)			.164	.180
	N			70	70
HbO_2	Pearson Correlation				.172
	Sig. (2-tailed)				.155
	N				70

*. Correlation is significant at the 0.05 level (2-tailed).
**. Correlation is significant at the 0.01 level (2-tailed).
Green shading = significance
Red shading = excluded significant correlation due to normality violation

Table 18. Spearman correlation (non-parametric) of normalized metrics for saline control group

		StO_2	THC	HbO_2	μ_s'
Tumor size	Pearson Correlation	-.363**	.195	-.312**	-.287*
	Sig. (2-tailed)	.002	.106	.009	.016
	N	70	70	70	70
StO_2	Pearson Correlation		-.451**	.840**	.311**
	Sig. (2-tailed)		.000	.000	.009
	N		70	70	70
THC	Pearson Correlation			.002	-.241*
	Sig. (2-tailed)			.987	.044
	N			70	70
HbO_2	Pearson Correlation				.153
	Sig. (2-tailed)				.205
	N				70

*. Correlation is significant at the 0.05 level (2-tailed).
**. Correlation is significant at the 0.01 level (2-tailed).
Green shading = significance

Table 19. Test of normality for isotype control group

		Shapiro-Wilk	
	Statistic	Statistic	Statistic
Tumor size	.728	51	.000
StO_2	.948	51	.026
THC	.916	51	.002
HbO_2	.905	51	.001
μ_s'	.902	51	.001

Table 20. Pearson correlation (parametric) of normalized metrics for isotype control group

		StO_2	THC	HbO_2	μ_s'
Tumor size	Pearson Correlation	-.302*	.128	-.280*	-.657**
	Sig. (2-tailed)	.031	.370	.047	.000
	N	51	51	51	51
StO_2	Pearson Correlation		-.092	.936**	.141
	Sig. (2-tailed)		.521	<.001	.322
	N		51	51	51
THC	Pearson Correlation			.252	-.059
	Sig. (2-tailed)			.074	.683
	N			51	51
HbO_2	Pearson Correlation				.141
	Sig. (2-tailed)				.323
	N				51

*. Correlation is significant at the 0.05 level (2-tailed).
**. Correlation is significant at the 0.01 level (2-tailed).
Green shading = significance
Red shading = excluded significant correlation due to normality violation

Table 21. Spearman correlation (non-parametric) of normalized metrics for isotype control group

		StO_2	THC	HbO_2	μ_s'
Tumor size	Pearson Correlation	-.484**	-.184	-.516**	-.624**
	Sig. (2-tailed)	<.001	.196	<.001	<.001
	N	51	51	51	51
StO_2	Pearson Correlation		-.009	.923**	.211
	Sig. (2-tailed)		.950	.000	.137
	N		51	51	51
THC	Pearson Correlation			.304*	.099
	Sig. (2-tailed)			.030	.489
	N			51	51
HbO_2	Pearson Correlation				.249
	Sig. (2-tailed)				.078
	N				51

*. Correlation is significant at the 0.05 level (2-tailed).
**. Correlation is significant at the 0.01 level (2-tailed).
Green shading = significance

Table 22. Test of normality for immunotherapy-treated group

		Shapiro-Wilk	
	Statistic	Statistic	Statistic
Tumor size	.789	60	.000
StO_2	.974	60	.240
THC	.890	60	.000
HbO_2	.887	60	.000
μ_s'	.974	60	.226

Table 23. Pearson correlation (parametric) of normalized metrics for immunotherapy-treated group

		StO_2	THC	HbO_2	μ_s'
Tumor size	Pearson Correlation	.076	.542**	.327*	-.390**
	Sig. (2-tailed)	.565	.000	.011	.002
	N	60	60	60	60
StO_2	Pearson Correlation		.552**	.915**	-.078
	Sig. (2-tailed)		<.001	<.001	.554
	N		60	60	60
THC	Pearson Correlation			.825**	-.315*
	Sig. (2-tailed)			<.001	.014
	N			60	60
HbO_2	Pearson Correlation				-.247
	Sig. (2-tailed)				.057
	N				60

*. Correlation is significant at the 0.05 level (2-tailed).
**. Correlation is significant at the 0.01 level (2-tailed).
Green shading = significance
Red shading = excluded significant correlation due to normality violation

Table 24. Spearman correlation (non-parametric) of normalized metrics for immunotherapy-treated group

		StO_2	THC	HbO_2	μ_s'
Tumor size	Pearson Correlation	-.058	.282*	.014	-.502**
	Sig. (2-tailed)	.660	.029	.916	<.001
	N	60	60	60	60
StO_2	Pearson Correlation		.502**	.929**	.039
	Sig. (2-tailed)		.000	.000	.767
	N		60	60	60
THC	Pearson Correlation			.717**	-.027
	Sig. (2-tailed)			.000	.841
	N			60	60
HbO_2	Pearson Correlation				-.016
	Sig. (2-tailed)				.905
	N				60

*. Correlation is significant at the 0.05 level (2-tailed).
**. Correlation is significant at the 0.01 level (2-tailed).
Green shading = significance

Table 25. Test of normality for chemotherapy-treated group

		Shapiro-Wilk	
	Statistic	Statistic	Statistic
Tumor size	.799	60	.000
StO_2	.934	60	.003
THC	.929	60	.002
HbO_2	.837	60	.000
μ_s'	.967	60	.100

Table 26. Pearson correlation (parametric) of normalized metrics for chemotherapy-treated group

		StO_2	THC	HbO_2	μ_s'
Tumor size	Pearson Correlation	.294*	.192	.275*	.261*
	Sig. (2-tailed)	.023	.141	.033	.044
	N	60	60	60	60
StO_2	Pearson Correlation		.400**	.926**	-.207
	Sig. (2-tailed)		.002	.000	.112
	N		60	60	60
THC	Pearson Correlation			.693**	.006
	Sig. (2-tailed)			.000	.964
	N			60	60
HbO_2	Pearson Correlation				-.150
	Sig. (2-tailed)				.254
	N				60

*. Correlation is significant at the 0.05 level (2-tailed).
**. Correlation is significant at the 0.01 level (2-tailed).
Green shading = significance
Red shading = excluded significant correlation due to normality violation

Table 27. Spearman correlation (non-parametric) of normalized metrics for chemotherapy-treated group

		StO_2	THC	HbO_2	μ_s'
Tumor size	Pearson Correlation	.203	.267*	.215	.302*
	Sig. (2-tailed)	.120	.040	.100	.019
	N	60	60	60	60
StO_2	Pearson Correlation		.297*	.912**	-.214
	Sig. (2-tailed)		.021	<.001	.100
	N		60	60	60
THC	Pearson Correlation			.601**	.048
	Sig. (2-tailed)			<.001	.714
	N			60	60
HbO_2	Pearson Correlation				-.165
	Sig. (2-tailed)				.208
	N				60

*. Correlation is significant at the 0.05 level (2-tailed).
**. Correlation is significant at the 0.01 level (2-tailed).
Green shading = significance

Table 28. Test of normality for combination therapy-treated group

		Shapiro-Wilk	
	Statistic	Statistic	Statistic
Tumor size	.930	56	.003
StO_2	.906	56	.000
THC	.609	56	.000
HbO_2	.909	56	.000
μ_s'	.601	56	.000

Table 29. Pearson correlation (parametric) of normalized metrics for combination therapy-treated group

		StO_2	THC	HbO_2	μ_s'
Tumor size	Pearson Correlation	-.012	.219	-.036	.377**
	Sig. (2-tailed)	.927	.105	.793	.004
	N	56	56	56	56
StO_2	Pearson Correlation		.364**	.970**	.404**
	Sig. (2-tailed)		.006	.000	.002
	N		56	56	56
THC	Pearson Correlation			.470**	.622**
	Sig. (2-tailed)			.000	.000
	N			56	56
HbO_2	Pearson Correlation				.345**
	Sig. (2-tailed)				.009
	N				56

*. Correlation is significant at the 0.05 level (2-tailed).
**. Correlation is significant at the 0.01 level (2-tailed).
Green shading = significance
Red shading = excluded significant correlation due to normality violation

Table 30. Spearman correlation (non-parametric) of normalized metrics for combination therapy-treated group

		StO_2	THC	HbO_2	μ_s'
Tumor size	Pearson Correlation	-.100	-.137	-.125	.319*
	Sig. (2-tailed)	.464	.315	.357	.017
	N	56	56	56	56
StO_2	Pearson Correlation		.199	.936**	.189
	Sig. (2-tailed)		.142	.000	.163
	N		56	56	56
THC	Pearson Correlation			.425**	-.311*
	Sig. (2-tailed)			.001	.020
	N			56	56
HbO_2	Pearson Correlation				.059
	Sig. (2-tailed)				.663
	N				56

*. Correlation is significant at the 0.05 level (2-tailed).
**. Correlation is significant at the 0.01 level (2-tailed).
Green shading = significance

6.11.3 Tumor associated macrophages

In our macrophage staining, we were able to stain for two different cell types: M1 and M2 macrophages using a triple staining procedure, which reduces the possibly of the common problem of including dendritic cells when counting macrophages. In general, M1 macrophages are considered anti-tumor and M2 macrophages are considered pro-tumor, although this is an oversimplification. M1 macrophages are counted if stained with both CD68 and CD80, whereas M2 macrophages are counted if stained with both CD68 and CD206. In a comparison between the isotype control and immunotherapy groups (Fig. 32), on both day 3 and day 7, the M1/M2 ratio in the isotype control group is elevated, as expected based on a reduction in the number of M2-polarized pro-tumor macrophages. The literature shows that an increase in the M1/M2 ratio is a positive prognostic indicator of cancer-specific survival (Edin *et al.*, 2012).

Specifically, on day 3, the M1/M2 ratio for the isotype control and immunotherapy groups are 45.1% ± 18.4% and 52.2% ± 14.2% ($p = 0.28$). On day 7, the M1/M2 ratio for the isotype control and immunotherapy groups are 29.5% ± 6.5% and 43.6% ± 16.1% ($p = 0.13$). These results, although insignificant, seem to indicate an increase in the M1/M2 ratio in tumors treated with anti-CCL2 immunotherapy. However, both groups show a decrease in the M1/M2 ratio over time. For example, in the isotype control group, M1/M2 ratio decreases from 45.1% ± 18.4% to 29.5% ± 6.5% ($p = 0.14$). In the anti-CCL2 immunotherapy group, M1/M2 ratio decreases from 52.2% ± 14.2% to 43.6% ± 16.1% ($p = 0.28$). Note that the decrease is more significant for the control group.

In the isotype control treatment group (i.e. mice treated with isotype antibodies as a control for anti-CCL2 immunotherapy), more and more M2 macrophages infiltrate the tumor over time, lowering the M1/M2 ratio significantly. In the immunotherapy group, there is a slight

but insignificant decrease in the M1/M2 ratio, potentially indicating that our anti-CCL2 immunotherapy is working to reduce monocyte infiltration as expected. Work in this area is ongoing and research will be needed in correlating M1/M2 ratios to HbO_2 values among treatment groups. We expect that a decrease in M2 macrophages, coupled with chemotherapy, will increase survival in mice compared to chemotherapy alone, although the precise interplay between TAMs and DRS-derived HbO_2 remains to be determined.

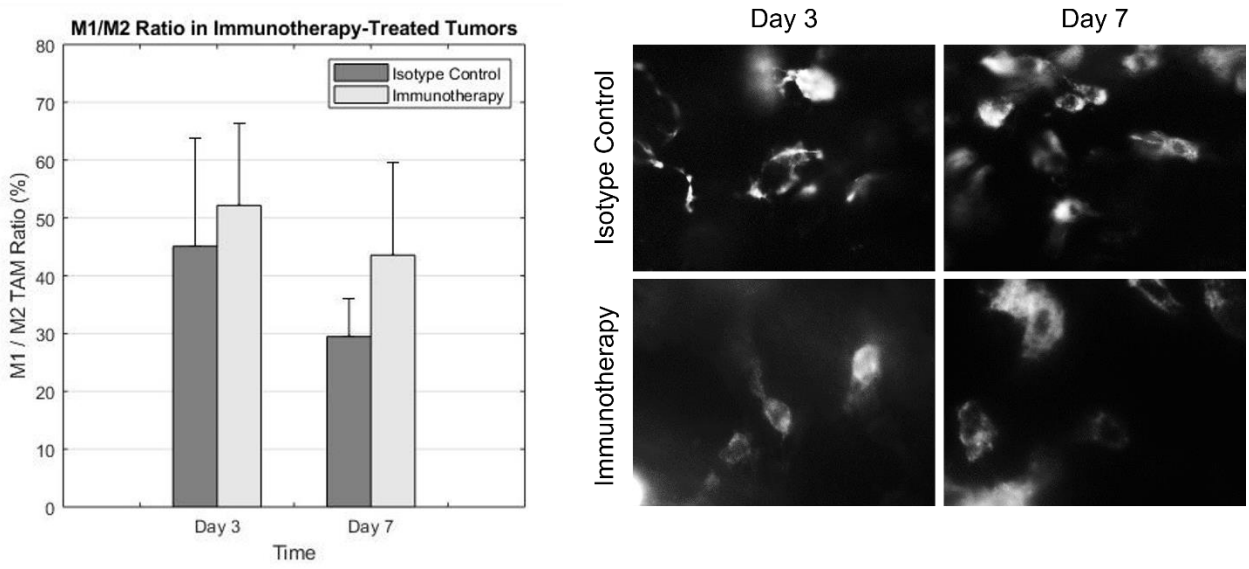

Figure 32. In both the isotype control (dark gray) and anti-CCL2 immunotherapy treated groups (light gray), the M1/M2 ratio decreased over time, although the M1/M2 ratio decreased more in the isotype control group. On both days 3 and 7, the M1/M2 is elevated in the immunotherapy-treated group, albeit insignificantly. An increase in the M1/M2 ratio has been shown to be a positive prognostic indicator of cancer-specific survival (Edin *et al.*, 2012).

6.11 Discussion

In this study, Balb/c mice were subcutaneously injected with murine CT26 colon carcinoma cells in the left flank. Tumors were allowed to grow until they reached 75 mm^3. Once the tumor reached 75 mm^3, mice underwent intraperitoneal treatment with either saline control, isotype control, anti-CCL2 neutralizing antibody immunotherapy, 5-FU chemotherapy, or a combination of anti-CCL2 immunotherapy and 5-FU chemotherapy for up to 7 days.

A two-way ANOVA with repeated measures was used to assess both the comparisons of treatments for days 1, 3, and 7 within metrics and comparisons to day 0 within treatment and within metrics. The normality of the residual error scores for the raw and normalized metrics was tested using the Shapiro-Wilk test. The Wilcoxon Signed Rank test was used to assess the differences between Day 0 and Days 1, 3, and 7 within each of the 5 treatments and for comparing all pairs of treatments on Days 1, 3, and 7 for any metrics in which normality failed ($W < 0.9$). These analyses computed the Pearson product-moment correlations between each pair of normalized metric scores within each of the five treatments. Shapiro-Wilk tests for normality were conducted for scores on all five normalized metrics within each treatment. Correlations between any pair of metrics within a treatment where one or both of the metrics had Shapiro-Wilk values below .88 were recomputed using the nonparametric Spearman's rho correlation.

The first topic of discussion is the effect of treatment on tumor size. Tumor size is the most common metric to assess response to anticancer therapy. Tumors were measured daily with external calipers. By the end of 7 days, tumors grew to 682 ± 85 mm^3 (128% growth per day), 690 ± 119 mm^3 (125% growth per day), 540 ± 82 mm^3 (96% growth per day), 262 ± 131 mm^3 (49% growth per day), and 175 ± 26 mm^3 (32% growth per day) for the saline control, isotype control, immunotherapy, chemotherapy, and combination groups, respectively (Figure 10, 11 and 16). Tables 12 and 14 shows the statistics for raw tumor size; however; tables 13 and 15, which shows statistics for normalized tumor size, is perhaps more important since growth is normalized to the tumor size at day 0. This allows for comparisons between mice that may have had different initial tumor sizes of 74 or 77 mm^3, for example. In all groups except for the combination therapy group, tumor size had significantly increased by day 3 (Table 13). In the combination therapy group, tumor size had significantly increased by day 7 (Table 13). So, it is noteworthy that tumors from all treatment groups experienced tumor growth. At day 3, tumors treated with

combination therapy (anti-CCL2 + 5-FU) showed significantly reduced tumor growth compared to saline control (p=0.011), isotype control (<0.001), and chemotherapy (p=0.012) groups. By day 7, all groups showed significantly different tumor growth rates, expect for the saline and isotype control groups (p=1.000), as expected. By day 7, combination therapy proved just slightly better than chemotherapy alone (p=0.046) with regards to tumor growth. Based on this data alone, it would appear that both immunotherapy and chemotherapy slowed tumor growth, albeit chemotherapy being more successful. A combination of the two treatments slowed tumor growth even further. One surprising result indicated that, according to Pearson correlations, tumor size significantly, albeit weakly, correlated with μ_s' (Figure 31(a), Tables 18, 21, 24, 27, and 30) in all treatment groups. There was a negative correlation of μ_s' vs. tumor size for the saline control (R=-0.287, p=0.016), isotype control (R=-0.624, p<0.001), and immunotherapy groups (R=-0.502, p<0.001), and a positive correlation of μ_s' vs. tumor size for the chemotherapy (R=-0.302, p=0.019) and combination treatment groups (R=0.319, p=0.017). However, the small R values give reason to question the importance of these results. Additionally, Wang et al. found that chemotherapy-treated breast cancer xenografts had reduced tumor cell density and proliferating cell density (Wang *et al.*, 2013), which would theoretically lead to a negative correlation of μ_s' vs. tumor size (Su *et al.*, 2015) in chemotherapy-treated mice, rather than the small positive correlation seen in our study. A potential confounding variable in this situation could be the skin layer overlying the tumor in this subcutaneous tumor model. It is reasonable to assume that, in larger tumors, the skin is stretched. Since chemotherapy and combination therapy treated mice had reduced tumor growth, it may be reasonable to assume that the skin was less stretched, although this was not explicitly tested. If this was the case, light from the DRS probe could potentially interact with the skin layer less in (Rajaram, Gopal, *et al.*, 2010) the control

groups compared to treatment groups. Skin has a higher scattering coefficient due to its collagen content (Lister *et al.*, 2012; Zonios *et al.*, 2008) compared to a tumor (Cerussi *et al.*, 2006; Spliethoff *et al.*, 2014; Su *et al.*, 2015), so "stretching" of the skin in a subcutaneous model could certain affect measured μ_s'. Some groups have solved this issue by creating a fiber-optic needle that penetrates the skin layer to sample μ_s' at the center of allograft or xenograft tumors (Spliethoff *et al.*, 2014). Interestingly, tumor size negatively and significantly correlated with StO_2 and HbO_2 (Figure 31(c, d), Tables 18, 21, 24, 27, and 30) in only the saline control (R=-0.363 and -0.312, p=0.002 and p=0.009) and isotype control groups (R=-0.484 and -0.516, p<0.001 and p<0.001), but not the treatment groups. This indicates that in control groups, as tumor size increases, StO_2 and HbO_2 decreases, indicating a more hypoxic tumor microenvironment with tumor growth. Furthermore, tumor hypoxia, as seen in the control tumors here, have been linked to tumor progression (Vaupel *et al.*, 2006), which is what these results indicate. Spectroscopically-derived StO_2 and HbO_2 (StO_2 * THC) have been shown to be correlated with tumor hypoxic fraction, validated with pimonidazole, an established hypoxia biomarker (Dadgar *et al.*, 2018). These studies by Dadgar et al. showed that DRS-based measurements of StO_2 and HbO_2 can indirectly and non-invasively quantify tumor hypoxia (Dadgar *et al.*, 2018). Although there was a correlation between tumor size and HbO_2 in control tumors in this study, other groups have shown that hypoxia cannot be predicted by tumor size alone (Walsh *et al.*, 2014), which perhaps partially explains why there was no correlation between tumor size and HbO_2 in experimental treatment groups. There were no correlations between tumor size and THC, except in the immunotherapy group (R=0.282, p=0.029). Although tumor size did correlate with many DRS-based metrics, it should be noted that volumetric measurements of allograft or xenograft tumors via external calipers is highly affected by error.

More accurate ways of measuring tumor size include micro-computed tomography (microCT) (Jensen *et al.*, 2008).

The next topic of discussion is the effect of treatment on the DRS-derived perfusion metrics, StO_2, THC, and HbO_2. StO_2 is the tissue oxygen saturation, which is a metric of assessing oxygen saturation, and is defined as the oxygen saturation averaged over the arterio-venous network (Christen *et al.*, 2014). Optical methods quantifying StO_2, including DRS and near-infrared spectroscopy (NIRS), has already made its way to the clinic, where it is currently being used to noninvasively alert clinicians of peripheral hypoperfusion and tissue hypoxia at the patient bedside (Epstein *et al.*, 2014). THC is the volume-averaged total hemoglobin, given as a concentration, of the tissue sampled by spectroscopic methods (G.J. Greening *et al.*, 2018; Rajaram, Gopal, *et al.*, 2010). HbO_2 is simply the amount of oxygenated hemoglobin from the total hemoglobin content and is mathematically a simple product of StO_2 and THC (Quincy Brown *et al.*, 2009; G.J. Greening *et al.*, 2018). Raw values for volume-averaged StO_2 ranged from 3% to 63% (Figure 12). These StO_2 values are comparable to other spectroscopy-based cancer studies (G.J. Greening *et al.*, 2018; G. J. Greening *et al.*, 2018; Palmer *et al.*, 2009; Spliethoff *et al.*, 2014). It is important to note that these raw values are lower than what is expected of arterial oxygen saturation (SaO_2), which is typically between 96% to 98% measured via pulse oximetry (Collins *et al.*, 2015). Raw values for volume-averaged THC ranged between 1.54 mg/mL to 3.42 mg/mL (Figure 13), corresponding to blood volume fractions of 0.95% to 2.28%, based on the well-established assumption that the concentration of hemoglobin in whole blood is 150 mg/mL (Prahl, 1999). These THC/blood volume fraction values are comparable to other spectroscopy-based cancer studies (Rajaram, Gopal, *et al.*, 2010; Spliethoff *et al.*, 2014). Based on these comparisons to literature, it was reasonable to assume that HbO_2 values were as

expected, although studies explicitly reporting spectroscopy-derived HbO_2 are uncommon. Raw values for volume-averaged HbO_2 ranged between 0.05 mg/mL to 1.79 mg/mL (Figure 14).

Tables 12 and 14 shows the statistics for raw StO_2, THC, and HbO_2; however; tables 13 and 15, which shows statistics for normalized StO_2, THC, and HbO_2, is perhaps more important since these metrics are normalized to the value at day 0. This allows for comparisons between mice that may have had different initial StO_2, THC, and HbO_2 values. Within each treatment, neither StO_2, THC, and HbO_2 significantly changed from baseline (Figures 17-19). However, there were several noteworthy trends that may show significance with increased sample power.

By day 7, StO_2 and HbO_2 in the saline control group decreased to 75% ± 5% and 78% ± 6% of baseline values, respectively, whereas THC barely increased to 104% ± 6% of baseline values, although all changes were insignificant (Figure 27-29). Similarly, by day 7, StO_2 and HbO_2 in the isotype control group decreased to 73% ± 21% and 70% ± 10% of baseline values, respectively, whereas THC remained at exactly that of baseline values (100% ± 15%), although all changes were insignificant (Figure 27-29). In the immunotherapy group, by day 7, StO_2 and HbO_2 increased to 102% ± 28% and 128% ± 56% of baseline values, respectively, whereas THC increased to 120% ± 26% of baseline values, although all changes were insignificant (Figure 27-29). It is worth noting that there was a large increase in standard deviation of the immunotherapy-treatment group compared to the isotype control group, indicating variability in treatment effect within subjects. In the chemotherapy group, by day 7, StO_2 and HbO_2 increased to 130% ± 37% and 136% ± 44% of baseline values, respectively, whereas THC increased to 106% ± 15% of baseline values, although all changes were insignificant (Figure 27-29). Again, standard deviations were much greater compared to the saline control group. Finally, in the combination-treatment group, by day 7, StO_2 and HbO_2 increased to 125% ± 22% and 137% ±

31% of baseline values, respectively, whereas THC barely increased to 108% ± 7% of baseline values, although again all changes were insignificant (Figure 27-29). Another noteworthy find was the oxyhemoglobin flare on day 1 in the chemotherapy-treatment group (144% ± 62% compared to day 0 baseline) (Figure 29). Although there was a high standard deviation with no significance, three mice had tumors had HbO_2 flares that doubled compared to baseline (213%, 230%, and 257%) and 6 of 11 mice experience HbO_2 flares in the chemotherapy-treatment group. However, subject-to-subject variability was high. In the future, the DRS-derived HbO_2 metric will be correlated to survival. For example, the question can be asked: do these mice with tumors that experience an increase in HbO_2 one day post-chemotherapy have increased survival compared to those that experience no HbO_2 flare or a decreased HbO_2 flare? In 2011, Roblyer et al. found that an HbO_2 flare one day post-treatment correlated with increased neoadjuvant chemotherapy response in human breast cancer patients (Roblyer *et al.*, 2011). This is important because many patients receiving neoadjuvant chemotherapy do not achieve any measurable response while undergoing toxic chemotherapy. Thus, optical spectroscopy techniques such as DRS may be beneficial in evaluating a patient's (or mouse) early response to therapy, and, if it has been shown to correlate with survival, can guide clinicians in deciding whether to continue with treatment, switch treatments, or proceed more quickly to surgery to reduce unnecessary toxic side effects (Roblyer *et al.*, 2011; A.S. Walker *et al.*, 2014). This indicates that DRS may be useful as a future complimentary tool to monitor early tumor therapeutic response in colon cancer. Next, at 7 days post-treatment, HbO_2, a marker currently being explored as a functional prognostic cancer marker, trended to increase in immunotherapy, chemotherapy, and combination therapy groups compared to their appropriate controls ($p=0.315$, 0.149, and 0.190).

StO_2 correlated with THC in the saline control, immunotherapy-treatment group, and chemotherapy-treatment groups, while not correlating with THC in the isotype control and combination-treatment groups (Figure 31). However, the author cautions to not look too deeply into these significant results. Since the change in THC over the 7-day treatment period was insignificant for all treatment groups and lacked any relevant or interesting trends, it can be concluded that, in this study, THC did not change in response to treatment. Therefore, any significance in the correlation between StO_2 and THC is likely a false positive due to low-powered data (Figure 31). There was always a necessary significant correlation between StO_2 and HbO_2 since these metrics are mathematically related.

While StO_2, and HbO_2 are often used as an indicator of tissue/tumor health, it has been suggested that these metrics can fail as reliable indicators in certain circumstances (Boas *et al.*, 2011). For example, StO_2 alone cannot detect differences in oxygen delivery or utilization between tumors of different treatment groups or even within a single treatment group. Furthermore, in breast cancer, StO_2 alone values measured via optical techniques can fail to distinguish malignant from non-malignant lesions (Boas *et al.*, 2011). However, by combining several metrics such as StO_2, THC, HbO_2, and μ_s', along with anatomical tumor size measured via external calipers, DRS may be able to overcome this limitation. Although not explicitly studied in these experiments, DRS can also provide data on scattering exponent, average blood vessel radius, fat content and water content (Rajaram *et al.*, 2016; Rajaram *et al.*, 2015; Rajaram, Reichenberg, *et al.*, 2010; Spliethoff *et al.*, 2016; Spliethoff *et al.*, 2014). However, since these studies indicated no changes in THC or μ_s' in response to therapy, or in response to simple tumor growth in control animals, and since HbO_2 values are determined in part by StO_2, it's possible DRS may be limited in providing reliable information to clinicians making vital decisions in

managing their patients' therapy regimens. DRS combined with other imaging techniques such as high-resolution microendoscopy (Parikh *et al.*, 2014), or spectroscopic techniques such as Raman spectroscopy (Jenkins *et al.*, 2016) or hyperspectral imaging (Awan *et al.*, 2018) may be more valuable than single-modality DRS.

6.12 Conclusion

Colorectal cancer is still one of the most prominent cancer types within the United States. Although current treatment standards (neoadjuvant therapy, surgery, and adjuvant therapy) treat a wide spectrum of cancer patients, recurrence, patient heterogeneity, toxicity, and poor survival rate remain problematic. Therefore, research into antibody-based immunotherapies in both clinical and pre-clinical settings is highly active. Clinical research into immune checkpoint inhibitors is more mature than cytokine-targeted immunotherapy. At present, cytokine-targeted immunotherapy is limited to anti-VEGF, anti-VEGFR, and anti-EGFR therapies for mCRC patients, although there is a growing interest in interleukin and chemokine therapies in both pre-clinical and early clinical trials. Additionally, monitoring CRC tumor response is a major problem, and investigators are continuing to engineer optical methods to improve the state-of-the-art. One of the biggest emerging challenges for immunotherapy in CRC is elucidating the genomic biomarkers for identifying patients likely to be responders or non-responders for certain immunotherapy regimens and monitoring response in real-time (Kather *et al.*, 2018). In this study, DRS probe was applied to subcutaneous murine colon tumors undergoing either antibody immunotherapy or standard 5-fluorouracil chemotherapy. Mice treated with a combination of these therapies showed reduced tumor growth compared to saline control, isotype control, immunotherapy, and chemotherapy groups 7 days post-treatment. Additionally, at 7 days post-treatment, oxyhemoglobin, a marker currently being explored as a functional prognostic cancer

marker, trended to increase in immunotherapy, chemotherapy, and combination therapy groups compared to controls. Also of interest, an oxyhemoglobin flare was shown in tumors treated with chemotherapy, indicating that DRS may be useful as a complimentary tool to monitor early tumor therapeutic response in colon cancer. However, subject-to-subject variability was high and studies correlating survival to early oxyhemoglobin flares are suggested. Additionally, single-modality DRS may be limited in providing clinicians reliable clinical information, and it is suggested to combine DRS with other endoscopically-compatible imaging or spectroscopic methods. Finally, ongoing research in the Muldoon laboratory at the University of Arkansas is analyzing the correlation of DRS-derived metrics with TAMs in the tumor microenvironment, which will provide valuable microscopic information about how immunotherapy and chemotherapy affect immune cell populations.

6.13 Acknowledgements

This material is based on work supported by the National Institutes of Health (1R15CA202662-01), the National Science Foundation Graduate Research Fellowship Program (G.G., DGE-1450079), the Arkansas Biosciences Institute, and the University of Arkansas Doctoral Academy Fellowship. Any opinions, findings, and conclusions or recommendations expressed in this material are those of the authors and do not necessarily reflect the views of the acknowledged funding agencies. I wish to thank Shelby Bess and Mattison Cato, undergraduates at the time of writing this dissertation, who were instrumental in cranking through data and performing data analysis. This project would not be where it is if it wasn't for Ms. Bess and Mr. Cato. Finally, I'd like to Dr. Narasimhan Rajaram for his guidance in experimental design, Dr. Quinn for his insights into statistical analysis, and Dr. Timothy Muldoon for his support, mentorship, and guidance in experimental design and data analysis.

6.14 Disclosures

The authors declare that there are no conflicts of interest related to this chapter.

References

"Surgical Resection with or without Preoperative Chemotherapy in Oesophageal Cancer: A Randomised Controlled Trial." *Lancet* 359.9319 (2002): 1727-33.

Akdis, M., *et al.* "Interleukins (from Il-1 to Il-38), Interferons, Transforming Growth Factor Beta, and Tnf-Alpha: Receptors, Functions, and Roles in Diseases." *J Allergy Clin Immunol* 138.4 (2016): 984-1010.

Akram, I. G., *et al.* "The Chemokines Ccr1 and Ccrl2 Have a Role in Colorectal Cancer Liver Metastasis." *Tumour Biol* 37.2 (2016): 2461-71.

Allavena, P., *et al.* "The Inflammatory Micro-Environment in Tumor Progression: The Role of Tumor-Associated Macrophages." *Critical Reviews in Oncology/Hematology* 66 (2008): 1-9.

Allen, F., *et al.* "Ccl3 Augments Tumor Rejection and Enhances Cd8(+) T Cell Infiltration through Nk and Cd103(+) Dendritic Cell Recruitment Via Ifngamma." *Oncoimmunology* 7.3 (2018): e1393598.

Althumairi, A. A., and S. L. Gearhart. "Local Excision for Early Rectal Cancer: Transanal Endoscopic Microsurgery and Beyond." *J Gastrointest Oncol* 6.3 (2015): 296-306.

Andre, T., *et al.* "Semimonthly Versus Monthly Regimen of Fluorouracil and Leucovorin Administered for 24 or 36 Weeks as Adjuvant Therapy in Stage Ii and Iii Colon Cancer: Results of a Randomized Trial." *J Clin Oncol* 21.15 (2003): 2896-903.

Angevin, E., *et al.* "A Phase I/Ii, Multiple-Dose, Dose-Escalation Study of Siltuximab, an Anti-Interleukin-6 Monoclonal Antibody, in Patients with Advanced Solid Tumors." *Clin Cancer Res* 20.8 (2014): 2192-204.

Armstrong, R. A. "When to Use the Bonferroni Correction." *Ophthalmic Physiol Opt* 34.5 (2014): 502-8.

Awan, R., *et al.* "Using Spectral Imaging for the Analysis of Abnormalities for Colorectal Cancer: When Is It Helpful?" *PLoS One* 13.6 (2018): e0197431.

Balmer, M. T., *et al.* "Doxorubicin and 5-Fluorouracil Induced Accumulation and Transcriptional Activity of P53 Are Independent of the Phosphorylation at Serine 15 in Mcf-7 Breast Cancer Cells." *Cancer Biol Ther* 15.8 (2014): 1000-12.

Baltussen, E. J. M., *et al.* "Diffuse Reflectance Spectroscopy as a Tool for Real-Time Tissue Assessment During Colorectal Cancer Surgery." *J Biomed Opt* 22.10 (2017): 1-6.

Banerjee, A., *et al.* "Hypothesis Testing, Type I and Type Ii Errors." *Ind Psychiatry J* 18.2 (2009): 127-31.

Barbera-Guillem, E., *et al.* "Vascular Endothelial Growth Factor Secretion by Tumor-Infiltrating Macrophages Essentially Supports Tumor Angiogenesis, and Igg Immune Complexes Potentiate the Process." *Cancer Research* 62.23 (2002): 7042-9.

Barros, M.H.M., *et al.* "Macrophage Polarisation: An Immunohistochemical Approach for Identifying M1 and M2 Macrophages." *PLOS ONE* 8.11 (2013): e80908.

Bauer, T.M., *et al.* "A First-in-Human Study of Pegylated Recombinant Human Il-10 (Am0010), Daily Administered for Four Months in Selected Advanced Solid Tumors." *Journal of Clinical Oncology* 32.15_suppl (2014): TPS3126-TPS26.

Becht, E., *et al.* "Immune and Stromal Classification of Colorectal Cancer Is Associated with Molecular Subtypes and Relevant for Precision Immunotherapy." *Clincal Cancer Research* 22.16 (2016): 4057-66.

Bénard, F., *et al.* "Systematic Review of Colorectal Cancer Screening Guidelines for Average-Risk Adults: Summarizing the Current Global Recommendations." *World J Gastroenterol* 24.1 (2018): 124-38.

Berger, A.W., *et al.* "Treatment Monitoring in Metastatic Colorectal Cancer Patients by Quantification and Kras Genotyping of Circulating Cell-Free DNA." *PLoS One* 12.3 (2017).

Beyersdorf, N., *et al.* "Cd28 Co-Stimulation in T-Cell Homeostasis: A Recent Perspective." *Immunotargets Ther* 4 (2015): 111-22.

Blanco-Calvo, M., *et al.* "Colorectal Cancer Classification and Cell Heterogeneity: A Systems Oncology Approach." *Int J Mol Sci* 16.6 (2015): 13610-32.

Boas, D. A., and M. A. Franceschini. "Haemoglobin Oxygen Saturation as a Biomarker: The Problem and a Solution." *Philos Trans A Math Phys Eng Sci* 369.1955 (2011): 4407-24.

Boland, P.M., and M. Fakih. "The Emerging Role of Neoadjuvant Chemotherapy for Rectal Cancer." *Journal of Gastrointestinal Oncology* 5.5 (2014): 362-73.

Boland, P.M., and W.W. Ma. "Immunotherapy for Colorectal Cancer." *Cancers* 9.5 (2017).

Brown, C. M., *et al.* "In Vivo Imaging of Unstained Tissues Using a Compact and Flexible Multiphoton Microendoscope." *J Biomed Opt* 17.4 (2012): 040505.

Buchbinder, E. I., and A. Desai. "Ctla-4 and Pd-1 Pathways: Similarities, Differences, and Implications of Their Inhibition." *Am J Clin Oncol* 39.1 (2016): 98-106.

Burmeister, K., *et al.* "Vascular Endothelial Growth Factor a Amplification in Colorectal Cancer Is Associated with Reduced M1 and M2 Macrophages and Diminished Pd-1-Expressing Lymphocytes." *PLoS One* 12.4 (2017).

Burris, H. A., *et al.* "Safety and Activity of Varlilumab, a Novel and First-in-Class Agonist Anti-Cd27 Antibody, in Patients with Advanced Solid Tumors." *J Clin Oncol* 35.18 (2017): 2028-36.

Optical Properties of Colorectal Muscle in Visible/Nir Range. SPIE Photonics Europe. 2018. SPIE. Print.

Carrato, A. "Adjuvant Treatment of Colorectal Cancer." *Gastrointest Cancer Res* 2.4 Suppl 2 (2008): S42-6.

Cercek, A., *et al.* "Neoadjuvant Chemotherapy First, Followed by Chemoradiation and Then Surgery, in the Management of Locally Advanced Rectal Cancer." *J Natl Compr Canc Netw* 12.4 (2014): 513-9.

Cerussi, A., *et al.* "In Vivo Absorption, Scattering, and Physiologic Properties of 58 Malignant Breast Tumors Determined by Broadband Diffuse Optical Spectroscopy." *J Biomed Opt* 11.4 (2006): 044005.

Cheadle, E. J., *et al.* "Eotaxin-2 and Colorectal Cancer: A Potential Target for Immune Therapy." *Clin Cancer Res* 13.19 (2007): 5719-28.

Cheeseman, S.L., *et al.* "A 'Modified De Gramont' Regimen of Fluorouracil, Alone and with Oxaliplatin, for Advanced Colorectal Cancer." *British Journal of Cancer* 87.4 (2008): 393-9.

Chen, J.J., *et al.* "Tumor-Associated Macrophages: The Double-Edged Sword in Cancer Progression." *Journal of Clinical Oncology* 23.5 (2005): 953-64.

Christen, T., *et al.* "Tissue Oxygen Saturation Mapping with Magnetic Resonance Imaging." *J Cereb Blood Flow Metab* 34.9 (2014): 1550-7.

Chun, E., *et al.* "Ccl2 Promotes Colorectal Carcinogenesis by Enhancing Polymorphonuclear Myeloid-Derived Suppressor Cell Population and Function." *Cell Reports* 12.2 (2015): 244-57.

Chung, W. S., *et al.* "Response Evaluation in Patients with Colorectal Liver Metastases: Recist Version 1.1 Versus Modified Ct Criteria." *AJR Am J Roentgenol* 199.4 (2012): 809-15.

Cohen, Martin H., *et al.* "Fda Drug Approval Summary: Bevacizumab Plus Folfox4 as Second-Line Treatment of Colorectal Cancer." *The Oncologist* 12.3 (2007): 356-61.

Collins, J. A., *et al.* "Relating Oxygen Partial Pressure, Saturation and Content: The Haemoglobin-Oxygen Dissociation Curve." *Breathe (Sheff)* 11.3 (2015): 194-201.

Cunningham, D., *et al.* "Perioperative Chemotherapy Versus Surgery Alone for Resectable Gastroesophageal Cancer." *N Engl J Med* 355.1 (2006): 11-20.

Cunningham, D., *et al.* "Cetuximab Monotherapy and Cetuximab Plus Irinotecan in Irinotecan-Refractory Metastatic Colorectal Cancer." *N Engl J Med* 351.4 (2004): 337-45.

Dadgar, S., *et al.* "Optical Spectroscopic Sensing of Tumor Hypoxia." *Journal of Biomedical Optics* 23.6 (2018): 067001.

de Gramont, A., *et al.* "Leucovorin and Fluorouracil with or without Oxaliplatin as First-Line Treatment in Advanced Colorectal Cancer." *J Clin Oncol* 18.16 (2000): 2938-47.

Dhillon, S. "Regorafenib: A Review in Metastatic Colorectal Cancer." *Drugs* 78.11 (2018): 1133-44.

Diaz, Luis A., *et al.* "Keynote-177: Randomized Phase Iii Study of Pembrolizumab Versus Investigator-Choice Chemotherapy for Mismatch Repair-Deficient or Microsatellite Instability-High Metastatic Colorectal Carcinoma." *Journal of Clinical Oncology* 35.4_suppl (2017): TPS815-TPS15.

Dienstmann, R., *et al.* "Prediction of Overall Survival in Stage Ii and Iii Colon Cancer Beyond Tnm System: A Retrospective, Pooled Biomarker Study." *Annals of Oncology* 28.5 (2017): 1023-31.

Dimberg, J., *et al.* "Expression of Cd137 and Cd137 Ligand in Colorectal Cancer Patients." *Oncol Rep* 15.5 (2006): 1197-200.

Dong, Y., *et al.* "Pd-1 and Its Ligands Are Important Immune Checkpoints in Cancer." *Oncotarget* 8.2 (2017): 2171-86.

Douillard, J. Y., *et al.* "Final Results from Prime: Randomized Phase Iii Study of Panitumumab with Folfox4 for First-Line Treatment of Metastatic Colorectal Cancer." *Ann Oncol* 25.7 (2014): 1346-55.

Dunne, Philip D., *et al.* "Cancer-Cell Intrinsic Gene Expression Signatures Overcome Intratumoural Heterogeneity Bias in Colorectal Cancer Patient Classification." *Nature Communications* 8 (2017): 15657.

Edin, S., *et al.* "The Distribution of Macrophages with a M1 or M2 Phenotype in Relation to Prognosis and the Molecular Characteristics of Colorectal Cancer." *PLoS One* 7.10 (2012): e47045.

Eisenhauer, E. A., *et al.* "New Response Evaluation Criteria in Solid Tumours: Revised Recist Guideline (Version 1.1)." *Eur J Cancer* 45.2 (2009): 228-47.

Epstein, C. D., and K. T. Haghenbeck. "Bedside Assessment of Tissue Oxygen Saturation Monitoring in Critically Ill Adults: An Integrative Review of the Literature." *Crit Care Res Pract* 2014 (2014): 709683.

Erreni, M., *et al.* "Tumor-Associated Macrophages (Tam) and Inflammation in Colorectal Cancer." *Cancer Microenviornment* 4 (2011): 141-54.

Fang, L., *et al.* "Determining the Optimal 5-Fu Therapeutic Dosage in the Treatment of Colorectal Cancer Patients." *Oncotarget* 7.49 (2016): 81880-7.

Ferrari, L., and A. Fichera. "Neoadjuvant Chemoradiation Therapy and Pathological Complete Response in Rectal Cancer." *Gastroenterology Report* 3.4 (2015): 277-88.

Forssell, J., *et al.* "High Macrophage Infiltration Along the Tumor Front Correlates with Improved Survival in Colon Cancer." *Clinical Cancer Research* 13.5 (2007): 1472-9.

Funada, Y., *et al.* "Prognostic Significance of Cd8+ T Cell and Macrophage Peritumoral Infiltration in Colorectal Cancer." *Oncology Reports* 10.2 (2003): 309-13.

Giantonio, B. J., *et al.* "Bevacizumab in Combination with Oxaliplatin, Fluorouracil, and Leucovorin (Folfox4) for Previously Treated Metastatic Colorectal Cancer: Results from the Eastern Cooperative Oncology Group Study E3200." *J Clin Oncol* 25.12 (2007): 1539-44.

Granata, V., *et al.* "Early Assessment of Colorectal Cancer Patients with Liver Metastases Treated with Antiangiogenic Drugs: The Role of Intravoxel Incoherent Motion in Diffusion-Weighted Imaging." *PLoS One* 10.11 (2015).

Greening, G. J., *et al.* "Effects of Isoflurane Anesthesia on Physiological Parameters in Murine Subcutaneous Tumor Allografts Measured Via Diffuse Reflectance Spectroscopy." *Biomed Opt Express* 9.6 (2018): 2871-86.

Greening, G.J., *et al.* "Towards Monitoring Dysplastic Progression in the Oral Cavity Using a Hybrid Fiber-Bundle Imaging and Spectroscopy Probe." *Scientific Reports* 6.26734 (2016).

Greening, G.J., *et al.* "Fiber-Bundle Microendoscopy with Sub-Diffuse Reflectance Spectroscopy and Intensity Mapping for Multimodal Optical Biopsy of Stratified Epithelium." *Biomedical Optics Express* 6.12 (2015): 4934-50.

Greening, G.J., *et al.* "Sampling Depth of a Diffuse Reflectance Spectroscopy Probe for in-Vivo Physiological Quantification of Murine Subcutaneous Tumor Allografts." *Journal of Biomedical Optics* 23.8 (2018).

Greening, Gage J., *et al.* "Effects of Isoflurane Anesthesia on Physiological Parameters in Murine Subcutaneous Tumor Allografts Measured Via Diffuse Reflectance Spectroscopy." *Biomedical Optics Express* 9.6 (2018): 2871-86.

Grothey, A., *et al.* "Regorafenib Monotherapy for Previously Treated Metastatic Colorectal Cancer (Correct): An International, Multicentre, Randomised, Placebo-Controlled, Phase 3 Trial." *Lancet* 381.9863 (2013): 303-12.

Group, FOxTROT Collaborative. "Feasibility of Preoperative Chemotherapy for Locally Advanced, Operable Colon Cancer: The Pilot Phase of a Randomised Controlled Trial." *Lancet Oncol* 13.11 (2012): 1152-60.

Guijarro, L. G., *et al.* "N-Acetyl-L-Cysteine Combined with Mesalamine in the Treatment of Ulcerative Colitis: Randomized, Placebo-Controlled Pilot Study." *World J Gastroenterol* 14.18 (2008): 2851-7.

Guinney, J., *et al.* "The Consensus Molecular Subtypes of Colorectal Cancer." *Nature Medicine* 21.11 (2015): 1350-6.

Guo, C., *et al.* "The Role of Tumor-Associated Macrophages in Tumor Vascularization." *Vascular Cell* 5.1 (2013).

Guo, Q., *et al.* "New Mechanisms of Tumor-Associated Macrophages on Promoting Tumor Progression: Recent Research Advances and Potential Targets for Tumor Immunotherapy." *Journal of Immunology Research* 2016 (2016): 1-12.

Habr-Gama, A., *et al.* "Complete Clinical Response after Neoadjuvant Chemoradiation Therapy for Distal Rectal Cancer: Characterization of Clinical and Endoscopic Findings for Standardization." *Diseases of the Colon & Rectum* 53.12 (2010): 1692-8.

Hammond, W. A., *et al.* "Pharmacologic Resistance in Colorectal Cancer: A Review." *Ther Adv Med Oncol* 8.1 (2016): 57-84.

He, J., *et al.* "Chemoresistance of Colorectal Cancer to 5-Fluorouracil Is Associated with Silencing of the Bnip3 Gene through Aberrant Methylation." *J Cancer* 8.7 (2017): 1187-96.

Herbeuval, J.P., *et al.* "Recruitment of Stat3 for Production of Il-10 by Colon Carcinoma Cells Induced by Macrophage-Derived Il-6." *The Journal of Immunology* 172.7 (2004): 4630-6.

Horiuchi, A., and N. Tanaka. "Improving Quality Measures in Colonoscopy and Its Therapeutic Intervention." *World J Gastroenterol* 20.36 (2014): 13027-34.

Huang, J., *et al.* "Comparison of Folfiri with or without Cetuximab in Patients with Resected Stage Iii Colon Cancer; Ncctg (Alliance) Intergroup Trial N0147." *Clin Colorectal Cancer* 13.2 (2014): 100-9.

Hubbard, J. M., and S. R. Alberts. "Alternate Dosing of Cetuximab for Patients with Metastatic Colorectal Cancer." *Gastrointest Cancer Res* 6.2 (2013): 47-55.

Hurwitz, H., *et al.* "Bevacizumab Plus Irinotecan, Fluorouracil, and Leucovorin for Metastatic Colorectal Cancer." *N Engl J Med* 350.23 (2004): 2335-42.

Ilic, I., *et al.* "Bevacizumab Combined with Chemotherapy Improves Survival for Patients with Metastatic Colorectal Cancer: Evidence from Meta Analysis." *PLoS One* 11.8 (2016): e0161912.

Issa, I. A., and M. Noureddine. "Colorectal Cancer Screening: An Updated Review of the Available Options." *World J Gastroenterol* 23.28 (2017): 5086-96.

Itatani, Y., *et al.* "The Role of Chemokines in Promoting Colorectal Cancer Invasion/Metastasis." *Int J Mol Sci* 17.5 (2016).

Jenkins, C. A., *et al.* "Role of Raman Spectroscopy and Surface Enhanced Raman Spectroscopy in Colorectal Cancer." *World J Gastrointest Oncol* 8.5 (2016): 427-38.

Jenkins, R. W., *et al.* "Mechanisms of Resistance to Immune Checkpoint Inhibitors." *Br J Cancer* 118.1 (2018): 9-16.

Jensen, M. M., *et al.* "Tumor Volume in Subcutaneous Mouse Xenografts Measured by Microct Is More Accurate and Reproducible Than Determined by 18f-Fdg-Micropet or External Caliper." *BMC Med Imaging* 8 (2008): 16.

Jeon, H.J., *et al.* "Adjuvant Chemotherapy Using the Folfox Regimen in Colon Cancer." *Journal of the Korean Society of Coloproctology* 27.3 (2011): 140-6.

Jure-Kunkel, M., *et al.* "Synergy between Chemotherapeutic Agents and Ctla-4 Blockade in Preclinical Tumor Models." *Cancer Immunol Immunother* 62.9 (2013): 1533-45.

Kaler, P., *et al.* "The Nf-Kb/Akt-Dependent Induction of Wnt Signaling in Colon Cancer Cells by Macrophages and Il-1β." *Cancer Microenviornment* 2.1 (2009): 69-80.

Kather, J. N., *et al.* "Genomics and Emerging Biomarkers for Immunotherapy of Colorectal Cancer." *Semin Cancer Biol* 52.Pt 2 (2018): 189-97.

Kawakami, H., *et al.* "Msi Testing and Its Role in the Management of Colorectal Cancer." *Curr Treat Options Oncol* 16.7 (2015): 30.

Keir, M. E., *et al.* "Tissue Expression of Pd-L1 Mediates Peripheral T Cell Tolerance." *J Exp Med* 203.4 (2006): 883-95.

Kekelidze, M., *et al.* "Colorectal Cancer: Current Imaging Methods and Future Perspectives for the Diagnosis, Staging and Therapeutic Response Evaluation." *World J Gastroenterol* 19.46 (2013): 8502-14.

Kim, H. Y. "Statistical Notes for Clinical Researchers: Post-Hoc Multiple Comparisons." *Restor Dent Endod* 40.2 (2015): 172-6.

Kirk, P.S., *et al.* "Inhibition of Ccl2 Signaling in Combination with Docetaxel Treatment Has Profound Inhibitory Effects on Prostate Cancer Growth in Bone." *International Journal of Molecular Sciences* 14.5 (2013): 10483-96.

Kitamura, H., *et al.* "Interleukin-6/Stat3 Signaling as a Promising Target to Improve the Efficacy of Cancer Immunotherapy." *Cancer Sci* 108.10 (2017): 1947-52.

Klampfer, L. "Cytokines, Inflammation and Colon Cancer." *Curr Cancer Drug Targets* 11.4 (2011): 451-64.

Landmann, R.G., and M.R. Weiser. "Surgical Management of Locally Advanced and Locally Recurrent Colon Cancer." *Clinics in Colon and Rectal Surgery* 18.3 (2005): 182-9.

Landskron, G., *et al.* "Chronic Inflammation and Cytokines in the Tumor Microenvironment." *Journal of Immunology Research* 149185 (2014).

Le, Dung T., *et al.* "Keynote-164: Phase 2 Study of Pembrolizumab for Patients with Previously Treated, Microsatellite Instability-High Advanced Colorectal Carcinoma." *Journal of Clinical Oncology* 34.15_suppl (2016): TPS3631-TPS31.

Leach, D. R., *et al.* "Enhancement of Antitumor Immunity by Ctla-4 Blockade." *Science* 271.5256 (1996): 1734-6.

Lee, L., *et al.* "Immune Checkpoint Inhibitors: An Introduction to the Next-Generation Cancer Immunotherapy." *J Clin Pharmacol* 56.2 (2016): 157-69.

Lee, S., and D. K. Lee. "What Is the Proper Way to Apply the Multiple Comparison Test?" *Korean J Anesthesiol* 71.5 (2018): 353-60.

Lenz, H. J. "Cetuximab in the Management of Colorectal Cancer." *Biologics* 1.2 (2007): 77-91.

Leone, F., *et al.* "Panitumumab in Combination with Infusional Oxaliplatin and Oral Capecitabine for Conversion Therapy in Patients with Colon Cancer and Advanced Liver Metastases. The Metapan Study." *Cancer* 119.19 (2013): 3429-35.

Levin, T.R. "Colorectal Cancer Screening: 80% by 2018. Colonoscopists Simply Cannot Do It Alone." *Gastrointestinal Endoscopy* 83.3 (2016).

Li, B., *et al.* "Immune Checkpoint Inhibitors: Basics and Challenges." *Curr Med Chem* (2017).

Li, J., *et al.* "Regorafenib Plus Best Supportive Care Versus Placebo Plus Best Supportive Care in Asian Patients with Previously Treated Metastatic Colorectal Cancer (Concur): A Randomised, Double-Blind, Placebo-Controlled, Phase 3 Trial." *Lancet Oncol* 16.6 (2015): 619-29.

Li, L. H., *et al.* "Monitoring Neoadjuvant Therapy Responses in Rectal Cancer Using Multimodal Nonlinear Optical Microscopy." *Oncotarget* 8.63 (2017): 107323-33.

Li, M., *et al.* "Targeting of Cancer-Associated Fibroblasts Enhances the Efficacy of Cancer Chemotherapy by Regulating the Tumor Microenvironment." *Molecular Medicine Reports* 13.3 (2016): 2476-84.

Lim, S.Y., *et al.* "Targeting the Ccl2-Ccr2 Signaling Axis in Cancer Metastasis." *Oncotarget* 7.19 (2016): 18697-710.

Lister, T., *et al.* "Optical Properties of Human Skin." *Journal of Biomedical Optics* 17.9 (2012).

Liu, Q., *et al.* "The Cxcl8-Cxcr1/2 Pathways in Cancer." *Cytokine Growth Factor Rev* 31 (2016): 61-71.

Liu, Y., and X. Cao. "The Origin and Function of Tumor-Associated Macrophages." *Cellular & Molecular Immunology* 12.1 (2015): 1-4.

Ludmir, E. B., *et al.* "Total Neoadjuvant Therapy for Rectal Cancer: An Emerging Option." *Cancer* 123.9 (2017): 1497-506.

Lynch, D., and A. Murphy. "The Emerging Role of Immunotherapy in Colorectal Cancer." *Annals of Translational Medicine* 4.16 (2016): 305.

"The Emerging Role of Immunotherapy in Colorectal Cancer." *Ann Transl Med* 4.16 (2016): 305.

Mager, L. F., *et al.* "Cytokine-Induced Modulation of Colorectal Cancer." *Front Oncol* 6 (2016): 96.

Mahalingam, Devalingam, *et al.* "First-in-Human, Phase I Study Assessing Imalumab (Bax69), a First-in-Class Anti-Oxidized Macrophage Migration Inhibitory Factor (Oxmif) Antibody in Advanced Solid Tumors." *Journal of Clinical Oncology* 33.15_suppl (2015): 2518-18.

Manzat Saplacan, R. M., *et al.* "The Role of Pdgfs and Pdgfrs in Colorectal Cancer." *Mediators Inflamm* 2017 (2017): 4708076.

Marech, I., *et al.* "Tumour-Associated Macrophages Correlate with Microvascular Bed Extension in Colorectal Cancer Patients." *Journal of Cellular and Molecular Medicine* 20.7 (2016): 1373-80.

McClellan, J.L., *et al.* "Linking Tumor-Associated Macrophages, Inflammation, and Intestinal Tumorigenesis: Role of Mcp-1." *American Journal of Physiology. Gastrointestinal and Liver Physiology* 303.10 (2012): 1087-95.

Mesia, R., *et al.* "A Phase 2 Open Label, Single-Arm Trial to Evaluate the Combination of Cetuximab Plus Taxotere, Cisplatin, and 5-Flurouracil as an Induction Regimen in Patients with Unresectable Squamous Cell Carcinoma of the Head and Neck." *Int J Radiat Oncol Biol Phys* 94.2 (2016): 289-96.

Miles, A., *et al.* "Colorectal Cancer: Advances in Prevention and Early Detection." *Biomed Res Int* 2015 (2015).

Mira, A., *et al.* "Stroma-Derived Hgf Drives Metabolic Adaptation of Colorectal Cancer to Angiogenesis Inhibitors." *Oncotarget* 8.24 (2017): 38193-213.

Mitsunaga, M., *et al.* "Fluorescence Endoscopic Detection of Murine Colitis-Associated Colon Cancer by Topically Applied Enzymatically Rapid-Activatable Probe." *Gut* 62.8 (2013): 1179-86.

Nadler, S. H., and G. E. Moore. "Fluorouracil Colon-Rectum Adjuvant Chemotherapy." *Arch Surg* 89 (1964): 592-5.

Nair, A. B., and S. Jacob. "A Simple Practice Guide for Dose Conversion between Animals and Human." *J Basic Clin Pharm* 7.2 (2016): 27-31.

Noguchi, T., *et al.* "Antibody-Based Therapy in Colorectal Cancer." *Immunotherapy* 5.5 (2013): 533-45.

O'Neil, B. H., *et al.* "Safety and Antitumor Activity of the Anti-Pd-1 Antibody Pembrolizumab in Patients with Advanced Colorectal Carcinoma." *PLoS One* 12.12 (2017): e0189848.

Ocvirk, J., *et al.* "Cetuximab Plus Folfox6 or Folfiri in Metastatic Colorectal Cancer: Cecog Trial." *World J Gastroenterol* 16.25 (2010): 3133-43.

Ohlsson, L., *et al.* "Ectopic Expression of the Chemokine Cxcl17 in Colon Cancer Cells." *Br J Cancer* 114.6 (2016): 697-703.

Overman, M. J., *et al.* "Nivolumab in Patients with Metastatic DNA Mismatch Repair-Deficient or Microsatellite Instability-High Colorectal Cancer (Checkmate 142): An Open-Label, Multicentre, Phase 2 Study." *Lancet Oncol* 18.9 (2017): 1182-91.

Palframan, R.T., *et al.* "Inflammatory Chemokine Transport and Presentation in Hev: A Remote Control Mechanism for Monocyte Recruitment to Lymph Nodes in Inflamed Tissues." *The Journal of Experimental Medicine* 194.9 (2001): 1361-73.

Palmer, G.M., *et al.* "Quantitative Diffuse Reflectance and Fluorescence Spectroscopy: A Tool to Monitor Tumor Physiology in Vivo." *Journal of Biomedical Optics* 14.2 (2009).

Pardoll, D. M. "The Blockade of Immune Checkpoints in Cancer Immunotherapy." *Nat Rev Cancer* 12.4 (2012): 252-64.

Parikh, N., *et al.* "In Vivo Diagnostic Accuracy of High Resolution Microendoscopy in Differentiating Neoplastic from Non-Neoplastic Colorectal Polyps: A Prospective Study." *The American Journal of Gastroenterology* 109.1 (2014): 68-75.

Passardi, A., *et al.* "Immune Checkpoints as a Target for Colorectal Cancer Treatment." *Int J Mol Sci* 18.6 (2017).

Patel, S. P., and R. Kurzrock. "Pd-L1 Expression as a Predictive Biomarker in Cancer Immunotherapy." *Mol Cancer Ther* 14.4 (2015): 847-56.

Peng, H., *et al.* "Reprogramming Tumor-Associated Macrophages to Reverse Egfr(T790m) Resistance by Dual-Targeting Codelivery of Gefitinib/Vorinostat." *Nano Lett* 17.12 (2017): 7684-90.

Petersen, R. K., *et al.* "Clinical Impact of Fdg-Pet/Ct on Colorectal Cancer Staging and Treatment Strategy." *Am J Nucl Med Mol Imaging* 4.5 (2014): 471-82.

Popivanova, B. K., *et al.* "Blocking Tnf-Alpha in Mice Reduces Colorectal Carcinogenesis Associated with Chronic Colitis." *J Clin Invest* 118.2 (2008): 560-70.

Popivanova, B.K., *et al.* "Blockade of a Chemokine, Ccl2, Reduces Chronic Colitis-Associated Carcinogenesis in Mice." *Cancer Research* 69.19 (2009): 7884-92.

Popovic, Z.V., *et al.* "Sulfated Glycosphingolipid as Mediator of Phagocytosis: Sm4s Enhances Apoptotic Cell Clearance and Modulates Macrophage Activity." *The Journal of Immunology* 179.10 (2007): 6770-82.

Prahl, S. "Optical Absorption of Hemoglobin." *Optical Properties Spectra*. Oregon Medical Laser Center 2015. Web.

Prahl, S.A. "Optical Absorption of Hemoglobin." 1999. Web. January 1, 2016.

Price, T. J., *et al.* "Panitumumab Versus Cetuximab in Patients with Chemotherapy-Refractory Wild-Type Kras Exon 2 Metastatic Colorectal Cancer (Aspecct): A Randomised, Multicentre, Open-Label, Non-Inferiority Phase 3 Study." *Lancet Oncol* 15.6 (2014): 569-79.

Quincy Brown, J., *et al.* "Quantitative Optical Spectroscopy: A Robust Tool for Direct Measurement of Breast Cancer Vascular Oxygenation and Total Hemoglobin Content in Vivo." *Cancer Research* 69.7 (2009): 2919-26.

Qureshi, O. S., *et al.* "Trans-Endocytosis of Cd80 and Cd86: A Molecular Basis for the Cell-Extrinsic Function of Ctla-4." *Science* 332.6029 (2011): 600-3.

Rajaram, N., *et al.* "Experimental Validation of the Effects of Microvasculature Pigment Packaging on in Vivo Diffuse Reflectance Spectroscopy." *Lasers in Surgery and Medicine* 42.7 (2010): 680-8.

Rajaram, N., *et al.* "Optical Spectroscopy of Tumor Oxygenation and Metabolism in Preclinical Head and Neck Tumors That Fail Radiation Therapy." *Molecular Cancer Research* 14.1 (2016).

Rajaram, N., *et al.* "Non-Invasive, Simultaneous Quantification of Vascular Oxygenation and Glucose Uptake in Tissue." *PLoS One* 10.1 (2015).

Rajaram, N., *et al.* "Pilot Clinical Study for Quantitative Spectral Diagnosis of Non-Melanoma Skin Cancer." *Lasers in Surgery and Medicine* 42.10 (2010): 716-27.

Riley, J. L. "Pd-1 Signaling in Primary T Cells." *Immunol Rev* 229.1 (2009): 114-25.

Roblyer, D., *et al.* "Optical Imaging of Breast Cancer Oxyhemoglobin Flare Correlates with Neoadjuvant Chemotherapy Response One Day after Starting Treatment." *PNAS* 108.35 (2011): 14626-31.

Ronnekleiv-Kelly, S. M., and G. D. Kennedy. "Management of Stage Iv Rectal Cancer: Palliative Options." *World J Gastroenterol* 17.7 (2011): 835-47.

Sacco, J. J., *et al.* "The Average Body Surface Area of Adult Cancer Patients in the Uk: A Multicentre Retrospective Study." *PLoS One* 5.1 (2010): e8933.

Sakuma, S., *et al.* "Fluorescence-Based Endoscopic Imaging of Thomsen-Friedenreich Antigen to Improve Early Detection of Colorectal Cancer." *Int J Cancer* 136.5 (2015): 1095-103.

Saltz, L. B., *et al.* "Bevacizumab in Combination with Oxaliplatin-Based Chemotherapy as First-Line Therapy in Metastatic Colorectal Cancer: A Randomized Phase Iii Study." *J Clin Oncol* 26.12 (2008): 2013-9.

Saltz, L. B., *et al.* "Randomized Phase Ii Trial of Cetuximab, Bevacizumab, and Irinotecan Compared with Cetuximab and Bevacizumab Alone in Irinotecan-Refractory Colorectal Cancer: The Bond-2 Study." *J Clin Oncol* 25.29 (2007): 4557-61.

Sanchez-Castanon, M., *et al.* "Immunotherapy in Colorectal Cancer: What Have We Learned So Far?" *Clinica Chimica Acta* 460 (2016): 78-87.

Schols, R.M., *et al.* "Automated Spectroscopic Tissue Classification in Colorectal Surgery." *Surgical Innovation* 22.6 (2015): 557-67.

Segal, N. H., *et al.* "Results from an Integrated Safety Analysis of Urelumab, an Agonist Anti-Cd137 Monoclonal Antibody." *Clin Cancer Res* 23.8 (2017): 1929-36.

Seidel, J. A., *et al.* "Anti-Pd-1 and Anti-Ctla-4 Therapies in Cancer: Mechanisms of Action, Efficacy, and Limitations." *Front Oncol* 8 (2018).

Selby, M. J., *et al.* "Preclinical Development of Ipilimumab and Nivolumab Combination Immunotherapy: Mouse Tumor Models, in Vitro Functional Studies, and Cynomolgus Macaque Toxicology." *PLoS One* 11.9 (2016): e0161779.

Setrerrahmane, S., and H. Xu. "Tumor-Related Interleukins: Old Validated Targets for New Anti-Cancer Drug Development." *Mol Cancer* 16 (2017).

Sharp, G. S., and W. W. Benefiel. "5-Fluorouracil in the Treatment of Inoperable Carcinoma of the Colon and Rectum." *Cancer Chemother Rep* 20 (1962): 97-101.

Siegel, R.L., *et al.* "Cancer Statistics, 2018." *A Cancer Journal for Clinicians* 68.1 (2018): 7-30.

Siegel, R.L., *et al.* "Cancer Statistics, 2016." *A Cancer Journal for Clinicians* 66.1 (2016): 7-30.

Singh, M., *et al.* "Effective Innate and Adaptive Anti-Melanoma Immunity through Localized Tlr-7/8 Activation." *The Journal of Immunology* 193.9 (2014): 4722-31.

Smith, K. M., and J. Desai. "Nivolumab for the Treatment of Colorectal Cancer." *Expert Rev Anticancer Ther* 18.7 (2018): 611-18.

Specenier, P. "Ipilimumab in Melanoma." *Expert Rev Anticancer Ther* 16.8 (2016): 811-26.

Spliethoff, J.W., *et al.* "In Vivo Characterization of Colorectal Metastases in Human Liver Using Diffuse Reflectance Spectroscopy: Toward Guidance in Oncological Procedures." *Journal of Biomedical Optics* 21.9 (2016): 10.1117/1.JBO.21.9.097004.

Spliethoff, J.W., *et al.* "Monitoring of Tumor Response to Cisplatin Using Optical Spectroscopy." *Translational Oncology* 7.2 (2014): 230-9.

Stewart, Michael W., *et al.* "Aflibercept." *Nature Reviews Drug Discovery* 11 (2012): 269.

Strickler, J. H., and H. I. Hurwitz. "Bevacizumab-Based Therapies in the First-Line Treatment of Metastatic Colorectal Cancer." *Oncologist* 17.4 (2012): 513-24.

Su, J. W., *et al.* "Precancerous Esophageal Epithelia Are Associated with Significantly Increased Scattering Coefficients." *Biomed Opt Express* 6.10 (2015): 3795-805.

Sugita, J., *et al.* "Close Association between Fas Ligand (Fasl; Cd95l)-Positive Tumor-Associated Macrophages and Apoptotic Cancer Cells Along Invasive Margin of Colorectal Carcinoma: A Proposal on Tumor-Host Interactions." *Japanese Journal of Cancer Research* 93.3 (2002): 320-8.

Sun, X., *et al.* "Immunotherapy in Human Colorectal Cancer: Challenges and Prospective." *World J Gastroenterol* 22.28 (2016): 6362-72.

Sundar, R., *et al.* "Nivolumab in Nsclc: Latest Evidence and Clinical Potential." *Ther Adv Med Oncol* 7.2 (2015): 85-96.

Svensson, S., *et al.* "Ccl2 and Ccl5 Are Novel Therapeutic Targets for Estrogen-Dependent Breast Cancer." *Clinical Cancer Research* 21.16 (2015): 3794-805.

Tabernero, J., *et al.* "Aflibercept Versus Placebo in Combination with Fluorouracil, Leucovorin and Irinotecan in the Treatment of Previously Treated Metastatic Colorectal Cancer: Prespecified Subgroup Analyses from the Velour Trial." *Eur J Cancer* 50.2 (2014): 320-31.

Toh, J. W. T., *et al.* "The Potential Value of Immunotherapy in Colorectal Cancers: Review of the Evidence for Programmed Death-1 Inhibitor Therapy." *Clin Colorectal Cancer* 15.4 (2016): 285-91.

Tsuji, S., *et al.* "Potential Responders to Folfox Therapy for Colorectal Cancer by Random Forests Analysis." *Br J Cancer* 106.1 (2012): 126-32.

Valderrama-Trevino, A. I., *et al.* "Hepatic Metastasis from Colorectal Cancer." *Euroasian J Hepatogastroenterol* 7.2 (2017): 166-75.

Valentini, A. M., *et al.* "Pd-L1 Expression in Colorectal Cancer Defines Three Subsets of Tumor Immune Microenvironments." *Oncotarget* 9.9 (2018): 8584-96.

Van Cutsem, E., *et al.* "Addition of Aflibercept to Fluorouracil, Leucovorin, and Irinotecan Improves Survival in a Phase Iii Randomized Trial in Patients with Metastatic Colorectal Cancer Previously Treated with an Oxaliplatin-Based Regimen." *J Clin Oncol* 30.28 (2012): 3499-506.

Van Cutsem, E., *et al.* "Imaging in Colorectal Cancer: Progress and Challenges for the Clinicians." *Cancers (Basel)* 8.9 (2016).

Van Cutsem, Eric, *et al.* "Improving Outcomes in Colorectal Cancer: Where Do We Go from Here?" *European Journal of Cancer* 49.11 (2013): 2476-85.

van de Ven, K., and J. Borst. "Targeting the T-Cell Co-Stimulatory Cd27/Cd70 Pathway in Cancer Immunotherapy: Rationale and Potential." *Immunotherapy* 7.6 (2015): 655-67.

Vaupel, P., *et al.* "Impact of Hemoglobin Levels on Tumor Oxygenation: The Higher, the Better?" *Strahlenther Onkol* 182.2 (2006): 63-71.

Wahl, R. L., *et al.* "From Recist to Percist: Evolving Considerations for Pet Response Criteria in Solid Tumors." *J Nucl Med* 50.Suppl 1 (2009): 122s-50s.

Walker, A. S., *et al.* "Future Directions for the Early Detection of Colorectal Cancer Recurrence." *J Cancer* 5.4 (2014): 272-80.

Walker, A.S., *et al.* "Future Directions for Monitoring Treatment Response in Colorectal Cancer." *Journal of Cancer* 5.1 (2014): 44-57.

Walpole, Sarah Catherine, *et al.* "The Weight of Nations: An Estimation of Adult Human Biomass." *BMC Public Health* 12.1 (2012): 439.

Walsh, J. C., *et al.* "The Clinical Importance of Assessing Tumor Hypoxia: Relationship of Tumor Hypoxia to Prognosis and Therapeutic Opportunities." *Antioxid Redox Signal* 21.10 (2014): 1516-54.

Wang, D., *et al.* "Cxcl1 Induced by Prostaglandin E2 Promotes Angiogenesis in Colorectal Cancer." *J Exp Med* 203.4 (2006): 941-51.

Wang, H., *et al.* "Interactions between Colon Cancer Cells and Tumor-Infiltrated Macrophages Depending on Cancer Cell-Derived Colony Stimulating Factor 1." *Oncoimmunology* 5.4 (2016): e1122157.

Wang, J. W., *et al.* "Assessment of Early Tumor Response to Cytotoxic Chemotherapy with Dynamic Contrast-Enhanced Ultrasound in Human Breast Cancer Xenografts." *PLoS One* 8.3 (2013): e58274.

Wang, Q., *et al.* "Analysis of Cd137 and Cd137l Expression in Human Primary Tumor Tissues." *Croat Med J* 49.2 (2008): 192-200.

Wang, X., *et al.* "Inflammatory Cytokines Il-17 and Tnf-Alpha up-Regulate Pd-L1 Expression in Human Prostate and Colon Cancer Cells." *Immunol Lett* 184 (2017): 7-14.

Wang, Y., *et al.* "Neutrophil Infiltration Favors Colitis-Associated Tumorigenesis by Activating the Interleukin-1 (Il-1)/Il-6 Axis." *Mucosal Immunol* 7.5 (2014): 1106-15.

Watanabe, M., *et al.* "Intraoperative Identification of Colonic Tumor Sites Using a near-Infrared Fluorescence Endoscopic Imaging System and Indocyanine Green." *Dig Surg* 34.6 (2017): 495-501.

West, N. R., *et al.* "Emerging Cytokine Networks in Colorectal Cancer." *Nat Rev Immunol* 15.10 (2015): 615-29.

Wolmark, N., *et al.* "Clinical Trial to Assess the Relative Efficacy of Fluorouracil and Leucovorin, Fluorouracil and Levamisole, and Fluorouracil, Leucovorin, and Levamisole in Patients with Dukes' B and C Carcinoma of the Colon: Results from National Surgical Adjuvant Breast and Bowel Project C-04." *J Clin Oncol* 17.11 (1999): 3553-9.

Wu, Y., *et al.* "Repeated Cycles of 5-Fluorouracil Chemotherapy Impaired Anti-Tumor Functions of Cytotoxic T Cells in a Ct26 Tumor-Bearing Mouse Model." *BMC Immunology* 17.1 (2016).

Xu, S., *et al.* "Treatment Outcome of Nimotuzumab Plus Chemotherapy in Advanced Cancer Patients: A Single Institute Experience." *Oncotarget* 7.22 (2016): 33391-407.

Yu, P., *et al.* "Simultaneous Blockade of Multiple Immune System Inhibitory Checkpoints Enhances Antitumor Activity Mediated by Interleukin-15 in a Murine Metastatic Colon Carcinoma Model." *Clin Cancer Res* 16.24 (2010): 6019-28.

Yuan, J., *et al.* "Novel Technologies and Emerging Biomarkers for Personalized Cancer Immunotherapy." *Journal for ImmunoTherapy of Cancer* 4.3 (2015).

Zhang, X., *et al.* "Macrophages Induce Resistance to 5-Fluorouracil Chemotherapy in Colorectal Cancer through the Release of Putrescine." *Cancer Letters* 381.2 (2016): 305-13.

Zhang, Y., and J. Wang. "Micrornas Are Important Regulators of Drug Resistance in Colorectal Cancer." *Biol Chem* 398.8 (2017): 929-38.

Zhao, X., *et al.* "Tumor Location Impacts Immune Response in Mouse Models of Colon Cancer." *Oncotarget* 8.33 (2017): 54775-87.

Zhou, Q., *et al.* "The Density of Macrophages in the Invasive Front Is Inversely Correlated to Liver Metastasis in Colon Cancer." *Journal of Translational Medicine* 8.13 (2010): 1-9.

Zhou, Z., *et al.* "Preoperative Chemotherapy for Locally Advanced Resectable Colon Cancer - a New Treatment Paradigm in Colon Cancer?" *Annals of Translational Medicine* 1.2 (2013): 11.

Zhu, X., *et al.* "Systemic Delivery of Neutralizing Antibody Targeting Ccl2 for Glioma Therapy." *Journal of Neuro-Oncology* 104.1 (2011): 83-92.

Zonios, G., and A. Dimou. "Light Scattering Spectroscopy of Human Skin *in Vivo*." *Optics Express* 17.3 (2008): 1256-67.

Zou, K., *et al.* "Specific Tumor-Derived Ccl2 Mediated by Pyruvate Kinase M2 in Colorectal Cancer Cells Contributes to Macrophage Recruitment in Tumor Microenvironment." *Tumor Biology* 39.3 (2017): 1-10.

Chapter 7: Conclusion

Colorectal cancer is the 4th most common and 2nd deadliest cancer. Problems exist with predicting which patients will respond best to certain therapy regimens. Diffuse reflectance spectroscopy has been suggested as a candidate to optically monitor a patient's early response to therapy and has been received favorably in experimentally managing other cancers such as breast and skin. In this dissertation, two diffuse reflectance spectroscopy probes were designed: one with a combined high-resolution microendoscopy modality, and one that was optimized for acquiring data from subcutaneous murine tumors.

For Specific Aim 1, our objective was to Develop and validate a quantitative hybrid imaging and spectroscopy microendoscope to monitor dysplastic progression within epithelial tissues. Co-registration of both techniques is important because this technique can be potentially used to not only detect dysplasia using two different modalities, but also to monitor personalized response of sub-surface dysplastic lesions to anti-tumor therapy at multiple source-detector separations. Our central hypothesis was that High-resolution microendoscopy and DRS can be combined within a single optical probe to co-register image and spectral data of *in vivo* epithelia. With this multimodal system, epithelial morphological data can be correlated with quantitative spectroscopy data of the subsurface microenvironment, including associated optical properties. This multimodal microendoscopy approach encompasses both structural and spectroscopic reporters of perfusion within the tissue microenvironment and can potentially be used to monitor tumor response to therapy. This hybrid imaging and spectroscopy platform may be capable of collecting a wealth of information about the structural and functional properties of tissue at various imaging sites in *ex vivo* and *in vivo* models. The potential of this technique to be coupled to the

biopsy port of a conventional endoscope makes further clinical translation and complimentary optical biopsy in the oral cavity and other epithelial tissues feasible. For both probes, percent errors for estimating tissue optical properties (reduced scattering coefficient and absorption coefficient) were less than 5% and 10%, respectively.

For Specific Aim 2, our objective was to demonstrate a method for producing thin phantom layers with tunable optical properties using poly(dimethylsiloxane) (PDMS) as a substrate material at six discrete wavelengths (591, 631, 659, 691, 731, and 851 nm) at varying concentrations of titanium dioxide and nigrosin. Our central hypothesis was that thin, PDMS-based optical phantoms can accurately simulate the geometry and optical properties of target epithelia and can be used to tst the sensitivity of various imaging and spectroscopy equipment to heterogeneities. From the presented data, we provide lookup tables to determine appropriate concentrations of scattering and absorbing agents to be used in the design of PDMS-based phantoms with specific optical coefficients. In addition, heterogeneous phantoms, mimicking the layered features of certain tissue types, may be fabricated from multiple stacked layers, each with custom optical properties. These thin, tunable PDMS optical phantoms can simulate many tissue types and have broad imaging calibration applications in endoscopy, diffuse optical spectroscopic imaging (DOSI), or optical coherence tomography (OCT), among others.

For Specific Aim 3, our objectives were to (1) Design a DRS probe with four SDSs (0.75, 2.00, 3.00, and 4.00 mm) to interrogate increasing tissue volumes between 450-900 nm. The goal was to quantify percent errors in extracting μ_a and μ_s', and to quantify sampling depth into subcutaneous Balb/c-CT26 colon tumor allografts. Using an optical phantom-based experimental method, lookup-tables were constructed relating μ_a, μ_s', diffuse reflectance, and sampling depth. (2) Examine whether blockade of monocyte recruitment via anti-CCL2 (macrophage

chemoattractant protein-1) leads to enhanced sensitivity of 5-FU (5-fluorouracil) therapy in a CT26-Balb/c mouse model of CRC, and whether this effect can be quantified via DRS. The oxyhemoglobin flare has not been quantified after combinatorial chemotherapy and immunotherapy, and furthermore, has not been quantified in colon cancer tumors. Can DRS be used to quantify the therapy-induced oxyhemoglobin flare in a mouse model of colon cancer? The central hypothesis is that tumors treated with immunotherapy will have increased tumor therapeutic response to chemotherapy, as measured via tumor size and DRS-derived metrics. This work shows that the DRS probe can accurately extract optical properties, and the resultant physiological parameters such as total hemoglobin concentration and tissue oxygen saturation, from sufficient depth within subcutaneous Balb/c-CT26 colon tumor allografts. Methods described here can be generalized for other murine tumor models. The diffuse reflectance spectroscopy probe was applied to subcutaneous murine colon tumors (n=61) undergoing either antibody immunotherapy or standard 5-fluorouracil chemotherapy. Mice treated with a combination of these therapies showed reduced tumor growth compared to saline control, isotype control, immunotherapy, and chemotherapy groups ($p<0.001$, <0.001, <0.001, and 0.046, respectively) 7 days post-treatment. Additionally, at 7 days post-treatment, oxyhemoglobin, a marker currently being explored as a functional prognostic cancer marker, trended to increase in immunotherapy, chemotherapy, and combination therapy groups compared to controls ($p=0.315$, 0.149, and 0.190). Also of interest, an oxyhemoglobin flare (average increase of 1.44x from baseline, $p=0.03$ compared to controls) was shown in tumors treated with chemotherapy, indicating that diffuse reflectance spectroscopy may be useful as a complimentary tool to monitor early tumor therapeutic response in colon cancer. There were no differences observed for total hemoglobin content, reduced scattering coefficient, scattering exponent, or blood vessel

radius. However, subject-to-subject variability was high and studies correlating survival to early oxyhemoglobin flares are suggested. In this study, 5-fluorouracil (5-FU) was chosen as the chemotherapy agent. Fluorouracil-based chemotherapy, especially 5-FU, has been a staple in CRC treatment for nearly 60 years. For example, the FOLFOX chemotherapy regimen for colon and colorectal cancer (CRC) consists of 5-FU, leucovorin, and oxaliplatin. Besides FOLFOX, there are three other first-line treatments for CRC including FOLFIRI, FOLFOXIRI, and XELOX. FOLFIRI consists of 5-FU, leucovorin, and irinotecan hydrochloride. FOLFOXIRI consists of 5-FU, leucovorin, oxaliplatin, and hydrochloride. XELOX is slightly different in that it consists of oxaliplatin and capecitabine. Thus, in three of four common first-line treatments, 5-FU is the common drug. To simplify study design, 5-FU was chosen as the only chemotherapy agent. It would also be interesting to perform this same study using oxaliplatin as the primary chemotherapy agent, since it is also used in three of four first-line treatments. In the body, 5-FU is converted to fluorodeoxyuridine monophosphate (FdUMP). FdUMP forms a complex with thymidylate synthase (TS), an enzyme that catalyzes deoxyuridine monophosphate (dUMP) to deoxythymidine monophosphate (dTMP), which is a DNA monomer and key for DNA replication. Thus, 5-FU-mediated depletion of dTMP results in cytotoxicity and apoptosis in the rapidly growing cells in CRC (Zhang *et al.*, 2008). However, there are several remaining questions.

The Tromberg group recently found that neoadjuvant chemotherapy causes an early (1-day post treatment initiation) flare in tumor oxyhemoglobin (HbO_2) in breast cancer patients that eventually show increased survival. Alternatively, breast cancer patients with tumors that did not have an early HbO_2 had decreased survival. Why is this? What are the biological mechanisms contributing to this early chemotherapy-derived HbO_2 flare? Can this HbO_2 be observed in other

tumors, including in murine xenograft and allograft models? The HbO_2 flare hasn't widely been discussed in animal models. Can optical methods such as diffuse reflectance spectroscopy be used to accurately monitor the HbO_2? Is the correlation of early HbO_2 flares with positive neoadjuvant chemotherapy response universal to other cancers besides breast cancer? How will early knowledge of tumor HbO_2 lead to improved therapy management? Many of these questions are currently open-ended and hot topics of research. These questions could be future avenues of research that the present dissertation work will help lead to. Thus, it is important to discuss what is currently known about these questions, what doors this dissertation research has closed, and what doors this dissertation research has opened.

First, discussion will focus on the biological origin of the HbO_2 flare. There are two current hypotheses in the field. First, it is possible that chemotherapy induction decreases cancer cellular metabolism leading to a decrease in the conversion of oxyhemoglobin to deoxyhemoglobin. Second, it is possible that chemotherapy induction increases perfusion to tissue. For the first hypothesis, HbO_2 is formed when oxygen (O_2) binds to heme, the iron-containing compound of hemoglobin in red blood cells. During gas exchange, HbO_2 forms in pulmonary capillaries and is transported to the rest of the body, where O_2 serves as the final electron acceptor during oxidative phosphorylation. As a brief review, oxidative phosphorylation is the primary cellular metabolism pathway in which O_2 is the final electron acceptor to produce adenosine triphosphate (ATP), the organic chemical that provides energy to most cellular processes. Thus, how does chemotherapy induction decrease cancer cellular metabolism and the conversion of oxyhemoglobin to deoxyhemoglobin? From the perspective of 5-FU, it is possible that the FdUMP-TS complex causes a decrease in cellular metabolism since TS is a known regulator of several critical cellular metabolic pathways (Chu *et al.*, 1996). However, since the

Tromberg group reported the HbO_2 in patients treated with a variety of different chemotherapy/immunotherapy drugs instead of 5-FU, including doxorubicin, cyclophosphamide, paclitaxel, carboplatin, trastuzumab, and bevacizumab, other mechanisms may be responsible (Tromberg *et al.*, 2017; Roblyer *et al.*, 2011). A 2016 study shows that chemotherapy increases the risk of metabolic syndrome in patients with breast cancer (Bicakli *et al.*, 2016). However, exact biological mechanisms are unknown. A 2018 study by Gorini et al. stated that, "Many cancer therapies produce toxic side effects whose molecular mechanisms await full elucidation." On interesting hypothesis is that because chemotherapy and radiation (including 5-FU) are known to increase intracellular reactive oxygen species (ROS) (Focaccetti *et al.*, 2015), the ROS can lead to a mitochondrial imbalance of the normally tightly-regulated ROS production and detoxification, leading to a shift towards glycolysis (Warburg effect) and impaired oxidative phosphorylation (Liemburg-Apers *et al.*, 2015), even in the presence of oxyhemoglobin (Liberti *et al.*, 2016). In brief review, the Warburg effect is the phenomenon of tumor cells favoring glycolysis for their energy demands, even when there is enough oxygen for oxidative phosphorylation. If indeed the assumption is true that chemotherapy can lead to further shifts away from oxidative phosphorylation, this would support the hypothesis that cancer therapy can lead to a decrease in the conversion of oxyhemoglobin to deoxyhemoglobin, resulting in an HbO_2 flare (Tromberg *et al.*, 2017; Roblyer *et al.*, 2011), although it is unclear how this would correlate with increased survival. The Tromberg group also notes that a drop in deoxyhemoglobin, as well as oxyhemoglobin, should accompany a decrease in metabolism (Roblyer *et al.*, 2011), although no changes in total hemoglobin (THC) were observed in our study. For the second hypothesis that chemotherapy induction increases perfusion to tumor tissue, it is suggested that ROS triggers downstream activation of HIF-1 transcription factor,

which progresses both angiogenesis and the metabolic switch to glycolysis (Constans *et al.*, 2011). Additionally, chemotherapy induction can cause an acute inflammatory response (Feng *et al.*, 2017; Lian *et al.*, 2017). Acute inflammatory response is marked by increased vascular permeability and vessel dilation over the course of hours to several days, potentially contributing to the increased HbO_2 observed in our group and the Tromberg group. However, based on this hypothesis, it would have been expected to observe an increase in tumor THC as well, something that was observed in the Tromberg group but not in the present study. However, it is entirely possibly that tumor THC changes were masked by the overlying skin layer or inability to sample the entire tumor or intra-tumoral heterogeneities. Many previous studies have shown that clinical outcome has a positive correlation with serum inflammatory biomarkers such as IL-1, IL-6, and TNF-α (Roblyer *et al.*, 2011). Forward studies can take several directions. First, switching from a subcutaneous model of colon cancer to a chemically-induced orthotopic model of colon cancer with a smaller probe compatible with the biopsy port of small animal colonoscopes may elucidate possible differences in both THC and HbO_2 in treated vs. control tumors. Furthermore, further thin-film phantom studies are needed to elucidate DRS sensitivity to THC-based heterogeneities.

This leads back into Specific Aim 2 in which there is a critical need to simulate epithelium-like structures in the field of biomedical optics (Greening *et al.*, 2014). The phantoms created in Specific Aim 2 can mimic simple squamous epithelium in terms of the geometry and optical properties. Therefore, it would be of interest to combine study design from Specific Aims 2 and 3 to test various DRS probes in monitoring a THC-based, rather than StO_2-based, HbO_2 flare. Small (~100 μm) geometrical heterogeneities could be created, both at the surface and sub-surface levels, with varying concentrations of hemoglobin-simulating absorbing agent to

elucidate DRS sensitivity to THC changes. Coupling this with measuring *in vivo* changes in tissues with known inflammation may provide more evidence for DRS in the clinical management of inflammatory-based diseases such as CRC.

References

Bicakli, D. H., *et al.* "Adjuvant Chemotherapy May Contribute to an Increased Risk for Metabolic Syndrome in Patients with Breast Cancer." *J Oncol Pharm Pract* 22.1 (2016): 46-53.

Chu, E., and C. J. Allegra. "The Role of Thymidylate Synthase in Cellular Regulation." *Adv Enzyme Regul* 36 (1996): 143-63.

Constans, J. M., *et al.* "Effects of Reactive Oxygen Species on Metabolism Monitored by Longitudinal1h Single Voxel Mrs Follow-up in Patients with Mitochondrial Disease or Cerebral Tumors." *Journal of Physics: Conference Series* 261 (2011): 012011.

Feng, X., *et al.* "Acute Inflammatory Response During Neoadjuvant Chemotherapy for Locally Advanced Breast Cancer: A Case Report." *Cureus* 9.6 (2017): e1332.

Focaccetti, C., *et al.* "Effects of 5-Fluorouracil on Morphology, Cell Cycle, Proliferation, Apoptosis, Autophagy and Ros Production in Endothelial Cells and Cardiomyocytes." *PLoS One* 10.2 (2015): e0115686.

Greening, G.J., *et al.* "Characterization of Thin Poly (Dimethylsiloxane)-Based Tissue Simulating Phantoms with Tunable Reduced Scattering and Absorption Coefficients at Visible and Nearinfrared Wavelength." *Journal of Biomedical Optics* 19.11 (2014): 115002.

Lian, Qiaoshi, *et al.* "Chemotherapy-Induced Intestinal Inflammatory Responses Are Mediated by Exosome Secretion of Double-Strand DNA Via Aim2 Inflammasome Activation." *Cell Research* 27 (2017): 784.

Liberti, M. V., and J. W. Locasale. "The Warburg Effect: How Does It Benefit Cancer Cells?" *Trends Biochem Sci* 41.3 (2016): 211-18.

Liemburg-Apers, D. C., *et al.* "Interactions between Mitochondrial Reactive Oxygen Species and Cellular Glucose Metabolism." *Arch Toxicol* 89.8 (2015): 1209-26.

Roblyer, D., *et al.* "Optical Imaging of Breast Cancer Oxyhemoglobin Flare Correlates with Neoadjuvant Chemotherapy Response One Day after Starting Treatment." *PNAS* 108.35 (2011): 14626-31.

Tromberg, B.J., *et al.* "Predicting Responses to Neoadjuvant Chemotherapy in Breast Cancer: Acrin 6691 Trial of Diffuse Optical Spectroscopic Imaging (Dosi)." *Cancer Research* 76.20 (2017): 5933-44.

Zhang, N., *et al.* "5-Fluorouracil: Mechanisms of Resistance and Reversal Strategies." *Molecules* 13.8 (2008): 1551-69.

Chapter 8: Appendix

Protocols and Methodology

Creating PDMS Phantoms

1. Place a THINKY cup on the scale and zero out the weight of the THINKY cup.
2. Dispense desired weight of Sylgard® 184 Silicone Elastomer Base into a THINKY cup.
    a. For making thin phantoms, dispense between 6.5-7.0 grams of elastomer base.
3. Record, to the nearest hundredth, the amount of Sylgard® 184 Silicone Elastomer Base dispensed.
4. Open the MATLAB program called PDMSphantom.m.
5. Run the program.
6. Type a reference wavelength. For most purposes, type "621".
7. Type the desired reduced scattering coefficient (cm^{-1}) at this reference wavelength.
8. Type the desired layer thickness (μm). If you are making a thick phantom, just type in any number.
9. Type in the measured weight of the PDMS elastomer base from step 3.
10. The output parameters will be displayed in the Command Window.
11. Weigh out an appropriate amount of titanium dioxide in a weigh boat and dispense into the THINKY cup containing the PDMS elastomer base.
12. Place the mixture inside the tan plastic THINKY cup holder.
13. Weigh the tan plastic THINKY cup holder.
14. Put the cup holder containing the THINKY cup in the THINKY machine.
15. Manually adjust the wheel so that the indicator is the same weight as measured in step 14.
16. Run the mixture through two cycles (8 total minutes) of the THINKY machine.
17. Using a micropipette, dispense the appropriate amount of curing agent inside the mixture.
18. Repeat steps 14-17.

19. For creation of thin phantoms, follow the following steps:

    a. Begin a timer upon removal of the final mixture from the THINKY machine.

    b. After exactly 1 minute from removal, place the THINKY cup onto plastic petri dish and place in the oven at 70ºC for exactly 3 minutes.

    c. Remove from the oven. Exactly 1 minute after removal, dispense the PDMS mixture onto a silicone wafer in the Spin Coater.

    d. Run the Spin Coater on the desired settings.

    e. After completion, remove the silicone wafer from the Spin Coater and immediately place in the oven at 70ºC for 2 hours.

    f. Remove the silicon wafer from the over after 2 hours of curing at 70°C.

20. For creation of thick phantoms or phantoms in a mold, follow the following steps:

    a. Remove the mixture from the THINKY machine.

    b. Poor mixture into desired mold.

    c. Place mold into vacuum chamber.

    d. Ensure that the downstream vacuum tubes in the fume hood are clamped off with surgical clamps such that the only path is from the vacuum to the vacuum chamber.

    e. Plug in the vacuum.

    f. Turn the knob on the vacuum so that air is getting sucked out. If you are unsure, you should start seeing bubbles appear at the top of the PDMS mixture between 1-5 minutes.

    g. Leave the phantom in the vacuum chamber for 1 hour.

    h. Slowly let air back into the vacuum chamber.

    i. Remove mold from vacuum chamber.

    j. Place mold in the oven for 2 hours at 70°C to complete the curing process.

SCS Spincoat G3P-8

---

1. Turn on the power in the back of the machine.
2. Turn on the vacuum pump.
3. Turn on the air valve. This will activate the main menu screen.
4. Change to channel 10 on the Spincoat G3P-8.
5. Click Mode on the control panel to get to the settings menu.
6. Scroll through the steps until you reach Step 0. Set the Ramp to 0, the RPM to 0, and the Dwell to 0.
7. Scroll through the steps until you reach Step 1. Set the Ramp to 0, the RPM to 0, and the Dwell to 1.
8. Scroll through the steps until you reach Step 2. Set the Ramp to 4, the RPM to any desired value, and the Dwell to 20.
9. Scroll through the steps until you reach Step 3. Set the Ramp to 4, the RPM to 0, and the Dwell to 1.
10. Scroll through the steps until you reach Step 5. Set the Ramp to 0, the RPM to 0, and the Dwell to 0.
11. Click Enter to save the settings.
12. Click Mode on the control panel to get back to the home screen.
13. Place the large circular white chuck onto the Spincoat G3P-8.
14. Test run the spin coater to make sure everything is working.
15. If everything is working, turn off the vacuum and air pump for now until the spin coater is ready to be used.
16. Place a silicone wafer on the chuck.
17. Close the lid.
18. Run

Creating Multi-Layered Phantoms

1. Remove the silicon wafer from the over after 2 hours of curing at 70°C.

2. Put on latex or nitrile gloves.

3. Without scratching the silicon wafer, peel off the PDMS layer. If all steps were followed completely, the layer should peel off fairly easily.

   Note: If you make a phantom layer that is 200 microns or thinner, peeling the layer off the silicon wafer will be difficult, but possible. Some tearing, especially at first, is expected.

4. Lay the layer as flat as possible on a clean surface, such as in the petri dish.

5. With a disposable scalpel or razor blade, cut a square approximately 1.5 x 1.5 centimeters.

6. Place this square layer over another layer using tweezers. Be careful not to squeeze the layer too hard.

7. After the application of one layer on top of another layer, you must place the entire system in a vacuum chamber.

8. Use the vacuum chamber to vacuum the system so that the single layer can adhere to the base layer underneath. Vacuum for at least 40 minutes or until there are no air bubbles between phantom layers

9. Once there are no air bubbles between layer interfaces, continue adding more layers and vacuuming until the multi-layered phantom is complete.

Software Implementation for the DRSME

Downloading Software for Dual-Camera System in LabVIEW

Note that software and firmware versions listed in this protocol will likely have been updated since the time of this publication.

1. Obtain 2 Point Grey monochrome Flea3 USB cameras (model number FL3-U3-13S2M-CS)
2. Go to the following URL: https://www.ptgrey.com/support/downloads
3. Login
4. Product Families: Flea3
5. Camera Models: FL3-U3-32S2M-CS
6. Operating System: Windows 7 64bit
7. Search
8. Click "Software"
9. Download *FlyCapture 2.9.3.11 SDK - Windows (64-bit) — 02/15/2016 - 251.1416MB* under the heading of *Latest FlyCapture2 Full SDK*
10. Click "Install" → Next → Check "I accept the terms in the License Agreement" → Next → Next
11. Enter the appropriate full name, organization, and email.
12. Check "Anyone who uses this computer"
13. Check "Automatically register with PGR via the internet" → Next → Next
14. Click "Complete"
15. Check "I will use USB Cameras" and then check "Install PGRUSBCam – Point Grey USB Camera Driver" and then uncheck "Install USBPro – Point Grey USB Interface Driver" → Next
16. Check "Click to Confirm"
17. Check "FlyCapture 2 will manage processor idle states"

18. Check “The installer will register the DirectShow dlls” → Next → Install → Finish

19. Go to the following URL: https://www.ptgrey.com/support/downloads

20. Login

21. Camera Family: Flea3

22. Model Number: FL3-U3-13S2M-CS

23. Operating System: Windows 7 x64

24. Search

25. Click “Firmware”

26. Download “Flea3 USB3 2.7.3.0 Firmware”

Creating Dual-Camera System in LabVIEW

---

1. Connect both Flea3 cameras to the computer

2. Open FlyCapture: Start menu → type "Point Grey FlyCap2" → Click "Point Grey FlyCap2"

3. Open the UpdatorGUI utility: Start menu → type "UpdatorGUI3" → Click "UpdatorGUI3"

4. Select one of the cameras

5. Click "Open" to select the firmware file (C:\Program Files (x86)\Point Grey Research\Flea3 USB3 2.7.3.0 Firmware\fl3-u3-2.07.3-00.ez2)

6. Click "Update"

7. Repeat steps 36-38 for the second camera (make sure you wait for the update to finish on the first camera before proceeding to the second camera)

8. Download National Instruments' Vision Acquisition Software

9. Extract all the files to C:\Program Files (x86)\National Instruments

10. Once installation of "NI Vision Acquisition Software February 2014" has finished, open the Driver Control GUI: Start menu → type "DriverContolGUI" → Click "DriverControlGUI"

11. Click the "USB" tab (loading may take a few moments)

12. Select "Point Grey USB3 Vision Camera"

13. Select "Third-Party Drivers" → then select the driver that is listed under the menu ("NI: niu3vk.inf 1.1.0.49152")

14. Click "Install Driver"

15. Repeat steps 42-46 for the second camera

16. Both cameras will now be listed as "NI-IMAQdx USB3 Vision Device"

17. Start → Type "MAX" → Click "NI MAX" (Make a shortcut for this on the desktop)

18. On the Configuration Tree, click "My System" → "Devices and Interfaces"

19. Both cameras will be listed as "Point Grey Research Flea3 FL3-U3-32S2M

Using Cameras in FlyCapture

---

1. Open the “DriverControl GUI.”
2. Navigate to the USB tab.
3. Locate one of the “NI-IMAQdx USB3 Vision Device” devices and highlight it.
4. On the right, select “Point Grey Drivers.”
5. In the drop down menu, click “USB Camera (Signed) 2.6.3.0”
6. Click “Install Driver”
7. The device will now be listed as “Point Grey USB3 Vision Camera”
8. Exit the DriverControlGUI.
9. Open FlyCapture.
10. Highlight the camera.
11. Click “Configure Selected” in the lower right corner.
12. Click “Advanced Camera Settings” in the menu on the left.
13. Under “Memory Channel,” select “Default”
14. Click “Restore” and then save.
15. Do this for the other camera and both will revert back to their original settings.

Running Spectrometer in LabVIEW

---

1. Go to http://www.oceanoptics.com/Technical/softwaredownloads.asp

2. Navigate to the OmniDriver+SPAM Windows Version (32-bit) – The current version is 2.37.

3. Click the "Windows Version (32-bit)" link to run the installer.

4. Run the Installer.

5. Select English as the language.

6. Select the "Redistributable version (for end-users)"

7. Select the Installation Directory (you shouldn't have to change this), but if you do it should be C:\Program Files (x86)\Ocean Optics\OmniDriverSPAM.

8. Check Yes for "Install VCREDIST silently" → Next

9. Finish the installation.

10. Visit the following link to set up an introductory LabVIEW GUI to run the USB2000+VIS-NIR-ES spectrometer with LabVIEW: https://www.youtube.com/watch?v=tT5C43D3rRA

11. *Note: The spectrometer will not run with LabVIEW and SpectraSuite at the same time.*

12. *Note: To access the Wrapper library that contains all the LabVIEW sub-vi's for the spectrometer, navigate to C:\Program Files (x86)\Ocean Optics\OmniDriverSPAM\labview\win32\Version8.5 and then click "Wrapper.llb"*

Arduino IDE and Libraries

1. Go to http://arduino.cc/en/main/software
2. Download Arduino 1.0.5 by clicking the link titled “Windows Installer”
3. Open the Installer.
4. Install the Arduino software.
5. Go to https://learn.adafruit.com/adafruit-motor-shield-v2-for-arduino/install-software
6. Click the green box that is titled “Download latest Adafruit Motor Shield V2 Library”
7. Navigate to C:\Program Files (x86)\Arduino\libraries
8. Create a new folder titled “Adafruit_Motorshield”
9. Open the contents of the downloaded .zip file
10. Copy all the material in the downloaded .zip file
11. Paste all the material from the .zip file to the “Adafruit_Motorshield” folder created in step 8.

LabVIEW Interface for Arduino (LIFA)

---

1. Go to http://www.ni.com/download/ni-visa-5.4.1/4626/en/
2. Click the link for NI Downloader: NIVISA541full_downloader.exe (634.78 MB)
3. Open the downloaded folder → Run
4. Save the application (.exe) file to C:\Program Files (x86)\National Instruments\LabVIEW 2012
5. The National Instruments Downloader will begin the N-VISA download (this may take several minutes).
6. When the download is complete, click "Open"
7. Click OK to the prompt.
8. In the "Unzip to folder:" box, copy "C:\National Instruments Downloads\NI-VISA\5.4.1"
9. Check "Override files without prompting"
10. Check "When done unzipping open: . \setup.exe"
11. Click "Unzip." A blue progress bar will appear.
12. Once complete, click "Yes," allowing the program to make changes on the computer.
13. Next → when prompted for a Destination Directory, copy "C:\Program Files (x86)\National Instruments\" into the box (without the quotation marks) → Next → Next → Next
14. Check "I accept the above 2 License Agreement(s)" → Next → Next
15. NI-VISA 5.4.1 will now be installing. This will take several minutes.
16. Once the installation is complete, restart the computer.
17. Go to http://jki.net/vipm
18. Download the free version of VI Package Manager.
19. Open the Installer.
20. Install VI Package Manager.
21. Open VI Package Manager.

22. Browse to “LabVIEW Interface for Arduino” – Version 2.2.0.79

23. Highlight the “LabVIEW Interface for Arduino” section.

24. Click the “Install Package(s)” button.

25. Accept the terms and conditions.

26. After a few moments, a confirmation window will appear. Click “Finish.”

27. Plug in the Arduino Uno R3 to the computer.

28. Navigate to C:\Program Files (x86)\Arduino and click “arduino.exe”

29. The Arduino IDE will open.

30. Click File → Open, and browse to LIFA_Base.ino found in C:\Program Files (x86)\National Instruments\LabVIEW 2012\vi.lib\LabVIEW Interface for Arduino\Firmware\LIFA_Base

31. Click LIFA_Base.ino

32. Click Tools → Board → Arduino Uno

33. Determine the COM port that corresponds to the Arduino by opening Device Manager and expanding “Ports (COM and LPT)”

34. Go back to the Arduino IDE

35. Click Tools → Serial Port → COMx (x is to be determined from step 17)

36. Click the “Upload” button.

37. If uploaded successfully, the firmware necessary to use the LabVIEW Interface for Arduino (LIFA) will be successfully installed.

38. Close the Arduino IDE.

39. Open LabVIEW 2012.

40. Go to the Block Diagram

41. Right-click → Search → Type “Arduino” → Place an “Init” and “Close” function onto the block diagram. Place the “Init” function somewhere on the left and the “Close” function somewhere on the right.

42. Right-click → Executive control → While Loop → Place the while loop in between (not surrounding) the “Init” and “Close” function.

43. On the “Init” function, right-click “VISA-resource” → Create → Constant → change to COMx (Determine the COM correct port that corresponds to the Arduino by opening Device Manager and expanding “Ports (COM and LPT)”)

44. On the “Init” function, right-click “Baud Rate (115200)” → Create → Constant → change the constant to 115200.

45. On the “Init” function, right-click “Board Type (Uno)” → Create → Constant → change to Uno

46. On the “Init” function, right-click “Connection Type (USB/Serial)” → Create → Constant → change to USB/Serial

47. Right-click → Search → Type “Arduino” → Digital Write Pin (place inside while loop).

48. Right-click → Search → Type “Arduino” → Set Digital Pin Mode (place inside while loop to the left of the icon you placed in step 8).

49. From “Init,” connect “Arduino Resource” to “Arduino Research” on “Set Digital Pin Mode”

50. From “Init,” connect “error out” to “error in” on “Set Digital Pin Mode”

51. From “Set Digital Pin Mode,” connect “Arduino Resource” to “Arduino Research” on “Digital Write Pin”

52. From “Set Digital Pin Mode,” connect “error out” to “error in” on “Digital Write Pin”

53. From “Digital Write Pin,” connect “Arduino Resource” to “Arduino Research” on “Close”

54. From “Digital Write Pin,” connect “error out” to “error in” on “Close”
55. Create a control on the Digital I/O Pin on “Set Digital Pin Mode” and change to 13 in the front panel.

56. Create a constant on the Pin Mode on “Set Digital Pin Mode” and change to Output

57. From the Digital I/O Pin on “Digital Write Pin,” run a wire to the wire that is connected to the Digital I/O Pin control created in step 17.

58. Go to the Front Panel.

59. Right-click → LED → Round LED → place in Front Panel

60. Once this is place, move to the block diagram and place the LED icon (Boolean) inside the while loop.

61. Right-click the LED icon in the block diagram → Change to Control

62. Right-click → Search → Type "Boolean to" → click "Boolean To (0,1) <<Conversion>> → click "Boolean To (0,1)"

63. Connect the output of the LED to the input of the Boolean converter and the output of the Boolean converter to the input of the "Digital Write Pin" input called "Value"

64. In the block diagram, click the icon that says "Clean Up Diagram"

65. Save the VI as "LIFA_Verification_Test.vi"

Reference Page 1 (Installing LIFA from VI Package Manager – Steps 17-26): http://digital.ni.com/public.nsf/allkb/A20FBBD3682066908625788600 4D5F4D

Reference Page 2 (Installing LIFA Firmware onto Arduino Uno – Steps 27 – 37): http://digital.ni.com/public.nsf/allkb/8C07747189606D148625789C005C2DD6?

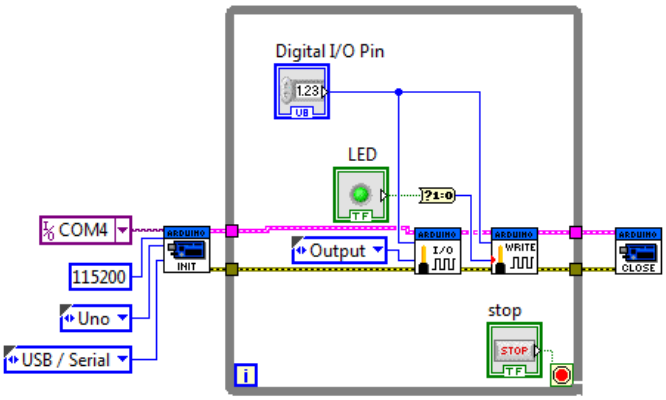

66. Load the correct firmware onto the Arduino by completing steps 27-36 of Section 8.

67. Exit the Arduino IDE then go back to the front panel on LabVIEW.

68. Click the "run" arrow on the front panel.

69. Turn the LED on and off. If the on-board LED on the Arduino blinks, then LabVIEW is successfully communicating with the Arduino.

Stepper Motor Control with LabVIEW

---

1. Purchase the EasyDriver Stepper Motor Driver from Sparkfun: https://www.sparkfun.com/products/10267

2. Solder connector pins on all the pins.

3. Plug the EasyDriver into a breadboard (across the middle ridge).

4. Run a jumper wire from "STEP" to the Arduino pin 2.

5. Run a jumper wire from "DIR" to the Arduino pin 3.

6. Run a jumper wire from "GND" (next to "STEP") to the Arduino GND pin.

7. In the top left of the EasyDriver PCB, you will see 4 pins in a row (2 "A" pins and 2 "B" pins). Going from A to B, connect the wires of the stepper motor in the following order: Grey, Green, Yellow, Red.

8. Plug in the 9.6V, 300mA wall wart to the top right of the EasyDriver PCB (GND and M+).

9. Flash the Arduino with the LIFA_Base firmware (steps 27-37 of section 8).

10. Open LabVIEW → Help → Find Examples → Search → Type "Arduino" → Open "Arduino Stepper Motor.vi"

11. Open the Block Diagram.

12. On the "Init" terminal, create constants for the following parameters: VISA resource, Baud Rate, Board Type, and Connection Type.

13. Keep the Baud Rate at 115200.

14. Change the VISA resource to whatever COM port your Arduino is using.

15. Open the Front Panel.

16. Set the "Set Speed" to around 400, "# of Steps to Move" to 1600 (one full rotation), "Set Acceleration" to 0, the "Stepper #" to 1.

17. Click Run.

18. Finally, click "Start Stepping." If everything worked properly, the stepper motor should make one counter clockwise rotation in 4 seconds (1600/400).

Cell Culture

Equipment and Materials

Item	Distributor	Item Number
CT26.WT Colon Carcinoma Cells	ATCC	CRL-2638
Gloves	VWR	89038-270
Laboratory Bench and Table Protector	VWR	89126-790
KimWipes	VWR	470224-038
95% Reagent Ethanol	VWR	BDH1156-4LP
100% Isopropyl Alcohol	VWR	MK303206
10% Bleach	VWR	89501-620
RPMI-1640 Medium	VWR	71002-878
Fetal Bovine Serum (FBS)	ATCC	30-2020
Antibiotic Antimycotic Solution (Pen/Strep)	Sigma-Aldrich	A5955-100ML
Amphotericin B (AmpB)/Gentamicin (GM)	Thermo Fisher	R01510
Dulbecco's Phosphate Buffered Saline	VWR	45000-434
Trypsin-EDTA Solution, 1X	VWR	VWRL0154-0100
Dimethyl Sulfoxide (DMSO)	VWR	97063-136
Sterile Saline (0.9% NaCl)	VWR	S5825
T75 Vented Cell culture Flask (Sterile)	VWR	10861-650
Nalgene Rapid-Flow Filter Units, 500 mL	VWR	16211-054
5 mL Serological Pipet Tip	VWR	89130-896
10 mL Serological Pipet Tip	VWR	89130-898
25 mL Serological Pipet Tip	VWR	89130-900

Pipetting Device	VWR	53498-001
Variable Volume Pipettors	VWR	75788-458
Universal Shelf Clip for 3 Pipettors	VWR	40000-272
10 µL Pipette Tips (Sterile-Aerosol)	VWR	89174-520
100 µL Pipette Tips (Sterile-Aerosol)	VWR	10126-388
1000 µL Pipette Tip (Sterile-Aerosol)	VWR	89174-530
1000 µL Pipette Tip (Non-Sterile)	VWR	83007-384
15 mL Conical-Bottom Centrifuge Tubes	VWR	89039-666
50 mL Conical-Bottom Centrifuge Tubes	VWR	89039-658
Water Bath	VWR	89501-464
Parafilm M, Bemis	VWR	52858-076
Nalgene Cryo 1°C “Mr. Frosty” Container	VWR	55710-200
Cryogenic Vials, 2 mL, externally threaded	VWR	66021-978
Microcentrifuge Tube	VWR	20170-038

Making RPMI-FBS Complete Growth Media

Step 1: Preparation and Storage of Solutions

1. Aliquot 100 mL of *Pen/Strep* into twenty 15 mL centrifuge tubes (5 mL each)
2. Store 20 aliquots of 5 mL *Pen/Strep* at -20°C
3. Store *AmpB/GM* (10 x 1 mL) at -20°C
4. Aliquot 500 mL of *FBS* into ten 50 mL centrifuge tubes (50 mL each)
5. Store 10 aliquots of 50 mL *FBS* at -20°C
6. Store *base RPMI media* at 4°C. Label

Step 2: Preparation

1. Obtain the following supplies and spray into the hood
    a. 50 mL Fetal bovine serum (FBS)
    b. 5 mL Antibiotic Antimycotic Solution (Pen/Strep)
    c. 1 mL Amphotericin B (AmpB)/Gentamicin (GM)
    d. One (1) Base Media
    e. Twelve (12) 50 mL centrifuge tubes (2 for waste and 10 for media)
    f. Three (3) 25 mL serological pipette tips
    g. Two (2) 5 mL serological pipette tip
    h. One (1) Rapid-Flow Filter Unit (“hourglass bottles”)

Step 3: Making and Filtering Media

1. Dispense 56 mL of base media into the two (2) 50 mL conical vials

2. Put 50 mL of FBS directly into the base media bottle
3. Put 5 mL of Antibiotic Antimycotic (Pen/Strep) into base media bottle
4. Put 1 mL of AmpB/GM directly into the base media bottle
5. Attach the aspiration tube to the filter bottle
6. Dispense approximately 20 mL of media into the filter bottle
7. Push down the foot pedal
8. Wait for 20 mL of media to dispense to the bottom of the filter bottle
9. Slowly pour in the rest of the media while continuing to push down foot pedal
10. Wait for all media to dispense to the bottom
11. Release the foot pedal
12. Detach the aspiration tube

Step 4: Aliquoting and Storing Media

1. Unscrew the top of the filter bottle and throw away in Biohazard trash.
2. Aliquot the 500 mL media into ten (10) 50 mL centrifuge tubes
3. Remove complete media solutions from the hood
4. Clean hood thoroughly with 70% EtOH
5. Wrap Parafilm around the caps of the 50 mL centrifuge tubes
6. Place 50 mL centrifuge tubes with media at 4°C

Feeding CT26 Cells

Step 1: Preparation

1. Place cell culture media in the 37.3°C water bath and wait 30 minutes
2. Clean hood with 70% EtOH

Step 2: Checking Cell Health

1. Spray gloves with 70% EtOH and rub hands together thoroughly
2. Remove tissue culture flask from incubator
3. Visually inspect the flask for mold or cloudiness
4. Set the flask on the microscope platform and turn lamp on
5. Focus the cells
6. Move the flask around above the objective to spot check for contamination
7. Spray the flask (but not the cap) with 70% EtOH, holding the bottle 12 inches away
8. Set flask it in the middle of the hood
9. Place all necessary serological pipettes in the left side of the hood
10. Obtain the 50 mL centrifuge tube with 37.3°C culture media
11. Spray in the 50 mL centrifuge tube with culture media into the hood
12. Obtain one (1) 50 mL centrifuge tube for waste
13. Loosen all caps slightly
14. Fully open the cap of the 50 mL waste tube

Step 3: Media Dispensing

1. Unscrew lid on tissue culture flask
2. Put the pipette tip in the corner of the flask and remove old media
3. Dispense old media into the 50 mL waste tube
4. Screw the lid back onto the tissue culture flask
5. Set the flask down in the hood

Step 4: Media Addition

1. Obtain 15 mL of media
2. Unscrew the cap of the tissue culture flask
3. Dispense 15 mL of media into the flask without introducing bubbles
4. Gently swirl liquid around in the bottom of the flask
5. Place flask in incubator until next feeding or passaging
6. Clean everything appropriately

Passaging CT26 Cells

Step 1: Preparation

1. Place cell culture media in the 37.3°C water bath.
2. Place PBS in the 37.3°C water bath
3. Place 0.25% Trypsin-EDTA in the 37.3°C water bath
4. Wait 30 minutes
5. Clean hood with 70% EtOH

Step 2: Checking Cell Health

1. Spray gloves with 70% EtOH and rub hands together
2. Remove tissue culture flask from incubator
3. Visually inspect the flask for mold or cloudiness
4. Set the flask on the microscope platform and turn lamp on
5. Focus the cells
6. Move the flask around above the objective to spot check for contamination
7. Spray the flask (but not the cap) with 70% EtOH, holding the bottle 12 inches away
8. Set flask it in the middle of the hood
9. Place all necessary serological pipettes in the left side of the hood
10. Obtain the 50 mL centrifuge tube with 37.3°C culture media
11. Spray in the 50 mL centrifuge tube with culture media into the hood
12. Obtain two (2) 50 mL centrifuge tube for waste
13. Obtain one (1) 15 mL centrifuge tube for centrifuging

14. Loosen all caps slightly

Step 3: Media Dispensing

1. Unscrew lid on tissue culture flask
2. Put the pipette tip in the corner of the flask and remove old media
3. Dispense old media into the 50 mL waste tube
4. Screw the lid back onto the tissue culture flask
5. Set the flask down in the hood

Step 4: PBS Rinse

1. Obtain 10 mL of PBS
2. Unscrew lid on tissue culture flask
3. Dispense the PBS in the tissue culture flask
4. Screw lid back on tissue culture flask
5. Gently swirl flask with a rocking motion for 20 seconds
6. Unscrew lid on tissue culture flask
7. Remove PBS
8. Screw lid back on tissue culture flask
9. Dispense PBS in 50 mL waste tube

Step 5: Trypsin Re-Suspension

1. Unscrew lid on tissue culture flask
2. Obtain 5 mL of Trypsin-EDTA

3. Dispense the trypsin in the tissue culture flask
4. Screw lid back on tissue culture flask
5. Gently swirl flask with a rocking motion for 30 seconds
6. Put the flask in the incubator for 3 minutes
7. Remove flask from incubator
8. Tap flask to break up cells from the bottom
9. Place flask underneath the inverted microscope to ensure that cells are detaching
10. Put tissue culture flask back in hood

Step 6: Media Addition #1

1. Obtain 4 mL of media
2. Unscrew lid on tissue culture flask
3. Dispense 4 mL of media into the flask (with the trypsin – total 9 mL)
4. Gently swirl flask with a rocking motion for 20 seconds

Step 7: Transfer to Centrifuge Tube

1. Obtain a 15 mL centrifuge tube
2. Remove all liquid from the tissue culture flask
3. Dispense the liquid (9 mL) into the 15 mL centrifuge tube
4. Set 15 mL centrifuge tube aside

Step 8: Media Rinse

1. Obtain 4 mL of media

2. Dispense 4 mL of media into the “empty” tissue culture flask
3. Gently swirl flask with a rocking motion for 10 seconds
4. Remove 4 mL of media
5. Dispense the 4 mL of media into the centrifuge tube (total volume of 13 mL)

Step 9: Centrifuging Cells #1

1. Obtain the 15 mL centrifuge tube with 13 mL liquid
2. Place the 15 mL centrifuge tube in the centrifuge
3. Place the appropriate counter balance
4. Spin the tubes at 200 RCF for 5 minutes at 4°C
5. Without disturbing the pellet, place the 15 mL centrifuge tube back in the hood

Step 10: Dispensing of Supernatant #1

1. Unscrew the cap of the centrifuge tube
2. Remove supernatant (media/Trypsin-EDTA), leaving the pellet intact
3. Screw the cap gently back on the tube

Step 11: Media Addition #2

1. Obtain 10 mL of media
2. Unscrew the cap of the centrifuge tube
3. Dispense 10 mL of media into the tube (10 mL total)
4. Pipette up and down to mix cells

Step 12: Counting Cells

1. Dispense 80 μL of media into a microcentrifuge tube
2. Dispense 20 μL of cells in media to the microcentrifuge tube
3. Mix the tube well
4. Obtain the hemacytometer
5. Load both chambers by pipetting the suspension under the cover slip
6. Place the hemacytometer on the microscope platform
7. View the first chamber
8. Count the cells in the top left, top right, bottom right, bottom left, and middle 4x4 boxes.
9. Total the cell count from the first 5 boxes
10. View the second chamber
11. Count the cells in the top left, top right, bottom right, bottom left, and middle 4x4 boxes
12. Total the cell count from the second 5 boxes

Step 13: Plating New Cells

1. Obtain one (1) new T75 tissue culture flask.
2. Fill the tissue culture flask with 15 mL of media
3. Place the required cell/media volume into the tissue culture flask
4. Screw lid back on tissue culture flask
5. Gently swirl flask with a rocking motion for 10 seconds
6. Place tissue culture flask quickly in the incubator
7. Clean everything appropriately

Freezing CT26 Cells

Step 1: Preparing Freezing Container

1. Obtain an empty (no cryovials) Mr. Frosty Freezing Container from the -80°C freezer
2. Set on a paper towel
3. Unscrew the cap

Step 2: Complete Passaging Steps

1. Complete either a P1, P2, or a P3 passage (*see the appropriate protocol*)
2. Place DMSO in 37.3° water bath

Step 3: Preparation for Freezing

1. Obtain DMSO (50 µL required aliquot per freeze vial)
2. Obtain the desired number of cryo-vials for storage
3. Label the cryo-vials with date, initials, cell type, number of cells, and passage number
4. Slightly unscrew the caps of the cryo-vials so they are loose

Step 4: Creating Freeze Media

1. Dispense the appropriate amount of media into each cryo-vial
2. Obtain the centrifuge tube (with media and cells)
3. Dispense the appropriate amount of cells/media into each cryo-vial
4. Dispense the 50 µL DMSO into each cryo-vial
5. Cap the cryo-vials

6. Gently mix
7. Place cryo-vials into Mr. Frosty container
8. Ensure Mr. Frosty has at least 1 inch of 100% isopropyl alcohol and refill as necessary
9. Place Mr. Frosty container in -80°C freezer for 12 hours
10. After 12 hours, remove Mr. Frosty container
11. Transfer cryo-vials to liquid nitrogen dewar
12. Clean everything appropriately

Thawing CT26 Cells

Step 1: Preparation

1. Place cell culture media in the 37.3°C water bath.
2. Place PBS in the 37.3°C water bath
3. Place 0.25% Trypsin-EDTA in the 37.3°C water bath
4. Wait 30 minutes
5. Clean hood with 70% EtOH
6. Obtain a 50 mL centrifuge tube for liquid waste storage
7. Obtain one T75 tissue culture flask and spray it into the hood.

Step 2: Preparing T75 Flask

1. Label T75 flask with initials, date, *CT26*, *P#*, and $5x10^5$
2. Loosen cap on the empty T75 flask
3. Dispense 14 mL of cell culture media into the T75 flask

Step 3: Preparing Cells

1. Remove the cryovial with cells from liquid nitrogen Dewar
2. Bring cryovial with cells to the 37.3°C warm water bath
3. Thaw the cells in the water bath without submerging the cryovial lid
4. When a small chunk of ice remains inside, remove from the water bath
5. Wipe the vial with 70% EtOH on a Kimwipe. *Do not directly spray the vial*
6. Place the cryovial vial into the hood

7. Loosen cap on cell vial

Step 4: Plating Cells in T75 Flask

1. Fill the tissue culture flask with contents of the thawed cryovial
2. Screw caps gently back on tissue culture flask
3. Gently swirl flask with a rocking motion for 30 seconds
4. Place tissue culture flask quickly in the incubator
5. Clean everything appropriately

Step 5: Feeding Cells

1. Feed cells within 24 hours (*see the appropriate protocol*)

Aliquoting CT26 Cells in Sterile Saline for Injection

Step 1: Preparation

1. Place cell culture media in the 37.3°C water bath.
2. Place dPBS in the 37.3°C water bath
3. Place saline in the 37.3°C water bath
4. Place 0.25% Trypsin-EDTA in the 37.3°C water bath
5. Wait 30 minutes
6. Clean hood with 70% EtOH
7. Obtain a small bucket of ice and set aside in freezer

Step 2: Checking Cell Health

1. Spray gloves with 70% EtOH and rub hands together
2. Remove tissue culture flask from incubator
3. Visually inspect the flask for mold or cloudiness
4. Set the flask on the microscope platform and turn lamp on
5. Focus the cells
6. Move the flask around above the objective to spot check for contamination
7. Spray the flask (but not the cap) with 70% EtOH, holding the bottle 12 inches away
8. Set flask it in the middle of the hood
9. Place all necessary serological pipettes in the left side of the hood
10. Obtain the 50 mL centrifuge tube with 37.3°C culture media
11. Spray in the 50 mL centrifuge tube with culture media into the hood

12. Obtain two (2) 50 mL centrifuge tube for waste

13. Obtain one (1) 15 mL centrifuge tube for centrifuging

14. Loosen all caps slightly

Step 3: Media Dispensing

1. Unscrew lid on tissue culture flask
2. Put the pipette tip in the corner of the flask and remove old media
3. Dispense old media into the 50 mL waste tube
4. Screw the lid back onto the tissue culture flask
5. Set the flask down in the hood

Step 4: PBS Rinse

1. Obtain 10 mL of PBS
2. Unscrew lid on tissue culture flask
3. Dispense the PBS in the tissue culture flask
4. Screw lid back on tissue culture flask
5. Gently swirl flask with a rocking motion for 20 seconds
6. Unscrew lid on tissue culture flask
7. Remove PBS
8. Screw lid back on tissue culture flask
9. Dispense PBS in 50 mL waste tube

Step 5: Trypsin Re-Suspension

1. Unscrew lid on tissue culture flask
2. Obtain 5 mL of Trypsin-EDTA
3. Dispense the trypsin in the tissue culture flask
4. Screw lid back on tissue culture flask
5. Gently swirl flask with a rocking motion for 30 seconds
6. Put the flask in the incubator for 3 minutes
7. Remove flask from incubator
8. Tap flask to break up cells from the bottom
9. Place flask underneath the inverted microscope to ensure that cells are detaching
10. Put tissue culture flask back in hood

Step 6: Media Addition #1

1. Obtain 4 mL of media
2. Unscrew lid on tissue culture flask
3. Dispense 4 mL of media into the flask (with the trypsin – total 9 mL)
4. Gently swirl flask with a rocking motion for 20 seconds

Step 7: Transfer to Centrifuge Tube

1. Obtain a 15 mL centrifuge tube
2. Remove all liquid from the tissue culture flask
3. Dispense the liquid (9 mL) into the 15 mL centrifuge tube
4. Set 15 mL centrifuge tube aside

Step 8: Media Rinse

1. Obtain 4 mL of media
2. Dispense 4 mL of media into the “empty” tissue culture flask
3. Gently swirl flask with a rocking motion for 10 seconds
4. Remove 4 mL of media
5. Dispense the 4 mL of media into the centrifuge tube (total volume of 13 mL)

Step 9: Centrifuging Cells #1

1. Obtain the 15 mL centrifuge tube with 13 mL liquid
2. Place the 15 mL centrifuge tube in the centrifuge
3. Place the appropriate counter balance
4. Spin the tubes at 200 RCF for 5 minutes at 4°C
5. Without disturbing the pellet, place the 15 mL centrifuge tube back in the hood

Step 10: Dispensing of Supernatant #1

1. Unscrew the cap of the centrifuge tube
2. Remove supernatant (media/Trypsin-EDTA), leaving the pellet intact
3. Screw the cap gently back on the tube

Step 11: Saline Addition #1

1. Obtain 10 mL of saline
2. Unscrew the cap of the centrifuge tube
3. Dispense 10 mL of saline into the tube (10 mL total)

4. Pipette up and down to mix cells

Step 12: Counting Cells

1. Dispense 80 μL of media into a microcentrifuge tube
2. Dispense 20 μL of cells in saline to the microcentrifuge tube
3. Mix the tube well
4. Obtain the hemacytometer
5. Load both chambers by pipetting the suspension under the cover slip
6. Place the hemacytometer on the microscope platform
7. View the first chamber
8. Count the cells in the top left, top right, bottom right, bottom left, and middle 4x4 boxes.
9. Total the cell count from the first 5 boxes
10. View the second chamber
11. Count the cells in the top left, top right, bottom right, bottom left, and middle 4x4 boxes
12. Total the cell count from the second 5 boxes

Step 13: Centrifuging Cells #2

1. Put the 15 mL centrifuge tube with cells into the centrifuge
2. Place the appropriate counter balance
3. Spin the tubes at 200 RCF for 5 minutes at 4°C
4. Without disturbing the pellet, place the 15 mL centrifuge tube back in the hood

Step 14: Dispensing of Supernatant #2

4. Unscrew the cap of the centrifuge tube
5. Remove supernatant (sterile saline), leaving the pellet intact

Screw the cap gently back on the tube

Step 15: Saline Addition #2

1. Obtain appropriate volume of warm sterile saline
2. Dispense appropriate volume of saline into the tube
3. Slowly pipette up and down to mix cells

Step 16: Aliquot Cells into Microcentrifuge Tubes

1. Obtain desired number of sterile microcentrifuge tubes
2. Pipette $1x10^5$ CT26 cells/sterile saline into each microcentrifuge tube
3. Cap tubes
4. Label tubes with *CT26*
5. Place tubes on ice (pre-prepared from earlier step)
6. Clean everything appropriately

Subcutaneous Injection of CT26 Cells into Balb/c Mice

Equipment and Materials

Item	Distributor	Item Number
Gloves	VWR	89038-270
KimWipes	VWR	470224-038
Distilled Water	Walmart	009594226
Sterile Saline (0.9% NaCl)	VWR	S5825
95% Reagent Ethanol	VWR	BDH1156-4LP
10% Bleach	VWR	89501-620
28G U-100 BD Micro-Fine IV Syringe	VWR	BD329410
Microcentrifuge Tubes	VWR	20170-038
Alcohol Swab	VWR	BD326859
Water Bath	VWR	89501-464
Ear Punch, Scissor Style	VWR	10806-292
Aluminum Dissecting Pan	Carolina	629210
Lab Coat (Men's)	VWR	10141-300
Lab Coat (Women's)	VWR	10141-316
Analytical Balance	VWR	10159-998
Eye Gel	CVS	332692
Warm Water Pump	Global Medical	TP700
Warm Water Pump Pad	Kent Scientific	TPZ-0510EA
Valved In-Line Hose Barb Coupling Body	Fresh Water Systems	42100
Non-Valved In-Line Hose Barb Coupling	Fresh Water Systems	40900

Rodent Trimmer Set	Braintree Scientific	CLP-9990 1201
Nair Hair Remover Lotion	Walmart	000287746

Subcutaneous Injection of CT26 Cells into Balb/c Mice

Step 1: Preparation

1. Clean all surfaces with 70% EtOH
2. Set out the metal dissection pan
3. Set up the anesthesia cart (*see appropriate instructions*)
4. Turn on the hot water pump pad at least 30 minutes before the first injection
5. Obtain necessary amount of 28G needles
6. Obtain microcentrifuge tubes with aliquot of $1x10^5$ CT26 cells in sterile saline in ice
7. Draw up entire aliquot (150 μL) of $1x10^5$ CT26 cells in sterile saline
8. Get rid of any air bubbles in the needle

Step 2: Anesthetizing Mouse

1. Let mice become aware of presence for 30 seconds
2. Remove mouse from cage
3. Place the mouse in the mouse-isoflurane chamber
4. Secure the lid on the mouse-isoflurane chamber
5. Anesthetize mouse
6. Remove mouse without grabbing the tail
7. Place the mouse on the nosecone
8. Put eye drop gel in the mouse's eyes
9. Ensure the mouse is on the nose cone for 30 seconds before proceeding
10. Ear punch the mouse appropriately

11. Shave the tumor cell injection site

Step 3: Subcutaneous Injection into Flank

1. Hold the 28G needle at a 5-10° angle
2. Place the needle 5 mm away from the spine at the level of the thigh
3. Stretch the skin taught with the left hand
4. Insert the needle so that it goes just underneath the skin at the upper thigh
5. Lift the needle up to test that you have good skin penetration
6. Inject slowly
7. Withdraw needle
8. Remove mouse from anesthesia
9. Warm mouse up with your hand
10. Place the mouse back in its cage once it's awake
11. Clean everything appropriately

Treatment Preparation

Equipment and Materials

Item	Distributor	Item Number
5-Fluorouracil	Sigma-Aldrich	F6627-1G
CCL2 (MCP-1) Monoclonal Antibody (2H5)	Bio X Cell	BE0185-A005MG
CCL2 (MCP-1) Isotype Control	Bio X Cell	BE0091-A005MG
15 mL Conical-Bottom Centrifuge Tubes	VWR	89039-666
Dimethyl Sulfoxide (DMSO)	VWR	97063-136
Microcentrifuge Tubes	VWR	20170-038
80-Place Storage System	VWR	30128-276
Sterile Saline (0.9% NaCl)	VWR	101320-574
Gloves	VWR	89038-270
KimWipes	VWR	470224-038
Variable Volume Pipettors	VWR	75788-458
Universal Shelf Clip for 3 Pipettors	VWR	40000-272
10 µL Pipette Tips (Sterile-Aerosol)	VWR	89174-520
10 µL Pipette Tips (Sterile)	VWR	89368-970
100 µL Pipette Tips (Sterile-Aerosol)	VWR	10126-388
100 µL Pipette Tips (Sterile)	VWR	89140-162
1000 µL Pipette Tip (Sterile-Aerosol)	VWR	89174-530
1000 µL Pipette Tip (Sterile)	VWR	83007-380

Preparation of 5-Fluorouracil Chemotherapy

Quantity per Container	1 g
Dose Schedule	Daily
Dose per Day	15 mg/kg/day
5-FU per Injection (15 g to 30 g mouse)	0.225 – 0.450 mg
5-FU per Injection in Microcentrifuge Tube	1 mg
Injections (cohort 1)	2
Injections (cohort 2)	4
Injections (cohort 3)	7
Injection Method	Intraperitoneal

Step 1: Making 5-FU

1. Determine the number of injections you want to make
2. Prepare the biosafety cabinet
3. Obtain container of 5-FU and spray into hood
4. Obtain a 50 mL centrifuge tube
5. Label the 50 mL centrifuge tube with *40 mg/mL 5-FU/DMSO*, initials, and date
6. Dispense 25 mL DMSO into 50 mL centrifuge tube
7. Dispense entire bottle (1 g) of 5-FU into 50 mL centrifuge tube
8. Remove solution from the hood
9. Vortex for 30 minutes at room temperature or until completely dissolved

Step 2: Pre-Preparation of 5-FU

1. Obtain a 15 mL centrifuge tube
2. Dispense 5 mL of 40 mg/mL 5-FU/DMSO into 15 mL centrifuge tube
3. Dispense 5 mL of sterile saline into 15 mL centrifuge tube
4. Label the 15 mL centrifuge tube with *20 mg/mL 5-FU/Saline*
5. Remove solution from the hood
6. Vortex for 1 minute or until completely dissolved
7. Store both solutions permanently at -20°C

Step 3: Preparing 5-FU for Injection

1. Obtain normal sterile saline
2. Remove 20 mg/mL 5-FU/Saline from -20°C
3. Obtain desired amount of 1.5 mL microcentrifuge tubes
4. Sterilize microcentrifuge tubes in autoclave
5. Place 23 µL of 20 mg/mL 5-FU/Saline in microcentrifuge tubes
6. Place 130 µL of saline in each tube to get a 3 mg/mL concentration of 5-FU/saline
7. Place 20 mg/mL 5-FU/Saline solution back in -20°C
8. Store aliquots at -20°C

Calculations:

1. **Minimum Daily Dose of 5-FU per Mouse (15 g mouse)**

$$\left[\frac{15\ mg}{kg}\right] \cdot \left[\frac{1\ kg}{1000\ g}\right] \cdot [15\ g] = 0.225\ mg$$

2. **Maximum Daily Dose of 5-FU per Mouse (30 g mouse)**

$$\left[\frac{15\ mg}{kg}\right] \cdot \left[\frac{1\ kg}{1000\ g}\right] \cdot [30\ g] = 0.450\ mg$$

3. **Total Number of 5-FU Injections**

$$[2\ groups] \cdot \left[\frac{5\ mice}{cohort \cdot group}\right] \cdot \left[\left(\frac{2\ inject.}{cohort\ 1}\right) + \left(\frac{4\ inject.}{cohort\ 2}\right) + \left(\frac{7\ inject.}{cohort\ 3}\right)\right]$$

$$= 130\ injections$$

4. **Total 5-FU used:**

$$[130\ injections] \cdot \left[\frac{0.450\ mg}{injection}\right] = 58.5\ mg$$

5. **DMSO Measurement for 40 mg/mL 5-FU/DMSO Storage Solution**

$$V_{DMSO} = \left[\frac{1\ mL}{40\ mg}\right] \cdot [x\ mg] = 25\ mL$$

6. **Recovering 0.450 mg of 5-FU (for a 30 g mouse) per Microcentrifuge Tube**

$$\left[\frac{1\ mL}{20\ mg\ 5FU}\right] \cdot [0.450\ mg\ 5FU] \cdot \left[\frac{1000\ \mu L}{1\ mL}\right] = 22.5\ \mu L$$

7. **Required Saline per 5-FU Aliquot**

$$V_{Total}(\mu L) = \left[\frac{20\ mg\ 5FU}{1\ mL}\right] \cdot \left[\frac{23\ \mu L}{1}\right] \cdot \left[\frac{1\ mL}{3\ mg\ 5FU}\right] = 153\ \mu L$$

$$V_{aliquot}(\mu L) = 23\ \mu L$$

$$V_{Saline}(\mu L) = V_{Total}(\mu L) - V_{aliquot}(\mu L) = 130\ \mu L$$

8. **Required Volume of 3 mg/mL 5-FU/saline Per Mouse**

$$\left[\frac{1\ mL\ saline}{3\ mg\ 5FU}\right] \cdot \left[\frac{1000\ \mu L}{1\ mL}\right] \cdot \left[\frac{15\ mg\ 5FU}{kg}\right] \cdot \left[\frac{1\ kg}{1000\ g}\right] \cdot Weight\ of\ Mouse\ (g)$$

$$= x\ \mu L\ 5FU/saline$$

Justification for 5-FU Dosage in Mice

5-FU Chemotherapy in Humans

- 2,400 mg/m^2 given during treatment – repeated every 2 weeks
- Body surface area (BSA) is the unit in humans

5FU Dose (based on Body Surface Area) in Humans: $\left[\frac{2{,}400\ mg\ 5FU}{m^2 \cdot 2\ week\ dose}\right]$

Average Ratio of Body Surface Area to Weight in Humans: $\left[\frac{1.6\ m^2}{60\ kg}\right]$

Standard Human-to-Mouse FDA Conversion Factor: $\left[\frac{12.3}{3}\right]$

Conversion of Human BSA-based Dosage to Mouse Weight-based Dosage:

$$\left[\frac{2{,}400\ mg\ 5FU}{m^2 \cdot 2\ week\ dose}\right] \cdot \left[\frac{1.6\ m^2}{60\ kg}\right] \cdot \left[\frac{12.3}{3}\right] \cdot \left[\frac{1\ 2\ week\ dose}{14\ daily\ doses}\right] = \mathbf{18.7}\ \boldsymbol{\frac{mg\ 5FU}{kg}} \approx \mathbf{15}\ \boldsymbol{\frac{mg\ 5FU}{kg}}$$

Preparation of anti-CCL2 Immunotherapy

Quantity per Container	5 mg
Dose Schedule	Every Other Day (0, 2, 4, 6)
Dose per Day	4 mg/kg/day
Anti-CCL2 per Injection (15 g to 30 g mouse)	60 – 120 μg
Injections (cohort 1)	1
Injections (cohort 2)	2
Injections (cohort 3)	4
Injection Method	Intraperitoneal (I.P.)

Step 1: Making Anti-CCL2 (or Isotype Control)

1. Determine number of injections you want to make
2. Obtain desired amount of 1.5 mL microcentrifuge tubes
3. Sterilize microcentrifuge tubes in autoclave
4. Prepare the biosafety cabinet
5. Obtain stock anti-CCL2 solution
6. Obtain normal sterile saline
7. Spray everything into biosafety hood
8. Label tubes with initials, date, and *150 μg anti-CCL2/Saline*
9. Aliquot **20 μL (150 μg anti-CCL2 protein)** of stock anti-CCL2 into each tube
10. Aliquot 106 μL sterile saline into each tube to create a 1.2 mg/mL anti-CCL2/saline solution
11. Place anti-CCL2 stock solution back in 4°C fridge

12. Place 1.2 mg/mL anti-CCL2 solutions back in 4°C fridge

13. Store aliquots at 4°C for no more than 2 months

Calculations:

1. **Minimum Dose of Anti-CCL2 per Injection per Mouse (15 g mouse)**

$$\left[\frac{4\ mg}{kg}\right] \cdot \left[\frac{1\ kg}{1000\ g}\right] \cdot [15\ g] = 0.06\ mg = 60\ \mu g$$

2. **Maximum Dose of Anti-CCL2 per Injection per Mouse (30 g mouse)**

$$\left[\frac{4\ mg}{kg}\right] \cdot \left[\frac{1\ kg}{1000\ g}\right] \cdot [30\ g] = 0.12\ mg = 120\ \mu g$$

3. **Total Number of Anti-CCL2 Injections (per group)**

$$[2\ groups] \cdot \left[\frac{5\ mice}{cohort \cdot group}\right] \cdot \left[\left(\frac{1\ inject.}{cohort\ 1}\right) + \left(\frac{2\ inject.}{cohort\ 2}\right) + \left(\frac{4\ inject.}{cohort\ 3}\right)\right]$$

$$= 70\ injections$$

4. **Total Anti-CCL2 used:**

$$[70\ injections] \cdot \left[\frac{0.12\ mg}{injection}\right] = 8.4\ mg$$

5. **Required Volume of anti-CCL2/Saline (not diluted) Per Mouse:**

$$V_{anti-CCL2}(\mu L)$$

$$= \left[\frac{0.7\ mL\ solv.}{5.3\ mg\ antiCCL2}\right] \cdot \left[\frac{4\ mg}{kg\ mouse}\right] \cdot \left[\frac{kg\ mouse}{1000\ g\ mouse}\right] \cdot \left[\frac{1000\ \mu L\ solv.}{1\ mL\ solv.}\right]$$

$$\cdot mouse\ weight(g)$$

6. **Required Volume of Saline for 1.2 mg/mL Aliquot of anti-CCL2**

$$V_{saline}(\mu L) = \left(\left[\frac{5.3\ mg}{0.7\ mL}\right] \cdot [0.020\ mL\ (from\ eq.\ 5, 25g\ mouse)] \cdot \left[\frac{1\ mL}{1.2\ mg}\right]\right) - 0.020\ mL$$

$$= 106\ \mu L$$

7. Required Volume of anti-CCL2/Saline (diluted) Per Mouse

$$V_{anti-CCL2\ dil.} = \left[\frac{1\ mL\ solv.}{1.2\ mg\ antiCCL2}\right] \cdot \left[\frac{4\ mg}{kg\ mouse}\right] \cdot \left[\frac{kg\ mouse}{1000\ g\ mouse}\right] \cdot \left[\frac{1000\ \mu L\ solv.}{1\ mL\ solv.}\right]$$

$$\cdot\ mouse\ weight(g)$$

Preparation of Isotype Control Antibodies

Quantity per Container	**5 mg**
Dose Schedule	Every Other Day (0, 2, 4, 6)
Dose per Day	4 mg/kg/day
Anti-CCL2 per Injection (15 g to 30 g mouse)	60 – 120 μg
Injections (cohort 1)	1
Injections (cohort 2)	2
Injections (cohort 3)	4
Injection Method	Intraperitoneal (I.P.)

Step 1: Making Isotype Control

1. Determine number of injections you want to make
2. Obtain desired amount of 1.5 mL microcentrifuge tubes
3. Sterilize microcentrifuge tubes in autoclave
4. Prepare the biosafety cabinet
5. Obtain stock isotype control solution
6. Obtain normal sterile saline
7. Spray everything into biosafety hood
8. Label tubes with initials, date, and *150 μg isotype control/Saline*
9. Aliquot **20 μL (150 μg Isotype Control)** of stock isotype control into each tube
10. Aliquot 106 μL saline into each tube to create a 1.2 mg/mL isotype control/saline solution
11. Place isotype control stock solution back in 4°C fridge

12. Place 1.2 mg/mL anti-CCL2 solutions back in 4°C fridge

13. Store aliquots at 4°C for no more than 2 months

Calculations:

1. **Minimum Dose of Isotype Control per Injection per Mouse (15 g mouse)**

$$\left[\frac{4\ mg}{kg}\right] \cdot \left[\frac{1\ kg}{1000\ g}\right] \cdot [15\ g] = 0.06\ mg = 60\ \mu g$$

2. **Maximum Dose of Isotype Control per Injection per Mouse (30 g mouse)**

$$\left[\frac{4\ mg}{kg}\right] \cdot \left[\frac{1\ kg}{1000\ g}\right] \cdot [30\ g] = 0.12\ mg = 120\ \mu g$$

3. **Total Number of Isotype Control Injections (per group)**

$$[2\ groups] \cdot \left[\frac{5\ mice}{cohort \cdot group}\right] \cdot \left[\left(\frac{1\ inject.}{cohort\ 1}\right) + \left(\frac{2\ inject.}{cohort\ 2}\right) + \left(\frac{4\ inject.}{cohort\ 3}\right)\right]$$

$$= 70\ injections$$

4. **Total Isotype Control used:**

$$[70\ injections] \cdot \left[\frac{0.12\ mg}{injection}\right] = 8.4\ mg$$

5. **Required Volume of Isotype Control/Saline (not diluted) Per Mouse:**

$$V_{isotype}(\mu L) = \left[\frac{0.7\ mL\ solv.}{5.3\ mg\ isotype}\right] \cdot \left[\frac{4\ mg}{kg\ mouse}\right] \cdot \left[\frac{kg\ mouse}{1000\ g\ mouse}\right] \cdot \left[\frac{1000\ \mu L\ solv.}{1\ mL\ solv.}\right]$$

$$\cdot\ mouse\ weight(g)$$

6. **Required Volume of Saline for 1.2 mg/mL Aliquot of Isotype Control**

$$V_{saline}(\mu L) = \left(\left[\frac{5.3\ mg}{0.7\ mL}\right] \cdot [0.020\ mL\ (from\ eq.\ 5, 25g\ mouse)] \cdot \left[\frac{1\ mL}{1.2\ mg}\right]\right) - 0.020\ mL$$

$$= 106\ \mu L$$

7. **Required Volume of Isotype Control/Saline (diluted) Per Mouse**

$$V_{isotype\ dil.} = \left[\frac{1\ mL\ solv.}{1.2\ mg\ isotype}\right] \cdot \left[\frac{4\ mg}{kg\ mouse}\right] \cdot \left[\frac{kg\ mouse}{1000\ g\ mouse}\right] \cdot \left[\frac{1000\ \mu L\ solv.}{1\ mL\ solv.}\right]$$

$$\cdot\ mouse\ weight(g)$$

Tissue Preparation

Equipment and Materials

Item	Distributor	Item Number
Gloves	VWR	89038-270
KimWipes	VWR	470224-038
Leica CM1860 Cryostat	Leica	CM1860
Low-Profile 819 Disposable Blades	VWR	10015-014
SuperFrost Plus Microscope Slides	VWR	48311-703
Coverslips (22 x 50)	VWR	16004-314
Microscope Slide Storage Box (Red)	VWR	89510-824
Tissue-Tek Cryomold (25x20x5)	VWR	25608-916
Razor Blades	VWR	55411-050
Artificial Tears Ointment	Walmart	305366550917
Plastic Divider Box (x2)	DigiKey	510-1030-ND
Plastic Divider Tabs (x6)	DigiKey	510-1035-ND
Steel Cooker	Amazon	B00H3377W6
Nalgene Dewar Flask (1 L)	VWR	633880-052
Dissecting Forceps (12”)	VWR	470018-958
Tissue-Tek O.C.T. Compound	VWR	25608-930
Low Temperature Organic Thermometer	VWR	89062-908
Lab Markers, Black	VWR	52877-310
Parafilm M Roll	VWR	52858-076
Nair Hair Removal Lotion	Amazon	B009ZCFSO2

Small Animal Surgical Cordless Trimmer	Braintree Scientific	CLP-9868 14
Aluminum Foil	VWR	89107-726
Isopentane (2-Methylbutane)	VWR	AA19387-AP
Liquid Nitrogen Tank	Airgas	NI NF180LT22

Tissue Dissection and Freezing

Step 1: Preparation of Supplies

1. Pre-cut the necessary amount of 5” x 5” aluminum foil squares (1 per tumor)
2. Label aluminum foil with the mouse identification number
3. Pre-prep 25 x 20 cryomolds (1 per tumor) with 2 mm of OCT in the base
4. Label cyromolds with *initials, date, mouse number*¸ either *IHC* and the *T* shape
5. Obtain plastic bag
6. Label plastic bag with *initials, date, mouse number*, and *IACUC protocol number*
7. Obtain steel cooker and Styrofoam container
8. Obtain white cutting board and ruler

Step 2: Anesthetize Mouse

1. Prep anesthesia machine
2. Place mouse in induction chamber
3. Anesthetize mouse with 1.5% isoflurane and 1 L/min O_2

Step 3: Preparation of Liquid Nitrogen

1. In the chemical fume hood, dispense ~250 mL of isopentane into the steel cooker
2. Fill Styrofoam container with liquid nitrogen
3. In the chemical fume hood, place steel cooker (with isopentane) in liquid nitrogen
4. Place thermometer in steel cooker so that the tip is submerged in liquid nitrogen
5. Begin swirling around the isopentane to distribute heat

6. Turn up mouse anesthesia to 4.0% isoflurane and 1 L/min O_2
7. Continually monitor temperature of isopentane

Step 4: Preparation of Mouse

1. Once mouse is fully anesthetized, transfer to nosecone
2. Maintain mouse on 4.0% isoflurane with 1 L/min O_2
3. Obtain a black lab marker
4. Draw a 5 mm line through the DRS measurement axis of each measurement location.
5. Dissect tumor with scissors
6. Set tumor on white cutting board with ruler in background and photograph
7. Continually monitor temperature of isopentane

Step 5: Flash Freezing Tumor in Liquid Nitrogen

1. Place tumor in the OCT filled cryomold
2. Fill the cyromold with more OCT to cover the tumor
3. Remove isopentane from liquid nitrogen
4. Grab the edge of cryomold with 12” dissecting forceps
5. When the temperature of isopentane is 73-78°C, dip cryomold in isopentane for 15 seconds
6. Remove cryomold from isopentane
7. Place more OCT on any exposed parts of the tumor and cryomold
8. Dip cryomold in isopentane for 15 seconds
9. Set the frozen cryomold on the aluminum foil square
10. Wrap the frozen cryomold in aluminum foil

11. Transport the foil-wrapped tissue sample to the -80°C freezer

Step 6: Euthanizing Mouse

1. Euthanize the mouse via cervical dislocation
2. Keep euthanized mouse on 4.0% isoflurane for 60 seconds following cervical dislocation
3. Place the euthanized mouse in plastic bag
4. Place the plastic bag with the mouse in the freezer in the small animal facility for disposal

Tips for Monitoring Isopentane Temperature

1. Continually use the thermometer to stir the isopentane
2. When the isopentane reaches 65-70°C, remove from liquid nitrogen – the temperature will continue to drop
3. Place the isopentane back in the liquid nitrogen when the temperature rises to 65°C
4. Do not let the temperature get below 90°C – this can ruin the thermometer
5. Only place the tumor/cryomold/OCT in the isopentane when the temperature is 73-78°C

Cryotome Sectioning

Step 1: Preparing the Cryotome and Materials

1. Obtain microscope slides (x8)
2. Transfer cryotome blades from -20°C freezer to the cryotome
3. Place the frozen tissue sample(s) into the cryotome
4. Leave the frozen tissue sample(s) and blades in the cryotome (at -20°C) for 20 minutes
5. Using the pencil, label the microscope slides (on the rough side) (x8) with the following (*i.e. example shown in picture*): 1) mouse identification number, 2) *Balb/c*, 3) *CT26*, 4) initials, and 5) slide number (out of 8)

Step 2: Preparing and Mounting the Blade

1. Check to see if there is a blade in the blade holder. If there is a blade in the blade holder, look for a small black handle on the right side of the main carrier that is located in the center of the cryotome and pull the black handle towards you. *(This releases the blade)*
2. Remove the old blade
3. Obtain a new blade
4. Using the magnet on the bottom of the white brush, place the blade into the blade holder, making sure that the sharp portion of the blade is facing up

5. Once the blade is in place, push the small black handle back

Step 3: Adjusting Angles

1. Obtain calipers
2. Ensure that the distance between the 2 cylinders is 6mm, measured with at least 3 points

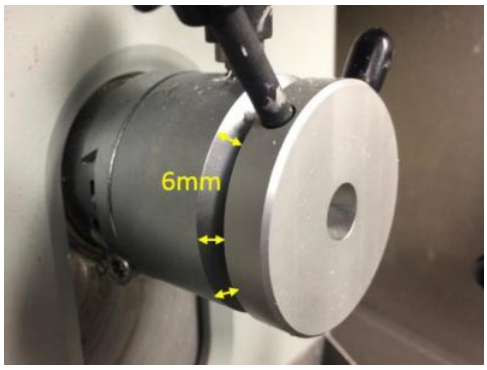

3. Ensure the angle of the blade is at ~7°

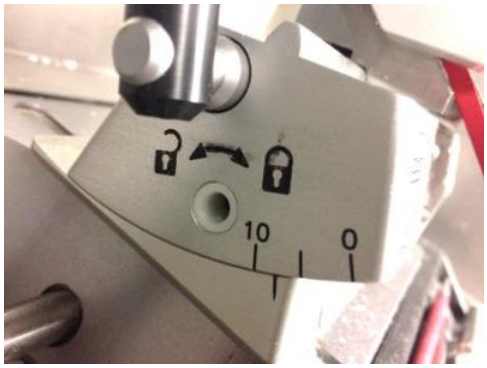

4. Ensure the glass blade cover is directly aligned over the top of the blade (i.e. cover and blade edge are parallel)

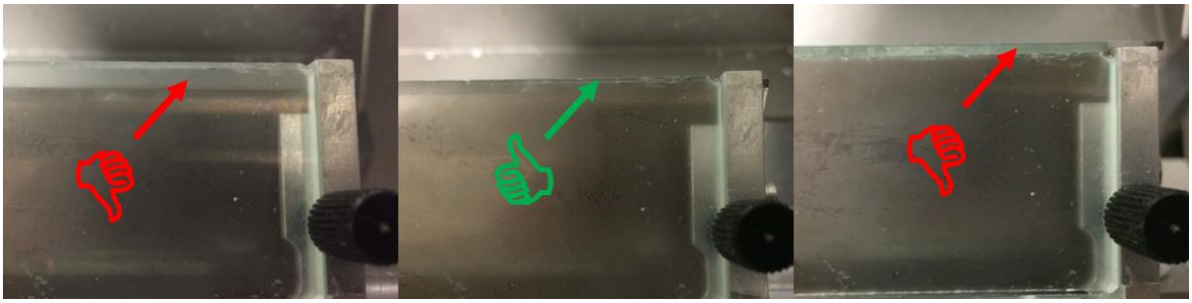

Step 4: Cutting Away Excess OCT

1. Obtain OCT/tumor sample
2. Obtain a razorblade
3. Cut away excess OCT surrounding the tumor so there is just 2-4 mm of OCT surrounding the tumor. *Note: this doesn't have to be perfect; we've noticed cutting away some excess OCT helps with getting good tissue sections*

Step 5: Preparation of Sample on Chuck

1. Obtain the chuck
2. Place a dime-sized amount of OCT onto the chuck
3. Take the sample out of the cryomold
4. Place the non-cutting edge of sample onto the chuck making sure that the correct corner is point up. (*The cutting edge is the flat square face. Note: the tissue sample should be in a diamond shape*)
5. Place the chuck with the sample onto the blue freezing panel
6. Close the lid of the cryotome and let the chuck/sample freeze for 5 minutes
7. Set the cutting thickness to 100 µm

Step 6: Preparation of Sample for Sectioning

1. Turn the wheel until the sample is close to the blade
2. Move the sample forward using the fast and slow track buttons on the left side of the cryotome. *(The blade should not be hitting the plastic guard or the carrier)*

3. Start turning the rotating arm on the right side of the cryotome to start slicing away excess OCT
4. Once the blade has sliced through approximately 1/3 way through the tumor, set the cutting thickness to 10 µm

Step 7: Sample Sectioning (10 µm)

1. Turn the wheel at ~1 turn per second.
2. Lift the cover and place the rough side of the slide onto the sample
3. *The OCT will melt onto the slide and the actual tissue will remain intact*
4. Leave the microscope slide in the cryotome to maintain temperature
5. Use the same microscope slide for the 2nd tissue slice
6. Repeat until you have four (4) **good** microscope slides (8 good tissue slices)

Step 8: Sample Sectioning (5 µm)

1. Set the cutting thickness to 5 µm
2. Lift the cover and place the rough side of the slide onto the sample
3. *The OCT will melt onto the slide and the actual tissue will remain intact*
4. Leave the microscope slide in the cryotome to maintain temperature
5. Use the same microscope slide for the 2nd tissue slice
6. Repeat until you have four (4) **good** microscope slides (8 good tissue slices)

Step 10: Storing Slides

1. Once complete, place all slides into a microscope storage box

2. Immediately places the microscope slide storage box in the -80°C freezer
3. Save the excess tumor, wrap it in foil, and place it back in the -80°C freezer
4. Clean the cryotome appropriately

Tissue Analysis

Equipment and Materials

Item	Distributor	Item Number
Anti-CD68 (anti-mouse) Alexa Fluor 488	BioLegend	137012
Anti-CD80 (anti-mouse) Brilliant Violet 421	BioLegend	104725
Anti-CD206 (anti-mouse) Alexa Fluor 594	BioLegend	141726
NucBlue™ Fixed Cell ReadyProbe (DAPI)	Thermo Fisher	R37606
Universal Antibody Dilution Buffer	Sigma-Aldrich	U3510-100ML
Hematoxylin Solution, Mayer's	VWR	100504-404
Eosin Y	VWR	10143-130
Bluing Reagent Solution	VWR	95057-852
Xylene	VWR	EM-XX0060-4
Cytoseal XYL	VWR	48212-196
100% Reagent Ethanol	VWR	EM-EX0276-4S
95% Reagent Ethanol	VWR	BDH1156-4LP
Microcentrifuge Tubes	VWR	20170-038
80-Place Storage System	VWR	30128-276
15 mL Conical-Bottom Centrifuge Tubes	VWR	89039-666
50 mL Conical-Bottom Centrifuge Tubes	VWR	89039-658
Gloves	VWR	89038-270
KimWipes	VWR	470224-038
Acetone	VWR	BDH1101-4LP
SuperFrost Plus Microscope Slides	VWR	48311-703

Coverslips (22 x 50)	VWR	16004-314
EasyDip™ Kit with Rack	VWR	CA10154-052
EasyDip™ Slide Staining Jars – White	VWR	87000-126
Whatman Grade 1 Qualitative Filter Paper	VWR	10035-812
Laboratory Bench and Table Protector	VWR	89126-790
Powder Funnel (Wide Stem)	VWR	16126-912
Phosphate Buffered Saline (PBS), 1X	VWR	45000-446
Phosphate Buffered Saline (PBS) Tablet	Sigma-Aldrich	P4417-100TAB
Tween 20	Sigma-Aldrich	P9416-50ML
Triton-X100	Sigma-Aldrich	X100-100ML
Goat serum	Sigma-Aldrich	G9023-10ML
Sodium Azide	Sigma-Aldrich	S2002-5G
Bovine Serum Albumin	Sigma-Aldrich	A8806-5G
Fluoromount-G Slide Mounting Medium	VWR	100241-874
Sterile Saline (0.9% NaCl)	VWR	S5815
Pipetting Device	VWR	53498-001
5 mL Serological Pipet Tip	VWR	89130-896
Rapid-Flow Sterilization Filter Unit	VWR	28199-098
Analytical Balance	VWR	10159-998
Variable Volume Pipettors	VWR	75788-458
Universal Shelf Clip for 3 Pipettors	VWR	40000-272
Universal Shelf Clip for 3 Pipettors	VWR	40000-272
10 µL Pipette Tips (Sterile-Aerosol)	VWR	89174-520

10 µL Pipette Tips (Sterile)	VWR	89368-970
100 µL Pipette Tips (Sterile-Aerosol)	VWR	10126-388
100 µL Pipette Tips (Sterile)	VWR	89140-162
1000 µL Pipette Tip (Sterile-Aerosol)	VWR	89174-530
1000 µL Pipette Tip (Sterile)	VWR	83007-380

Immunohistochemistry Reagent Preparation

Step 1: Cold Acetone

1. Obtain 250 mL of acetone
2. Label with initials, date, and *Acetone* and store at -20° C

Step 2: Dilution Buffer for IHC: Universal Antibody Dilution Buffer

1. Purchase pre-made Universal Antibody Dilution Buffer
2. Store at room temperature

   Universal Antibody Dilution Buffer Percentages

   - 1.0% BSA
   - 0.3% Tris HCl
   - 0.025% Triton-X

Step 3: Making PBS-t Washing Solution

1. Obtain a bottle that can hold at least 600 mL
2. Fill with 600 mL of MilliPore filtered water
3. Add three PBS tablets to the canister
4. Obtain Tween-20
5. Obtain 1.2 mL of Tween-20
6. Dispense 1.2 mL of Tween-20 into the canister of 600 mL PBS
7. Cap canister
8. Place magnetic stirrer in PBS-t

9. Place PBS-t on magnetic plate at RT and 300 RPM until everything is dissolved
10. Label canister as *PBS-t, mm/dd/yyyy, and initials*

Step 4: Blocking Buffer for IHC (Goat Serum-Based)

1. Prepare biosafety hood
2. Obtain 50 mL centrifuge tube of sterile 1X PBS from 4°C
3. Obtain Goat Serum from -20°C
4. Place the Goat Serum in the 37.3°C water bath until liquid. *Do not submerge the lid*
5. Place the 1X PBS tube in the 37.3°C water bath for 15 minutes. *Do not submerge the lid*
6. Obtain Bovine Serum Albumin (BSA) from 4°C
7. Obtain Triton-X100 from 23°C
8. Obtain Tween-20 from 23°C
9. Obtain Sodium Azide from 23°C
10. Obtain one (1) empty 50 mL centrifuge tube
11. Label the 50 mL tube with date, initials, and *Blocking Buffer: 4% Goat Serum, 0.5% BSA*
12. Dispense 38.4 mL of 1X PBS into the empty 50 mL centrifuge tube
13. Obtain the analytical balance
14. Weigh 0.04 g (40 mg) of Sodium Azide (NaN_3) and dispense Sodium Azide (NaN_3) into 50 mL centrifuge tube
15. Weigh 0.2 g (200 mg) of BSA and dispense BSA into 50 mL centrifuge tube
16. Dispense 40 µL of Triton-X100 into the 50 mL centrifuge tube
17. Dispense 20 µL of Tween-20 into the 50 mL centrifuge tube
18. Vortex the solution for 2 minutes

19. Prepare biosafety hood

Complete all of the following steps in the Biosafety hood in ENRC 2545

20. Spray the 50 mL centrifuge tube (with the blocking buffer) into the hood
21. Spray the Goat Serum into the hood
22. Obtain Rapid-Flow Sterilization Filter Unit and spray into the hood
23. Using a sterile 1000 µL pipette, dispense 1,600 µL of goat serum into the 50 mL centrifuge tube
24. Mix well
25. Perform sterile vacuum filtration
26. Label the beaker with initials, date, and *Blocking Buffer: 4% Goat Serum, 0.5% BSA*
27. Aliquot into microcentrifuge tubes (1.6 mL) and label with *B*
28. Store at 4°C
29. Clean the hood

Blocking Solution Percentages (B)

- 4% Goat Serum
- 0.5% BSA
- 0.1% NaN_3
- 0.1% Triton-X
- 0.05% Tween-20

CD68-CD80-CD206 Stain

Step 1: Preparing Blocking Solution

1. Obtain empty microcentrifuge tubes
2. Remove goat-based blocking solution from 4°C
3. Dispense 800 µL of goat-based blocking solution into microcentrifuge tubes (each tube ≈ 10 sections)
4. Label microcentrifuge tubes with *B*
5. Obtain necessary quantity of full microcentrifuge tubes per number of tissue sections (each tube ≈ 10 sections)

Step 2: Preparing Slides for Staining

1. Remove slides from the -80°C freezer
2. Remove the slides you want to stain with anti-CD68/80/206
3. Label the slides appropriately with a pencil
4. Place the slides in a -20°C freezer. Start a timer
5. Bring the rest of the slides not being stained back to the -80°C freezer for permanent storage

Step 3: Preparation of Solution Boxes

1. Fill **2nd staining jar** with ~90 mL of **new** room temperature PBS-t
2. Fill **3rd staining jar** with ~90 mL of **new** room temperature PBS-t
3. Fill **4th staining jar** with ~90 mL of **new** room temperature PBS-t.

Step 4: Preparing Macrophage Antibody Cocktail (MAC)

1. Store the undiluted 0.5 mg/mL anti-CD68 solution (100 μg/200 μL total) in the 4° C fridge
2. Store the undiluted 0.5 mg/mL (lot-specific) anti-CD80 in the 4° C fridge
3. Store the undiluted 0.5 mg/mL anti-CD206 solution (100 μg/200 μL total) in the 4° C fridge
4. Determine number of tissue sections to be stained. *One microcentrifuge tube can hold 10 trials*
5. Multiply the number of tissue sections by 100 μL (*x*)
6. Multiply the number of tissue sections by 1.0 μL (*a – M*). (1:100)
7. Multiply the number of tissue sections by 5.0 μL (*b – M1*). (1:100)
8. Multiply the number of tissue sections by 0.8 μL (*c – M2*). (1:125)
9. Obtain microcentrifuge tubes (≤10 tissue sections = 1 tube, 11-20 tissue sections = 2 tubes, etc.)
10. Label microcentrifuge tubes appropriately
11. Dispense *x* μL of the Universal Antibody Dilution Buffer into each microcentrifuge tube
12. Dispense *a* μL of undiluted anti-CD68 antibody into the microcentrifuge tube
13. Dispense *b* μL of undiluted anti-CD80 antibody into the microcentrifuge tube
14. Dispense *c* μL of undiluted anti-CD206 antibody into the microcentrifuge tube
15. Gently and sufficiently pipette up and down within the microcentrifuge tube to mix using 1000 μL pipette
16. Wrap microcentrifuge tubes with aluminum foil and store at 4°C for 4 hr. maximum

Step 5: Preparing Acetone

1. 17 minutes after step 2.4, remove acetone from the -20°C freezer
2. Fill **1st staining jar** with ~90 mL of -20°C acetone

3. Place Celsius thermometer in 1st staining jar with acetone

Step 6: Fixation with Acetone

1. When the acetone reaches -5°C to -3°C, remove slides from the -20°C freezer
2. Place the slides (up to 10) in the black slide holder
3. Place the slide holder in acetone (**Jar 1**) for 10 minutes
4. Remove from acetone (**Jar 1**)
5. Air dry and let drip for 5 seconds

Step 7: Wash with PBS-t (#1)

1. Place the slide holder in PBS-t (**Jar 2**) for 3 minutes
2. Remove slides from PBS-t (**Jar 2**)
3. Air dry and let drip for 5 seconds

Step 8: Adding Blocking Solution

1. Obtain one paper towel and split in half
2. Lay out one-half of the paper towel. Set the other half aside for now
3. Obtain the Eppendorf tube labeled *B*
4. Obtain the 10-100 μL micropipette and place an appropriate pipette tip on the end
5. Remove the slide holder from the PBS-t (**Jar 2**)
6. Air-dry and let drip for 5 seconds
7. Remove 3 slides from the slide holder and place on the paper towel half
8. Keep the other slides (if more than 3) in the slide holder and place back in the PBS-t

9. Use the 2nd paper towel half and dry off the top of the slides at the areas around the tissue
10. Slowly drip ~80 µL (depends on tissue size) blocking solution onto each tissue section
11. Place the slides in the dark humidified chamber at room temperature
12. Repeat steps 5-11 for more than 3 slides. *Do no more than 3 slides at a time*
13. Leave slides in dark humidified chamber for 50 minutes
14. After 50 minutes, reapply ~80 µL blocking solution
15. Leave slides in dark humidified chamber for additional 40 minutes (90 minutes total)

Step 9: Adding Macrophage Antibody Cocktail

1. Obtain one paper towel and split in half
2. Lay out one of the paper towel halves. Set the other paper towel half aside for now
3. Obtain the microcentrifuge tube with the macrophage antibody cocktail
4. Remove 1 slide from the humidified chamber. Keep the others in the chamber for now
5. Drain off blocking solution onto the 1st paper towel half
6. Set slide down on the 1st paper towel half
7. Use the 2nd paper towel half and dry off the top of the slides at the areas around the tissue
8. Slowly drip ~90 µL of the macrophage antibody cocktail onto each tissue section
9. Place the slides in the dark humidified chamber at room temperature for 90 minutes
10. Immediately after step 10, finish the remaining slides. *Do no more than 3 slides at a time to avoid tissue drying*

Step 10: Wash with PBS-t (#2)

1. Obtain one paper towel

2. Remove one slide from the dark humidified chamber
3. Drain off the excess macrophage antibody cocktail onto the paper towel
4. Place the slide in the slide holder
5. Repeat steps 1-4 for up to 10 slides
6. Place the slide holder in PBS-t (**Jar 3**) for 3 minutes
7. Remove slides from PBS-t (**Jar 3**)
8. Air dry and let drip for 5 seconds
9. Dip the slide holder *slowly* in the PBS-t (**Jar 3**) 20 times. *Let each "dip cycle" be 3 seconds (60s total)*
10. Gently "swirl" the black slide holder in the staining jar for 1 minute
11. Set the black slide holder stable in PBS-t (**Jar 3**) for 1 more minute

Step 11: Wash with PBS-t (#3)

1. Obtain one paper towel and set on the IHC table
2. Remove one slide from the dark humidified chamber
3. Drain off the excess macrophage antibody cocktail onto the paper towel.
4. Place the slide in the slide holder
5. Repeat steps 1-4 for up to 10 slides
6. Place the slide holder in PBS-t (**Jar 4**) for 3 minutes
7. Remove slides from PBS-t (**Jar 4**)
8. Air dry and let drip for 5 seconds
9. Dip the slide holder *slowly* in the PBS-t (**Jar 4**) 20 times. *Let each "dip cycle" be 3 seconds (60s total)*

10. Gently “swirl” the black slide holder in the staining jar for 1 minute
11. Set the black slide holder stable in PBS-t (**Jar 4**) for 1 more minute

Step 12: Mounting with Fluoromount G

1. Obtain two paper towels and split in half and split one of them in half
2. Obtain a 22x50 coverslip.
3. Obtain Fluoromount G
4. Obtain a 5 mL serological pipette and open
5. Lay out one of the paper towel halves. Set the other paper towel half aside for now
6. Remove the slide holder from the PBS-t (**Jar 5**)
7. Air-dry and let drip for 5 seconds
8. Remove 3 slides from the slide holder and place on the 1st paper towel half
9. Keep the other slides (if more than 3) in the slide holder and place back in the PBS-t
10. Use the 2nd paper towel half and dry off the top of the slides at the areas around the tissue
11. Place the 5 mL serological pipette tip barely in the Fluoromount G and then remove
12. Drip the Fluoromount G onto the tissue sections – *only enough to cover the tissue, don’t use too much*
13. Gently place a coverslip on the slide
14. Use tweezers to gently press the coverslip onto the slide
15. Use tweezers to gently press out all air bubbles on the samples
16. Place the slides with coverslips on paper towel
17. Wipe off any excess mounting solution. *Although if there is excess, you used too much*
18. Repeat steps for additional slides. *Do no more than 3 slides at a time*

Step 13: Attaching Coverslip to Slide with Nail Polish

1. Apply nail polish along the edges of the coverslip
2. Ensure the edges are completely covered
3. Set all completed slides in drying chamber to finish drying
4. After 1 hour, store completed slides permanently in slide rack
5. Store in the dark at room temperature
6. Clean everything appropriately

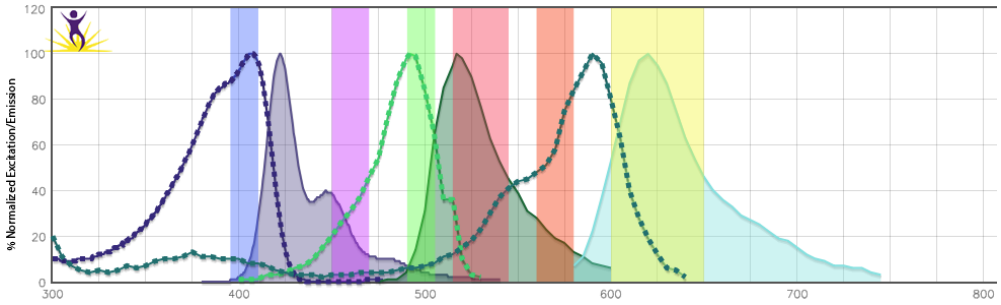

Hematoxylin and Eosin (H&E) Staining

Step 1: Preparing Hematoxylin

1. Aliquot Hematoxylin into two (2) 50 mL centrifuge tubes (45 mL each)
2. Label 50 mL centrifuge tube lids with *Hematoxylin*, initials, and date
3. Cover the tubes with aluminum foil
4. Store at 23°C in the dark
5. Dispense 90 mL of hematoxylin into hematoxylin jar

Step 2: Preparing Eosin

1. Aliquot eosin into two (2) 50 mL centrifuge tubes (45 mL each)
2. Label 50 mL centrifuge tube lids with *Eosin*, initials, and date
3. Cover the tubes with aluminum foil
4. Store at 23°C in the dark
5. Dispense 90 mL of eosin into eosin jar

Step 3: Preparing Slides for Staining

1. Remove slides from the -80°C freezer
2. Remove the slides you want to stain with hematoxylin and eosin
3. Label the slides appropriately with a pencil
4. Place the petri dish in the -20°C freezer for 12 minutes. Start a timer
5. Bring the rest of the slides not being stained back to the -80°C freezer for permanent storage

Step 4: Preparing Work Station

Fill all jars. All jars receive 80 mL of liquid

1. Obtain 600 mL beaker
2. Obtain 250 mL beaker
3. **Jar #2**: Hematoxylin
4. **Jar #3:** Bluing Solution
5. **Jar #4:** Distilled H_2O
6. **Jar #5**: Eosin
7. **Jar #6:** EtOH (70%)
8. **Jar #7**: EtOH (95%)
9. **Jar #8**: EtOH (100%)
10. **Jar #9**: Xylene (*must remain in the chemical fume hood at all times*)
11. 12 minutes after step 3.4, remove acetone from the -20°C freezer
12. Fill **1st staining jar** with ~90 mL of -20°C acetone
13. Place thermometer in acetone
14. Proceed to **Step 6** once the acetone reaches 0°C (*may need to stir to disperse heat*)

Step 5: H&E Staining

Each "dip" cycle lasts one (4) seconds, such that the slides are submerged and then taken out of solution

1. Obtain 6 µm sliced sections. *There should be two sections per slide*
2. Set slides in cold acetone (Jar #1) for 6 minutes
3. Gently shake off and air dry sections in your gloved hands for 5 seconds

4. Set slides in hematoxylin (Jar #2) for 5 minutes. *Drain well (i.e. let excess liquid drip off)*
5. While waiting for step 5 to finish, fill a 600 mL beaker with cool tap water
6. After step 6 is complete, set slides in full 600 mL beaker
7. Run cool tap water in beaker for 7 minutes
8. Remove slides from bucket. *Drain well*
9. Dip slides in bluing solution (Jar #3) 15 times. *Drain well*
10. Dip slides in distilled H_2O (Jar #4) 2 times. *Drain well*
11. Set slides in eosin (Jar #5) for 30 seconds. *Drain well*

Step 6: Ethanol Dehydration

Each "dip" cycle lasts one (4) seconds, such that the slides are submerged and then taken out of solution

1. Dip slides in 70% EtOH (Jar #6) 15 times (slow 4-second dips). *Drain well*
2. Dip slides in 95% EtOH (Jar #7) 15 times (slow 4-second dips). *Drain well*
3. Dip slides in 100% EtOH (Jar #8) 15 times (slow 4-second dips). *Drain well*
4. Dip slides in 95% EtOH (Jar #7) 15 times (slow 4-second dips). *Drain well*
5. Dip slides in 100% EtOH (Jar #8) 15 times (slow 4-second dips). *Drain well*

Step 7: Xylene Clearing

1. Place black slide holder (with slides) in a 250 mL beaker
2. Transfer 250 mL beaker to the chemical fume hood near the xylene (Jar #9)
3. Set slides in xylene (Jar #9) for 4 minutes. *Drain well*

Step 8: Coverslip Mounting

All steps must be completed in an approved chemical fume hood

1. Lay out paper towel in hood (*avoid xylene/Cytoseal dripping on the fume hood surface*)
2. Lay out three 22x50 mm coverslips on the Kimwipes
3. Remove slides from xylene. *Drain well*
4. Remove three slides from the black slide holder
5. Set the 3 slides on the Kimwipes near the coverslips so the rough/labeled side is facing up
6. Set slides back in xylene (Jar #9) temporarily (*avoid slides drying out*)
7. Place Cytoseal XYL drops (5-7 mm diameter) on the tissue sections
8. Set the 22x40 coverslips on the slides at a slow, controlled, 45° angle
9. Cytoseal XYL should spread without leaving air bubbles. Use tweezers to facilitate spread
10. Set the cover-slipped slides to the side to dry
11. Repeat steps 2-10 until all slides are finished
12. Wipe off Cytoseal container well so it doesn’t harden on the tip
13. Obtain nail polish
14. Apply nail polish along the edges of the coverslip
15. Ensure the edges are completely covered
16. Clean everything appropriately

Tissue Analysis

Equipment and Materials

Item	**Distributor**	**Item Number**
Upright microscope	Nikon	89501-464
Monochrome digital camera	Nikon	Ds-Qi1Mc
PC-based camera control unit	Nikon	DS-U3
SOLA Light Engine® fluorescent lamp	Lumencor	SOLA SM 6-LCR-SB
DAPI filter set	Chroma	49000
FITC filter set	Chroma	SP101
Texas red filter set	Chroma	41004
Objective lens, 20X/0.50NA	Nikon	CFI Plan Fluor 20X
NIS-Elements F Ver4.60.00 for 64bit edition	Nikon	N/A

Imaging Macrophage-Stained Slides

Step 1: Preparing Microscope

1. Close the shutter for the fluorescence lamp
2. Switch to the 20X objective
3. Turn on the Nikon camera, microscope, and Lumencor fluorescent lamp
4. Open up NIS Elements F 4.00.00
5. Select "*Camera Ds-Qi iMc-U3….*"
6. For the Ds-Qi1Mc Settings:
    - Change the mode to normal
    - Fast focus at "1280x1024 no binning"
    - Change the quality capture to "1280x1024 no binning"
    - Set the exposure to 100 ms (*can be changed later*)
    - Set the analog gain to 1.0x
    - Click commands: ROI, then select to use Current ROI

Step 2: Preparing Slide Position

1. Obtain the desired slide.
2. Set the slide on the microscope slide stage
3. Turn the filter wheel to the DAPI filter
4. Open the shutter for the fluorescence lamp
5. Adjust the translation stage so the light is hitting some part of the desired tissue section
6. Apply course focus

7. Locate the top of the tissue either by the hair or a marking on the slide.
8. Apply fine focus to bring the M1 macrophages in-focus
9. Manually adjust the exposure (between 50-250 ms) to reduce background noise.

Step 3: Saving M1 Macrophage Images with DAPI Filter

1. Bring the M1 macrophages (DAPI filter) in-focus
2. Click “Capture” then “Save as”
3. Save as a TIFF file
4. Click “LIVE”

Step 4: Saving Non-Polarized Macrophage Images with FITC Filter

1. Do not move the slide or translation stage
2. Bring the non-polarized macrophages (FITC filter) in-focus
3. Click “Capture” then “Save as”
4. Save as a TIFF file
5. Click “LIVE”

Step 5: Saving M2 Macrophage Images with Texas Red

1. Do not move the slide or translation stage
2. Bring the M2 macrophages (Texas Red filter) in-focus
3. Click “Capture” then “Save as”
4. Save as a TIFF file
5. Click “LIVE”

Step 2: Run Code

1. Ensure there are at least three TIFF files in the appropriate folder: M1 (DAPI), non-polarized (FITC), and M2 (Texas Red) images

   Note: Ideally, there will be 12 images for each region-of-interest: 4 from each filter to account for cells slightly out of the plane-of-focus in the 5 μm thick slide. This is how the code, tamcount.m, is set up to run
2. Open and run *tamcount.m*
3. A black-and-white image will appear full screen
4. With the mouse, click the center of each mostly-in-focus TAM you see. *It is very important to click the center*
   a. TAMs will often appear as elongated "rings" or "C shapes" with a dark center and white ring/C
5. Once you are done clicking the center of each TAM, hit the enter button
6. A new black-and-white image will appear full screen
7. Repeat these steps until you are finished with all 12 images

Notes:

1. Be sure the click the *center* of each TAM. Use your best judgement
2. There may be instances in which the same TAM appears in-focus across multiple images – it is okay to select the same TAM twice (or more) in back-to-back images. The code will automatically identify duplicates and only include one in the count
3. Something being *in-focus* or *out-of-focus* is slightly subjective. Use your best judgement

Other General Procedures

Equipment and Materials

Item	Distributor	Item Number
Tabletop Animal Anesthesia System	VWR	89012-492
Mobile Cart for Anesthesia System	Amazon	OF-STC111-B
Gloves	VWR	89038-270
KimWipes	VWR	470224-038
Microcentrifuge Tubes	VWR	20170-038
Alcohol Swab	VWR	BD326859
80-Place Storage System	VWR	30128-276
Water Bath	VWR	89501-464
Warm Water Pump	Global Medical	TP700
Warm Water Pump Pad	Kent Scientific	TPZ-0510EA
Valved In-Line Hose Barb Coupling Body	Fresh Water Systems	42100
Non-Valved In-Line Hose Barb Coupling	Fresh Water Systems	40900
Analytical Balance	VWR	10159-998
Alcohol Swab	VWR	BD326859
28G U-100 BD Micro-Fine IV Syringe	VWR	BD329410
Compressed Air Cylinder, Size 200L	Airgas	AI USP200
Compressed O_2 Cylinder, Size 200L	Airgas	OX USP200
Isothesia (Isoflurane) Solution	Henry Schein	1169567762
Regulator for Air Cylinder	Airgas	HCL3000762
Regulator for O_2 Cylinder	Airgas	HCL3000714

O_2 DISS Femaile Hex Nut – ¼" Hose Barb	Med. Support Products	0115
Activated Charcoal Filter VaporGuard	VWR	89012-608
Cylinder Bench Clamp	VWR	60142-003

Anesthetizing Mice with Isoflurane

Step 1: Preparing Warm Water Pad.

1. Place the heated water pump in the hood
2. Place the heated water pad in the hood
3. Connect the water pad to the pump using the in-line hose barb coupling
4. Turn on the heated water pump
5. Place a large Kimwipe over the heated water pad (so the mouse won't lay directly on the pad)
6. Wait 20 minutes until the water is warm

Step 2: Preparing the Anesthesia Machine

1. Place the carbon filter in the back of the hood, such that it is 2 inches from the back wall
2. Place the mouse-isoflurane chamber in the hood, such that it is 6 inches from the front of the hood
3. Place the analytical scale in the hood
4. Place a large folded paper towel in the mouse-isoflurane chamber
5. Open both valves (tank valve and nosecone valve)
6. Tape the nosecone down on the edge of the warm water pump pad such that it is parallel to the surface
7. Slightly loosen the top gray knob of the oxygen tank to start gas flow
8. Adjust the silver isoflurane tank knob between 1.5 and 4 (% isoflurane)
    a. 1.5%: Immobility (no analgesia, use for giving shots)
    b. 2%: Shallow Anesthesia

c. 3%: Medium Anesthesia

d. 4%: Deep Anesthesia (used for euthanasia)

e. 5%: Very Deep Anesthesia (not used in any of our studies)

9. Set the green isoflurane tank knob to 1.0 (1.0 L/min oxygen)

Step 3: Anesthetizing Mice

1. Obtain a mouse
2. Pick the mouse up by the tail
3. Place the mouse in the mouse-isoflurane chamber
4. Secure the lid by locking the black hinge
5. When mouse passes out, remove the mouse by the tail
6. Place the mouse on the nosecone such that its eyes are at the level of the cone bottom
7. Put eye drop gel in the mouse's eyes
8. Ensure the mouse is on the nose cone for 30 seconds
9. Remove mouse from nosecone and quickly weigh the mouse
10. Put mouse back on nosecone for 20 seconds
11. Perform desired task
12. Remove mouse from nosecone
13. Place mouse in hands and wait until it wakes up (time depends on anesthesia level)
14. Place mouse back in cage

Intraperitoneal Injection (I.P.) of Mice

Step 1: Preparation for Injection

1. Set up the isoflurane tank and chamber
2. With 28G syringe, draw up required volume to nearest 10 μL
3. Get rid of all air bubbles
4. Set the 28G needle aside
5. Remove mouse from cage
6. Put mouse in isoflurane chamber until sedated
7. Remove mouse from isoflurane chamber and weigh mouse
8. Remove mouse from scale and place under nosecone in biosafety cabinet

Step 2: Intraperitoneal (IP) Injection

1. Obtain 28G needle from the Kimwipe
2. Turn the needle so that the bevel points up and the numbers on the syringe barrel can be read
3. Bring the needle to a 35° ± 5° angle from the abdomen
4. Place the needle 2 mm off the abdominal midline (*you can see where the hair parts*)
5. Place the needle on the same line as the visible knee bones
6. Push needle in until ~1/2 of the needle length is inserted
7. Depress the plunger until the solution has been fully administered (2-second plunge)
8. *Do not allow the needle to move around inside the abdomen*
9. Pull the needle straight out and place the syringe/needle into a Sharps container without recapping

10. Leave mouse in hand or on warm water pad until awake

11. Place the mouse back in the cage

Potential Complications

Note: These complications were not experienced throughout the study. IACUC should be contacted immediately if these complications are experienced

1. Aspiration of green material: bowel has been punctured
2. Aspiration of yellow liquid: bladder has been punctured
3. Aspiration of blood: abdominal blood vessel has been punctured

Humane Endpoint Criteria

Mice will be euthanized based their appropriate endpoint per study, or on humane endpoint criteria, whichever comes first:

Humane endpoint criteria are as follows.

1. Tumor Volume = 1500 mm^3
2. Maximum Tumor Diameter = 20 mm (or 2 cm)
3. Body Condition Score < 2
4. Weight Loss ≥ 20% (~3-4 g)
5. Chronic Pain or Distress
    a. Changes in Health and Well-Being (monitored by IACUC and Investigator)
    b. Impaired mobility (the inability to reach food and water)
    c. Inability to remain upright
    d. Interference with a vital physiological function:
        i. Respiration, mastication, swallowing, urination, defecation, or locomotion
    e. Location of the tumor causing interference with movement
    f. Hunched abnormal posture for more than 48 hours
    g. Labored breathing and cyanosis [bluish pinnae (ears) or feet or mucous membranes]
    h. Clinical dehydration and/or prolonged decreased food intake
    i. Muscle atrophy and signs of lethargy and lack of physical activity
    j. Chronic diarrhea or constipation for more than 48 hours

k. Hematological or biochemical values that indicate organ failure

l. Severe anemia [pale pinnae (ears) or feet or mucous membranes]

m. Bloodstained or mucopurulent discharge from any orifice

n. Lack of grooming behavior; rough/unkempt hair coat for more than 48 hours

o. Enlarged lymph nodes or spleen

p. Significant abdominal distension

q. Cranial deformity/neurological signs

r. Exophthalmos (bulging eye)

s. Ulceration or necrosis of tumor

t. Restlessness/inability to get comfortable

u. Unconsciousness with no response to external stimuli

Institutional Review Board (IRB) Approval

UNIVERSITY OF ARKANSAS

Office of Research Compliance
Institutional Review Board

October 21, 2015

MEMORANDUM

TO:	Gage Greening Haley James Mary Dierks Timothy Muldoon
FROM:	Ro Windwalker IRB Coordinator
RE:	New Protocol Approval
IRB Protocol #:	15-09-149
Protocol Title:	*Microendoscopic Imaging and Spectroscopy of in vivo Human Skin and Oral Mucosa*
Review Type:	☐ EXEMPT ☒ EXPEDITED ☐ FULL IRB
Approved Project Period:	Start Date: 10/21/2015 Expiration Date: 10/08/2016

Your protocol has been approved by the IRB. Protocols are approved for a maximum period of one year. If you wish to continue the project past the approved project period (see above), you must submit a request, using the form *Continuing Review for IRB Approved Projects*, prior to the expiration date. This form is available from the IRB Coordinator or on the Research Compliance website (https://vpred.uark.edu/units/rscp/index.php). As a courtesy, you will be sent a reminder two months in advance of that date. However, failure to receive a reminder does not negate your obligation to make the request in sufficient time for review and approval. Federal regulations prohibit retroactive approval of continuation. Failure to receive approval to continue the project prior to the expiration date will result in Termination of the protocol approval. The IRB Coordinator can give you guidance on submission times.

This protocol has been approved for 80 participants. If you wish to make *any* modifications in the approved protocol, including enrolling more than this number, you must seek approval *prior to* implementing those changes. All modifications should be requested in writing (email is acceptable) and must provide sufficient detail to assess the impact of the change.

If you have questions or need any assistance from the IRB, please contact me at 109 MLKG Building, 5-2208, or irb@uark.edu.

109 MLKG • 1 University of Arkansas • Fayetteville, AR 72701-1201 • (479) 575-2208 • Fax (479) 575-6527 • Email irb@uark.edu

UNIVERSITY OF ARKANSAS INSTITUTIONAL REVIEW BOARD
PROTOCOL FORM

The University Institutional Review Board recommends policies and monitors their implementation, on the use of human beings as subjects for physical, mental, and social experimentation, in and out of class. . . . Protocols for the use of human subjects in research and in class experiments, whether funded internally or externally, must be approved by the (IRB) or in accordance with IRB policies and procedures prior to the implementation of the human subject protocol. . . Violation of procedures and approved protocols can result in the loss of funding from the sponsoring agency or the University of Arkansas and may be interpreted as scientific misconduct. *(see Faculty Handbook)*

Supply the information requested in items 1-14 as appropriate. **Type** entries in the spaces provided using additional pages as needed. In accordance with college/departmental policy, submit the original **and** one copy of this completed protocol form and all attached materials to the appropriate Human Subjects Committee. In the absence of an IRB-authorized Human Subjects Committee, submit the original of this completed protocol form and all attached materials to the IRB, Attn: Compliance Officer, MLKG 109, 575-2208. Completed form and additional materials may be emailed to irb@uark.edu. The fully signed signature page may be scanned and submitted with the protocol, by FAX (575-6527) or via campus mail.

1. Microendoscopic imaging and spectroscopy of *in vivo* human skin and oral mucosa

2. (Students **must** have a faculty member supervise the research. The faculty member must sign this form and all researchers and the faculty advisor should provide a campus phone number.)

	Name	Department	Email Address	Campus Phone
Principal Researcher	Gage Greening	BMEG	ggreenin@uark.edu	
Co-Researcher	Haley James	CHEM	hmjames@uark.edu	
Co-Researcher	Mary Dierks	BIOL	mkdierks@uark.edu	
Faculty Advisor	Timothy Muldoon	BMEG	tmuldoon@uark.edu	(479) 575-5324

3.Researcher(s) status. Check all that apply.

☒ Faculty ☐ Staff ☒ Graduate Student(s) ☒ Undergraduate Student(s)

4. Project type

☒ Faculty Research ☐ Thesis / Dissertation ☐ Class Project ☐ Independent Study /
☐ Staff Research ☐ M.A.T. Research ☐ Honors Project Educ. Spec. Project

5. Is the project receiving extramural funding? (Extramural funding is funding from an external research sponsor.)

☐ No ☒ Yes. Specify the source of funds: National Institutes of Health (1R03CA182052-01)

6.Brief description of the purpose of proposed research and all procedures involving people. Be specific. Use additional pages if needed. (**Do not** send thesis or dissertation proposals. Proposals for extramural funding must be submitted in full.)

Purpose of research: The overall purpose of this project is to 1) assess the spectral characteristics of healthy human skin and correlate this functional spectral data with microendoscopic images of normal skin tissue, and 2) assess the spectral characteristics of healthy human oral mucosa. To accomplish this, we will use a simple, non-invasive fiber-optic probe in direct contact with a target site on the subject (either the skin or inner lip) to deliver and collect light (< 2 mW total). Two light sources will be used: A blue 455 nm LED will be used to acquire images and a broadband 450-750 nm tungsten halogen lamp will be used to acquire spectroscopic information. Following collection of low-power light, subsequent post-processing of spectral data will be used to extract quantitative functional information, including optical properties, hemoglobin concentration and blood oxygen saturation. Additionally, functional features will be correlated to qualitative image data during post-processing. This will aid in correlating image and spectral data from a normal data set.

Procedures involving people: Upon receiving informed consent, the investigator will sterilize the tip of the fiber probe using 70% ethanol or an alcohol swab prior to taking data from the volunteer's inner lip and an exposed 1 cm^2 area of the volunteer's skin (such as the hand, arm, or forehead). For the inner lip, investigator will place the tip of the fiber-optic probe (2 mm in diameter) in direct contact with the volunteer's inner lip. Once in direct contact, the volunteer will undergo non-invasive data collection for 60 seconds. Following the 60 seconds of data collection, the probe will be removed from the inner lip. For the skin, the 1 cm^2 skin site will be shaved with a disposable razor if there is any hair. After shaving, the skin site will be marked with a standard yellow highlighter, which is fluorescent when in the presence of the blue light supplied by the LED. The investigator will place the tip of the fiber-optic probe in direct contact with the marked area of the volunteer's skin. Once in direct contact, the volunteer will undergo non-invasive data collection for 60 seconds. Following the 60 seconds of data collection, the probe will be removed from the skin area and the volunteer may wash away any remaining highlighter ink. No biographical information will be collected from the normal volunteers.

7. Estimated **number of participants** (complete all that apply)

_____ Children under 14	_____ Children 14-17	40 UA students (18yrs and older)	40 Adult non-students

8. Anticipated dates for contact with participants:

First Contact 10/01/2015 Last Contact 10/01/2018

9. Informed Consent procedures: The following information must be included in any procedure: identification of researcher, institutional affiliation and contact information; identification of Compliance Officer and contact information; purpose of the research, expected duration of the subject's participation; description of procedures; risks and/or benefits; how confidentiality will be ensured; that participation is voluntary and that refusal to participate will involve no penalty or loss of benefits to which the subject is otherwise entitled. See *Policies and Procedures Governing Research with Human Subjects*, section 5.0 Requirements for Consent.

☒ Signed informed consent will be obtained. **Attach copy of form**.
☐ Modified informed consent will be obtained. **Attach copy of form**.
☐ Other method (e.g., implied consent). **Please explain on attached sheet**.
☐ Not applicable to this project. **Please explain on attached sheet**.

10. Confidentiality of Data: All data collected that can be associated with a subject/respondent must remain confidential. Describe the methods to be used to ensure the confidentiality of data obtained.

Following informed consent, data files will simply be numbered by the collection date and subject number. No information linking the subject number to the data file will be retained.

11. Risks and/or Benefits:

Risks: Will participants in the research be exposed to more than minimal risk? F Yes F No Minimal risk is defined as risks of harm not greater, considering probability and magnitude, than those ordinarily encountered in daily life or during the performance of routine physical or psychological examinations or tests. Describe any such risks or discomforts associated with the study and precautions that will be taken to minimize them.

Volunteers will not experience any more discomfort than is experienced when the bottom of a pen is placed in gentle contact with the skin or inner lip. Highlighter ink in contact with the skin provides no risk, expect for temporary and minor discoloration in the 1 cm^2 image area. The volunteer may experience minor discomfort due to shaving of any hair of the skin image site, although discomfort is not expected.

Benefits: Other than the contribution of new knowledge, describe the benefits of this research, especially any benefits to those participating.

Patients will not receive any benefits from participation in this study.

12. Check all of the following that apply to the proposed research. Supply the requested information below or on attached sheets:

- ☐ A. Deception of or withholding information from participants. Justify the use of deception or the withholding of information. Describe the debriefing procedure: how and when will the subject be informed of the deception and/or the information withheld?
- ☐ B. Medical clearance necessary prior to participation. Describe the procedures and note the safety precautions to be taken.
- ☐ C. Samples (blood, tissue, etc.) from participants. Describe the procedures and note the safety precautions to be taken.
- ☐ D. Administration of substances (foods, drugs, etc.) to participants. Describe the procedures and note the safety precautions to be taken.
- ☐ E. Physical exercise or conditioning for subjects. Describe the procedures and note the safety precautions to be taken.
- ☐ F. Research involving children. How will informed consent from parents or legally authorized representatives as well as from subjects be obtained?
- ☐ G. Research involving pregnant women or fetuses. How will informed consent be obtained from both parents of the fetus?
- ☐ H. Research involving participants in institutions (cognitive impairments, prisoners, etc.). Specify agencies or institutions involved. Attach letters of approval. Letters must be on letterhead with original signature; electronic transmission is acceptable.
- ☐ I. Research approved by an IRB at another institution. Specify agencies or institutions involved. Attach letters of approval. Letters must be on letterhead with original signature; electronic transmission is acceptable.
- ☐ J. Research that must be approved by another institution or agency. Specify agencies or institutions involved. Attach letters of approval. Letters must be on letterhead with original signature; electronic transmission is acceptable.

13. Checklist for Attachments

The following are attached:
☒ Consent form (if applicable) or
☐ Letter to participants, written instructions, and/or script of oral protocols indicating clearly the information in item #9.
☐ Letter(s) of approval from cooperating institution(s) and/or other IRB approvals (if applicable)
☐ Data collection instruments

Microendoscopic imaging and spectroscopy of *in vivo* human skin and oral mucosa

Principal Researcher: Gage J. Greening, B.S.
Faculty Advisor: Timothy J. Muldoon, M.D., Ph.D.

INVITATION TO PARTICIPATE

You are invited to participate in a research study to aid in the understanding of the optical properties of human skin and oral mucosa. This information will allow the investigators to correlate these skin optical properties with image data of your skin epidermal tissue or analyze optical properties of the oral mucosa. You are asked to participate in this study because you can provide us with normal-appearing epithelial cells from either the skin or oral mucosa, which will help us develop a normal data set.

WHAT YOU SHOULD KNOW ABOUT THE RESEARCH STUDY

Who is the Principal Researcher?

Gage J. Greening, B.S., Graduate Research Associate, Department of Biomedical Engineering.
Office: Engineering Research Center #2912; email: ggreenin@uark.edu

Who is the Faculty Advisor?

Timothy J. Muldoon, M.D., Ph.D., Assistant Professor, Department of Biomedical Engineering.
Office: Engineering Research Center #2920; phone: 479-575-3967; email: tmuldoon@uark.edu

What is the purpose of this research study?

The purpose of this study is to collect reflected light, using a fiber optic probe, from certain tissue sites (skin and oral mucosa), indicating the health of the tissue.

Who will participate in this study?

Subjects must be over 18, and have never been previously diagnosed with a skin premalignant lesion, skin cancer, oral premalignant lesion, or oral cancer of any kind.

What am I being asked to do?

Your participation will require the following:

After an appropriate skin site has been identified, hair will be removed in a 1 cm^2 area using a disposable sterile razor.

After hair removal, the 1 cm^2 skin site will be marked with a standard yellow highlighter.

A 2 mm diameter fiber-optic probe will be placed in gentle contact with the skin site.

Data collection, with the probe still placed in gentle contact with the skin, will occur for no more than 60 seconds. After data collection, you may wash away any remaining or excess yellow highlighter ink.

The same 2 mm diameter fiber-optic probe will be placed in gentle contact with the inner lip.

Data collection, with the probe still placed in gentle contact with the inner lip, will occur for no more than 60 seconds.

What are the possible risks or discomforts?

There are no anticipated risks for this study. You may feel brief discomfort from the electric razor and experience temporary and minor skin discoloration due to the yellow highlighter ink.

What are the possible benefits of this study?
There are no direct benefits to the participants in this study.

How long will the study last?
The total time commitment for this study will be five minutes. You may not volunteer multiple times for this study.

Will I receive compensation for my time and inconvenience if I choose to participate in this study?
You will not receive any compensation for this study.

Will I have to pay for anything?
There is no cost associated with participation in this study.

What are the options if I do not want to be in the study?
If you do not want to be in this study, you may refuse to participate. Also, you may refuse to participate at any time during the study. Your relationship with the University will not be affected in any way if you refuse to participate.

How will my confidentiality be protected?
All information will be kept confidential to the extent allowed by applicable State and Federal law.
All data will be kept anonymous and informed consent documents will be kept by the Principal Investigator in a locked drawer.

Will I know the results of the study?
At the conclusion of the study you will have the right to request feedback about the results. You may contact the faculty advisor, Timothy J. Muldoon, M.D., Ph.D. (email: tmuldoon@uark.edu) or Principal Researcher, Gage J. Greening, B.S. (email: ggreenin@uark.edu). You will receive a copy of this form for your files.

What do I do if I have questions about the research study?
You have the right to contact the Principal Researcher or Faculty Advisor as listed below for any concerns that you may have.

Faculty Advisor: Timothy J. Muldoon, M.D., Ph.D. (email: tmuldoon@uark.edu)
Principal Researcher: Gage J. Greening, B.S. (email: ggreenin@uark.edu).

You may also contact the University of Arkansas Research Compliance office listed below if you have questions about your rights as a participant, or to discuss any concerns about, or problems with the research.

Ro Windwalker, CIP
Institutional Review Board Coordinator
Research Compliance
University of Arkansas
109 MLKG Building
Fayetteville, AR 72701-1201
479-575-2208
irb@uark.edu

I have read the above statement and have been able to ask questions and express concerns, which have been satisfactorily responded to by the investigator. I understand the purpose of the study as well as the potential benefits and risks that are involved. I understand that participation is voluntary. I understand that significant new findings developed during this research will be shared with the participant. I understand that no rights have been waived by signing the consent form. I have been given a copy of the consent form.

_____

Institutional Animal Care and Use Committee (IACUC) Approval

UNIVERSITY OF ARKANSAS

Office of Research Compliance

To:	Timothy Muldoon
Fr:	Craig Coon
Date:	April 7th, 2017
Subject:	IACUC Approval
Expiration Date:	April 6th, 2020

The Institutional Animal Care and Use Committee (IACUC) has APPROVED your protocol # **17072:** *Quantifying tumor perfusion response with diffuse reflectance spectroscopy in murine allograft model of colon carcinoma following immunomodulation of tumor-associated macrophages*.

In granting its approval, the IACUC has approved only the information provided. Should there be any further changes to the protocol during the research, please notify the IACUC in writing (via the Modification form) prior to initiating the changes. If the study period is expected to extend beyond April 6th, 2020 you must submit a newly drafted protocol prior to that date to avoid any interruption. By policy the IACUC cannot approve a study for more than 3 years at a time.

The following individuals are approved to work on this study: Haley James, Timothy Muldoon, Gage Greening, and Sandra Prieto. Please submit personnel additions to this protocol via the modification form prior to their start of work.

The IACUC appreciates your cooperation in complying with University and Federal guidelines involving animal subjects.

CNC/aem

Animal Use Protocol
University of Arkansas, Fayetteville
Coversheet

IACUC use only:			
Protocol number:	17072	Category(s) of animal use:	
Date Received:	3-29-17	☐ Agricultural	
Approval Date:	4-7-17	☒ Biomedical	
Start Date:	4-7-17	☐ Field	
End Date:	4-6-20	LATA Training Verified	☒ Yes ☐ No

Instructions:

- *This is a MicroSoft Word (MSWord) "form". Use MSWord to fill in the information asked for in either the blanks ("____"), or the box (" ☐ ") provided. You can put as much information in the blanks or boxes as needed.* (Note -- It may cause minor complications to use the "Tab" key to move from box to box since the boxes are a cell in a table [consisting of one cell]. Therefore, it should cause less problems to avoid using the tab key. However, if you need to use the Tab key in the cell, you will need to use the Ctrl-Tab combination.)
- *Submit an electronic copy of your completed protocol to iacuc@uark.edu and be sure to sign the appropriate form(s) with a scanned signature. However, completed forms sent in via uark.edu mail system are considered "signed" even without a scanned signature.*
- *Failure to follow these instructions and adequately fill out the required information may result in the protocol being returned.*
- *The deadline for getting this form to Tony Munn, is 12:00 Noon on Monday of the week of the IACUC meeting when it will be acted upon.*

Project Title: Quantifying tumor perfusion response with diffuse reflectance spectroscopy in murine allograft model of colon carcinoma following immunomodulation of tumor-associated macrophages

Project length (3 years maximum): 3 years

Start date: 4-7-17 End date: 4-6-20

	Principal Investigator:	**Co-Investigator(s)** *(if applicable):*	
Name:	Timothy J. Muldoon		
Department/Division:	Biomedical Engineering		
Campus Mail Address:	126 Engineering Hall		
Telephone:	575-5324/575-3967		
Fax:	575-4346		
E-mail:	tmuldoon@uark.edu		

Individual(s) responsible for animal care:

Name:	Timothy J. Muldoon		
Office address:	2920 ENRC		
Office City, State, Zip:	Fayetteville, AR 72701		
Office phone:	575-5324/575-3967		
Home address:	1822 N. Best Friend Ln		
Home City, State, Zip:	Fayetteville, AR 72704		
Home phone:	832-816-5349 (cell)		

Individual(s) responsible for euthanasia:

Name:	Timothy J. Muldoon		
Office address:	2920 ENRC		
Office City, State, Zip:	Fayettville, AR 72701		
Office phone:	575-5324/575-3967		
Home address:	1822 N. Best Friend Ln		
Home City, State, Zip:	Fayetteville, AR 72704		
Home phone:	832-816-5349 (cell)		

Animal Use Protocol
University of Arkansas, Fayetteville
Coversheet

Animals used

Species: Mus musculus
Common name: mouse
Calculated number to be used (by species; not a combined number): 160 Balb/c mice
-- Note: This number (or these numbers) must agree with those listed in Section 2B (Experimental Design) of the Narrative.
Supplier (all purchases must be from a licensed supplier)
Name: The Jackson Laboratory
Address: Bar Harbor, ME

Locations (building and room)
Animal housing: 4617 ENRC
Surgical facility: N/A
Data collection: 4617 / 2540 / 2541

Animal Use Protocol
University of Arkansas, Fayetteville
Checklist

Title of Project: Quantifying tumor perfusion response with diffuse reflectance spectroscopy in murine allograft model of colon carcinoma following immunomodulation of tumor-associated macrophages

Principal Investigator: Muldoon

Type of Project:

Select one → ☒ Research ☐ Teaching → Course Number(s) _____

Category of research and teaching for which this protocol was written:

Select one → ☒ Biomedical ☐ Agricultural ☐ Field

Funding Source (check all that apply):

☒ NIH ☐ NSF ☐ USDA ☐ private industry ☒ U of A ☐ State of Arkansas

☐ other (identify): _____

Level of Pain or Stress: Check only one level, which should be the most severe level the animals will be subjected to during the course of the study ***(Please read these carefully)***

	Level	Examples and Comments
☒ Level 1	Level 1 Experiments on vertebrate animals that are expected to produce little or no discomfort.	• Simple procedures such as injections and blood sampling; • observational field behavior; • physical examinations; • experiments on anesthetized animals that do not regain consciousness; • food/water deprivation for short periods and methods of euthanasia that induce rapid unconsciousness.
☐ Level 2	Level 2 Experiments that involve some minor stress or short-duration pain to vertebrate animals.	• With anesthesia, "cut downs" or implantation of catheters; • behavioral experiments on conscious animals that involve restraint; • immunization employing Freund's adjuvant; • noxious stimuli from which escape is possible; • surgical procedures under anesthesia that may result in postsurgical discomfort (possibly requiring analgesics); • **experimental** infection producing *no significant pain or distress*.
☐ Level 3	Level 3 Experiments that involve *significant unavoidable stress or pain* to vertebrate animals.	• Deliberate induction of behavioral stress; • major surgical procedures under anesthesia that result in significant postoperative discomfort or an anatomic or physiologic deficit that will *result in pain or distress*; • noxious stimuli from which escape is impossible; • prolonged periods of physical restraint; • procedures that produce pain or distress in which anesthetics are not used (toxicity testing, radiation sickness, certain injections, stress and shock research, or **experimental** infection **producing systemic disease that will *result in pain, distress, or death***).
	Level 3 mandates responsibility on the part of the investigator to explore alternative procedures.	
☐ Level 4	Level 4 Procedures that involve inflicting severe pain on unanesthetized, conscious animals.	• Use of muscle relaxants or paralytic drugs without the use of anesthetics; • surgery, severe burn or trauma infliction on unanesthetized animals; • attempts to induce psychotic-like behavior or severe stress or terminal stress.

Many of these procedures are specifically prohibited and therefore may result in withdrawal of federal funds and/or institutional USDA registration.

Note: The preceding levels correspond to the following animal use categories on the APHIS annual report form: Level 1 = Category C or D; Level 2 = Category D; Levels 3 and 4 = Category E.

Animal Use Protocol
University of Arkansas, Fayetteville
Checklist

Surgical Procedures:
If any of the methods/techniques listed below will be used, check the appropriate space and *provide the requested details in Section 2D of the Narrative (Surgical Procedures)*:

- ☒ none
- ☐ non-survival surgery (euthanasia will be administered before recovery from anesthesia)
- ☐ survival surgery (animal will be allowed to recover from anesthesia)
- ☐ multiple survival surgeries *(this requires explicit justification in Narrative)*

Non-Surgical Procedures:
If any of the methods/techniques listed below will be used, check the appropriate space and *provide the requested details in Section 2C of the Narrative (Non-Surgical Procedures)*:

- ☐ Non-surgical invasive procedures (blood collection, catheterization, intubation, etc.).
  Provide appropriate details (volume, site, frequency, etc.)
- ☒ Exposure of a living animal to a hazardous, toxic, and/or radioactive substance.
  Provide substance name, route of administration, dose, volume, frequency
- ☐ Exposure of a living animal to an infectious agent. Notice, if this is checked, you must also check, either Level 2 or Level 3 pain in the previous section!
  Provide name of agent, means of exposure, and amount and frequency of exposure. Specify in "Method of Euthanasia" section, the criterion you will use to determine if euthanasia is necessary to relieve suffering.
- ☐ Immunization protocol.
  Provide name of adjuvant(s) used; injection site; volume per site; frequency of injection; method, frequency, and volume of blood withdrawn (including anesthetic, if used).
  Note: this does NOT apply to standard prophylactic vaccinations.
- ☐ Prolonged restraint.
  Provide method, duration, frequency, procedure by which animal is adapted to restraint device.
- ☐ Food/water deprivation.
  Provide duration, frequency, extent (total/partial), methods used to assess and monitor distress.
  Note: removal of food and/or water for 24 hours in preparation for surgery or some other procedure is NOT considered to be food/water deprivation.
- ☐ Abnormal environment.
  Provide information on departure from normal conditions (temperature, humidity, light, duration, etc.).
- ☐ Aversive stimuli.
  Provide type and intensity of stimulus, duration, justification for use.
- ☐ Hybridoma protocol.
  Provide priming agent, cells injected, schedule for collection of ascites, number of abdominal taps, size of needle used.
  Important: Provide justification for use of the *in vivo* mouse ascites method versus the various *in vitro* methods currently available, providing adequate documentation.
- ☐ Use of neuromuscular blocking agents (muscle paralytics) during surgery.
  Provide a rationale for their use and explain how you will determine that adequate anesthesia is maintained.

☐ Use of death (without euthanasia) as an endpoint of the study.
Provide justification why an earlier endpoint is not acceptable.

Method of Euthanasia -- Identify the method(s) of euthanasia to be used; it (they) must comply with the most recent AVMA Guidelines on Euthanasia
http://www.avma.org/issues/animal_welfare/euthanasia.pdf

☐ none needed

☐ overdose of anesthetic (specify agent, dose, and route of administration)

☐ inhalation of carbon dioxide

☐ physical means under general anesthesia (identify the specific means that will be used; cervical dislocation, etc.)

☒ physical means without anesthesia
- the use of captive bolt pistol on large farm animals, cervical dislocation on chickens, and some other physical methods [such as gunshot] **are permitted, if done properly by trained personnel;**
- *OTHERWISE, physical means without anesthesia* ***(such as cervical dislocation of mice)*** *can be used only when scientifically justified and requires specific written justification).*
  If to be used, write justification here: _____

☐ other (identify here and describe): _____

Disposal of remains:

☒ Incineration at University Farm (this is the disposal site for dead animals that are placed in the freezer at CLAF)

☐ Other (describe): _____

Animal Use Protocol
University of Arkansas, Fayetteville
Narrative

1. **ABSTRACT** (approximately 100-300 words)

Please provide, in lay language,

- a concise but specific statement of the scientific objective for the proposed research,
- the rationale behind this objective,
- the species of animal to be used, and
- an **overview** of the procedures to be followed.

This statement should stand alone and be comprehensible to a non-scientist.

This is NOT the place for a lengthy introduction! PLEASE…

Abstract here :

We are interested in developing novel imaging methods for early detection and management of colorectal cancer. Dysplasia of colonic epitheleium has been known to be exacerbated due to inflammatory response, and both spontaneous and colitis (inflammatory) models are associated with myriad structural and spectral changes that can be observed using optical and spectroscopy systems. We are developing a hybrid microendoscopy / diffuse reflectance spectroscopy device that could be used at the point-of-care to visualize regions of dysplasia and to better monitor early tumor response to combination therapy involving chemotherapy and immunomodulation therapy

The overall goal of this study will be to compare the biomarkers (in terms of microscopic-level structural changes as well as specific diffuse reflectance spectral changes) that are observed in the development of subcutaneous tumors in the CT26-Balb/c mouse model of colon carcinoma. We will evaluate tumors at various stages of development using an subcutaneous injection of murine colon carcinoma cells. These mice will be useful to study the spectroscopic and immunological response in tumors, in a longitudinal study after various days of tumor growth. We will evaluate non-invasive diffuse reflectance spectroscopy twice daily, and for a select number of mice we will inject with anti-CCL2 (known for blocking macrophage-induced inflammatory response and decreasing size of tumors) in order to compare immunological response to differences in inflammation (comparison of tumor-associated macrophages in excised tissue).

2. **METHODS**

Using the headings listed below, describe the methods to be used in your project. The level of detail for procedures involving animals should be comparable to that in the Methods section of a journal article (i.e., sufficient to enable another researcher competent in your field to replicate your study). Please, **do not** cut & paste from your grant proposal, it usually includes information that the IACUC does not need to review. Also, do not repeat information in the different sections below any more than is absolutely necessary to communicate clearly what you plan to do. (In other words, do not repeat descriptions in B, C, and/or D.)

A. Housing

(**Note**: Cage size, amount of room per animal, etc. must conform to the dimensions listed in one of the following;

- ILAR *Guide for the Care and Use of Laboratory Animals,*
- *Animal Welfare Act (USDA) Regulations,*
- PHS *Policy on Humane Care and Use of Laboratory Animals, or*
- FASS *GUIDE For the Care and Use of Agricultural Animals in Agricultural Research and Teaching.*

The only exceptions are those protocols that are to be done under "commercial conditions", these must be appropriately documented and approved.)

Describe how the animals will be housed, including

- cage or pen size (indicate dimensions),
- number per cage where applicable (indicating area of floor space allotted to each animal), and
- a concise description of routine husbandry practices

Describe here :

Mice will be housed 5 per cage (males and females house separately) in Allentown JAG75 (75 sq. in.) micro-isolator cages, in room 4617 ENRC. Mice will be maintained on a 12:12 hr light-dark cycle and given standard rodent chow (Labdiet 5K20 or equivalent) and water ad libitum. Cages are changed twice per week. Beginning one week prior to imaging procedure, the study animal will be fed a low-fluorescence diet (Harlan AIN-93G purified diet). This diet is alfalfa-free, and is considered standard for most optical imaging protocols in mice. The remainder of the study will be conducted as described in the original protocol document. A daily log of room temperature, humidity and animal health is maintained in room 4617 ENRC.

B. Experimental design

Provide an overview of the experimental design, including:

- numbers of groups (include some sort of **table**, **list**, **chart**, etc., indicating treatment groups, etc.)
  Tables listing groups with respective treatments and numbers of animals/group are extremely useful
- numbers of animals in each group
  (Note: These numbers must agree with the number listed on the Coverpage)
- a schedule or timetable of the treatments animals will be exposed to
- duration of treatments
- the terminal fate of the animals (sent to processing, subjected to a terminal procedure under anesthesia, euthanized for tissue collection, etc.)

Describe here :

CT26 induction of colon carcinoma in Balb/c mice

Procedure: Prior to CT26 cell injection, each animal will be anesthetized via isofluorane in an externally ventilated chamber. The animal will be weighed, placed on a feedback-controlled heating pad, and a nosecone will supply a maintenance dose of 1.5% isofluorane and oxygen from a precision vaporizer. Fur at the injection site will be shaved. Single injections will be performed subcutaneously using a 27 gauge needle at a dose of $1x10^5$ cells per 100 µL HBSS. These injections will be conducted in a certified chemical fume hood (ENRC 2545) to provide continuous isofluorane exhaust. For control mice, an equal volume of sterile saline will be injected. All safety precautions will be followed per published standard operating procedures. Animals will be observed closely for stress on days following injection and weighed daily. The total time elapsed since the initiation of CT26 cell induction will be used to track animal cohorts throughout the experiment. Experiments will proceed once the subcutaneous CT26-tumor reaches a size of 200 mm^3, as measured via $½*(length \times width^2)$.

The study presented here will analyze combination therapy in the CT26-Balb/c mouse model of colon carcinoma, and evaluate the effectiveness of non-invasive spectroscopy as a tool for monitoring early tumor perfusion response. Combination therapy includes 5-Fluorouracil (5-FU) chemotherapy (IP) and neutralizing anti-CCL2. Anti-CCL2 neutralizes monocyte chemoattractant protein 1 (CCL2), a cytokine which recruits monocytes/macrophages to the tumor site and has been implicated in tumor growth and progress. We hypothesis that combining standard chemotherapy with the neutralization of the CCL2 cytokine will reduce tumor burden, and reflectance spectroscopy can predict a decrease in tumor burden prior to reduction in tumor size. Once the tumor reaches 200 mm^3, Balb/c mice will be separated into 4 groups (each group consisting of 40 mice).

Table 1: Breakdown of experimental and control groups

Group	Sample Size	CT26 Injection	5-FU Therapy	Anti-CCL2
1	40	X		
2	40	X	X	
3	40	X		X
4	40	X	X	X
TOTAL	**160**			

The key experimental group (group 4) will receive the combination therapy of 5-FU and anti-CCL2. A second group (group 2) will receive 5-FU therapy only (**20 mg/kg/day given daily**) to isolate the effects of standard chemotherapy (Wu et al.). A third group will receive anti-CCL2 only (**7 mg/kg/week given every 3rd day**) to isolate the effects of the neutralizing antibody (Zhu et al.). This yields a total dose of up to 10 mg/kg/mouse over the course of the study. Finally, a control group will receive injections of sterile saline at equivalent concentrations. Intraperitoneal (IP) injections of 5-FU and anti-CCL2 will be given to the mice under anesthesia via isofluorane. The animal will be weighed, placed on a feedback-controlled heating pad, and a nosecone will supply a maintenance dose of 1.5% isofluorane and oxygen from a precision vaporizer.

Systemic Toxicity: *Several studies of combination therapy involving anti-CCL2 and chemotherapy have reported no significant systemic toxicity at higher concentrations of anti-CCL2 than what is used for this proposed study (Kirk et al., Rozel et al.). Otherwise, standard procedures will be followed for sacrificing mice that experience severe side-effects. For example, at any time, if mice become moribund or cachetic, fail to eat, or drink or develop dehydration, they will be euthanized via cervical dislocation. Any animal experiencing rapid weight loss, debilitating diarrhea, rough hair coat, hunched posture, labored breathing, lethargy, persistent recumbence, jaundice, anemia, significantly abnormal neurological signs, bleeding from any orifice, self-induced trauma, impaired mobility, becomes moribund or otherwise unable to obtain food or water will be immediately euthanized via cervical dislocation.*

The four groups of 40 mice each will be further split into four cohorts of 10 mice each. Each cohort of 10 mice will undergo endpoint immunohistochemistry (IHC) on days 1, 3, 6 or 10. When the desired time point is reached for each individual, mice will be euthanized by cervical dislocation without anesthesia. At each endpoint, we will mark the location of spectral measurements on the skin covering the tumor using histopathology ink, then perform in vivo pimonidazole injection (IV) prior to surgical tumor resection to map regions of hypoxia. The tumor will then be placed in OCT and flash frozen via isopentane in liquid nitrogen. Tumors will be sectioned transversely through the site of reflectance measurements to spatially correlate IHC measurements with spectral data. Immunofluorescent staining of sequential sections will be performed using murine anti-CD31 antibody (blood

vessel density), murine monoclonal anti-pimonidazole antibody (tumor hypoxia), hematoxylin and eosin, anti-CD-68 (total macrophage number), iNOS (M1 macrophage count), anti CD-206 (M2 macrophage count), and DAPI (total cell content and macrophage fraction). Murine serum will be collected at each end-point for quantification of soluble CCL2 via ELISA. The following table shows the schedule for end-point IHC for each group and cohort of mice.

Table 2: End-point immunohistochemistry (IHC) schedule

Time-Point for IHC (Days post Treatment)	Group 1	Group 2	Group 3	Group 4	TOTAL
Day 1 (Cohort 1)	10	10	10	10	40
Day 3 (Cohort 2)	10	10	10	10	40
Day 6 (Cohort 3)	10	10	10	10	40
Day 10 (Cohort 4)	10	10	10	10	40
				TOTAL	**160**

C. Non-surgical procedures involving animals

Be particularly detailed regarding any procedures that are:

- invasive,
- involve stress, or
- cause tissue damage.

Be sure this section explains (and agrees with) what is indicated on the Checklist.

Describe here :

CT26 cells have been used in mice for a model of murine colon carcinoma in a number of recent cross-sectional studies, including magnetic resonance imaging to monitor photodynamic therapy (Schreurs et al.) and combined gene and radiotherapy (Bezborodova et al.). It is a common cell line for testing immunotherapy protocols and studying the host immune response to various chemotherapy and radiotherapy treatment. CT26 is an N-nitroso-N-methylurethane-(NNMU) induced colon carcinoma cell line and is considered Biosafety Level 1. The Balb/c mouse strain (Jackson Labs) is a commonly used strain for CT26 tumor allografts (Xiao et al.).

CT26 aliquots will be prepared in the following manner in accordance with existing Biosafety Protocol IBC #13031. Cells will be cultured in RPMI-1640 media supplemented with 10% fetal bovine serum (FBS, ATCC). CT26 cells will be re-suspended in sterile balanced salt solution (HBSS, ThermoFisher Scientific) to a concentration of $1x10^5$ cells per 100 µL HBSS and placed in individual microcentrifuge tubes for a single subcutaneous injection into the flank of each Balb/c mouse. Solutions will be prepared in a certified biological fume hood (ENRC 2545).

Upon receipt of 6-week-old Balb/c mice, animals will be housed in the ENRC mouse facility in rm. 4617 (separated by gender) for up to two weeks to acclimate. They will be placed in mouse cages that measure ≈16.5"L x 10"W x 6"H with the cage cards color-coded specific to strain and [at the Principal Investigator's (PI) discretion] uniquely numbered via ear-punch. Animals will be provided with a bedding mixture of ≈ 75% Sanichips (aspen chip bedding) and 25% Tekfresh (a paper product bedding) and fed a standard high-fat rodent diet (Labdiet 5K20 or equivalent) ad libitum and provided tap water ad libitum. Clean cages and water bottles are routinely provided once weekly.

All procedures done under anesthesia (isofluorane): Subcutaneous injection of CT26 cells at the beginning of study; Some mice (80) will receive intraperitoneal injection of anti-CCL2 monocolonal antibodies; finally, some mice (80) will receive intraperitoneal injection of 5-Fluorouracil chemotherapy

Twice daily reflectance spectroscopy measurements will be performed on each mouse on the tumor site starting on the day the tumor reaches 200 mm^3, and each subsequent day after for 10 days (up to 22 spectra per mouse). Spectroscopy measurements are non-invasive, but will be performed while the mouse is under anesthesia for convenience.

D. Surgical procedures

Note:

- Written records of surgery and anesthesia must be kept for each animal.
- Animals must be observed daily following surgery and observations must be recorded from the time surgery is completed until incisions are healed.
- These records must be made available for semi-annual inspection by the IACUC.

Be sure this section explains what is indicated on the Checklist.

1. **Surgeon(s)** (list his or her qualifications for the doing the procedures to be carried out)

List here :

N/A

2. **Procedure** (must use aseptic techniques)

Describe here :

N/A

3. Medication

For all medications, specify:

- agent,
- route of administration (e.g., IM),
- dose (indicate mg of drug/kg of body wt. and also include both concentration of the drug being used [usually expressed as mg of drug/ml of solution] and ml of solution/kg of body wt. to be given)
- frequency of administration (when appropriate)

A. Pre-operative medication and preparation

Describe here :

N/A

B. Anesthesia and other medication during surgery

Describe here :

N/A

C. Post-operative medication and observation

Describe here :

N/A

E. Euthanasia

If animals to become seriously ill or injured (**even if this is not an expected occurrence**), specify the criterion you will use to determine if, and when euthanasia will be used to relieve suffering. If euthanasia is not included as part of the protocol, indicate what will happen to the animals at the end of the study.

Again, information included should conform to what is indicated on the Checklist.

Describe here :

At any time, if mice become moribund or cachetic, fail to eat, or drink or develop dehydration, they will be euthanized via cervical dislocation. Any animal experiencing rapid weight loss, debilitating diarrhea, rough hair coat, hunched posture, labored breathing, lethargy, persistent recumbence, jaundice, anemia, significantly abnormal neurological signs, bleeding from any orifice, self-induced trauma, impaired mobility, becomes moribund or otherwise unable to obtain food or water will be immediately euthanized via cervical dislocation.

When the desired time point is reached for each individual, mice will be euthanized by cervical dislocation without prior anesthesia. This is the preferred method of euthanasia for these types of studies since it avoids chemical contamination and hypoxia of tissues following the use of other forms of euthansia (ketamine/xylazine, pentobarbital, isofluorane, CO2, etc). This is a conditionally approved method of euthanasia according to the AVMA Guidelines.

3. QUALIFICATIONS OF INDIVIDUALS PERFORMING WORK WITH ANIMALS

Please list all individuals who will be carrying out procedures involving animals during this project. Please indicate who will be performing each procedure and their qualifications for that procedure. If individuals are to be trained in a procedure during this project, please indicate who will provide the training and supervision and their qualifications.

A. Principal Investigator (a current vita should be on file with the IACUC)

Any Additional Information here :

Timothy J. Muldoon- >10 years working with mice and rats for optical imaging studies. Dr. Muldoon has experience with small animal anesthesia (isofluorane and IP ketamine), carcinogen administration (SC injection and topical application methods) and euthanasia methods (including cervical dislocation) for both mice and rats.

B. Students (attach resume or provide a brief description of qualifications)

Any Additional Information here :

Gage Greening (Graduate Reasearch Assistant):
- >2 year of rodent handling experience. Procedures performed: cervical dislocation and necropsy.

Sandra Gordon (Graduate Reasearch Assistant):
- >2 year of rodent handling experience. Procedures performed: cervical dislocation and necropsy.

Haley James (Graduate Reasearch Assistant):
- >2 year of rodent handling experience. Procedures performed: cervical dislocation and necropsy.

Timothy J. Muldoon (PI) will be fully responsible for training and supervising the staff in regards to animal care and handling.

C. Lab Technicians (attach resume or provide a brief description of qualifications)

Any Additional Information here :

D. Individuals Providing Training or Supervision (attach resume or provide a brief description of qualifications)

Any Additional Information here :

Timothy J. Muldoon

All personnel listed on this protocol must complete the 2 base modules;
(1) *The Humane Care and Handling of Laboratory Animals* and
(2) *Policy and Procedures,*
of the Laboratory Animal Training Association (LATA) online training program. Any questions

regarding this training should be directed to Tony Munn (575-2994 or iacuc@uark.edu).

Please fill out the table on the following page regarding the completion of this training.

LATA Training Documentation

Person:	List Names →	Timothy J. Muldoon	Gage Greening	Haley James	Sandra (Prieto) Gordon	____	____	____
Responsibility – PI, Tech, Student, or Other		☒ ☐ ☐ ☐ PI T S O	☐ ☐ ☒ ☐ PI T S O	☐ ☐ ☒ ☐ PI T S O	☐ ☐ ☒ ☐ PI T S O	☐ ☐ ☐ ☐ PI T S O	☐ ☐ ☐ ☐ PI T S O	☐ ☐ ☐ ☐ PI T S O
Required Modules:								
Base Modules								
The Humane Care and Use of Laboratory Animals	Date Completed →	08/29/2014	08/28/2014	04/21/2016	08/29/2014	____	____	____
Policy and Procedures	Date Completed →	08/29/2014	08/28/2014	04/21/2016	08/29/2014	____	____	____
Optional Modules:								
Species Modules								
The Humane Care and Use of the Laboratory Rat	Date Completed →	____	____	____	____	____	____	____
The Humane Care and Use of the Laboratory Mouse	Date Completed →	____	____	____	____	____	____	____
The Humane Care and Use of the Laboratory Hamster	Date Completed →	____	____	____	____	____	____	____
The Humane Care and Use of the Laboratory Guinea Pig	Date Completed →	____	____	____	____	____	____	____
The Humane Care and Use of the Laboratory Rabbit	Date Completed →	____	____	____	____	____	____	____
The Humane Care and Use of the Laboratory Goat	Date Completed →	____	____	____	____	____	____	____
The Humane Care and Use of Laboratory Swine	Date Completed →	____	____	____	____	____	____	____
The Humane Care and Use of Laboratory Fish	Date Completed →	____	____	____	____	____	____	____
Techniques Modules								
Aseptic Surgery of Rodents	Date Completed →	____	____	____	____	____	____	____
Anesthesia and Analgesia of Rodents	Date Completed →	____	____	____	____	____	____	____
Safety Module								
Occupational Health and Safety	Date Completed →	____	____	____	____	____	____	____

Person:	List Names →	____	____	____	____	____	____	____
Responsibility – PI, Tech, Student, or Other		☐ ☐ ☐ ☐ PI T S O	☐ ☐ ☐ ☐ PI T S O	☐ ☐ ☐ ☐ PI T S O	☐ ☐ ☐ ☐ PI T S O	☐ ☐ ☐ ☐ PI T S O	☐ ☐ ☐ ☐ PI T S O	☐ ☐ ☐ ☐ PI T S O
Required Modules:								
Base Modules								
The Humane Care and Use of Laboratory Animals	Date Completed →	____	____	____	____	____	____	____
Policy and Procedures	Date Completed →	____	____	____	____	____	____	____
Optional Modules:								
Species Modules								
The Humane Care and Use of the Laboratory Rat	Date Completed →	____	____	____	____	____	____	____
The Humane Care and Use of the Laboratory Mouse	Date Completed →	____	____	____	____	____	____	____
The Humane Care and Use of the Laboratory Hamster	Date Completed →	____	____	____	____	____	____	____
The Humane Care and Use of the Laboratory Guinea Pig	Date Completed →	____	____	____	____	____	____	____
The Humane Care and Use of the Laboratory Rabbit	Date Completed →	____	____	____	____	____	____	____
The Humane Care and Use of the Laboratory Goat	Date Completed →	____	____	____	____	____	____	____
The Humane Care and Use of Laboratory Swine	Date Completed →	____	____	____	____	____	____	____
The Humane Care and Use of Laboratory Fish	Date Completed →	____	____	____	____	____	____	____
Techniques Modules								
Aseptic Surgery of Rodents	Date Completed →	____	____	____	____	____	____	____
Anesthesia and Analgesia of Rodents	Date Completed →	____	____	____	____	____	____	____
Safety Module								
Occupational Health and Safety	Date Completed →	____	____	____	____	____	____	____

Animal Use Protocol
University of Arkansas, Fayetteville
Assurance Statements for Biomedical Research and Teaching

4. STATEMENT OF COMPLIANCE:

As the individual responsible for this research or teaching project,

I confirm that the information contained herein is accurate and, to the best of my knowledge, conforms to all applicable University, PHS, and USDA policies on the use of animals in research and teaching.

I confirm that I have completed the following online LATA training modules:
1) The Humane Care and Use of Laboratory Animals,
2) Policy and Procedures.

I confirm that all individuals involved with the animals used in this project will complete the above online LATA training modules and will be instructed in the humane care, handling, and use of animals, prior to participation in the project, and I will have reviewed their qualifications.

I agree not to proceed with any portion of this project or purchase animals until I receive written approval from the University of Arkansas Institutional Animal Care and Use Committee (IACUC).

I agree that no substantive change will be made in the procedures contained in this proposal without prior written notification to and approval by the IACUC.

I agree to allow inspection of my research facilities by members of the IACUC and the Animal Welfare Veterinarian and to comply promptly if informed of any violations of the University of Arkansas, Fayetteville's Policy on Animal Care and Use.

I understand that failure to comply with the University of Arkansas, Fayetteville's Policy on Animal Care and Use will jeopardize the University's Animal Welfare Assurance on file with the PHS (and with it all federal funding for the University), and may ultimately lead to revocation of my privileges to conduct animal research at the University of Arkansas.

DO NOT COMPLETE THIS SECTION IF PROTOCOL IS SPECIFIED AS AGRICULTURAL or FIELD RESEARCH

The regulations for the Animal Welfare Act (United States Department of Agriculture) and the Public Health Service require that protocols for biomedical research and teaching involving animals the following concerns be specifically addressed in writing by the Principal Investigator. Items in brackets [] identify the source of the requirement [AWA = Animal Welfare Act regulations; NIH = NIH Guide for Care and Use of Laboratory Animals, 1996 edition].

A. **Animals should not be used if other methods exist that would provide substantially the same information. Indicate why the use of live animals is required in this research.** [AWA 2.31 (e) (2); NIH p. 8] :
Indicate here :

Studies that evaluate real-time spectroscopic data about hemoglobin oxygenation and inflammatory response require access to live animals. To date, there are no in vitro systems that could be used as a substitute.

B. **Justify your choice of species by listing some of the important characteristics of the species that make it suitable for use in the proposed research. Cost alone is not sufficient rationale.** [AWA 2.31 (e) (2); NIH p. 8] :
Justify here :

Studies that evaluate immune-based approaches to cancer management require mice with a high likelihood of developing colorectal tumors. In this case, the strain of mouse chosen is highly susceptible to developing colon carcinoma in response to administration of CT26 cells. To date, there are no in vitro systems that could be used as a substitute. The mouse is the lowest mammal with this type of genetic modification which is available, and the purpose of this study (evaluation of colon tumor development and progression following immune-modulation therapy using novel microendoscopy optics) requires a live animal model.

C. **The number of animals used should be the minimum number that can be expected to provide valid results. Describe how the number of animals to be used was determined to comply with this requirement, i.e., that the number animals to be used can be expected to provide valid results.** [AWA 2.31 (e) (2); NIH p. 8] : *A statistical explanation is needed.*
Describe here :

Based on an a priori power analysis, the analysis of 40 animals per time point will be sufficient to achieve α=0.05 and power (1-β) = 0.72 for a moderate effect size (Pearson's correlation, r=0.3). This is a conservative estimate based on a 20% difference in diffuse reflectance spectra between normal and dysplastic tissues. Based on the above, we anticipate using 40 animals per group (4 groups including control) for a total of 160 animals.

D. **The principal investigator submitting protocols for biomedical research should not unnecessarily duplicate previous experiments, and must consider less invasive alternatives to procedures that may cause more than momentary or slight pain or distress to animals (i.e., Level 3 or higher). Provide a statement that a literature review has been carried out demonstrating that this research does not unnecessarily duplicate previous experiments, and that appropriate alternative research methods are not available for any proposed procedures that are Level 3 or higher. The database used must be identified (check below).** [AWA 2.31 (d) (1) (I, ii, and iii); NIH p. 8] : **(Note, this requirement does not apply to protocols for teaching projects.)**
Provide statement here :

The proposed studies do not duplicate previous experiments. Our lab is the only one correlating multimodal spectral data with markers for tumor-associated macrophages (TAMs) and localized inflammation following combination treatment with standard 5-FU chemotherapy and immunomodulation of TAMs. To our knowledge, no other lab has performed similar studies to the proposed research.

Animal Use Protocol
University of Arkansas, Fayetteville
Assurance Statements for Biomedical Research and Teaching

(Be sure to list date(s) of search for each database used and the keywords that were used.)

	Database	Date(s) of Search	Key Words Used
☐	Medline	____	____
☐	Agricola	____	____
☐	Index Medicus	____	____
☐	Biol. Abstracts	____	____
☐	Animal Welfare Information Center (National Agricultural Library)	____	____
☒	Other (please specify below): PubMed	03/27/2017	diffuse reflectance spectroscopy; Balb/c; CT26; immune; modulation; 5-FU; colon; colorectal; cancer; carcinoma; tumor macrophage; endoscopy

UNIVERSITY OF ARKANSAS

Office of Research Compliance

To:	Timothy Muldoon
Fr:	Craig Coon
Date:	January 17th, 2018
Subject:	IACUC Approval
Expiration Date:	January 15th, 2021

The Institutional Animal Care and Use Committee (IACUC) has APPROVED your protocol # **18060:** *Quantifying tumor perfusion response with diffuse reflectance spectroscopy in murine models of colon carcinoma following therapy and immunomodulation of tumor-associated macrophages*.

In granting its approval, the IACUC has approved only the information provided. Should there be any further changes to the protocol during the research, please notify the IACUC in writing (via the Modification form) prior to initiating the changes. If the study period is expected to extend beyond January 15th, 2021 you must submit a newly drafted protocol prior to that date to avoid any interruption. By policy the IACUC cannot approve a study for more than 3 years at a time.

The following individuals are approved to work on this study: Timothy Muldoon, Gage Greening, Hayley James, and Sandra Prieto. Please submit personnel additions to this protocol via the modification form prior to their start of work.

The IACUC appreciates your cooperation in complying with University and Federal guidelines involving animal subjects.

CNC/tmp

18060

Animal Use Protocol
University of Arkansas, Fayetteville
Coversheet

IACUC use only:			
Protocol number: _____		Category(s) of animal use:	
Date Received: _____		☐ Agricultural	
Approval Date: _____		☐ Biomedical	
Start Date: _____		☐ Field	
End Date: _____		LATA Training Verified	☐ Yes ☐ No

Instructions:

- *This is a MicroSoft Word (MSWord) "form". Use MSWord to fill in the information asked for in either the blanks ("____"), or the box (" ☐ ") provided. You can put as much information in the blanks or boxes as needed.*
- *Submit an electronic copy in MSWORD FORMAT of your completed protocol to iacuc@uark.edu and be sure to sign the appropriate form(s) by inserting signature into provided boxes. Alternatively completed forms sent in via uark.edu mail system are considered "signed" even without a scanned signature.*
- *Failure to follow these instructions and adequately fill out the required information may result in the protocol being returned.*
- *The deadline for getting this form to iacuc@uark.edu is 12:00 Noon on the LAST FRIDAY of every month*

Project Title: Quantifying tumor perfusion response with diffuse reflectance spectroscopy in murine models of colon carcinoma following therapy and immunomodulation of tumor-associated macrophages

Project length (3 years maximum): 3 years

* Start date: 11/6/2017 End date: 11/5/2020

	Principal Investigator:	**Co-Investigator(s)** *(if applicable)*:	
Name:	Timothy J. Muldoon	_____	_____
Department/Division:	Biomedical Engineering	_____	_____
Campus Mail Address:	126 Engineering Hall	_____	_____
Telephone:	575-5324/575-3967	_____	_____
Fax:	575-4346	_____	_____
E-mail:	tmuldoon@uark.edu	_____	_____

Individual(s) responsible for animal care:

Name:	Timothy J. Muldoon	Gage Greening	Haley James
Office address:	2920 ENRC	2910 ENRC	2910 ENRC
Office City, State, Zip:	Fayetteville, AR 72701	Fayetteville AR 72701	Fayetteville AR 72701
Office phone:	575-5324/575-3967	816-519-8091(cell)	870-378-4209 (cell)
Home address:	1822 N. Best Friend Ln	Sandra Gordon	_____
Home City, State, Zip**:	Fayetteville, AR 72704	2910 ENRC, Fayetteville AR 72701	_____
Home phone**:	832-816-5349 (cell)	479-220-0490 (cell)	_____

Individual(s) responsible for euthanasia:

Name:	Timothy J. Muldoon	Gage Greening	Haley James
Office address:	2920 ENRC	2910 ENRC	2910 ENRC
Office City, State, Zip:	Fayetteville, AR 72701	Fayetteville AR 72701	Fayetteville AR 72701
Office phone:	575-5324/575-3967	816-519-8091(cell)	870-378-4209 (cell)
Home address:	1822 N. Best Friend Ln	Sandra Gordon	
Home City, State, Zip**:	Fayetteville, AR 72704	2910 ENRC, Fayetteville AR 72701	
Home phone**:	832-816-5349 (cell)	479-220-0490 (cell)	

*Start date will be the date of approval by the committee

Animal Use Protocol
University of Arkansas, Fayetteville
Coversheet

**This information is necessary to provide the IACUC with emergency contact information.

Animals used

Species: Mus musculus
Common name(s): mouse
*Gender(s): male : female , 1:1

*Note: Biomedical studies that exclude the female gender of species must include justification for doing so. (for more information see NIH Notice Number: NOT-OD-15-02)

**Calculated number to be used (by species; not a combined number): 160 Balb/c mice, 160 athymic mice

**Note: This number (or these numbers) must agree exactly with those listed in Section 2B (Experimental Design) of the Narrative. Be clear and concise. Include replacement and breeder animals specific to the project. The IACUC cannot approve a protocol with inconsistencies in number of animals, and the submission will be returned for correction.

Supplier (all purchases must be from a licensed supplier)
Name: The Jackson Laboratory
Address: Bar Harbor, ME

Locations (building and room where animals will be housed or used)
Animal housing: 4617 ENRC, CLAF
Surgical facility: ENRC 2545
Data collection: ENRC 2545

Animal Use Protocol
University of Arkansas, Fayetteville
Checklist

Title of Project: Quantifying tumor perfusion response with diffuse reflectance spectroscopy in murine models of colon carcinoma following therapy and immunomodulation of tumor-associated macrophages

Principal Investigator: Muldoon

Type of Project:

Select one → ☒ Research ☐ Teaching → Course Number(s) _____

Category of research and teaching for which this protocol was written:

Select one → ☒ Biomedical ☐ Agricultural ☐ Field

Funding Source (check all that apply):

☒ NIH ☐ NSF ☐ USDA ☐ private industry ☒ U of A ☐ State of Arkansas

☒ other (identify): Arkansas Biosciences Institute

Level of Pain or Stress: Check only one level, which should be the most severe level the animals will be subjected to during the course of the study *(Please read these carefully)*

	Level	Examples and Comments
☐ Level 1	Level 1 Experiments on vertebrate animals that are expected to produce little or no discomfort.	• Simple procedures such as injections and blood sampling; • observational field behavior; • physical examinations; • experiments on anesthetized animals that do not regain consciousness; • food/water deprivation for short periods and methods of euthanasia that induce rapid unconsciousness.
☒ Level 2	Level 2 Experiments that involve some minor stress or short-duration pain to vertebrate animals.	• With anesthesia, "cut downs" or implantation of catheters; • behavioral experiments on conscious animals that involve restraint; • immunization employing Freund's adjuvant; • noxious stimuli from which escape is possible; • surgical procedures under anesthesia that may result in postsurgical discomfort (possibly requiring analgesics); • **experimental infection** producing ***no significant pain or distress***.
☐ Level 3	Level 3 Experiments that involve *significant unavoidable stress or pain* to vertebrate animals.	• Deliberate induction of behavioral stress; • major surgical procedures under anesthesia that result in significant postoperative discomfort or an anatomic or physiologic deficit that will *result in pain or distress*; • noxious stimuli from which escape is impossible; • prolonged periods of physical restraint; • procedures that produce pain or distress in which anesthetics are not used (toxicity testing, radiation sickness, certain injections, stress and shock research, or **experimental infection producing systemic disease that will *result in pain, distress, or death*).**
	Level 3 mandates responsibility on the part of the investigator to explore alternative procedures.	
☐ Level 4	Level 4 Procedures that involve inflicting severe pain on unanesthetized, conscious animals.	• Use of muscle relaxants or paralytic drugs without the use of anesthetics; • surgery, severe burn or trauma infliction on unanesthetized animals; • attempts to induce psychotic-like behavior or severe stress or terminal stress.

Many of these procedures are specifically prohibited and therefore may result in withdrawal of federal funds and/or institutional USDA registration.

Note: The preceding levels correspond to the following animal use categories on the APHIS annual report form: Level 1 = Category C or D; Level 2 = Category D; Levels 3 and 4 = Category E.

Animal Use Protocol
University of Arkansas, Fayetteville
Checklist

Surgical Procedures:
If any of the methods/techniques listed below will be used, check the appropriate space and *provide the requested details in Section 2D of the Narrative (Surgical Procedures)*:

- ☐ none
- ☒ non-survival surgery (euthanasia will be administered before recovery from anesthesia)
- ☐ survival surgery (animal will be allowed to recover from anesthesia)
- ☐ multiple survival surgeries *(this requires explicit justification in Narrative)*

Non-Surgical Procedures:
If any of the methods/techniques listed below will be used, check the appropriate space and *provide the requested details in Section 2C of the Narrative (Non-Surgical Procedures)*:

- ☐ Non-surgical invasive procedures (blood collection, catheterization, intubation, etc.).
  Provide appropriate details (volume, site, frequency, etc.)
- ☒ Exposure of a living animal to a hazardous, toxic, and/or radioactive substance.
  Provide substance name, route of administration, dose, volume, frequency
- ☐ Exposure of a living animal to an infectious agent. Notice, if this is checked, you must also check, either Level 2 or Level 3 pain in the previous section!
  Provide name of agent, means of exposure, and amount and frequency of exposure. Specify in "Method of Euthanasia" section, the criterion you will use to determine if euthanasia is necessary to relieve suffering.
- ☐ Immunization protocol.
  Provide name of adjuvant(s) used; injection site; volume per site; frequency of injection; method, frequency, and volume of blood withdrawn (including anesthetic, if used).
  Note: this does NOT apply to standard prophylactic vaccinations.
- ☐ Prolonged restraint.
  Provide method, duration, frequency, procedure by which animal is adapted to restraint device.
- ☐ Food/water deprivation.
  Provide duration, frequency, extent (total/partial), methods used to assess and monitor distress.
  Note: removal of food and/or water for 24 hours in preparation for surgery or some other procedure is NOT considered to be food/water deprivation.
- ☐ Abnormal environment.
  Provide information on departure from normal conditions (temperature, humidity, light, duration, etc.).
- ☐ Aversive stimuli.
  Provide type and intensity of stimulus, duration, justification for use in the narrative.
- ☐ Hybridoma protocol.
  Provide priming agent, cells injected, schedule for collection of ascites, number of abdominal taps, size of needle used.
  Important: Provide justification for use of the *in vivo* mouse ascites method versus the various *in vitro* methods currently available, providing adequate documentation.
- ☐ Use of neuromuscular blocking agents (muscle paralytics) during surgery.
  Provide a rationale for their use and explain how you will determine that adequate anesthesia is maintained in the narrative.
- ☐ Use of death (without euthanasia) as an endpoint of the study/procedure.
  Provide justification why an earlier endpoint is not acceptable in the narrative

Method of Euthanasia used as a procedure in this project-- Identify the method(s) of euthanasia to be used as part of this specific research project; it (they) must comply with the most recent AVMA Guidelines on Euthanasia
http://www.avma.org/issues/animal_welfare/euthanasia.pdf

- ☐ not used as part of this project (see page 8 to provide description of euthanasia to address animal welfare issues)
- ☐ overdose of anesthetic (specify agent, dose, and route of administration)
  Agent_____ Dose: _____ Route: _____
- ☐ inhalation of carbon dioxide
- ☒ physical means under general anesthesia (identify the specific means that will be used; cervical dislocation, etc.)
- ☐ physical means without anesthesia
  - **if done properly by trained personnel;** the use of captive bolt pistol on large farm animals, cervical dislocation on chickens, and some other physical methods [such as gunshot] **are permitted without justification (see avma guide)**
    State Method to be used here:_____
  - **OTHERWISE,** physical means without anesthesia ***(such as cervical dislocation of mice)*** can be used only when scientifically justified and requires specific written justification).
    State and Justify these methods here: _____
- ☐ other (identify here and describe): _____

Disposal of remains:

- ☒ Incineration at University Farm *
- ☐ Other (describe): _____

*in addition to poultry, this is also the disposal site for non-contaminated carcasses that are placed in the freezer at CLAF or ENRC

Animal Use Protocol
University of Arkansas, Fayetteville
Narrative

I. ABSTRACT (approximately 100-300 words)

Please provide, in **lay language**,

- a concise but specific statement of the scientific objective for the proposed research,
- the rationale behind this objective,
- the species of animal to be used, and
- a quick overview of the procedures to be followed.

This statement should stand alone and be comprehensible to a **non-scientist**.

This is NOT the place for a lengthy introduction! PLEASE…

Abstract here :

We are interested in developing novel imaging methods for early detection and management of colorectal cancer. Dysplasia of colonic epithelium has been known to be exacerbated due to inflammatory response, and both spontaneous and colitis (inflammatory) models are associated with myriad structural and spectral changes that can be observed using optical and spectroscopy systems. We are developing a hybrid microendoscopy / diffuse reflectance spectroscopy device that could be used eventually in human patients at the point-of-care to visualize regions of dysplasia and to better monitor early tumor response to combination therapy involving chemotherapy and immunomodulation therapy. This protocol will examine the use of diffuse reflectance spectroscopy in subcutaneous tumors only in murine models.

The overall goal of this study will be to compare the biomarkers (in terms of microscopic-level structural changes as well as specific diffuse reflectance spectral changes) that are observed in the development of subcutaneous tumors using the CT26-Balb/c mouse model of colon carcinoma as well as in xenografts in athymic mice derived from human colon carcinoma cell lines (HCT-116 and RKO lines). We will evaluate tumors at various stages of development using an subcutaneous injection of colon carcinoma cells. These mice will be useful to study the spectroscopic and immunological response in tumors, in a longitudinal study after various days of tumor growth. We will evaluate non-invasive diffuse reflectance spectroscopy daily. For a select number of mice (allograft model only) we will inject with anti-CCL2 (known for blocking macrophage-induced inflammatory response and decreasing size of tumors) in order to compare immunological response to differences in inflammation (comparison of tumor-associated macrophages in excised tissue). We will also examine tumor response to conventional 5-fluorouracil therapy in a select number of mice (both allograft and xenograft models).

II. METHODS

Using the headings listed below, describe the methods to be used in your project. The level of detail for procedures involving animals should be comparable to that in the Methods section of a journal article (i.e., sufficient to enable another researcher competent in your field to replicate your study). Please, **do not** cut & paste from your grant proposal, it usually includes information that the IACUC does not need to review. Also, do not repeat information in the different sections below any more than is absolutely necessary to communicate clearly what you plan to do. (In other words, do not repeat descriptions in B, C, and/or D.)

A. Housing

(**Note**: Cage size, amount of room per animal, etc. must conform to the dimensions listed in one of the following:

- ILAR Guide for the Care and Use of Laboratory Animals:
- *Animal Welfare Act (USDA) Regulations*
- PHS Policy on Humane Care and Use of Laboratory Animals, or
- FASS GUIDE For the Care and Use of Agricultural Animals in Agricultural Research and Teaching.

The only exceptions are those protocols that are to be done under "commercial conditions", these must be appropriately documented and approved.)

Describe how the animals will be housed, including

- cage or pen size (indicate dimensions),
- number per cage where applicable (indicating area of floor space allotted to each animal), and
- a concise description of routine husbandry practices

Describe here :

Mice will be housed 5 per cage (males and females house separately) in Allentown JAG75 (75 sq. in.) micro-isolator cages, in room 4617 ENRC (Balb/c mice for allograft studies) or in microisolator cages in a dedicated room in the CLAF under conditions appropriate for athymic nude mice (xenograft studies). Mice will be

maintained on a 12:12 hr light-dark cycle and given standard rodent chow and water ad libitum. Cages are changed twice per week. A daily log of room temperature, humidity and animal health is maintained in room 4617 ENRC.

B. Experimental design

Provide an overview of the experimental design, including:

- numbers of groups (include some sort of **table**, **list**, **chart**, etc., indicating treatment groups, etc.) Tables listing groups with respective treatments and numbers of animals/group are extremely useful
- numbers of animals in each group
  (Note: These numbers must agree with the number listed on the Coverpage)
- a schedule or timetable of the treatments animals will be exposed to
- duration of treatments
- the terminal fate of the animals (sent to processing, subjected to a terminal procedure under anesthesia, euthanized for tissue collection, etc.)

Describe here :

Subcutaneous cell line injection procedures: Prior to subcutaneous injection of prepared cell lines (under approved Biosafety Protocol #13031), each animal will be anesthetized via isofluorane in an externally ventilated chamber. Opthalmic ointment will be applied to the eyes to ensure. The animal will be weighed, placed on a circulating water heating pad to maintain temperature, and a nosecone will supply a maintenance dose of 1.5% isofluorane and oxygen from a precision vaporizer. Fur at the injection site will be shaved. Single injections will be performed subcutaneously using a 27 gauge needle at a dose of $1x10^5$ (CT-26 murine carcinoma cells) or $1x10^6$ (HCT-116 or RKO human cancer cell line cells) per 100 µL HBSS. Tumors will only be implanted in the flank, one tumor per mouse. For consistency, all tumors will be placed on one side of the mouse (i.e. right flank OR left flank), which will be noted on the cage card. All anesthesia and injections will be conducted in a certified chemical fume hood (ENRC 2545) to provide continuous isofluorane exhaust. For control mice, an equal volume of sterile saline will be injected. All safety precautions will be followed per published standard operating procedures. Animals will be observed closely for stress on days following injection and weighed daily. The total time elapsed since the initiation of cell line induction will be used to track animal cohorts throughout the experiment. Experiments will proceed once the subcutaneous tumor reaches a size of 75 mm^3, as measured via $½*(length \times width^2)$. See also Section C below.

Diffuse reflectance spectroscopy procedures: Once mouse tumors reach 75mm^3 in size, all mice (therapy and control groups, see below), will undergo non-invasive daily tumor spectroscopy measurements in order to quantify tumor hemoglobin and oxygen saturation. To perform spectroscopy measurements, each mouse will be anesthetized as described above. A custom, handheld spectroscopy probe will be gently placed at the site of the tumor, and reflectance spectroscopy data acquired. This procedure takes approximately 5 minutes per mouse. See also Section C below.

Therapy administration procedures: The study presented here will examine conventional (5-FU based) and emerging immunomodulatory methods (via administration of anti-CCL2 antibody) of anti-cancer therapy in both murine allografts and murine xenografts (for human cancer cell lines), and evaluate the effectiveness of non-invasive spectroscopy as a tool for monitoring early tumor perfusion response. Anti-CCL2 neutralizes monocyte chemoattractant protein 1 (CCL2), a cytokine which recruits monocytes/macrophages to the tumor site and has been implicated in tumor growth and progress. We hypothesis that combining standard 5-FU therapy with the neutralization of the CCL2 cytokine will reduce tumor burden, and reflectance spectroscopy can predict a decrease in tumor burden prior to reduction in tumor size. This effect will be compared to conventional xenograft models of 5-FU response using human cancer cell lines (without anti-CCL2 modulation, since these animals are immunosuppressed). Balb/c (allograft) mice will be separated into 4 groups (40 mice per group), examining 5-FU therapy, anti-CCL2 therapy, combination therapy or control, while athymic nude mouse models (RKO and HCT-116 cell lines) will be separated into two groups each, examining 5-FU therapy or control only (see complete table on facing page):

Table 1: Breakdown of experimental and control groups

Group	Sample Size	CT26 Injection	RKO Injection	HCT-116 Injection	5-FU Therapy	Anti-CCL2
1	40	X				
2	40	X			X	
3	40	X				X
4	40	X			X	X
5	40		X		X	
6	40		X			
7	40			X	X	
8	40			X		
TOTAL	**320 (all strains)**	160 (Balb/c)	80 (Athymic)	80 (Athymic)		

5-FU therapy groups will receive **20 mg/kg/day given daily** (Wu et al.). Anti-CCL2 therapy groups will receive **7 mg/kg/week given every 3rd day** (Zhu et al.). This yields a total dose of up to 10 mg/kg/mouse over the course of the study. Combination therapy groups will receive both 5-FU and anti-CCL2 antibody at the indicated dose and schedule. Finally, a control group will receive injections of sterile saline at equivalent concentrations. Intraperitoneal (IP) injections of 5-FU, anti-CCL2, and/or control saline will be given to the mice under anesthesia via isofluorane. To perform therapeutic administration, each animal will be weighed placed on a circulating water heating pad to maintain temperature, and a nosecone will supply a maintenance dose of 1.5% isofluorane and oxygen from a precision vaporizer. Injections will be placed on alternate sides each day. All therapy administration procedures will be performed in an externally ventilated fume hood in ENRC 2545.

Systemic Toxicity: *Several studies of combination therapy involving anti-CCL2 and chemotherapy have reported no significant systemic toxicity at higher concentrations of anti-CCL2 than what is used for this proposed study (Kirk et al., Rozel et al.). Otherwise, standard procedures will be followed for sacrificing mice that experience severe side-effects. For example, at any time, if mice become moribund or cachetic, fail to eat, or drink or develop dehydration, they will be euthanized via cervical dislocation. Cachexia will be defined as a greater than 10% loss in body weight (compared to the body weight of each mouse on the day of injection) OR a 1 point decrease in body condition score. A body condition score chart will be placed in the procedure room for this study (ENRC 2545). Any animal experiencing rapid weight loss, debilitating diarrhea, rough hair coat, hunched posture, labored breathing, lethargy, persistent recumbence, jaundice, anemia, significantly abnormal neurological signs, bleeding from any orifice, self-induced trauma, impaired mobility, becomes moribund or otherwise unable to obtain food or water will be immediately euthanized via cervical dislocation.*

Endpoint immunohistochemistry (Balb/c allograft model only): For all mice in this study, euthanasia will be performed via cervical dislocation following anesthesia as described in Section E. Efficacy of anti-CCL2 therapy will be quantified in immunocompetent Balb/c mouse groups only. The four groups of 40 mice each will be further split into four cohorts of 10 mice each. Each cohort of 10 mice will undergo endpoint immunohistochemistry (IHC) on days 1, 3, 6 or 10. At each endpoint, we will mark the location of spectral measurements on the skin covering the tumor using histopathology ink, then perform in vivo pimonidazole injection (IV) prior to surgical tumor resection to map regions of hypoxia. Following a 90 minute incubation period following recovery from anesthesia, the mouse is again anesthetized, and the tumor removed prior to euthanized by cervical dislocation as described in section E. Non-survival surgery procedures are discussed in Section D The tumor will then be placed in OCT and flash frozen via isopentane in liquid nitrogen. Tumors will be sectioned transversely through the site of reflectance measurements to spatially correlate IHC measurements with spectral data. Immunofluorescent staining of sequential sections will be performed using murine anti-CD31 antibody (blood vessel density), murine monoclonal anti-pimonidazole antibody (tumor hypoxia), hematoxylin and eosin, anti-CD-68 (total macrophage number), iNOS (M1 macrophage count), anti CD-206 (M2 macrophage count), and DAPI (total cell content and macrophage fraction). Murine serum will be collected at each end-point for quantification of soluble CCL2 via ELISA. The following table shows the schedule for end-point IHC for each group and cohort of mice (facing page):

Table 2: End-point immunohistochemistry (IHC) schedule for Balb/c mice only

Time-Point for IHC (Days post Treatment)	Group 1	Group 2	Group 3	Group 4	TOTAL
Day 1 (Cohort 1)	10	10	10	10	40
Day 3 (Cohort 2)	10	10	10	10	40
Day 6 (Cohort 3)	10	10	10	10	40
Day 10 (Cohort 4)	10	10	10	10	40
				TOTAL	**160**

Endpoint histology and / or cell culture (nude mouse xenografts only). Athymic xenograft models will follow a simpler endpoint schedule, and all mice will be euthanized following anesthesia on Day 10 post-therapy following procedures outlined in section E. Tumors will be removed and will either be immediately placed in OCT and flash frozen via isopentane in liquid nitrogen prior to conventional cryosectioning and hematoxylin and eosin staining or processed for in vitro cell culture following procedures outlined in approved Biosafety protocol #13031.

C. Non-surgical procedures involving animals

Blood draws should indicate method, volume and frequency: Be particularly detailed regarding any procedures that are.

- invasive,
- involve stress, or
- cause tissue damage.

Be sure this section explains (and agrees with) what is indicated on the Checklist.

Describe here :

Subcutaneous cell line injection. Cell suspension aliquots will be prepared in the following manner in accordance with existing Biosafety Protocol IBC #13031. Cells will be cultured in RPMI-1640 media supplemented with 10% fetal bovine serum (FBS, ATCC). Cells will be re-suspended in sterile balanced salt solution (HBSS, ThermoFisher Scientific) to a concentration of $1x10^5$ (CT-26 murine carcinoma cells) or $1x10^6$ (HCT-116 or RKO human cancer cell line cells) per 100 µL HBSS and placed in individual microcentrifuge tubes for a single subcutaneous injection into the flank of each mouse. Solutions will be prepared in a certified biological fume hood (ENRC 2540A).

Housing procedures. Upon receipt of 6-week-old mice (Balb/c or athymic), animals will be housed in the mouse facility in (ENRC 4617 for Balb/c OR CLAF for athymic) and separated by sex for up to two weeks to acclimate. They will be placed in mouse cages that measure ≈16.5"L x 10"W x 6"H with the cage cards color-coded specific to strain and [at the Principal Investigator's (PI) discretion] uniquely numbered via ear-punch. Animals will be provided with a bedding mixture of ≈ 75% Sanichips (aspen chip bedding) and 25% Tekfresh (a paper product bedding) and fed a conventional rodent diet ad libitum and provided tap water ad libitum. Clean cages and water bottles are routinely provided once weekly.

Procedures performed under anesthesia: Subcutaneous injection of cells at the beginning of study; Some mice will receive intraperitoneal injection of anti-CCL2 monocolonal antibodies, intraperitoneal injection of 5-Fluorouracil, intraperitoneal injection of both, or saline control vehicle.

Diffuse reflectance spectroscopy methods. Daily reflectance spectroscopy measurements will be performed on each mouse on the tumor site starting on the day the tumor reaches 75 mm^3, and each subsequent day after for 10 days (up to 11 spectra per mouse). Spectroscopy measurements are non-invasive, but will be performed while the mouse is under anesthesia for convenience.

D. Surgical procedures

Note: Written records of surgery and anesthesia must be kept for each animal.
Animals must be observed daily following surgery and observations must be recorded from the time surgery is completed until incisions are healed. These records must be made available for semi-annual inspection by the IACUC.

1. Surgeon(s) (list his or her qualifications for the doing the procedures to be carried out)

List here :

Timothy J. Muldoon- >10 years working with mice and rats for optical imaging studies. Dr. Muldoon has experience with small animal anesthesia (isofluorane and IP ketamine), carcinogen administration (SC injection and topical application methods) and euthanasia methods (including cervical dislocation) for both mice and rats. Also experienced with both survival surgery and non-survival surgery in mice and rats.

Gage Greening- >2 year of rodent handling experience. Procedures performed: subcutaneous tumor cell injection, IP therapy injection, anesthesia, diffuse reflectance spectroscopy methods, cervical dislocation, necropsy, tumor removal under anesthesia (trained by Dr. Muldoon)

Haley James- >2 year of rodent handling experience. Procedures performed: subcutaneous tumor cell injection, IP therapy injection, anesthesia, diffuse reflectance spectroscopy methods, cervical dislocation, cervical dislocation. necropsy, tumor removal under anesthesia (trained by Dr. Muldoon)

Sandra Gordon- >2 year of rodent handling experience. Procedures performed: subcutaneous tumor cell injection, IP therapy injection, anesthesia, diffuse reflectance spectroscopy methods, cervical dislocation, cervical dislocation. necropsy, tumor removal under anesthesia (trained by Dr. Muldoon)

2. Procedure (must use aseptic techniques)

Note: Include your method for determining that animal has reached plane of anesthesia, how often it will be checked that animal is remaining in plane of anesthesia, and how it will be determined that animal has fully recovered from effects of anesthesia

Describe here :

For endpoint tumor removal in Balb/c mice only: Following injection of pimonizazole as described in Section B above, mice will be anesthetized using isofluorane and placed on a circulating water heating pad to maintain temperature, and a nosecone will supply a maintenance dose of up to 4% isofluorane (deep anesthestization is required) and oxygen from a precision vaporizer (all work performed inside a certified chemical fume hood in ENRC 2545). Anesthesia depth will be confirmed via hind paw pinch prior to beginning procedure. The tumor will be resected surgically using a scalpel, forceps, and scissors and immediately flash frozen in OCT using isopentane and liquid nitrogen. The mouse will also be immediately euthanized following tumor removal via cervical dislocation.

Justification: Pimonidazole is taken up by hypoxic cells present within the tumor mass, and converted to a molecule which can be detected via anti-pimonidazole antibody using immunohistochemistry methods. As such, any change in tumor perfusion or hypoxia immediately prior to resection of the tumor would induce experimental error in subsequent quantification of tumor hypoxia via this method. Tumor resection must be performed while the tissues are perfused and while the animal is sufficiently anesthetized in order to minimize this error.

3. Medication

For all medications, specify:

- agent,
- route of administration (e.g., IM),
- dose (indicate mg of drug/kg of body wt. and also include both concentration of the drug being used [usually expressed as mg of drug/ml of solution] and ml of solution/kg of body wt. to be given)

• frequency of administration (when appropriate)

a. Pre-operative medication and preparation
Describe here :

N/A

b. Anesthesia and other medication during surgery
Describe here :

N/A

c. Post-operative medication and observation
Describe here :

N/A

d. Explain Observations, Procedures, and frequency that they are performed to determine animal is in the plane of anesthesia, remains in the plane of anesthesia, and has fully recovered from anesthesia
Describe here:

During procedures involving anesthesia, personnel performing the procedure will ensure the study animal is in the plane of anesthesia via a hindpaw pinch immediately prior to beginning a procedure, and again every 5 minutes, observing closely for reflexive limb withdrawal. Following termination of the procedure, isoflurane anesthesia will be withdrawn and the animal will be observed until fully mobile while remaining on their heating pad. The will be observed for full mobility again after being relocated to their designated cage.

E. Euthanasia & Final Fate of Animals (Mandatory)
(1)If animals to become seriously ill or injured **(even if this is not an expected occurrence)**, specify the criterion you will use to determine if, and when euthanasia will be used to relieve suffering. (2) If all animals will not be euthanized by the end of the project, indicate what will happen to these animals when the study has finished (e.g. returned to colony, herd, sent to processing plant etc).
Describe here :

At any time, if mice become moribund or cachetic (defined as >10% loss in body mass OR a one point decrease in body condition score), fail to eat, or drink or develop dehydration, they will be euthanized via cervical dislocation following anesthestization. Any animal experiencing rapid weight loss, debilitating diarrhea, rough hair coat, hunched posture, labored breathing, lethargy, persistent recumbence, jaundice, anemia, significantly abnormal neurological signs, bleeding from any orifice, self-induced trauma, impaired mobility, becomes moribund or otherwise unable to obtain food or water will be immediately euthanized via cervical dislocation. When the desired time point is reached for each individual, mice will be euthanized by cervical dislocation while under up to 4% isofluorane anethesia following the procedures previously described. A hindpaw pinch prior to the procedure will be used to confirm depth of anesthesia. This is a conditionally approved method of euthanasia according to the AVMA Guidelines.

III. TRAINING/ QUALIFICATIONS OF INDIVIDUALS PERFORMING WORK WITH ANIMALS

Any questions regarding this training should be directed to (575-2994 or iacuc@uark.edu).

A. MANDATORY ONLINE TRAINING

1. **PRIOR TO MAY 1 2017** All individuals should have taken the following modules from the **LATA website:**
   a. *The Humane Care and Handling of Laboratory Animals*

b. *Policy and Procedures*

2. **AFTER MAY 1 2017:** All new individuals who have not taken the LATA training should take the following modules from the **CITI website:**
   a. *Working with the IACUC*

B. PERSONNEL PERFORMING WORK AT CLAF OR ENRC ONLY

1. Individuals starting work at **CLAF or ENRC after May 1, 2017** must complete the additional **CITI Training module:**
   a. *Post-Procedure Care of Mice and Rats in Research: Minimizing Pain and Distress*
2. Those Individuals working with animals at CLAF or ENRC must complete a health survey form, and submit it to the **Pat Walker Health Center**

C. Study Roster

1. Please complete the table on page 9 indicating the role of the individual, at which website they completed training, and a brief summary of their qualifications
   a. **Principal Investigator** (PI) (a current vita should be on file with the IACUC)
   b. **Students** (S) (attach resume or provide a brief description of qualifications)
   c. **Technician-**(T) (attach resume or provide a brief description of qualifications)
   d. **Other** (O) Please define this person's role in the Additional Information box
   e. **Training:** If you have students who do not have any background in animal research, please indicate a trainer under additional information

NOTE: All training will be verified. **If training records cannot be found** for any individual listed, **the submission will not be forwarded** to the committee for consideration until training is complete

STUDY ROSTER

NAME	ROLE ON STUDY	ONLINE TRAINING	Qualifications and Additional Information
Timothy J. Muldoon	☒ ☐ ☐ ☐ PI T S O	☒ CITI ☒ LATA	>10 years working with mice and rats for optical imaging studies. Dr. Muldoon has experience with small animal anesthesia (isofluorane and IP ketamine), carcinogen administration (SC injection and topical application methods) and euthanasia methods (including cervical dislocation) for both mice and rats. Dr. Muldoon will be responsible for training students in mouse handling procedures, subcutaneous cell injections, tumor volume measurements, diffuse reflectance spectroscopy measurements, therapy administration, and euthanasia and necropsy procedures.
Gage Greening	☐ ☐ ☒ ☐ PI T S O	☒ CITI ☒ LATA	>2 year of rodent handling experience. Mr. Greening will be responsible for performing daily mouse health

			checks, subcutaneous cell injections, diffuse reflectance spectroscopy measurements, tumor volume measurements, therapy administrations, and euthanasia and necropsy procedures. Mice which are Mr. Greening's primary responsibility (Balb/c) will be labeled as such on the cage card.
Haley James	☐ ☐ ☒ ☐ PI T S O	☒ CITI ☒ LATA	>2 year of rodent handling experience. Procedures performed: cervical dislocation and necropsy. Ms. James will be responsible for performing daily mouse health checks, subcutaneous cell injections, diffuse reflectance spectroscopy measurements, tumor volume measurements, therapy administrations, and euthanasia and necropsy procedures. Mice which are Ms. James' primary responsibility (athymic) will be labeled as such on the cage card.
Sandra Gordon	☐ ☐ ☒ ☐ PI T S O	☒ CITI ☒ LATA	>2 year of rodent handling experience. Mrs. Gordon will be responsible for performing daily mouse health checks, subcutaneous cell injections, diffuse reflectance spectroscopy measurements, tumor volume measurements, therapy administrations, and euthanasia and necropsy procedures. Mice which are Mrs. Gordon's primary responsibility (Balb/c) will be labeled as such on the cage card.
____	☐ ☐ ☐ ☐ PI T S O	☐ CITI ☐ LATA	____
____	☐ ☐ ☐ ☐ PI T S O	☐ CITI ☐ LATA	____
____	☐ ☐ ☐ ☐ PI T S O	☐ CITI ☐ LATA	____
____	☐ ☐ ☐ ☐ PI T S O	☐ CITI ☐ LATA	____
____	☐ ☐ ☐ ☐ PI T S O	☐ CITI ☐ LATA	____
____	☐ ☐ ☐ ☐ PI T S O	☐ CITI ☐ LATA	____
____	☐ ☐ ☐ ☐ PI T S O	☐ CITI ☐ LATA	____
____	☐ ☐ ☐ ☐ PI T S O	☐ CITI ☐ LATA	____
____	☐ ☐ ☐ ☐ PI T S O	☐ CITI ☐ LATA	____
____	☐ ☐ ☐ ☐ PI T S O	☐ CITI ☐ LATA	____
____	☐ ☐ ☐ ☐ PI T S O	☐ CITI ☐ LATA	____
____	☐ ☐ ☐ ☐ PI T S O	☐ CITI ☐ LATA	____

____	☐ ☐ ☐ ☐ PI T S O	☐ CITI ☐ LATA	____
____	☐ ☐ ☐ ☐ PI T S O	☐ CITI ☐ LATA	____
____	☐ ☐ ☐ ☐ PI T S O	☐ CITI ☐ LATA	____

IV. STATEMENT OF COMPLIANCE:

As the individual responsible for this research or teaching project,

I confirm that the information contained herein is accurate and, to the best of my knowledge, conforms to all applicable University, PHS, and USDA policies on the use of animals in research and teaching.

I confirm that I have completed the following online LATA training modules:
1) The Humane Care and Use of Laboratory Animals,
2) Policy and Procedures.

I confirm that all individuals involved with the animals used in this project will complete the above online LATA training modules and will be instructed in the humane care, handling, and use of animals, prior to participation in the project, and I will have reviewed their qualifications.

I agree not to proceed with any portion of this project or purchase animals until I receive written approval from the University of Arkansas Institutional Animal Care and Use Committee (IACUC).

I agree that no substantive change will be made in the procedures contained in this proposal without prior written notification to and approval by the IACUC.

I agree to allow inspection of my research facilities by members of the IACUC and the Animal Welfare Veterinarian and to comply promptly if informed of any violations of the University of Arkansas, Fayetteville's Policy on Animal Care and Use.

I understand that failure to comply with the University of Arkansas, Fayetteville's Policy on Animal Care and Use will jeopardize the University's Animal Welfare Assurance on file with the PHS (and with it all federal funding for the University), and may ultimately lead to revocation of my privileges to conduct animal research at the University of Arkansas.

Assurance Statement of Compliance

DO NOT COMPLETE THIS SECTION IF PROTOCOL IS SPECIFIED AS AGRICULTURAL or FIELD RESEARCH

The regulations for the Animal Welfare Act (United States Department of Agriculture) and the Public Health Service require that protocols for biomedical research and teaching involving animals the following concerns be specifically addressed in writing by the Principal Investigator. Items in brackets [] identify the source of the requirement [AWA = Animal Welfare Act regulations; NIH = NIH Guide for Care and Use of Laboratory Animals, 1996 edition].

A. **Animals should not be used if other methods exist that would provide substantially the same information. Indicate why the use of live animals is required in this research.** [AWA 2.31 (e) (2); NIH p. 8] :
Indicate here :

Studies that evaluate real-time spectroscopic data about hemoglobin oxygenation and inflammatory response require access to live animals. To date, there are no in vitro systems that could be used as a substitute.

B. **Justify your choice of species by listing some of the important characteristics of the species that make it suitable for use in the proposed research. Cost alone is not sufficient rationale.** [AWA 2.31 (e) (2); NIH p. 8]:
Justify here:

Studies that evaluate immune-based approaches to cancer management require mice with a high likelihood of developing colorectal tumors. In this case, the strain of mouse chosen is highly susceptible to developing colon carcinoma in response to administration of CT26 cells. In order to study the functional response to anti-cancer therapy of human cells, athymic nude mice are used. To date, there are no in vitro systems that could be used as a substitute. The mouse is the lowest mammal with this type of genetic modification which is available, and the purpose of this study (evaluation of colon tumor development and progression following conventional and/or immune-modulation therapy using novel spectroscopy methods) requires a live animal model.

C. **The number of animals used should be the minimum number that can be expected to provide valid results. Describe how the number of animals to be used was determined to comply with this requirement, i.e., that the number animals to be used can be expected to provide valid results.** [AWA 2.31 (e) (2); NIH p. 8]: *A statistical explanation is needed.*
Describe here :

Based on an a priori power analysis, the analysis of 40 animals per time point will be sufficient to achieve α=0.05 and power (1-β) = 0.72 for a moderate effect size (Pearson's correlation, r=0.3). This is a conservative estimate based on a 20% difference in diffuse reflectance spectra between normal and dysplastic tissues. Based on the above, we anticipate using 40 animals per group - 8 groups total divided among Balb/c mice (160 total) and athymic nude mice (160 mice total).

D. **The principal investigator submitting protocols for biomedical research should not unnecessarily duplicate previous experiments, and must consider less invasive alternatives to procedures that may cause more than momentary or slight pain or distress to animals (i.e., Level 3 or higher). Provide a statement that a literature review has been carried out demonstrating that this research does not unnecessarily duplicate previous experiments, and that appropriate allternative research methods are not available for any proposed procedures that are Level 3 or higher. The database used must be identified (check below).** [AWA 2.31 (d) (1) (I, ii, and iii); NIH p. 8] :
(Note, this requirement does not apply to protocols for teaching projects.)
Provide statement here :

The proposed studies do not duplicate previous experiments. Our lab is the only one correlating multimodal spectral data with markers for tumor-associated macrophages (TAMs) and localized inflammation following combination treatment with standard 5-FU

chemotherapy and immunomodulation of TAMs. To our knowledge, no other lab has performed similar studies to the proposed research.

(Be sure to list date(s) of search for each database used and the keywords that were used.)

	Database	Date(s) of Search	Key Words Used
☐	Medline	____	____
☐	Agricola	____	____
☐	Index Medicus	____	____
☐	Biol. Abstracts	____	____
☐	Animal Welfare Information Center (National Agricultural Library)	____	____
☒	Other (please specify below): ____	10/30/2017	diffuse reflectance spectroscopy; Balb/c; CT26; immune; modulation; 5-FU; colon; colorectal; cancer; carcinoma; tumor macrophage; endoscopy

UNIVERSITY OF ARKANSAS
Office of Research Compliance

To: Timothy Muldoon
FR: Craig Coon
Date: March 5th, 2018
Subject: IACUC Approval
Expiration Date: January 15th, 2021

The Institutional Animal Care and Use Committee (IACUC) has APPROVED your Modification to protocol # 18060 *Quantifying tumor perfusion response with diffuse reflectance spectroscopy in murine models of colon carcinoma following therapy and immunomodulation of tumor-associated macrophages* to modify anesthetic parameters.

In granting its approval, the IACUC has approved only the information provided. Should there be any further changes to the protocol during the research, please notify the IACUC in writing (via the Modification form) prior to initiating the changes. If the study period is expected to extend beyond January 15th, 2021 you must submit a newly drafted protocol prior to that date to avoid any interruption. By policy the IACUC cannot approve a study for more than 3 years at a time.

The IACUC appreciates your cooperation in complying with University and Federal guidelines involving animal subjects.

CNC/tmp

UNIVERSITY OF ARKANSAS

Office of Research Compliance

To: Timothy Muldoon
FR: Craig Coon
Date: October 8th, 2018
Subject: IACUC Approval
Expiration Date: January 15th, 2021

The Institutional Animal Care and Use Committee (IACUC) has APPROVED your Modification to protocol # 18060 *Quantifying tumor perfusion response with diffuse reflectance spectroscopy in murine models of colon carcinoma following therapy and immunomodulation of tumor-associated macrophages* to utilize non-tumor bearing mice for macrophage confirmation.

In granting its approval, the IACUC has approved only the information provided. Should there be any further changes to the protocol during the research, please notify the IACUC in writing (via the Modification form) prior to initiating the changes. If the study period is expected to extend beyond January 15th, 2021 you must submit a newly drafted protocol prior to that date to avoid any interruption. By policy the IACUC cannot approve a study for more than 3 years at a time.

The IACUC appreciates your cooperation in complying with University and Federal guidelines involving animal subjects.

CNC/tmp

MATLAB Code

SiliconePhantom.m

```
%% Gage J. Greening
% University of Arkansas
% College of Engineering
% Department of Biomedical Engineering
% Translational Biophotonics and Imaging Laboratory
% February 9, 2017

clear all; close all; clc;



% This MATLAB script will determine the following user-specified variables
% in order to construct a PDMS-based optical tissue phantom using
% titanium dioxide as the scattering agent.

    % 1. Application wavelength                       [nm]
    % 2. Desired Reduced Scattering Coefficient       [1/cm]
    % 3. Desired thickness of thin layer              [um]
    % 4. Weight of PDMS elastomer base measured       [g]

% Then, this MATLAB script will output the following parameters

    % 1. Volume of PDMS elastomer base                [uL]
    % 2. Volume of Curing Agent                       [uL]
    % 3. Concentration of TiO2                        [g/g PDMS elastomer
base]
    % 4. Amount of TiO2                               [g]
    % 5. Spin Speed in Spincoater                     [rpm]



%% Determine the 5 user-specified variables
fprintf('\nSilicone Phantom Design Module\n');
fprintf('by Gage J. Greening\n')
fprintf('Department of Biomedical Engineering, University of Arkansas\n');
fprintf('From the Journal of Biomedical Optics, Manuscript #115002-2, Nov.
2014\n\n');
fprintf('Substrate Material: Poly(dimethylsiloxane) (PDMS)\n');
fprintf('Scattering Agent: Titanium Dioxide\n');
fprintf('Absorbing Agent: Red Food Dye\n');
fprintf('Acceptable Wavelengths: 591, 621, 659, 691, 731, and 851 nm\n\n');

fprintf('Input Parameters\n');
wl_s   = input('Reference Wavelength for Scattering [nm]?:        ');   % 1.
Scattering wavelength
wl_a   = input('Reference Wavelength for Absorption [nm]?:        ');   % 2.
Absorption wavelength
us     = input('Desired Reduced Scattering Coefficient [1/cm]?:   ');   % 3.
Desired Reduced Scattering Coefficient
ua     = input('Desired Absorption Coefficient [1/cm]?:           ');   % 4.
Desired Absorption Coefficient
thick  = input('Desired Layer Thickness [um]?:                    ');   % 5.
Desired thickness of thin layer
```

```
base   = input('Weight of PDMS Elastomer Base [g]?:                ');   % 6.
Weight of PDMS elastomer base measured


%% 1. Concentration of Scattering Agent

if wl_s == 591
    scat_conc = (0.0003797*us) + (-0.0001878);

elseif wl_s == 621
    scat_conc = (0.0004367*us) + (-0.000174);

elseif wl_s == 659
    scat_conc = (0.0004904*us) + (-0.0001579);

elseif wl_s == 691
    scat_conc = (0.0005377*us) + (-0.00009323);

elseif wl_s == 731
    scat_conc = (0.0005852*us) + (-0.00007569);

elseif wl_s == 851
    scat_conc = (0.0007266*us) + (-0.00007963);

else
    disp('Tested wavelength not specified: choose from 591, 631, 659, 691,
731, or 851 nm');
end

scat_conc_new = scat_conc*1000;

%% Volume of PDMS elastomer base
vol_base = (base) * (1/1030) * (1/1000) * (100^3) * (1/1000) * (1000000/1);

%% Amount of Curing Agent
mass_ca = (base/10);
% The average experimental density of curing agent is 889 kg/m^3
vol_ca = (mass_ca)*(1/889)*(1/1000)*(1000/1)*(1000000/1);

%% Amount of Scattering Agent
scat_amt = scat_conc*(base);

%% Amount of Absorpting Agent

% Read in the Excel file of the absorption coefficient of the stock solution
mua = xlsread('abs.csv');
row = wl_a - 449;

if ua < mua(row,2)
    abs_conc = (ua/(mua(row,2))) * 0.417;
else
    abs_conc = (ua/(mua(row,3))) * 0.782;
end
```

```
abs_amt = abs_conc * (base);

%% Spin Speed in Spincoater
speed = ((115900)*(thick^-0.9985))-15.09;

%% Display all the values necessary to complete construction of the PDMS-
based tissue phantom

fprintf('\nOutput Parameters\n');
fprintf('Volume of PDMS Elastomer Base:\t\t\t\t\t  %.1f uL\n',vol_base);
fprintf('Volume of Curing Agent:\t\t\t\t\t\t  %.1f uL\n',vol_ca);
fprintf('Concentration of Scattering Agent:\t\t\t\t  %.4f
mg/g\n',scat_conc_new);
fprintf('Amount of Scattering Agent:\t\t\t\t\t  %.4f g\n',scat_amt);
fprintf('Concentration of Absorbing Agent:\t\t\t\t  %.4f uL/g\n',abs_conc);
fprintf('Amount of Absorbing Agent:\t\t\t\t\t  %.2f uL\n',abs_amt);
fprintf('Spin Speed:\t\t\t\t\t\t\t\t\t  %.0f rpm\n\n',speed);
```

lutfunc1.m

```
%% Gage J. Greening
% University of Arkansas
% College of Engineering
% Department of Biomedical Engineering
% March 19, 2016
% lutfunc1.m

function [lambda, Qsca, Qback, g] = lutfunc1(l_min, l_max, dl, r,
sphere_type)

%%%%%%%%%%%%%%%%%%%%%%%%%%  mie_lambda  %%%%%%%%%%%%%%%%%%%%%%%%%%%%%%%%%
% This function calculates scattering crosssections, Qsca, and anisotropy
% parameter, g, vs. wavelength.
%
% Inputs:
%       - l_min:        minimum wavelength [um]
%       - l_max:        maximum wavelength [um]
%       - dl:           wavelength step [um]
%       - r:            radius of particle [um]
%       - bead_type:    type of sphere (bead (1) or tissue (2))
%
% Outputs:
%       - lambda:   wavelength [nm]
%       - Qsca:     Total scattering efficiency [1/um^3]
%       - Qback:    Backscattering efficiency [1/um^3]
%       - g:        Anisotropy parameter
%%%%%%%%%%%%%%%%%%%%%%%%%%%%%%%%%%%%%%%%%%%%%%%%%%%%%%%%%%%%%%%%%%%%%%%%%%%%




for lambda = l_min:dl:l_max,

    switch lower(sphere_type)
        case {'tissue'}
```

```
            n_sph = 1.424;
            n_med = 1.36;
            m = n_sph/n_med;
        case  {'beads'}
            n_sph = 1.5663;
            %A=1.31279;
            %B=0.015763;
            %C=0.004382;
            %D=0.0011455;
            %n_med=(A+B./lambda-C./lambda.^2+D./lambda.^3);
            n_med = 1.33;
            %m=1.59/n_med;
            m=(n_sph + .00785/(lambda.^2) + .000334/(lambda.^4))/n_med;
            %m=(n_sph + .010002/(lambda^2))/n_med;
            %m=(1.5663 + (0.00785/lambda^2) - (0.000334/lambda^4))/n_med;
    end
    k=2*pi*n_med/lambda;
    x=r*k;
    F = lutfunc2(m,x);   % returns [Re(m) Im(m) x Qext Qsca Qabs Qback g
Qratio]
    Qsca(round((lambda-l_min)/dl+1))   = F(5);
    g(round((lambda-l_min)/dl+1))      = F(8);
    Qback(round((lambda-l_min)/dl+1))  = F(7);

end
lambda = l_min:dl:l_max;
```

lutfunc2.m

```
%% Gage J. Greening
% University of Arkansas
% College of Engineering
% Department of Biomedical Engineering
% March 19, 2016
% lutfunc2.m

function result = lutfunc2(m, x)
% Computation of Mie Efficiencies for given
% complex refractive-index ratio m=m'+im"
% and size parameter x=k0*a, where k0= wave number in ambient
% medium, a=sphere radius, using complex Mie Coefficients
% an and bn for n=1 to nmax,
% s. Bohren and Huffman (1983) BEWI:TDD122, p. 103,119-122,477.
% Result: m', m", x, efficiencies for extinction (qext),
% scattering (qsca), absorption (qabs), backscattering (qb),
% asymmetry parameter (asy=<costeta>) and (qratio=qb/qsca).
% Uses the function "Mie_abcd" for an and bn, for n=1 to nmax.
% C. Mätzler, May 2002.

if x==0                 % To avoid a singularity at x=0
    result=[real(m) imag(m) 0 0 0 0 0 0 1.5];
elseif x>0              % This is the normal situation
    nmax=round(2+x+4*x^(1/3));
    n1=nmax-1;
    n=(1:nmax);cn=2*n+1; c1n=n.*(n+2)./(n+1); c2n=cn./n./(n+1);
```

```
    x2=x*x;
    f=lutfunc3(m,x);
    anp=(real(f(1,:))); anpp=(imag(f(1,:)));
    bnp=(real(f(2,:))); bnpp=(imag(f(2,:)));
    g1(1:4,nmax)=[0; 0; 0; 0]; % displaced numbers used for
    g1(1,1:n1)=anp(2:nmax);    % asymmetry parameter, p. 120
    g1(2,1:n1)=anpp(2:nmax);
    g1(3,1:n1)=bnp(2:nmax);
    g1(4,1:n1)=bnpp(2:nmax);
    dn=cn.*(anp+bnp);
    q=sum(dn);
    qext=2*q/x2;
    en=cn.*(anp.*anp+anpp.*anpp+bnp.*bnp+bnpp.*bnpp);
    q=sum(en);
    qsca=2*q/x2;
    qabs=qext-qsca;
    fn=(f(1,:)-f(2,:)).*cn;
    gn=(-1).^n;
    f(3,:)=fn.*gn;
    q=sum(f(3,:));
    qb=q*q'/x2;
    asy1=c1n.*(anp.*g1(1,:)+anpp.*g1(2,:)+bnp.*g1(3,:)+bnpp.*g1(4,:));
    asy2=c2n.*(anp.*bnp+anpp.*bnpp);
    asy=4/x2*sum(asy1+asy2)/qsca;
    qratio=qb/qsca;
    result=[real(m) imag(m) x qext qsca qabs qb asy qratio];
end;
```

lutfunc3.m

```
%% Gage J. Greening
% University of Arkansas
% College of Engineering
% Department of Biomedical Engineering
% March 19, 2016
% lutfunc3.m

function result = lutfunc3(m, x)

% Computes a matrix of Mie coefficients, a_n, b_n, c_n, d_n,
% of orders n=1 to nmax, complex refractive index m=m'+im",
% and size parameter x=k0*a, where k0= wave number
% in the ambient medium, a=sphere radius;
% p. 100, 477 in Bohren and Huffman (1983) BEWI:TDD122
% C. Mätzler, June 2002

nmax=round(2+x+4*x^(1/3));
n=(1:nmax); nu = (n+0.5); z=m.*x; m2=m.*m;
sqx= sqrt(0.5*pi./x); sqz= sqrt(0.5*pi./z);
bx = besselj(nu, x).*sqx;
bz = besselj(nu, z).*sqz;
yx = bessely(nu, x).*sqx;
hx = bx+i*yx;
b1x=[sin(x)/x, bx(1:nmax-1)];
b1z=[sin(z)/z, bz(1:nmax-1)];
```

```
y1x=[-cos(x)/x, yx(1:nmax-1)];
h1x= b1x+i*y1x;
ax = x.*b1x-n.*bx;
az = z.*b1z-n.*bz;
ahx= x.*h1x-n.*hx;

an = (m2.*bz.*ax-bx.*az)./(m2.*bz.*ahx-hx.*az);
bn = (bz.*ax-bx.*az)./(bz.*ahx-hx.*az);
cn = (bx.*ahx-hx.*ax)./(bz.*ahx-hx.*az);
dn = m.*(bx.*ahx-hx.*ax)./(m2.*bz.*ahx-hx.*az);
result=[an; bn; cn; dn];
```

step1_createPhantoms

```
%% Gage J. Greening
% University of Arkansas
% College of Engineering
% Department of Biomedical Engineering
% May 3, 2016
% step1_createPhantoms.m

% This program provides the amount of beads to generate each phantom and
% the amount of ink needed at each step. Although this program generates
% exact numbers for the volume to be added, it might not be always possible
% to pipet out the exact numbers. In such cases, correct x1 and volumeDist
% to represent actual volumes added.

clear all; close all; clc;

% The total volume of solution
tot_vol = input('Phantom Volume (mL): ');

% The reduced scattering coefficients (us') of the phantoms at 630 nm
redscatCoef = [3.43, 4.94, 7.14, 10.31, 14.88, 21.48] / 10;

% Diameter of the beads (um)
actBeadSize = 0.99;

% Standard deviation of the bead size (um)
stdev = 0.03;

% Percent solid of beads
perSol = 2.6;

%% Use the function 'lutfunc1.m' to determine scattering efficiency

% Input parameters for the mie2 function (also described in mie2.m)
minwave = 0.30;         % Minimum wavelength (um)
maxwave = 0.80;         % Maximum wavelength (um)
wavestep = 0.001;       % Wavelength step (um)
radius = actBeadSize/2; % Radius of beads (um)

% Output parameters for the mie2 function (also described in mie2.m)
    % lambda:   Wavelength
    % Qsca:     Total scattering efficiency [1/um^3]
```

```
    % Qback:    Backscattering efficiency [1/um^3]
    % g:        Anisotropy coefficient

[lambda, Qsca, Qback, g] =
lutfunc1(minwave,maxwave,wavestep,radius,'beads');

% Convert lambda (um) to lambda_nm (nm) for plotting purposes
lambda_nm = lambda.*1000;

% Calculation of the scattering cross section (Tsca = scattering cross
section)
Tsca = Qsca.*pi*(radius)^2;     % [1/um^3] * [um^2] = [um^-1] ????

% Calculation of the reduced scattering cross section
redScat = Tsca.*(1-g);

%% Absorption Coefficient

% The stock solution is made with the following:
    % 2,000 uL yellow food dye
    % 800 uL red food dye
    % 400 uL blue food dye
    % 16,800 uL deionized water
    % 20,000 uL total volume

% Read in the Excel file of the absorption coefficient of the stock solution
mua_init = xlsread('Dye Combination Stock - Dilution of 10x -
05192017.csv');

% Absorption coefficient of the stock solution (without 1st column of
% wavelength)
mua_init_c1 = mua_init(:,1);
mua_init_c2 = mua_init(:,2)*10;     % 10x stock solution
for i = 1:501                       % absorbance data btw 300-800 nm
    if mua_init_c2(i) < 0
        mua_init_c2(i) = 0.001;
    end
end

% Desired maxiumum absorption coefficient of calibration phantoms
max_mua = input('Maximum Absorption Coefficient (1/cm): ');
wavelength_min = input('Minimum Wavelength (nm): ');
wavelength_min_index = (wavelength_min - (mua_init_c1(1) - 1));
wavelength_max = input('Maximum Wavelength (nm): ');
wavelength_max_index = (wavelength_max - (mua_init_c1(1) - 1));

% The scale of the desired max ua and the ua of the stock solution
scale = max_mua /
max(mua_init_c2(wavelength_min_index:wavelength_max_index));

% The absorption coefficient of the calibration phantoms
mua = scale * mua_init_c2;

% The volume of the stock solution needed to yield the desired ua
```

```
mLAbsorber = zeros(1,2*length(redscatCoef));
mLAbsorber(length(redscatCoef)+1:2*length(redscatCoef)) = (tot_vol)*scale;

%% Create the phantoms

% Density [1/um^3]
density = redscatCoef(1,:)./redScat(331)/1000;
% #part per ml of bead solution
partBeads = tot_vol.*density.*10^12;
%Total number of beads in Solution
totBeads = (6.*(perSol./100).*10^12)./(1.05*pi.*actBeadSize.^3);
%mL of beads to use to create phantom
mLBeads = partBeads./totBeads;
mLBeads = horzcat(mLBeads,mLBeads);
%mL of water used to create phantom
mLWater(1:length(redscatCoef)) = tot_vol - (mLBeads(1:length(redscatCoef)) +
mLAbsorber(1:length(redscatCoef)));
mLWater(length(redscatCoef)+1:2*length(redscatCoef)) = tot_vol -
(mLBeads(length(redscatCoef)+1:2*length(redscatCoef)) +
mLAbsorber(length(redscatCoef)+1:2*length(redscatCoef)));
%volumeDist is a table with mLs beads in the first column and the
%corresponding mLs of water in the second.
volumeDist = [mLBeads' mLAbsorber' mLWater' mLBeads'+mLWater'+mLAbsorber'];

% Volume distribution in uL (microliters)
volumeDist = round(volumeDist*1000);

%% Reduced Scattering Coefficient

% If less than 6 phantoms are needed to span the desired range of reduced
% scattering coefficients, comment out the extra phantoms.

redScatCS = redScat;        % Reduced scattering cross section [cm^2]

% Reduced scattering coefficients for all phantoms put in terms of cm
musp1 = redScatCS.*(density(1,1))*10000;    % Reduced scattering cross
section * volume density = musp for phantom 1 [cm^-1]
musp2 = redScatCS.*(density(1,2))*10000;    % Reduced scattering cross
section * volume density = musp for phantom 2 [cm^-1]
musp3 = redScatCS.*(density(1,3))*10000;    % Reduced scattering cross
section * volume density = musp for phantom 3 [cm^-1]
musp4 = redScatCS.*(density(1,4))*10000;    % Reduced scattering cross
section * volume density = musp for phantom 4 [cm^-1]
musp5 = redScatCS.*(density(1,5))*10000;    % Reduced scattering cross
section * volume density = musp for phantom 5 [cm^-1]
musp6 = redScatCS.*(density(1,6))*10000;    % Reduced scattering cross
section * volume density = musp for phantom 6 [cm^-1]

% Currently, the resolution of the reduced scattering coefficients is 1.
% Interpolate these values such that they correlate with the resoultion of
% the spectrometer (~0.35).
load('Wavelength.mat');
musp1 = interp1(lambda_nm,musp1,wavelength_501);
musp1 = musp1(wavelength_min_index:wavelength_max_index);
musp2 = interp1(lambda_nm,musp2,wavelength_501);
```

```
musp2 = musp2(wavelength_min_index:wavelength_max_index);
musp3 = interp1(lambda_nm,musp3,wavelength_501);
musp3 = musp3(wavelength_min_index:wavelength_max_index);
musp4 = interp1(lambda_nm,musp4,wavelength_501);
musp4 = musp4(wavelength_min_index:wavelength_max_index);
musp5 = interp1(lambda_nm,musp5,wavelength_501);
musp5 = musp5(wavelength_min_index:wavelength_max_index);
musp6 = interp1(lambda_nm,musp6,wavelength_501);
musp6 = musp6(wavelength_min_index:wavelength_max_index);

muspmin =
[min(musp1);min(musp2);min(musp3);min(musp4);min(musp5);min(musp6)];
muspmax =
[max(musp1);max(musp2);max(musp3);max(musp4);max(musp5);max(musp6)];

% Plot the reduced scattering and absorption coefficients
figure(1)
subplot(1,2,1);
plot(wavelength_501(wavelength_min_index:wavelength_max_index),musp1,'Linewi
dth',2);
hold on;
subplot(1,2,1);
plot(wavelength_501(wavelength_min_index:wavelength_max_index),musp2,'Linewi
dth',2);
hold on;
subplot(1,2,1);
plot(wavelength_501(wavelength_min_index:wavelength_max_index),musp3,'Linewi
dth',2);
hold on;
subplot(1,2,1);
plot(wavelength_501(wavelength_min_index:wavelength_max_index),musp4,'Linewi
dth',2);
hold on;
subplot(1,2,1);
plot(wavelength_501(wavelength_min_index:wavelength_max_index),musp5,'Linewi
dth',2);
hold on;
subplot(1,2,1);
plot(wavelength_501(wavelength_min_index:wavelength_max_index),musp6,'Linewi
dth',2);
[yaxis]=get(get(gca,'children'),'ydata');
legend('Phantom 1,7','Phantom 2,8','Phantom 3,9','Phantom 4,10','Phantom
5,11','Phantom 6,12');
title('\mu_s^'' vs. wavelength for LUT calibration phantoms');
xlabel('Wavelength (nm)');
ylabel('\mu_s^'' (cm^-^1)');
axis square; axis([wavelength_min wavelength_max 0 max(musp6)*1.1]);

mua_zeros = zeros(length(wavelength_501),1);
mua_zeros(:) = 0.001;
subplot(1,2,2);
plot(wavelength_501(wavelength_min_index:wavelength_max_index),mua_zeros(wav
elength_min_index:wavelength_max_index),'Linewidth',2);
hold on;
```

```
subplot(1,2,2);
plot(wavelength_501(wavelength_min_index:wavelength_max_index),mua(wavelengt
h_min_index:wavelength_max_index),'Linewidth',2);
legend('Phantom 1-6','Phantom 7-12');
title('\mu_a vs. wavelength for LUT calibration phantoms');
xlabel('Wavelength (nm)');
ylabel('\mu_a (cm^-^1)');
axis square; axis([wavelength_min wavelength_max 0 max(mua)*1.1]);

% Write data to table

table = {'Phantom', 'Polystyrene Beads (uL)', 'Absorber (uL)', 'Deionized
Water (uL)', 'Total Volume (mL)', 'Min. us'' (cm-1)', 'Max. us'' (cm-1)',
'Min. ua (cm-1)', 'Max. ua (cm-1)'};

for i = 2:13
    table{i,1} = i-1;
    table{i,2} = volumeDist(i-1,1);
    table{i,3} = volumeDist(i-1,2);
    table{i,4} = volumeDist(i-1,3);
    table{i,5} = volumeDist(i-1,1)+volumeDist(i-1,2)+volumeDist(i-1,3);
end

for i = 2:7
    table{i,6} = muspmin(i-1,1);
    table{i,7} = muspmax(i-1,1);
    table{i,8} = 0;
    table{i,9} = 0;
end

for i = 8:13
    table{i,6} = muspmin(i-7,1);
    table{i,7} = muspmax(i-7,1);
    table{i,8} = 0;
    table{i,9} = max_mua;
end

table_double = cell2mat(table(2:13,:));

total_beads = sum(table_double(:,2));
total_dye  =sum(table_double(:,3));
total_water = sum(table_double(:,4));
total_volume = sum(table_double(:,5));

table{16,1} = 'Total (mL)';
table{16,2} = total_beads/1000;
table{16,3} = total_dye/1000;
table{16,4} = total_water/1000;
table{16,5} = total_volume/1000;

filename = 'PhantomSpecifications.xlsx';
xlswrite(filename,table,'PhantomSpecifications','A1');

% Save an Excel file with absorption coefficients
table2(:,1) = wavelength_501(wavelength_min_index:wavelength_max_index);
```

```
table2(:,2) = mua_zeros(wavelength_min_index:wavelength_max_index);
filename = 'PhantomAbsCoeffZeros.xlsx';
xlswrite(filename,table2,'PhantomAbsCoeffZeros','A1')

table3(:,1) = wavelength_501(wavelength_min_index:wavelength_max_index);
table3(:,2) = mua(wavelength_min_index:wavelength_max_index);
filename = 'PhantomAbsCoeff.xlsx';
xlswrite(filename,table3,'PhantomAbsCoeff','A1')

% Save variables

mua_P01toP06 = mua_zeros';
mua_P07toP12 = mua';

save('temp.mat','volumeDist','musp1','musp2','musp3','musp4','musp5','musp6'
,'mua_P01toP06','mua_P07toP12','table','wavelength_min','wavelength_max');

clear all;

load('Wavelength.mat');
load('temp.mat');

%
save('temp.mat','musp1','musp2','musp3','musp4','musp5','musp6','mua_P08toP1
4','mua_P01toP07','sample','wavelength_301','wavelength_857');
```

step2_createLUT.m

```
%% Gage J. Greening
% University of Arkansas
% College of Engineering
% Department of Biomedical Engineering
% March 6, 2017
% step2_createLUT.m

clc; close all;

%% Load in the calibration curve taken with the reflectance standard
fprintf('Load Calibration Curve:\n\n');
filename = uigetfile;
C = csvread(filename);
wavelength_long = C(1:2228,1);      % cut off at 800 nm
calibration_curve = C(1:2228,2);    % cut off at 800 nm

%% Load in the dark noise curve taken when all lights are off
fprintf('Load Darknoise Curve:\n\n');
filename = uigetfile;
D = csvread(filename);
darknoise_curve = D(1:2228,2);      % cut off at 800 nm

%% Interpolate phantom generation data to match wavelengths of spectrometer

% Set the standard 1 nm resolution wavelength range
wavelength_range = wavelength_min:1:wavelength_max;
```

```
% Create interpolated musp values based on spectrometer resolution
musp_interp(:,1) = interp1(wavelength_range,musp1,wavelength_long);
musp_interp(:,2) = interp1(wavelength_range,musp2,wavelength_long);
musp_interp(:,3) = interp1(wavelength_range,musp3,wavelength_long);
musp_interp(:,4) = interp1(wavelength_range,musp4,wavelength_long);
musp_interp(:,5) = interp1(wavelength_range,musp5,wavelength_long);
musp_interp(:,6) = interp1(wavelength_range,musp6,wavelength_long);
musp_interp(:,7) = interp1(wavelength_range,musp7,wavelength_long);

% Create interpolated mua values based on spectrometer resolution
mua_ranges = input('Ranges of Absorption Coefficients: ');
fprintf('Load Phantoms Absorption Curves, starting with zeros:\n\n');
fprintf('\n');
for i = 1:mua_ranges
    filename = uigetfile;
    A = csvread(filename);
    abs_coeff(:,i) = A(:,2);
end
mua_interp(:,1) = interp1(wavelength_range,abs_coeff(:,1),wavelength_long);
mua_interp(:,2) = interp1(wavelength_range,abs_coeff(:,2),wavelength_long);
mua_interp(:,3) = interp1(wavelength_range,abs_coeff(:,3),wavelength_long);

phantom_number = input('Number of Phantoms: ');
fprintf('Load Phantom Raw Reflectance Data:\n\n');
for i = 1:phantom_number
    filename = uigetfile;
    P = csvread(filename);
    phantom(:,i) = P(1:2228,2);
end

phantom_calibrated = zeros(length(calibration_curve),phantom_number);
for i = 1:phantom_number
    phantom_calibrated(:,i) = (phantom(:,i) - darknoise_curve(:,1)) ./
((calibration_curve(:,1) - darknoise_curve(:,1)) * 5);
end

%% Create mesh

% Reduced Scattering Coefficient
musp(:,1:7) = musp_interp;
musp(:,8:14) = musp_interp;
musp(:,15:21) = musp_interp;
musp(isnan(musp)) = 0;

% Absorption Coefficient
for i = 1:7
mua(:,i) = mua_interp(:,1);
mua(:,i+7) = mua_interp(:,3);
mua(:,i+14) = mua_interp(:,2);
end
mua(isnan(mua)) = 0;

% Calibrated Reflectance
ref(:,:) = phantom_calibrated(:,:);
```

```
% Convert matrices to vectors
vector_musp = musp(:);
vector_mua = mua(:);
vector_ref = ref(:);

% Create LResolution for Lookup Table

musp_min = min(vector_musp(vector_musp>0));
musp_max = max(vector_musp);
mua_min = min(vector_mua(vector_mua>0));
mua_max = max(vector_mua);
ref_min = min(vector_ref(vector_ref>0));
ref_max = max(vector_ref(vector_ref<1));

res_musp = linspace(musp_min,musp_max,200);
res_mua = linspace(mua_min,mua_max,200);

% Create Lookup Table
lut = griddata(vector_musp,vector_mua,vector_ref,res_musp',res_mua);
surf(res_musp',res_mua,lut); hold on;
scatter3(vector_musp,vector_mua,vector_ref,'k');
axis([5, 40, -1, 10, 0, 0.3]);
xlabel('\mu_s^'' (cm^-^1)');
ylabel('\mu_a (cm^-^1)');
zlabel('Reflectance (A.U.)');
title('Lookup Table');
box on; grid on; axis square; colormap(jet); colorbar;

% Save necessary variables
save('specLookupTable.mat','res_musp','res_mua','lut');
```

calcOP_hb_3000_hb.m

```
function R = calcOP_hb_3000_hb(InitialValues,lambda,Hb,HbO2,mel)

% The goal of this function is to determine R

%%%%%%%%%%%%%%%%%%%%%%%%%%%%%%%%%%%%%%%%%%%%%%%%%%%%%%%%%%%%%%%%%%%%%%%
% lambda in um
%%%%%%%%%%%%%%%%%%%%%%%%%%%%%%%%%%%%%%%%%%%%%%%%%%%%%%%%%%%%%%%%%%%%%%%

A                   = InitialValues(1);
B                   = InitialValues(2);
C                   = InitialValues(3);
cHb                 = InitialValues(4);
alpha               = InitialValues(5);
S                   = InitialValues(6);

if cHb<0
    cHb = 0;
end

% Reduced Scattering Coefficient
mu_sp = (A*10).*(lambda./0.730).^(-B);
```

```
% Absorption Coefficient
mu_a1 = (2.303*(150).*(alpha.*HbO2(:,2) + (1-alpha).*Hb(:,2)));
mu_a = 0.01*cHb.*mu_a1.*(1 - exp(-S.*mu_a1))./(S.*mu_a1);
% mu_a = mu_a + (2.303*0.1.*C*mel(:,2));

% Loading the appropriate LUT
load('calcOP.mat');
R = interp2(musp3000',mua3000,lut3000,mu_sp,mu_a);

end
```

calcOP_hb_3000_oxy.m

```
function R = calcOP_hb_3000_oxy(InitialValues,lambda,Hb,HbO2,mel)

% The goal of this function is to determine R

%%%%%%%%%%%%%%%%%%%%%%%%%%%%%%%%%%%%%%%%%%%%%%%%%%%%%%%%%%%%%%%%%%%
% lambda in um
%%%%%%%%%%%%%%%%%%%%%%%%%%%%%%%%%%%%%%%%%%%%%%%%%%%%%%%%%%%%%%%%%%%

A                   = InitialValues(1);
B                   = InitialValues(2);
C                   = InitialValues(3);
cHb                 = InitialValues(4);
alpha               = InitialValues(5);
S                   = InitialValues(6);

if cHb<0
    cHb = 0;
end

% Reduced Scattering Coefficient
mu_sp = (A*10).*(lambda./0.590).^(-B);

% Absorption Coefficient
mu_a1 = (2.303*(150).*(alpha.*HbO2(:,2) + (1-alpha).*Hb(:,2)));
mu_a = 0.01*cHb.*mu_a1.*(1 - exp(-S.*mu_a1))./(S.*mu_a1);
% mu_a = mu_a + (2.303*0.1.*C*mel(:,2));

% Loading the appropriate LUT
load('calcOP.mat');
R = interp2(musp3000',mua3000,lut3000,mu_sp,mu_a);

end
```

chisqOP_hb_3000_hb.m

```
%%%%%%%%%%%%%%%%%%%%%%%%%%%%%%%%%%%%%%%%%%%%%%%%%%%%%%%%%%%%%%%%%%%%
%This function calculates the chi-squared error between the
%OP model and measured data (Rmeas)
%%%%%%%%%%%%%%%%%%%%%%%%%%%%%%%%%%%%%%%%%%%%%%%%%%%%%%%%%%%%%%%%%%%%
function chisq = chisqOP_hb_3000_hb(InitialValues,Rmeas,lambda,Hb,HbO2,mel)
```

```
R = calcOP_hb_3000_hb(InitialValues,lambda,Hb,HbO2,mel);
chisq = sum(((R - Rmeas)./R).^2);
```

chisqOP_hb_3000_oxy.m

```
%%%%%%%%%%%%%%%%%%%%%%%%%%%%%%%%%%%%%%%%%%%%%%%%%%%%%%%%%%%%%%%%%%%%%%%
%This function calculates the chi-squared error between the
%OP model and measured data (Rmeas)
%%%%%%%%%%%%%%%%%%%%%%%%%%%%%%%%%%%%%%%%%%%%%%%%%%%%%%%%%%%%%%%%%%%%%%%
function chisq = chisqOP_hb_3000_oxy(InitialValues,Rmeas,lambda,Hb,HbO2,mel)

R = calcOP_hb_3000_oxy(InitialValues,lambda,Hb,HbO2,mel);
chisq = sum(((R - Rmeas)./R).^2);
```

PostProcess3mm.m

```
%% Gage Greening
% University of Arkansas
% College of Engineering
% Department of Biomedical Engineering
% June 30, 2016



%% Loading in Calibration and Dark Noise Data

clear all; close all; clc;

% Load in the calibration curve
[filename, ~] = uigetfile('*.csv', 'Select the calibration dataset');
cal = load(filename);
cal = cal;

% Load in the dark noise curve
dn = csvread('3mm_75ms_DARKNOISE.csv');
data(:,1) = dn(:,1);



%% Initialize variables

samples = input('Number of Spectra: ' );
% samples = input('Number of Spectroscopy Measurements: ');
name = ['3-1';'3-2';'3-3';'3-4';'3-5';'3-6';'3-7';'3-8';'3-9'];
name2 = ['3-10';'3-11';'3-12';'3-13';'3-14';'3-15';'3-16';'3-17';'3-18';'3-
19';'3-20';'3-21';'3-22';'3-23';'3-24';'3-25';'3-26';'3-27';'3-28';'3-
29';'3-30';'3-31';'3-32';'3-33';'3-34';'3-35'];
temp = zeros(2048,2);
temp2 = zeros(2048,2);
specraw = zeros(2048,samples);



%% Create Matrix with Raw Spectra

% Raw spectra
for i = 1:9
    temp = csvread([name(i,:),'.csv']);
```

```
    specraw(:,i) = temp(:,2);
end
for i = 10:samples
    temp2 = csvread([name2(i-9,:),'.csv']);
    specraw(:,i) = temp2(:,2);
end

% (Raw spectra - darknoise) / (5(calibration - darknoise))
for i = 1:samples
    data(:,i+1) = (specraw(:,i)-dn(:,2))./((cal(:,2)-dn(:,2))*5);
end



%% Boundary Conditions: Wavelength

% Set the minimum and maximum wavelengths: Oxygenation
wmin_oxy = 515;
wmax_oxy = 595;

% Set the minimum and maximum wavelengths: [Hb] and scattering
wmin_hb = 475;
wmax_hb = 750;

% Load in the absorbance values for hemoglobin and melanin
load('HbO2.txt');
load('Hb.txt');
load('mel.txt');



%% Boundary Conditions: Optical Properties

% Set the initial values: Oxygenation [A B cMel cHb SaO2 S wmin wmax]
InitParams1 =    [0.400   -1.00   0.000   2.000    0.20    0.001   wmin_oxy
wmax_oxy];
InitVal1 = InitParams1(1:6);
lb1 =            [0.000   -4.00   0.000   0.0000   0.000   0.000];
ub1 =            [1.000   0.000   0.000   12.000   1.000   0.010];

% Set the initial values: Hemoglobin [A B cMel cHb SaO2 S wmin wmax]
InitParams2 =    [0.400   0.500   0.000   2.000    0.20    0.001   wmin_hb
wmax_hb];
InitVal2 = InitParams2(1:6);
lb2 =            [0.000   -1.00   0.000   0.0000   0.000   0.000];
ub2 =            [1.000   1.500   0.000   12.000   1.000   0.010];



%% Model Fit

for i = 1:samples
    % Choose wavelength range by index: Oxygenation
    [~, lambdaMinIndex1] = min((data(:,1) - InitParams1(7)).^2);
    [~, lambdaMaxIndex1] = min((data(:,1) - InitParams1(8)).^2);
    lambda1 = data(lambdaMinIndex1:lambdaMaxIndex1,1)/1000;
    % Choose wavelength range by index: Hemoglobin
```

```
    [~, lambdaMinIndex2] = min((data(:,1) - InitParams2(7)).^2);
    [~, lambdaMaxIndex2] = min((data(:,1) - InitParams2(8)).^2);
    lambda2 = data(lambdaMinIndex2:lambdaMaxIndex2,1)/1000;

    % Scale = initParams(6): Oxygenation
    eHbO21   = [lambda1 interp1q(HbO2(:,1)/1000,HbO2(:,2),lambda1)];
    eHb1    = [lambda1 interp1q(Hb(:,1)/1000,Hb(:,2),lambda1)];
    emel1    = [lambda1 interp1q(mel(:,1)/1000,mel(:,2),lambda1)];
    % Scale = initParams(6): Hemoglobin
    eHbO22   = [lambda2 interp1q(HbO2(:,1)/1000,HbO2(:,2),lambda2)];
    eHb2    = [lambda2 interp1q(Hb(:,1)/1000,Hb(:,2),lambda2)];
    emel2    = [lambda2 interp1q(mel(:,1)/1000,mel(:,2),lambda2)];

    % Generate first guess at reflectance based on initial parameters:
Oxygenation
    RFirstGuess1 = calcOP_hb_3000_oxy(InitVal1,lambda1,eHb1,eHbO21,emel1);
    % Generate first guess at reflectance based on initial parameters:
Hemoglobin
    RFirstGuess2 = calcOP_hb_3000_hb(InitVal2,lambda2,eHb2,eHbO22,emel2);

    % Get measured reflectance data: Oxygenation
    Rmeas1(:,i) = data(lambdaMinIndex1:lambdaMaxIndex1,i+1);
    % Get measured reflectance data: Hemoglobin
    Rmeas2(:,i) = data(lambdaMinIndex2:lambdaMaxIndex2,i+1);

    % Adjust fit parameters
    % FitOptimize =optimset('MaxFunEvals',6000,'MaxIter',6000,'TolX',5E-
5,'TOlFun',5E-5,'LevenbergMarquardt','on');
    fitOptimize =
optimset('LargeScale','off','MaxFunEvals',6000,'MaxIter',6000,'TolX',5E-
5,'TOlFun',5E-5);

    %[FitVals chisq] =
fminsearch('chisqOP',InitVal,fitOptimize,Rmeas,lambda,eHbO2): Oxygenation
    [FitVals1(i,:), chisq1(i,:)] =
fmincon('chisqOP_hb_3000_oxy',InitVal1,[],[],[],[],lb1,ub1,[],fitOptimize,Rm
eas1(:,i),lambda1,eHb1,eHbO21,emel1);
    %[FitVals chisq] =
fminsearch('chisqOP',InitVal,fitOptimize,Rmeas,lambda,eHbO2): Hemoglobin
    [FitVals2(i,:), chisq2(i,:)] =
fmincon('chisqOP_hb_3000_hb',InitVal2,[],[],[],[],lb2,ub2,[],fitOptimize,Rme
as2(:,i),lambda2,eHb2,eHbO22,emel2);



    Fit1(:,i) = calcOP_hb_3000_oxy(FitVals1(i,:),lambda1,eHb1,eHbO21,emel1);
    Fit2(:,i) = calcOP_hb_3000_hb(FitVals2(i,:),lambda2,eHb2,eHbO22,emel2);

    if exist('chisq1')==0
        chisq1(i) = sum(((Fit1(:,i) - Rmeas1(:,i))./Fit1(:,i)).^2);
    end
    if exist('chisq2')==0
        chisq2(i) = sum(((Fit2(:,i) - Rmeas2(:,i))./Fit2(:,i)).^2);
    end

end
```

```
% Multiply lambda by 1000 to get values in nm
lambda1 = lambda1 * 1000;
lambda2 = lambda2 * 1000;

clc;

% Creating optical property tables (for both wavelength ranges)
Quantify1 = zeros(samples,7); % Initializing the 1st table per number of
samples
Quantify2 = zeros(samples,7); % Initializing the 2nd table per number of
samples
for i = 1:samples
    % Table for fit values: Accurate Oxygenation (515-595 nm)
    Quantify1(i,1:6) = FitVals1(i,:); Quantify1(i,7) = chisq1(i);
    % Table for fit values: Accurate Hemoglobin (475-750 nm)
    Quantify2(i,1:6) = FitVals2(i,:); Quantify2(i,7) = chisq2(i);
end

% Creating table of relevant optical properties
% 1st column: Oxygenation
% 2nd column: Oxygenation Chi-Squared Value
% 3rd column: Hemoglobin Content
% 4th column: Hemoglobin Content Chi-Squared Value
% 5th column: Reduced Scattering Coefficient
table1 = zeros(samples,4);
table1(:,1) = Quantify1(:,5);
table1(:,2) = Quantify1(:,7);
table1(:,3) = Quantify2(:,4);
table1(:,4) = Quantify2(:,7);
table1(:,5) = Quantify2(:,1);

% Exclude samples that don't meet Chi-Squared criteria
table2 = zeros(size(table1));
for i = 1:samples
    if table1(i,2) > 2 | table1(i,4) > 6 | table1(i,1) < 0.01 | table1(i,3)
< 1.2
        table2(i,:) = NaN;
    else
        table2(i,:) = table1(i,:);
    end
end
table2(isnan(table2(:,1)),:) = [];

% Create a 3rd table with the average oxygenation and hemoglobin
table3(1,1) = mean(table2(:,1));
table3(2,1) = mean(table2(:,3));
table3(3,1) = mean(table2(:,5)*10);

disp(table3);
```

tamcount.m

```
%% Gage Greening
% University of Arkansas
% College of Engineering
```

```
% Department of Biomedical Engineering
% May 24, 2018
% tamcount.m

clear all; close all; clc;

%% Load in 12 image files
Files = dir('*.tif');
numfiles = length(Files);
mydata = cell(1, numfiles);

for k = 1:numfiles
  mydata{k} = imread(Files(k).name);
end

x = mydata{1};
[height width] = size(x);

error = round(height * 0.06);

%% Mark the macrophages you see in the images; click ENTER when done for
each image
figure
a=imshow(mydata{1}); set(gcf, 'Units', 'Normalized', 'OuterPosition', [0.5
0.5 0.5 0.5]);
imcontrast(a);
[x01,y01] = getpts;

figure
b=imshow(mydata{2}); set(gcf, 'Units', 'Normalized', 'OuterPosition', [0.5
0.5 0.5 0.5]);
imcontrast(b);
[x02,y02] = getpts;

figure
c=imshow(mydata{3}); set(gcf, 'Units', 'Normalized', 'OuterPosition', [0.5
0.5 0.5 0.5]);
imcontrast(c);
[x03,y03] = getpts;

figure
d=imshow(mydata{4}); set(gcf, 'Units', 'Normalized', 'OuterPosition', [0.5
0.5 0.5 0.5]);
imcontrast(d);
[x04,y04] = getpts;

figure
e=imshow(mydata{5}); set(gcf, 'Units', 'Normalized', 'OuterPosition', [0.5
0.5 0.5 0.5]);
imcontrast(e);
[x05,y05] = getpts;

figure
```

```
f=imshow(mydata{6}); set(gcf, 'Units', 'Normalized', 'OuterPosition', [0.5
0.5 0.5 0.5]);
imcontrast(f);
[x06,y06] = getpts;

figure
g=imshow(mydata{7}); set(gcf, 'Units', 'Normalized', 'OuterPosition', [0.5
0.5 0.5 0.5]);
imcontrast(g);
[x07,y07] = getpts;

figure
h=imshow(mydata{8}); set(gcf, 'Units', 'Normalized', 'OuterPosition', [0.5
0.5 0.5 0.5]);
imcontrast(h);
[x08,y08] = getpts;

figure
i=imshow(mydata{9}); set(gcf, 'Units', 'Normalized', 'OuterPosition', [0.5
0.5 0.5 0.5]);
imcontrast(i);
[x09,y09] = getpts;

figure
j=imshow(mydata{10}); set(gcf, 'Units', 'Normalized', 'OuterPosition', [0.5
0.5 0.5 0.5]);
imcontrast(j);
[x10,y10] = getpts;

figure
k=imshow(mydata{11}); set(gcf, 'Units', 'Normalized', 'OuterPosition', [0.5
0.5 0.5 0.5]);
imcontrast(k);
[x11,y11] = getpts;

figure
l=imshow(mydata{12}); set(gcf, 'Units', 'Normalized', 'OuterPosition', [0.5
0.5 0.5 0.5]);
imcontrast(l);
[x12,y12] = getpts;

close all;

%% Exclude duplicate M1 TAMs

plot(x01,y01,'k*'); hold on;
plot(x02,y02,'k*'); hold on;
plot(x03,y03,'k*'); hold on;
plot(x04,y04,'k*'); hold on;

max_length_M1tams(1) = length(x01);
max_length_M1tams(2) = length(x02);
max_length_M1tams(3) = length(x03);
max_length_M1tams(4) = length(x04);
```

```
M1tams_x =
zeros(max_length_M1tams(1)+max_length_M1tams(2)+max_length_M1tams(3)+max_len
gth_M1tams(4),1);
M1tams_y =
zeros(max_length_M1tams(1)+max_length_M1tams(2)+max_length_M1tams(3)+max_len
gth_M1tams(4),1);

M1tams_x(1:length(x01),1) = x01;
M1tams_x(1+length(x01):length(x01)+length(x02),1) = x02;
M1tams_x(1+length(x01)+length(x02):length(x01)+length(x02)+length(x03),1) =
x03;
M1tams_x(1+length(x01)+length(x02)+length(x03):length(x01)+length(x02)+lengt
h(x03)+length(x04),1) = x04;

M1tams_y(1:length(x01),1) = y01;
M1tams_y(1+length(x01):length(x01)+length(x02),1) = y02;
M1tams_y(1+length(x01)+length(x02):length(x01)+length(x02)+length(x03),1) =
y03;
M1tams_y(1+length(x01)+length(x02)+length(x03):length(x01)+length(x02)+lengt
h(x03)+length(x04),1) = y04;

M1tams = zeros(length(M1tams_x),2);
M1tams(:,1) = round(M1tams_x); M1tams(:,2) = round(M1tams_y);
M1tams(:,3) = M1tams(:,1).*M1tams(:,2);
M1tams_update = M1tams;

distance = zeros(length(M1tams(:,1)),length(M1tams(:,1)));
for i = 1:length(M1tams(:,1))
    for j = 1:length(M1tams(:,1))
        if i > j
            distance(i,j) = sqrt(((M1tams(i,1) - M1tams(j,1))^2) +
((M1tams(i,2) - M1tams(j,2))^2));
        else
            distance(i,j) = 0;
        end
    end
end
distance(distance==0) = NaN;

distance_logic = zeros(length(M1tams(:,1)),length(M1tams(:,1)));
for i = 1:length(M1tams(:,1))
    for j = 1:length(M1tams(:,1))
        if distance(i,j) < error
            distance_logic(i,j) = 1;
        else
            distance_logic(i,j) = 0;
        end
    end
end

for i = 1:length(M1tams(:,1))
    for j = 1:length(M1tams(:,1))
        if distance_logic(i,j) == 1
            M1tams_update(i,1) = 0; M1tams_update(i,2) = 0;
```

```
        end
    end
end

temp = find(M1tams_update(:,1) > 0);
count_M1 = length(temp);
M1tams_update = M1tams_update(temp,:);

%% Exclude duplicate TAMs

plot(x05,y05,'k*'); hold on;
plot(x06,y06,'k*'); hold on;
plot(x07,y07,'k*'); hold on;
plot(x08,y08,'k*'); hold on;

max_length_Mtams(1) = length(x05);
max_length_Mtams(2) = length(x06);
max_length_Mtams(3) = length(x07);
max_length_Mtams(4) = length(x08);

Mtams_x =
zeros(max_length_Mtams(1)+max_length_Mtams(2)+max_length_Mtams(3)+max_length
_Mtams(4),1);
Mtams_y =
zeros(max_length_Mtams(1)+max_length_Mtams(2)+max_length_Mtams(3)+max_length
_Mtams(4),1);

Mtams_x(1:length(x05),1) = x05;
Mtams_x(1+length(x05):length(x05)+length(x06),1) = x06;
Mtams_x(1+length(x05)+length(x06):length(x05)+length(x06)+length(x07),1) =
x07;
Mtams_x(1+length(x05)+length(x06)+length(x07):length(x05)+length(x06)+length
(x07)+length(x08),1) = x08;

Mtams_y(1:length(x05),1) = y05;
Mtams_y(1+length(x05):length(x05)+length(x06),1) = y06;
Mtams_y(1+length(x05)+length(x06):length(x05)+length(x06)+length(x07),1) =
y07;
Mtams_y(1+length(x05)+length(x06)+length(x07):length(x05)+length(x06)+length
(x07)+length(x08),1) = y08;

Mtams = zeros(length(Mtams_x),2);
Mtams(:,1) = round(Mtams_x); Mtams(:,2) = round(Mtams_y);
Mtams(:,3) = Mtams(:,1).*Mtams(:,2);
Mtams_update = Mtams;

distance = zeros(length(Mtams(:,1)),length(Mtams(:,1)));
for i = 1:length(Mtams(:,1))
    for j = 1:length(Mtams(:,1))
        if i > j
            distance(i,j) = sqrt(((Mtams(i,1) - Mtams(j,1))^2) +
((Mtams(i,2) - Mtams(j,2))^2));
        else
            distance(i,j) = 0;
        end
```

```
    end
end
distance(distance==0) = NaN;

distance_logic = zeros(length(Mtams(:,1)),length(Mtams(:,1)));
for i = 1:length(Mtams(:,1))
    for j = 1:length(Mtams(:,1))
        if distance(i,j) < error
            distance_logic(i,j) = 1;
        else
            distance_logic(i,j) = 0;
        end
    end
end

for i = 1:length(Mtams(:,1))
    for j = 1:length(Mtams(:,1))
        if distance_logic(i,j) == 1
            Mtams_update(i,1) = 0; Mtams_update(i,2) = 0;
        end
    end
end

temp = find(Mtams_update(:,1) > 0);
count_total = length(temp);
Mtams_update = Mtams_update(temp,:);

%% Exclude duplicate M2 TAMs

plot(x09,y09,'k*'); hold on;
plot(x10,y10,'k*'); hold on;
plot(x11,y11,'k*'); hold on;
plot(x12,y12,'k*'); hold on;

max_length_M2tams(1) = length(x09);
max_length_M2tams(2) = length(x10);
max_length_M2tams(3) = length(x11);
max_length_M2tams(4) = length(x12);

M2tams_x =
zeros(max_length_M2tams(1)+max_length_M2tams(2)+max_length_M2tams(3)+max_len
gth_M2tams(4),1);
M2tams_y =
zeros(max_length_M2tams(1)+max_length_M2tams(2)+max_length_M2tams(3)+max_len
gth_M2tams(4),1);

M2tams_x(1:length(x09),1) = x09;
M2tams_x(1+length(x09):length(x09)+length(x10),1) = x10;
M2tams_x(1+length(x09)+length(x10):length(x09)+length(x10)+length(x11),1) =
x11;
M2tams_x(1+length(x09)+length(x10)+length(x11):length(x09)+length(x10)+lengt
h(x11)+length(x12),1) = x12;

M2tams_y(1:length(x09),1) = y09;
M2tams_y(1+length(x09):length(x09)+length(x10),1) = y10;
```

```
M2tams_y(1+length(x09)+length(x10):length(x09)+length(x10)+length(x11),1) =
y11;
M2tams_y(1+length(x09)+length(x10)+length(x11):length(x09)+length(x10)+lengt
h(x11)+length(x12),1) = y12;

M2tams = zeros(length(M2tams_x),2);
M2tams(:,1) = round(M2tams_x); M2tams(:,2) = round(M2tams_y);
M2tams(:,3) = M2tams(:,1).*M2tams(:,2);
M2tams_update = M2tams;

distance = zeros(length(M2tams(:,1)),length(M2tams(:,1)));
for i = 1:length(M2tams(:,1))
    for j = 1:length(M2tams(:,1))
        if i > j
            distance(i,j) = sqrt(((M2tams(i,1) - M2tams(j,1))^2) +
((M2tams(i,2) - M2tams(j,2))^2));
        else
            distance(i,j) = 0;
        end
    end
end
distance(distance==0) = NaN;

distance_logic = zeros(length(M2tams(:,1)),length(M2tams(:,1)));
for i = 1:length(M2tams(:,1))
    for j = 1:length(M2tams(:,1))
        if distance(i,j) < error
            distance_logic(i,j) = 1;
        else
            distance_logic(i,j) = 0;
        end
    end
end

for i = 1:length(M2tams(:,1))
    for j = 1:length(M2tams(:,1))
        if distance_logic(i,j) == 1
            M2tams_update(i,1) = 0; M2tams_update(i,2) = 0;
        end
    end
end

temp = find(M2tams_update(:,1) > 0);
count_M2 = length(temp);
M2tams_update = M2tams_update(temp,:);

%% Reorder matrices from left to right

TAM_M0 = sortrows(Mtams_update);
TAM_M1 = sortrows(M1tams_update);
TAM_M2 = sortrows(M2tams_update);

figure(1)
subplot(1,3,1)
imagesc(mydata{3}); colormap gray; axis image; hold on;
```

```
plot(M1tams_update(:,1),M1tams_update(:,2),'b*'); hold off;
title('M1 Macrophages (CD80)');
figure(1)
subplot(1,3,2)
imagesc(mydata{7}); colormap gray; axis image; hold on;
plot(Mtams_update(:,1),Mtams_update(:,2),'g*'); hold off;
title('All Macrophages (CD68)');
figure(1)
subplot(1,3,3)
imagesc(mydata{11}); colormap gray; axis image; hold on;
plot(M2tams_update(:,1),M2tams_update(:,2),'r*'); hold off;
title('M2 Macrophages (CD206)');

%% Exclude M1 TAMs without associated M0 (CD68) stain

r = cell(length(TAM_M1),1);
c = cell(length(TAM_M1),1);
s = cell(length(TAM_M1),1);
check = zeros(length(TAM_M1),1);
TAM_M1_new = TAM_M1;
newerror = 0.05;
for i = 1:length(TAM_M1)
    r{i} = find(TAM_M0(:,1)>TAM_M1(i,1)-(width*newerror) &
TAM_M0(:,1)<TAM_M1(i,1)+(width*newerror));
    c{i} = find(TAM_M0(:,2)>TAM_M1(i,2)-(width*newerror) &
TAM_M0(:,2)<TAM_M1(i,2)+(width*newerror));
    s{i} = intersect(r{i},c{i});
    check(i) = any(s{i});
    if check(i) == 1
        TAM_M1_new(i,1) = TAM_M1(i,1);
        TAM_M1_new(i,2) = TAM_M1(i,2);
        TAM_M1_new(i,3) = TAM_M1(i,3);
    else
        TAM_M1_new(i,1) = 0;
        TAM_M1_new(i,2) = 0;
        TAM_M1_new(i,3) = 0;
    end
end
temp = find(TAM_M1_new(:,1) > 0);
TAM_M1_new = TAM_M1_new(temp,:);

%% Exclude M2 TAMs without associated M0 (CD68) stain

r = cell(length(TAM_M2),1);
c = cell(length(TAM_M2),1);
s = cell(length(TAM_M2),1);
check = zeros(length(TAM_M2),1);
TAM_M2_new = TAM_M2;
newerror = 0.05;
for i = 1:length(TAM_M2)
    r{i} = find(TAM_M0(:,1)>TAM_M2(i,1)-(width*newerror) &
TAM_M0(:,1)<TAM_M2(i,1)+(width*newerror));
    c{i} = find(TAM_M0(:,2)>TAM_M2(i,2)-(width*newerror) &
TAM_M0(:,2)<TAM_M2(i,2)+(width*newerror));
    s{i} = intersect(r{i},c{i});
    check(i) = any(s{i});
```

```
    if check(i) == 1
        TAM_M2_new(i,1) = TAM_M2(i,1);
        TAM_M2_new(i,2) = TAM_M2(i,2);
        TAM_M2_new(i,3) = TAM_M2(i,3);
    else
        TAM_M2_new(i,1) = 0;
        TAM_M2_new(i,2) = 0;
        TAM_M2_new(i,3) = 0;
    end
end
temp = find(TAM_M2_new(:,1) > 0);
TAM_M2_new = TAM_M2_new(temp,:);

%% M1/M2 Ratio

ratio = length(TAM_M1_new) / length(TAM_M2_new);
fprintf('\nM1/M2 Ratio: %.2f\n\n',ratio);

%% Final Data

close all;

figure(2)
subplot(1,3,1)
imagesc(mydata{3}); colormap gray; axis image; hold on;
plot(M1tams_update(:,1),M1tams_update(:,2),'b*'); hold off;
title('M1 Macrophages (CD80)');
figure(2)
subplot(1,3,2)
imagesc(mydata{7}); colormap gray; axis image; hold on;
plot(Mtams_update(:,1),Mtams_update(:,2),'g*'); hold off;
title('All Macrophages (CD68)');
figure(2)
subplot(1,3,3)
imagesc(mydata{11}); colormap gray; axis image; hold on;
plot(M2tams_update(:,1),M2tams_update(:,2),'r*'); hold off;
title('M2 Macrophages (CD206)');

a = 'M1/M2 Ratio = ';
b = num2str(ratio*100);
c = '%';
d = strcat(a,b,c);

fig = gcf;
saveas(fig,'tamcount.jpg');



format compact;
M0_totalcount = length(Mtams_update(:,1));
M1_totalcount = length(TAM_M1_new(:,1));
M2_totalcount = length(TAM_M2_new(:,1));

fprintf('M1:\t\t %.1d\n',M1_totalcount);
fprintf('Total:\t %.1d\n',M0_totalcount);
fprintf('M2:\t\t %.1d\n',M2_totalcount);
```

samplingdepth.m

```
%% Gage Greening
% University of Arkansas
% College of Engineering
% Department of Biomedical Engineering
% samplingdepth_3mm.m

% Initialize Variables
close all; clear all; clc;
n = input('Number of Phantoms: ');
name = ['s (01)';'s (02)';'s (03)';'s (04)';'s (05)';'s (06)';'s (07)';'s
(08)';'s (09)';'s (10)';'s (11)';'s (12)';'s (13)';'s (14)';'s (15)';'s
(16)';'s (17)';'s (18)';'s (19)';'s (20)';'s (21)';'s (22)';'s (23)';'s
(24)';'s (25)';'s (26)';'s (27)';'s (28)';'s (29)';'s (30)';'s (31)';'s
(32)';'s (33)';'s (34)';'s (35)';'s (36)';'s (37)';'s (38)';'s (39)';'s
(40)';'s (41)';'s (42)';'s (43)';'s (44)';'s (45)';'s (46)';'s (47)';'s
(48)';'s (49)';'s (50)';'s (51)';'s (52)';'s (53)';'s (54)';'s (55)';'s
(56)';'s (57)';'s (58)';'s (59)';'s (60)';'s (61)';'s (62)';'s (63)';'s
(64)';'s (65)';'s (66)';'s (67)';'s (68)';'s (69)';'s (70)';'s (71)';'s
(72)';'s (73)';'s (74)';'s (75)';'s (76)';'s (77)';'s (78)';'s (79)';'s
(80)';'s (81)';'s (82)';'s (83)';'s (84)';'s (85)';'s (86)';'s (87)';'s
(88)';'s (89)';'s (90)';'s (91)';'s (92)';'s (93)';'s (94)';'s (95)';'s
(96)';'s (97)';'s (98)';'s (99)'];
wavelength = csvread('s (01).csv'); wavelength = wavelength(:,1);
temp = zeros(2048,2);
specori = zeros(2048,n);

% Determine matrix index for getting 1 nm resolution in spectra
x = linspace(1,1050,1050);
wavelength_550to890 = round(wavelength(575:1624));
p = polyfit(wavelength_550to890,x',2);
x1 = linspace(550,890,341);
y1 = round(polyval(p,x1))';

% Create matrix with all spectra of increasing distance from abs. layer
for i = 1:n
    temp = csvread([name(i,:),'.csv']);
    specori(:,i) = temp(:,2);
    for i = 1:2048
        for j = 1:n
            specori(i,j) = round(specori(i,j));
        end
    end
end
specori = specori - 300;

spectra_550to890 = specori(575:1624,:);
spectra = spectra_550to890([y1(1:341)],:);
wavelength = linspace(550,890,341)';

maxspec = spectra(:,n);
halfspec = round(maxspec./2);

x1 = zeros(341,1);
```

```
x2 = zeros(341,1);
sampdepth = zeros(341,1);
for i = 1:341
    x1 = find(spectra(i,:)<halfspec(i));
    x2(i) = max(x1);
    sampdepth = (((x2*50)/1000)-0.05);
end

scatter(wavelength,sampdepth); axis square; box on;
xlabel('Wavelength (nm)')
ylabel('Sampling depth (mm)');
title('Sampling depth of probe into optical phantom');

save('sd.mat','wavelength','sampdepth');
clc;
```

Input Text Files for PostProcess3mm.m

Wavelength	Hb.txt	HbO2.txt	mel.txt
250	1.747845	1.645147	30.92699
251	1.747845	1.640806	30.92699
252	1.747845	1.636465	30.65722
253	1.747845	1.652806	30.52234
254	1.747845	1.669147	30.38745
255	1.756279	1.685643	30.25257
256	1.764713	1.70214	30.11768
257	1.77414	1.726605	29.9828
258	1.783566	1.75107	29.84791
259	1.793302	1.777674	29.71303
260	1.803039	1.804279	29.57814
261	1.812868	1.833829	29.44326
262	1.822698	1.86338	29.31882
263	1.832868	1.896124	29.2008
264	1.843039	1.928868	29.08278
265	1.853364	1.962078	28.96475
266	1.86369	1.995287	28.84673
267	1.874047	2.029147	28.7287
268	1.884403	2.063008	28.61068
269	1.89476	2.086295	28.49265
270	1.905116	2.109581	28.37463
271	1.906791	2.118605	28.2566
272	1.908465	2.127628	28.13858
273	1.899597	2.136744	28.02055
274	1.890729	2.14586	27.90253
275	1.88186	2.138233	27.78451
276	1.872992	2.130605	27.66648
277	1.865488	2.118171	27.54846
278	1.857985	2.105736	27.43043
279	1.850481	2.075628	27.31241
280	1.842977	2.045519	27.19049
281	1.833333	2.012837	27.06691
282	1.82369	1.980155	26.94333

283	1.801922	1.937985	26.81975
284	1.780155	1.895814	26.69617
285	1.758357	1.85107	26.57258
286	1.736558	1.806326	26.449
287	1.698822	1.744124	26.32542
288	1.661085	1.681922	26.20184
289	1.593054	1.652992	26.07826
290	1.525023	1.624062	25.95467
291	1.472868	1.578977	25.83109
292	1.420713	1.533891	25.70751
293	1.375628	1.450171	25.58393
294	1.330543	1.36645	25.46035
295	1.262946	1.298078	25.33702
296	1.195349	1.229705	25.23869
297	1.136	1.164341	25.14036
298	1.076651	1.098977	25.04204
299	1.03786	1.060899	24.94371
300	0.99907	1.022822	24.84538
301	0.974729	1.001395	24.74706
302	0.950388	0.979969	24.64873
303	0.931225	0.970233	24.5504
304	0.912062	0.960496	24.45208
305	0.897178	0.963597	24.35375
306	0.882295	0.966698	24.25542
307	0.887814	0.970605	24.15709
308	0.893333	0.974512	24.05877
309	0.90524	0.978357	23.96044
310	0.917147	0.982202	23.86211
311	0.941116	1.002512	23.76379
312	0.965085	1.022822	23.66546
313	0.989085	1.046419	23.56745
314	1.013085	1.070016	23.47307
315	1.036093	1.096279	23.37869
316	1.059101	1.122543	23.28431
317	1.08155	1.146822	23.18993
318	1.104	1.171101	23.09555
319	1.129581	1.196031	23.00117
320	1.155163	1.220961	22.90679
321	1.184434	1.248124	22.81241
322	1.213705	1.275287	22.71803
323	1.242977	1.304093	22.62365
324	1.272248	1.332899	22.52927
325	1.299628	1.362543	22.42292
326	1.327008	1.392186	22.31477
327	1.349674	1.422977	22.20663
328	1.372341	1.453767	22.09849
329	1.390481	1.482791	21.99034
330	1.40862	1.511814	21.8822
331	1.426729	1.538574	21.77406
332	1.444837	1.565333	21.66592

333	1.462977	1.585023	21.55777
334	1.481116	1.604713	21.44963
335	1.51414	1.616062	21.34149
336	1.547163	1.627411	21.23335
337	1.583473	1.638915	21.1252
338	1.619783	1.650419	21.01706
339	1.65076	1.661519	20.90892
340	1.681736	1.67262	20.80077
341	1.701302	1.681736	20.69263
342	1.720868	1.690853	20.58449
343	1.740465	1.698853	20.46183
344	1.760062	1.706853	20.33825
345	1.779659	1.698636	20.21467
346	1.799256	1.690419	20.09109
347	1.820186	1.682295	19.96751
348	1.841116	1.674171	19.84392
349	1.867008	1.663256	19.72034
350	1.892899	1.652341	19.59676
351	1.918822	1.640434	19.47318
352	1.944744	1.628527	19.3496
353	1.970636	1.618109	19.22601
354	1.996527	1.60769	19.10243
355	2.02245	1.591194	18.97885
356	2.048372	1.574698	18.85527
357	2.060093	1.545705	18.73169
358	2.071814	1.516713	18.61756
359	2.081953	1.492806	18.53178
360	2.092093	1.468899	18.44601
361	2.100651	1.44955	18.36024
362	2.109209	1.430202	18.27447
363	2.116403	1.411504	18.1887
364	2.123597	1.392806	18.10292
365	2.130791	1.382326	18.01715
366	2.137985	1.371845	17.93138
367	2.145395	1.36431	17.84561
368	2.152806	1.356775	17.75984
369	2.161426	1.361922	17.67406
370	2.170047	1.36707	17.58829
371	2.178698	1.39355	17.50252
372	2.187349	1.420031	17.41675
373	2.195969	1.447535	17.33097
374	2.204589	1.475039	17.2452
375	2.21324	1.504465	17.15943
376	2.221891	1.533891	17.07366
377	2.230512	1.568744	16.98789
378	2.239132	1.603597	16.90211
379	2.245395	1.651132	16.81634
380	2.251659	1.698667	16.73057
381	2.251659	1.756062	16.6448
382	2.251659	1.813457	16.55902

383	2.278295	1.878977	16.46076
384	2.30493	1.944496	16.35346
385	2.34555	2.019783	16.24616
386	2.386171	2.09507	16.13886
387	2.42986	2.195597	16.03156
388	2.47355	2.296124	15.92425
389	2.537395	2.448434	15.81695
390	2.60124	2.600744	15.70965
391	2.696	2.771225	15.60235
392	2.79076	2.941705	15.49504
393	2.880186	3.114729	15.38774
394	2.969612	3.287752	15.28044
395	3.051659	3.439318	15.17314
396	3.133705	3.590884	15.06584
397	3.215783	3.721054	14.95853
398	3.29786	3.851225	14.85123
399	3.379907	3.989426	14.74393
400	3.461953	4.127628	14.63663
401	3.561891	4.267101	14.52932
402	3.661829	4.406574	14.42202
403	3.795008	4.596434	14.31472
404	3.928186	4.786295	14.20742
405	4.061364	5.138946	14.10012
406	4.194543	5.491597	13.99281
407	4.324837	6.019597	13.88551
408	4.455132	6.547597	13.80487
409	4.583814	6.892713	13.72623
410	4.712496	7.237829	13.64759
411	4.847287	7.496434	13.56895
412	4.982078	7.755039	13.49031
413	5.146822	7.941705	13.41168
414	5.311566	8.128372	13.33304
415	5.47631	8.109767	13.2544
416	5.641054	8.091163	13.17576
417	5.810295	8.04186	13.09712
418	5.979535	7.992558	13.01849
419	6.149147	7.72	12.93985
420	6.31876	7.447442	12.86121
421	6.491783	7.071628	12.78257
422	6.664806	6.695814	12.70393
423	6.907597	6.264465	12.6253
424	7.150388	5.833116	12.54666
425	7.310388	5.443938	12.46802
426	7.470388	5.05476	12.38938
427	7.617674	4.722047	12.31074
428	7.764961	4.389333	12.23211
429	7.980155	4.102202	12.15347
430	8.195349	3.81507	12.07483
431	8.377985	3.56738	11.99619
432	8.56062	3.31969	11.92096

433	8.56062	2.941488	11.85542
434	8.56062	2.563287	11.78988
435	8.52093	2.311256	11.72434
436	8.48124	2.059225	11.6588
437	8.128682	1.953178	11.59326
438	7.776124	1.847132	11.52772
439	7.091783	1.71876	11.46218
440	6.407442	1.590388	11.39664
441	6.019535	1.514419	11.3311
442	5.631628	1.43845	11.26556
443	5.007473	1.350574	11.20002
444	4.383318	1.262698	11.13448
445	4.030605	1.223008	11.06894
446	3.677891	1.183318	11.0034
447	3.182512	1.11138	10.93786
448	2.687132	1.039442	10.87231
449	2.144279	1.006667	10.80677
450	1.601426	0.973891	10.74123
451	1.286295	0.943256	10.67569
452	0.971163	0.91262	10.61015
453	0.765969	0.871442	10.54461
454	0.560775	0.830264	10.47907
455	0.518363	0.798822	10.41353
456	0.47595	0.76738	10.34799
457	0.438645	0.751876	10.28245
458	0.40134	0.736372	10.21691
459	0.381978	0.712992	10.15648
460	0.362617	0.689612	10.10642
461	0.343256	0.665116	10.05636
462	0.323895	0.64062	10.0063
463	0.311256	0.628893	9.956237
464	0.298617	0.617166	9.906176
465	0.289947	0.595972	9.856115
466	0.281278	0.574778	9.806055
467	0.27262	0.557705	9.755994
468	0.263963	0.540633	9.705933
469	0.257225	0.527752	9.655872
470	0.250487	0.514871	9.605812
471	0.243926	0.502552	9.555751
472	0.237364	0.490233	9.50569
473	0.235336	0.478555	9.455629
474	0.233309	0.466878	9.405569
475	0.231327	0.457088	9.355508
476	0.229346	0.447299	9.305447
477	0.228295	0.438518	9.255386
478	0.227243	0.429736	9.205326
479	0.226412	0.421296	9.155265
480	0.225581	0.412856	9.105204
481	0.228149	0.405665	9.055143
482	0.230716	0.398474	9.005083

483	0.233284	0.394434	8.955022
484	0.235851	0.390394	8.906236
485	0.238419	0.386434	8.858166
486	0.240986	0.382474	8.810097
487	0.243733	0.378639	8.762028
488	0.246481	0.374803	8.713958
489	0.252574	0.371002	8.665889
490	0.258667	0.3672	8.61782
491	0.264757	0.362567	8.569751
492	0.270847	0.357935	8.521681
493	0.27694	0.353057	8.473612
494	0.283033	0.34818	8.425543
495	0.289122	0.343473	8.377473
496	0.295212	0.338766	8.329404
497	0.301802	0.334189	8.281335
498	0.308391	0.329612	8.233265
499	0.315916	0.327076	8.185196
500	0.323442	0.32454	8.137127
501	0.330967	0.321932	8.089057
502	0.338493	0.319324	8.040988
503	0.346019	0.317941	7.992919
504	0.353544	0.316558	7.94485
505	0.36107	0.312899	7.89678
506	0.368595	0.30924	7.848711
507	0.376121	0.309628	7.800642
508	0.383647	0.310016	7.752572
509	0.391619	0.310319	7.704503
510	0.399591	0.310623	7.656434
511	0.408608	0.311516	7.608364
512	0.417625	0.312409	7.560295
513	0.426642	0.314571	7.512226
514	0.435659	0.316732	7.464156
515	0.444676	0.321169	7.416087
516	0.453693	0.325606	7.368018
517	0.46271	0.337296	7.319949
518	0.471727	0.348986	7.271879
519	0.480744	0.362109	7.22381
520	0.489761	0.375231	7.175741
521	0.499541	0.392657	7.127671
522	0.509321	0.410084	7.079602
523	0.521309	0.431935	7.031533
524	0.533296	0.453786	6.98398
525	0.545284	0.478803	6.938063
526	0.557271	0.50382	6.892146
527	0.569256	0.530902	6.846229
528	0.58124	0.557985	6.800313
529	0.593228	0.588735	6.754396
530	0.605216	0.619485	6.708479
531	0.617212	0.649867	6.662562
532	0.629209	0.680248	6.616645

533	0.640868	0.703876	6.570728
534	0.652527	0.727504	6.524811
535	0.664186	0.749426	6.478895
536	0.675845	0.771349	6.432978
537	0.687473	0.786543	6.387061
538	0.699101	0.801736	6.341144
539	0.710729	0.81355	6.295227
540	0.722357	0.825364	6.24931
541	0.734419	0.825798	6.203393
542	0.746481	0.826233	6.157477
543	0.758574	0.816961	6.11156
544	0.770667	0.80769	6.065643
545	0.78276	0.790419	6.019726
546	0.794853	0.773147	5.973809
547	0.804372	0.748279	5.927892
548	0.813891	0.723411	5.881976
549	0.820992	0.695163	5.836059
550	0.828093	0.666915	5.790142
551	0.833271	0.641017	5.74827
552	0.83845	0.615119	5.715836
553	0.84186	0.592949	5.683402
554	0.845271	0.570778	5.650968
555	0.845426	0.552651	5.618534
556	0.845581	0.534524	5.586101
557	0.842667	0.526611	5.553667
558	0.839752	0.518698	5.521233
559	0.836837	0.512164	5.488799
560	0.833922	0.505631	5.456365
561	0.822202	0.505684	5.423931
562	0.810481	0.505736	5.391498
563	0.797271	0.51578	5.359064
564	0.784062	0.525823	5.32663
565	0.770543	0.54582	5.294196
566	0.757023	0.565817	5.261762
567	0.74245	0.594319	5.229328
568	0.727876	0.622822	5.196894
569	0.713333	0.656341	5.164461
570	0.698791	0.68986	5.132027
571	0.685364	0.726109	5.099593
572	0.671938	0.762357	5.067159
573	0.659349	0.794419	5.034725
574	0.64676	0.826481	5.002291
575	0.634171	0.843783	4.969857
576	0.621581	0.861085	4.937424
577	0.608989	0.854791	4.90499
578	0.596397	0.848496	4.872556
579	0.585175	0.812651	4.840122
580	0.573953	0.776806	4.807688
581	0.563538	0.724093	4.775254
582	0.553122	0.67138	4.742821

583	0.542707	0.604214	4.710387
584	0.532291	0.537048	4.677953
585	0.520809	0.474729	4.645519
586	0.509327	0.412409	4.613085
587	0.495557	0.359408	4.580651
588	0.481786	0.306406	4.548217
589	0.460462	0.264837	4.517434
590	0.439138	0.223268	4.497694
591	0.417011	0.192785	4.477953
592	0.394884	0.162301	4.458213
593	0.37244	0.140676	4.438473
594	0.349997	0.119051	4.418732
595	0.328487	0.103585	4.398992
596	0.306977	0.088118	4.379252
597	0.285724	0.078977	4.359512
598	0.264471	0.069836	4.339771
599	0.246012	0.059724	4.320031
600	0.227553	0.049612	4.300291
601	0.219377	0.045457	4.280551
602	0.2112	0.041302	4.26081
603	0.203023	0.037147	4.24107
604	0.194847	0.032992	4.22133
605	0.186673	0.030366	4.20159
606	0.178499	0.02774	4.181849
607	0.170471	0.026642	4.162109
608	0.162443	0.025544	4.142369
609	0.154428	0.024447	4.122629
610	0.146412	0.023349	4.102888
611	0.139805	0.022251	4.083148
612	0.133197	0.021153	4.063408
613	0.126769	0.020056	4.043668
614	0.120341	0.018958	4.023927
615	0.117107	0.018084	4.004187
616	0.113873	0.017209	3.983271
617	0.110636	0.016558	3.957
618	0.107398	0.015907	3.93073
619	0.104161	0.015256	3.904459
620	0.100924	0.014605	3.878188
621	0.098471	0.013953	3.851917
622	0.096019	0.013302	3.825646
623	0.093798	0.012651	3.799375
624	0.091578	0.012	3.773104
625	0.089355	0.011485	3.746833
626	0.087132	0.010971	3.720563
627	0.085169	0.010592	3.694292
628	0.083206	0.010214	3.668021
629	0.081516	0.009836	3.64175
630	0.079826	0.009457	3.615479
631	0.078136	0.009079	3.589208
632	0.076447	0.008701	3.562937

633	0.074896	0.008322	3.536666
634	0.073346	0.007944	3.510396
635	0.07235	0.007684	3.484125
636	0.071355	0.007423	3.457854
637	0.070357	0.007281	3.431583
638	0.069358	0.007138	3.405312
639	0.068363	0.006995	3.379041
640	0.067367	0.006853	3.35277
641	0.066372	0.00671	3.326499
642	0.065377	0.006567	3.300229
643	0.064381	0.006425	3.276784
644	0.063386	0.006282	3.262801
645	0.06243	0.006167	3.248819
646	0.061474	0.006053	3.234836
647	0.060641	0.005966	3.220853
648	0.059808	0.005879	3.20687
649	0.058975	0.005792	3.192888
650	0.058141	0.005705	3.178905
651	0.057308	0.005619	3.164922
652	0.056475	0.005532	3.15094
653	0.055642	0.005445	3.136957
654	0.054809	0.005358	3.122974
655	0.053976	0.005278	3.108991
656	0.053142	0.005197	3.095009
657	0.052309	0.005122	3.081026
658	0.051476	0.005048	3.067043
659	0.05075	0.005002	3.05306
660	0.050024	0.004955	3.039078
661	0.049355	0.004912	3.025095
662	0.048687	0.004868	3.011112
663	0.048017	0.004825	2.99713
664	0.047348	0.004781	2.983147
665	0.046679	0.004738	2.969164
666	0.046011	0.004695	2.955181
667	0.045342	0.004657	2.941199
668	0.044673	0.00462	2.927216
669	0.044004	0.004589	2.913233
670	0.043335	0.004558	2.899251
671	0.042666	0.004527	2.885268
672	0.041998	0.004496	2.871285
673	0.041368	0.004462	2.857302
674	0.040739	0.004428	2.84332
675	0.040171	0.0044	2.829337
676	0.039603	0.004372	2.815354
677	0.039035	0.00435	2.801372
678	0.038468	0.004329	2.787389
679	0.0379	0.004316	2.773406
680	0.037332	0.004304	2.759423
681	0.036764	0.004291	2.745323
682	0.036197	0.004279	2.728408

683	0.035629	0.004267	2.711492
684	0.035062	0.004254	2.694576
685	0.034494	0.004242	2.67766
686	0.033926	0.004229	2.660745
687	0.033358	0.004242	2.643829
688	0.032791	0.004254	2.626913
689	0.032302	0.004267	2.609997
690	0.031813	0.004279	2.593082
691	0.031414	0.004291	2.576166
692	0.031015	0.004304	2.55925
693	0.030616	0.004316	2.542335
694	0.030218	0.004329	2.525419
695	0.029819	0.00435	2.508503
696	0.02942	0.004372	2.491587
697	0.02902	0.004403	2.474672
698	0.028621	0.004434	2.457756
699	0.02822	0.004465	2.44084
700	0.027818	0.004496	2.423924
701	0.027405	0.004527	2.407009
702	0.026992	0.004558	2.390093
703	0.02658	0.004589	2.373177
704	0.026167	0.00462	2.356261
705	0.025754	0.004657	2.339346
706	0.025341	0.004695	2.32243
707	0.024946	0.004738	2.305514
708	0.024551	0.004781	2.288598
709	0.024217	0.004825	2.271683
710	0.023883	0.004868	2.254767
711	0.023549	0.004912	2.237851
712	0.023216	0.004955	2.220935
713	0.022882	0.004998	2.209274
714	0.022548	0.005042	2.201263
715	0.022215	0.005095	2.193252
716	0.021881	0.005147	2.185242
717	0.021547	0.005209	2.177231
718	0.021214	0.005271	2.16922
719	0.020885	0.005333	2.16121
720	0.020556	0.005395	2.153199
721	0.020241	0.005457	2.145188
722	0.019925	0.005519	2.137178
723	0.019609	0.005581	2.129167
724	0.019294	0.005643	2.121156
725	0.018978	0.005709	2.113146
726	0.018662	0.005774	2.105135
727	0.018267	0.005842	2.097124
728	0.017873	0.00591	2.089113
729	0.017481	0.005978	2.081103
730	0.017088	0.006047	2.073092
731	0.017088	0.006115	2.065081
732	0.017088	0.006183	2.057071

733	0.017088	0.006251	2.04906
734	0.017088	0.006319	2.041049
735	0.017085	0.006406	2.033261
736	0.017082	0.006493	2.027098
737	0.017072	0.006598	2.020936
738	0.017062	0.006704	2.014774
739	0.017181	0.006809	2.008611
740	0.0173	0.006915	2.002449
741	0.017655	0.00702	1.996287
742	0.01801	0.007126	1.990125
743	0.018365	0.007231	1.983962
744	0.018719	0.007336	1.9778
745	0.019174	0.007448	1.971638
746	0.019629	0.00756	1.965476
747	0.020149	0.007678	1.959313
748	0.02067	0.007795	1.953151
749	0.021229	0.007913	1.946989
750	0.021787	0.008031	1.940826
751	0.02264	0.008149	1.934664
752	0.023493	0.008267	1.928502
753	0.023698	0.008385	1.92234
754	0.023903	0.008502	1.916177
755	0.024048	0.008608	1.910015
756	0.024193	0.008713	1.903853
757	0.024193	0.008806	1.897691
758	0.024193	0.008899	1.891528
759	0.024101	0.008992	1.885366
760	0.024008	0.009085	1.879204
761	0.023697	0.009178	1.873041
762	0.023387	0.009271	1.866879
763	0.023008	0.009364	1.860717
764	0.022629	0.009457	1.854555
765	0.022249	0.009557	1.844935
766	0.021869	0.009656	1.834974
767	0.021487	0.009761	1.825013
768	0.021106	0.009867	1.815052
769	0.020722	0.009972	1.805091
770	0.020339	0.010078	1.79513
771	0.019956	0.010183	1.785169
772	0.019573	0.010288	1.775208
773	0.019189	0.010394	1.765247
774	0.018806	0.010499	1.755286
775	0.018423	0.010592	1.745325
776	0.01804	0.010685	1.735364
777	0.017662	0.010766	1.725403
778	0.017284	0.010847	1.715442
779	0.016979	0.010927	1.705481
780	0.016673	0.011008	1.69552
781	0.016368	0.011088	1.685559
782	0.016063	0.011169	1.675598

783	0.015758	0.01125	1.667512
784	0.015453	0.01133	1.659546
785	0.015148	0.011402	1.651579
786	0.014843	0.011473	1.643613
787	0.014567	0.011535	1.635647
788	0.014291	0.011597	1.627681
789	0.014051	0.011659	1.619715
790	0.013811	0.011721	1.611749
791	0.013571	0.011783	1.603782
792	0.01333	0.011845	1.595816
793	0.01309	0.011907	1.58785
794	0.01285	0.011969	1.579884
795	0.012649	0.012081	1.571918
796	0.012449	0.012192	1.563951
797	0.012289	0.012353	1.555985
798	0.01213	0.012515	1.548019
799	0.01197	0.012583	1.540053
800	0.01181	0.012651	1.532087
801	0.005	0.005	1.524121
802	0.005	0.005	1.516154
803	0.005	0.005	1.508188
804	0.005	0.005	1.500222
805	0.005	0.005	1.492256
806	0.005	0.005	1.48429
807	0.005	0.005	1.476323
808	0.005	0.005	1.468357
809	0.005	0.005	1.460391
810	0.005	0.005	1.452425
811	0.005	0.005	1.444459
812	0.005	0.005	1.436493
813	0.005	0.005	1.428526
814	0.005	0.005	1.42056
815	0.005	0.005	1.412594
816	0.005	0.005	1.404628
817	0.005	0.005	1.396662
818	0.005	0.005	1.388696
819	0.005	0.005	1.380729
820	0.005	0.005	1.372763
821	0.005	0.005	1.364797
822	0.005	0.005	1.356831
823	0.005	0.005	1.348865
824	0.005	0.005	1.340898
825	0.005	0.005	1.332932
826	0.005	0.005	1.324966
827	0.005	0.005	1.317
828	0.005	0.005	1.309034
829	0.005	0.005	1.301068
830	0.005	0.005	1.293101
831	0.005	0.005	1.285135
832	0.005	0.005	1.277169

833	0.005	0.005	1.269203
834	0.005	0.005	1.261237
835	0.005	0.005	1.25327
836	0.005	0.005	1.245304
837	0.005	0.005	1.237338
838	0.005	0.005	1.229372
839	0.005	0.005	1.221406
840	0.005	0.005	1.21344
841	0.005	0.005	1.205473
842	0.005	0.005	1.197507
843	0.005	0.005	1.189541
844	0.005	0.005	1.181575
845	0.005	0.005	1.173609
846	0.005	0.005	1.165642
847	0.005	0.005	1.157676
848	0.005	0.005	1.14971
849	0.005	0.005	1.141744
850	0.005	0.005	1.133778
851	0.005	0.005	1.125812
852	0.005	0.005	1.117845
853	0.005	0.005	1.109879
854	0.005	0.005	1.101913
855	0.005	0.005	1.093947
856	0.005	0.005	1.085981
857	0.005	0.005	1.078014
858	0.005	0.005	1.070048
859	0.005	0.005	1.062082
860	0.005	0.005	1.054116
861	0.005	0.005	1.04615
862	0.005	0.005	1.038184
863	0.005	0.005	1.030217
864	0.005	0.005	1.022251
865	0.005	0.005	1.014285
866	0.005	0.005	1.006319
867	0.005	0.005	0.998353
868	0.005	0.005	0.990387
869	0.005	0.005	0.98242
870	0.005	0.005	0.974454
871	0.005	0.005	0.966488
872	0.005	0.005	0.958522
873	0.005	0.005	0.950556
874	0.005	0.005	0.942589
875	0.005	0.005	0.934623
876	0.005	0.005	0.926657
877	0.005	0.005	0.918691
878	0.005	0.005	0.910725
879	0.005	0.005	0.902759
880	0.005	0.005	0.894792
881	0.005	0.005	0.886826
882	0.005	0.005	0.87886

883	0.005	0.005	0.870894
884	0.005	0.005	0.862928
885	0.005	0.005	0.854961
886	0.005	0.005	0.846995
887	0.005	0.005	0.839029
888	0.005	0.005	0.831063
889	0.005	0.005	0.823097
890	0.005	0.005	0.815131
891	0.005	0.005	0.807164
892	0.005	0.005	0.799198
893	0.005	0.005	0.791232
894	0.005	0.005	0.783266
895	0.005	0.005	0.7753
896	0.005	0.005	0.767333
897	0.005	0.005	0.759367
898	0.005	0.005	0.751401
899	0.005	0.005	0.743435
900	0.005	0.005	0.735469

Engineering Sketches

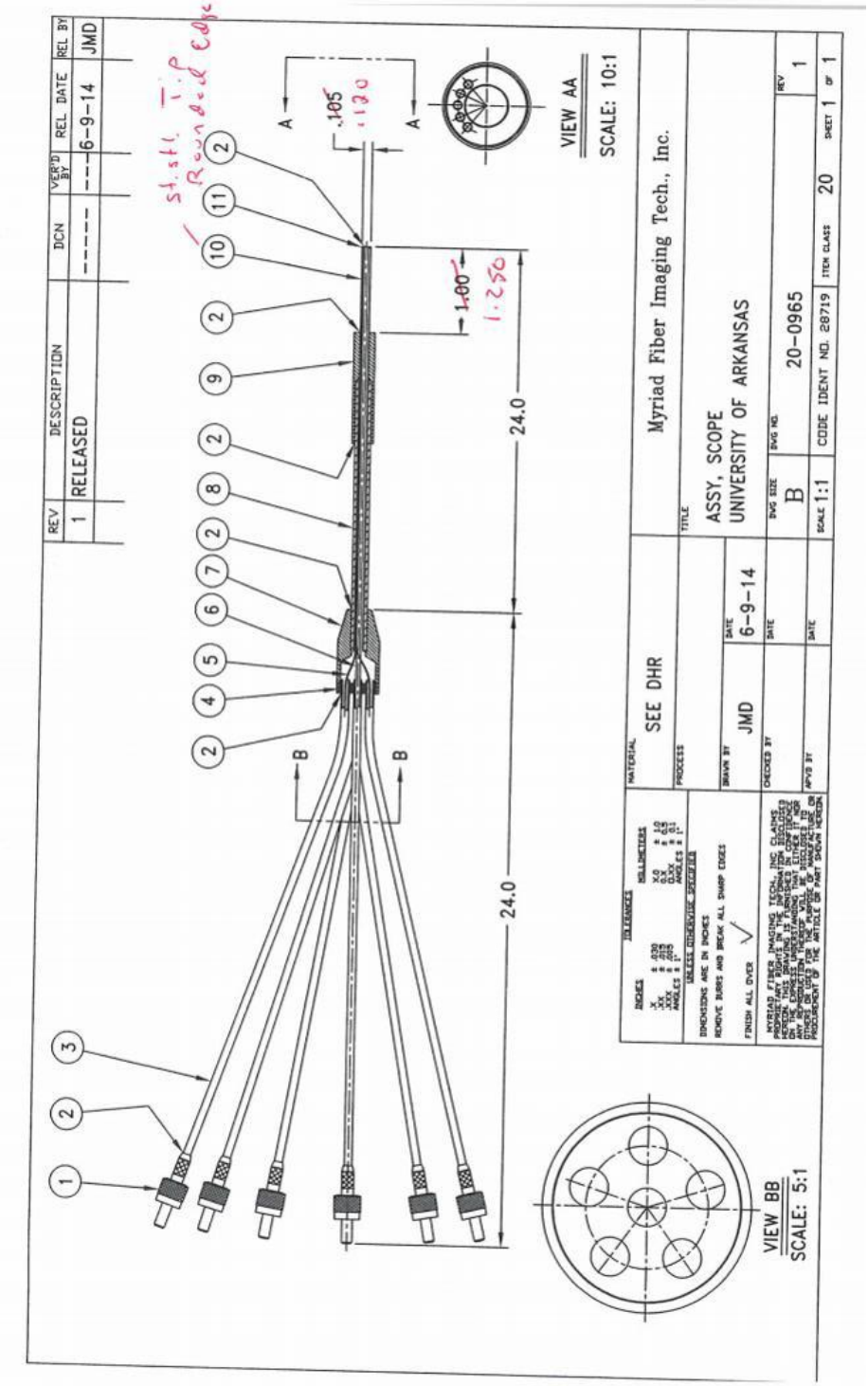

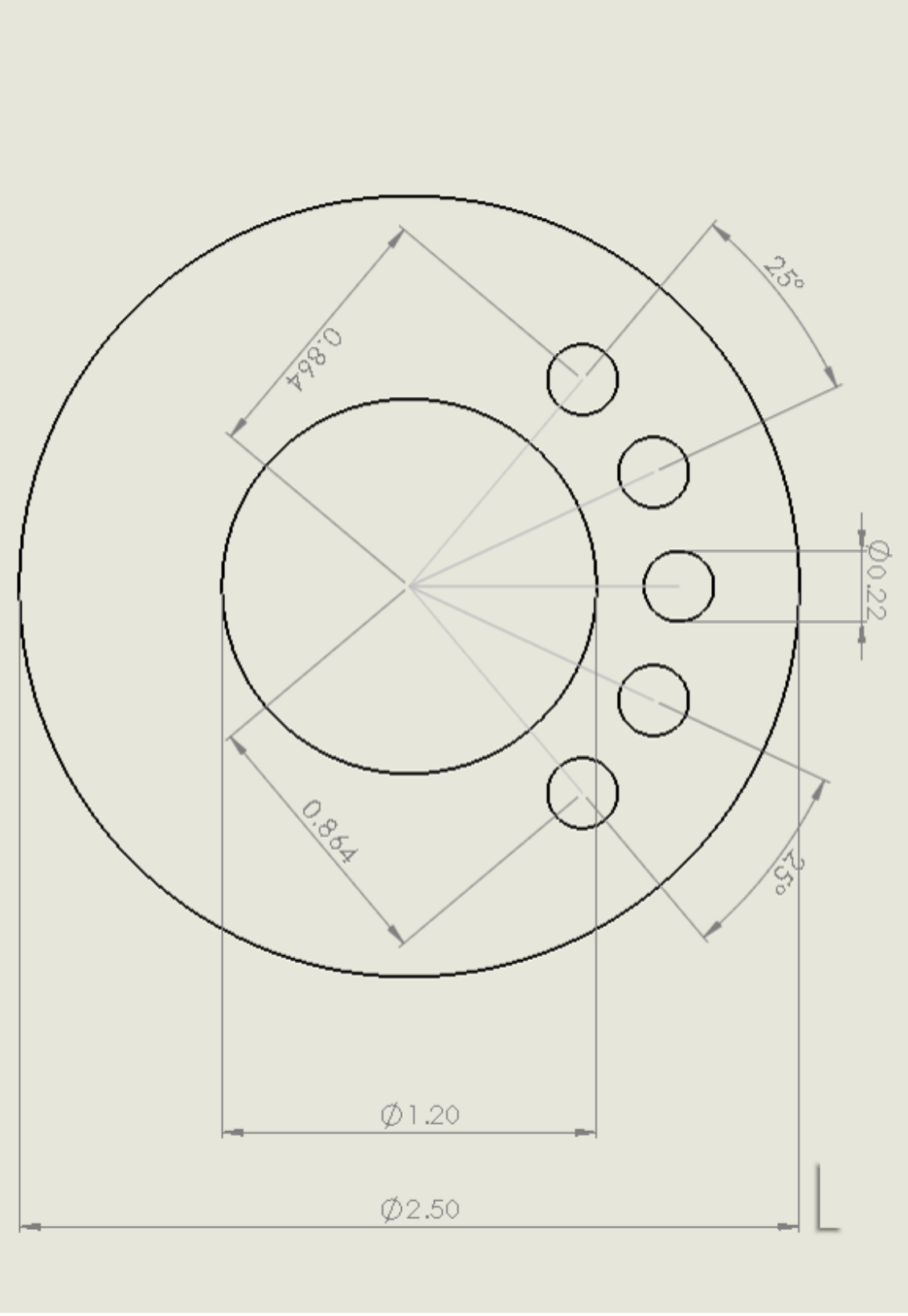
0.864
25°
Ø0.22
0.864
25°
Ø1.20
Ø2.50

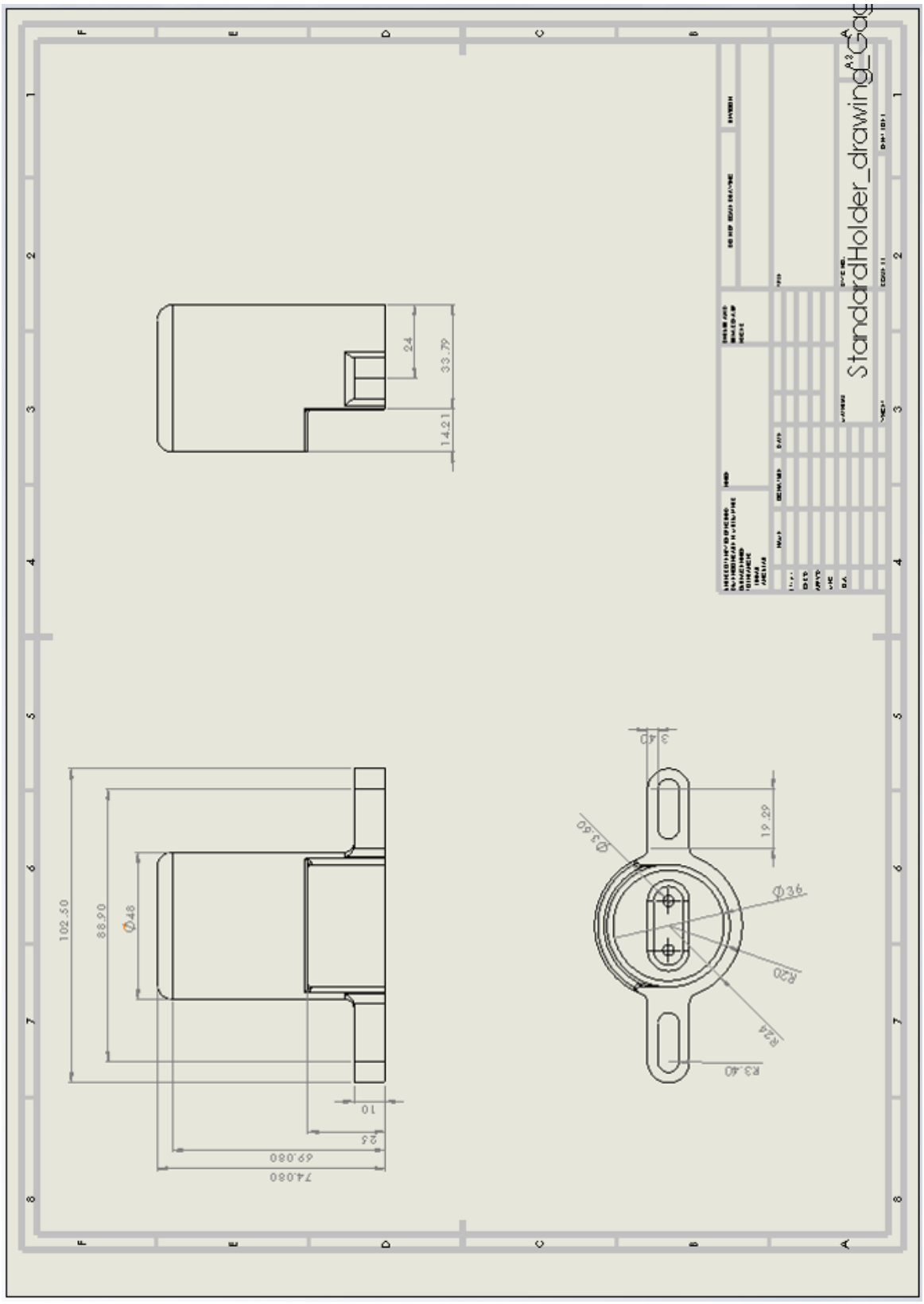
StandardHolder_drawing
24
33.79
14.21
102.50
88.90
Ø48
10
23
69.080
74.080
3.40
19.29
Ø3.60
Ø36
R20
R24
R3.40

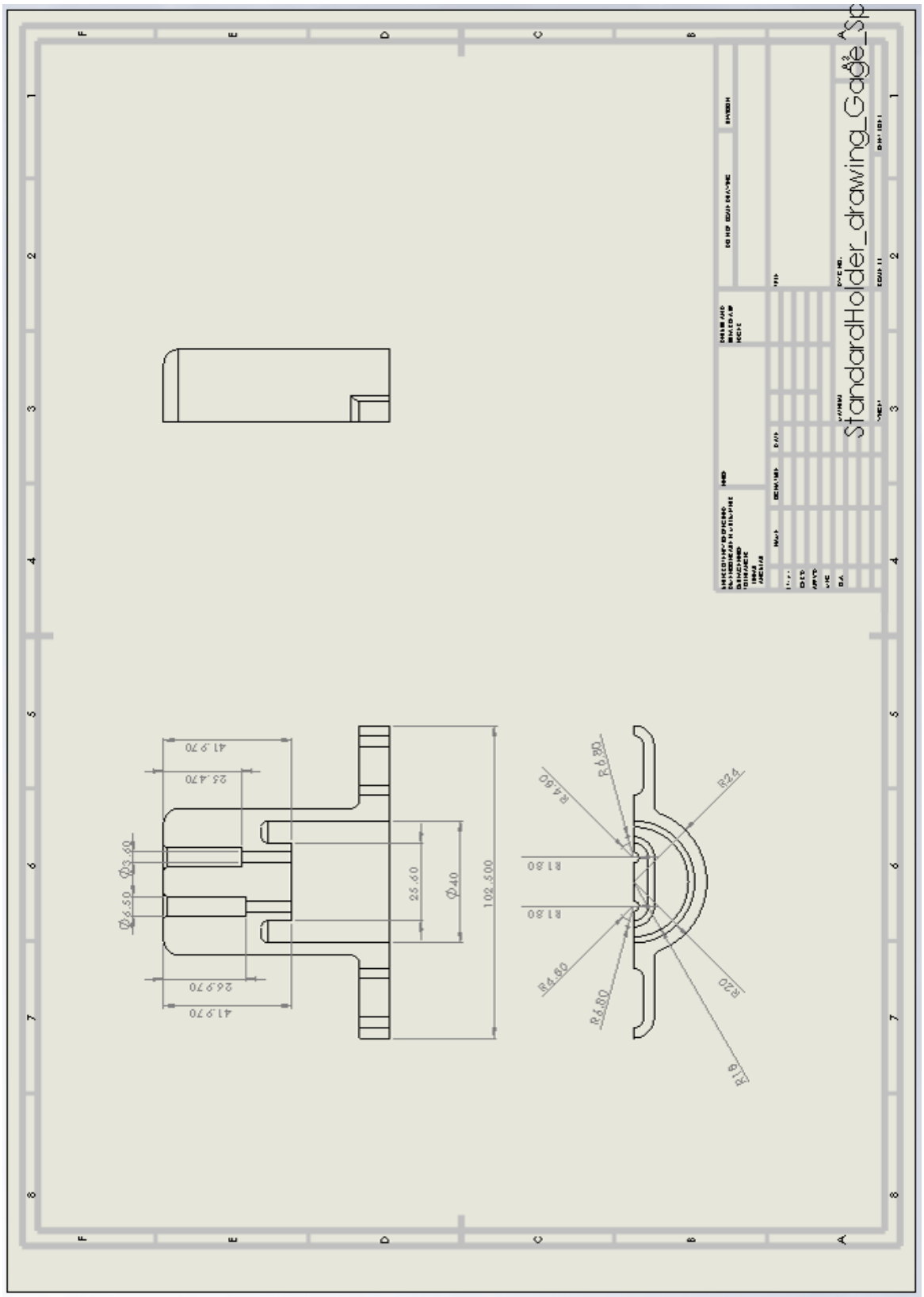
StandardHolder_drawing_Gage_Sp
41.970
25.470
Ø3.600
Ø6.500
26.970
41.970
25.600
Ø40
102.500
R6.80
R4.80
R1.80
R1.80
R4.80
R6.80
R24
R20
R19

Item	Quantity	Description	
1	1	**Multi-channel (1 x 5) UV-VIS linear array**	
	2		
		Hi OH fiber:	1 x SUV200/220PI silica/silica fiber Silica core: 200 um +/- 2% Silica clad: 220 um +/- 2% Polyimide jacket: 245 um +/- 5% NA: 0.22 +/- 0.02 High OH for wavelength range 190-1200 nm 4 x SUV400/440PI silica/silica fiber Silica core: 400 um +/- 2% Silica clad: 440 um +/- 2% Polyimide jacket: 470 um +/- 5% NA: 0.22 +/- 0.02 High OH for wavelength range 190-1200 nm
		Length:	
		Total:	1.00 +/- 0.10 m from tip to tip
		Common:	0.67 +/- 0.05 m from front of ferrule to back of breakout joint
		Legs:	0.33 +/- 0.05 m from back of breakout joint to front of SMA's
		Sheathing:	
		Common:	Black PVC coated monocoil 4.8 mm OD
		Legs:	Black PVC furcation tube 3.0 mm OD
		Terminations:	
		Common end:	Brass ferrule 6.35 OD x 50 mm long Fibers arranged in a slit line per customer sketch 1 x 400 um fiber in center of the ferrule 2 x 400 um fibers to the right of the center fiber With 1 mm and 2 mm center to center spacing 1 x 400 um fiber to the left of the center fiber With 2 mm center to center spacing 1 x 200 um fiber to the left of the center fiber With 1.25 mm center to center spacing ***Spacing tolerance between each fibers: +/- 0.01 mm***
		Legs:	Standard 905 SMA connectors with hex nuts, reinforced with strain relief
		Joint:	Brass

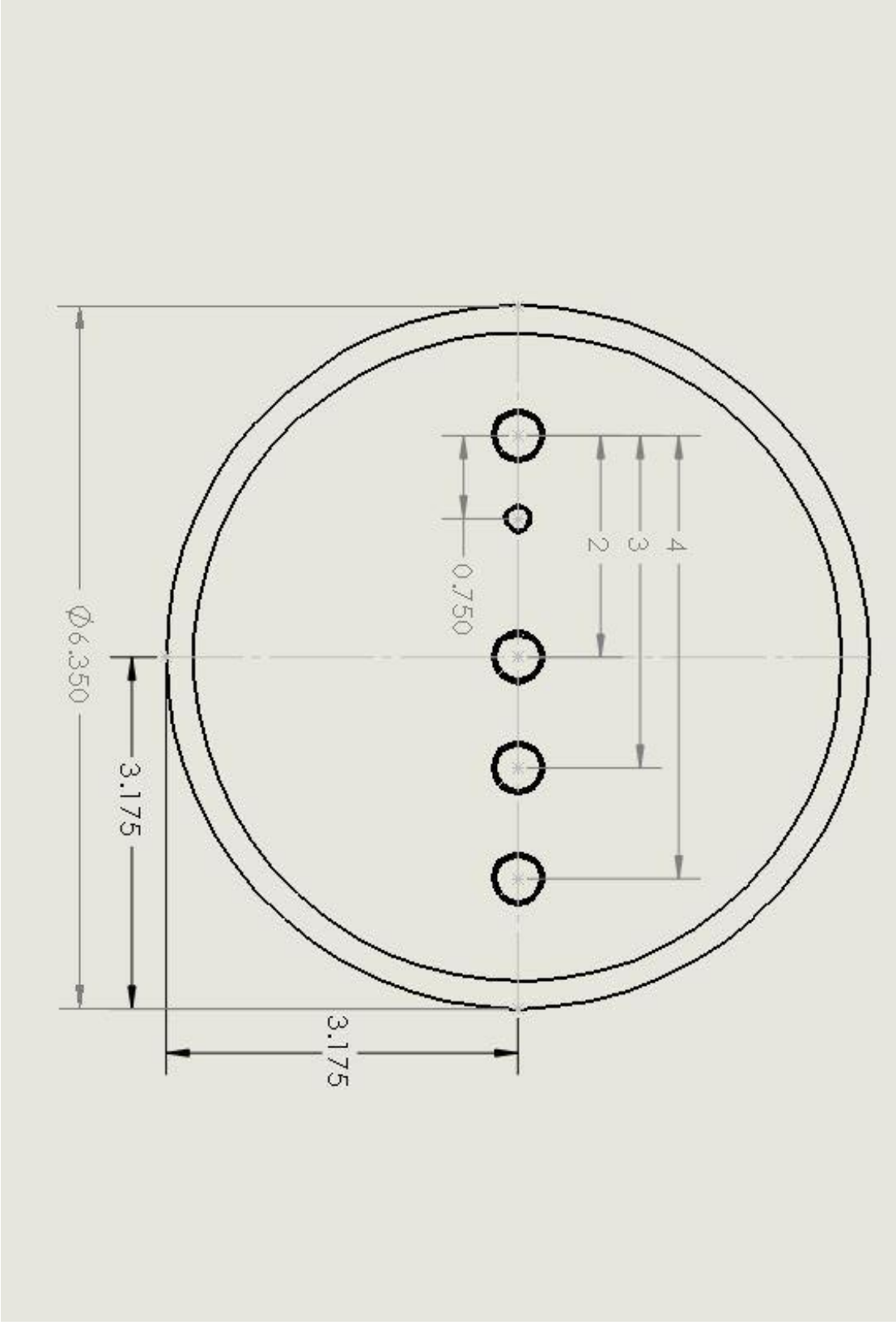
Ø6.350
3.175
3.175
0.750
2
3
4